XI International conference

Plasma Physics and Plasma Technology

Contributed papers

Minsk, Belarus
September 15 – 19, 2025

B.I. Stepanov Institute of Physics
National Academy of Sciences of Belarus

The National Academy of Sciences of Belarus
B.I. Stepanov Institute of Physics of the National Academy of Sciences of Belarus
Joint Institute for High Temperatures of the Russian Academy of Sciences

XI International Conference

PLASMA PHYSICS AND PLASMA TECHNOLOGY

(PPPT-11)

Minsk, Belarus
September 15 – 19, 2025

CONTRIBUTED PAPERS

Minsk
«Kovcheg»
2025

UDC 533.3(082)

CONFERENCE ORGANIZERS:
The National Academy of Sciences of Belarus
B.I. Stepanov Institute of Physics of the National Academy of Sciences of Belarus
Joint Institute for High Temperatures of the Russian Academy of Sciences

CO-ORGANIZERS:
A.V. Luikov Heat and Mass Transfer Institute of NAS of Belarus
Al-Farabi Kazakh National University
Scientific Council of the Russian Academy of Sciences on Low-Temperature Plasma Physics
Scientific-Technical Association «Optics and Lasers»
The Belarusian Physical Society

SPONSORED BY:
The National Academy of Sciences of Belarus
SOLAR LS
SOL instruments Ltd.
SLS Prime Technology

EDITORS:
N.V. Tarasenko, A.A. Nevar

COMPUTER PROCESSING:
M.S. Usachonak

The reports in these Contributed Papers are presented by the individual authors. The views expressed are their own and do not necessarily represent the views of the Publishers or Sponsors. Whilst every effort has been made to ensure the accuracy of the information contained in this book, the Publisher or Sponsors cannot be held liable for any errors or omissions however caused.

All rights reserved.
No part of this publication may be reproduced, stored in a retrieval system, in any form or by any means, electronic, mechanical, photocopying, recording, or otherwise, without the prior permission of the copying owner

ISBN 978-985-884-542-1

© B.I. Stepanov Institute of Physics of
National Academy of Sciences of Belarus, 2025
© Registration, “Kovcheg LTD”, 2025

Chairmen: N.V. Tarasenko (Belarus)
O.F. Petrov (Russia)

Vice-chairmen: A.N. Chumakov (Belarus)
L.V. Simonchik (Belarus)

Scientific secretary: A.A. Nevar (Belarus)

Advisory Committee

A.G. Shumilin (Belarus), S.A. Tikhomirov (Belarus), M.V. Bogdanovich (Belarus), S.V. Gaponenko (Belarus)

International Program Committee

Yu.S. Akishev (Russia), V.I. Arkhipenko (Belarus), V.M. Astashynski (Belarus), M.V. Bel`kov (Belarus), G. Chen (China), I.I. Filatova (Belarus), W. Han (China), A.V. Kazak (Belarus), K.V. Kozadaev (Belarus), M. Kuraica (Serbia), M. Kuzmanovic (Serbia), Yu.A. Lebedev (Russia), Z.A. Mansurov (Kazakhstan), A.L. Mosse (Belarus), I.S. Nikonchuk (Belarus), B. Obradovic (Serbia), O.G. Penjazkov (Belarus), I.L. Pobol (Belarus), I. Rafatov (Türkiye), V. Rogalin (Russia), L. Shi (China), N. Skvortsova (Russia), A.S. Smetannikov (Belarus), I.P. Smyaglikov (Belarus), R. Soni (India), V.A. Titov (Russia), M. Trtica (Serbia), F. Trukhachev (Belarus), Ya.V. Vodopyanov (Russia), M.S. Usachonak (Belarus), V.V. Uglov (Belarus)

Local Organizing Committee

Chairman: M.I. Nedelko,
Secretary: P.A. Ivanova

V.E. Aniskevich, N.A. Bosak, O.M. Borzdova, E.A. Vabishchevich, N.V. Varapaj, S.V. Goncharik, A.A. Kirillov, V.V. Kouhar, V.A. Lyushkevich, S.I. Kolomytskii, V.G. Kornev, D.A. Korolko, V.V. Lychkovski, A.S. Pilipovich, A.O. Radomtsev, A.A. Tabolich, N.V. Tomkovich, D.V. Shabrov, A.R. Shumeijko

TOPICS

1. Modeling of plasma processes, plasma dynamics, optical and thermodynamic properties of plasmas

2. Electrical discharges and other plasma sources, novel plasma generation approaches

3. Atmospheric pressure plasmas, plasma in and in contact with liquid, plasma-liquid interactions

4. Non-ideal and dusty plasmas, extreme plasma regimes, fusion and astrophysical plasmas

5. Laser and plasma interactions with materials, laser ablation, modification of materials by plasma and laser treatment, sputtering and deposition

6. Plasma spectroscopy and other diagnostic methods, plasma chemistry

7. Plasma applications and advanced plasma technologies *(plasma for nanomaterials synthesis and processing, plasma in medicine and biology, plasma in agriculture, water treatment and decontamination, plasma in spectrochemical analysis, plasma in catalysis, plasma metallurgy, etc.)*

CONTENTS

1. Modeling of plasma processes, plasma dynamics, optical and thermodynamic properties of plasmas

NUMERICAL STUDY OF CHARACTERISTICS OF ATMOSPHERIC PRESSURE GLOW DISCHARGE IN HELIUM GAS
G. Islamov, E. Eylenceoglu, I. Rafatov 2

WAVE TRANSPORT OF MATTER BY WAVES IN MAGNETIZED AND DEMAGNETIZED PLASMA (A SHORT REVIEW)
F.M. Trukhachev, N.V. Gerasimenko, M.M. Vasiliev, O.F. Petrov 6

THE CALCULATIONS OF EQUATION OF STATE AND ELECTRONIC TRANSPORT COEFFICIENTS OF LOW-TEMPERATURE TIN PLASMA
E. M. Apfelbaum 10

EQUILIBRIUM COMPOSITION OF TRANSIENT GRAPHITE PLASMA
M. Ristić, M. Marković, A. Šajić, D. Ranković, M. Kuzmanović 14

TAKING INTO ACCOUNT THE VIBRATIONAL EXCITATION EFFECTS OF NITROGEN AND OXYGEN PARTICLES TO SIMULATE OZONE PRODUCTION IN DIELECTRIC BARRIER DISCHARGE PLASMA-CHEMICAL REACTOR
I.A. Ruchkin, M.E. Pinchuk, O.M. Stepanova 18

ION FLUX SPATIAL DISTRIBUTION IN AN END-HALL SOURCE
V. Shakialeuski, D. Kotov 22

4D VYSIKAYLO'S EQUATION FOR DESCRIBING THE TRANSPORT OF NON-UNIFORM PROFILES OF 26

AMBIPOLAR QUASI-NEUTRAL PLASMA WITH CURRENT
P.I. Vysikaylo

ON THE INFLUENCE OF CONTROL PARAMETERS IN PLASMA CHEMICAL ETCHING ON THE SPATIAL UNIFORMITY OF PLASMA IN A REACTOR
Y. Zakharov, A. Efremov 30

NUMERICAL MODELING OF STREAMER DISCHARGE USING ADAPTIVE MESH AND MASS CORRECTION
A.S. Kirillov, E.A. Shershunova, V.V. Voevodin, V.A. Yamshchikov, Ya.E. Zharkov 33

APPLICATION OF OPEN FOAM PACKAGE FOR MODELING HIGHFREQUENCY DISCHARGE WITH LIQUID JET ELECTRODES
F. Khairullin, Al. Gaisin, V. Zheltukhin 37

FISSILE PLASMA GAS DYNAMICS
S. Kunakov, A. Shapiyeva 41

2. Electrical discharges and other plasma sources, novel plasma generation approaches

COAXIAL BARRIER DISCHARGE IN ARGON FLOW: ROLE OF SURFACE IONIZATION WAVES IN THE PLASMA STRUCTURES FORMATION
Yu. Akishev, M. Medvedev, A. Petryakov 46

SURFACE STREAMER DEVELOPMENT IN BARRIER DISCHARGE IN TRANSVERSE MAGNETIC FIELD
Yu. Akishev, I. Kochetov, A. Petryakov 50

ATMOSPHERIC PRESSURE PLASMA JETS AS A TOOL FOR PLASMA MEDICINE
A.V. Kazak, L.V. Simonchik 54

COMPACT COLD ATMOSPHERIC PLASMA SOURCES BASED ON PIEZOELECTRIC TRANSFORMERS: DEVELOPMENT AND APPLICATIONS
N.N. Bogachev, E.M. Konchekov, L.V. Kolik, A.S. Bakshaev, D.V. Malakhov, V.P. Stepin, T.I. Pavlik, N.G. Gusein-zade, S.V. Gudkov 58

CHARACTERISTICS OF THE PULSED PLASMA ACCELERATOR DEPENDING ON ENERGY INPUT
A.A. Kozlov, V.E. Zavalova, Yu.V. Karpushin, V.P. Polishchuk, M.V. Protasov 62

A METHOD FOR DETERMINING THE EROSION OF A METAL CATHODE DURING THE COMBUSTION OF A HIGH-CURRENT VACUUM DISCHARGE BASED ON THE INTERACTION OF TWO CO-DIRECTIONAL PLASMA JETS
A. Kuzminykh, A. Rousskikh, A. Zhigalin, V.I. Oreshkin, V.A. Gasilov 66

EXTRACTED ION BEAM DRIFT ANALYSIS IN A BERNAS-TYPE SOURCE
N.V. Mamedov, A.A. Avdienko, A.A. Starostenko, A.V. Sorokin 70

MODULATION OF THE BEAM CURRENT IN AN ELECTRON SOURCE WITH A MULTI-ARC TWO-GRID PLASMA EMITTER
M.A. Mokeev, V.N. Devyatkov, D.A. Gorkovskaia, M.S. Vorobyov, N.N. Koval, V.V. Nedoshivin 74

TURBULENT DECAY OF THE THERMAL CAVERN OF THE HF CORONA DISCHARGE
I. Moralev, I. Selivonin 78

ON THE CHARGE EXTRACTED FROM A MICROHOLLOW CATHODE PLASMA REACTOR
K. Romanov, E. Shershunova, S. Nebogatkin 81

THEORETICAL AND EXPERIMENTAL STUDY OF NEUTRON SOURCES AND PLASMA GENERATORS
A.G. Polyanskiy, S.V. Ryzhkov 85

EXPERIMENTS ON THE IONIZATION WAVES INTERACTION IN LONG TUBES
V. Zaletov, A. Shishpanov 89

IONIZATION WAVES THAT FORMING CAPACITIVE DISCHARGE AT LOW AND MODERATE GAS PRESSURES
V. Zaletov, A. Shishpanov 92

PLASMA SOURCE OF UV RADIATION WITH EXCITATION BY COMBINED DISCHARGE
K. Znosko 96

CURRENT-VOLTAGE CHARACTERISTICS OF AN INCANDESCENT AND HOLLOW CATHODE ARC DISCHARGE
I.I. Azhazha, V.V. Shugurov, Yu.Kh. Akhmadeev 100

FARADAY PROBE SYSTEM FOR MEASURING THE DENSITY AND ENERGY SPECTRUM OF COMPENSATED ION AND ION-PLASMA BEAMS USED IN THIN-FILM DEPOSITION TECHNOLOGY
R. Dubin, D. Ksenzov, A. Yasunas 103

PATTERNS OF EMISSION PLASMA GENERATION PRODUCED BY NON-SELF-SUSTAINED GLOW DISCHARGE IN HOLLOW CATHODES OF DIFFERENT VOLUMES AT LOW PRESSURE
A. Egorov, V. Yakovlev, V. Denisov, S. Kovalsky, E. Ostroverchov 107

METHODS FOR INCREASING THE STABILITY OF ELECTRON BEAM GENERATION IN A PLASMA CATHODE SOURCE BASED ON A LOW-PRESSURE ARC
D.A. Gorkovskaia, M.A. Mokeev, M.S. Vorobyov, V.N. Devyatkov, N.N. Koval, A.A. Grishkov, S.Yu. Doroshkevich, M.G. Volis 111

IMPEDANCE MATCHING IN DUAL-FREQUENCY CAPACITIVE DISCHARGE SYSTEMS FOR MICROELECTRONICS EQUIPMENT
P. Gvozdov, A. Yasunas 115

COMPETING ELECTRON EMISSION MECHANISMS IN A LOW-PRESSURE ARC-BASED GRIDDED PLASMA EMITTER
R.A. Kartavtsov, M.S. Vorobyov, A.A. Grishkov, N.N. Koval, M.A. Mokeev, S.Y. Doroshkevich, P.V. Moskvin, D.A. Gorkovskaya 119

3. Atmospheric pressure plasmas, plasma in and in contact with liquid, plasma-liquid interactions

MICROWAVE DISCHARGE IN LIQUIDS: PHYSICS AND APPLICATION
T.S. Batukaev, I.V. Bilera, G.V. Krashevskaya, Yu.A. Lebedev 124

LONG-LIVED REACTIVE OXYGEN AND NITROGEN SPECIES IN LIQUIDS TREATED WITH CAPILLARY DISCHARGE
V. Gudkova, A. Davydov, M. Zimina, V. Borzosekov, I. Naumova, N. Gusein-zade, V. Titov 128

MODIFICATION OF THE SURFACE OF ELECTRODES IN A BARRIER DISCHARGE IN AIR
I. Selivonin, A. Lazukin, I. Moralev 132

PLASMA-LIQUID SYNTHESIS OF MXENES AND THEIR PHOTOCATALYTIC PROPERTIES
N. Sirotkin, A. Khlyustova 136

SIZE PROPERTIES OF NANOPARTICLES FORMED IN PLASMA OF ELECTRIC EXPLOSION IN DISTILLED WATER
A. Zelianko 140

EFFECT OF THE PLASMA-FORMING GAS ON THE GENERATION OF LONG-LIVED REACTIVE OXYGEN AND NITROGEN SPECIES IN LIQUID IN THE PRESENCE OF COPPER ELECTRODE EROSION
M. Zimina, V. Gudkova, I. Moryakov, V. Borzosekov 144

4. Non-ideal and dusty plasmas, extreme plasma regimes, fusion and astrophysical plasmas

ENERGETICS AND EVOLUTION OF ACTIVE BROWNIAN MOTORS IN COULOMB SYSTEMS IN PLASMA, VISCOUS LIQUID AND SUPERFLUID HELIUM 149
O. Petrov, M. Vasiliev

ELECTROMAGNETIC RADIATION IN PLASMAS: NON-PLANCKIAN THERMAL EMISSION AND ASYMPTOTIC TUNNELING 152
S.V. Gaponenko, D.V. Novitsky, L.V. Simonchik, M.S. Usachonak

AB INITIO PSEUDOPOTENTIALS AND YUKAWA LIKE SCRENING IN MODERATE DENITIES PLASMA, INITIAL RESULTS 156
N. M. Sakan, Z. Simić, V. A. Srećković, M. Dechev, B. Stankov

SAGDEEV'S ION-ACOUSTIC SOLITON WITH TRAPPED ELECTRONS 160
S. Kuznetsov

FEATURES OF ROTATION OF PLASMA-DUST STRUCTURES IN DIFFERENT PHASES OF A STRIATION IN A UNIFORM AND NON-UNIFORM MAGNETIC FIELD 164
S. Pavlov, E. Dzlieva, M. Morozova, L. Novikov, S. Tarasov, V. Karasev

DYNAMICS OF AN ACTIVE BROWNIAN PARTICLE WITH A CENTRE-OF-MASS SHIFT IN A HARMONIC TRAP 168
E.A. Sametov, E.A. Lisin

ELECTRIC CURRENTS IN VYSIKAYLO'S CUMULATIVE-DISSIPATIVE STRUCTURES OF THE UNIVERSE 172
P.I.Vysikaylo

FEATURES OF PLASMA FORMATION DURING THE EXPLOSION OF FLAT CONDUCTORS IN MEGAGAUSS MAGNETIC FIELDS 176
I. Datsko, S. Chaikovsky, V. Van'kevich, N. Labetskaya, V. Oreshkin, N. Ratakhin

DUSTY PLASMA IN A GLOW DISCHARGE IN HELIUM IN A STRONG MAGNETIC FIELD
L. Dyachkov, E. Dzlieva, L. Novikov, S. Pavlov, V. Karasev 180

ON THE DYNAMICS AND CHARGE OF A DUST PARTICLE IN A STRONG MAGNETIC FIELD
V. Karasev, E. Dzlieva, L. Novikov, M. Gasilov, D. Janitsin, M. Golubev, S. Pavlov 184

5. Laser and plasma interactions with materials, laser ablation, modification of materials by plasma and laser treatment, sputtering and deposition

OPTOPLASTIC EFFECT OBSERVED IN METALS EXPOSED TO NANOSECOND ULTRAVIOLET LASER PULSES V.E. Rogalin, T.V. Malinskiy, S.I. Mikolutskiy, Yu.V. Khomich, V.A. Yamshchikov 189

XPS STUDY OF PLASMA-MODIFIED POLYMER SURFACES: FUNCTIONALIZATION AND DEPOSITION USING GLOW DISCHARGE IN A GAS FLOW
D. Zuza, V. Nekhoroshev, A. Korzhova, A. Bryuzgina 192

PREPARATION AND CHARACTERIZATION OF LASER NANO-HYDROXYAPATITE CLADDED ON TI6AL4V SUBSTRATES FOR BIOMEDICAL APPLICATIONS
Man. Ganjali, Mo. Ganjali, A. Rasouli Azad 196

ENHANCEMENT OF TI-6AL-4V SURFACE PROPERTIES THROUGH GRAPHENE-REINFORCED HYDROXYAPATITE COATINGS: HARDNESS AND WEAR RESISTANCE EVALUATION
A. Sohrabi, Mo. Ganjali, F. Torknik, Ma. Ganjali 200

PLASMA LINEAR MULTICUSP MAGNETIC TRAP FOR MATERIAL TESTING AND PLASMA PHYSICS APPLICATIONS
D.I. Kavyrshin, S.D. Fedorovich, V.P. Budaev, Quang Vinh Tran, M.V. Lukashevsky, A.V. Karpov 204

SYNTHESIS OF SILICON-TIN ALLOYED NANOPARTICLES BY LASER ABLATION OF SILICON COVERED BY TIN FILM IN LIQUID
V. Kornev, N. Tarasenka, M. Nedelko, A. Manshina, A. Kuchmizhak, N. Tarasenko 208

EFFECT OF PLASMA AND ION-BEAM TREATMENT ON GLASS SURFACE MORPHOLOGY
K.T. Logunov, D.A. Kotov, A.V. Aksiuchyts 212

MODIFICATION OF CR-VN COATINGS ON SILICON BY LOW INTENCITY NANOSECOND BICHROMATIC IRRADIATION
V. Lychkouski, A. Chumakov, I. Nikonchuk, V. Aniskevich 216

MORPHOLOGY CHANGE OF CR-VN COATINGS ON SILICON USING LOW INTENCITY NANOSECOND LASER IRRADIATION
V. Lychkouski, A. Chumakov, I. Nikonchuk, V. Aniskevich 220

LASER MODIFICATION OF CR-VN COATING ON STEEL IN LIQUID
V. Lychkouski, A. Chumakov, I. Nikonchuk, V. Aniskevich 224

COMPOSITE MATERIAL BASED ON NATURAL HIGH MOLECULAR WEIGHT COMPOUND FILLED WITH ACRYLIC EMULSIONS MODIFIED BY LOW ENERGY ION FLOW
K.I. Maksimova, I.I. Latfullin, G.R. Rakhmatullina, R.R. Kayumov 228

THE EFFECT OF THE LOW-ENERGY ION FLUX OF A LOW-PRESSURE HF PLASMA OF ARGON WITH AN ADMIXTURE OF NITROGEN AND OXYGEN ON THE MECHANICAL CHARACTERISTICS OF METALS AND ALLOYS
I.S. Abdullin, K.S. Mastyukov, S.V. Mironov, A.V. Shestov 232

EFFECT OF PULSE BICHROMATIC IRRADIATION OF OXYGEN-FREE COPPER SURFACE
S.I. Mikolutskiy, A.N. Chumakov, V.V. Lychkovsky, Yu.V. Khomich, V.E. Rogalin, V.Yu. Zheleznov 236

MEASUREMENT OF OPTICAL NONLINEARITY COEFFICIENTS OF INTEGRATED MICRORESONATORS
D. Morozov, A. Vorobyev, V. Pavlov, I. Stepanov, N. Dmitriev, D. Chermoshentsev, I. Bilenko 240

IMPACT OF LASER IRRADIATION AND TRANSITION METALS DOPING ON THE PHOTO-ACTIVATED CONDUCTIVITY OF COPPER OXIDE-BASED NANOSTRUCTURES
S. T. Pashayan, V.G. Kornev, N. V. Tarasenko, S. V. Zlotski, S.V. Husakova, V.M. Anishchik 242

THE INFLUENCE OF PLASMA ASSISTANCE IN THE APPLICATION OF TITANIUM DIOXIDE BY THE VACUUM ARC METHOD
N.A. Prokopenko, Yu.F. Ivanov, E.A. Petrikova, N.N. Koval, M.S. Vorobyov, M.A. Mokeev, I.I. Azhazha 246

FINISH CLEANING OF THE SUBSTRATE SURFACE DUE TO SECONDARY EMISSION IN A LASER EROSION PLASMA ION SOURCE FOR THE FORMATION OF NANOSTRUCTURES.
V.K. Goncharov, M.V. Puzyrev 250

FABRICATION OF LEAD ZIRCONATE TITANATE FILMS BY COMBINED LASER ABLATION/LASER MODIFICATION TECHNIQUE
A.O. Radomtsev, A.A. Nevar, M.I. Nedelko, N.V. Tarasenko 254

DEPOSITION AND CHARACTERIZATION OF TITANIUM NITRIDE THIN FILMS AS COATINGS FOR PACEMAKER ELECTRODE PROTOTYPES
Yu. Rukina, O. Obrezkov, Yu. Martynenko, S. Shevchuk 258

SYNTHESIS OF NANOPARTICLES BY LASER ABLATION OF COPPER TARGET IN A SURFACTANT SOLUTION FOLLOWING PHOTOINDUCED COALESCENCE
N.A. Savastenko, N.V. Tarasenko, A.V. Butsen, A.A. Nevar, O.M. Tursunkulov 262

VORTEX MOTION IN A SYSTEM OF ACTIVE BROWNIAN PARTICLES UNDER LASER IRRADIATION
R.V. Senoshenko, E.A. Kononov, M.M. Vasiliev, O.F. Petrov 266

DEVELOPMENT OF VAPOR-PLASMA FORMATION UNDER LASER ACTION ON A SAMPLE LOCATED IN A LIQUID
S. Vasiliev, A. Sitkevich 268

ROLE OF CHARGES IN WETTABILITY OF PLASMA-TREATED POLYTETRAFLUOROETHYLENE
M.Yu., Yablokov, A.A. Kuznetsov 272

DIGITAL UPGRADE OF ANALOG OPTICAL DEVICES IN LASER SURFACE PROCESSING APPLICATIONS
V. Zheleznov 276

LASER POLISHING OF NATURAL LEATHER
A.G. Anisovich, M.I. Markevich, V.I. Zhuravleva, T.Zh. Kodirov, U.O. Khudanov 280

SURFACE MORPHOLOGY, OPTICAL AND ELECTROPHYSICAL PROPERTIES OF FILMS La0.82Sr0.18Co0.9Ni0.1O3-d
N.A. Bosak, M.V. Bushinsky, L.V. Baran, V.V. Malyutina-Bronskaya, O.S. Mantytskaya, A.S. Kuzmitskaya, N.V. Podvitsky 284

LASER ABLATION IN LIQUID FOR PREPARATION OF MULTIELEMENT NANOPARTICLES: STOICHIOMETRY PRESERVATION
N. Tarasenko, A. Butsen 288

NONLINEAR MULTIVARIATE CALIBRATION OF LOW-ALLOY STEEL COMPOSITION BY APPLYING SUPPORT VECTOR REGRESSION TO LOW-RESOLUTION SPECTRA OF COMPACT LIBS SETUP
M.V. Belkov, K.Yu. Catsalap, M.A. Khodasevich 292

STRUCTURE AND HIGH-TEMPERATURE OXIDATION RESISTANCE OF AUSTENITIC STAINLESS STEEL SURFACE LAYER ALLOYED BY COMPRESSION PLASMA FLOWS IMPACT
N.N. Cherenda, D.A. Bronov, V.M. Astashynski, A.M. Kuzmitski 296

6. Plasma spectroscopy and other diagnostic methods, plasma chemistry

DIAGNOSTICS OF ATMOSPHERIC PRESSURE DISCHARGES VIA SPECTRAL LINE SHAPE ANALYSIS
B. Obradović, G. Sretenović, N. Cvetanović, S. Ivković, V. Kovačević, I. Krstić, M. Kuraica 301

APPLICATION OF SPECTRAL PYROMETRY TO DETERMINE DISCHARGE TEMPERATURE IN THE LIQUID ANODE METHOD
Yu.S. Baryshnikov, R.O. Kurakin, F.A. Orlov, S.A. Ponyaev 303

MODELING OF THE FORMATION OF BACTERICIDAL COMPONENTS OF AIR GLOW DISCHARGE PLASMA JETS
A.V. Kazak, A.A. Kirillov, L.V. Simonchik, V.M. Chukhalionak 307

SPATIAL DISTRIBUTION OF ELECTRIC FIELD STRENGTH IN A GLOW DISCHARGE AT ATMOSPHERIC PRESSURE IN HELIUM WITH NON-PLANAR ELECTRODES
P.A. Ivanova, A.V. Kazak, L.V. Simonchik, I. Rafatov, V.V. Shkurko 311

PLASMA VELOCITY IN MPK-A40 FOR DIFFERENT ENERGIES
I.B. Krstić, N.T. Boca, G.B. Sretenović, V.V. Kovačević, B.B. Obradović, M.M. Kuraica 315

USING THE TM110 MODE OF A CYLINDRICAL CAVITY TO DIAGNOSTIC THE PLASMA DENSITY IN A GAS DISCHARGE TUBE
N.N. Bogachev, V.P. Stepin, V.I. Zhukov, S.E. Andreev, D.M. Karfidov, M.S. Usachonak 319

INFLUENCE OF INITIAL COMPOSITION OF THE Cl2/HBr/Ar MIXTURE ON PLASMA CHARACTERISTICS AND ETCHING PROFILE EVOLUTION
F. Oksanichenko, A. Efremov 323

A COMPARISON OF PARAMETERS OF STARK BROADENING OBTAINED UNDER DIFFERENT PRESSURES IN LASER PLASMA
A.M. Popov, S.M. Zaytsev, B.S. Chilikin 327

VACUUM DISCHARGE WITH STRIP LINE CURRENT DRIVER AS EUV RADIATION SOURCE
L. Stepanov, N. Matyukhin, P. Antsiferov 329

STUDIES OF ERROR BUDGET IN CF-LIBS IN CONNECTION WITH TEMPERATURE BEHAVIOUR OF PARTITION FUNCTION
N. Sushkov, A. Popov 331

PLASMA DIAGNOSTICS DURING A SKIN EXPLOSION OF CONDUCTORS IN MEGAGAUSS MAGNETIC FIELDS
V. Van'kevich, I. Datsko, N. Labetskaya, A. Rousskikh, A. Zhigalin, A. Kuzminykh, V. Oreshkin 335

EXPERIMENTAL DETERMINATION OF THE STARK BROADENING PARAMETERS OF THE NA I AND K I LINES IN LASER PLASMA
B. Chilikin, S. Zaytsev, A. Popov 339

MODEL-BASED APPROACH TO CHARACTERIZE PLASMA COMPOSITION AND ETCHING/POLYMERIZATION KINETICS IN VARIOUS FLUOROCARBON GASES MIXED WITH ARGON AND/OR OXYGEN
A. Efremov, K.-H. Kwon 341

FEATURES OF THE FORMATION OF EROSIVE PLASMA IN THE TWO-PULSE CLAY ABLATION MODE
N. Kurian, S. Anufrik 345

DYNAMICS OF SPECTRAL LINE INTENSITY ALONG THE AXIS OF THE EROSION PLASMA TORCH ON AN ALUMINUM TARGET
A. Liskovich 349

OPTICAL EMISSION SPECTROSCOPY OF COAXIAL DBD PLASMA AT ATMOSPHERIC PRESSURE
K.T. Logunov, D.A. Kotov, A.V. Aksiuchyts 354

RECOMBINATION RADIATION REGIME OF LASER PRODUCED LITHIUM PLASMA (Li)
N. Matiukhin, M. Krivokorytov, V. Gubarev, L. Stepanov 358

7. Plasma applications and advanced plasma technologies

THE ALOE – DEVICE FOR PLASMA MEDICINE
A.V. Kazak, L.V. Simonchik 363

ANTIMICROBIAL ACTIVITY OF AN ATMOSPHERIC PRESSURE GLOW DISCHARGE JET
V.M. Pashkova, N.V. Dudchik, O.A. Emelyanova, L.V. Simonchik, A.V. Kazak 367

PLASMACHEMICAL SYNTHESIS OF MICRO- AND NANO-SIZED MATERIALS IN CHAIN REACTIONS INITIATED BY MICROWAVE PULSES OF THE POWERFUL GYROTRON IN POWDERS
N.N. Skvortsova, N.S. Akhmadullina, V.D. Borzosekov, N.G. Gusein-zade, E.M. Konchekov, D.V. Malakhov, E.A. Obraztsova, V.D. Stepakhin, N.K. Kharchev, O.N. Shishilov 371

SUPPORT OF THE EXPERIMENT IN THE LABORATORY OF PLASMA AERODYNAMICS USING NUMERICAL MODELING: GAS DYNAMICS, COMBUSTION, ELECTRICAL DISCHARGES
A. Firsov 375

AMMONIA CONVERSION IN THE PLASMACHEMICAL REACTOR WITH A NON-SELF-SUSTAINED DC GLOW DISCHARGE AT ATMOSPHERIC PRESSURE
A.V. Kazak, A.A. Kirillov, L.V. Simonchik, M.U. Tomkavich 379

COPPER–IRON ALLOY CONTACTS IN HIGH CURRENT PROTECTION DEVICES
M.E. Pinchuk, A.A. Bogomaz, V.A. Kolikov, I.V. Bagriy, I.Yu. Pervashov, A.V. Budin 383

TOWARDS IMPLEMENTING ATMOSPHERIC PRESSURE PLASMA JET FOR PAPER DOCUMENT RESTORATION
M.E. Pinchuk, E.A. Tileva, O.M. Stepanova, I.V. Tseveleva, D.G. Grudkin, V.N. Snetov 385

STRUCTURE OF TNTZ TITANIUM ALLOY WITH ZN NANOPARTICLES TREATED WITH COMPRESSIVE PLASMA FLOWS
V.V. Uglov, S.V. Zlotski 388

TANTALUM DIBORIDE SURFACE AFTER TREATMENT WITH COMPRESSION PLASMA FLOWS
V.V. Uglov, I.V. Kondrus, M.O. Kovalenko, A.Ya. Pak, A.A. Svinukhova 392

MULTIFUNCTIONAL SETUP FOR EXPERIMENTS ON ADVANCED APPLICATIONS OF ELECTRON-BEAM PLASMA
T. Vasilieva, A. Diaz Mesa, M. Vasiliev 396

METAL-PUFF Z-PINCH BASED ON FOIL EVAPORATION AND IONIZATION
A. Zhigalin, A. Rousskikh, V. Oreshkin, A. Shishlov, R. Cherdizov, V. Kokshenev, N. Kurmaev 400

EXPERIMENTAL STUDY OF COMBINED COOLING SYSTEM USING EHD STREAMS
A.S. Kirillov, V.Yu. Khomich, O.I. Korzhova, S.I. Moshkunov, V.V. Voevodin, Ya.E. Zharkov 404

CAPABILITIES OF LIQUID-ASSISTED LASER AND PLASMA METHODS FOR SYNTHESIS OF COMPOSITE NANOSTRUCTURES
N. Tarasenko, V. Kornev, N. Tarasenka, A.Nevar, M. Nedelko 408

OPTICALLY PUMPED RARE GAS LASER
Yu.A. Adamenkov, M.A. Gorbunov, A.A. Kalacheva, V.A. Shaidulina, A.V. Yuriev 412

ON THE INFLUENCE OF ELECTRON VELOCITY SPREAD ON THE OPERATION OF COMPTON FELS DRIVEN BY LASER PLASMA ACCELERATORS
S. Anishchenko 416

X-RAY RADIOGRAPHY OF SUBSTANCE STRUCTURE OF ALUMINUM TUBE DURING EXPLOSION ON THE GIT-12 FACILITY
A. Artyomov, A. Rousskikh, V. Oreshkin, A. Zhigalin 420

OPTIMIZATION OF THE ELECTROLYTIC PLASMA POLISHING PROCESS OF TC4 ALLOY USING TAGUCHI METHOD
S.I. Bahayeu, I.P. Smyaglikov, A.A. Parshuto, E.A. Klimova 424

DIFFUSION FLUX ENHANCEMENT IN DEPOSITION PROCESS
D.A. Butniakov, I.A. Sorokin, D.V. Kolodko 428

ACCOUNTING FOR THE MARANGONI EFFECT DURING ELECTROMAGNETIC MIXING IN AN ELECTRIC ARC LIQUID METAL MELT
M.Yu. Dokukin 432

PLASMA-CHEMICAL PROCESS OF RESTORING THE PROPERTIES OF METAL POWDERS AFTER THEIR USE IN ADDITIVE MANUFACTURING
A.A. Fadeev, A.V. Samokhin, N.V. Alekseev, M.A. Sinaisky, D.E. Kirpichev, A.A. Dorofeev, I.V. Kulbakin 436

SIMULTANEOUS GENERATION AT THREE WAVELENGTHS IN OPTICALLY PUMPED HE-AR-KR MEDIUM
A.A. Kalacheva, Yu.A. Adamenkov, M.A. Gorbunov, V.A. Shaydulina, A.V. Yuriev 440

PLASMA-CHEMICAL MICROWAVE METHOD FOR ONE-STAGE SYNTHESIS OF HETEROGENEOUS CATALYSTS
N.K. Kharchev, N.N. Skvortsova, N.S. Akhmadullina, V.D. Borzosekov, N.G. Gusein-zade, E.M. Konchekov, D.V. Malakhov, E.A. Obraztsova, V.D. Stepakhin, O.N. Shishilov 444

COMPARISON OF PARTIAL LEAST SQUARES (PLS) AND THE ORIGINAL MULTIPARAMETRIC CALIBRATION FOR THE ANALYSIS OF STEELS WITH HIGH COMPOSITIONAL VARIABILITY USING LASER-INDUCED BREAKDOWN SPECTROSCOPY (LIBS) 448
V. Kiris, M. Belkov

SYNTHESIS OF COMPLEX OXIDES UNDER THE INFLUENCE OF AIR PLASMA OF PULSED HIGH-VOLTAGE DISCHARGE ON A MECHANICAL MIXTURE OF SIMPLE OXIDES AND ON METAL ELECTRODES AND THEIR MAGNETIC PROPERTIES 452
V.G. Kuryavyi, I.A. Tkachenko, A.V. Gerasimenko

APPLICATION OF PLASMA AND MICROWAVE TECHNIQUES FOR FABRICATION OF ADVANCED LUMINESCENT CARBON NANODOTS 456
V.A. Lapina, A.A. Nevar, T.A. Pavich, A.R. Shumejko, N.V. Tarasenko

EFFECTS OF PLASMA TREATMENT ON THE SOME PHYSICOCHEMICAL PROPERTIES OF TECHNOGENIC SALINE SOIL 460
V.A. Lyushkevich, I.I. Filatova, S.V. Goncharik, J.N. Kalatskaja, I.A. Ovchinnikov, D.A. Kotov, A.V. Aksiuchyts

THE STUDY OF THE OSCILLATIONS AND STRUCTURE OF A FLOW INTERACTING WITH A SECONDARY GAS TRANSVERSE JET IN THE PRESENCE OF SPARK DISCHARGES 464
Y. Miroshnikov, L. Volkov, A. Firsov, I. Moralev

CONTROL OF THE INSTABILITIES IN SHEAR FLOWS USING PLASMA ACTUATORS 467
I. Moralev

LIBS ANALYSIS OF CARBON-CONTAINING SAMPLES BASED ON MOLECULAR SPECTRA REGISTRATION 471
M.I. Nedelko, A.A. Nevar, A.O. Radomtsev, N.V. Tarasenko

FORMATION OF SUBMICRON TITANIUM CARBIDE PARTICLES BY ELECTRICAL DISCHARGE TREATMENT OF TITANIUM TC4 MICROPOWDERS
A. Shumeijko, A. Nevar, V. Aniskevich, M. Nedelko, N. Tarasenko, Y. Song 475

USING OF THE PLASMA ARC EJECTOR FOR WASTE TREATMENT
P. Petrenko, A. Pereslavtsev, A. Artemov, S. Voschinin, N. Chemodanov 479

OZONE-HYDROXYL MIXTURE FOR WATER PURIFICATION AND DISINFECTION
I.M. Piskarev, N.A. Aristova, I.P. Ivanova, I.I. Vasina 483

SYNCHRONOUS PURIFICATION OF DIESEL ENGINE EXHAUST GASES FROM NITROGEN OXIDES AND SOOT USING NANOSECOND CORONA DISCHARGE PLASMA SYSTEMS
A.Z. Ponizovsky, S.G. Gosteev, O.S. Kuzhel, S.P. Kryuchkov, V.A. Maevsky, A.S. Smirnov, I.G. Agrelov, S.N. Filippov 487

OPTIMIZATION OF PLASMA FURNACE DESIGN FOR LOW RADIOACTIVE WASTE PROCESSING
V. Sauchyn, A. Liavonchyk, I. Khvedchyn, U. Skavysh, Hr. Dalholenka, M. Polkanov, I. Kadyrov 491

PLASMA TECHNOLOGY FOR SEWAGE SLUDGE PROCESSING
V. Sauchyn, U. Skavysh, A. Liavonchyk, I. Khvedchyn, Hr. Dalholenka, N. Kurbanov 495

SIMULATION THE GAS DYNAMICS IN THE FLAT REACTOR WITH RECTANGULAR CROSS-SECTION FOR THIN FILM DEPOSITION BY CVD
V. Shakialeuski, N. Leonovich, D. Kotov 499

ESTIMATION OF A PLASMA DENSITY AND ELECTRON ENERGY AT ANOMALOUS ABSORPTION OF ORDINARY MICROWAVE IN PLASMA FILAMENT
M.S. Usachonak, L.V. Simonchik, E.Z. Gusakov, A.Yu. Popov 503

1. MODELING OF PLASMA PROCESSES, PLASMA DYNAMICS, OPTICAL AND THERMODYNAMIC PROPERTIES OF PLASMAS

NUMERICAL STUDY OF CHARACTERISTICS OF ATMOSPHERIC PRESSURE GLOW DISCHARGE IN HELIUM GAS

G. Islamov, Eylenceoglu E., I. Rafatov

Department of Physics, Middle East Technical University, Ankara 06800, Türkiye
rafatov@metu.edu.tr

Glow discharges are a classic subject of low-temperature plasma physics [1, 2]. Currently, atmospheric pressure glow discharges (APGDs) are of interest due to their simple design and practical applications (see, e.g. [3]). Here, we report results of one- and two-dimensional numerical studies of APGD in helium gas. The numerical model is based on the drift and diffusion theory of gas discharges and includes a detailed description of plasma-chemical kinetics [4].

Table 1: Species that are considered in the numerical model.

No	Term	Energy (eV)	Designation
0	He	0	1^1S_0
1	He^* (1)	19.82	2^3S_1
2	He^* (2)	20.62	2^1S_0
3	He^* (3)	20.96	$2^3P_0{}^0$, $2^3P_0{}^1$, $2^3P_2{}^0$
4	He^* (4)	21.22	$2^1P_0{}^1$
5	He^* (5)	23.02	3^3S_0, 3^1S_1, $3^3P_0{}^2$, $3^3P_0{}^1$, $3^3P_0{}^0$, 3^3D_3, 3^3D_2, 3^3D_1, 3^1D_2
6	He^+	24.59	He^+
7	He_2^*	17.97	He_2 ($^3\sum_u{}^+$)
8	He_2^{**}	18.36	He_2 ($^1\sum_g{}^+$)
9	He_2^+	22.24	$He_2{}^+$
10	He_3^+	22.12	$He_3{}^+$

To verify the performance of the model, the current-voltage characteristic (CVC) and current density-voltage characteristic (CDVC) curves have been obtained and analyzed. The effects of the following factors were investigated: the temperature regime (cooled vs uncooled) on the cathode, the value of the secondary electron emission (SEE) coefficient, and the thermal diffusion. The effect of the thermal diffusion manifests itself from very low values of the discharge current; it leads to an upward shift of the CVC curves by a few tens of volts (see Fig. 1). The effect of cathode heating on the CVC begins to show up at sufficiently high discharge currents, of the order of one tenth of an ampere. It leads to a significant distortion (up to several tens of volts) of the part of the CVC corresponding to a normal discharge, which in the case of a cold cathode has a flat profile usual for the normal discharge mode.

In the case of microdischarge at atmospheric pressure, due to intense heating of the plasma at sufficiently high currents, it becomes necessary to identify the

discharge mode. The question is whether it is positioned to the left of the minimum of the Paschen curve and, therefore, whether it is in obstructed mode.

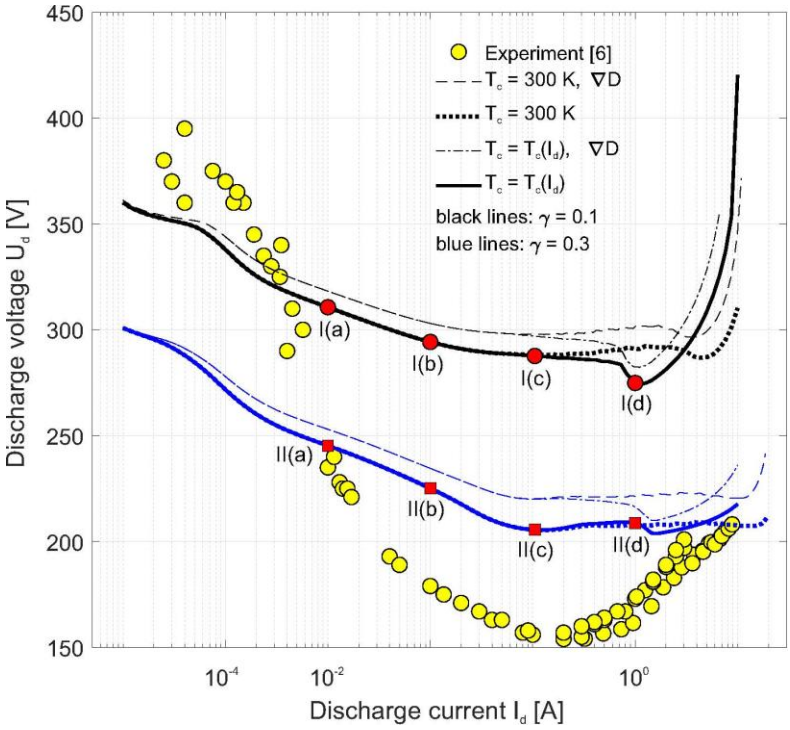

Figure 1: CVCs obtained from 2D simulations in helium APGD. Calculations were performed for $\gamma = 0.1$ and 0.3, and imposing constant (300 K) and varying (linearly with the discharge current) temperature T_c on the cathode. The inclusion of thermal diffusion in the model is indicated by '∇D' term in the legend. The experimental data is taken from [6].

With this in mind, the patterns of transition of helium APGD to the obstructed regime with increasing current were investigated. The results revealed that this transition differs from that observed in APGD in argon [5]. In particular, for a microdischarge in argon, on the right branch of the CVC, the current density, the total ionization rate, and the maximal electron density saturate or even decrease with an increase in the discharge voltage, accompanied by an increase in the gas temperature. On the contrary, in a microdischarge in helium, the current density, as well as the total ionization rate, increase monotonically with increasing discharge voltage. The analysis showed that for gas gaps of $d = 0.5$ mm and 1 mm, the helium APGD is not obstructed. With a gas gap of $d = 0.1$ mm, the discharge state is very close to obstructed regime, and with $d = 0.05$ mm it is obstructed.

Calculations have shown that the numerical model is capable of reproducing the formation of a normal glow discharge in atmospheric pressure helium in the correct parameter regime (see Fig. 2). An analysis revealed good agreement between the calculated values of the current density and electric field on the cathode surface and the experimental data. However, formation of a classical normal glow discharge, with current density on the cathode surface nearly constant with increasing discharge current, is observed in the case of a cooled cathode. In the case of an uncooled cathode, at sufficiently high discharge currents, the current density on the cathode surface no longer remains approximately equal to the normal current density, known from the literature [1],

but drops drastically.

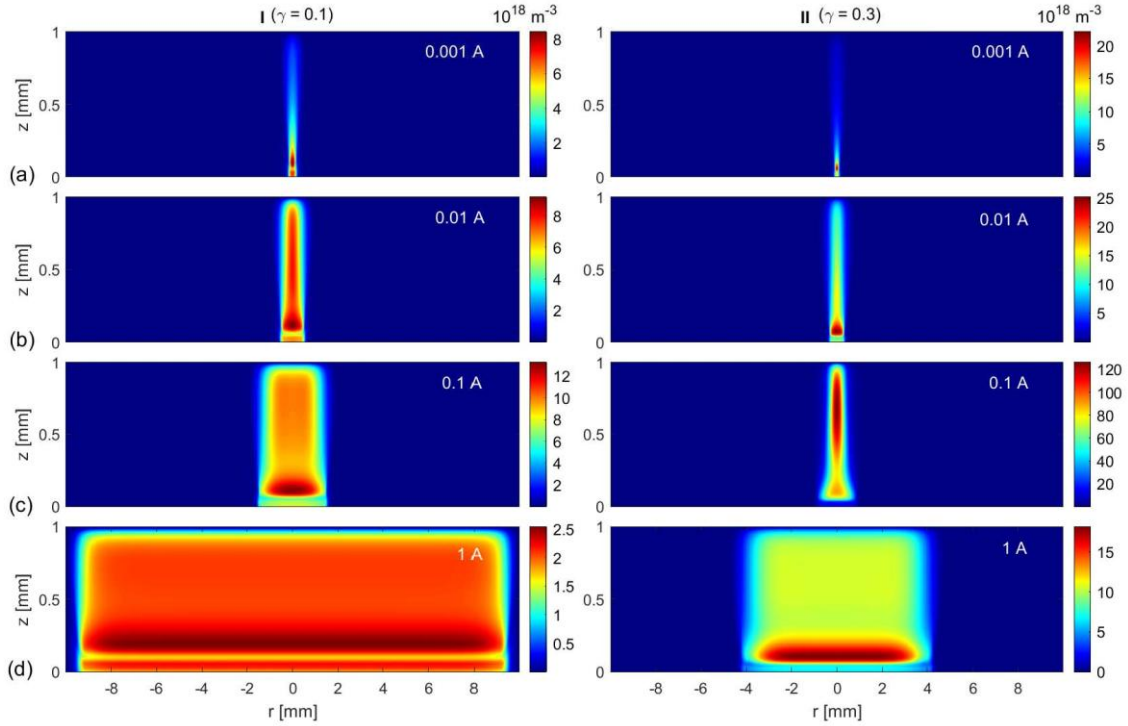

Figure 2: Profiles of the total ion density n_i in helium APGD. The left column "I" corresponds to $\gamma = 0.1$ and the right column "II" corresponds to $\gamma = 0.3$. The values of discharge current are $I_\mathrm{d} = 0.001$ A, 0.01 A, 0.1A and 1 A, from (a) to (d), in each column. The discharge states correspond to those designated from I(a) and II(a) to I(d) and II(d) on CVC curve in Fig. 1. The gas gap is $d = 1$ mm, the radius of the discharge tube is $l = 10$ mm.

As usual in fluid models of glow discharges, the effective value of the SEE coefficient from the cathode, without having a noticeable qualitative effect on the helium APGD parameter profiles, exhibits a significant quantitative effect on them (see Fig. 2). Recall that the SEE is generally considered as one the main sources of uncertainty in fluid models of glow discharges.

The above analysis concerned regular discharges formed along the axis of the system. The spontaneous emergence of cathode spots was also observed. In particular, multiplication of the cathode spots with increasing current was identified (see Fig. 3). In this case, for each individual spot, the average current density on the cathode surface remained approximately equal to the normal current density for helium APGD. Calculations have shown that due to the intense heating of plasma at relatively high discharge currents (of the order of tens of mA or more), cathode spots do not form dynamically stable patterns at these discharge currents [4]. We have observed that an increase in the discharge current can lead to an increase in the number of cathode spots by either of two ways. The first one is the pattern 'self-completion' process. It is accompanied by the growth of perturbation in the region surrounding the primary spots, followed by the

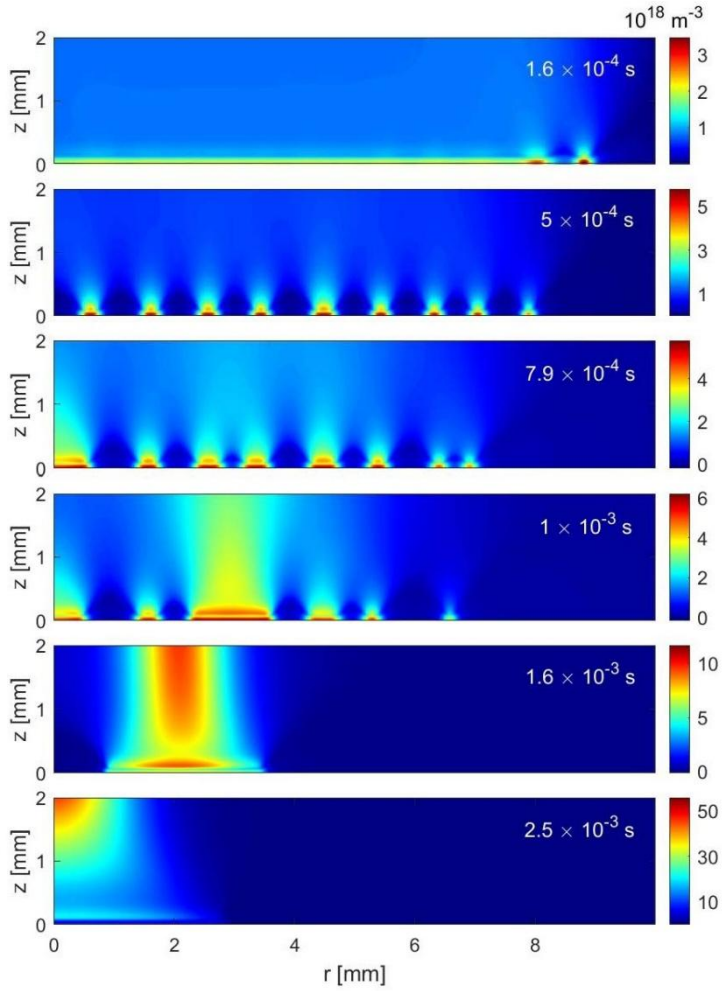

emergence of new spots in the vicinity of old ones. Another scenario that was observed at sufficiently high discharge currents is that the number of spots increases via the division of existing spots.

Figure 3: Temporal evolution of the ion density n_i on the cathode surface in helium APGD with gas heating taken into account. The discharge state depicted in the bottom panel is in a steady state. The discharge current is $I_d = 0.5$ A, the gas gap $d = 5$ mm, the radius of the discharge tube $l = 10$ mm, and $\gamma = 0.1$. The cathode temperature is set to $T_c = 300$ K. A part of the gas gap along the cathode surface, limited by a distance of 2 mm from its surface, is shown.

Acknowledgements. This work was supported by the Grant 221N363 from the Scientific and Technological Research Council of Türkiye (TUBITAK).

References

1. **Raizer Y.P.** Gas Discharge Physics. Springer (2011).
2. **Lieberman M. and Lichtenberg A.** Principles of Plasma Discharges and Materials Processing. Wiley (2005).
3. **Fridman G., Friedman G., Gutsol A., Shekhter A.B., Vasilets V.N. and Fridman A.** Plasma Process. Polym., 5 (2008) 503-33.
4. **Islamov G., Eylenceoglu E. and Rafatov I.** Plasma Sources Sci. Technol., 34 (2025) 025016.
5. **Bogdanov E., Kudryavtsev A. and Chirtsov A.** Tech. Phys., 56 (2011) 55-60.
6. **Arkhipenko V., Kirillov A., Safronau Y.A. and Simonchik L**. Eur. Phys. J. D, 60 (2010) 455-63.

WAVE TRANSPORT OF MATTER BY WAVES IN MAGNETIZED AND DEMAGNETIZED PLASMA (A SHORT REVIEW)

F.M. Trukhachev [1,2], N.V. Gerasimenko[2], M.M. Vasiliev[1], O.F. Petrov[1]

[1]Joint Institute for High Temperatures, Russian Academy of Sciences, Izhorskaya str.13/2, Moscow, 125412, Russia
[2] Belarusian-Russian University, Mira Ave, 43, 212000, Mogilev, Belarus.

A brief review of the processes of wave transport of matter is made. From the results of the review it follows that the transport of matter by real waves is a very common phenomenon. Classical definitions of a wave are strictly valid only for the linear case and systems with fixed boundaries (strings, membranes).

According to traditional definitions, waves are usually called some disturbances of the medium that propagate in space. It is also believed that material waves do not transfer the substance of the propagation medium, but only energy and momentum [1],[2]. In modern physics textbooks, the ban on wave transfer of matter is presented as one of the fundamental properties of nature. However, this is not so. The wave community knows that the traditional definition of a wave is valid for systems with fixed boundaries or for the linear case in a system with free boundaries. Real waves have a non-zero amplitude, sometimes quite large. Such waves (with a finite amplitude) begin to demonstrate non-linear effects. One of these effects is the non-zero drift of the substance in which the waves propagate. These phenomena can be classified as follows:

1 - Resonant particles. Some particles can be captured by the wave. Such particles are called trapped (or resonant) [3], they move together with the wave with its phase velocity. Resonant particles, as a rule, do not greatly affect the parent wave, moreover, they may not be taken into account in the first approximation. For small amplitudes, resonant particles are small. Large-amplitude waves are capable of capturing and accelerating a significant part of the particles of the medium, which is used in particle accelerators [4].

Landau damping [5] is a clear example of a phenomenon involving trapped (resonant) particles. This phenomenon was discovered by Lev Landau in 1945 and consists of the damping of Langmuir waves in a collisionless plasma. The Langmuir wave is one of the fundamental plasma modes [6], it is a longitudinal wave of electron concentration, while the ion concentration remains constant. The wave frequency is close to the plasma frequency $\omega_p = \sqrt{4\pi n_e e^2/m_e}$, where n_e, m_e is the electron density and mass, respectively. In the simplest case, Langmuir plasma waves obey the simple dispersion relation

$\omega^2 = \omega_p^2 + 3k^2T_e/m_e$, where T_e is the electron temperature, k=2π/λ is the wave number. The nature of the phenomenon lies in the absorption of wave energy by electrons moving at speeds close to the phase velocity of the wave. Such electrons are "trapped" in the potential well of the periodic potential of the wave. Slower particles take energy from it and accelerate, while faster electrons slow down and give their energy to the wave. Because there are more slow particles, the loss of wave energy when interacting with slow plasma particles exceeds the energy gain when interacting with fast electrons. As a result, the wave attenuates. Under the action of the wave, the electron distribution function is deformed in the region of $v = \omega/k$, so that its integral remains equal to 1, but the particle flux becomes greater than zero, which corresponds to a positive particle flux. It is important to note that waves of medium amplitude do not attenuate completely. They perturb the distribution function so that the number of slow and fast particles becomes equal. In this case, the particle flux remains positive.

Langmuir waves of large amplitude are capable of accelerating electrons to relativistic energies (tens of GeV). This property is used in linear accelerators (acceleration in wave wakefield) [4].

It is important to note that the plasma wave itself can exist without captured particles, i.e. the presence of a resonant particle flux is not a condition for the existence of a wave.

2 - Stokes drift. Another type of transport phenomena is the "Stokes drift" [7]. In this situation, a wave of any amplitude moves all particles of the medium in which it moves, to a finite distance [8]. In the case of small amplitudes, the Stokes drift is usually neglected, as are other nonlinear effects. However, for large amplitudes, the Stokes drift appears stronger, and a nonlinear distortion of the wave profile occurs [9]. In the linear approximation, all the main parameters of the wave can be written in the form

$$\psi = \psi_0 + \hat{\psi}_1 \exp(-\mathrm{i}\omega t + \mathrm{i}kx).$$

For the particle velocity, this expression, accurate to phase, can be rewritten as

$$v_i(x,t) = \hat{v}_{i1} \sin(\mathrm{k}x - \omega t).$$

It is obvious that the average velocity of ions is zero. However, if the amplitude of the ion-sound wave, although small, is different from zero, Stokes drift occurs. The analysis of Stokes drift for acoustic waves is clearly presented in [8]. The solution for the above harmonic Eulerian velocity field can be written as

$$X(t) = \frac{a}{\omega}\cos(kX_0 - \omega t) + \frac{ka^2}{2\omega^2}\sin[2(kX_0 - \omega t)] + \frac{ka^2}{2\omega}t$$

The expression $v_{St} = \frac{ka^2}{2\omega}$ describes the mean velocity of the particle in the positive direction. It is obvious that the Stokes drift is a second-order nonlinear effect. As the wave amplitude decreases, the value of v_{St} decreases rather quickly (quadratically) and for small-amplitude waves, the Stokes drift becomes negligible.

3 – Soliton transport. The third type of phenomena under consideration is the transfer of matter by acoustic solitons [10]. Solitons are solitary waves that exist due to the balance of nonlinearity and dispersion. The one-way transfer of matter by KdV solitons is described in [11]. Compressive solitons transfer matter in the direction of their motion, while rarefactive solitons transfer matter in the opposite direction. In the present work, only KdV solitons are considered, which will be referred to below as simply "solitons". The one-way transfer of matter is an integral (fundamental) property of solitons. In other words, unlike the first two cases, soliton transfer cannot be neglected for waves of any amplitude (including arbitrarily small ones).

Despite the large number of articles, the physics of solitons is far from complete. This applies in particular to magnetosonic solitons, which is confirmed by the small number of publications. This state of affairs is apparently associated with the three-dimensional geometry of the problem even for one-dimensional solitons. In a recent work, the authors of this review carried out a hydrodynamic analysis of the properties of magnetosonic compressive solitons. Profiles were calculated numerically for the case of arbitrary amplitudes, analytical formulas were obtained for small amplitudes. The main result: it was shown that magnetosonic solitons carry out a significant one-way transfer of charged particles across the external magnetic field. Moreover, unidirectional transfer is their fundamental property by analogy with ion-acoustic solitons [26].

The phenomena considered extend beyond the physics of plasma waves. Wave transport of matter is characteristic of waves on the surface of a liquid, internal waves in a liquid, acoustic waves, etc.

As follows from the above facts, the classical definition of a wave is valid only for linear waves or systems under confinement (string, membrane, etc.). Real waves of finite amplitude transfer matter along with energy and momentum. Moreover, in relation to solitons, matter transfer is a fundamental property. Our future task is to expand the areas of practical application of the presented results.

References

[1] I.E. Irodov, Wave processes. Basic laws: a tutorial / Moscow 2020. - 266 p. — ISBN 978-5-00101-673-1 (In Russian).
[2] F.S Crawford, Jr (1968). Waves (Berkeley Physics Course, Vol. 3), McGraw-Hill, ISBN 978-0070048607.
[3] I. B. Bernstein, Exact nonlinear plasma oscillations. Physical Review. V. 108. P. 546. (1957).
[4] A. Modena, [et al.], Electron acceleration from the breaking of relativistic plasma waves. Nature. V. 377. P. 606–608. (1995).
[5] L. D. Landau, J. Phys. (USSR) 10, 25 (1946).
[6] L. Tonks, I. Langmuir Oscillations in ionized gases. Physical Review. 33 (8): 195–210 (1929).
[7] G.G. Stokes, On the theory of oscillatory waves, Trans. Camb. Philos. Soc. 8. P. 441–455. (1847).
[8] G. Falkovich. Fluid Mechanics (A short course for physicists). – Cambridge University Press. – 2011. – 171 pp. ISBN 978-1-107-00575-4.
[9] Konno K. Propagation of Ion Acoustic Cnoidal Wave. Journal of the Physical Society of Japan. V. 46. P. 1907. (1979).
[10] F. M. Trukhachev, N. V. Gerasimenko, M. M. Vasiliev, O. F. Petrov. Matter transport as fundamental property of acoustic solitons in plasma. Phys. Plasmas. V. 30. P. 112302. (2023).
[11] A. E. Dubinov X. I. Lebedeva, Ambiplasma separation into matter and antimatter by a train of baryon-acoustic solitons in the problem of the baryon asymmetry of the Universe, Chaos, Solitons & Fractals 152, 111391, (2021).

THE CALCULATIONS OF EQUATION OF STATE AND ELECTRONIC TRANSPORT COEFFICIENTS OF LOW-TEMPERATURE TIN PLASMA

E. M. Apfelbaum

Joint Institute for High Temperatures of RAS,
Izhorskaya str. 13. bldg. 2, Moscow 125412, Russia, apfel_e@mail.ru

The information about thermophysical properties of various substances play important role in various fundamental tasks and applications in different areas of physics, including, of course, the physics of plasmas as well [1]. Among these properties we will consider below the thermodynamical ones, i. e. the pressure, internal energy etc., which consist the equations of state (EOS), and the electronic transport coefficients, i. e. the electrical conductivity, thermal conductivity and thermal power. The mentioned values together with many others are investigated for more than a century in various areas of phase diagram. In result presently there are many calculated and measured data even within the plasma region. The latter for the most of metals is located at elevated temperatures, i. e. at $T > 5$ -10 kK. (Below T is the temperature, ρ is the mass density, P is the pressure, U is the specific (per mass) internal energy, V is the volume). It is difficult to obtain so high T states in experiments even without any further measurements [2]. Within the theories the main obstacle is concluded in the presence of Coulomb interaction, which is difficult to describe accurately, so this task is not solved completely up to now in spite of significant progress both in theoretical and calculations techniques [3]. Nevertheless, the existing data for the considered properties for many substances appear to be enough to create the databases namely for plasma states [4,5]. Thus, for plasma of some materials the problem with thermophysical properties is solved at least partially. However there are many other substances, for which the are too little corresponding data or they are even absent in plasma states. Tin (Sn) is one of these substances, although it plays important role in various technology processes, for instance extreme ultra violet lithography [6]. For Sn plasma up to recent time one can find in the literature only three semi-empirical models [6-8], while any measurements were absent (for ρ less then the critical one, of course). In [6] there are simple relations for thermodynamics and thermal conductivity of almost ideal plasma of Sn for T =10-100 eV (~ 100 -1000 kK) and $\rho \leq 0.01$ g/cm^3. The EOSes ofeered in [7] and [8] are calibrated to reproduce the shock-wave data near solid state density $\rho_0 = 7.31$ g/cm^3. Thus, the data under study in the region of low temperature plasma (LTP) of Sn, located at T=10 -100 kK and $\rho < \rho_0$, has been absent both in theory and measurements.

To correct this situation we have recently developed a model for the

calculations of the properties under study for Sn LTP [9]. Our model is constructed on the same approaches, that were previously used for other elements, for which the data on investigated properties were scarce, like, for instance, Ga, Bi, In [10-12]. For the thermodynamics we have used the chemical approach, which is widely used in the physics of plasmas [1]. To calculate transport coefficients the relation time approximation, described in many manuals (see, for instance, [13]), was used. The characteristic examples of application of both approaches one can find, for instance, in [14,15]. So here we will present only the main relations of our model and the results of calculations that was not published previously in [9].

Within the chemical approach a substances is represented as some mixture of various components. For the case of Sn plasma at T = 10 - 100 K it is enough to include into considerations the following constituents: atoms, electrons and positive ions with charge up to +5 |e| (e is the electron charge). The free energy F of this mixture can be presented in an additive form, i. e.:

$$F(N_0, N_1, ..., N_5, N_e, V, T) = F_{\text{id}} + F_{\text{Ch-Ch}} + F_{\text{N-Ch}} + F_{\text{N-N}} \qquad (1)$$

All thermodynamical functions, including P, U will be calculated as corresponding derivatives of F. So they will have the same additive structure. Besides V and T the free energy F is also dependent on the mixture composition, i. e. on the numbers of separate components N_s (or concentrations $n_s = N_s/\text{V}$), where subscript $s = 1,..5$, numerates the ions, according to their charge, while $s = 0$ or $s = a$ is for atoms, $s = e$ is for electrons. The term F_{id} is the free energy of mixture of non-interacting components. The translation contributions to F_{id} are known exactly [1]. Besides F_{id} includes the internal partition functions of all components, which can be calculated by various techniques [1,9-12]. In present calculations we used the same approach as in [9]. The subscript Ch-Ch (charge - charge) marks the contributions due to Coulomb interaction. In our model it is described by the expressions, obtained in [16], where the formulas for $P_{Ch\text{-}Ch}$ and $U_{Ch\text{-}Ch}$ are also presented. The other terms in (1) are due to neutral - charge (N-Ch) and neutral - neutral (N -N) contributions. They were obtained by means of the second virial coefficient approximation with corresponding interaction potential [9-12]. The minimization of F with respect to N_s with account of the mass and charge conservation laws gives rise to the system of coupled equations for N_s, which expresses the action mass laws for corresponding ionization - recombination processes [1]. Its solution produces the composition, i. e. the set of n_s for given T and ρ. The following substitution of n_s into (1) allows us to calculate F. The derivatives of F define the other thermodynamical functions, including P and U.

Furthermore, the concentrations $n_s = N_s/V$ were used within the relaxation time approximation (RTA) to get the transport coefficients [1,9-12,15]. Corresponding expressions within RTA for electrical conductivity σ, thermal

conductivity κ and thermal power S_t are the following:

$$\sigma = -\frac{2|e|^2\sqrt{2m_e}}{3\pi^2\hbar^3} I_{3/2},\quad \kappa = \frac{2\sqrt{2m_e}}{3\pi^2\hbar^3 T}\left(-I_{7/2} + \frac{(I_{5/2})^2}{I_{3/2}}\right),\quad S_t = \frac{1}{|e|T}\left(\mu_e - \frac{I_{5/2}}{I_{3/2}}\right),$$

$$I_y = \int_0^\infty \varepsilon^y \tau(\varepsilon)\frac{\partial f_0}{\partial \varepsilon} d\varepsilon,\quad \varepsilon = m_e u^2/2 \qquad (2)$$

$$f_0 = \left[\exp\left(\frac{\varepsilon-\mu}{k_B T}\right)+1\right]^{-1},\quad \nu(\varepsilon) = \tau^{-1}(\varepsilon) = \sum_{i=1,\ldots,5} n_i A^m_{i-e}(\varepsilon)u + n_a A^m_{a-e}(\varepsilon)u$$

In (2) $A^m_{a,i-e}(\varepsilon)$ is the momentum cross-section of electrons on heavy particles (atoms and positive ions), m_e, e, $\hbar$, k_B are the fundamental constants, ε is the free electron energy, f_0 is the Fermi–Dirac distribution function, τ is the relaxation time. The generalized Rutherford formula was used for electro-ion scattering, see [9]. The cross-section e - Sn is given in [17]. The correction due to electron-electron collisions in (2) is introduced by means of an additional factor, i. e. for conductivity, for instance, $\sigma \to \gamma_{ee}\sigma$. Here we have used the expression for γ_{ee} obtained in [18].

In Fig. 1 and 2 we have presented the comparison of the results for two models for P and U correspondingly ρ = 0.1 g/cm^3. This density value is 10 times higher than the density at the isochore, studied previously in [9]. For P there is a good agreement, while for U it is not so. The reason is that model [6] does not account for internal partition functions of separate components. Besides the chosen density is more than upper limit for model [6] (see above). In Fig. 3 and 4 we have presented the conductivity and the Lorenz number for the same density, but only within our model.

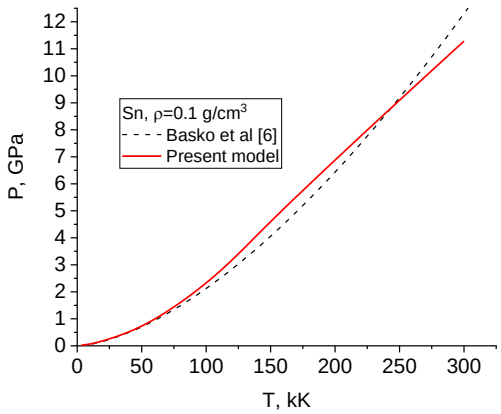

Fig. 1. Pressure P of Sn plasma at ρ=0.1 g/cm^3 in two models.

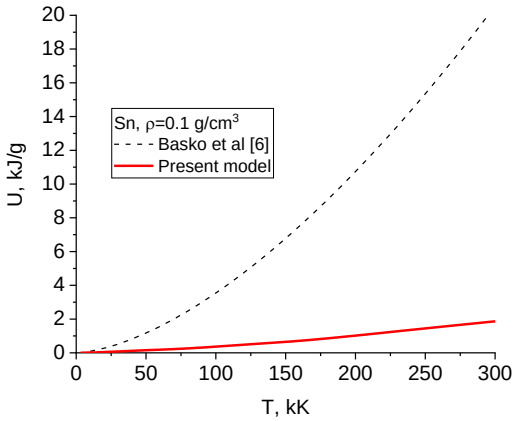

Fig. 2. The same as in Fig. 1 but for internal energy U per mass.

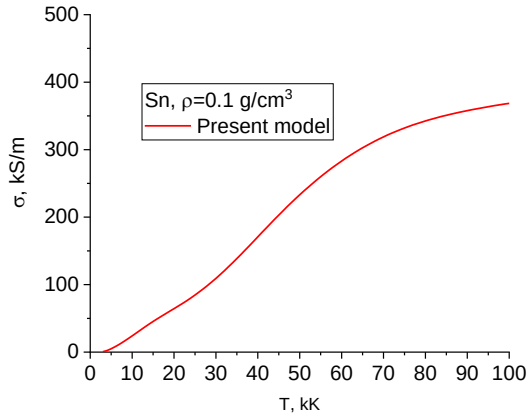

Fig. 3. The same as in Fig. 1 but for electrical conductivity σ and only for our model.

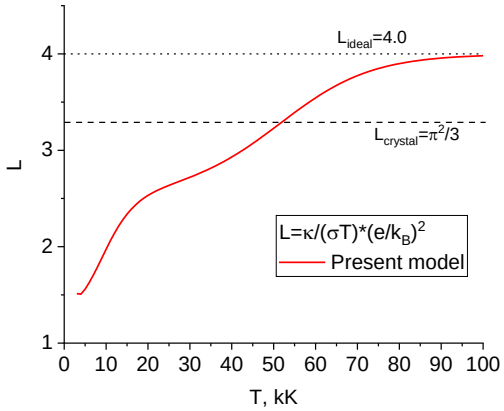

Fig. 4. The same as in Fig. 1 but for the Lorenz number L and only for our model.

Acknowledgements. This work was supported by the Ministry of Science and Higher Education of the Russian Federation (State Assignment No. 075-00269-25-00).

References

1. **Fortov V. E., Yakubov I, T, Khrapak A. G.** Physics of strongly coupled plasma. Oxford: OUP (2006).
2. **DeSilva A. W., Rakhel A. D.** Contributions to Plasma Physics. 45 (2005) 236–242.
3. **Stanek L. J. et al**. Physics of Plasmas. 31 (2024) 052104.
4. **Clérouin J. et al**. Physics of Plasmas. 19 (2012) 082702.
5. **Militzer B. et al.** Physical Review E. 103 (2021) 013203.
6. **Basko M. M et. al.** S. Phys. Plasmas. 22 (2015) 053111.
7. **Khishenko K. V.** J. Phys, Conf, Ser. 121 (2008) 022025.
8. **Rehn D. A. et. al.** Phys. Rev. B. 103 (2021) 184102.
9. **Apfelbaum E. M.** Physics of Plasmas. 32 (2025) doi: 10.1063/5.0276569.
10. **Apfelbaum E. M.** Physics of Plasmas. 27 (2020) 042706.
11. **Apfelbaum E. M.** Plasma Physics Reports. 48 (2022) 1087–1093.
12. **Apfelbaum E. M.** Physics of Plasmas. 30 (2023). 042709.
13. **Pitaevskii L. P., Lifshitz E. M.** Physical Kinetics: Volume 10. Butterworth-Heinemann (2012).
14. **Kuhlbrodt S., Redmer R.** Phys. Rev. E. 62 (2000) 7190–7200.
15. **Khomkin A. L., Shumikhin A. S.** High Temperature. 52 (2014) 335–344.
16. **Potekhin A. Y. et al.** Phys. Rev. E. 79 (2009) 016411.
17. **Umer H. et. al** Atomic Data and Nuclear Data Tables. 154 (2023) 101586.
18. **Reinholz H. et. al.** Phys. Rev. E. 91 (2015) 043105.

EQUILIBRIUM COMPOSITION OF TRANSIENT GRAPHITE PLASMA

M. Ristić[1], M. Marković[1], A. Šajić[1], D. Ranković[2], M. Kuzmanović[1]

[1]University of Belgrade, Faculty of Physical Chemistry, P. O. Box 47, 11158 Belgrade, Serbia, miroslav@ffh.bg.ac.rs
[2]University of Belgrade, Vinča Institute of Nuclear Sciences, P. O. Box 522, 11351 Belgrade, Serbia

Abstract

The goal of this work was to discuss the influence of pressure change and air mixing of ablated material on the equilibrium composition of plasma obtained on a graphite target with impurities, which is a material of great interest for nuclear technology. Special care is devoted to the influence of pressure and mixing on the equilibrium relationship between temperature *T* and electron number density *N*e, which is important for plasma diagnostics. The conclusion relates to the interval of plasma pressure and temperature from 10 to 0.1 bar and 5000-15,000 K, for the expected degree of mixing of the ablated material and air, relevant for the LIBS technique.

INTRODUCTION

Knowledge of the composition of gas plasma as a function of temperature and pressure is of great importance both in plasma spectroscopy and plasma technology. Under the conditions of validity of local thermodynamic equilibrium (LTE), the equilibrium composition of the plasma can be calculated by solving a system of equations consisting of the Saha equations, the mass conservation law and the electroneutrality equation. This approach has been successfully applied to describe the equilibrium composition of time transient plasmas such as laser-induced plasma (LIP), which is of interest for the LIBS technique (Laser-Induced Breakdown Spectroscopy) /1/. The action of a nanosecond laser pulse on a solid target leads to its local vaporization and the formation of a hot and dense plasma that usually expands in air, at atmospheric pressure. Experimental measurements and theoretical modeling of laser-induced plasma expansion have shown that during the time evolution of the plasma, near the end of its expansion, the pressure can even be lower than ambient /2/.

Graphite is a material of great interest in nuclear technology. The LIBS technique is particularly interesting for application in nuclear technology, due to its ability to depth-profiling elemental composition. The aim of this work was to consider the influence of pressure and mixing between the ablated material and air on the equilibrium composition of time transient plasma.

METHODOLOGY

The equilibrium plasma composition was calculated using a previously developed application, which is described in detail in references /3,4/. The ionization potential lowering (IPL) is determined by Stewart-Pyatt model. Special attention was paid to the influence of IPL on the value of partition functions; for some elements, especially at higher temperatures, this influence can be significant. Iterations are further performed until the difference between two adjacent iterations of Ne value is lower than 10^5 m^{-3}. The equilibrium composition was calculated for a sample containing 96% mole fraction of C and 1% each of Be, B, Ca and Mg.

RESULTS AND DISCUSSION

The equilibrium plasma composition for pressure of 1 atm is given at Fig.1, with and without IPL correction. Depending on the ionization energy and ion charge, the influence of the PLE correction becomes significant with increasing

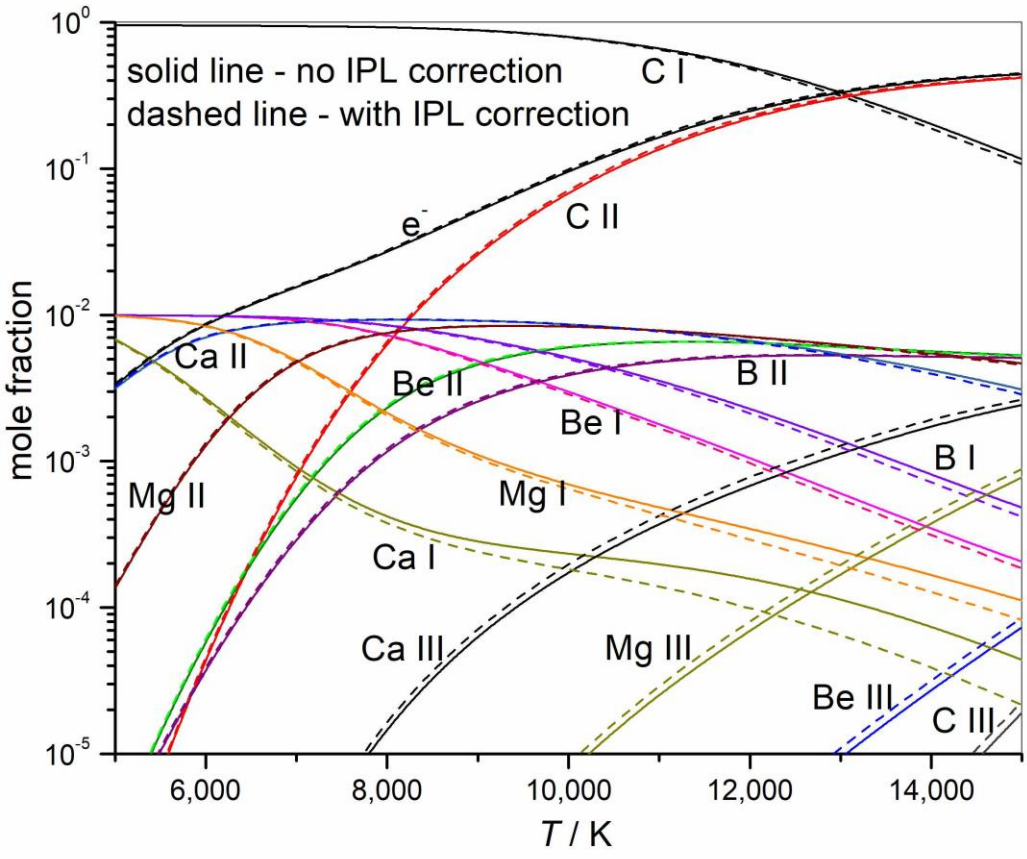

Fig. 1. Equilibrium plasma composition as a function of temperature

temperature. For atoms and single charged ions, the PLE correction lowers their mole fractions, while for double charged ions it increases them. Knowledge of the equilibrium composition of plasma is important for optical spectroscopy,

both for the assessment of optimal excitation conditions, for analytical applications, and for the application of spectroscopic methods for plasma diagnostics. For this approach in the LIBS technique, the limiting problem is knowing the plasma pressure and the degree of mixing of the ablated material with the surrounding air, during the time evolution of the plasma.

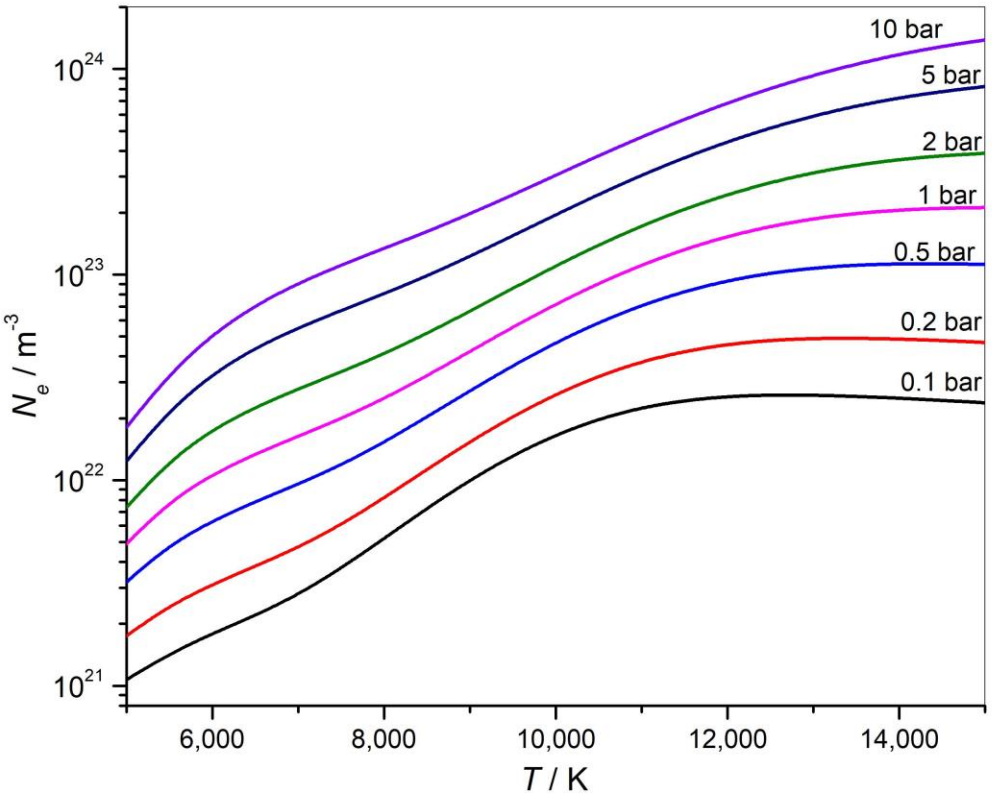

Fig. 2. Number density of electrons (Ne) in function of temperature for graphite plasma at various pressures

For a given composition of the ablated material, the plasma pressure can be estimated (at least roughly) by independent measurements of Ne and T, Fig. 2. The effect of mixing ablated material and air on the equilibrium composition is illustrated in Fig. 3, using the example of Ne temperature dependence: due to the high ionization energies of N and O, the degree of mixing has little effect on Ne, and thus on the degree of ionization of individual atoms, and further indirectly on the relative ratios of the fractions of ablated elements from the target.

Fig. 3 is interesting for plasma diagnostics: for a given target composition and a previously determined plasma pressure, the distribution of Ne as a function of T depends weakly on the degree of mixing with air. If Ne is determined using some of the spectroscopic diagnostics method, T can be estimated with satisfactory accuracy using Fig. 3. Also, if T is previously measured, Ne can be estimated using Fig. 3.

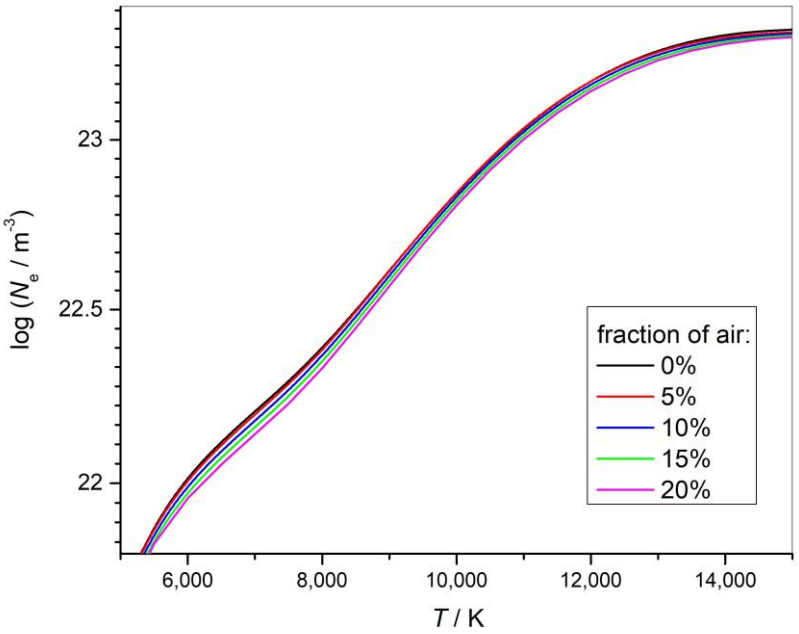

Fig. 3. Dependence Ne of T for graphite plasma at various degree of air mixing

CONCLUSION

The obtained results show that the application of the LTE concept for calculating the composition of transient plasma can be useful for optimizing spectrochemical analysis parameters and plasma diagnostics. The dependence of Ne on T at different pressures is sensitive enough that, based on previously measured T and Ne, one can at least roughly estimate the pressure. The degree of mixing of the ablated material and air does not significantly affect the function Ne(T), for a given pressure and mixture composition.

Acknowledgements. The research was funded by the Ministry of Education, Science and Technological Development of the Republic of Serbia, Contract numbers: 451-03-137/2025-03/200146, 451-03-136/2025-03/200146, and 451-03-136/2025-03/200017.

References

1. **Shabanov S.V**, **Gornushkin I.B.** Appl. Phys. A, 121(2015) 1087-1107.
2. **Ershov-Pavlov E.A, Katsalap K. Yu, Stepanov K. L, Stankevich Yu. A.** Spectrochim. Acta Part B At. Spectrosc. 63 (2008) 1024-1037.
3. **Ristić M, Krstevski N, Ranković D, Marković M, Šajić A, Kuzmanović M.** Plasma Phys. Control. Fusion 66 (2024) 125014.
4. **Ristić M, Krstevski N, Marković M, Šajić A, Kuzmanović M.** J. Serb. Chem. Soc. Jul. (2025) 1-13.

TAKING INTO ACCOUNT THE VIBRATIONAL EXCITATION EFFECTS OF NITROGEN AND OXYGEN PARTICLES TO SIMULATE OZONE PRODUCTION IN DIELECTRIC BARRIER DISCHARGE PLASMA-CHEMICAL REACTOR

I.A. Ruchkin[1,2], M.E. Pinchuk[1], O.M. Stepanova[1]

[1]Institute for Electrophysics and Electric Power, Russian Academy of Sciences, 18, Dvortsovaya nab., St. Petersburg, 191186, Russia, iruchkin98@gmail.com
[2]Ioffe Institute, Russian Academy of Sciences, St. Petersburg, 194021, Russia

The ozone production in a plasma-chemical reactor based on a coaxial dielctric-barrier discharge [1] has been simulated using the ZDPlaskin software module [2]. The relevancy in accounting the vibrational excitation of nitrogen $N_2(v\leq8)$ and oxygen $O_2(v\leq4)$ molecules when modeling the kinetics of plasma-chemical reactions in dry air at atmospheric pressure is discussed.

The two sets of reactions are considered: with and without taking into account the vibrationally excited molecules $N_2(v)$ and $O_2(v)$. In the first case, the model was composed of 806 reactions and 53 particles from the kinet_N2_O2_v1.03 set [3], which was added with the reactions of interaction of $N_2(v)$ and $O_2(v)$ with other particles [4]. In the second case, we used the approach that assumed that $N_2(v)$ and $O_2(v)$ can be neglected [5,6], that reduced the set to 561 reactions. For the calculation, we used the reaction cross sections from the SIGLO database [7]. The time dependences of the reduced field $E/N(t)$ and electron concentration $n_e(t)$ were obtained from the current and voltage oscillograms (figures 1 and 2).

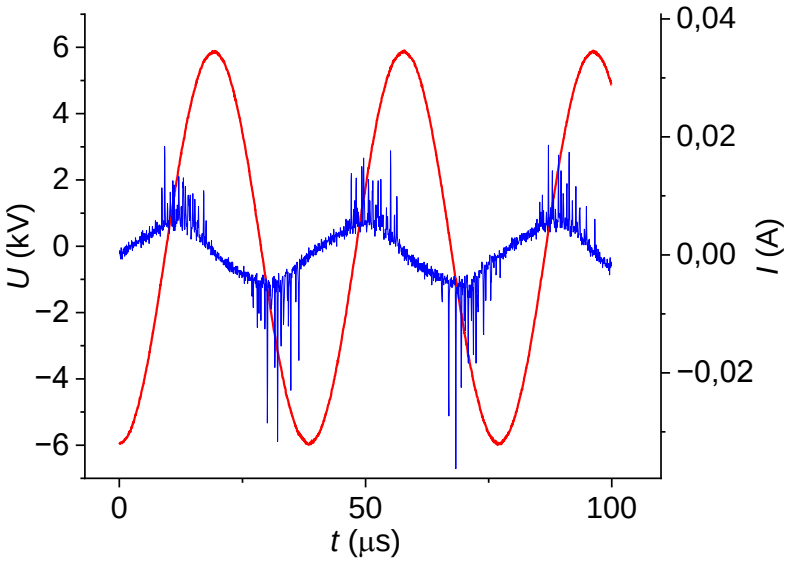

Figure 1 – Time dependences of current $I(t)$ and voltage $U(t)$

The reduced electric field $E/N(t)$, V·cm^2 is determined as follows:

$$\frac{E}{N} = \frac{U(t)kT}{\left(d+\frac{s}{\varepsilon}\right)p}, \quad (1)$$

where $E(t)$ is the electric field, V/m; d is the distance between the electrode and the inner wall of the discharge quartz tube, cm; s is the thickness of the tube wall, cm; $\varepsilon = 4$ is the relative permittivity of quartz, N is the concentration of neutral particles, m^{-3}; $p = 101325$ Pa is the atmospheric pressure; $k = 1.38 \cdot 10^{-23}$ J/K is the Boltzmann constant; T is the gas temperature, K.

The electron concentration $n_e(t)$, cm^{-3} is calculated using formula (2):

$$n_e(t) = \frac{P(t)}{E(t)^2 e \mu_e}, \quad (2)$$

where $P(t)$ is the power density, W/cm^3; $e = 1.6 \cdot 10^{-19}$ C is the electron charge; μ_e is the electron mobility, cm^2/(V·s), calculated using Bolsig+ [8].

The power density is determined by formula (3):

$$P(t) = \frac{I(t)U(t)}{V} = \frac{4I(t)U(t)}{d^2 \pi H}, \quad (3)$$

where V is the discharge volume, cm^3; H is the height of the discharge area, cm. In this work, an assumption about the diffuse form of existence of the discharge in the reaction volume is made, however, it is known from the literature that the discharge volume occupied by microdischarges is approximately 0.1–10% of the volume of the reaction volume [9].

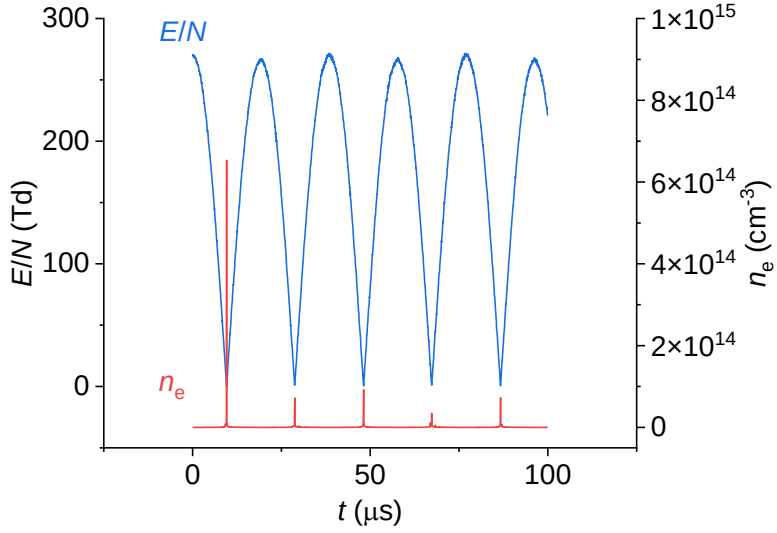

Figure 2 – Time dependences of E/N and n_e

Figure 3 shows the calculated kinetic curves for ozone at 400 K.

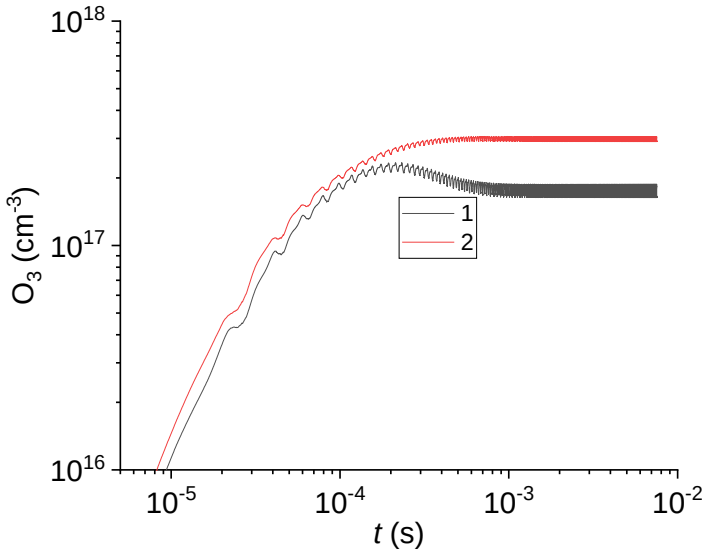

Figure 3 – Time dependence of ozone concentration: 1 – $N_2(v)$ and $O_2(v)$ are taken into account, 2 – $N_2(v)$ and $O_2(v)$ are excluded

The calculated ozone concentrations were determined from figure 3 when equilibrium was reached. When taking into account $N_2(v)$ and $O_2(v)$, the calculated O_3 concentration was approximately equal to $1.8 \cdot 10^{17}$ cm^{-3}; whereas when vibrationally excited species were excluded, it increased almost twofold and was equal to $3 \cdot 10^{17}$ cm^{-3}.

In order to reveal the influence of vibrationally excited species on ozone formation, we considered the main reactions of ozone production using the PumpKin software package [10]:

R1 $O+O_2+N_2 \rightarrow O_3+N_2$ (45%);

R2 $O+O_2+O_2 \rightarrow O_3+O_2$ (36%);

R3 $O+O_2+O \rightarrow O_3+O$ (17%).

The N_2 and O_2 required for R1-R3 are expended to form $N_2(v)$ and $O_2(v)$. As a result of the reaction R4 $O_2+O \rightarrow O_2(v1)+O$, about 16% of oxygen is consumed. On the contrary, only 7% of oxygen enters into the R1 reaction, 6% into the R2 reaction and 3% into the R3 reaction.

For $N_2(v)$ and $O_2(v)$, vibrational-vibrational (V-V) interactions and vibrational-translational (V-T) relaxation processes predominate [4,11]. The data [4,12] indicates that the interaction of $N_2(v)$ and $O_2(v)$ with other types of particles results in the formation of O_3, NO, N_2O, NO_2, and others. $N_2(v)$ and $O_2(v)$ do not directly participate in the formation of the above types of particles, but they consume nitrogen and oxygen of the initial mixture. In particular, there are two dominating reactions of NO production:

R5 $O+NO_2 \rightarrow NO+O_2$ (53%), and

R6 $N(2D)+O_2 \rightarrow NO+O$ (37%).

In this paper, the influence of $N_2(v)$ and $O_2(v)$ on the kinetics of ozone production in a dielectric-barrier discharge in dry air at atmospheric pressure is studied. As a result of the 0D modeling approach, it is found that when taking into account $N_2(v\leq8)$ and $O_2(v\leq4)$, the ozone concentration decreases approximately twofold. The formation of vibrationally excited particles is a competing process with respect to ozone synthesis, so it is advisable to include them in modeling the kinetics of plasma-chemical reactions.

Acknowledgements. The study has been supported by a grant from the Russian Science Foundation № 24-29-00816, https://rscf.ru/en/project/24-29-00816/.

1. **Pinchuk M., Stepanova O., Kurakina N. and Spodobin V.** Journal of Physics Conference Series, 830(2017) 012060.
2. S. Pancheshnyi, et. al., Computer code ZDPlasKin, URL: http://www.zdplaskin.laplace.univ-tlse.fr
3. N_2-O_2 mixtures. ZDPlaskin, URL: http://www.zdplaskin.laplace.univ-tlse.fr/index.html@p=340.html
4. **Zhong H., Mao A., Liu N., Wang Z., Ombrello T. and Ju Y.** Combustion and Flame, 256(2023) 112948.
5. **Pierotti G., Popoli A., Pintassilgo C.D. and Cristofolini A.** Plasma Chemistry and Plasma Processing, 44(2024) 1575-1594.
6. **Sakiyama Y., Graves D.B., Chang H.W., Shimizu T. and Morfill G.E.** Journal of Physics D: Applied Physics, 45(2012) 425201.
7. **Phelps A.V. and Pitchford L.C.** Physical Review A, 31(1985) 2932-2949.
8. BOLSIG+. Electron Boltzmann equation solver, URL: https://www.bolsig.laplace.univ-tlse.fr/
9. **Bang S., Snoeckx R. and Cha M.S.** Plasma Chemistry and Plasma Processing, 43(2023) 1453–1472.
10. **Markosyan A.H., Luque A., Gordillo-Vázquez F. J. and Ebert U.** Computer Physics Communications, 185(2014) 2697-2702.
11. **Capitelli M., Ferreira C.M., Gordiets B.F. and Osipov A.I.** Plasma kinetics in atmospheric gases. Berlin: Springer-Verlag (2000).
12. **Wang W., Patil B., Heijkers S., Hessel V., Bogaerts A.** ChemSusChem, 10(2017) 2145-2157.

ION FLUX SPATIAL DISTRIBUTION IN AN END-HALL SOURCE

V. Shakialeuski, D. Kotov

Belarusian State University of Informatics and Radioelectronics, 6 Petrusya Brovki str. Minsk, Belarus, ivadim2703@gmail.com, kotov@bsuir.by

1. Introduction

Despite the widespread use of end-Hall ion sources (EHIS) in industry for surface modification and ion-assisted deposition of coatings, there is a limited number of studies focused on modeling low-voltage anode discharges in crossed E×H fields and the formation of ion fluxes from the discharge region—most of which are empirical in nature. Therefore, this study explores the application of numerical methods based on the Monte Carlo technique for charged particles to evaluate the spatial distribution of ions leaving the discharge zone of an end-Hall ion source.

The primary mechanism of ion flux formation in the discharge region of an end-Hall sources involves gas atom ionization by electron impact inside a conical anode, which expands toward the end of the device and is bounded below by a reflector beneath which permanent magnets are positioned. Most electrons are emitted from a thermionic cathode. Plasma localization and ion flux generation within the discharge zone are maintained by the E×H fields /1/. Since analytical descriptions of the processes within this region are challenging, we employ numerical modeling. The most reliable approach to describing discharges in crossed E×H fields is solving the Lorentz force equation for charged particles using the Monte Carlo method. Determining the ion flux from the discharge region of the end-Hall ion source thus reduces to solving the Lorentz equation for electrons and subsequently for ions, using the data obtained to estimate their spatial distribution /2/.

The Lorentz equation is written as follows

$$m\vec{a} = q\left(\vec{v} \times \vec{\mathrm{B}}\right) + q\vec{E} \qquad (1)$$

where m – particle mass, kg; a – acceleration, m/s²; q – charge, C; v – velocity, m/s; B – magnetic field induction, T; E – electric field intensity, V/m.

This equation is a second-order differential equation, which, in Cartesian coordinates, is transformed into a system of three equations to determine the velocity vector projections along each axis. These are solved using numerical iterative methods. To solve equation (1), it is necessary to calculate the electric and magnetic fields for the given configuration of the EHIS. In our case, the finite element method was used for this purpose. The effect of gas pressure on charged

particle motion was accounted for using a probabilistic model based on estimating the mean free path for hard spheres /2/. Next, a simulation of multiple electrons with varying initial positions and velocities must be performed, which allows for determining their overall spatial distribution—this distribution defines the discharge's spatial structure. Using the resulting electron coordinates as initial conditions for ions, the ion trajectories leaving the discharge zone are computed, allowing for estimation of the ion flux onto the substrate surface. In our case, relativistic corrections for electron mass variation were also included.

2. Results and Discussion

To numerically solve of equation (1), the Runge-Kutta-Fehlberg method of fifth-order accuracy was used. The method was implemented using the Python 3.11 programming language together with the Taichi library, which enabled GPU acceleration of computations. The equation (1) was solved using time steps of 10^{-11} for electrons and 10^{-7} s for ions. Particle spatial position data were recorded at the 10,000th iteration.

Due to the complex configuration of the magnetic and electric systems of the End-Hall Ion Source, which includes numerous ferromagnetic components, the finite element method was employed to solve Laplace's equation for computing the magnetic and electric fields. The resulting field distributions were exported from COMSOL Multiphysics into our simulation code via the COMSOL API. The EHIS discharge zone configuration used for calculating the electric and magnetic fields is shown in Figure 1 /3/.

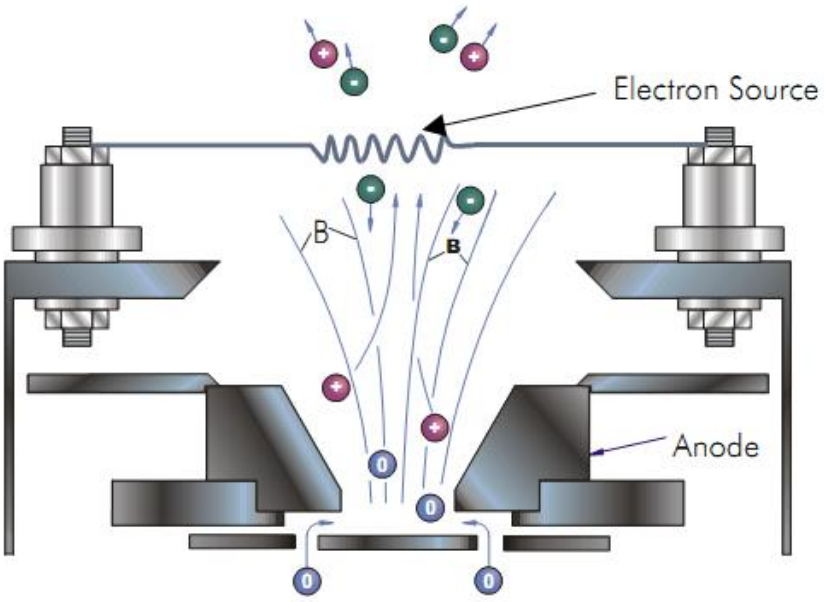

Fig. 1. Cross-section of the discharge zone of the End-Hall Ion Source used in the simulations.

The initial velocities of electrons were set according to a Maxwellian distribution with an energy of 2 eV. The initial positions of the electrons were located on the surface of the thermionic cathode. Figure 2 shows the calculated spatial distribution of the electron and ion components in the active zone of the EHIS, relative to the model's axis. As can be seen, electrons are concentrated in the region of crossed electric and magnetic fields along the anode surface, which is consistent with experimental data [1].

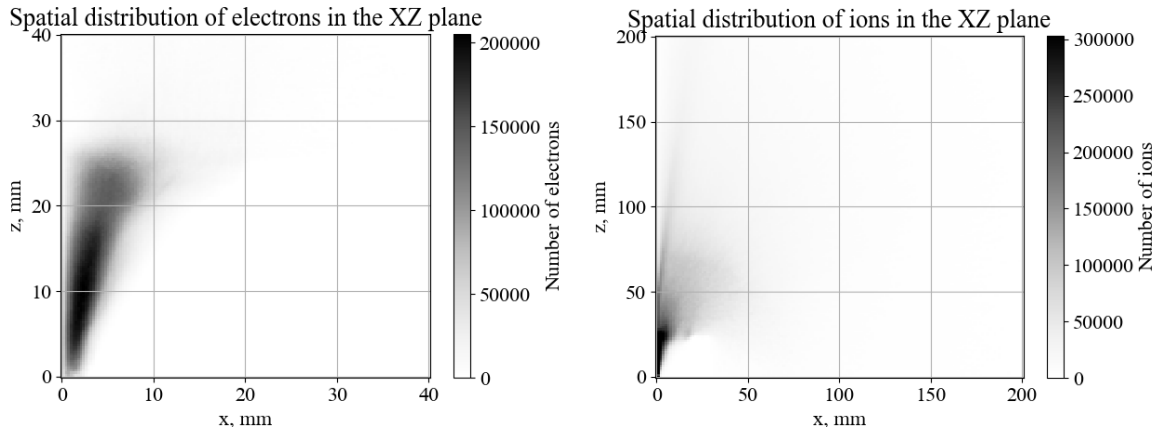

Fig. 2. Simulation of the spatial distribution of the electron and ion fluxes in the active zone of the EHIS.

Figure 3 presents a visualization of the spatial distribution of ions (in green) and electrons for the EHIS model used in the calculations.

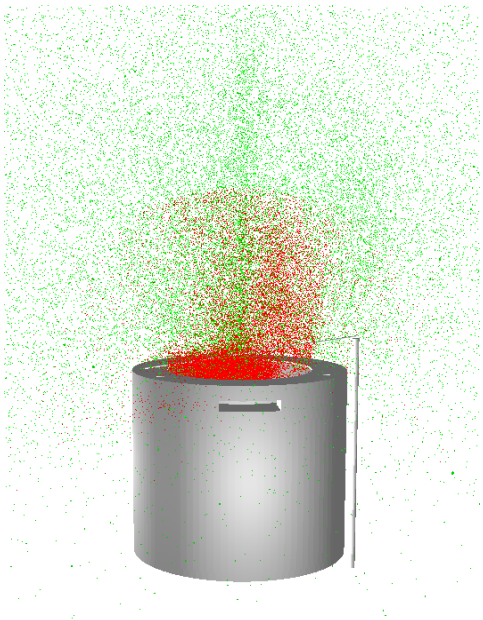

Fig. 3. Visualization of the spatial distribution of ions (green) and electrons (red).

As can be seen, the majority of electrons are concentrated in the discharge zone. Less than 10% of the electrons leave the discharge zone, being ejected by the thermionic cathode. The thermionic cathode influences the ion dispersion; however, the main flow of ions moves along the EHIS axis, which is consistent with experimental data.

It should also be noted that the electron trajectory was calculated within a radius of 100 mm from the center of the discharge zone, since electrons that leave the discharge zone do not influence the ionization process. Upon reaching this specified radius, new initial conditions were assigned to the electron.

4. Conclusion

Thus, a calculation method is proposed, using the Monte Carlo method, for the distribution of the generated ion flux, originating from the electron distribution in the discharge zone of the EHIS. However, it is necessary to adapt the calculation model to the geometric parameters of the discharge zone of the EHIS. Using the method allows determining the ion beam current distribution profile, taking into account the operating pressure, as well as the ion energy.

References

1. **Zhurin V. V.** John Wiley & Sons (2012), 326 p.
2. **Ido S.** Vacuum, 47 (1996), P. 1035-1038.
3. **Kaufman H. R.** Patent 4862032 USA (1989).

4D VYSIKAYLO'S EQUATION FOR DESCRIBING THE TRANSPORT OF NON-UNIFORM PROFILES OF AMBIPOLAR QUASI-NEUTRAL PLASMA WITH CURRENT

P.I.Vysikaylo

Moscow Institute of Physics and Technology, Russia, E-mail filvys@yandex.ru

Cumulation (self-focusing) of charged particles in non-uniform plasma (with current) is a universal property of cumulative-dissipative structures with characteristic sizes from 10^{-15} to 10^{26} m. These phenomena are observed from the femto- to the macroworld (non-uniform atmospheres and ionospheres of all planets of the Solar system, intergalactic lightning). Here we draw attention to the solution and visualization of this solution of the non-stationary nonlinear 3D equation of the Navier-Stokes type. We applied this equation to describe phenomena in a non-uniform plasma with current. In this paper, a more complete classification of 3D processes of ambipolar transport in plasma with current and a classification of non-uniform 3D profiles of plasma parameters are given. We verify the theoretical models by experiments on the study of non-uniform plasma, locally perturbed by a beam of fast electrons. This leads to self-formation of: 1) shock waves of the electric field (layer of positive volume charge), stopped for photography by pumping gas, and 2) transition 3D profiles and plasma 3D Vysikaylo's nozzles already in quasi-neutral inhomogeneous plasma. We have for the first time analytically, numerically and experimentally investigated 3D processes of nonlinear ambipolar transport caused by violation of electrical neutrality and 3D interaction of electric fields with matter (charged particles) in inhomogeneous plasma with current. For the first time it has been proven that the coefficients of ambipolar diffusion, due to violation of electroneutrality, are vectors determined by the vector of the electric field, related to the concentration of electrons ($\boldsymbol{E}/n_e$).

The author has constructed for the first time the most complete non-stationary nonlinear 3D perturbation theory for describing the nonlinear interaction of an electric field with a non-uniform plasma with current. A modified non-stationary Navier-Stokes equation for the electron concentration is obtained (taking into account the violation of plasma electroneutrality in the approximation of small ion current compared to electron current) and its quasi-stationary solution is visualized, describing Vysikaylo's shock waves of the electric field and plasma nozzles (analogs of Laval's nozzles). The work is of scientific and practical interest for interdisciplinary research and the development of a method for generalized mathematical transfer of mathematical models from some areas of natural sciences to others, where their development

is not yet sufficiently complete. This work is of interest to researchers of nonlinear 4D self-organization of plasma in the electric field of cumulative-dissipative structures in semiconductors, gas-discharge plasma, the ionosphere of the Earth and other planets, the heliosphere, stellar spheres, lightning, intergalactic lightning, etc.

Our model includes equations for the balance of ion numbers:

$$\partial n_i/\partial t + \mathrm{div}(n_i(\boldsymbol{V}_i + \boldsymbol{U})) = I_i - R_i, \quad (1)$$

Here n_i – concentration of positive (or negative, if present) ions; $\boldsymbol{V}_i+\boldsymbol{U}= \mu_i\boldsymbol{E} +\boldsymbol{U}$ – drift velocity of ions, which is a function of the parameter E/N. $\boldsymbol{U}$ – the rate of pumping of neutral gas, which entrains ions. It is constant and does not depend on the parameter E/N. The same way (as gas pumping or an external electric field) one can take into account any forces acting on certain components of the plasma, for example, gravitational forces acting on ions (gravitational forces acting on ions /1/), magnetic fields acting on electrons, etc. see references in /1/. I_i, R_i – ion sources and sinks. To equation (1) it is necessary to add the electrodynamic equations:

$$\mathrm{rot}\,\boldsymbol{E} = 0 \text{ и } \mathrm{div}\,\boldsymbol{E} = 4\pi\rho; \quad \rho = e(\sum_{\alpha=1}^{m} z_a n_a - n_e);, \quad (2)$$

Here z_α – ion charge; m – number of different types of ions.

Instead of the balance equation for electrons (as in the case of ions), we will take into account the total current density. To do this, we add the balance equations for electrons and all possible ions (multiplying them by the corresponding charge) and take into account that charged particles of different signs in the volume are born and die simultaneously, using (2), we get:

$\nabla\boldsymbol{j} = 0$. Here $\boldsymbol{j}/e = (\partial\boldsymbol{E}/\partial t)/(4\pi e) - n_e\boldsymbol{V}_e + \sum_{\alpha=1}^{m} z_a n_a \boldsymbol{V}_\alpha + \nabla(D_e n_e)\ldots$ D_e – electron diffusion coefficient, (… - denotes ion diffusion). Electrons and ions in plasma are born and die together, in the current continuity equation the sources and sinks are mutually compensated (as are the flows caused by the non-stationarity and non-uniformity of the plasma concentration and electric field strength, as well as the non-stationarity and non-uniformity of the electron velocity distribution function in the sources and sinks). From (2): $n_i = n_e + \nabla\boldsymbol{E}/(4\pi e) \sum_{\alpha=1}^{m-1} z_a n_a$, and, the equation for $\boldsymbol{j}$ taking into account the displacement current – $(\partial\boldsymbol{E}/\partial t)/(4\pi)$:

$$\boldsymbol{j}/e = 1/(4\pi e)(\partial\boldsymbol{E}/\partial t) - n_e\boldsymbol{V}_e + (\sum_{\alpha=1}^{m-1} z_a n_a \boldsymbol{V}_\alpha + z_i\boldsymbol{V}_i\,(n_e + \nabla\boldsymbol{E}/(4\pi e) - \sum_{\alpha=1}^{m-1} z_a n_a) + \nabla(D_e n_e)\ldots, \quad (3)$$

Here 5th member with $z_i\boldsymbol{V}_i\ \nabla\boldsymbol{E}/(4\pi e)$ takes into account the influence of the violation of plasma electroneutrality on the modification of the internal electric field – $\boldsymbol{E}$ /1/.

Since electrons have a smaller mass, they are more mobile and the main

current transfer is the electron drift in an external electric field. Therefore, the main assumption of Vysikaylo's perturbation theory for plasma with current is the smallness of the ion current compared to the electron current. Therefore, we will consider the ratio of $n_e\boldsymbol{V}e$ to the other terms in (3) to be small parameters: τ_M/τ, 1, $(\mu_i/\mu_J)l_E/L$, l_u/L ... Here τ is the characteristic time of charge change, $\tau_M = 1/(4\pi e\mu_J n_e)$ – Maxwellian time of neutralization of space charge, μ_J – effective plasma mobility, taking into account the mobility of ions and electrons, $\boldsymbol{l}_{E0} = \boldsymbol{E}_0/(4\pi e n_e)$ – vectorized characteristic size of the change in electric field strength. The system of equations (1) - (3) taking into account the violation of plasma electroneutrality (2) can be solved using Vysikaylo's perturbation theory, if the parameters: $\Omega\tau_M$, $(\mu_i/\mu_J)l_E/L$ and l_u/L « 1 /1/. The smallness of the parameter $(\mu_i/\mu_J)l_E/L << 1$ can be observed at $l_{E0}/L >> 50$, since $\mu_i/\mu_J \approx \mu_i/\mu_e$. Within the framework of Vysikaylo's perturbation theory, it is possible to advance in zero order to a region with a significant violation of electroneutrality [2,5]. The zero approximation in Vysikaylo's perturbation theory splits into two approximations:

1) quasi-neutral or drift approximation, here: $l_{E0}/L << 1$ (see /1/) and

2) with a significant violation of plasma electroneutrality (Vysikaylo's approximation), when $l_{E0}/L \sim 1$ (or even when $l_{E0}/L >> 50$, but $(\mu_i/\mu_J)l_E/L << 1$ (the main current is carried by electrons $\mu_J \approx \mu_e >> \mu_i$ is the ion mobility).

Schottky in 1924 presented (3) in the form: $\boldsymbol{j}/e = -n_e\boldsymbol{V}_e + \nabla(D_e n_e) = n_e\mu_e\boldsymbol{E} + \nabla(D_e n_e)$ or $\boldsymbol{E} = \boldsymbol{E}_0 + \boldsymbol{E}_1 = \boldsymbol{j}/(e\, n_e\mu_e) + \nabla(D_e n_e)/(n_e\mu_e)$ (4)
and substituting (4) into (1) he obtained for the first time the Schottky's ambipolar diffusion coefficient $D_a = \mu_i D_e/\mu_e$. According to section 2.2 /1/, taking into account the electric field $\boldsymbol{E}_1$ is the first (or diffusion approximation) approximation of Vysikaylo's perturbation theory for a small parameter l_u/L « 1.

All processes in gas discharge plasma are determined by the parameter E/N. This was already known to Stoletov. Detailed experimental measurements of the profiles of the processes of birth, death, transfer of charged and excited plasma particles from the parameter E/N were obtained by Townsend and his followers, see references in [2,5,7,8]. For this reason, the Schottky's diffusion field – $\boldsymbol{E}_1$ should be taken into account in all these processes. Such an account leads to a number of ambipolar drifts and ambipolar diffusions [2,5,7,8]. This is the modification of the Schottky method. It was performed by Vysikaylo in 1987. According to this modification, the most significant term is the ambipolar drift, caused by taking into account the diffusion field $\boldsymbol{E}_1$ in the ion source - $\nu_i\nu_i^*(D_{e0}/\mu_{e0})\ \nabla n_e$. This term takes into account the non-uniformity of the electric field in the ionization term ($I_i = \nu_i n_e$, $\nu^*_{i0} = \partial \ln \nu^*_{i0}/\partial \ln\gamma$, $\gamma = E_0/N$).

A similar account should be taken of the inhomogeneity of the electric field ($\boldsymbol{E} = \boldsymbol{E}_0 + \boldsymbol{E}_1$) in the Euler equation for momentum transfer (and taking into

account the term with $\boldsymbol{V}_{i,e}\nabla\boldsymbol{V}_{i,e}$ as a small addition). This leads to the appearance of Vysikaylo-Euler's ambipolar diffusions for electrons and ions, see ref. in /1/.

Taking into account the displacement currents in (3) leads to the appearance of a perturbation of the electric field $\boldsymbol{E}_1 = [1/(4\pi e)]\ (\partial\boldsymbol{E}_0/\partial t)/(n_e\mu_{e0})$. This perturbation, when taken into account in equation (1) (using the Schottky method), leads to the appearance of mixed derivatives (the second derivative with respect to time and one with respect to coordinates) and the renormalization of all terms with mixed derivatives with respect to time and coordinates. This makes the problem quite complex and (given the importance of these processes) it requires complex equipment for photographing non-stationary structures in inhomogeneous plasma. We will restrict ourselves to the case of very small values of $\boldsymbol{E}_1$ in (1). Displacement currents and the ambipolar plasma flows arising from them are significant at the initial stages of the discharge. Below we will focus on photographs of the quasi-stationary stage of a non-uniform discharge with profiles of electric field shock waves (here the Vysikaylo-Poisson's diffusion is important) and Vysikaylo's plasma nozzles (here the ambipolar drifts and gas pumping are important). The gas pressure in the experiments was 15 Torr, so we will neglect the displacement currents and the ambipolar Schottky's and Vysikaylo-Euler's diffusions. Thus, we will limit ourselves to the ***zero approximation*** in Vysikaylo's perturbation theory /1/ and compare the theoretical results with photographs of the glow profiles of a ***quasi-stationary*** self-focusing inhomogeneous discharge.

In ***zero*** approximation, the drift velocity of electrons and ions is described by the relations: $\boldsymbol{V}_{e0} = \mu_{e0}\boldsymbol{E}_0$, $\boldsymbol{V}_{i0} = \mu_{i0}\boldsymbol{E}_0 + \boldsymbol{U}$. Here the mobilities of electrons– μ_{e0} и ионов – μ_{i0} are presented respectively. From (1) and (3) in the zero approximation ($\mu_{j0}n_e\nabla\boldsymbol{E}_0 = -\boldsymbol{E}_0\nabla(\mu_{J0}n_e)$) we obtain a non-stationary 3D equation for simple plasma /1/:

$$\partial n_e/\partial t - \partial[(\boldsymbol{l}_{E0}/\mu_{e0})\nabla](\mu_{e0}n_e)/\partial t + (\boldsymbol{j}/e)\nabla(\mu_{i0}/\mu_{e0}) + \boldsymbol{U}\nabla n_e - \nabla(\boldsymbol{U}(\boldsymbol{l}_{E0}/\mu_{e0})\nabla(\mu_{e0}n_e)) - \nabla\{\boldsymbol{l}_{E0}(\mu_{i0}\boldsymbol{E}_0/\mu_{e0}\nabla)(\mu_{e0}n_e)\} - \beta n_e(\boldsymbol{l}_{E0}/\mu_{e0})\nabla(\mu_{e0}n_e) + \mu_i m_i(\boldsymbol{g}/z_i e)\nabla n_i - (\mu_i\mu_e[\boldsymbol{E}\times\boldsymbol{H}]/c)\nabla n = I_{i0} - R_{i0};\quad \boldsymbol{l}_{E0} = \boldsymbol{E}_0/(4\pi e n_e). \qquad (5)$$

The four-dimensional Vysikaylo's equation (5) is derived from (1) by modifying the ion concentration n_i by $n_e - (\boldsymbol{l}_{E0}\nabla)(n_e\mu_{e0})/\mu_{e0}$. ***Equation (5) is the Navier-Stokes equation modified by Vysikaylo to account for the violation of plasma electroneutrality***. The terms with the vector $\boldsymbol{l}_{e0}$ in (5) arise due to the violation of electroneutrality.

References

1. **Vysikaylo P.I.**: (2024). 4D Perturbation Theory for Describing Nonlinear Interaction of Electric Field with Matter. Vysikaylo's Electric Field Shock Waves and Plasma Nozzles. J Sen Net Data Comm, 4(3), 01-24.

ON THE INFLUENCE OF CONTROL PARAMETERS IN PLASMA CHEMICAL ETCHING ON THE SPATIAL UNIFORMITY OF PLASMA IN A REACTOR

Y. Zakharov[1,2], A. Efremov[2]

[1]Moscow Institute of Physics and Technology (National Research University), 141701, Russia, Dolgoprudny, Moscow Region, Insitutskiy per., 9
[2]JSC "Molecular Electronics Research Institute" (MERI), 124460, Russia, Moscow, Zelenograd, Akademika Valieva st., 6/1

Plasma processes are widely used in microelectronics technology for depositing various functional layers and their patterning (etching) in inductively coupled plasma (ICP) reactors operating at RF (13.56 MHz) discharge [1, 3]. The key advantage of such systems is the ability to independently control the fluxes of reactive species and ion energy, enabling flexible adjustment of etch rate, selectivity, and profile anisotropy.

The primary technological challenge in plasma etching remains ensuring high uniformity (≥95%) across large-diameter wafers, which is complicated by spatial non-uniformities in reactive species concentrations. These non-uniformities arise due to spatial variations in particle generation rates via electron-impact processes (caused by inhomogeneous electromagnetic fields associated with inductor geometry and dimensions) and a sharp increase in radical and positive ion densities near the chamber walls (due to heterogeneous recombination, which dominates at pressures below 100 mTorr).

Achieving uniform plasma etching is further complicated by the multifactorial interdependence between control parameters (gas flow rate, pressure, input power, gas mixture composition) and the steady-state plasma conditions. Consequently, optimizing process parameters and reactor design requires a comprehensive approach and cannot be resolved solely through experimental methods. Significant progress in this field can be achieved through computational modeling of plasma processes, which enables the creation of a "digital twin" of the reactor and facilitates virtual experimentation without substantial time and material costs.

The objective of this study was to develop a two-dimensional (2D) plasma model for a planar reactor (with a top-mounted flat spiral inductor) under typical plasma etching conditions. The research focused on an Ar + Cl_2 plasma, with the initial gas mixture composition, input power, gas flow rate, and pressure serving as variable control parameters. This system was chosen due to its well-documented properties, which eliminate critical uncertainties in the kinetic scheme and ensure model validation through comparison with independent experimental and computational data. The simulations were performed using

COMSOL 6.2 software.

The modeling results demonstrated satisfactory agreement with experimental data on electron temperature and density when using the kinetic scheme recommended in [2]. The key trends in the spatial distribution of plasma parameters can be summarized as follows:

1) Gas pressure increase (Fig. 1) enhances plasma non-uniformity, causing a sharp decline in electron density from the axis toward the walls. This is attributed to the reduced mean free path and electron diffusion coefficient, hindering electron transport from the central reactor zone (where electron-impact ionization rates are highest) to the walls. The electron temperature decreases due to higher collision frequencies with gas particles and increased energy losses in elastic and inelastic processes.
2) Higher gas flow rate (Fig. 2) produces an effect similar to pressure but with a key distinction: the sharp drop in electron density is localized near the walls, while the central region (aligned with the wafer position) remains relatively uniform.
3) Increased input power (Fig. 3) has a minor effect on the spatial distribution of particle densities but raises the absolute values of electron temperature and density at any fixed point. This results from enhanced total ionization rates, higher Cl_2 dissociation degrees, and reduced electron energy losses due to the growing fraction of atomic species. Atomic species predominantly undergo electronic excitation, which has higher threshold energies compared to vibrational and electronic excitation in Cl_2 molecules.
4) Higher argon fraction in the plasma mixture (Fig. 4) reduces plasma uniformity by eliminating the region of constant electron density in the processing zone. This stems from the transition of electron diffusion mechanisms—from free diffusion (typical for electronegative gases) to ambipolar diffusion (dominant in electropositive gases) - leading to a lower electron diffusion coefficient. The decrease in absolute electron density is explained by Ar's higher ionization potential compared to chlorine-containing species.

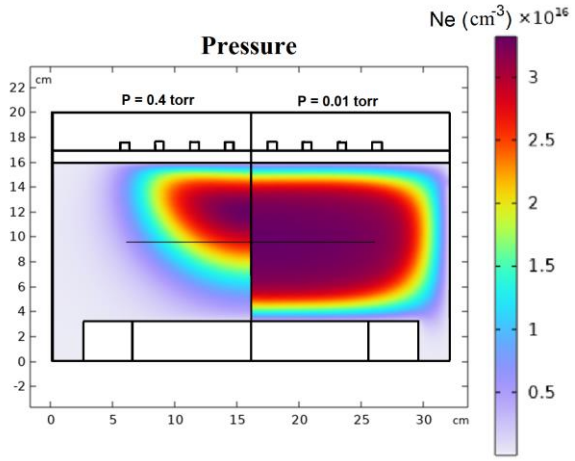

Fig. 1. Electron density variation with gas pressure in 50% Ar + 50% Cl_2 plasma.

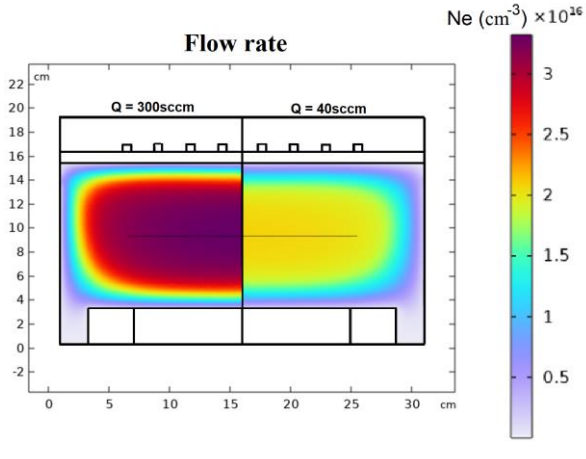

Fig. 2. Electron density variation with gas flow rate in 50% Ar + 50% Cl_2 plasma.

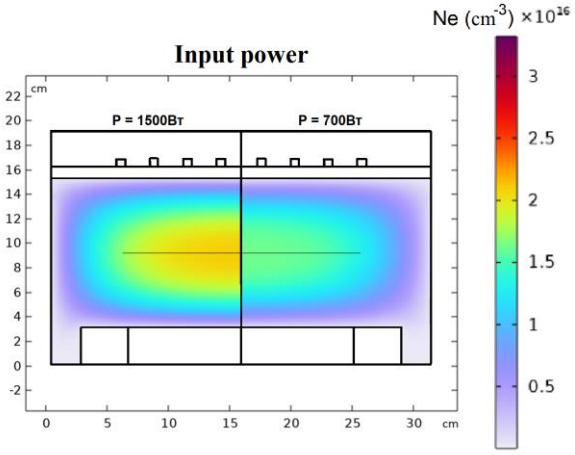

Fig. 3. Electron density variation with input power in 50% Ar + 50% Cl_2 plasma.

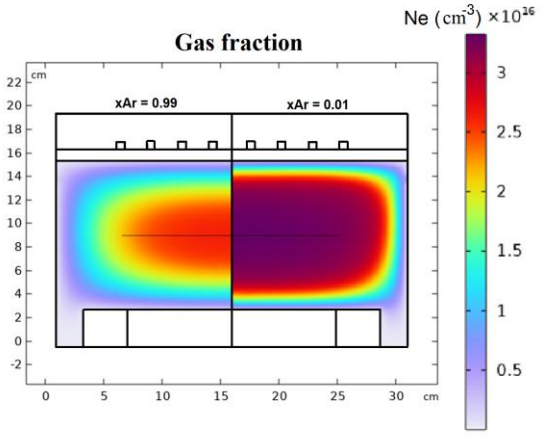

Fig. 4. Electron density variation with gas mixture composition.

Acknowledgements. This work was supported by the Molecular Electronics Research Institute.

References

1. Efremov A. M., Lee J., Kwon K.-H. A comparative study of CF_4, Cl_2 and HBr + Ar inductively coupled plasmas for dry etching applications // Thin Solid Films. 2017. V. 629. P. 39–48. DOI: 10.1016/j.tsf.2017.03.035.
2. Lieberman M. A., Lichtenberg A. J. Principles of Plasma Discharges and Materials Processing. — Hoboken: John Wiley & Sons, 2005.

NUMERICAL MODELING OF STREAMER DISCHARGE USING ADAPTIVE MESH AND MASS CORRECTION

A.S. Kirillov[1], Shershunova E.A.[1], V.V. Voevodin[1], V.A. Yamshchikov[1], Ya.E. Zharkov[1]

[1]IEE RAS, Russia, Saint-Petersburg, Palace Embankment, 18a, 191181,
E-mail: yarik77794@mail.ru

Abstract: This work presents a numerical approach for modeling streamer discharges using an adaptive mesh combined with optimization-based mass correction of logarithmic fields. The method ensures local mass conservation and accurate front resolution. Numerical results demonstrate a 3.2× reduction in computational cost compared to fixed-grid simulations while preserving key discharge characteristics.

A streamer discharge represents a non-equilibrium formation of a plasma channel in a strong electric field and plays a significant role both in natural phenomena and in applied technologies, including plasma actuators based on surface dielectric barrier discharges (SDBDs) [1]. The efficiency of such actuators is largely determined by the structure of the streamer front and the distribution of surface charges, necessitating precise resolution of local electric field characteristics. In numerical practice, hydrodynamic models are most commonly employed for streamer simulation, offering a compromise between physical accuracy and computational feasibility. However, the presence of steep gradients near the streamer head demands fine spatial resolution, which significantly increases the computational burden. To enhance numerical stability, logarithmic transformations and various temporal or spatial filters are often applied; although effective in suppressing instabilities, these techniques may compromise solution accuracy and lead to violations of local charge conservation.

Adaptive mesh refinement (AMR) methods help reduce computational costs and are known for their robustness [2], but most existing implementations do not account for the specific features of logarithmic formulations. Such remeshing procedures may result in charge loss at cell interfaces, undermining the consistency of the solution. To address this issue, the present work introduces an adaptive remeshing strategy coupled with an optimization-based correction of logarithmic concentration fields. This approach ensures strict local mass conservation while maintaining accurate resolution of the streamer front.

The simulation is conducted for a canonical surface dielectric barrier discharge configuration (Fig. 1), comprising a 3.4 mm air gap and a 2.8 mm dielectric substrate with a relative permittivity of 3.5. A surface high-voltage (HV) electrode with a rectangular cross-section (40 μm in height and a 5 μm edge

radius) is positioned at the interface between the two media. A voltage pulse of positive polarity, linearly rising to 8 kV over 30 ns, is applied to the HV electrode. One edge of the surface electrode is electrostatically shielded by a second electrode embedded within the dielectric and maintained at the same potential.

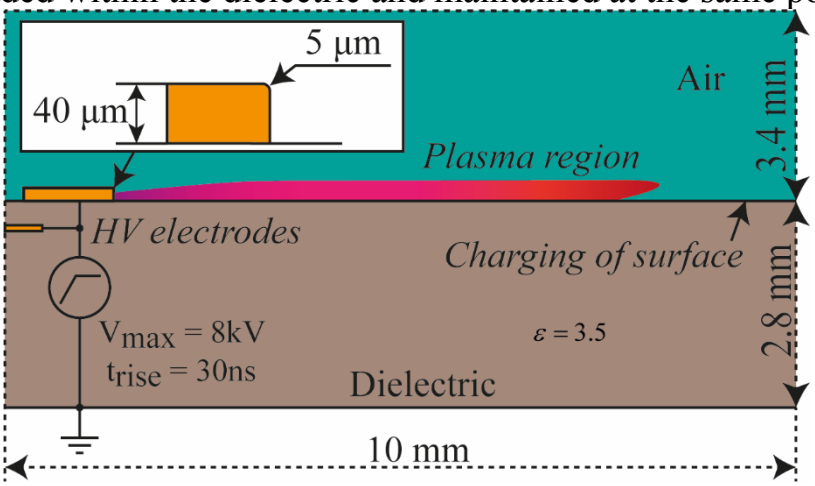

Figure 1 – Domain Setup with Electrode and Dielectric Parameters

Numerical modeling was performed using a drift-diffusion plasma model in the mean electron energy approximation, coupled with the Poisson equation for the electric potential and a surface charge accumulation model on the dielectric interface

$$\begin{gathered}\frac{\partial n_e}{\partial t}+\nabla\cdot\left(-\mu_e n_e \mathrm{E}-D_e\nabla n_e\right)=S_{\mathrm{ion}}+S_{\mathrm{ph}}-R_{\mathrm{att}},\\ \frac{\partial n_e\varepsilon}{\partial t}+\nabla\cdot\left(-\mu_e n_e\varepsilon \mathrm{E}-D_e\nabla\left(n_e\varepsilon\right)\right)=\mathrm{E}J_e-\sum_j R_j\Delta\varepsilon_j,\\ \frac{\partial n_i}{\partial t}+\nabla\cdot\left(-z_i\mu_i n_i \mathrm{E}-D_i\nabla n_i\right)=S_{\mathrm{i}}-R_{\mathrm{i}},\\ \nabla^2 V=-e\left(-n_e+\sum_{i=1}^{N_{\mathrm{ions}}} z_{\mathrm{i}} n_{\mathrm{i}}\right)\varepsilon_{\mathrm{m}}^{-1},\quad \frac{\partial\rho_s}{\partial t}=-en\cdot\left(\Gamma_e-\sum_{i=1}^{N_{\mathrm{ions}}} z_{\mathrm{i}}\Gamma_i\right).\end{gathered} \tag{1}$$

Here, μ_e and μ_ε, D_e and D_ε – denote the mobilities and diffusion coefficients of electrons and their mean energy, respectively; S_{ion}, S_{ph}, R_{att} – are source terms accounting for impact ionization, photoionization, and electron loss due to attachment; E, J_e, R_j, $\Delta\varepsilon_j$ – represent the electron heating due to the electric field E at current density J_e and the cooling effect from inelastic collisions characterized by reaction rates R_j and energy losses $\Delta\varepsilon_j$; z_i – is the charge sign of ion species; S_i and R_i – are the corresponding source and loss terms; Γ_e и Γ_i – denote the fluxes of electrons and ions near the dielectric boundary; n is the unit normal to the surface.

Photoionization processes in the model are accounted for using the SP_3 approximation of the radiative transfer equation. The photon source term is based

on a generalized de-excitation reaction of singlet excited states of the N_2 molecule, with characteristic energies around 12.8 eV. Transport and energy coefficients were obtained using the BOLSIG+ solver, while chemical reaction kinetics were constructed based on data from the SIGLO and IAA databases [3].

To implement the adaptive remeshing algorithm with mass-conservative field transfer, an interface between MATLAB and COMSOL Multiphysics was employed. This approach facilitates development and debugging by enabling control from MATLAB while delegating the solution of physical models to COMSOL.

The algorithm, schematically shown in Fig. 2, consists of an initialization stage (including the generation of a mesh adaptation map, a list of time points, the model interface, and correction parameters) and an iterative cycle comprising:

(I) simulation of streamer propagation until a remeshing criterion is met, based on the detection of streamer head exiting the high-resolution zone; (II) update of the mesh adaptation map; (III) remeshing and interpolation of fields; (IV) solution of the correction problem using Karush–Kuhn–Tucker (KKT) conditions; (V) upload of the corrected fields into the model via weak-form expressions.

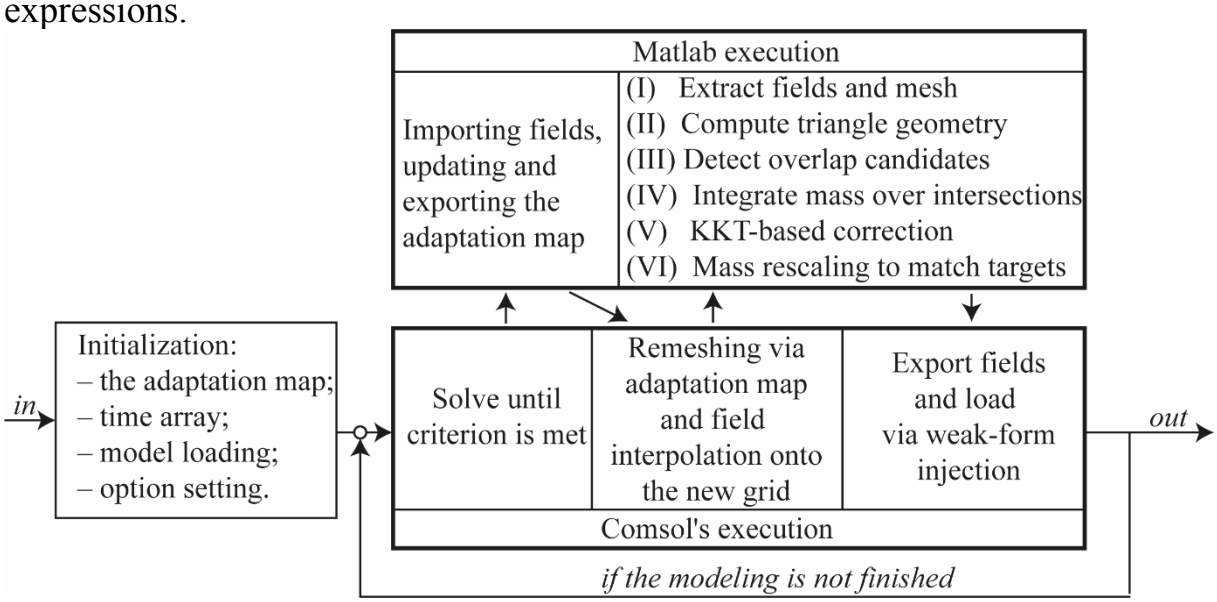

Figure 2 – Sequence of Adaptive Mesh Update and Field Adjustment

To ensure accurate transfer of logarithmic fields onto the new adaptive mesh, an optimization-based correction procedure is employed, incorporating Karush–Kuhn–Tucker (KKT) conditions to strictly enforce target mass constraints. The minimization problem is formulated as a variationally regularized system, with modifications to the Hessian that include Tikhonov regularization, a discrete graph Laplacian, and a directionally scaled diagonal approximation of $J^{\mathrm{T}}J$. Each subproblem is solved within a trust region using a dogleg strategy, with step sizes adjusted based on a trust-ratio criterion. Field components are identified

automatically, partitioned using METIS, and processed iteratively. Global consistency is restored by applying a smoothing procedure that reconciles local corrections with the overall field distribution.

Numerical studies have shown that the use of an adaptive mesh reduces computation time by a factor of 3.2 compared to a fixed mesh, while preserving the waveform of the high-voltage electrode current and the surface-directed thrust. The spatial distributions of charged particle densities exhibit good agreement between both models.

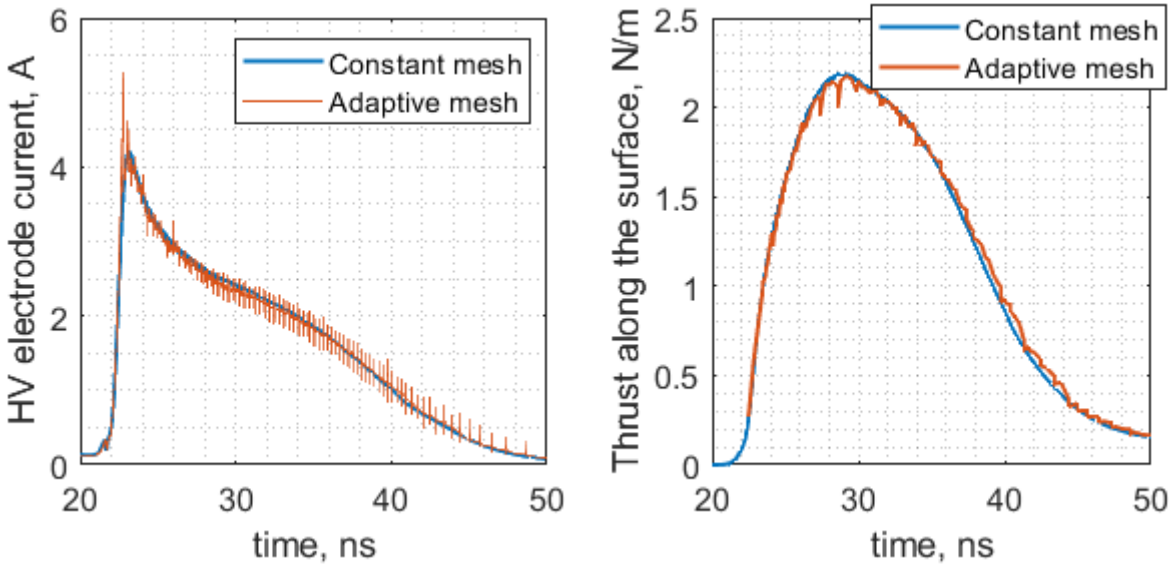

a) *b*)

Figure 3 – Comparison of simulated waveforms of the high-voltage electrode current (a) and surface thrust (b) obtained using fixed and adaptive meshes

Acknowledgements. The results of the study were obtained with financial support from the Russian Federation represented by the Ministry of Education and Science of Russia (Grant for major scientific projects in priority areas of scientific and technological development, agreement No. 075-15-2024-558).

References

1. **Dufour T., Sretenovic G., Jorissen K., Reniers F.** The electrohydrodynamic force distribution in surface AC DBD actuators: Do streamers dictate ionic wind profiles // J. Phys. D: Appl. Phys. – 2021. – Vol. 54, No. 22. – Art. 225201. – DOI: 10.1088/1361-6463/abf53e.

2. **Bochev P., Gunzburger M., Peterson J., Shashkov M.** Formulation, analysis and numerical study of an optimization-based conservative interpolation (remap) of scalar fields for arbitrary Lagrangian–Eulerian methods // J. Comput. Phys. – 2011. – Vol. 230, No. 13. – P. 5199–5225. – DOI: 10.1016/j.jcp.2011.03.017.

3. Siglo and IAA database [Electronic resource] // LXCat. – URL: https://us.lxcat.net/ (accessed January 5, 2025).

APPLICATION OF OPEN FOAM PACKAGE FOR MODELING HIGH-FREQUENCY DISCHARGE WITH LIQUID JET ELECTRODES

F. Khairullin, Al. Gaisin, V. Zheltukhin

A.N. Tupolev's Kazan National Research Technical University,
10, K. Marx St., Kazan, Russia
khayrullin.farkhad@mail.ru, almaz87@mail.ru, vzheltukhin@gmail.com

Electric discharge with liquid electrodes is used in industry for surface treatment and obtaining materials with specified properties. In the field of ecology and health care, this discharge can be used to clean the surface of solids, water and air.

This type of discharge is generated by direct or alternating current in the interelectrode gap, where one or both electrodes are a flowing or non-flowing liquid. Solutions of salts of various concentrations in water are used as liquid electrodes. Depending on the set voltage, pressure, configuration and type of electrodes, speed and nature of the flow of the medium, there are different types and forms of combustion of an electric discharge. In this area of science, the issues of understanding the processes occurring both in plasma generated by an electric discharge and in flows of homogeneous and multiphase interacting media are relevant.

The mechanisms of electrical breakdown in discharges with liquid electrodes are basically the same as in the case of metal electrodes. The main difference between discharges with liquid electrodes and the same discharges with solid electrodes is that in the first case, the breakdown and subsequent maintenance of the discharge is preceded by the formation of a vapor-gas phase, which is the plasma-forming medium.

For the breakdown of a gas, the presence of free electrons in it is essential, since it is they that perceive the energy of the electric field and create an electron avalanche, which is the primary cause of the breakdown. There are several mechanisms of electron emission from the surface occurs: photoelectron, thermionic, secondary electron, ion-electron, and field emission. To implement the first four mechanisms, at the moment of jet rupture and formation of an electrical gap, there are not enough initiating factors. Therefore, the most probable mechanism seems to be field emission. To implement it, it is necessary to create an electric field with a strength of $E = 10^9–10^{10}$ V/m [1].

To predict the properties of materials and understand the mechanism of the effect of discharge by liquid electrodes on the material, an urgent task is to establish the dependence of the discharge parameters. The complexity of this task is reflected in the presence of three interacting environments: the liquid jet, the plasma of the vapor-gas discharge and the surrounding neutral gas.

At present, a general theory of discharge with liquid electrodes has not been established. The objective of this work is to develop a simplified mathematical model of discharge by liquid electrodes.

The most complete description of the hydrodynamic model of a jet discharge with liquid electrodes in the pressure range $p=10^3$–10^5 Pa, discharge current 10–20 A, voltage 10^{-1}–10 kV presented in the work [1].

The experimental setup consists of an electrolytic bath, an aluminum tube and an electrolyte. The basic diagram of the installation for the case of a cathode electrolyte is shown in Fig. 1.

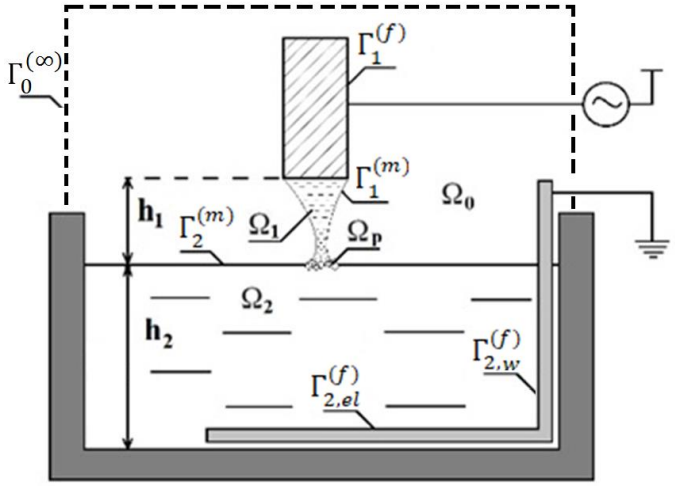

Fig. 1. Diagram of discharge regions with liquid electrodes

For the numerical implementation of the mathematical model of a jet discharge with liquid electrodes, we will consider several simplified models, the implementation of which will allow us to convey the main properties of the discharge at a qualitative level and will subsequently allow us to combine them and construct a numerical model that takes into account the main processes in the discharge.

1. Breakdown modeling

It is known that for a breakdown to occur, the presence of free (primary) charged particles and an electric field that gives them directed movement is necessary. In previous studies, the mechanism of formation of ring plasma structures was substantiated based on experimental and numerical studies [2]. The discharge occurs in places where the jet narrows or where it transitions into a droplet flow as a result of the electric field being strengthened when the jet radius is reduced to 1 mm.

In the work [1] it is shown that breakdown occurs at the point of narrowing of the jet, or its transition to the drop phase (Fig. 2), where the amplitude of the current density in the jet reaches values $\geq 10^6 \mathrm{A/m^2}$, and the electric field strength on the surface of the jet exceeds 10^9 V/m.

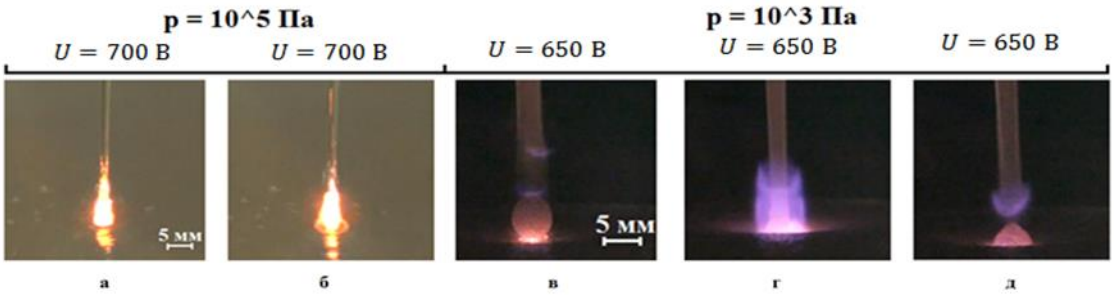

Fig. 2. Electric discharge between the jet cathode and the liquid anode at different currents and interelectrode distances/

In a jet discharge, the electric field is created by two sources: the potential difference between the electrodes and the current of charged particles in the jet. Therefore, to calculate the EMF it is necessary to use the complete system of Maxwell's equations.

$$\nabla \times \vec{H} = \vec{j} + \frac{\partial \vec{D}}{\partial t}, \qquad \nabla \times \vec{E} = -\frac{\partial \vec{B}}{\partial t}, \tag{1}$$

$$\nabla \cdot \vec{B} = 0, \ \nabla \cdot \vec{D} = e(n_+ - n_-), \text{at } r \in \Omega, \tag{2}$$

where n_+ is a number density of positive ions, n_- is a number density of negative ions and electrons, $\vec{B}$, $\vec{H}$ are magnetic induction and magnetic intensity vectors, consequently, $\vec{B} = \mu_0 \mu \vec{H}$, $\vec{D} = \varepsilon_0 \varepsilon \vec{E}$, $\varepsilon_0, \varepsilon$ are electric constant and relative permittivity of the electrolyte, Ω is the model domain. Equation (3) is supplemented by the charge conservation equation.

$$\frac{\partial q_i}{\partial t} + \nabla \cdot \vec{j}_i = W_i - \sum_m k_{im}^{(r)} n_i^+ n_m^-, \tag{3}$$

where $\vec{j}_i = e\left(Z_i n_i b_i \vec{E} - D_i \nabla n_i + \vec{V} n_i\right)$, index i indicates the type of ions, $q_i = eZ_i n_i$ is charge densities, W_i is dissociation rate of neutrals such molecules, ion pairs, etc., $k_{im}^{(r)}$ is recombination coefficients of charged particles indexed i,m, Z_i is charge number of the ion with sign, b_i, D_i is mobility and diffusion coefficients, $\vec{V}$ is liquid flow velocity.

2. Jet flow modeling

Let us consider the flow of electrolyte through a small diameter hole under the action of gravity in a two-dimensional approximation. At the initial moment of time, water begins to flow out of the hole to fill the bathtub. The water entry velocity at the inlet section into the inlet chamber is 0.1 m/s. The case is a free surface problem with an abrupt transition between two liquid and gaseous phases [3].

Fluid Dynamics models are used to describe fluid flow [4]. The model includes the following equations:

$$\rho_k \left[\frac{\partial V_k}{\partial t} + \left(\vec{V}_k \cdot \nabla\right)\vec{V}_k\right] = -\nabla p_k' + \eta_k \Delta \vec{V}_k + g\rho_k + q_k \vec{E}_k, \tag{4}$$

$$\nabla \cdot \vec{V}_k = 0, \text{ at } r \in \Omega_k, \ k = 0, 2, \ p \quad (5)$$

Here the index k means that the corresponding quantity is defined in the domain Ω_k: ρ_k is density of liquid, $\vec{V}_k = V_{k,x}\vec{e}_x + V_{k,y}\vec{e}_y + V_{k,z}\vec{e}_z$ is velocity field, $V_{k,x}, V_{k,y}, V_{k,z}$ are its components, $\vec{e}_x, \vec{e}_y, \vec{e}_z$ are coordinate system orts, p'_k is total (hydrodynamic and electrostrictive) pressure, η_k is coefficient of dynamic viscosity, g is acceleration of gravity, q_k is spatial electric charge, $\vec{E}_k$ is electric field strength, $\vec{r} = x\vec{e}_x + y\vec{e}_y + z\vec{e}_z$ is radius vector.

To create and maintain a vapor-gas discharge plasma, it is necessary to include the equation for conservation of thermal energy in the model.

$$\rho_k C_{p,k} \frac{\partial T_k}{\partial t} - \nabla\left(\lambda_{T,k} \nabla T_k - \rho_k C_{p,k} V_k T_k\right) = \vec{j}\vec{E}, \text{at } r \in \Omega_k, k = 1,2, \quad (4)$$

where $C_{p,k}$ – heat capacity, $\lambda_{T,k}$ – thermal conductivity, T_k – temperature of the electrolyte in the region Ω_k.

To solve this problem, an open integrated platform for numerical modeling of continuum mechanics problems, OpenFOAM (Open Source Field Operation And Manipulation), is used [5].

The modeling of the vapor-gas shell is a jet flow with a preceding breakdown between the liquid electrolyte and the anode. A stable turbulent flow with an initial electrolyte velocity of 0.05 m/s forms a cylinder with a radius of 1.00–1.25 mm and a thickness of 20 mm. The maximum breakdown thickness value depends on the current frequency and the liquid flow rate.

References

1. **Gaisin A.F.** High-frequency and direct current electrical discharges with liquid and solid electrodes. Kazan, (2019).
2. **Zheltukhin V.S. et al.** Breakdown mechanism of high-frequency discharge with jet electrolytic electrodes, Letters to the Journal of Technical Physics, 48:17 (2022), 24–27.
3. **Bruggeman P.G. et al.** Plasma Chemistry Model of Surface Microdischarge in Humid Air and Dynamics of Reactive Neutral Species. Journal of Physics D: Applied Physics, 45, (2012).
4. **Hemida H.** OpenFOAM tutorial: Free surface tutorial using interFoam and rasInterFoam. Göteborg, (2008).
5. **Jasak H.** OpenFOAM: Open source CFD in research and industry, International Journal of Naval Architecture and Ocean Engineering, 1 (2009) 89–94.

FISSILE PLASMA GAS DYNAMICS

S. Kunakov[1], A. Shapiyeva[2]

[1]Suleyman Demirel University, Almaty, Kazakhstan, sandybeck.kunakov@gmail.com
[2]International Information Technology University, Almaty, Kazakhstan, aikombi@gmail.com

A fissile gas, composed of atoms capable of undergoing neutron-induced fission, exhibits complex behavior due to internal coupling between nuclear reaction products and neutral gas components. This study develops a self-consistent theoretical framework for the gas dynamics of weakly ionized fissile plasma. Starting from the Boltzmann kinetic equations for neutral particles, fission fragments, and electrons, we derive the macroscopic hydrodynamic equations. The model reveals that the energy exchange processes significantly alter the transport properties of the medium, impacting both the chemical and thermodynamic structure of the gas.

1. Introduction

Fissile gases such as ^{3}He and $^{235}UF_6$ are known to undergo fission when irradiated with thermal neutrons, releasing high-energy fragments and electrons. These products initiate ionization, excitation, and energy transfer to neutral particles, thereby forming a weakly ionized plasma. Conventional hydrodynamic models often neglect these interactions. Here, we present a theoretical formulation that consistently incorporates these nuclear-driven microphysical effects into a macroscopic framework, extending prior studies /1,2,3/.

2. Kinetic Formulation

We consider a multi-component system described by Boltzmann kinetic equations for neutrals, neutrons (treated parametrically), fission fragments, and electrons. The dominant nuclear reactions include:

$$^3He + n \rightarrow p + T + 0.76\ MeV \quad (1)$$

$$^{235}UF_6 + n \rightarrow ff_1 + ff_2 + 165\ MeV \quad (2)$$

These reactions generate fast particles that interact with the gas via elastic and inelastic collisions, leading to energy and momentum redistribution. Elastic collisions dominate the early thermalization stage, especially between heavy fission fragments and neutral atoms /4,5/.

Electron dynamics are modeled by including sources from direct fission, impact ionization, and recombination, while the loss mechanisms include attachments to electronegative species and recombination with positive ions /6/.

3. Hydrodynamic model

From the kinetic equations, we derive macroscopic balance laws for mass, momentum, and energy. The continuity equation for neutrals includes losses due to neutron-induced fission and inelastic interactions.

$$\frac{\partial n_a}{\partial t} + \nabla \cdot (n_a \vec{u}) = -S_{fission} - \sum_k S_k, \tag{3}$$

where S_k accounts for ionization and excitation by fission products.

Energy transfer from fragments and electrons leads to rapid heating of the gas, altering local temperature and flow. The energy equation includes contributions from the kinetic degradation of fission fragments and primary electrons:

$$\frac{\partial}{\partial t}\left(\frac{3}{2}\rho_a R T_a + \frac{1}{2}\rho_a u^2\right) = -\nabla \cdot \vec{q} + \sum_k S_k E_k \tag{4}$$

The electric field formed by charge separation is modeled by the Poisson equation:

$$\nabla \cdot \vec{E} = 4\pi e(\sum_j n_j - n_e) \tag{5}$$

Transport coefficients differ significantly from classical values due to the weak ionization and high energy nature of interactions. Heat flux becomes a nonlinear function of both temperature gradients and particle distributions:

$$\vec{q}(t,\vec{r}) = \lambda \nabla T_a + \chi_{a,e}(T_a - T_e) + \sum_j \chi_{a,j}\left(T_a - T_j\right). \tag{6}$$

4. Conclusion

This work presents a complete framework for modeling the gas dynamics of weakly ionized fissile plasma, incorporating nuclear reaction sources, energy transfer mechanisms, and microscopic interactions into a unified hydrodynamic picture. The model can be applied to nuclear reactors and astrophysical environments, where fission-driven energy exchange dominates the plasma

evolution.

As an illustrative simulations (Figure 1, Figure 2), temperature fields near a uranium sphere in a helium-3 flow under neutron irradiation were computed using COMSOL Multiphysics, showing strong spatial variations consistent with theoretical predictions.

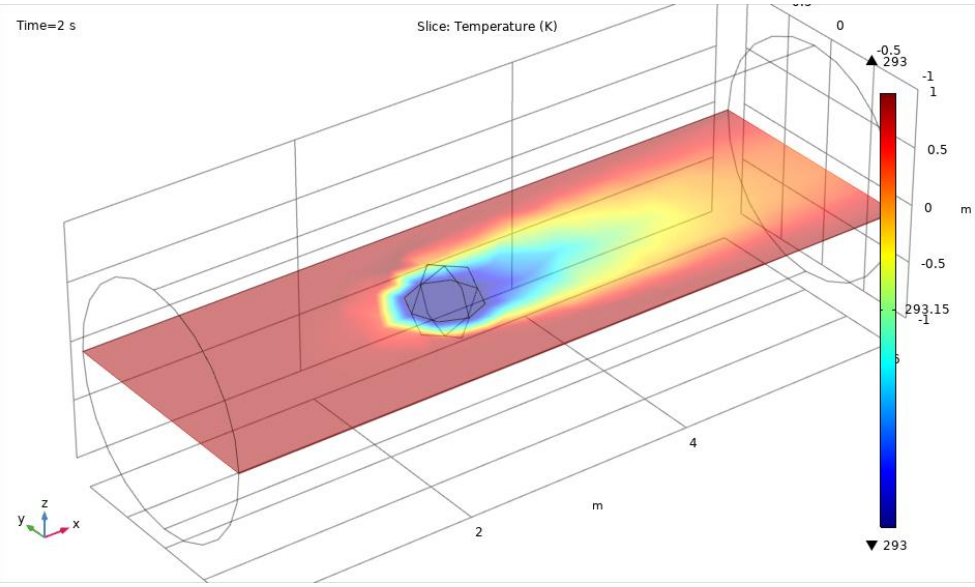

Figure 1. Temperature distribution around a uranium sphere in a helium-3 flow in the presence of an external neutron flux (1 atm)

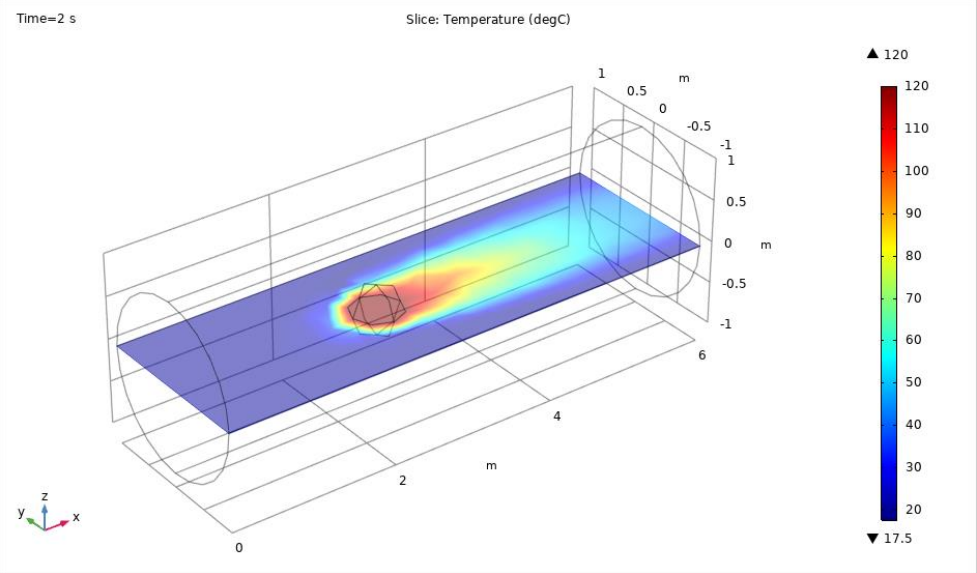

Figure 2. The uranium sphere heated by internal fission processes in the presence of an external neutron flux (0.1atm) streamlined by helium flow.

5. References

1. **Guyot J. C., Miley G. H.** Nucl. Sci. Eng., 48(1972), 373 - 386.
2. **Shapiyeva A., Son E., Kunakov S.**. Contrib. Plasma Phys., e202100174(2022).
3. **Chapman S., Cowling T. G.** The Mathematical Theory of Non-Uniform Gases. Cambridge Univ. Press. (1990).
4. **Gryzinski M.** Phys. Rev., 138(1965), 336.
5. **Holstein T.** Phys. Rev., 70(1946), 367.
6. **Compton R. N.** J. Chem. Phys., 66(1977), 4478–4485.

2. ELECTRICAL DISCHARGES AND OTHER PLASMA SOURCES, NOVEL PLASMA GENERATION APPROACHES

COAXIAL BARRIER DISCHARGE IN ARGON FLOW: ROLE OF SURFACE IONIZATION WAVES IN THE PLASMA STRUCTURES FORMATION

Yu. Akishev, M. Medvedev, A. Petryakov

State Research Center of Russian Federation Troitsk Institute for Innovative and Fusion Research, Moscow, Troitsk, Pushkovykh str., 12, 108840, Russia, akishev@triniti.ru,

Currently, there are many papers devoted to studying the ionization waves in a coaxial barrier discharge in argon. They state that there are two forms of streamers, that is, like a "snake" (Fig.1a) /1/ and straight-line (Fig.1b) /2/ streamers.

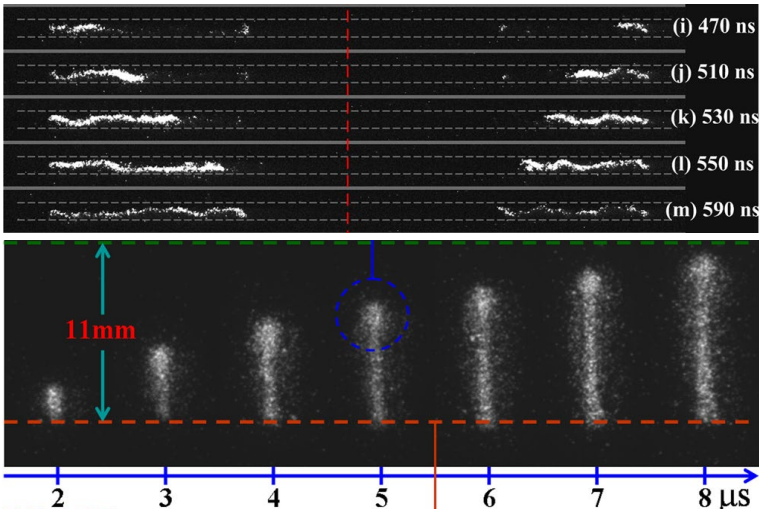

Figure 1. Snake-like (a) and straight-line (b) streamers in a barrier discharge.

However, all these works investigated the propagation of the ionization waves which start from the discharge tube output. We are the first to trace the formation of ionization waves of the snake-like and straight-line streamers starting from their formation in the discharge zone within the tube. Their formation was traced using a high-speed ICCD camera. The coaxial barrier discharge in argon flow at atmospheric pressure was excited by successive trains of sinusoidal voltage, the frequency repetition of which was varied (Figure 2).

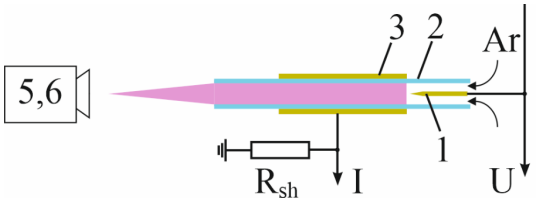

Figure 2. Scheme of the experimental setup.

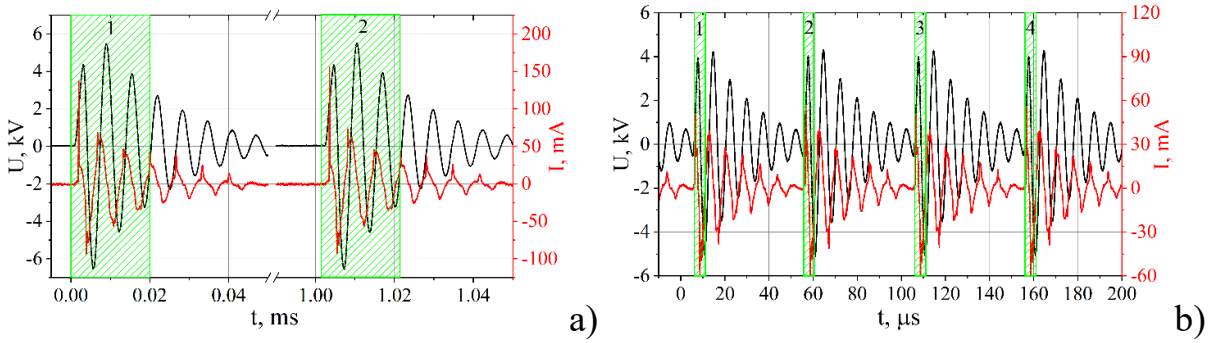

Figure 3. Voltage and current waveforms of sinusoidal zugs at two repetition frequency: a) F=1 kHz; b) F=20 kHz.

A significant difference in the forms of ionization waves in dependence on the repetition frequency F was revealed. The snake-like inside the tube and straight-line streamers outside the tube are shown in figure 4 for the repetition frequency F=100 Hz.

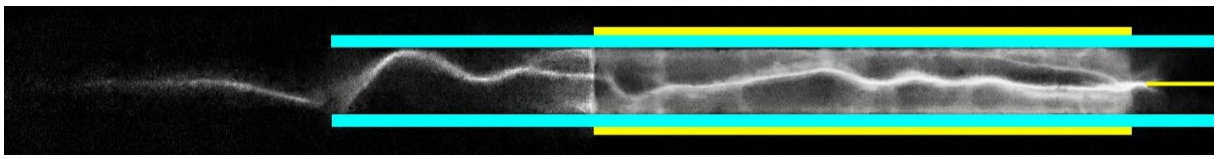

Figure 4. Images of plasma structures in the quartz tube and plasma jet outside the tube. At short exposure time, weak diffuse glow of plasma jet is not detected. Flow direction is from right to left. F = 100 Hz.

In Figure 5, the plasma structure development inside (Fig.5a) and outside (Fig.5b) the discharge tube after the very first breakdown at first positive half-period in the zug is shown. F = 100 Hz. There is no snake-like streamer inside the discharge zone; there is no straight-line streamer outside the tube.

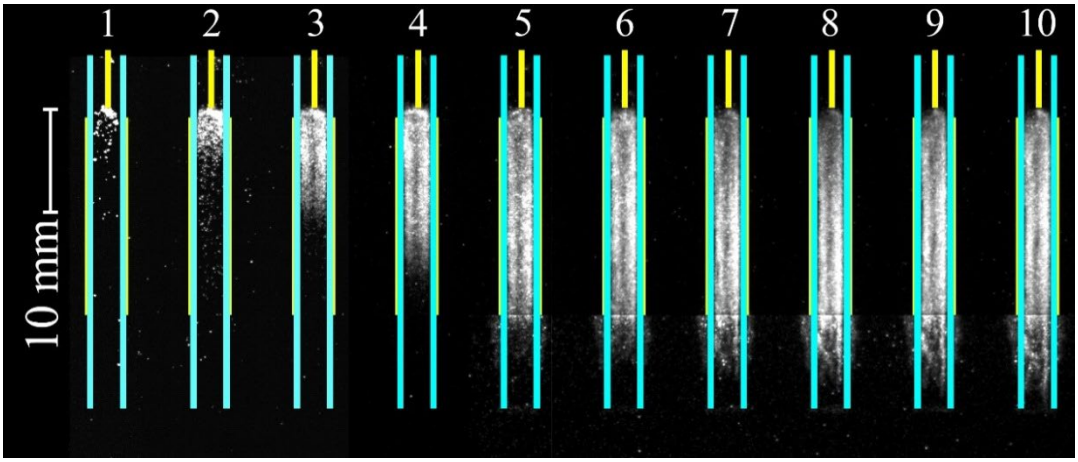

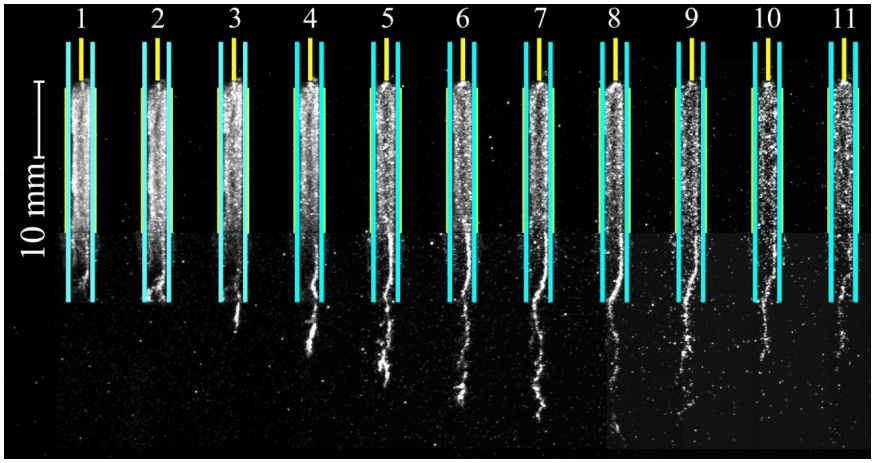

b)

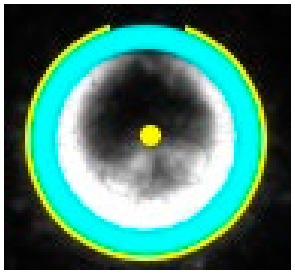

c)

Figure 5. The images demonstrating the plasma structure development inside (a) and outside (b) the discharge tube. c) image taken from the tube face.

Besides, the simultaneous existence of both the diffuse and constricted plasma structures was revealed. These structures are formed jointly by two types of the surface ionization waves, diffuse and constricted ones, arising and disappearing each half-cycle of the periodical applied voltage. The constricted plasma structures have a spatial “memory”. Do plasma structures have a "memory"? Yes, however, it is surprising that they save their spatial pattern only for a time that is much shorter compared to that needed for gas to pass through the discharge zone.

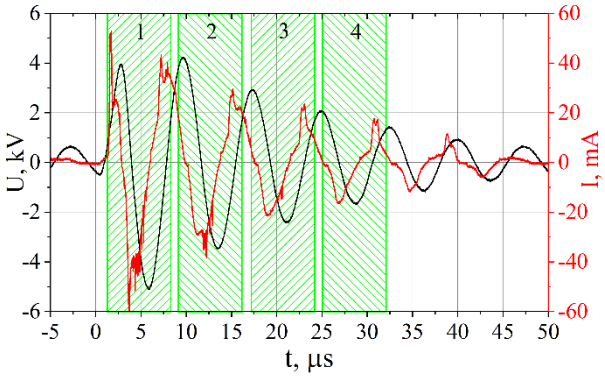

a)

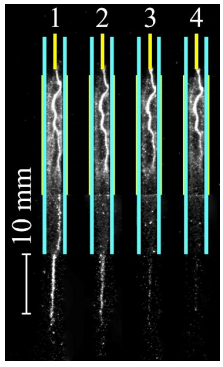

b)

Figure 6. Several cycles in one zug(a) and the images of plasma structure inside the tube (b). Figures 1-4 in a) and b) correspond to the same moments.

Inside one zug, the plasma structure inside the tube repeats from one breakdown to another, that is, each subsequent breakdown follows the path formed by the previous breakdown.

Conclusion.

1) The plasma structure dynamics in a coaxial barrier discharge is determined by the development of surface ionization waves, the propagation of which is accompanied by the surface charge deposition on the tube wall.

2) The conductivity current of surface ionization waves is transferred through the tube wall by a displacement current.

3) Two types of surface ionization wave occur in the discharge zone: diffuse and constricted ones. Diffuse waves propagate both in the forward direction, i.e. from the high-voltage needle towards the tube outlet, and in the opposite direction. The propagation of constricted waves is vitally supported by the electric current of diffuse waves.

4) The equation describing the motion of diffuse waves has the form of a diffusion equation for potential.

5) The plasma jet consists of a bright, constricted plasma filament surrounded by diffuse, faintly luminous plasma. With a low frequency of zugs, the plasma filament has the snake-like shape. With a high frequency of zugs, the plasma filament is straight-line.

Acknowledgement. This work was supported by the Russian Science Foundation (grant No. 24-45-20006).

References

1. **S. Wu, Z. Wang, Q. Huang, X. Tan, X. Lu et al.** Phys. Plasmas 20, 023503 (2013)
2. **A. Kudryavtsev et al.** JOURNAL OF APPLIED PHYSICS 122, 093301 (2017)

SURFACE STREAMER DEVELOPMENT IN BARRIER DISCHARGE IN TRANSVERSE MAGNETIC FIELD

Yu. Akishev, I. Kochetov, A. Petryakov

State Research Center of Russian Federation Troitsk Institute for Innovative and Fusion Research, Moscow, Troitsk, Pushkovikh str. 12, petryakov@triniti.ru

Nonequilibrium low-temperature plasma created by electrical discharges at atmospheric pressure on the surface of solid dielectrics is widely used in various applications. In many cases, surface barrier discharges excited by sinusoidal or pulse-periodic voltage are used to form non-thermal plasma. In the electrode system of surface barrier discharge, a thin rod and a flat plate covered with a dielectric are used. In this case, the rod is perpendicular to the plane (Fig. 1). The surface discharges exist in the form of bright non-stationary thin current filaments called streamers (Fig. 1) with a diameter of 100 - 200 μm.

Surface streamers always originate at the pointed rod and spread from it along the barrier surface. In the process of their propagation, streamers deposit an electric charge on the barrier, the sign of which coincides with the polarity of the voltage applied to the tip. The characteristic propagation velocity of these streamers depends on many parameters, including the type and pressure of gas, the amplitude value and the polarity of the applied voltage. The streamer velocity varies in the range from 10^4 to 10^8 cm/s. The plasma structure formed on the barrier by surface streamers depends on the polarity of the voltage at the tip, and this structure does not repeat from half-period to half-period. Surface streamers exist for a short time and arise anew in each half-period of the applied voltage. The reason for their self-destruction is the charge they deposit.

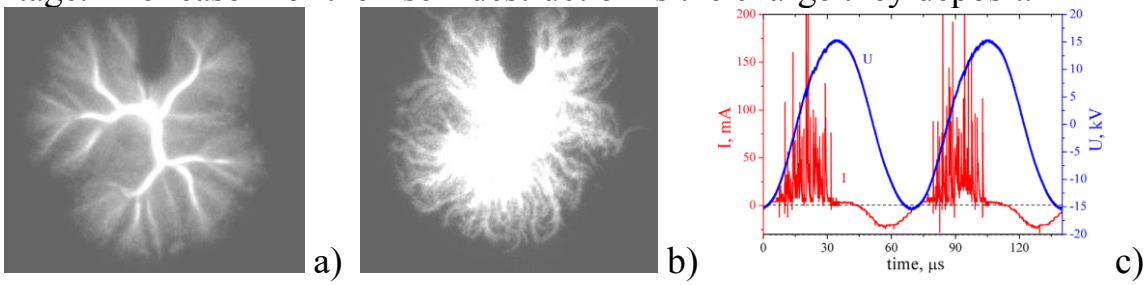

Fig 1. Typical surface barrier discharge electrode system in pin-plane geometry (top view). The pointed end of the rod rests against the dielectric barrier. Surface streamers created by sinusoidal voltage are shown on the barrier surface. a) negative half-period streamers; b) positive half-period streamers; c) discharge current and voltage waveforms.

The superposition of longitudinal and transverse magnetic fields significantly affects the parameters of volume and surface streamers. The terms

longitudinal and transverse magnetic fields define the relationship between the direction of streamer movement and the direction of the magnetic field. If the streamer moves along the magnetic field, the field is longitudinal, if perpendicular to it, the field is transverse.

The transverse magnetic field has the greatest effect on streamers, since it changes the electron transfer coefficients and the electron impact ionization frequency, which affects the speed of streamer propagation. This effect is due to a change in the electron energy distribution function (EEDF) in the presence of a transverse magnetic field, which is shown in Fig. 2a /1/. As can be seen, with an increase in the induction of the transverse magnetic field, the high-energy tail of the distribution function is greatly depleted. This leads to the fact that the average electron energy in the plasma decreases noticeably (Fig. 2b).

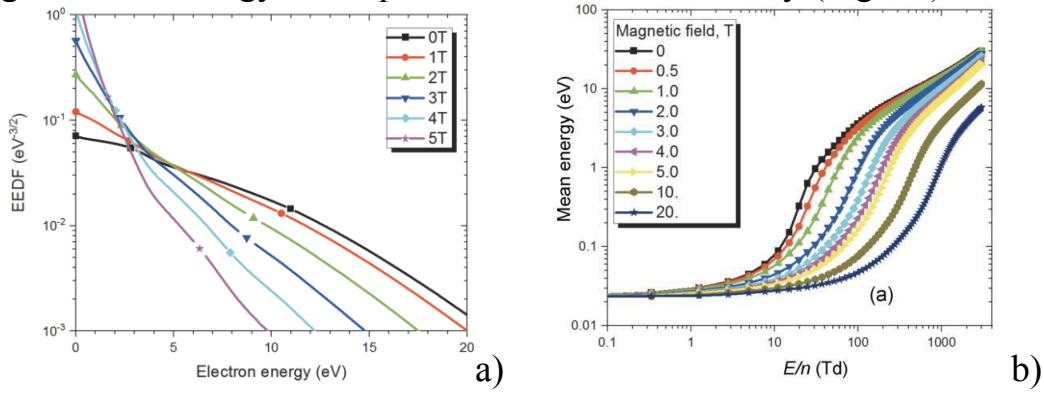

Fig 2. a) the EEDF in CO_2 at E/N=300 Td, P=50 Torr and different magnetic field values. The electric and magnetic fields are perpendicular to each other, b) Average electron energy as a function of the reduced electric field strength at different transverse magnetic fields. CO_2, P = 50 Torr.

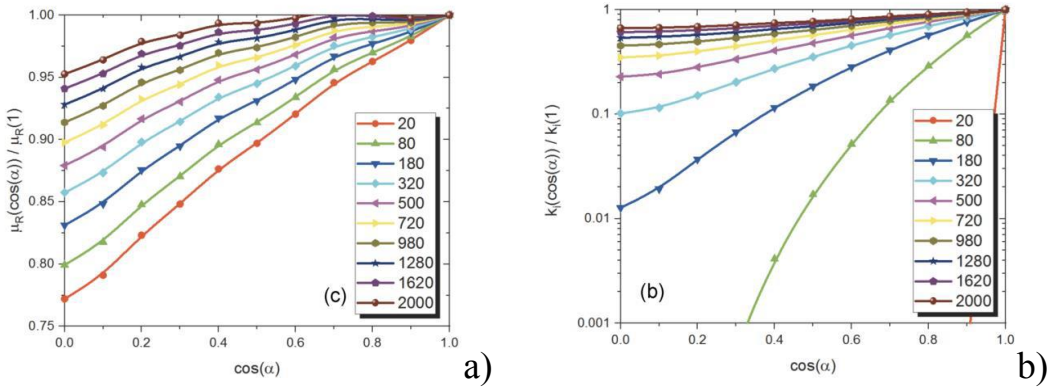

Fig. 3. a) Electron mobility across the magnetic field as a function of cos(α) at B=3 T and different values of E/N (scale in Td). CO_2 gas, P = 50 Torr. b) Dependence of the ionization rate coefficient in CO_2 on cos(α) at B = 3 T and different values of the reduced electric field strength E/N (in Td)

In general, the properties of electrons depend not only on the values of the electric E and magnetic B field vectors, but also on the angle α between these

vectors. Fig. 3a shows the dependence of the electron mobility across the magnetic field on cos(α) at B = 3 T and various values of the electric field E/N. Fig. 3b shows the dependence of the ionization rate coefficient in CO_2 on cos(α) at B = 3 T and various E/N. As can be seen, with a decrease in E/N, the influence of the transverse magnetic field on the properties of electrons is increasingly pronounced. The negative influence of the magnetic field can be compensated for by increasing the applied voltage, at which the discharge mode will shift to the region of large E/N, where the influence of the field is less.

In addition, there is the force effect of magnetic field on the streamer, caused by the Ampere force. The streamer can be considered as a current-carrying conductor placed in a transverse magnetic field. In this case, the Ampere force can bend the streamer trajectory and, thus, significantly increase the length of the streamer until the moment the streamer crosses the gas gap. Noted effect contributes to an increase in the volume of the medium activated by the streamer. In the case of streamer propagation over a surface, it is necessary to take into account the orientation of the transverse magnetic field relative to this surface. In the case of a field parallel to the surface, the Ampere force will either press the streamer to the surface or squeeze it away.

It should be noted that there are very few published works on the experimental study of surface barrier discharge with a transverse magnetic field in the literature, and information on studies of such a discharge in an electronegative gas - air, as far as we know, is absent. As reference data, we present the results on the effect of a transverse magnetic field on surface streamers in an electropositive gas - nitrogen. Photographs of streamers are taken from the article /2/.

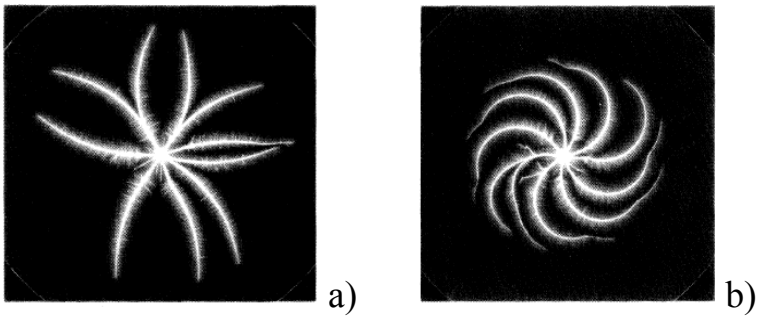

Fig 4. Surface streamer imprints on photographic film used as a dielectric barrier. Streamer shape: a) in the absence of a transverse magnetic field; b) in the presence of a transverse magnetic field. Surface barrier discharge in nitrogen.

As can be seen in Fig. 5, in the absence of a transverse magnetic field, the shape of the surface streamers is almost rectilinear, the streamers are slightly curved, and in different directions. In the presence of a transverse magnetic field, the shape of the streamers becomes strongly twisted, and all streamers are

twisted in one direction, determined by the direction of the Ampere force. Even with the naked eye it is visible that the surface streamers twisted by the magnetic field are longer and therefore process a larger surface of the barrier.

Experimental data on surface barrier discharge in air in a transverse magnetic field. The discharge is excited by a sinusoidal voltage at a frequency f = 100 kHz.

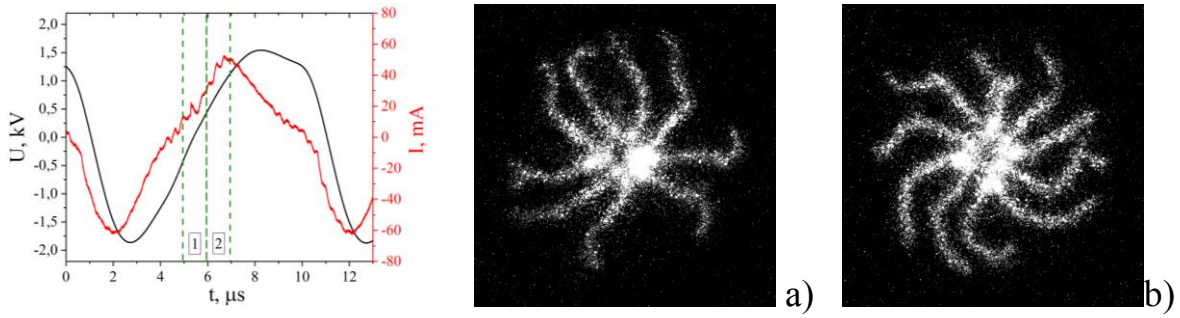

Fig 5. The voltage and current waveforms and images of surface streamers of a barrier discharge in air (top view): a) no magnetic field B=0; b) a transverse magnetic field B ≠ 0 is applied, which twists the streamers into spirals.

The experiments were performed at the same value of the reduced magnetic field induction B/N (B and N are the magnetic field induction and the gas density) at which P. Uhlig et al. experimented with a barrier discharge in nitrogen.

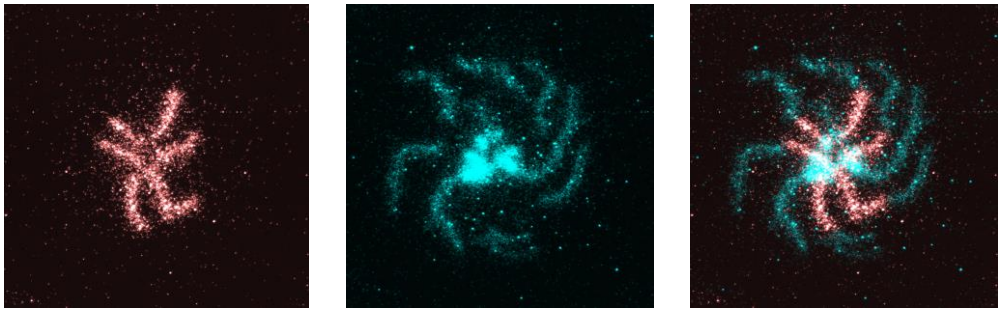

Fig. 6. Color images of surface streamers at B ≠ 0, showing their stepwise propagation across the dielectric barrier.

Acknowledgements This work was supported by the Russian Science Foundation (grant No. 25-49-00039)

References

1. **A. Yu. Starikovskiy, N. L. Aleksandrov, and M. N. Shneider**. Streamer self-focusing in an external longitudinal magnetic field. Phys. Rev. E **103**, 063201.
2. **P. Uhlig, J. C. Maan, and P. Wyder**. Spatial Evolution of Filamentary Surface Discharges in High Magnetic Fields. Phys. Rev. Let., **63**, 1968-1973

ATMOSPHERIC PRESSURE PLASMA JETS AS A TOOL FOR PLASMA MEDICINE

A.V.Kazak, L.V.Simonchik

B. I. Stepanov Institute of Physics of the National Academy of Sciences of Belarus, 220072, Nezavisimosti ave. 68-2, Minsk, Belarus,
Email: a.pavlova@ifanbel.bas-net.by

Introduction. Cold atmospheric plasma (CAP) has emerged as a powerful biomedical tool that combines the principles of low-temperature plasma physics with advanced therapeutic strategies. Operating at near-room temperatures (typically below 40 °C), CAP enables safe interaction with biological tissues without causing thermal injury. Its unique bioactivity is attributed to a cocktail of reactive oxygen and nitrogen species (RONS), UV photons, charged particles, and transient electric fields that can modulate biochemical signaling, induce oxidative stress, and inactivate pathogens selectively /1,2/. Over the last decade, CAP has transitioned from basic laboratory research to preclinical and clinical settings. CAP's ability to stimulate immunogenic cell death has also opened promising avenues in oncology, where it can enhance the efficacy of chemotherapy and trigger systemic anti-tumor immunity /3,4/.

Furthermore, plasma-activated liquids (PALs) offer a means of delivering plasma-generated reactive species to remote or internal targets, such as tumors or mucosal surfaces, without direct exposure to plasma jets. These solutions retain long-lived species like hydrogen peroxide and nitrate, allowing for flexible and systemic applications /5,6/.

Finally, the integration of artificial intelligence (AI) and computational modeling is paving the way for personalized plasma medicine. Recent studies highlight the potential of AI in optimizing CAP parameters and predicting therapeutic outcomes based on patient-specific biomarkers /7/.

This article provides an in-depth review of CAP jet applications in medicine, including established uses and emerging innovations, underlying mechanisms, and perspectives for future interdisciplinary research.

Medical Applications of CAP Jets. Let's consider the main areas where plasma jets are currently used.

1. Cancer Therapy. CAP jets can selectively target cancer cells by inducing oxidative stress, membrane disruption, and immunogenic cell death (ICD), without harming surrounding healthy tissues. Recent reviews in Cancers and Applied Sciences have highlighted CAP's ability to induce apoptosis and ICD through HMGB1 release and calreticulin exposure, thereby stimulating systemic anti-tumor immunity /8-9/

2. Chronic Wound Healing. CAP promotes tissue regeneration by stimulating angiogenesis, reducing inflammation, and eliminating pathogens. Studies published in Wound Repair and Regeneration and Clinical Plasma Medicine confirm accelerated healing of chronic wounds through CAP-induced modulation of the local microenvironment /10-11/

3. Antimicrobial Disinfection. CAP offers broad-spectrum antimicrobial activity, capable of disrupting biofilms and sterilizing surfaces without chemicals. Research in Frontiers in Microbiology and the Journal of Hospital Infection supports its efficacy against antibiotic-resistant bacteria and hospital-acquired infections /12-13/

4. Dermatology and Aesthetics. CAP is used for non-invasive dermatologic treatments due to its anti-inflammatory and antimicrobial effects./14-15/

5. Dentistry. CAP facilitates bacterial biofilm removal and improves surface conditioning for restorations and implants.

6. Veterinary Medicine. CAP applications are extending to animal care, with promising results in wound management and infection control.

CAP Jet Mechanisms of Action. Depending on the case under consideration, the underlying mechanism may differ.

On Non-biological Surfaces. Surface activation: Improves hydrophilicity and cell adhesion on polymers and metals. Degradation of pollutants: Breaks down endocrine-disrupting chemicals and allergens. Sterilization: Effective against spores, fungi, and multidrug-resistant organisms.

On Cells. Oxidative stress induction: RONS damage DNA, proteins, and lipids, leading to apoptosis or senescence. Membrane permeability: CAP enhances transmembrane delivery of molecules. Cell death pathways: Apoptosis, ferroptosis, and ICD.

On Tissues. Wound repair: Stimulates fibroblast migration, neovascularization, and re-epithelialization. Drug delivery: Transient opening of skin barriers improves topical drug uptake. Tumor regression: Local CAP treatment causes tumor necrosis and modulates the tumor microenvironment.

Plasma-Activated Liquids (PALs). Plasma-activated liquids (PALs) extend the benefits of CAP to remote or internal applications by delivering long-lived RONS in solution. Recent publications in Biomaterials and Scientific Reports have demonstrated the cytotoxic potential of PALs on cancer cells and their antimicrobial activity against resistant pathogens. /16/

Commercial Devices. Currently, several devices based on atmospheric pressure plasma jets have been certified:

- kINPen® MED: Certified in Europe for chronic wound treatment.
- PlasmaDerm®: Used for eczema and skin regeneration.
- PlasmaJet®: Surgical CAP device for dissection and coagulation.
- Sterilize-X: Portable CAP system for room and surface disinfection.

- Canady Helios Cold Plasma (CHCP): a CAP system used in surgery for localized inactivation of cancer cells at resection margins.
- Helios: a device is designed for effective treatment of living tissues with non-equilibrium cold plasma obtained in a helium environment.
- Plazon: a liquid-cooled arc plasma generator with an air intake and built-in micro-compressor that produces a hot plasma stream, which is then rapidly cooled ("quenched") to 20–40°C, maintaining a high concentration of nitrogen oxide (NO). Suitable for surgery, early therapy of chronic ulcers, and potentially dermatology.

Air plasma jets based on glow microdischarge at atmospheric pressure combine the key advantages of CAP technologies: the absence of vacuum and permissible heating of the sample (about 40 °C), the use of inexpensive and safe air instead of inert gases, and high stability and homogeneity of the flow at a low power of the discharge power source. This ensures the disinfection of target samples and local action, minimal thermal tissue damage, stimulation of healing, re-epithelialization, and angiogenesis due to the optimal spectrum of ROS/RNS and UV radiation, as well as improved migration of keratinocytes and fibroblast activity. In addition, devices based on air glow microdischarge demonstrate long-term stability of gas discharge conditions and safety, meeting electrical safety standards.

- ALOE: The device we developed is based on the creation of an atmospheric pressure air plasma jet of a glow microdischarge on direct current and has already been used by us for the inactivation of microorganisms /17/ and their associations /18/, wound healing in an animal model /19/. In 2025, a registration certificate (No. IM-7.117470) was received from the Ministry of Health of the Republic of Belarus for this device for use in dentistry and maxillofacial surgery.

Future Directions. The extensive information accumulated by now on plasma devices indicates that the current state of science is characterized by an abundance of unsystematized and mutually inconsistent empirical material, which is difficult to use for constructing physical models of both discharges and the jets they create. In such a situation, the selection of optimal conditions for a discharge that provide the desired parameters of the devices is often carried out by trial and error, which leads to large expenditures of time and resources. Also, in plasma medicine there is no concept of "Dose" that would help compare the results of the impact of various devices on biological materials. Therefore, a commission was created and it was supposed to issue recommendations for standardizing the conduct of clinical trials of such devices by July 1.

Exploratory studies in npj Digital Medicine and IEEE Transactions on Radiation and Plasma Medical Sciences propose using AI models to predict optimal CAP parameters for individualized therapy /20-21/

It is proposed to increase the effectiveness of plasma jets by combining them with chemotherapy, immunotherapy and nanocarriers. It is also proposed to use such sources in neurology, ophthalmology and organ preservation.

Conclusion. Cold atmospheric plasma jets represent a groundbreaking frontier in biomedicine. Their versatility, safety, and multifactorial action make them ideal candidates for applications ranging from antimicrobial therapy to oncology and tissue engineering. As interdisciplinary research progresses, CAP-based treatments are poised to redefine therapeutic standards across human and veterinary medicine.

References

1. **Choi, J. H., Kang, S. U., & Kim, Y. S.** Cancers, 15, 5 (2023), 1472.
2. **Cheng, X., Sherman, J. H., & Ratovitski, E. A.** Applied Sciences, 13,13 (2023), 7729.
3. **Lackmann, J. W., et.al.** Frontiers in Microbiology, 12 (2021), 683973.
4. **Emmert, S., et.al.** Journal of the European Academy of Dermatology and Venereology, 27, 5 (2013), 564–570.
5. **Lee, S. H., & Hong, J. Y.** Dermatologic Surgery, 47, 3 (2021), 348–355.
6. **Tanaka, H., et.al.** Biomedical Research International, (2011), 1–7.
7. **Zhang, Q., et.al.**. npj Digital Medicine, 6, 1 (2023), 56.
8. **Shrikant B. Mali** Oral Oncology Reports, 9 (2024), 100133.
9. **Sunil Kumar Dubey, et.al.** Drug Discov Today,27,9 (2022), 2425–2439.
10. **Strohal, R., et al.** Sci Rep. 12(2022), 3645.
11. **Bolgeo T, et.al**. J. Pers Med. 13, 5, (2023), 736.
12. **Maho, T., et.al** Applied Sciences, 11, 20 (2021), 9598.
13. **Sarthak Das, et.al.** Health Sciences Review, 4 (2022), 100037.
14. **Khalaf, A.T. et al.** Eur. J Med Res 29 (2024), 487.
15. **Karrer, S., et.al.** Applied Sciences, 11, 23 (2021), 11181.
16. **Solé-Martí X, et.al** Cancers (Basel). 13, 3 (2021):452.
17. **A.V Kazak et al**. Journal of Applied Spectroscopy, 91, 3 (2024) 511-519
18. **L. V. Simonchik et al**., Plasma Medicine. 7,2 (2017) 109 -115.
19. **A.V Kazak et.al**.29th SPIG: contributioned papers, Belgrade, Serbia (2018) 246-249.
20. **Ramaswamy, V.D., Keidar, M.**. Appl. Sci., 14 (2024), 355
21. **D. Gidon, et.al**. IEEE Transactions on Radiation and Plasma Medical Sciences, vol. 3, no. 5 (2019), pp. 597-605.

COMPACT COLD ATMOSPHERIC PLASMA SOURCES BASED ON PIEZOELECTRIC TRANSFORMERS: DEVELOPMENT AND APPLICATIONS

N.N. Bogachev[1,2], E.M. Konchekov[1,3], L.V. Kolik[1], A.S. Bakshaev[2], D.V. Malakhov[1], V. P. Stepin[1], T.I. Pavlik[1,4], N.G. Gusein-zade[1,4], S.V. Gudkov[1]

[1]Prokhorov General Physics Institute of the Russian Academy of Sciences, Moscow, Russia, bgniknik@yandex.ru
[2]MIREA – Russian Technological University, Moscow, Russia
[3]Peoples' Friendship University of Russia named after Patrice Lumumba, Moscow, Russia
[4]Pirogov Russian National Research Medical University, Moscow, Russia

Low-temperature atmospheric pressure plasma (cold atmospheric plasma, CAP) has firmly established itself among modern interdisciplinary technologies, finding applications in a wide range of fields, including medicine, biology, the food industry, agriculture, and ecology. The uniqueness of CAP lies in its ability to generate a complex mix of physically and chemically active components, such as ultraviolet radiation, electric fields, moderate heat fluxes, and, most importantly, reactive oxygen and nitrogen species (RONS). This occurs while maintaining a sufficiently low temperature, enabling the treatment of living tissues and other sensitive materials. However, the transition from laboratory use of CAP to its widespread practical application has long been hindered by the need to develop compact, energy-efficient, and safe plasma sources. One promising approach to solving this critical challenge is the development and study of plasma sources based on piezoelectric transformers [1,2].

The core element of such sources is the use of a Rosen-type piezoelectric transformer (PT). Leveraging the inverse and direct piezoelectric effects, the PT can increase voltage from 30-150 V to 3-12 kV at its resonant frequency, while being compact and highly efficient. The applied input voltage is converted into mechanical vibrations, which, in turn, generate high voltage on the output section. This high voltage initiates and sustains a discharge in various gas media.

A key advantage of this approach is the significant simplification and miniaturization of the plasma source's power system. This achieves unprecedented compactness and portability, as the bulky and heavy mains-powered high-voltage power supply becomes unnecessary. The device can be powered by batteries, which is crucial for field applications. The system's energy efficiency is also high due to minimal energy loss during piezoelectric energy conversion at the resonant frequency. The piezoelectric transformer itself functions as a resonant element within the circuit, and its resonant frequency is influenced by the electrical characteristics of the load, such as the treated surface or medium. Consequently, maintaining optimal operational efficiency requires

active control and adjustment of the input signal frequency supplied to the transformer.

Three generations of PT-based plasma sources have been developed at the GPI RAS (Fig. 1). The evolution through these generations primarily reflects advancements in their tuning capabilities, operational control systems, physical dimensions, and potential for scaling the technology.

The initial architecture (Fig. 1a) employs a straightforward two-stage design. A Very Low Frequency (VLF) generator provides a periodic signal, which is subsequently amplified by a conventional ferromagnetic transformer to the high voltage necessary to excite the piezotransformer into resonance. The PT then further transforms this voltage to the multi-kilovolt level required for plasma ignition. This design prioritizes simplicity and robustness; however, its operational frequency is fixed, limiting the ability to dynamically track the PT's resonant frequency shift under varying load conditions, which can lead to suboptimal power transfer efficiency.

The enhanced design (Fig. 1b) introduces greater control and efficiency. A 220 V AC mains input is rectified and down-converted to a stable 24 V DC bus. This DC supply powers a Pulse-Width Modulation (PWM) generator, which controls a MOSFET transistor switch. The switch pulses the DC voltage across the primary winding of a voltage transformer. The transformed high-voltage output then drives the PT. This architecture allows for manual or simple feedback control of the PWM frequency, enabling coarse tuning to the PT's mechanical resonance. This results in improved power coupling efficiency and stability compared to the first-generation design.

The most advanced architecture (Fig. 1c) is a fully integrated, portable system centered around a digital microcontroller (STM32G474). It is powered by a 12 V battery, managed by a Battery Management System (BMS) and charger circuit. On-board DC-DC converters provide a regulated 3.3 V supply for the logic components and a variable 12-30 V rail for the power stage. The microcontroller generates a precise, tunable PWM signal. A dedicated gate driver IC (IR2101) ensures optimal switching of the power MOSFET, which pulses the variable voltage rail to the PT's primary. This design enables active frequency tracking and automatic resonance locking, ensuring maximum efficiency and stable plasma operation even with dynamic load changes. Additional features include user interface components (screen, buttons, status LEDs) and optional remote communication via RS485, making it ideal for field-deployable and research applications requiring high reproducibility.

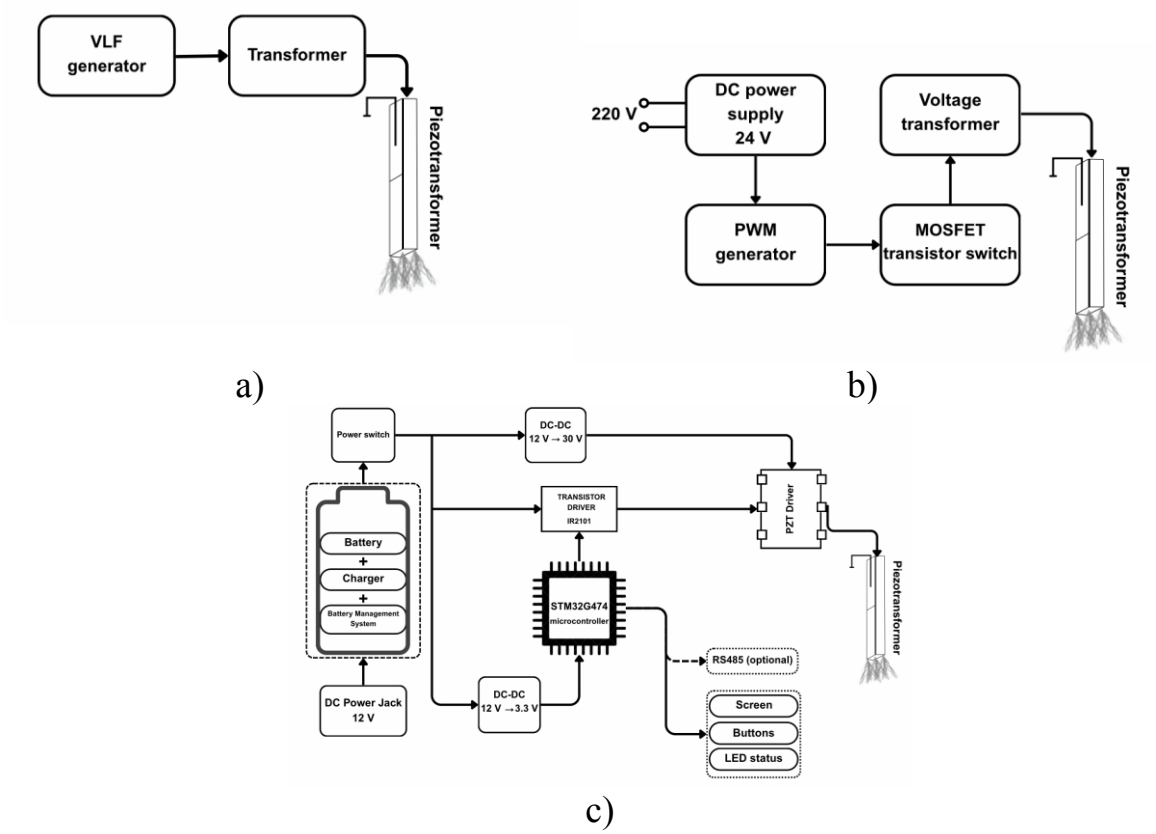

Fig. 1. Piezotransformer plasma sources: a) first generation with VLF generator, b) second generation with transistor switch, c) third generation with logic control

One of the distinctive features of this technology is its versatility. Depending on the interchangeable nozzles or electrodes used, the developed piezoelectric transformer-based source is capable of generating various types of atmospheric pressure discharges, including corona, spark, plasma jet, and dielectric barrier discharge (DBD) configurations (Fig. 2). For example, a spark discharge in argon is well-suited for the intensive generation of RONS in liquids, while barrier discharges and plasma jets are more appropriate for the delicate treatment of surfaces.

As part of our comprehensive analysis, we have conducted measurements of the electrical parameters of these sources and acquired the optical emission spectra for the discharges. Furthermore, we have extensively researched methods for producing plasma-activated liquids with varying concentrations of reactive oxygen and nitrogen species (RONS). The application of these plasmas and activated liquids for the treatment of surfaces and within liquid media has been a central focus. The resulting solutions and direct plasma treatments have been evaluated for their efficacy in agricultural and biomedical applications [3,4].

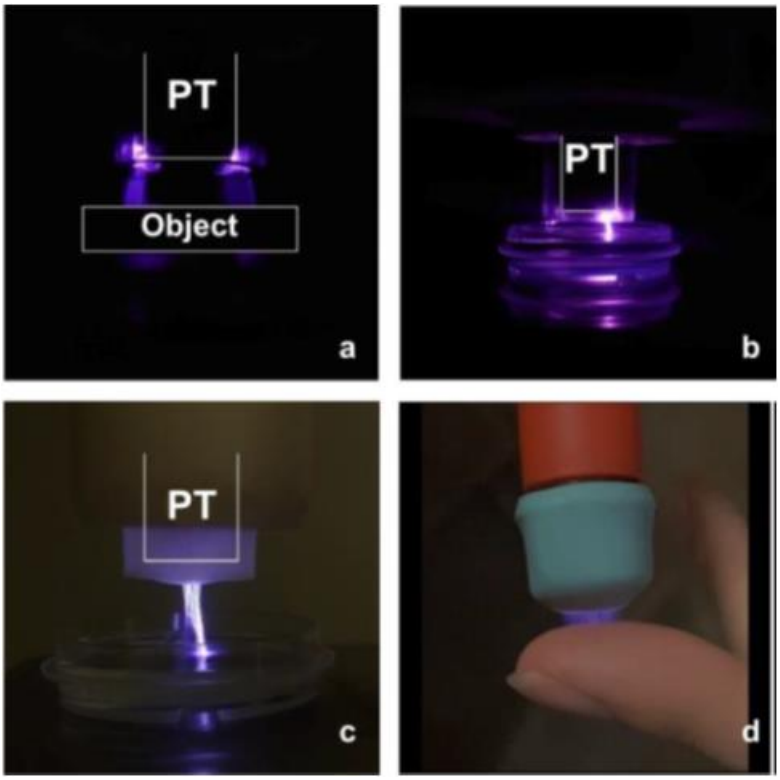

Fig. 2. Four types of gas discharge that can be generated by a single piezotransformer source of low-temperature atmospheric plasma: a – corona discharge, b – spark discharge, c – plasma jet in noble gas (for example Ar) or air, d – dielectric barrier discharges

Acknowledgements. The study was supported by the grant of the Russian Science Foundation No. 24-29-00842, https://rscf.ru/project/24-29-00842/.

References

1. **Teranishi, K., Suzuki S, Itoh H.** Japanese Journal of Applied Physics, 43.9S (2004), 6733.
2. **Artem'ev, K. V., et al.** Russian Physics Journal, 62 (2020), 2073-2080.
3. **Konchekov, E. M., et al.** Frontiers in Physics, 8 (2021), 616385.
4. **Pavlik, T., et al.** Plasma Medicine, 13, 1 (2023), 13-27.

CHARACTERISTICS OF THE PULSED PLASMA ACCELERATOR DEPENDING ON ENERGY INPUT

A.A. Kozlov, V.E. Zavalova, Yu.V. Karpushin, V.P. Polishchuk, M.V. Protasov

Joint Institute for High Temperatures,
Russian Academy of Sciences, Moscow, 125412 Russia

The characteristics of hydrogen plasma in an accelerator with multichannel injection were studied. An arc discharge with a current 0.5 MA was ignited up to 200 μs at the initial hydrogen density of ~$3 \cdot 10^{16}$ cm^{-3} . The current and voltage in the discharge, the density and temperature of electrons in the plasma were measured.

Two types of experiments were conducted. The first type dealt with the study of electron density in depending of the energy increasing in the capacity store in using a single inlet valve. The second type of studies were conducted for several (two and three) gas inlet valves. Because we have already demonstrated the feasibility of using a multi-channel injector (MCI) of the working gas (hydrogen) in a pulsed plasma accelerator (PPA) [1] and its positive effect on the homogeneity of the generated plasma, then the role of valves in increasing plasma mass is of interest.

The experimental setup is shown in Fig. 1. Up to six electrodynamics valves simultaneously distributed in one section of the MCI could be used to inject gas.

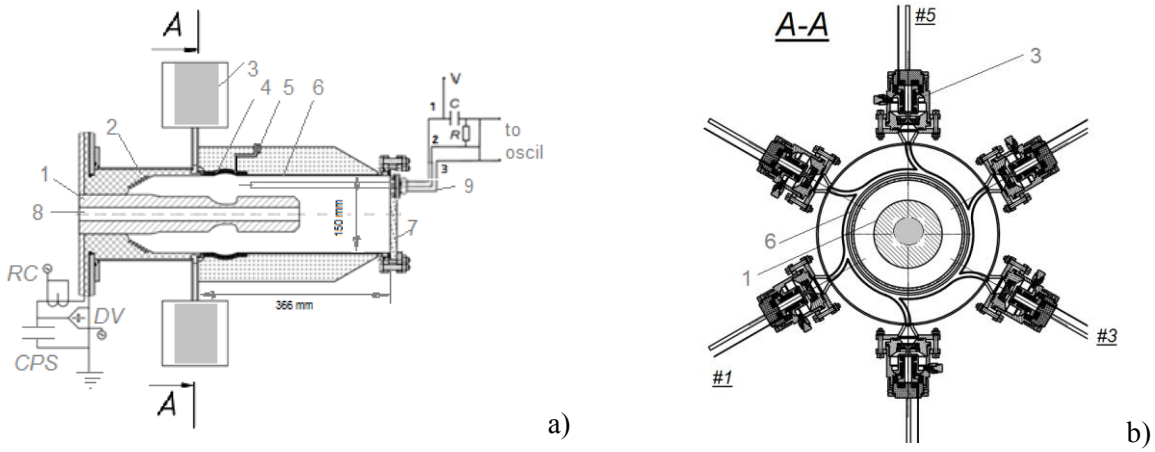

Fig.1 Sketch of the MCI model in longitudinal (a) and transverse (b) cross sections. Design elements: (1) central electrode (cathode); (2) insulator with a developed surface; (3) electrodynamics gas inlet valve; (4) solenoid (was not powered); (5) collector for the solenoid power supply; (6) outer electrode (anode) with bandage; (7) flange with a Wilson seal (can be replaced with an organic glass viewing window); (8) vacuum pumping channel; (9) socket with bracket for mounting probes

The capacitive storage CPS was used the energy source for the discharge. The energy input into the discharge varied from 2 to 60 kJ. The diagnostic system included measurements of currents and voltage in the discharge (Rogowski coils and voltage divider), and plasma parameters determination (triple Langmuir probe [2] and spectral method). High-speed video recording of the plasma bunch formation was used.

The results of the first type of experiments, with use one valve, are presented in Fig.2-5, CPS has capacity 36 μF, a quarter period was 8 μs. CPS was charged to voltages 10 kV, 15 kV, 20 kV, 25 kV and 30 kV, that corresponded to the stored energies ~2 kJ, 4kJ, 7 kJ, 11 kJ and 16 kJ.

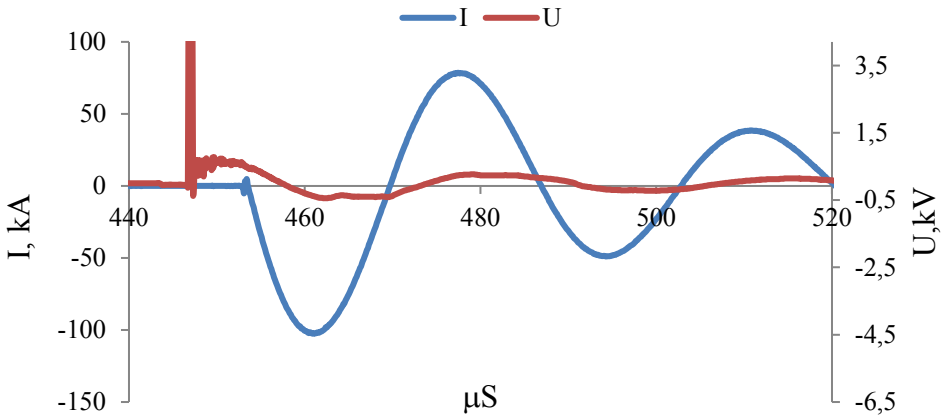

Fig. 2. Example of current and voltage on the discharge gap with a source energy of 4 kJ

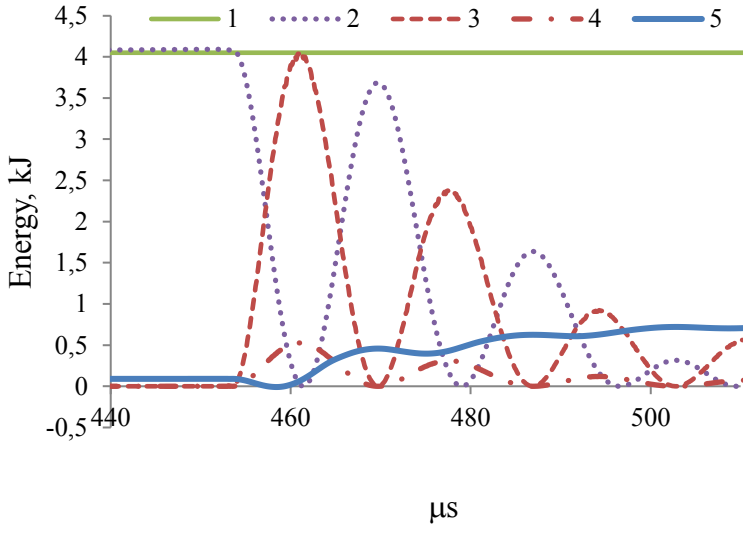

Fig.3. Energy balance in MCI with use energy source of 4 kJ,
1- stored, 2- electric, 3- entire circuit magnetic energy, 4 - plasma load magnetic energy, 5- thermal energy.

For the first type of experiments it was shown that increase of the electron density (and the mass of the plasma) directly proportional to the energy increase of the capacitive storage up to 16 kJ when using one valve. The thermal energy is Joule energy, which goes directly to plasma formation, in this case makes up no more than 20 percent of the stored energy (fig.3). The maximum electron concentration reached ~ $1 \cdot 10^{14}$ cm^{-3}, the average electron temperature value was ~20 eV. The dynamics of the electron density exactly repeated the dynamics of the discharge current.

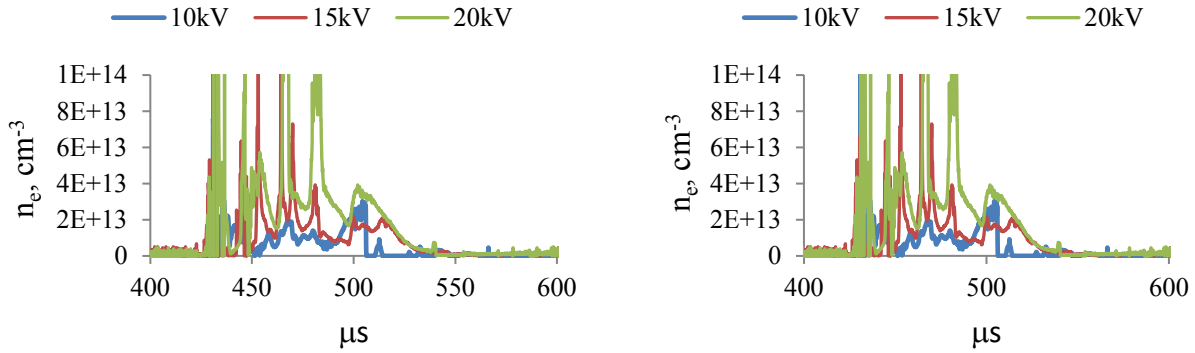

Fig. 4. Changes in the electron density n_e depending on the energy input into the MCI discharge for the first experiment.

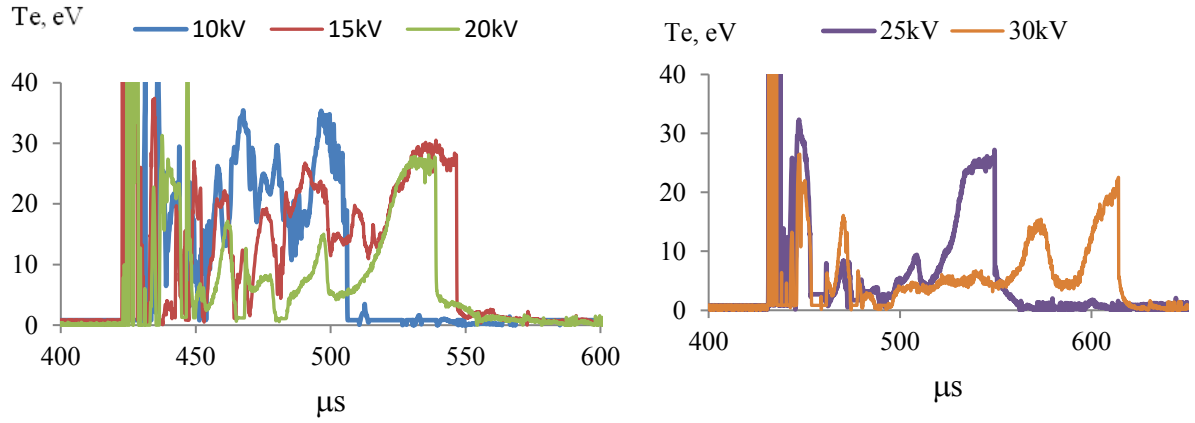

Fig. 5. Changes in electron temperature T_e depending on the energy input into the MCI discharge

A figure 6 illustrates the results of second type of experiment, with use three valves number 1, 3, 5 (see fig.1b). CPS has capacity 102 μF, a quarter period was 15 μs. CPS was charged to voltages17 kV, 24 kV, and 30 kV, that corresponded to the stored energies ~15 kJ, 30kJ and ~46 kJ.

В результате исследования плазмообразования при одновременном подключении трех клапанов можно констатировать, следующее. Пробой разрядного промежутка наступал раньше вследствие увеличения в три раза

порции впрыскиваемого рабочего газа, но на ионизацию газа требовалась уже большая энергия.

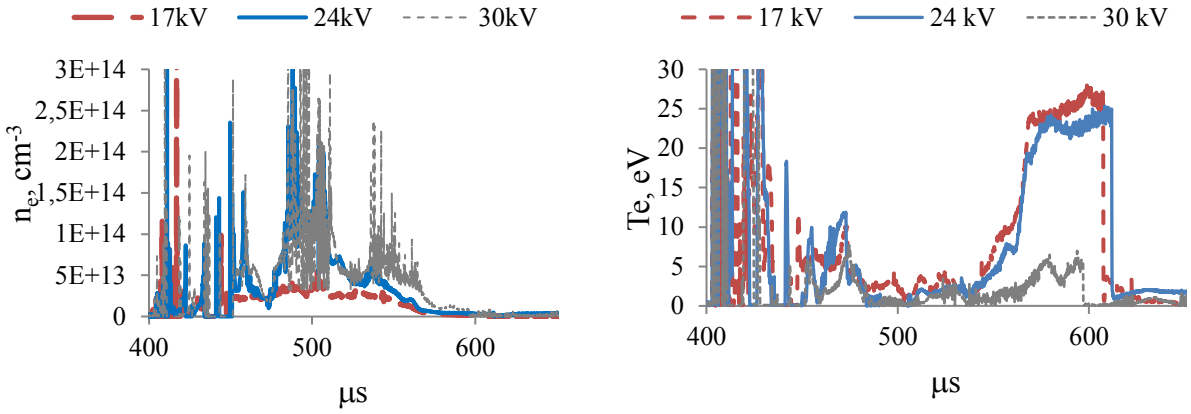

Fig. 6. Changes in electron density n_e and electron temperature T_e depending on the energy input into the MCI discharge.

Средняя концентрация электронов при энергии накопителя 15 кДж была 2 cm^{-3}, 30 кДж была 5 $\cdot 10^{13}$ cm^{-3}, для 46 кДж средняя концентрация электронов составляла ~6 $\cdot 10^{13}$ cm^{-3} при этом измеренный в разряде ток имел максимальное значение 0.3 МА. The maximum electron concentration reached ~ $2.5 \cdot 10^{14}$ cm^{-3}. Температура электронов нарастала к концу импульса тока, в противоположность концентрации электронов. Когда концентрация электронов снижалась до $\cdot 10^{11}$-$\cdot 10^{12}$ cm^{-3}, соответствующего значению тлеющего разряда, температура с нескольких электрон-вольт подскакивала до двух десятков.

Acknowledgements. This work was also supported by the Ministry of Science and Higher Education of the Russian Federation (State Assignment no. 075-00269-25-00).

References

1. **Zavalova V.E., Kozlov A.A., Kozlov A.V., Polistchook V.P., Karpushin Yu.V., Shurupov M.A.** Multichannel injection of hydrogen in a pulsed plasma accelerator. Proceedings of 9th International Congress on Energy Fluxes and Radiation Effects (EFRE–2024) | Tomsk, Russia. DOI: 10.56761/EFRE2024.C1-P-023104
2. **Zavalova V.E., Kozlov A.A., Kozlov A.V., Polistchook V.P., Karpushin Yu.V., Gusev A. N., Shurupov M.A.** Generation of a Plasma Bunch in a Multichannel Injector/ Plasma Physics Reports, 2025, Vol. 51, No. 1, pp. 92–102. DOI: 10.1134/S1063780X24601974

A METHOD FOR DETERMINING THE EROSION OF A METAL CATHODE DURING THE COMBUSTION OF A HIGH-CURRENT VACUUM DISCHARGE BASED ON THE INTERACTION OF TWO CO-DIRECTIONAL PLASMA JETS

A. Kuzminykh[1], A. Rousskikh[1], A. Zhigalin[1], V.I. Oreshkin[1], V.A. Gasilov[2]

[1]Institute of High Current Electronics of the Siberian Branch of the Russian Academy of Sciences, Tomsk 634055, Russia, rualexe@mail.ru
[2]Federal Research Center Keldysh Institute of Applied Mathematics of the Russian Academy of Sciences, Moscow, Russia, vgasilov@yandex.ru

Introduction.

During the burning of a high-current vacuum arc discharge, the active evaporation of electrode materials occurs. The amount of material evaporated from the surface of the electrode as a result of the flowing of electrical current through it is characterized by the ion erosion coefficient. In experiments on the generation of plasma jets and Z-pinches /1-3/, the ion erosion of metals plays a crucial role and is the source of matter for the formation of plasma streams or shells.

Experimental setup.

When a high-current plasma gun with a single cathode is used, a single plasma jet is created. The structure of the jet is maintained by the flowing current along its axis /1/. When two such jets are created, located relatively close to each other, they begin to interact. This interaction is explained by the attraction and further fusion of the jets, which is caused by the Ampere force acting on them from the side of the currents flowing along the axes of each of the jets.

In these experiments, used a pulse power generator IMRI-5 as an arc discharge source. This pulse power generator has the following characteristics: the current amplitude in the short-circuit mode is 450 kA and the current rise time is 450 nanoseconds.

To determine the arc current, its derivative, and the voltage drop across the arc, a Rogowski coil, an inductive loop, and an inductive voltage divider were used. The signal was recorded using a TDS2024B oscilloscope.

An HSFC-Pro 4-frame camera with an exposure time of 10 ns and a delay time between frames of 100 ns was used to register the image in the visible range.

Two plasma guns were used as the load (see Fig. 1). The cathodes in the form of two rods were located in a cylindrical kaprolon insulator, to which the anode was located coaxially, and the upper ends of the electrodes and the insulator were

in the same plane. A vacuum arc discharge was initiated upon a breakdown along the surface of the insulator end face. The diameter of the cathodes was 3 mm. The diameter of the insulator was 24 mm, and the distance between the cathodes was 12 mm. All the electrodes were made of aluminum.

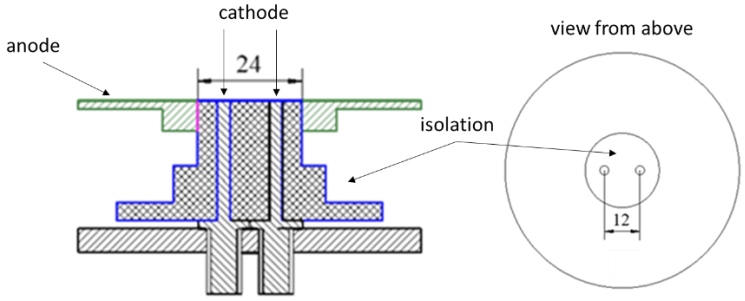

Figure 1 – Generator load.

Calculation of linear mass.

Let us consider an infinitesimal volume dV of one of the jets, the trajectory of which begins from the cathode and ends at the point of contact of the jets (see Fig. 2).

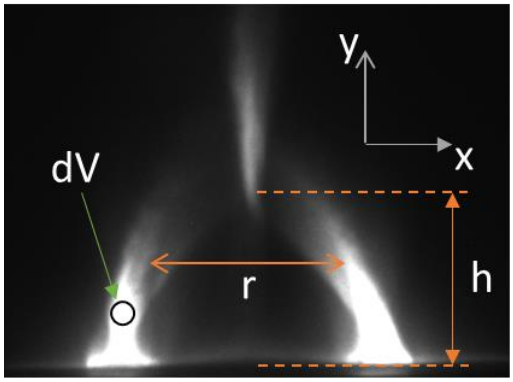

Figure 2 – A photo of the interaction of two plasma jets taken by a 4-frame HSFC-Pro camera with an exposure time of 10 ns. Notation: h is the distance from the cathode to the point of collision of the jets, r is the distance between the axes of the jets.

Along the horizontal X-axis, the dV plasma is affected by the Lorentz force from the magnetic field generated by the current of another jet.

Projected on the horizontal X-axis, the acceleration has the form

$$a(t) = \frac{\mu_0}{2\pi r}\frac{I^2}{dm/dL} = \frac{\mu_0}{2\pi r}\frac{I^2}{m_p}, \qquad (3)$$

where m_p –mass per unit length, μ_0 – magnetic constant, r – distance to the axis of the second jet, I – current flowing in the second jet. We assume that the current in both jets is the same and is equal to half of the total current of the generator.

If assume that the plasma jet propagates uniformly along the Y axis, then by experimentally determining the plasma velocity v_y, can understand when the plasma volume dV was emitted from the cathode relative to the moment of recording the image and thereby determine in which range of the generator current the volume dV was moving.

Let us divide the time of movement of the plasma volume dV under consideration, in the section dt. Let the plasma move uniformly accelerated along the X-axis in each of these sections.

When selecting the linear mass, it is necessary to choose a trajectory such that at the last moment of time the volume dV reaches the experimentally observed coordinate of the intersection of the jets. (see Fig. 3)

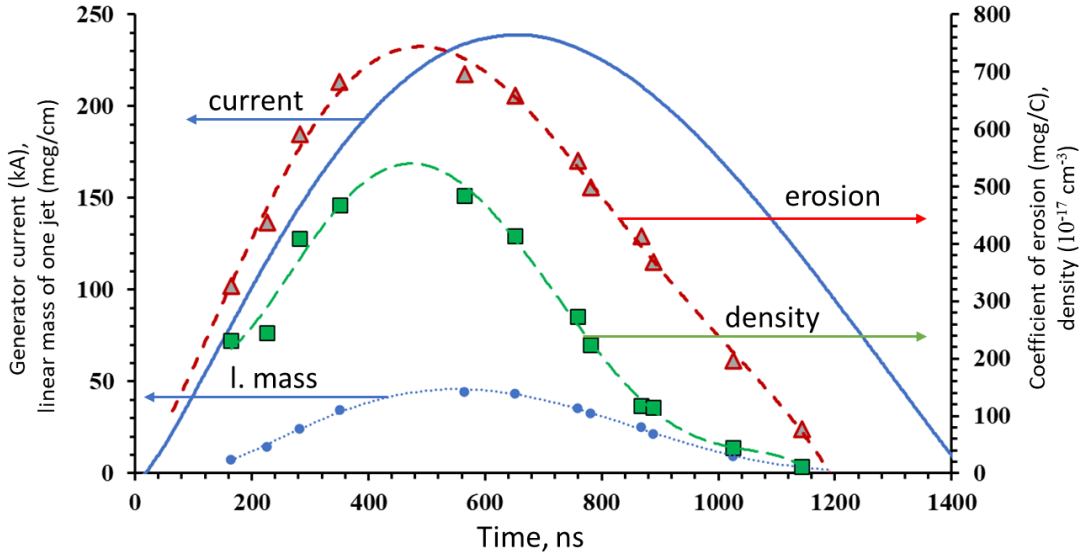

Figure 3 – The results of the analysis of several images. The total current of the generator (solid, blue). Linear mass (dotted line, blue). The coefficient of erosion (red). Ion density (green).

Calculation of the erosion coefficient.

Knowing the velocity of the jet propagation upward from the cathode v_y, and the linear mass m_p, it is possible to calculate how much mass was emitted from the cathode during dt. From here, the erosion coefficient can be determined using the formula

$$\gamma = \frac{dm}{dQ} = \frac{m_p dL}{I_0 dt} = \frac{m_p v_y dt}{I_0 dt} = \frac{m_p v_y}{I_0}, \qquad (7)$$

where dL – the distance that the dV volume managed to travel during dt, I_0 – the current of the jet at a given time.

Using the method described above for calculating the linear mass and the coefficient of erosion, in images taken at different points in time, it is possible to observe the development of these characteristics over time (see Fig. 3).

Conclusion.

This paper presents a relatively simple method for estimating the coefficient of ion erosion of metals. The corresponding calculations for aluminum were also given in the work. In further work on this topic, it is planned to carry out verification and comparative analysis with other methods for estimating the coefficient of ion erosion. It is also planned to compile a database of the values of the ion erosion coefficient for different materials during combustion of a high-current vacuum arc discharge on their surface.

Acknowledgements. This work was supported by the Russian Science Foundation (grant No. 25-61-00018).

References

1. **Rousskikh A.G., Zhigalin A.S., Oreshkin V.I., Labetskaya N.A., Kuzminykh A.M.** Formation of Directed Plasma Jets During the Combustion of a High-Current Vacuum-Arc Discharge. // Plasma Physics Reports, 2024, V. 50, Is.7, P. 800 - 809. https://doi.org/10.1134/S1063780X24600890
2. **R.K. Cherdizov, R.B. Baksht, V.A. Kokshenev, V.I. Oreshkin, A.G. Rousskikh, A.V. Shishlov, D.L. Shmelev and A.S. Zhigalin**, Effect of tailored density profiles on the stability of imploding Z-pinches at microsecond rise time megaampere currents, Plasma Physics and Controlled Fusion. 64 (2022) 015011 (9pp) https://doi.org/10.1088/1361-6587/ac35a5.
3. **Oreshkin V.I., Baksht R.B., Cherdizov R.K., Oreshkin E.V., Ratakhin N.A., Rousskikh A.G., Shishlov A.V., Vankevich V.A. and Zhigalin A.S.**, Studies on the implosion of pinches with tailored density profiles, Plasma Phys. Control. Fusion 63 (2021) 045022 (12pp) https://doi.org/10.1088/1361-6587/abe959

EXTRACTED ION BEAM DRIFT ANALYSIS IN A BERNAS-TYPE SOURCE

N.V. Mamedov[1,2], A.A. Avdienko [1], A.A. Starostenko [3], A.V. Sorokin [3]

[1] Research Institute of Precision Machine Manufacturing (JSC NIITM), Zelenograd, Russia,
[2] National Research Nuclear University MEPhI, Moscow, Russia
[3] Budker Institute of Nuclear Physics SB RAS, Novosibirsk, Russia

Ion sources (IS) with crossed ExH fields of the Bernas type play a critical role in ion implantation systems, where the generation of stable and high-current ion beams is required [1–5]. This type of source (see Figs. 1 and 2) is a modified version of a Penning-type hot-cathode ion source.

Inside the discharge chamber, a tungsten filament (thermionic cathode) is placed in a helical configuration, located in close proximity (typically 1–5 mm) to cathode. At the opposite end of the chamber, an electron reflector (anticathode) is installed, held at the same electrical potential as the cathode. In the standard operating mode of this ion source, cathode heating is achieved by means of an electron beam emitted from the thermionic filament. The filament is powered with a voltage of up to 5 V and a current of up to 60 A. A bias voltage of up to 700 V is applied between the filament and the cathode, resulting in a thermoelectron current of up to 3 A. Electrons accelerated by this potential strike the cathode end surface, causing resistive heating and initiating thermionic emission from the cathode itself. Only those electrons emitted from the cathode surface facing the anode — i.e., the interior of the discharge chamber — contribute to the discharge process.

The discharge chamber is located within a longitudinal magnetic field generated by an external electromagnet. The magnetic assembly consists of a pole piece, a core (around which the excitation coil is wound), and a C-shaped yoke that closes the magnetic circuit. The magnetic field strength in the discharge region can be adjusted in the range from 0 to 0.05 T, or up to 0.2 T, depending on the required plasma parameters and the specific geometry of the ion source [2, 4, 5]. This magnetic field, directed from the cathode to the anticathode, confines electrons along the axis of the discharge chamber, where they undergo oscillatory motion between the two electrodes. Such an ExH configuration suppresses the radial drift of electrons and ensures their confinement within the plasma. This confinement increases the electron residence time in the discharge region, which, in turn, promotes stable ignition and sustained maintenance of the plasma. The plasma formed between the cathode and anticathode is characterized by an approximately uniform axial density distribution [4,5]. As a result, a narrow ion beam with high cross-sectional uniformity along its long axis can be extracted through a longitudinal

slit aperture in the anode.

Bernas-type source ion extraction system is performed using a two-electrode extraction system. The discharge chamber was biased under a high positive potential relative to ground, up to +80 kV. Suppression electrode (biased to -3 kV), which serves to reflect secondary electrons returning to the ion source, and a grounded focusing electrode are further from the anode.

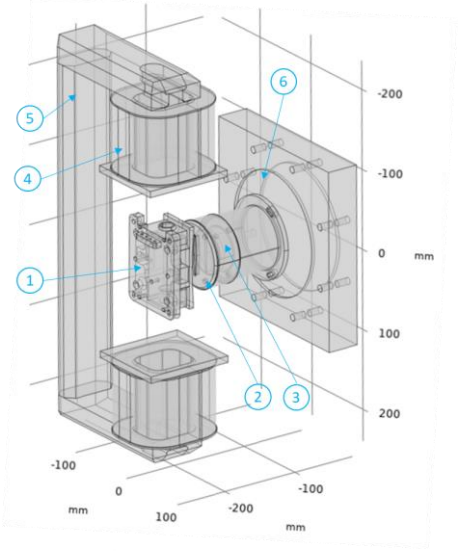

Fig. 1. 3D view of a Bernas-type ion source

1 – Discharge chamber
2 – Suppressor electrode
3 – Focusing electrode
4 – Electromagnet coils
5 – Electromagnet yoke
6 – Beamline gate valve

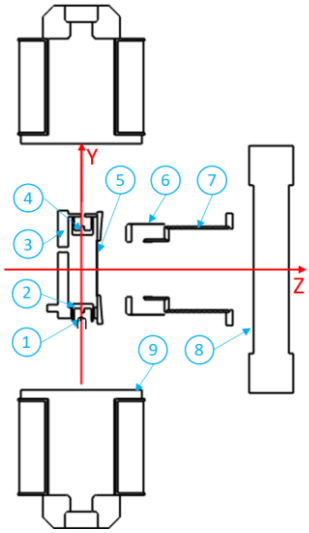

Fig. 2. Cross-sectional view of the Bernas-type ion source in the YZ plane

1 – Thermionic filament (thermocathode)
2 – Cathode
3 – Discharge chamber housing
4 – Anticathode (electron reflector)
5 – Extraction slit
6 – Suppressor electrode
7 – Focusing electrode
8 – Beamline gate valve
9 – Electromagnet

However, a significant drawback of the Bernas-type ion source is the influence of stray magnetic fields extending beyond the discharge chamber due to ion extracted in a direction transverse to the magnetic field. These residual fields induce lateral beam deflection, resulting in substantial ion losses on the extraction electrodes. To mitigate such losses, beam alignment correction systems are employed. One common solution is a hexapod — a six-degree-of-freedom positioning platform that allows precise spatial translation and rotation of the ion source via six independently controlled actuators. Accurate

adjustment of the hexapod requires preliminary modeling of the required positional and angular offsets of the source relative to the axis of the extraction system.

The simulation accounted for beam divergence due to its space charge, as well as secondary processes arising from ion–gas interactions, including ion-induced ionization, resonant charge exchange, and elastic scattering. Initial beam parameters were based on data reported in [1, 3, 5]. Two scenarios were considered: one neglecting stray magnetic fields, and the other incorporating their influence. As a result, key beam characteristics were determined — including total current, emittance, and density distribution — as well as the beam displacement at the exit of the ion-optical system (at the beamline gate valve). To parameterize these displacements, the ion source was virtually shifted relative to the extraction axis, and its angular misalignment was varied. This allowed the establishment of correlations between current losses, transverse beam size, and emittance as functions of the misalignment magnitude. Figure 3 illustrates examples of ion beam trajectory simulations (at a typical extraction current of 5 mA and a magnetic field strength of approximately 0.2 mT at the center of the source), both without source misalignment correction and with a lateral offset of $\Delta x = 7$ mm and a rotational tilt of $\alpha = 10°$.

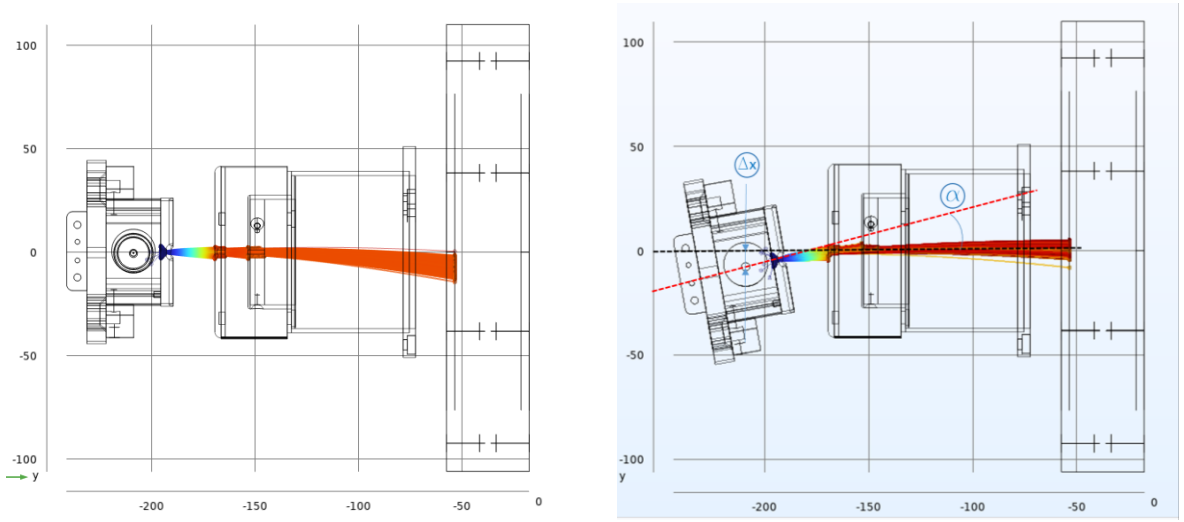

(a) Without source alignment correction (b) With lateral offset x = 7 mm and angular tilt 10

Fig. 3. Examples of ion beam trajectory simulations in COMSOL environment

Figure 4 shows examples of the ion beam profile (Ar^+, 5 mA, 80 keV) at the beamline gate valve: (a) with and without the presence of a magnetic field; (b) with a magnetic field of 0.1 T, under source axis displacement of 5 mm and angular misalignments of 5°, 7°, and 10°, respectively. Figure 5 shows the full width at half maximum (FWHM) of the beam in the transverse directions (X, Y) under magnetic field B_2, for a lateral displacement of 7 mm and various angular

tilts of the ion source axis. The obtained data will be used to calibrate the hexapod system prior to commissioning.

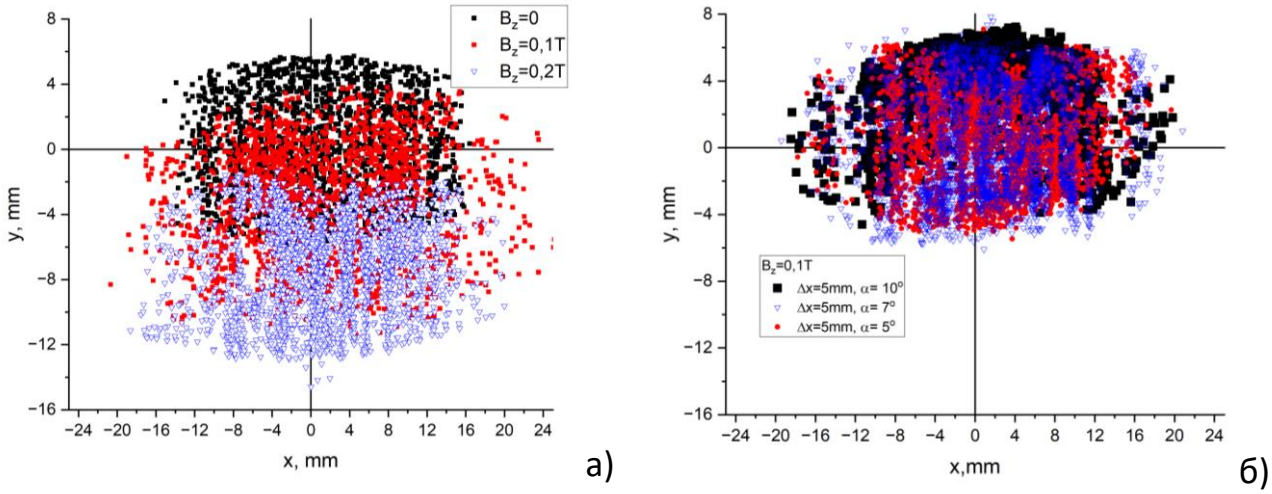

а) б)

Fig. 4. Examples of the ion beam profile (Ar^+, 5 mA, 80 keV) at the beamline gate valve.

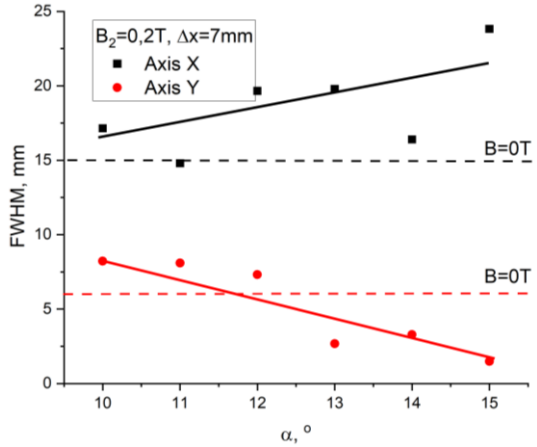

Fig. 5. Full width at half maximum (FWHM) of the beam in the transverse directions (X, Y) under magnetic field B_2, with a 7 mm lateral displacement and various angular tilts of the ion source axis.

References

1. Michiro Sugitani. Rev. Sci. Instrum 85, 02C315 (2014) doi: 10.1063/1.4854155
2. S. R. Walther, B. Pedersen and C. M. McKenna. Particle Accelerator Conference, 1991. Accelerator Science and Technology., Conference Record of the 1991 IEEE doi: 10.1109/PAC.1991.164876
3. Shigeki Sakai, Nariaki Hamamoto, Yutaka Inouchi, Sei Umisedo, and Naoki Miyamoto. Rev. Sci. Instrum 85, 02C313 (2014) doi.org/10.1063/1.4852315
4. T. V. Kulevoy; et al. Rev. Sci. Instrum 77, 03C110 2006 doi:: 10.1063/1.2165267
5. I. Roudskoy ; et al. Rev. Sci. Instrum 79, 02B313 2008 doi: 10.1063/1.2823897
6. www.comsol.com

MODULATION OF THE BEAM CURRENT IN AN ELECTRON SOURCE WITH A MULTI-ARC TWO-GRID PLASMA EMITTER

M.A. Mokeev[1], V.N. Devyatkov[1], D.A. Gorkovskaia[1],
M.S. Vorobyov[1,2], N.N. Koval[1], V.V. Nedoshivin[1,2]

[1]High Current Electronics Institute of the Siberian Branch of the RAS,
Russia, 634055, Tomsk, Akademichesky Avenue, 2/3, Tomsk, Russia,
maks_mok@mail.ru, vlad@opee.hcei.tsc.ru, diana191@inbox.ru,
koval@opee.hcei.tsc.ru, nedoshivin_vlad@mail.ru
[2]National Research Tomsk Polytechnic University, Russia, 634050,
Tomsk, Lenina Avenue, 30, vorobyovms@yandex.ru

In modern applications involving modification of the surface of various materials or its heating, it has been shown that expanding the range of parameters of the generated electron beam is a relevant and in-demand task. For such applications, pulsed electron beams are the most effective tool, allowing both short-term high-energy effects (melting, alloying) and modes with preheating or maintaining the surface temperature of the sample aimed at changing the morphology or eliminating internal stresses without destroying the structure. Additionally, pulsed electron beams with a constant current amplitude, set by fixed parameters of the accelerating voltage and the arc discharge current, limit the applicable types of modifiable materials, differing in thermal conductivity, heat resistance and other physical properties. In particular, this approach to electron beam generation at low operating gas pressures (~10^{-2} Pa) makes it impossible to modify ceramic surfaces with an electron beam with a quasi-constant power /1,2/.

One of the methods of expanding the power range of an electron beam is the implementation of combined modulation of both the parameters of the arc discharge and the voltage on the control grid, which determines the proportion of electrons passing through its cells into the accelerating gap. The presence of a multi-arc system makes it possible to increase the electron beam current to the kiloampere level, and grid control makes it possible to achieve electron beam currents up to tenths of an ampere /3.4/.

Figure 1 shows a diagram of an electron source with a multi-arc plasma emitter having grid control of the electron beam current. A multi-arc plasma emitter (PE) with grid control includes: a multi-cathode node, a power supply system, an additional fine-structured grid and a source of reference and modulated voltage.

The principle of operation of a multi-arc electron source is described in more detail in /4/. For modulated control of the electron beam current, either modulation of the arc discharge current or grid control can be used when a modulated voltage is applied to the control grid *8*. To implement the second control method, two sources are connected in series between grids *6* and *8*: a reference voltage source and a modulated voltage source. The reference voltage source is a block of capacitor banks charged via a voltage multiplier powered by an adjustable autotransformer, which provides the possibility of smooth regulation of the output voltage in the range from 0 to -60 V. The modulated voltage source is a source consisting of a set of capacitive

storage devices connected in series, to each of which IGBT modules are connected, allowing the appropriate voltage to be applied between grids *6* and *8*, which allows for amplitude and latitude modulation of the electron beam current. This power supply has 4 key-capacitor pairs, thus there are 16 variations in the amplitude of the bias voltage. Transistor control allows the generation of voltage pulses of reverse polarity with respect to the reference voltage in order to compensate for the voltage between the emission and control grids generated by the reference voltage source.

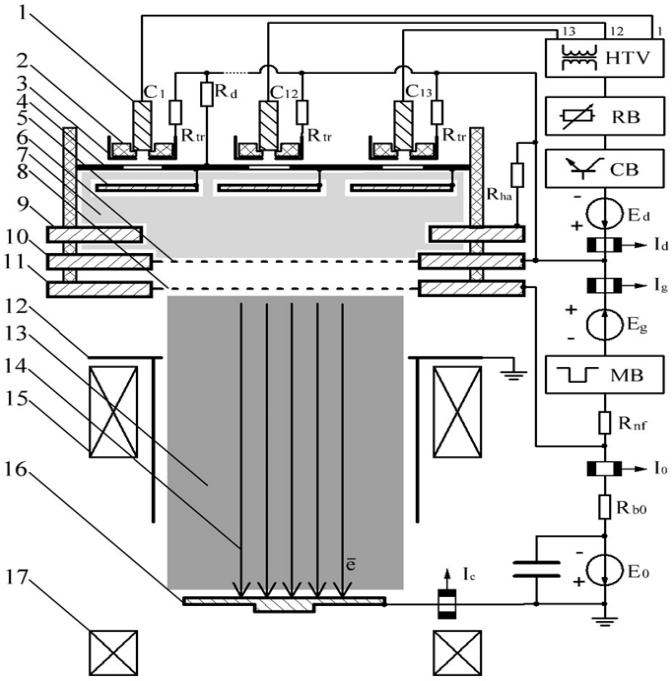

Figure 1 – Experimental setup of a grid–controlled multi–arc plasma emitter: 1 – cathode, 2 – insulator, 3 – igniting electrode, 4 – diaphragm, 5 – redistributing electrode, 6 – emission grid; 7 – emission (cathode) plasma; 8 – control grid; 9 – intermediate anode; 10 – anode; 11 – emission electrode; 12 – extraction electrode; 13 – beam (anode) plasma; 14 – electron beam; 15, 17 – magnetic coils; 16 – collector.

As the negative bias increases, a potential barrier is created on the control grid, reducing the number of electrons extracted from the emission plasma into the accelerating gap. When a pulse voltage is applied by a modulated voltage source, the potential barrier on the control grid decreases and the number of emitted electrons increases. Depending on the amplitude of the pulse voltage, it is possible to adjust the amount of current in the accelerating gap.

When using a voltage modulation source, it is possible to control the current in the accelerating gap with a constant arc discharge current. Figure 2 shows characteristic waveforms demonstrating the ability to control the beam current at a reference voltage U_g = -20 V, U_0 = 15 kV, p (Ar) = 20 mPa, τ = 500 μs.

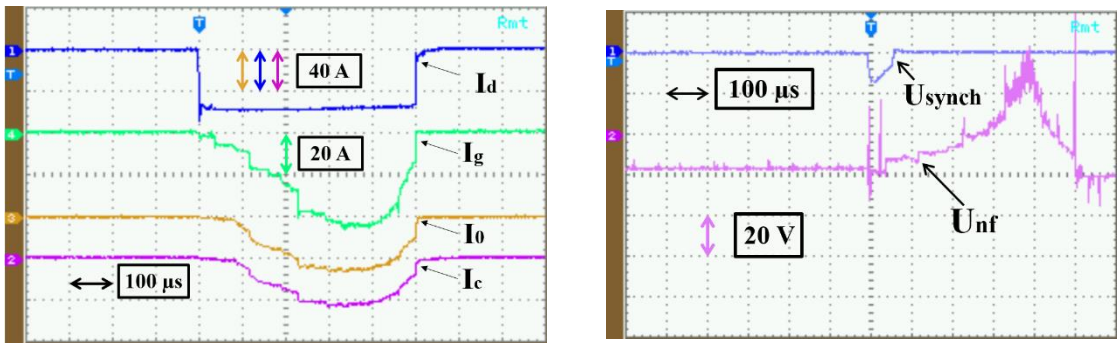

a b

Figure 2 – Characteristic oscillograms of the arc discharge current I_d, the current on the control grid I_g, the current in the accelerating gap I_0, the current on the collector I_c (a) and the inter-grid voltage U_{nf} (b).

Figure 3 shows the oscillograms of the collector current and the current in the accelerating gap, obtained using the modulation of the arc discharge current at a constant locking inter-grid voltage U_g = -20 V, U_0 = 25 kV, p (Ar) = 20 mPa, τ = 500 µs.

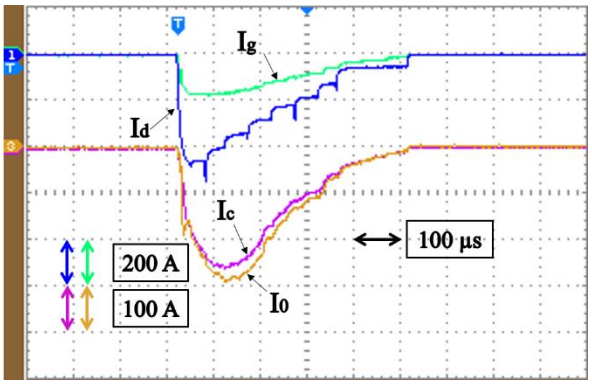

Figure 3 – Characteristic oscillograms of the arc discharge current I_d, the current on the control grid I_g, the current in the accelerating gap I_0, the current on the collector I_c in the mode of increasing power.

The combined control of the amplitude of the beam current allows simultaneous change of the amplitude of the arc discharge current and the value of the inter-grid voltage, which is also focused on expanding the range and precision of the power of the generated electron beam. In this case, due to the combined control of the arc discharge current and the control inter-grid voltage during a single pulse of submillisecond duration, it is possible to implement both high-energy beam current pulses designed to melt the surface of the material, and relatively low-current ones designed for cleaning and preheating the target. The presented approach to electron beam generation opens up new possibilities for its use in scientific and technological purposes.

Acknowledgements. The work was supported by the Ministry of Science and Higher Education of the Russian Federation (Number: FWRM-2021-0006).

References

1. **N.N. Koval, E.M. Oks, Y.S. Protasov, N.N. Semashko,** Emission Electronics, 2009, p. 595.
2. **N.N. Koval, Yu.F. Ivanov.** Evolution of the structure of the surface layer of steel subjected to electron-ion-plasma processing methods, 2016, p. 304.
3. **M.S. Vorobyov, P.V. Moskvin, V.I. Shin, T.V. Koval, V.N. Devyatkov, S.Yu. Doroshkevich, N.N. Koval, M.S. Torba, K.T. Ashurova,** Technical Physics, 92 (6), 883 (2022).
4. **V.N. Devyatkov, M.A. Mokeev, M.S. Vorobyov, N.N. Koval, P.V. Moskvin, R.A. Kartavtsov, S.Yu. Doroshkevich, M.S. Torba,** Technical Physics Letters, 50 (10), 20 (2024).

TURBULENT DECAY OF THE THERMAL CAVERN OF THE HF CORONA DISCHARGE

I. Moralev*, I. Selivonin

Joint Institute for High Temperatures, Moscow, Russia
*morler@mail.ru

High-frequency corona discharge is formed at atmospheric and higher pressures when an alternating voltage with frequencies ranging from 0.1 to 30 MHz and amplitudes on the order of several kilovolts is applied between the tip and a surrounding bulk electrode. Extensive research has been dedicated to studying the propagation and properties of these discharges, driven both by the insulation design of high-frequency high-voltage devices [1] and by issues related to lean mixtures ignition in car engines [2]. This type of discharge combines a high gas temperature at the channel axis (up to 3 kK) and sufficiently large electric fields in the region surrounding the discharge channel [1]–[3]. As a result of the development of a HF corona, a heated region with a reduced gas density – a thermal cavity – forms in the gas. The processes of thermal cavity dissipation have been well studied for a spark discharge [4]. It has been shown that the hydrodynamics of a spark thermal cavity is determined by the superposition of the formation of large-scale vortices on the electrodes and channel bendings due to baroclinic effects and the generation of small-scale turbulence as a result of the Richtmyer-Meshkov instability. Detailed studies of the discharge dynamics and thermal cavity for HF corona are carried out in this paper.

The discharge propagation was studied in dry air and methane-air mixtures at pressures from 1 to 4 atm and room temperature (Fig.1). The discharge was fed by sinusoidal voltage with radio-pulses modulation with a duration of 0.2-3 ms, base frequency of 850 kHz and an amplitude of voltage of 10-20 kV. The characteristic power dissipated in the discharge during radio-pulse was 3-100 W, estimated net power – 10-30W/(cm atm). Discahrge structure was studies using schlieren device and optical camera. It is shown that the discharge channels propagate within 50 μs from the occurrence of the discharge, while the temperature in the discharge already in the first 500 μs exceeds 1500 K. After that propagation velocity drops to several meters per second.

Starting from approximately 20-300 μs after initiation, both the low-density cavern and the discharge channel exhibit sinuous deformations. Deformation amplitude grows exponentially with time, with increment on the order of 1-5 10^4 s^{-1}. The initial instability wavelength is on the order of 2-3 cavern diameters and decreases with increasing pressure. Due to the generation

of subharmonics of the initial disturbance, this wavelength increases over time, reaching several millimeters by around 1 ms.

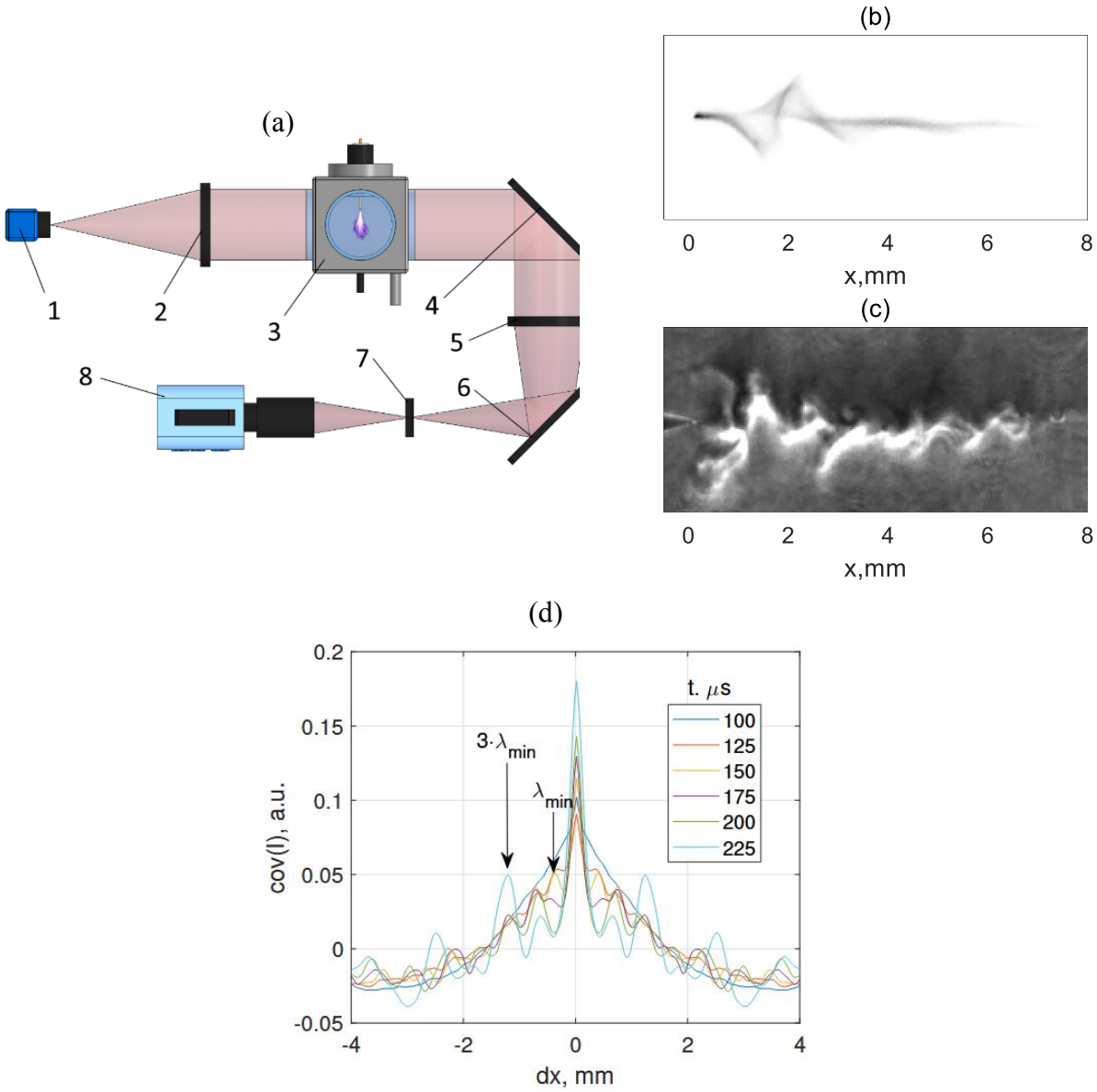

Fig. 1. (a) – Experimental setup: 1 - laser, 2,4,5,6 - lens, 3- high pressure chamber, 7- knife, 8 – high-speed camera; (b) – Integral image of the discharge for 500 μs (brightness inverted); (c) – Schlieren pattern of the flow at the time 300 μs from the beginning of the pulse and integral image of the discharge (P=2 atm, U=18 kV); (d) Subharmonics generation of the initial instability, visualized by the covariance of the intensity profiles along the filament

The underlying mechanism of this instability requires further investigation. Currently, the Kelvin-Helmholtz instability and nonlinear acoustic forces are considered the primary candidates.

Furthermore, it has been demonstrated that the discharge morphology is closely linked to discharge cavern deformation by this secondary flow, with

bends in the filament leading to discharge branching. This effect resembles the formation of apokamp discharges in pulsed-repetitive nanosecond discharges, studied in [5]. Typical propagation velocity of the new filaments is on the order of several meters per second (<20 m/s) and is on the order of the elongation velocity of the main channel. It is assumed that these new branches are associated with the filamentation of the glow discharge present at the bends of the RF filament. This suggests that gasdynamic deformations play a significant role in shaping the evolution and structure of the discharge.

The work was supported by the Russian Science Foundation within the framework of scientific project № 24-29-00791.

References

1. **M. A. Aronov and V. P. Larionov, Eds.,** Electrical insulation of the high frequency high voltage devices (in Rus.). // Moscow: Znak, 1994.
2. **F. Auzas, P. Tardiveau, V. Puech, M. Makarov, and A. Agneray,** "Heating effects of a non-equilibrium RF corona discharge in atmospheric air," // J. Phys. D. Appl. Phys., vol. 43, no. 49, 2010.
3. **M. Laan and J. Susi**, "Determination of N2 C3πu → B3πg (0 – 0) Band Absorption in the Propagating HF Discharge Channel," in XVII International Conference on Phenomena in Ionized Gases (July 8-12, 1985, Budapest, Hungary), 1985, p. 1014.
4. **M. A. Shurupov, S. B. Leonov, A. A. Firsov, D. A. Yarantsev, and Y. I. Isaenkov,** "Gasdynamic instabilities during decay of the submicrosecond spark discharge channel," //High Temp., vol. 52, no. 2, pp. 169–178, 2014.
5. **E. A. Sosnin et al.,** "Apokamps produced by repetitive discharges in air,"// Phys. Plasmas, vol. 25, no. 8, 2018.

ON THE CHARGE EXTRACTED FROM A MICROHOLLOW CATHODE PLASMA REACTOR

K. Romanov, E. Shershunova, S. Nebogatkin

Institute for Electrophysics and Electric Power RAS, 18 Dvortsovaya nab. lit. A, St.-Petersburg, 191181, Russia, email: eshershunova@ieeras.ru

1. Introduction. Plasma technologies utilizing cold plasma find applications in various fields, including medicine /1-3/, chemistry and biochemistry /1/, agriculture /4-6/, material processing /7, 8/ and others. Discharges with a microhole cathode are characterized as gas discharges between a cathode with a microaperture and an anode. /9/. Such devices first studied over 20 years ago, operate at atmospheric pressure, and attract attention due to their small size, low energy consumption, and low ignition voltage /10, 11/. The increasing use of microplasma requires /12/ detailed study of discharge parameters, which depend on voltage, flow rate, and target characteristics /13/. Charge extracted from a coaxial reactor with a microhole cathode due to argon flow and the application of direct current (DC) or pulse voltage were evaluated in this work. The influence of target distance and gas flow rate on the transferred charge was studied. Differences in charge transfer depending on the voltage shape and flow rate were identified, and optical emission spectra of the plasma were recorded.

2. Experimental setup. The experimental setup is described in detail in reference /14/. A photograph of the reactor is shown in Fig. 1. In the experiments two high-voltage sources were used: a rectangular pulse generator developed at the IEE RAS with an amplitude of up to 6 kV, a pulse repetition frequency of 3 kHz, and a pulse duration of 600 ns /15/ (pulse mode), as well as a commercially available DC voltage source Plazon HVSA-30/10, with an output voltage up to 30 kV and a current up to 10 mA (DC mode).A quartz tube with an external diameter of 24 mm served as a chamber of the plasma reactor. The anode was a 1 mm diameter tungsten needle. High voltage was applied to the anode through a ballast resistor. The cathode was a nickel foil with a 1 mm hole, placed 1 mm from the anode tip. The discharge in the reactor occurred between the needle and the nickel electrode. A conductive target with a diameter of 25 mm was placed at a distance from the reactor nozzle (from 2 to 10 mm). The

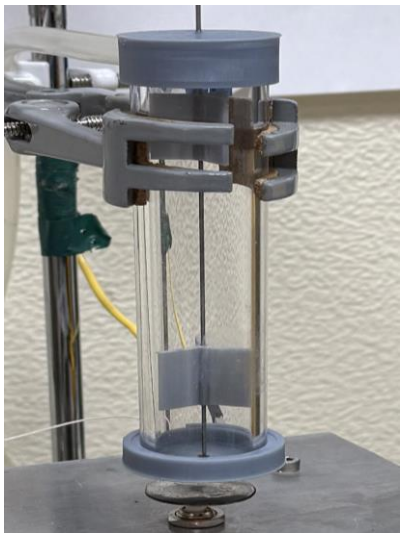

Fig. 1 – Photo of the reactor

target was grounded through a capacitor to measure the charge carried out from the reactor. The voltage on the reactor electrodes, the voltage across the capacitor, and the discharge current in the reactor were measured using specialized capacitive and resistive sensors and displayed on an oscilloscope with a bandwidth of 200 MHz (Keysight DSOX2024A). The optical emission spectrum of the plasma discharge was recorded using an optical fiber spectrometer Brolight BIM-6002 with an accuracy of 1 nm.

3.1 Results. DC mode. In DC mode, ignition voltage was 230–260 V at argon flow rates of 2–8 L/min (42-169 m/s) and distance to the target up to 10 mm. A graph illustrating the dependence of the amount of charge carried out on the flow velocity and the distance to the target was obtained (Fig. 2). It was established that the amount of charge reaching the target increases with increasing gas flow rate. The ion drift velocity in a weak electric field was calculated. Theoretical studies indicate that ions initially introduced into the drift zone are primarily Ar^+ ions /16/. According to the reference /17/ the mobility of argon ions (Ar^+) in the weak field is 1.54 $cm^2/(V \cdot s)$. Thus, the obtained value of the ion drift velocity (~10 m/s) is comparable to the gas flow velocity.

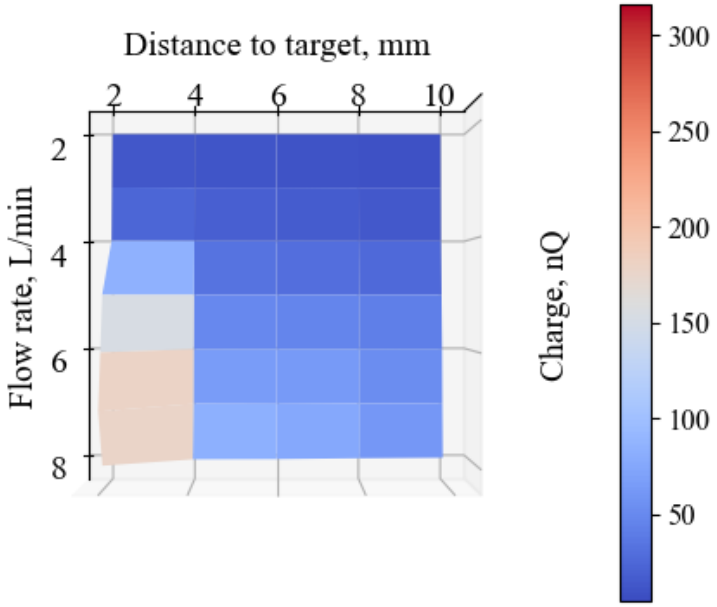

Fig. 2 –The amount of extracted charge versus the flow rate and the distance to the target for the DC mode

An optical emission spectrum of the discharge was obtained (Fig. 3). The 680–850 nm spectrum shows characteristic argon emission lines, indicating the presence of excited argon atoms in the plasma /18/.

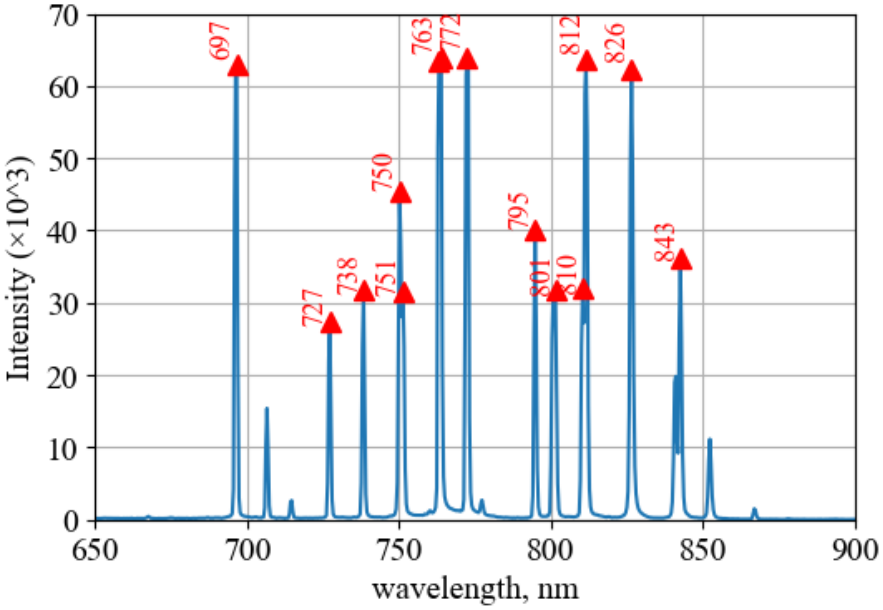

Fig. 3 – The obtained spectrum for the DC mode

3.2 Results. Pulse mode. For the pulse mode, the ignition voltage ranged from 1900 to 2600 V at the same gas flow rates and distances to the target as in the DC mode. The dependence of the charge amount on the flow velocity and the distance to the target is shown in Fig. 4. Based on estimates, the value of the ion drift velocity was approximately 100 m/s. The optical emission spectrum does not differ from the spectrum observed under constant voltage power supply; however, the intensities of the lines are higher by an order of magnitude.

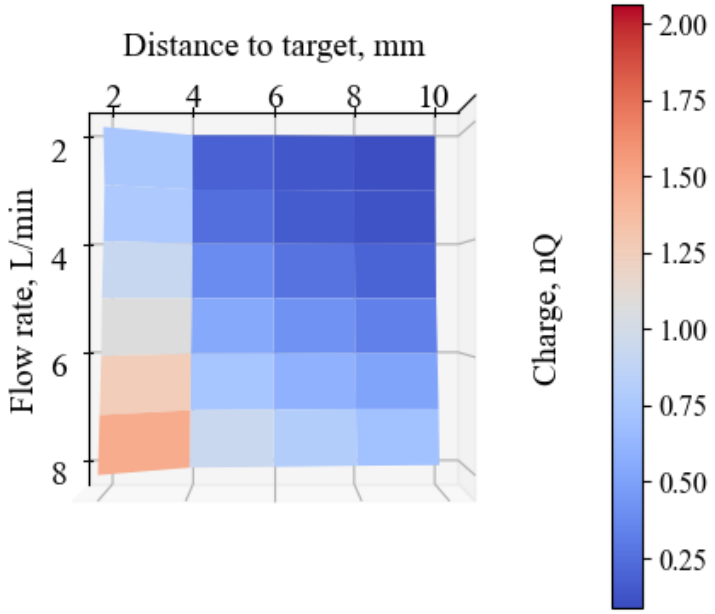

Fig. 4 –The amount of extracted charge versus the flow rate and the distance to the target for the pulse mode

4. Conclusions. In this work, an experimental study of a discharge with a microhole cathode in argon was conducted. It was established that the carried charge depended on the power supply mode, the distance to the target, and the gas flow rate. In the direct current (DC) mode, the discharge ignition occurs at relatively low voltages (230–260 V). In the pulse mode, significantly higher voltages (1900–2600 V) are required. It was found that the gas flow rate and the distance to the target influenced the amount of extracted, which could be utilized in practical applications of such microdischarges. Spectra were obtained for the two modes (DC and Pulse). Their overall appearance is similar: characteristic argon emission lines are present in the range of 680–850 nm. For the Pulse mode, the optical emission spectrum does not differ in composition from the spectrum observed under constant voltage power supply; however, the intensity of the lines is higher by an order of magnitude.

Acknowledgements. This work was supported by the Ministry of Education and Science of the Russian Federation (FFGR-2025-0001).

References

1. **Wende K. et al.** Biological Chemistry, 400(2018) 19-38.
2. **Laroussi M.** Frontiers in Physics, 8(2020) 74.
3. **Bernhardt T. et al.** Oxidative medicine and cellular longevity, 1(2019) 3873928.
4. **Domonkos M. et al.** Applied Sciences, 11(2021) 4809.
5. **Misra N. N. et al.** Academic Press, 2016.
6. **Thirumdas R. et al.** Trends in food science & technology, 77(2018) 21-31.
7. **Hnatiuc E. et al.** IEEE, (2012) 497-502.
8. **Anisovich A.G. et al.** Foundry and Metallurgy, 2(2019) 85-91. (in Russian)
9. **Schoenbach K H et al.** Phys. Plasmas, 7(2000) 2186
10. **Moshkunov S. I. et al.** Journal of Physics, 15(2021) 012032.
11. **Moshkunov S. I. et al.** Plasma Physics Reports, 48(2022) 449-452.
12. **Becker K H et al.** J. Phys. D: Appl. Phys, 39(2006) R55
13. **Shershunova E. A. et al.** IEEE Transactions on Plasma Science, 47(2019) 4909.
14. **Shershunova E. A. et al.** Applied Physics, 5(2025) [in press] (in Russian)
15. **Moshkunov S. I. et al.** Letters to the Journal of Technical Physics, 45(2019) 34-36 (in Russian).
16. **McAfee Jr K. et al.** Physical Review, 160(1967) 130.
17. **Madson J. M., Oskam H. J.** Physics Letters A., 25(1967) 407-408.
18. **Gorbunkov V.I. et al.** Omsk State Technical University, 3(2019) 123-130 (in Russian)

THEORETICAL AND EXPERIMENTAL STUDY OF NEUTRON SOURCES AND PLASMA GENERATORS

A.G. Polyanskiy, S.V. Ryzhkov

Bauman Moscow State Technical University (BMSTU),
2-nd Baumanskaya, 5, 1, Moscow, 105005, Russia, svryzhkov@bmstu.ru

Introduction.

The beginning of the development of neutron tubes (neutron generators) on the territory of the Russian Federation dates back to 1947. At this point in time, the key parameters of neutron tubes are considered to be: the time of the beginning and end of the neutron pulse (at a certain threshold of its value), the magnitude of the integral neutron output, the specific intensity of the neutron pulse (neutron/mcs) and its duration, the deviation of the average neutron flux level during repeated inclusions and the stability of operation.

The neutron spectrometers, which are being created in collaboration with other neutron centers of the country, will make it possible to study both atomic and supratomic structures of condensed media, as well as thermal vibrations of atoms and molecules, as well as the course of kinetic processes under various external influences and the isotopic composition of matter.

The possibilities of producing neutron beams in a wide range of energies are also of great importance /1-7/. The latter circumstance makes it possible to "probe" the medium for the presence and properties of inhomogeneities with sizes from subatomic to tens of nanometers. The range of applications of neutron research methods is becoming wider and extends, for example, from the study of proteins or biological processes in cell membranes, including the study of catalysts, batteries and magnetic substances, as well as determining the service life of turbine blades and gas turbines in energy production. We can also mention the importance of neutron research methods for solving fundamental and still unresolved problems of condensed matter physics: heavy fermion systems, insulators, valence fluctuation systems, high-temperature superconductors.

The greatest information about the studied medium is carried by neutrons, the wavelength of which (or at least the inverse of the transmitted pulse in small-angle scattering) is commensurate with the characteristic sizes of objects, whether it is the nucleus of an atom, a biological molecule or a nanoinclusion in a material.

Neutron generators.

The use of neutron generators (including neutron sources) is associated, firstly, with the possibility of implementing remote analysis of the elemental

composition of matter on their basis, and, secondly, direct effects on nuclear materials and some types of cells of living organisms.

The generation of monochromatic neutrons is always based on one of the neutron-converting reactions. The most convenient for neutron generation are those characterized by the absence of a threshold and a sufficiently large cross-section of neutron-forming reactions (the critical value of the cross-section depends on the target value of the neutron yield) at relatively low energies (about 50 keV) of the incident nuclei. Such reactions are primarily reactions with isotopes of hydrogen, since the Coulomb barrier is minimal for nuclei with a charge number about 1. Neutron generators at other reactions cannot be made portable primarily due to the need to obtain accelerating voltages of the order of 1 MeV, so further we will talk about devices operating on deuterium-deuterium (DD) or deuterium-tritium (DT) fusion reactions /8-11/.

Neutrons are produced as a result of a thermonuclear reaction in converter targets containing deuterium or tritium, when they are "bombarded" with accelerated deuterium ions (which come from an ion source). The converter targets of neutron generators, which make it possible to obtain high-intensity neutron fluxes, are usually solid-state and consist of thin layers (up to several tens of microns) of titanium, scandium or zinc deposited on a copper substrate. The energy lost by the beam of charged particles in the converter target is determined by the current and energy of the ion beam coming from the ion source, and can reach large values (up to tens of kW per square centimeter). Obviously, in this case, such targets require effective cooling.

Applications.

The coaxial high-power neutron generator for medical applications /12-14/ has the ability to operate in high-power beam mode. This is made possible due to the unique location of the target. The basic scheme of a coaxial neutron generator consists of a high-frequency induction ion source with an internal antenna, a target cylinder surrounding the source and an insulator cylinder surrounding the target.

As noted in the article /15/, a pure thermonuclear fusion probe suffers from predicted low Q-factor values (energy gain). Much higher energy production can be achieved in a thermonuclear reactor, where the neutron source of the thermonuclear plasma is surrounded by a fission shell. Thermonuclear neutrons are capable of initiating energetic fission reactions in the surrounding mantle. The mirror machine can probably be designed in such a way as to provide sufficient space for a 1.1 m wide fission shell inside the current coils, and the energy production as a result of fission reactions can in this case exceed the power of thermonuclear fusion by more than two orders of magnitude ($P_{fis}/P_{fus} \approx 150$), which implies a realistic reactor mode for the device

thermonuclear fusion based on a mirror. The device that generates energy can operate at an electron temperature of about 1 keV. Transmutation of long-lived radioactive isotopes (minor actinides) from spent fission reactor nuclear fuel can reduce geological storage from 100,000 years to just 300 years. Since the energy of thermonuclear neutrons D-T exceeds the threshold value for the most important transmutation reactions necessary for the treatment of nuclear waste, there may be interest in a mirror transmutation device, even if clean energy is not produced.

Recent theoretical calculations have shown the possibility of using the gas dynamic trap (GDT) in Novosibirsk as a subcritical burner for thermonuclear neutron transmutation. In this paper, the possibilities of mirror-based thermonuclear fusion systems are discussed. The means of achieving sufficient terminal insulation for a rectilinear mirror thermonuclear fusion system with a thermal barrier are briefly analyzed. Alternatively, leakage at the ends can be avoided by connecting the ends of the magnetic mirror to the stellarator tube, while thermonuclear neutrons are formed in the part of the mirror where the high-energy ionic component is contained. A zero-dimensional model has been developed for such a mirror-stellarator system. The calculation results indicate some possible parameter modes for industrial transmutation and power generation. The article /16/ presents the project and strategy for the development of a continuously operating thermonuclear volumetric neutron source with a high flux ($> 10^{18}$ n s^{-1}).

The proposed installation is based on a gas-dynamic magnetic plasma confinement device with injection of a high-power neutral beam (~ 50 MW). The project roadmap includes the construction of several pilot plants that solve a specific set of physical and engineering tasks, ranging from the continuous operation of critical subsystems to advanced plasma physics problems typical of axisymmetric mirror plasma retention plants. The project is aimed at establishing the widest possible international cooperation to create a multi-purpose experimental facility that could solve a number of problems most important for the introduction of economical thermonuclear energy around the world. The document discusses in detail the basic principles of operation of a gas-dynamic neutron source, presents the parameters, expected performance and basic principles for the construction of intermediate and final devices, as well as outlines ways to solve scientific and engineering problems that make up the project.

Conclusion.

One of the urgent applied tasks of modern physics is the search for new promising (hybrid) technical systems aimed at creating a source of high-energy particles (for example: neutron fluxes generated in thermonuclear installations).

Such advanced technologies based on the use of plasma, fusion reactions, magnetic inertial confinement (through the use of super-strong magnetic fields) and powerful heating sources such as lasers and accelerators are necessary in industries and in the transition to the energy of the future. One of the urgent tasks of nuclear energy is the reprocessing of spent nuclear fuel, which is necessary for the transition to a closed fuel cycle in order to more fully involve reactor fuel resources by isolating minor actinides for the reuse of refitted fuel. The paper describes thermonuclear neutron sources that can be used for processing irradiated nuclear fuel to extract fissile isotopes, for plasma separation of spent nuclear fuel and separation of components of spent nuclear fuel by plasma method in azimuthal magnetic and radial electric fields.

This research has been supported by Russian Minobrnauki, No. 0705-2024-0022

References

1. **Velikhov E.P., Ilgisonis V.I.** Prospects for Thermonuclear Research // Herald of the Russian Academy of Sciences, 91 (2021) 284–291.
2. **Kuzenov V.V., Ryzhkov S.V.** Physica Scripta, 96(12) (2021) 125613.
3. **Garanin S.G., Ivanovskii A.V., Kulikov S.M., Mamyshev V.I., Pevny S.N. and Rogachev V.G.** Plasma Physics Reports, 48 (2022) 111-120.
4. **Ilgisonis V.I., Ilyin K.I., Novikov S.G., Olenin Yu.A.** Plasma Phys. Rep., 47 (2021) 1085-1091.
5. **Bystritskii V.M., Bystritskiy V.M., Dudkin G.N., et** al. JETP Letters, 99:9 (2014) 497–502. DOI: https://doi.org/10.1134/S0021364014090033
6. **Polyanskiy A.G.** Review of target for laser-irradiated neutron sources // Heat Transfer Research (2024). DOI: 10.1615/HeatTransRes.2024055057
7. **Kuzenov V.V., Ryzhkov S.V.** Fusion Science and Technology, 79 (2023) 399-406. DOI: https://doi.org/10.1080/15361055.2022.2112037.
8. **Grabovski E.V., et al.** JETP Lett., 103 (2016) 350–356. https://doi.org/10.1134/S0021364016050040.
9. **Polyanskiy A.G., Ryzhkov S.V.** Models of Compact Neutron and Particle Sources under the Action of Laser Radiation // AIP Conf. Proc. (2025).
10. **Ryzhkov S.V.** Applied Sciences, 13 (2023) 6658.
11. **Polyanskiy A.G.** // High Temperature Material Processes, 28 (2024) 11-19.
12. **Antonov N.N., Vorona N.N., et al.** Tech. Phys., 61:2 (2016) 180–186.
13. **Polishchuk V.P., et al.** High Temperature, 58:4 (2020) 476–494.
14. **Samokhin A.A., Smirnov V.P., et al.** Tech. Phys., 61:2 (2016) 283–289.
15. **Ågren O., et al.** // Fusion Science and Technology, 55:2T (2009) 46-51.
16. **Bagryansky P.A., Chen Z., et al.** // Nucl. Fusion, 60 (2020) 036005.

EXPERIMENTS ON THE IONIZATION WAVES INTERACTION IN LONG TUBES

V. Zaletov, A. Shishpanov

Saint Petersburg State University,
198504 Rassian Federation, Saint Petersburg, Peterhof, Ul'yanovskaya 3,
vlad.zaletov@mail.ru, a.shishpanov@spbu.ru

The ionization waves (IW) interaction /1/ is a poorly studied process that occurs in nature as a streamer collision during the lightning leader progress /2/, but is rarely observed in laboratory conditions. The present work is devoted to the study of the IW interaction occurring in discharge tubes at low and moderate gas pressures. The main difference between such IWs and air streamers consists in that their plasma contacting the tube wall, creating a charge on it with potential of the same order as the applied voltage. They also have high reproducible parameters in the pulse-periodic mode of generation, which allows obtaining reliable data on the processes involving them.

We conducted an experiment on the interaction of different polarities IWs. The waves propagated towards each other from opposite ends of a sealed gas-discharge tube filled with neon at different pressures. The length of the tubes was 40-80 cm, with inner diameter of 1.3 cm. To prevent the development of current surges in the circuit, one or both waves were started from the external electrode. To reproduce the result of the IW interaction, the problem of identical initial waves at each discharge was solved in the experiment. Each IW was powered from an independent DC voltage source using a circuit consisting of a switch and ballast resistance connected in series with the electrode. The switches created rectangular voltage pulses with frequencies below 10 Hz and duration in range 100 μs – 2s. The tube was placed in a grounded metal screen, 5 cm in diameter, with a longitudinal slot, in which a pair of capacitive probes could move to record the IW signals at different points along its trajectory. The probe design and the interpretation of the obtained signals, as well as the details of the experiment are described in /3/. The probe signals allowed to find instantaneous IW velocities, and the longitudinal component *E*-field before and after interaction.

It was found that the interaction of the ionization waves of different polarity led to the formation of only one IW of positive polarity with velocity of several times greater than the same of every initial IWs near the electrodes. Depending on the pressure and the polarities ratio of the external and internal electrodes, the resulting wave could acquire a velocity characteristic of fast ionization waves, reaching about 10^9 cm/s.

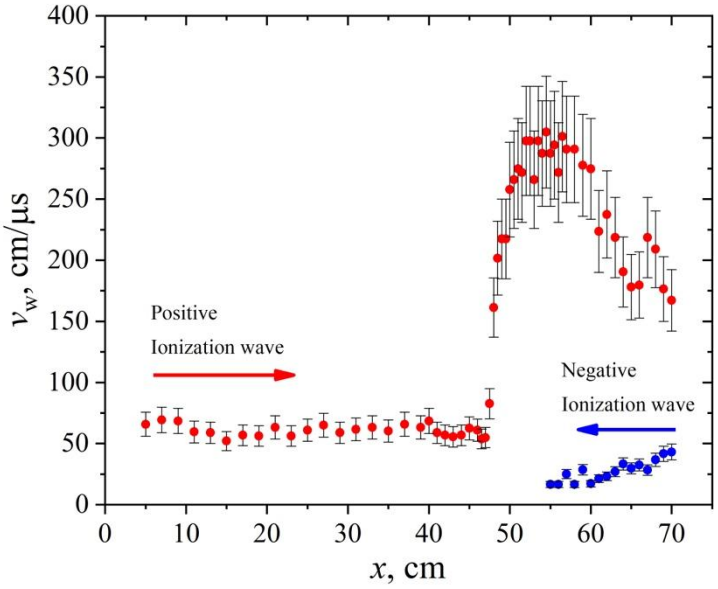

Figure 1. Example of velocity-distance diagrams of interaction ionization waves: ● - positive ionization wave, ● – negative. Ne 0,5 Torr, frequency 10 Hz, voltages on the electrodes at the wave's ignition moments are ±1,5 kV.

Figure 1 illustrates this phenomenon by the dependencies of the counter ionization waves instantaneous velocities on the distance traveled. This is an example of rather weak wave interaction at pressure 0,5 Torr and ignition voltages ±1,5 kV. The region of the fast wave existence is clearly seen at the graph, which is the 25 cm tube section. At the beginning of the region (first 5 cm), velocity of the resulting IW increases sharply and reaches a maximum, after that it gradually decreases. The strong scatter of the fast wave velocities can be associated both with the instability of the interaction process and with random errors in measuring the short travel time across small section between the probes (10 mm). The fast wave velocity is on average 5-6 times higher than of the initial waves near the electrodes. It is evident that in the fast wave existence region, a negative wave which passed these points before the interaction is recorded while near the positive electrode, it was not detected. This result shows that the interaction of different polarity IWs leads to the formation of a new wave, rather than the waves passing through each other like solitons. It is also worth noting the sharp transition of the positive wave to a fast one during interaction (Figure 1), which occurs at a distance of less than 1 cm - the gap width between the capacitive probes that scanned the tube.

Figure 2 shows another illustration of the IW interaction which is the results of measuring the *E*-field longitudinal component for each IW-partner as a function of the coordinate and time at a pressure of 50 Torr in case of low-frequencies discharge pulses (with a period of 4 s). Using these graphs as an example, we will highlight the common features in the behavior of interacting waves. 1) The *E*-field strength at the positive wave front, regardless of the electrode type, was greater than that of the negative one. It also turned out to be higher for the internal electrode IW compared to electrodeless waves. 2) The *E*-field strength of the resulting IW does not show a significant increase in amplitude compared to the initial waves, but the high field region becomes significantly larger (up to 2 times

in the presented example) than that of the initial IW. 3) Even with high synchronization of the initial wave appearance moments, the process of their interaction was unstable. This was manifested in registration time jitter of the signal corresponding to their fusion.

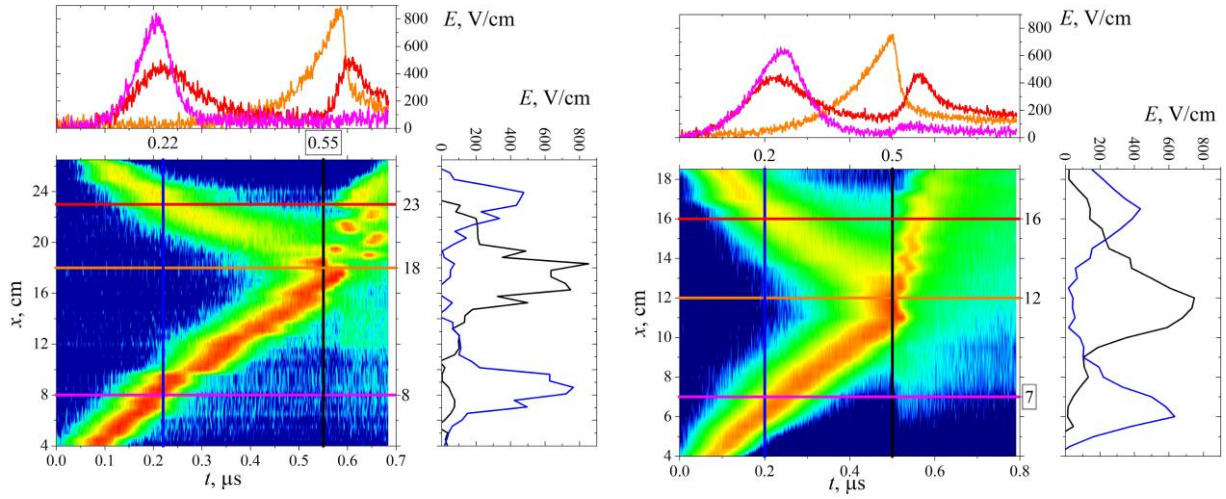

(a) (b)

Figure 2. Longitudinal components of the *E*-field strength as a function of time and distance. Ne, 50 Torr. Red color corresponds to field values > 900 V/cm, and blue light corresponds to values < 50 V/cm. The negative polarity electrode is placed at the top of the graph (U_0 = -3 kV). The positive polarity electrode is placed at the origin of the coordinates (U_0 = 3 kV) and it could be internal (a) or external (b) electrode.

Acknowledgements. The work of V.Zaletov and A.Shishpanov was supported by the Ministry of Science and Higher Education of the Russian Federation (agreement 075-15-2025-343 dated 29/04/2025 for Saint Petersburg Leonhard Euler International Mathematical Institute at Saint Petersburg State University)

References

1. **J. Qiu, C. Zhang, Z. Liu, D. Hu and T. Shao**, IEEE International Conference on Plasma Science (ICOPS), Denver, USA, 2018, pp. 1-1.
2. **Cooray V., Arevalo L., Rahman M., Dwyer J., Rassoul H**. Journal of Atmospheric and Solar-Terrestrial Physics, 71 (2009) 1890-1898
3. **Shishpanov A.I., Zaletov V.V., Bazhin P.S.** Bulletin of the Lebedev Physics Institute, 51, (2024) 256-261.

IONIZATION WAVES THAT FORMING CAPACITIVE DISCHARGE AT LOW AND MODERATE GAS PRESSURES

V. Zaletov, A. Shishpanov

Saint Petersburg State University, 198504 Rassian Federation,
Saint Petersburg, Peterhof, Ul'yanovskaya 3, vlad.zaletov@mail.ru, a.shishpanov@spbu.ru

Ionization waves (IW) constitute an extensive class of phenomena accompanying plasma formation under diverse conditions. Numerous works /1-3/ have studied the IW propagation velocity as a function of electromagnetic characteristics; however, direct comparison of these results is hindered by significant variations in experimental conditions, including gas type and pressure, discharge chamber geometry and voltage waveform. The research presented aims to identify universal patterns in the behavior of IW generated within glass tubes during a capacitive discharge at low and moderate gas pressures.

In the experiment, detailed in /4/, we employed two sets of sealed glass tubes: one set filled with neon at pressures ranging from 0.5 to 50 Torr, and another set contained various inert gases (helium, neon, argon, krypton, xenon) at a fixed pressure of 1 Torr. All the tubes have an internal diameter of 1.3 - 1.5 cm and lengths of 40-80 cm. A capacitive discharge was initiated from a single internal electrode which was an aluminum hollow cylinder. A switching unit generated rectangular voltage pulses with frequencies below 1 Hz of both polarities (amplitude 3 kV, duration up to 10 ms). The tube was enclosed within a grounded cylindrical screen with longitudinal slit. A pair of capacitive probes, whose design is described in /4/, can displace along the tube through the slit. The probe signal reflects the temporal evolution of the local plasma potential.

It was found that the IW potential (φ_w) attenuation along the tube follows an exponential decay: $\varphi_w = \varphi_0 \exp(-\alpha x)$, where φ_0 is the initial potential, α is the attenuation coefficient. This pattern was previously known just for the fast ionization waves and discussed in /1/. Our experimental results demonstrate that the electric field amplitude diminishes analogously. Figure 1(a) illustrates this pattern showing behavior of the electric field peak in the IW front at various distances from the electrode. The field behavior also exhibits weak pressure dependence, consistent with prior results /5/. Furthermore, the coefficients governing field attenuation coincide precisely with those for potential decay, as illustrated in Figure 1(b). A decrease in pressure results in a decrease in the attenuation coefficient, suggesting its minimum under our conditions possibly occurs at p below 1 Torr.

In argon, krypton, and xenon, the electric field manifests spatial and temporal characteristics like those in neon. However, under positive polarity, the IW field

in neon is approximately 40% greater than in other gases (Fig. 2(a)).

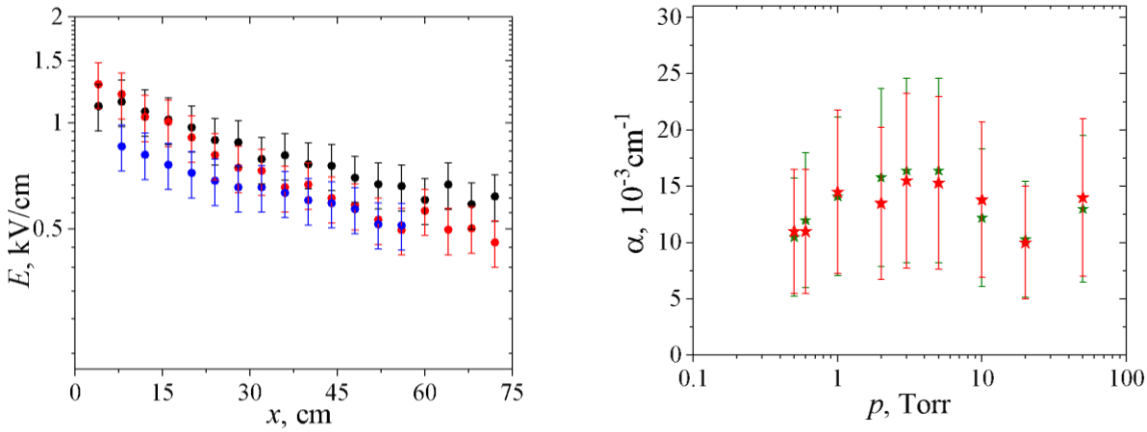

(a) (b)

Figure 1. (a) Electric field strength peaks at different distances from the electrode. ● - 0,5 Torr, ● - 5 Torr, ● - 20 Torr. (b) Attenuation coefficients of the field strength (★) and ionization wave potential amplitude (★) at different pressures. Neon, $U_0 = 3$ kV.

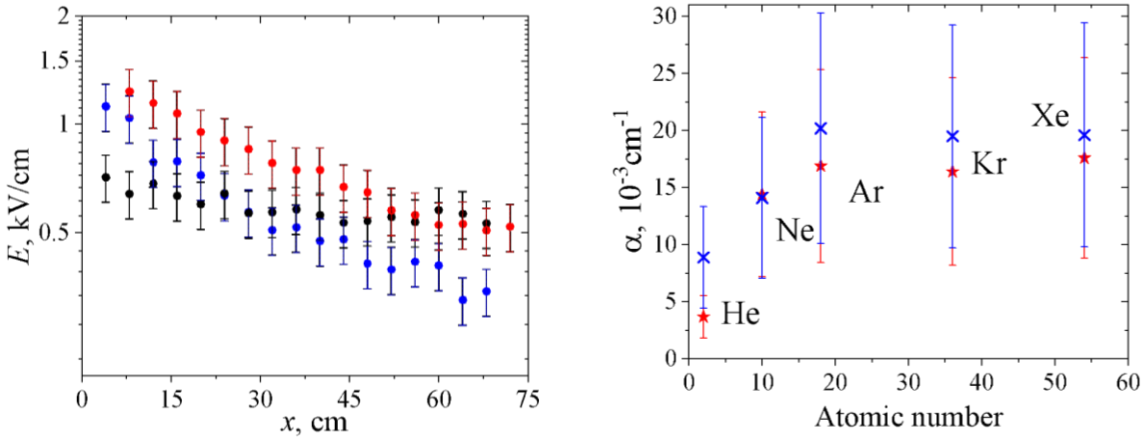

(a) (b)

Figure 2. (a) Electric field strength peak of the positive ionization wave at different distances from the electrode. ● - helium, ● - neon, ● - xenon. (b) Field strength attenuation coefficients for positive (★) and negative (×) ionization waves in different noble gases. $U_0 = 3$ kV, $p = 1$ Torr.

For helium in case of positive voltage polarity, the initial field strength is roughly 1.5 times lower than in other gases, yet it exhibits negligible attenuation during propagation. Consequently, by the tube midpoint, field values in helium become comparable to those in other gases and ultimately exceed them by the termination of the wave's propagation. A similar trend, albeit less pronounced, occurs under negative polarity, with the IW field in helium approaching values in other gases only near the tube's end. Figure 2(b) shows field attenuation

coefficients obtained from longitudinal measurements in different noble gases. These coefficients increase with atomic mass and are consistently higher for negative ionization waves.

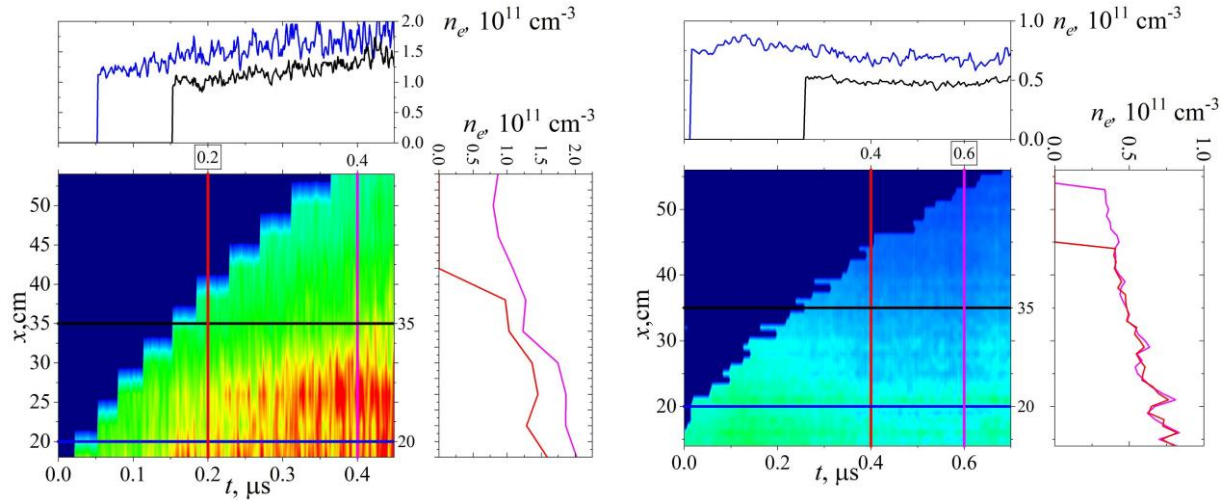

(a) (b)

Figure 3. Dependences on distance to the electrode end time of the electron density behind the ionization wave front. The red color corresponds to $n_e > 2 \cdot 10^{11}$ cm^{-3}, while for $n_e < 2 \cdot 10^{10}$ cm^{-3} the color is blue. Neon 5 Torr. (a) $U_0 = 3$ kV, (b) $U_0 = -3$ kV.

Electron densities (n_e) behind the wave front in neon were computed from IW current and electric field measurements at fixed voltage (±3 kV) for various pressures, employing methodology used in /5/. Examples of such calculations at 5 Torr are shown in Fig. 3. It illustrates several trends found. For negative IW, n_e remains remarkably constant throughout propagation. In contrast, the plasma channel of positive IW exhibits significant temporal evolution of electron density, with n_e increasing up to twofold by the wave's path termination (upper curves, Figure 3(a)). Crucially, for both polarities, the electron density generated at the front decays with increasing distance from the electrode. This behavior, observed universally across the pressure range, directly results from the IW field attenuation.

Notably, positive IW yielded electron densities 2 to 6 times higher than negative waves at the same applied voltages. Nevertheless, across the entire pressure range at 3 kV, n_e consistently remained on the order of 10^{10}-10^{11} cm^{-3}. Fig. 4 depicts n_e and the degree of ionization (k) versus pressure. The maximum in n_e occurs near 10 Torr for positive polarity and near 3 Torr for negative one. Conversely, k decreases monotonically with rising pressure, which is in accordance with findings in /5/.

The IW current can be interpreted as the charging current of a cylindrical capacitor, $I = CvU_0$ /1/, where C is the linear capacitance, v is the instantaneous wave velocity and U_0 is the electrode potential. Assuming that the potential drop

behind the front is caused by current through a resistive medium, it follows that $I = 2\pi r^2 \sigma \alpha U_0$, where r is the tube radius and $\sigma \sim n_e/N$ is the plasma conductivity behind the front. The attenuation coefficient α decreases with falling pressure, while σ increases. Consequently, their product should exhibit a maximum, which would be reflected in the pressure dependence of the wave velocity. We observed this maximum experimentally, and its existence has been repeatedly confirmed in other works (see for example: /1/).

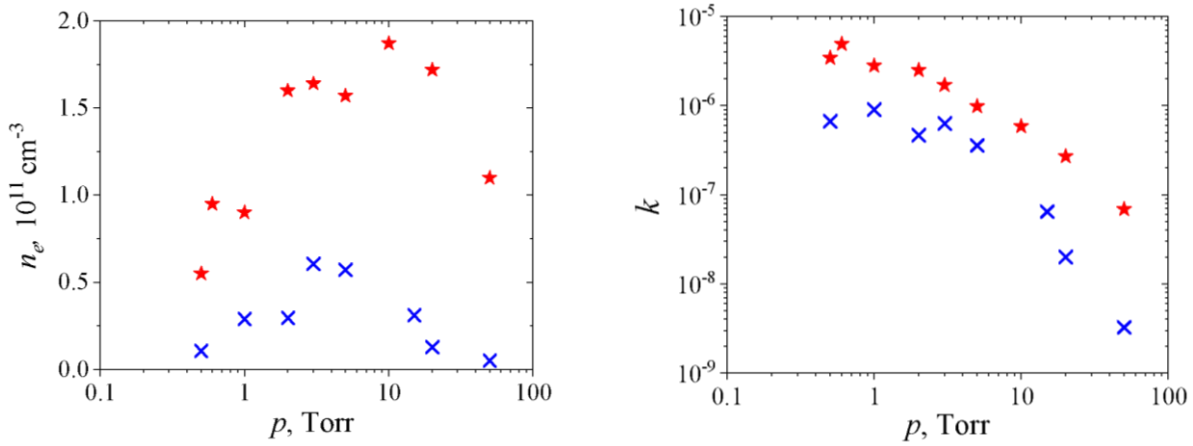

(a) (b)

Figure 4. Electron concentration (a) and ionization degree (b) as a function of pressure. Values obtained for a point 20 cm from the electrode at the moment when ionization wave front reached the tube termination. Neon, positive (★) and negative (✕) voltage polarities (amplitude 3 kV).

Acknowledgements. The work of V.Zaletov and A.Shishpanov was supported by the Ministry of Science and Higher Education of the Russian Federation (agreement 075-15-2025-343 dated 29/04/2025 for Saint Petersburg Leonhard Euler International Mathematical Institute at Saint Petersburg State University)

References

1. **Vasilyak, L.M. et al.** Physics-Uspekhi, 37, (1994) 247.
2. **Ionikh Yu. Z.** Plasma Physics Reports, 46, (2020) 1015-1044.
3. **Lu, XinPei, and Kostya Ken Ostrikov** Appl. Phys. Rev., 5, (2018) 031102.
4. **Shishpanov A.I., Zaletov V.V., Bazhin P.S.** Bulletin of the Lebedev Physics Institute, 51, (2024) 256-261.
5. **Anikin, N.B., et al.** Journal of Physics D: Applied Physics, 31, (1998) 826.

PLASMA SOURCE OF UV RADIATION WITH EXCITATION BY COMBINED DISCHARGE

K. Znosko

State University of Grodno, Ozheshko Street 22, 230023, Grodno, Belarus,
znosko@rambler.ru

For practical use in various fields of science, technology and industry, sources of ultraviolet (UV) radiation are required. At present, a large number of UV radiation sources have been developed that operate on various physical principles /1, 2/. The need for UV radiation sources is currently mainly satisfied by mercury or quartz lamps. However, exciplex sources on inert gas halides are more effective /3, 4/. To excite the working medium in these sources, volume, glow, barrier, capacitive, high-frequency and other discharges are used. The use of a particular discharge type is determined by the intended purpose of the UV source. Today, there is a wide variety of designs of such sources /2-9/.

From the point of view of the contact of the working medium with the discharge electrodes, electric discharge radiation sources are divided into two classes. The first class includes sources whose discharge electrodes are located directly in the working medium and are in contact with it. These include radiation sources with excitation by volume, spark, glow, self-sustained and other discharges /8, 9/. Their main disadvantage is the spraying of the electrode material that occurs during the discharge. This leads to contamination of the working medium with metal particles injected from the surface of the electrodes. The second class includes radiation sources whose working medium does not have direct contact with the discharge electrodes. These are sources with excitation by barrier, capacitive, high-frequency and other discharges /10-12/. In this case, the electrodes are isolated from the working medium by the walls of the discharge flask. This class of gas-discharge radiation sources is also called "electrodeless".

Capacitive discharge has found wide practical application for excitation of the working medium in UV radiation sources /2, 4-6, 11, 12/. UV radiation sources with excitation by capacitive discharge have high resource characteristics and operational stability. However, their disadvantage is the low specific radiation power with a sufficiently high efficiency. This is a consequence of fundamental physical limitations on the power input into the discharge, caused by too small interelectrode capacitance.

Although studies of pulsed gas discharge plasma have been conducted for a long time, including for the purposes of gas-discharge lasers /13, 14/, the task of creating highly effective sources of UV radiation has not yet been fully solved. The results of modeling show that it is also not always possible to successfully control the kinetics of plasma-chemical processes occurring in the working environment /15, 16/.

To correct the above-mentioned drawback of the capacitive discharge, it is proposed to use a combined discharge to excite the working environment. To form a discharge in the working environment using a capacitive discharge, and to deposit energy into it (with some delay) by a self-sustained discharge. The spraying of the electrode material into the working environment does not occur from their entire surface, but only from the "hot" points to which the streamers that arise during the formation of the self-sustained discharge are attached. The imposition of a self-sustained discharge on a capacitive discharge will lead to an increase in the degree of uniformity of the discharge, will lead to the absence of streamers and the preservation of the purity of the working environment.

This paper presents the results of an experimental study of the emission properties of a UV radiation source operating on a mixture of inert gases with a halogen carrier when excited by a combined discharge.

To conduct experimental studies, a model of a gas-discharge emitter was developed and created, shown in Figure 1. It consisted of a quartz flask (1) of cylindrical shape, 40 mm in diameter and 300 mm in length, on the ends of which discharge electrodes (2) were located on flanges (3-5). When screwing the nuts on the studs (4), the sealing ring (6) is deformed, ensuring a hermetic connection of the flanges with the cylindrical flask. The flanges (3) had a longitudinal-transverse channel (7) for evacuating the emitter and filling it with a gas mixture. On the outer surface of the quartz flask (1) there were ring electrodes of the capacitive discharge (8).

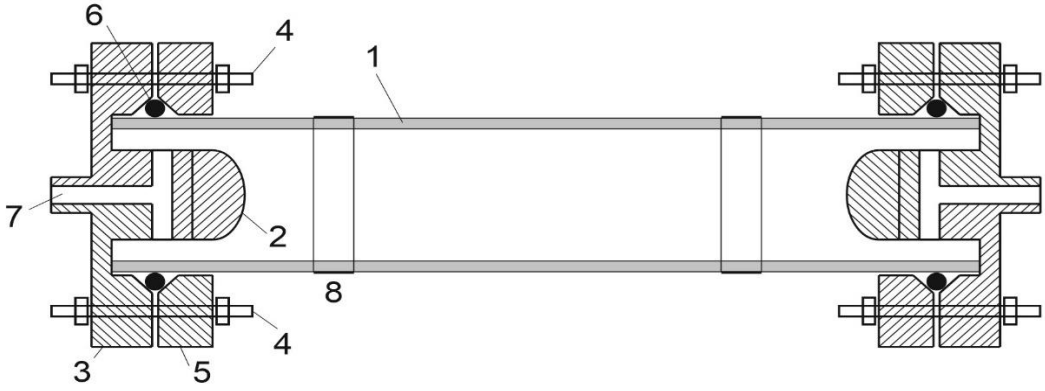

Figure 1 – Longitudinal section of a gas-discharge emitter

To create a discharge, a power source was developed that generated high-voltage paired pulses. The first pulse was fed directly to the ring electrodes (8) and formed a capacitive discharge in the emitter. The second pulse was fed to the end electrodes and contributed energy to the plasma formed by the capacitive discharge. Thus, combined formation and excitation of the discharge in the working environment of the emitter was realized. The power source allowed the pulse repetition rate to be adjusted within 10–50 kHz.

A series of experiments aimed at optimizing the composition of the working medium were carried out. Figure 2 shows the dependences of the average UV radiation power on the HCl pressure in the working medium. The Xe pressure was 10 Torr (1), 20 Torr (2), 30 Torr and 40 Torr (4). The Ne pressure was 60 Torr. The dependences of the radiation power on the Xe pressure at HCl pressures of 2 Torr (1), 2.5 Torr (2) and 3 Torr (3) are shown in Figure 3. The dependences of the radiation power on the Ne pressure are shown in Figure 4. The partial pressures of HCl and Xe were: 2 Torr and 20 Torr (1), 2.5 Torr and 25 Torr (2), 3 Torr and 30 Torr (3). The repetition rate of paired pulses for exciting the working medium with a combined discharge was 25 kHz. It was found that the optimal working environment is the following composition: 2.5 Torr HCl + 25 Torr Xe + 60-80 Torr Ne.

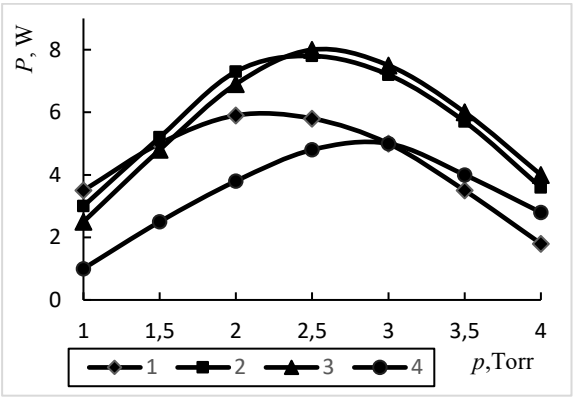

Figure 2

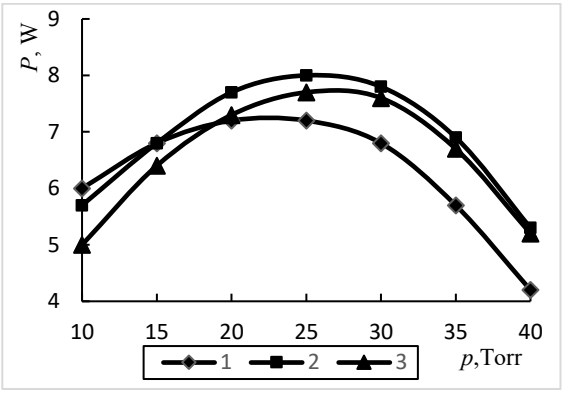

Figure 3

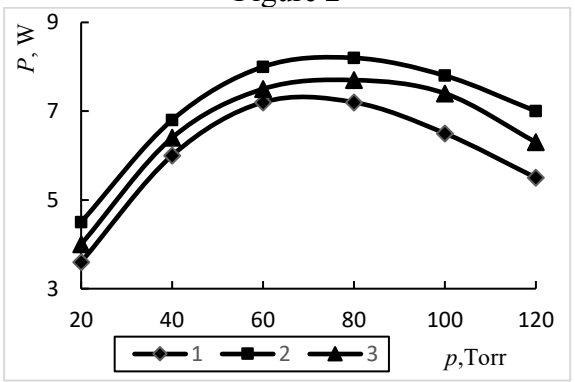

Figure 4

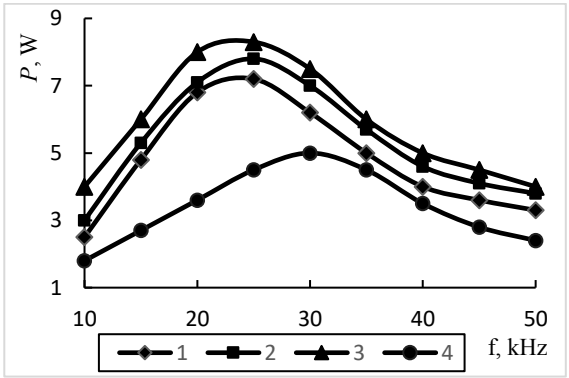

Figure 5

Figure 5 shows the dependences of the UV radiation power on the pulse repetition rate. The working medium with the component ratio HC1:Xe:Ne – 1:15:30, pressure 92 Torr (1), HC1:Xe:Ne – 1:10:20, pressure 93 Torr (2), HC1:Xe:Ne – 1:10:24, pressure 88 Torr (3), HC1:Xe:Ne – 1:10:24, pressure 44 Torr (4) was used. The most optimal pulse repetition rate was 23 kHz. With an increase in the pulse repetition rate, the radiation power increases. However, at frequencies exceeding 25 kHz, a decrease in the radiation power is observed. This

occurs because at high frequencies, the cores of pulse transformers enter saturation and a decrease in the excitation energy in a single pulse occurs.

Thus, the use of combined excitation allows forming a diffuse discharge in mixtures of inert gases with a halogen carrier and obtaining high radiation efficiency on its basis. The use of a combined discharge leads to a fourfold increase in the power of UV radiation compared to using only a capacitive discharge. The average power of the UV source was 8 W when operating at a frequency of 23 kHz and an efficiency of 8% relative to the power source energy.

References

1. **Rokhlin G.N.** Discharge light sources. 2nd ed. Moscow, (1991).
2. **Lomaev M.I., Panchenko A.N., Sosnin E.A. [et al.].** Gas-discharge sources of spontaneous ultra-violet radiation: Excilamps. Tomsk, (1999).
3. **Erofeev M.V., Tarasenko V.F.** Journal of Physics D: Applied Physics, 39 (2006) 3609-3614.
4. **Lomaev M. I., Skakun V. S., Sosnin E. A. [et al.].** Advances in Physical Sciences, 173 (2003) 201-217.
5. **Znosko K.F.** Vesnik of Yanka Kupala State University of Grodno. Series 2. Mathematics. Physics…, 8 (2018) 102-112.
6. **Znosko K.F., Belash V.Ch.** Vesnik of Yanka Kupala State University of Grodno. Series 6. Engineering Science, 9 (2019) 28-39.
7. **Shuaibov A.K., Dashchenko A.I.** Quantum electron., 30 (2000) 279-281.
8. **Panchenko A.N., Tarasenko V.F.** Quantum electron., 36 (2006) 169-173.
9. **Znosko K.F.** Vesnik of Yanka Kupala State University of Grodno. Series 6. Engineering Science, 9 (2019) 81-91.
10. **Lomaev M.I., Skakun V.S., Tarasenko V.F. [et al.].** Journal of optical, 79 (2012) 83-91.
11. **Anufrik S.S., Volodenkov A.P., Znosko K.F.** Vesnik of Yanka Kupala State Univer. of Grodno. Series 2. Mathemat. Phys…, No.1 (186), (2015)113-124.
12. **Znosko K.F., Belash V.Ch.** Vesnik of Yanka Kupala State University of Grodno. Series 2. Mathematics. Physics…, 9 (2019) 74-85.
13. **Belash V.Ch., Znosko K.F.** Vesnik of Yanka Kupala State University of Grodno. Series 2. Mathematics. Physics…, 8 (2018) 83-92.
14. **Anufrik S., Volodenkov A., Znosko K.** International Conference on Lasers, Applications, and Technologies 2007: Advanced Lasers and Systems. Minsk, 2007, vol. 6731, art. 673106.
15. **Anufrik S.S., Volodenkov A.P., Znosko K.F.** 8th International conference on laser and fiber-optical networks modeling, LFNM 2006: Proceed. of the conf., 29 June - 1 July, 2006. Kharkiv, Ukraine, art. 4018200, 80-83.
16. **Anufrik S., Volodenkov A., Znosko K.** High Temperature Material Processes, 18 (2014) 181-196.

CURRENT-VOLTAGE CHARACTERISTICS OF AN INCANDESCENT AND HOLLOW CATHODE ARC DISCHARGE

I. I. Azhazha, V. V. Shugurov, Yu. Kh. Akhmadeev

Institute of High-Current Electronics SB RAS, Tomsk, Russia, 634055,
vanya.azhazha@gmail.com, shugurov@inbox.ru, ahmadeev@opee.hcei.tsc.ru

In this paper, the characteristics of an incandescent and hollow cathode arc discharge (PINK) are investigated in a system with a "hot" anode, the current-voltage characteristics of the discharge are plotted, and the probe characteristics of the plasma are measured. The research was carried out on the surface electron-ion-plasma engineering installation "COMPLEX", developed in the laboratory of plasma-emission electronics of the IHCE SB RAS, included in the register of unique scientific installations of Russia "UNIKUUM".

The system with a "hot" anode is a PINK plasma generator, the anode of which is a crucible with boron-containing powder (B). All the current-voltage characteristics were recorded both for the PINK discharge itself in its usual design, when the discharge anode is a chamber, and for the case when the discharge anode is a powder crucible (a system with a "hot" anode).

Keywords: *plasma; arc evaporator; discharge; crucible; argon; discharge characteristics; hot anode*.

Introduction

Modern technological progress is closely related to the creation and widespread use of new inorganic materials with specific antifriction properties. In addition, there are materials that are similar in hardness and other properties to diamond [1]. Such materials include a cubic modification of boron nitride (cBN), which has a low coefficient of friction and a high modulusем of elasticity, which depend on the syngony and composition of the material [2]. Due to the high cost of cBN, recently they have been extensively engaged in research and development of materials with similar characteristics. Подобными характеристиками обладают BAlMg antifriction coatings BAlMg (BAM) have similar characteristics [3].

Antifriction coatings are widely used not only in electronics (Microelectromechanical systems - MEMS relays, switches, fast-acting accelerometers), but also in the production of internal combustion engines, in the system of contacting surfaces (friction – rolling pairs) and other areas of mechanical engineering and production.

In this paper, a comparative study of the operating modes of the PINK plasma generator in the configuration with an anode-chamber and in systemse with a "hot" anode is carried out, as well as the effect of the metal plasma of the arc plasma generator on the properties of the coatings obtained, compared with the parameters obtained in preliminary experiments [4].

The main part

The research was carried out on the electron-ion-plasma surface engineering installation "COMPLEX" (Fig. 1), developed in the Laboratory of plasma-emission Electronics of the IHCE SB RAS, which is included in the register of unique scientific installations in Russia.

Inoltamperny, the characteristics (VAC) were recorded both for the PINK discharge itself in its usual design, when the discharge anode is a chamber, and for the case when the discharge anode is a crucible with powder (a system with a "hot" anode) at different pressures and different working gas ratios Ar, Ar+$_{N2}$. The pressure change step was 0.1 Pa in the pressure range 0.1-0.8 Pa. The step of the working gas ratio (in %) Ar/N_2 was 100/0, 80/20, 60/40, 50/50, 40/60, 20/80, 0/100.

The roughness and friction coefficient were measured on a tribometer TRIBOtechnic, and the hardness was measured on a PMT-3M hardness tester.

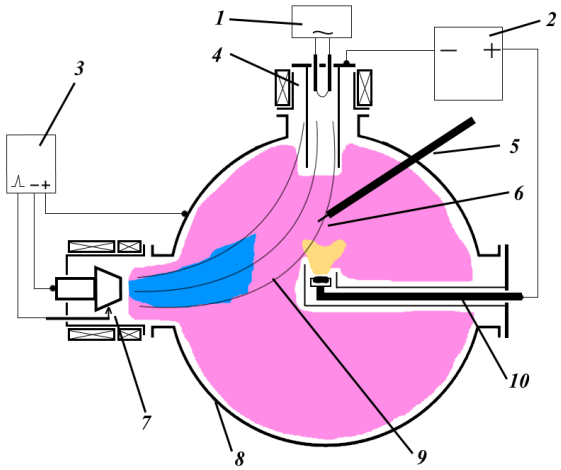

Fig. 1. Schematic diagram of an experimental setup for sputtering boride coatings and studying plasma. 1 - PINK glow unit, 2-PINK discharge power supply unit, 3-arc evaporator power supply unit, 4-PINK gas plasma generator, 5-probe input, 6-Langmuir probe, 7-arc evaporator, 8-vacuum chamber, 9-magnetic field lines

An ammeter and voltmeter built into the system's power supplies were used to measure the current-voltage characteristics of the discharge. The current-voltage characteristics were measured in two systems: in the standard one (Fig. 2), when the discharge anode is a chamber, and in the upgraded one (Fig. 3), when the discharge anode is a so - called "hot anode" - a crucible for spraying powder of a certain composition.

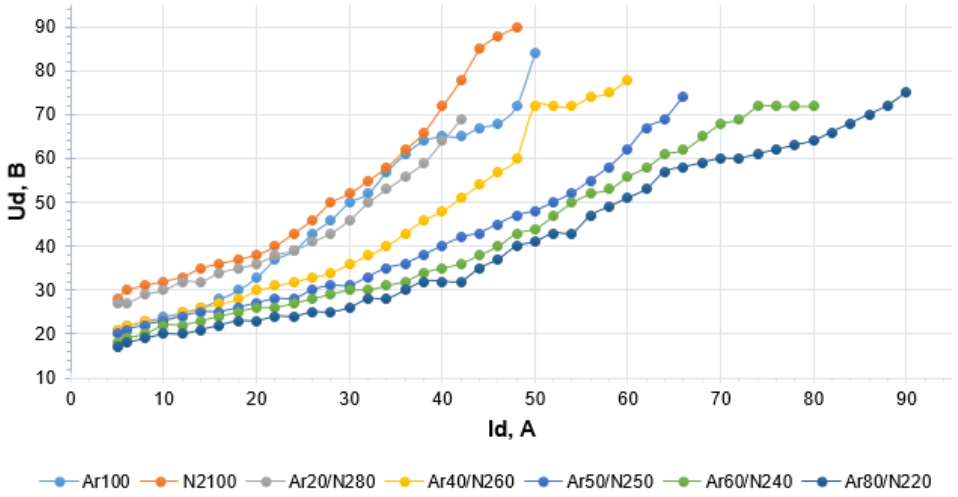

Fig. 2. Dependence of the discharge burning voltage on the discharge current in the standard system (P_{Ar} = 0.3 Pa)

The dependences obtained in an electrode system with an anode-chamber (Fig. 2) are characteristic when a nonmonotonic increase in the discharge burning voltage occurs with an increase in the current.

Switching the discharge to the anode-crucible leads to a slower current increase (Fig. 3)

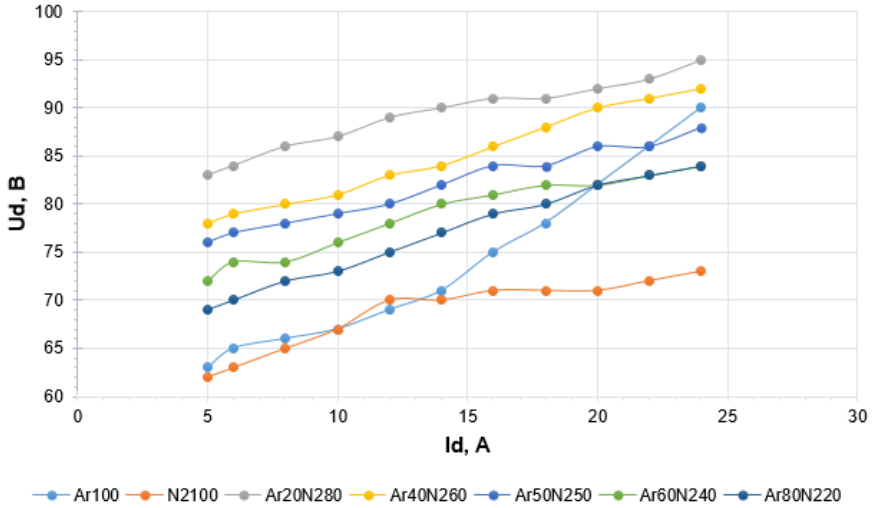

Fig. 3. Dependence of the discharge burning voltage on the discharge current in a system with a "hot" anode (P_{Ar} = 0.3 Pa)

For the Ar/N_2 50/50 curve, a voltage surge from 15 A is visible, which indicates the ignition of a parasitic discharge on the crucible holder equipment.

Conclusion

In the course of this work, the current-voltage characteristics of the plasma were obtained, which make it possible to control the parameters of coatings in the deposition process in a wide range.

Coatings of the BAM composition with a hardness of about 30 GPa, a roughness of 0.3 microns, and a coefficient of friction in the range of $5\ 10^{-6} – 5\ 10^{-7}$.

This work was supported by the Ministry of Science and Higher Education of the Russian Federation (number: FWRM-2021-0006)

List of sources used

1. Koval N. N., Ivanov Yu. F., Teresov A.D., Akhmadeev Yu. Kh., Krysina O. V., Petrikova E. A., Shugurov V. V., Lopatin I. V. Development of complex technology of electron-ion-plasma engineering of the surface of materials and products. *Nanoengineering.* 2015; 4(46): 4-13.
2. Yu.F. Ivanov, A.P. Laskovnev, A.D. Teresov, V.V. Uglov, E.A. Petrikova, V.I. Shymanski, N.N Cherenda. Modification of technically pure titanium with nitrogen in a low-pressure arc discharge plasma assisted by plasma generator "PINK". *News of higher educational institutions. Physics*. 2016; 9(2): 189-192.
3. Tkachev D. A., Zhukov I. A., Valikhov V. D., Shugurov V. V., Azhazha I. I., Akhmadeev Yu. K.Ion-plasma deposition of antifriction coatings $AlMgB_{14}$ and $AlMgB_{14\text{-}50}$wt. % TiB_2. *Problems of mechanical engineering and machine reliability* 2024; 5(1): 97-106.
4. Ivanov Yu. F., Shugurov V. V., Azhazha I. I., Petrikova E. A., Tolkachev O. S. Structure and properties of the Al-Mg-B coatingformed by the ion-plasma method on the surface of a high-entropy alloy.
Vacuum engineering and Technologies 2023; 1(1): 199-202.

FARADAY PROBE SYSTEM FOR MEASURING THE DENSITY AND ENERGY SPECTRUM OF COMPENSATED ION AND ION-PLASMA BEAMS USED IN THIN-FILM DEPOSITION TECHNOLOGY

R. Dubin, D. Ksenzov, A. Yasunas

[1]Freegy LLC, Republic of Belarus, Minsk, Nekrasova str., h.39-1, office №438,
worldwar9350@gmail.com, alex.yasunas@gmail.com

Using the full spectrum of technological capabilities of Ion Beam Sputtering (IBS) and Ion Beam Assisted Deposition (IBAD) requires understanding, precise control, and reproducibility of ion beam parameters – current density, ion energy, and their spatial distributions. Comprehensive characterization of these parameters enables controlled and repeatable fabrication of thin-film properties: density, adhesion, stoichiometry, microstructure, and consequently optical characteristics (refractive index, absorption, scattering) and long-term stability. Diagnostic methods for ion beam parameters include Faraday cups, calorimetry, mass spectrometry, optical emission spectroscopy, and Langmuir probes /1/.

For setup, optimization, and monitoring of ion sources in industrial conditions, the probe method for diagnostics of ion beam parameters using a three-electrode Faraday probe equipped with a suppressor electrode (hereinafter Faraday probe) is most suitable (see Fig. 1). This article discusses the operating principle and design of the "FCUP-E" automated system for measuring charged particle beam parameters using a Faraday probe. The measurement system includes: Faraday probe, ammeter block with vacuum flange, and external control unit.

The Faraday probe measures ion current and energy within a charged particle beam (see Fig. 1a). Positioned in the vacuum chamber at the measurement location, it interfaces with an external control unit. Figure 1b shows the probe's electrical configuration during measurements.

The "FCUP-E" system characterizes ion flux energy spectra via the retarding field method. A negative potential sufficient to limit the electron current from the plasma to the collector and the secondary electron current emitted from the collector to the probe housing is applied to the suppressor electrode (3).

A retarding potential difference is applied between the collector and the grounded probe housing. Only ions whish energy is sufficient to overcome the retarding potential difference reach the collector /2/. During measurement, the retarding potential is varied within the operator-specified range and with a given

step, which allows obtaining the ion retardation curve, from which the ion energy distribution is determined by differentiation.

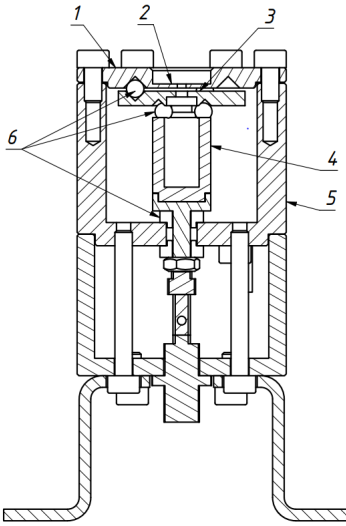

a) Front cover (1), aperture (2), suppressor electrode (3), collector – Faraday cup (4), case (5), insulators (6)

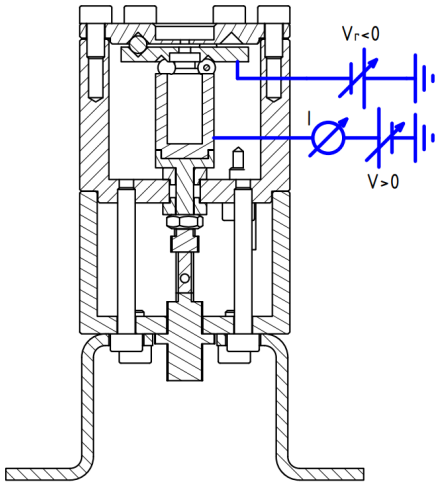

b) Faraday probe connection during retardation characteristic measurement

Fig. 1 – Design and connection diagram of the Faraday probe

The measurement block (see Fig. 2) can measure electric current in the range from 1 nA to 2.5 mA in a high-voltage circuit up to 2000 V. A transimpedance amplifier, isolating operational amplifier, and analog-to-digital converter (ADC) provide conversion of the measured current into voltage, based on which the controller calculates the current value depending on the measurement range. The nano-milliammeter block is based on a transimpedance amplifier, whose operation consists in converting the measured current into voltage without distortion.

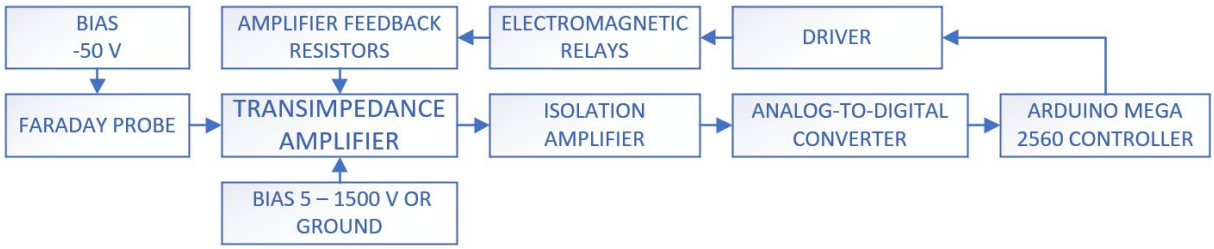

Fig. 2 – Block diagram of the nano-milliammeter

For this purpose, the operational amplifier is connected in a circuit with negative feedback through a resistor. Its inverting input is connected to the circuit

for measuring current in it, and the non-inverting input is connected to ground. The amplifier dynamically adjusts its output voltage so that the potential difference between the inputs remains close to zero. The output voltage of the amplifier is directly proportional to the current, which allows accurate measurement even of picoampere quantities /3/.

The high-voltage block is designed to supply bias voltage to the collector of the Faraday probe in the range from 0 to 1500 V. The 12-bit digital-to-analog converter (DAC) used, together with a linear voltage regulator, achieves a resolution of the high-voltage block output voltage of 0.37 V.

Using the developed system, retardation curves and ion energy distribution profiles were obtained for an ion source with single-grid (see Fig. 3) and three-grid (see Fig. 4) ion-optical systems.

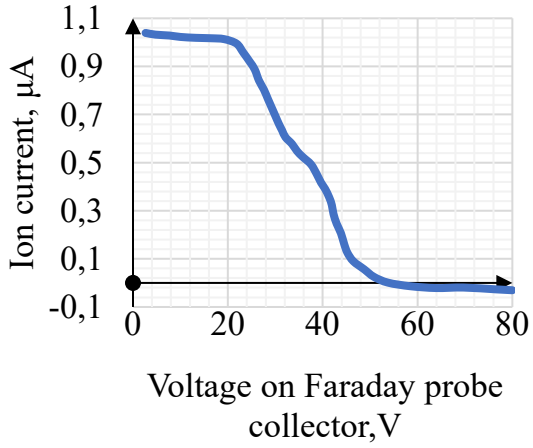

a) Retardation curve

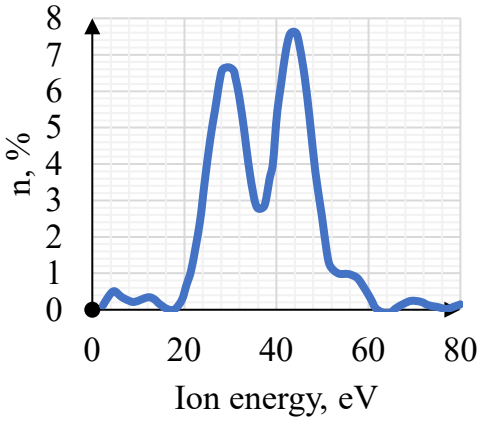

b) Ion energy distribution

Fig. 3 – Faraday probe characteristics of the single-grid ion source

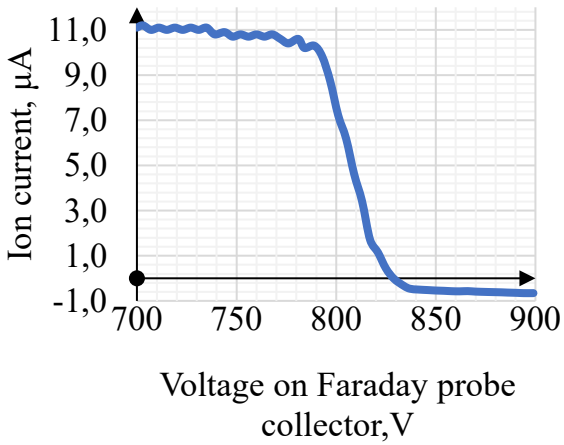

a) Retardation curve

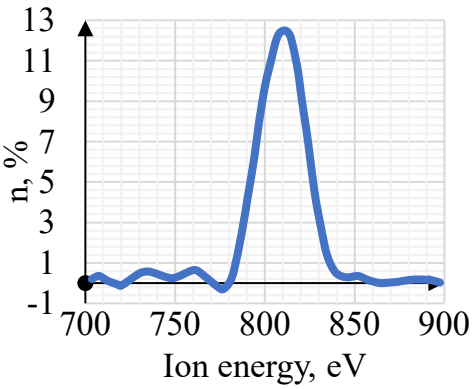

b) Ion energy distribution

Fig. 4 – Faraday probe characteristics of the three-grid ion source

The developed "FCUP-E" system enables comprehensive characterization of charged particle beams – including current, energy spectrum, spatial profile, and angular divergence – using a three-electrode Faraday probe. The system is intended for operation with electrostatic ion accelerators with volume ionization (grid-type ion sources such as Kaufman), electrostatic and magneto-plasmadynamic plasma accelerators (end-Hall plasma accelerators, anode-layer accelerators, etc.). The system provides current measurements from 1 nA to 2.5 mA and supports ion energies up to 1500 eV.

References

1. **Пушкарев А., Исакова Ю.** П91 «Диагностика мощных ионных пучков» (2016) 2–9.
2. **Chen, F., Chang J.** Lecture notes on Principles of Plasma Processing (2002) 95–96.
3. **Lacoste R.** «Picoammeter Design» Circuit Cellar (2010) 63–64.

PATTERNS OF EMISSION PLASMA GENERATION PRODUCED BY NON-SELF-SUSTAINED GLOW DISCHARGE IN HOLLOW CATHODES OF DIFFERENT VOLUMES AT LOW PRESSURE

A. Egorov, V. Yakovlev, V. Denisov, S. Kovalsky, E. Ostroverchov

Institute of High Current Electronics SB RAS, Tomsk, Russian Federation,
egorov.ao.work@gmail.com

The present study focuses on exploring the possibility for generating high-intensity electron beams from the plasma of a non-self-sustained glow discharge within a hollow cathode. For electron pulse beams with a large cross-sectional area, arc discharge-based sources /1, 2/ are commonly employed. Their primary advantage lies in high electron current density, reaching up to 10 A/cm^2, although the resulting plasma exhibits low temporal homogeneity due to the inherent physical properties of the discharge. This leads to unstable electron beam extraction when pulse durations approach the submillisecond range or when the cross-sectional area increases. Switching to a non-self-sustained glow discharge for plasma generation could enable extending the permissible operating ranges of the source—both in terms of time (up to 1 ms) and cross-sectional area (hundreds of cm^2).

Initial research on the discharge parameters and plasma characteristics /3/ was carried out using a Langmuir probe /4/ in a large-volume experimental chamber with a volume of approximately 0.34 m^3. The image of the vacuum chamber and the experiments diagram are presented in Figure 1.

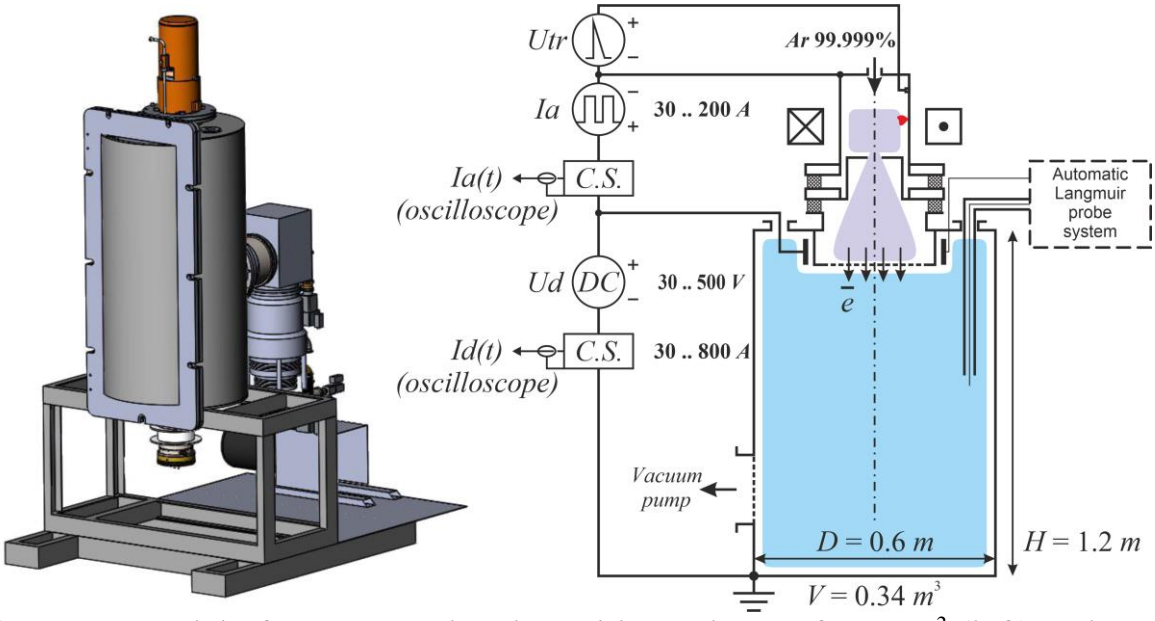

Fig. 1. 3D model of a vacuum chamber with a volume of 0.34 m^3 (left) and a

diagram of the experiments (right).

The main non-self-sustained glow discharge was established between a hollow cylindrical cathode and an annular anode positioned at the top of the cathode. Electrons were injected into the hollow cathode volume from an external arc discharge source, triggered by a high-voltage pulse. The chamber was evacuated using a turbomolecular vacuum pump to a minimum pressure of $5 \cdot 10^{-3}$ Pa, while the operating pressure ranged from 0.02 to 1 Pa during an inlet of 99.999% argon. The discharge voltage varied from 30 to 500 V, the auxiliary arc discharge current spanned from 30 to 200 A, and the pulse duration reached up to 1 ms. The typical dependencies of the glow discharge current on pressure and injection current are depicted in Figure 2.

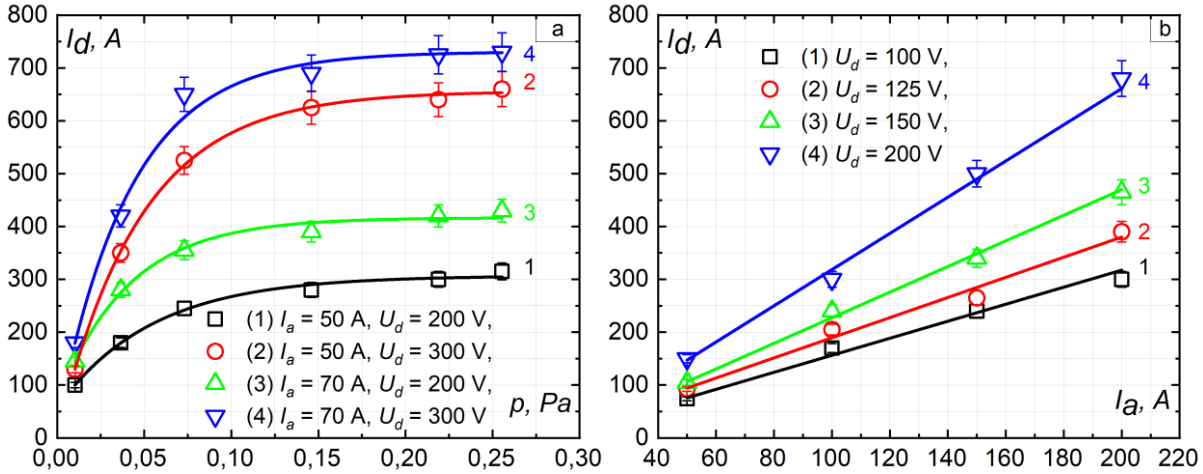

Fig. 2. (a) Dependences of glow discharge current on the working pressure. (b) Dependences of glow discharge current on arc discharge current at an argon pressure of 0.025 Pa.

At low pressure (0.025 – 0.25 Pa), pulse currents of up to 800 A were obtained at a discharge burning voltage of up to 400 V and a pulse duration of 1 ms. Plasma with a concentration of about 10^{12} cm^{-3} and an ionization degree of up to 16% was formed. The measured electron saturation current densities on the probe were 3.7 A/cm^2 (0.025 Pa), 5 A/cm^2 (0.05 Pa) and 6.7 A/cm^2 (0.25 Pa), which indicates the prospects for using pulsed plasma of a high-current glow discharge with a hollow cathode in devices for generating pulsed intense electron beams of large cross-sections.

The next step was to study the processes in a small volume, to be able to create a compact source of electron beam. For this purpose, a model with a hollow cathode volume of 0.007 m^3 was made. The image of the model and the scheme of experiments are presented in Figure 3.

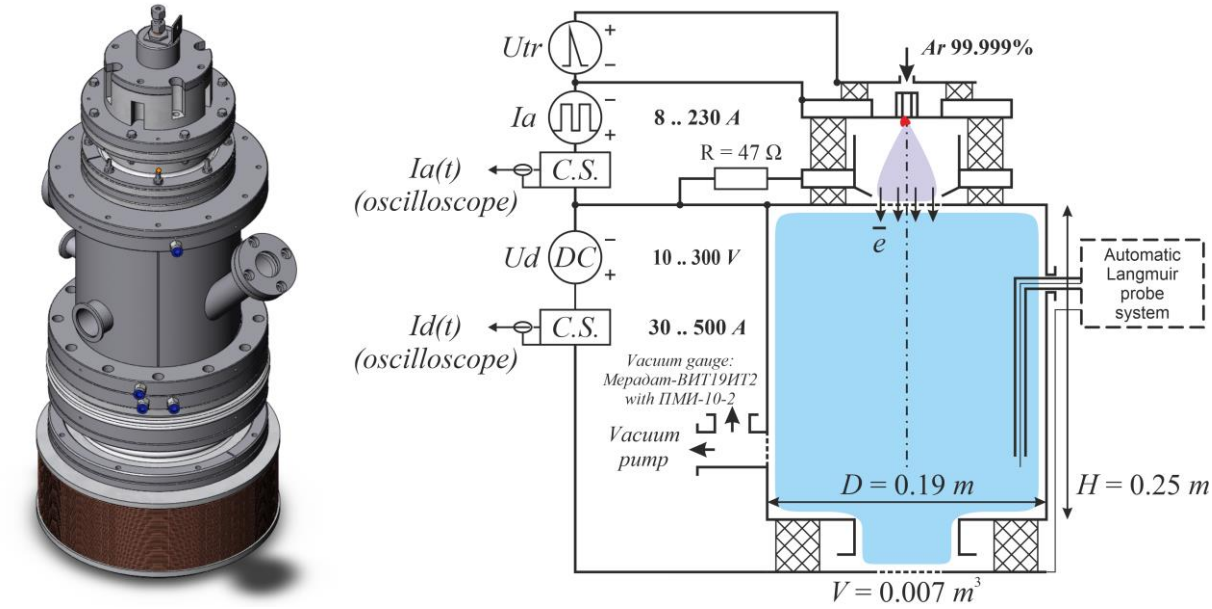

Fig. 3. 3D model of a vacuum chamber with a volume of 0.007 m^3 (left) and a diagram of the experiments (right).

In this case, a glow discharge was formed between a hollow cylindrical cathode and a mesh anode located in the lower part of the cavity. The discharge voltage varied from 10 to 300 V, the auxiliary arc discharge current was in the range from 8 to 230 A, the pulse duration was up to 1 ms. The system was pumped out by a turbomolecular pump from the hollow cathode cavity to a minimum pressure of $1 \cdot 10^{-2}$ Pa, the working pressure was 3.3 Pa. Gas was injected through the upper inlet of the stand into the arc cell cavity, the working gas was special purity argon. The main dependencies are shown in Figure 4.

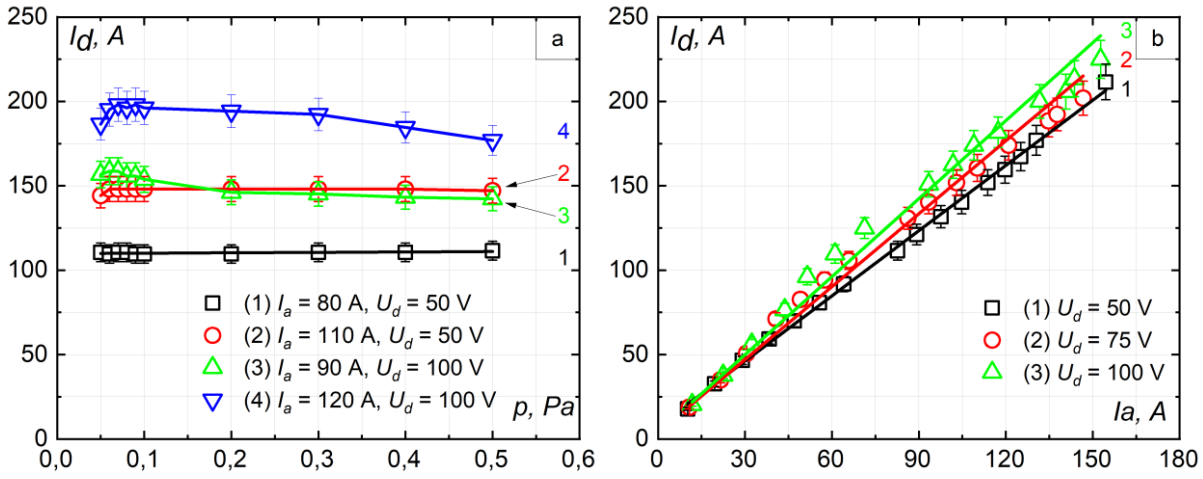

Fig. 2. (a) Dependences of glow discharge current on the working pressure. (b) Dependences of glow discharge current on arc discharge current at an argon pressure of 0.2 Pa, frequency 1 Hz, pulse duration 750 μs.

The pulse power was about 30 kW (current 250 A, voltage 120 V, with a duration of 500 μs). The plasma characteristics in the hollow cathode cavity were also studied using a Langmuir probe for 4 modes: currents of 60 and 120 A for an arc discharge and voltages of 50 and 100 V for a glow discharge. With an increase in the glow discharge voltage and arc discharge current, an increase in the maximum (from $2.1 \cdot 10^{18}$ to $3.6 \cdot 10^{18}$ m^{-3}) and average concentration (from $4.43 \cdot 10^{17}$ to $7.69 \cdot 10^{17}$ m^{-3}) is observed, as well as a decrease in the heterogeneity of the electron concentration distribution over the volume.

This work was performed within the framework of the State Assignment of the Ministry of Science and Higher Education of the Russian Federation (Project No. FWRM-2025-0001).

References

1. V.N. Devyatkov et al. // Laser Part. Beams. – 2003. – V.21. – p.243-248.
2. Korolev Y.D. and Koval N.N. 2018 J. Phys. D: Appl. Phys. 51 323001
3. Yakovlev V.V., Denisov V.V., Koval N.N., Kovalskiy S.S., Ostroverchov E.V., Egorov A.O., Savchuk M.V. // Izvestiya VUZov. Physika, Founders: National Research Tomsk State University ISSN: 0021-3411. DOI: 10.17223/00213411/63/10/109.
4. Kovaslkiy S.S., Denisov V.V., Koval N.N., Lopatin I.V. // Izvestiya VUZov. Physika, Founders: National Research Tomsk State University ISSN: 0021-3411. Volume 57, № 11/3. Page 78-82.

METHODS FOR INCREASING THE STABILITY OF ELECTRON BEAM GENERATION IN A PLASMA CATHODE SOURCE BASED ON A LOW-PRESSURE ARC

D.A. Gorkovskaia, M.A. Mokeev, M.S. Vorobyov, V.N. Devyatkov, N.N. Koval, A.A. Grishkov, S.Yu. Doroshkevich, M.G. Volis

High Current Electronics Institute of the Siberian Branch of the RAS,
Russia, 634055, Tomsk, Akademichesky Avenue, 2/3, Tomsk, Russia,
diana191@inbox.ru, maks_mok@mail.ru, vorobyovms@yandex.ru, vlad@opee.hcei.tsc.ru, koval@hcei.tsc.ru, grishkov@to.hcei.tsc.ru, doroshkevich096@gmail.com, volis.maks@mail.ru

In electron sources with plasma cathodes, special attention is paid to the study of the electrical strength of the high-voltage accelerating gap, which determines not only the limits of electron beam generation, but also its stability and reproducibility. Increasing the electrical strength allows to expand such parameters of the generated beam as: amplitude, duration and pulse repetition rate. Decrease in the electrical strength of the accelerating gap can be affected by charging of dielectric inclusions on the surface of the emission electrode, disturbance of plasma generators, disturbance of layer stabilisation of the emission plasma boundary, etc. /1-4/, often accompanied by uncontrolled growth of the beam current, which turns into electrical breakdown. In cases when a preliminary growth of the beam current is observed, one of the ways to improve the electrical strength can be considered the introduction of negative current feedback (NCF) in the accelerating gap, which will prevent the withdrawal of electrons from the emission plasma under the conditions of destabilising factors, such as gas pressure growth, melting of the target, spatial changes in the beam current density during its pulse, etc. The introduction of negative current feedback (NCF) in the accelerating gap can be considered. /5/.

In this work, in an electron source with a plasma cathode based on an arc discharge with grid stabilisation of the emission plasma boundary and a plasma anode with an open plasma boundary, studies have been carried out to increase the electrical strength of the accelerating gap by introducing an NCF compensating the uncontrolled growth of the electron beam current. The NCF organisation is a necessary tool for beam current stabilisation and can be used for fine-tuning of irradiation modes for the surface of various materials and products.

Figure 1 shows the scheme of the electron source with a grid plasma cathode with a grid plasma cathode based on a low-pressure arc discharge and a plasma anode with an open plasma boundary. The detailed principle of the source operation is described in papers /5,6/ and, in general, is as follows. Initiation of the cathode spot on the cathode *1* leads to ignition of the arc discharge between the cathode 1 and the hollow arc discharge anode *2*. After ignition of the arc discharge, the cathode plasma *3* is generated, electrons from which are extracted through the cells of the emission grid *4* and additional grid *5* under the action of a constant

accelerating voltage from the source U_0. Emission and acceleration of electrons up to the collector *10* lead to plasma generation in the electron beam transport space *8* and formation of anode beam plasma *7*.

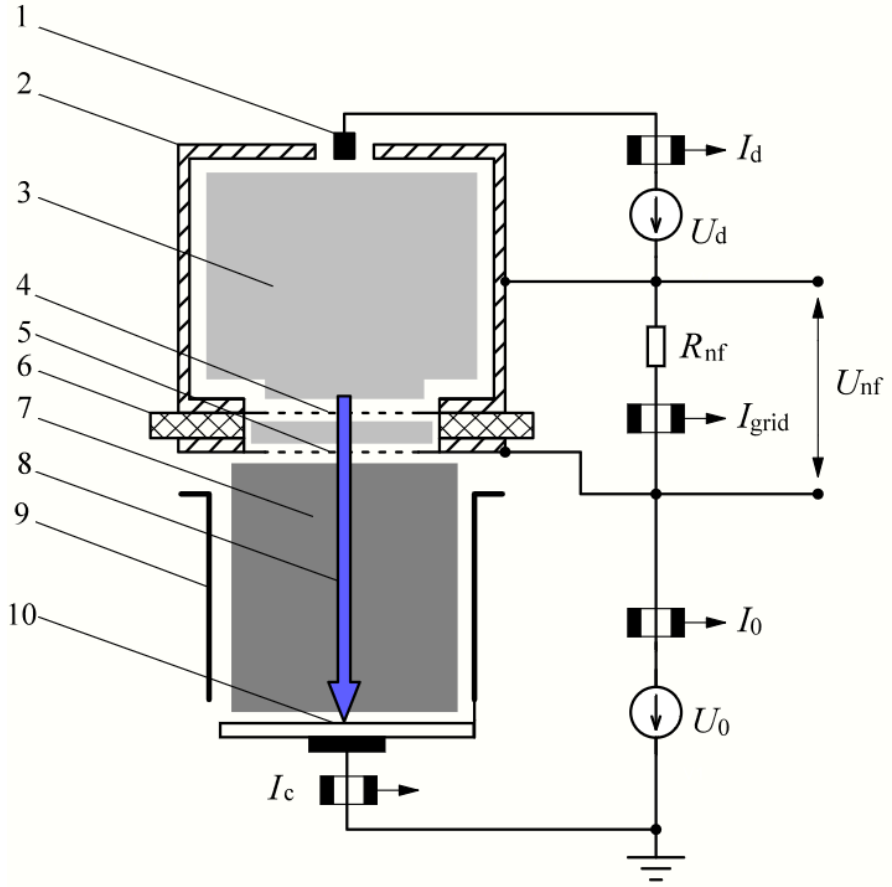

Figure 1 – Experimental setup of electron source with implementation of negative feedback mechanism: 1 - cathode, 2 - hollow anode of arc discharge and body of plasma electron emitter, 3 - cathode plasma, 4 - emission grid, 5 - additional grid, 6 - insulator, 7 - collector (anode) plasma, 8 - electron beam, 9 - extracting electrode combined with drift tube, 10 – collector

Realisation of the NCF mechanism in this source is achieved by introducing into the plasma emitter an additional grid *5*, which is under negative potential auto bias relative to the hollow anode *2* of the arc discharge. The value of the voltage between the grids is self-consistently determined by the nominal value of the resistor R_{nf}, specially installed in the electrical circuit, as well as by the amplitude of the current flowing between grids *4* and *5*, which, in the case of uncontrolled growth of the current in the accelerating gap, a portion of which is also shorted through grids *4* and *5*, leads to a decrease in the emission of electrons from the plasma emitter.

The experiment was conducted at different resistances (0.1 and 1 Ω) at constant arc current I_d = 200 A, residual gas pressure p(Ar) = 20 mPa and accelerating voltage U_0 = 3 - 11 kV. Figure 2 shows characteristic oscillograms of

currents (a, c) and voltages (b, d) taken at U_0 = 11 kV and R_{nf} = 1 Ω (a, b) and R_{nf} = 0.1 Ω (c, d).

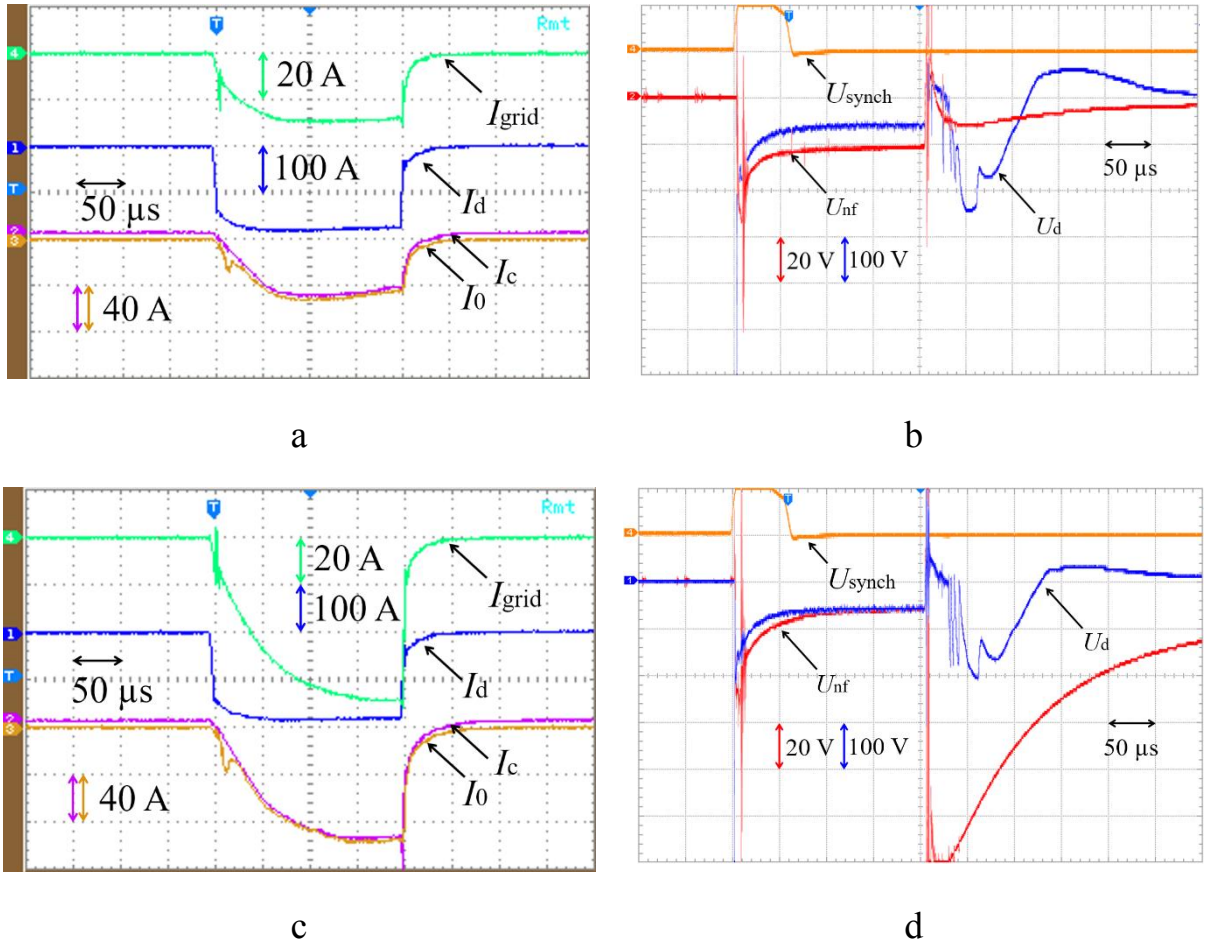

Figure 2 – Characteristic oscillograms of current on the control grid I_{grid}, arc discharge current I_d, collector current I_c, current in the accelerating gap I_0 (a, c); inter-grid voltage U_{nf}

From the presented oscillograms it can be seen that the resistor R_{nf}, connected between the emitter and additional grids, allows to create on it a voltage proportional to the current flowing through it, providing an increase in the locking voltage U_{nf}, which reduces the value of the extracted current from the emitter, increasing the stability of the source operation and the reproducibility of the beam parameters.

The comparative analysis of oscillograms also shows that an increase in resistance leads to a decrease in the rate of current rise in the accelerating gap, which is reflected in a decrease in the steepness of the beam current pulse front. A characteristic feature of the oscillograms of the beam current is the flat shape of the top of its pulse, which also indicates the mechanism of self-consistent increase in the locking voltage: the growth of the current in the accelerating gap leads to an increase in the voltage between the grids, which, in turn, limits further current growth, forming a flat top of the beam current pulse.

Figure 3 shows the dependence of the current in the accelerating gap on the value of the accelerating voltage at different values of the resistance R_{nf}.

The experiment has shown that increasing the resistance R_{nf} from 0.1 to 1 Ω reduces the beam current on average by 40 A, but the stability of electron beam generation in this case increases, which is expressed in a decrease in the number of electrical breakdowns and reproducibility of beam current pulses.

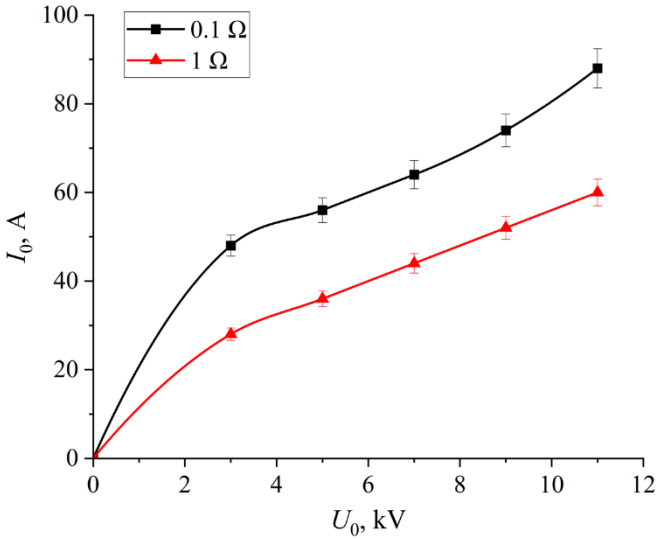

Figure 3 – Dependence of the current value in the accelerating gap on the value of the accelerating voltage at different values of resistance R_{nf}.

As a result, it has been shown that the introduction of a current controlled oscillation in the accelerating gap during the operation of an electron source with a plasma cathode under grid control conditions makes it possible to realise stable modes of electron beam generation in a source with a grid plasma cathode with good reproducibility at a beam power of up to 10 MW.

Acknowledgements. This research was supported by the Russian Science Foundation Grant No. 25-19-00745, https://rscf.ru/project/25-19-00745/.

References

1. **N.N. Koval, E.M. Ochs, Y.S. Protasov, N.N. Semashko**. Emission Electronics. Moscow: Bauman Moscow State Technical University (2009).
2. **Kreindel, Yu.E.** Plasma sources of electrons. Moscow: Atomizdat, (1977).
3. **N.N. Koval, Y.E. Kreindel, G.A. Mesyats, V.S. Tolkachev, P.M. Shchanin.** Letters in ZhTF. 9(1983) 568 -572.
4. **Ochs E.M.** Electron sources with plasma cathode: physics, technique, applications. Tomsk: Izdvo nauchno-technical lit. (2005).
5. **M.S. Vorobyov, P.V. Moskvin, V.I. Shin, T.V. Koval, V.N. Devyatkov, S.Y. Doroshkevich, N.N. Koval, M.S. Torba, K.T.** Ashurova. ZHTF. 92 (2022) 883 - 888.
6. **P. V. Moskvin, M. S. Vorobyev, A. A. Grishkov [et al].** Letters in ZhTF. 49(2023) 43 - 46.

IMPEDANCE MATCHING IN DUAL-FREQUENCY CAPACITIVE DISCHARGE SYSTEMS FOR MICROELECTRONICS EQUIPMENT

P. Gvozdov, A. Yasunas

[1]Freegy LLC, Republic of Belarus, Minsk, Nekrasova str., h.39-1, office №438,
22pavelgvozdov@gmail.com, alex.yasunas@gmail.com

High-frequency inductive and capacitive coupled plasma systems (ICP and CCP) are widely used in modern micro- and nanoelectronics technology. Increasing integration density and reduced feature sizes have revealed processes where single-frequency plasma systems cannot achieve the required processing speed and quality. For example, in Bosch deep reactive ion etching (DRIE), attempts to increase etch rate and anisotropy using single-frequency RF discharges exacerbate sidewall roughness and induce the notching effect /1, 2/. Dual-frequency power delivery systems – combining a high-frequency (HF) source for the ICP coil and a medium-frequency (MF) bias on the wafer holder – mitigate these effects while maintaining throughput. Similarly, CCP PECVD reactors use two power supplies: an HF source controlling ion flux (plasma density) and an MF source regulating ion energy /3/.

Impedance matching between the discharge system and the RF generator is essential for generator stability and process repeatability. Impedance mismatch increases reflected power, currents and voltages, leading to overheating of the elements and leads to process instability.

Effective dual-frequency matching networks must provide: 1) independent impedance matching at each operating frequency; 2) minimized cross-coupling between frequency channels; 3) sufficiently broad matching ranges to accommodate dynamic plasma impedance variations (dependent on pressure, power, gas composition, etc.).

The matching network design employed a transmission matrix method for two-port network analysis. The procedure involves: 1) deriving the transmission matrix for the target network topology; 2) calculating the set of load impedances matched to the generator's characteristic impedance (Z_0) at each frequency. For a dual-frequency system, the calculation is performed at both frequencies. For dual-frequency systems, this yields two distinct matching ranges, visualized on a Smith (Volpert-Smith) chart.

A dual-frequency matching device can be implemented using a bandpass-filter-like topology Figure 1 /4/.

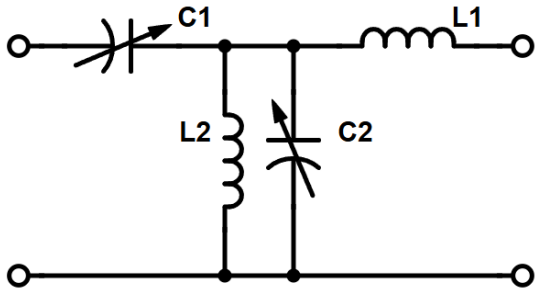

Fig.1 Dual-frequency matching network schematic.

The transmission matrix for calculating the matching ranges is:

$$\begin{bmatrix} 1+\frac{Z_1}{Z_2}+\frac{Z_1}{Z_3} & Z_1+Z_4+\frac{Z_1\cdot Z_4}{Z_2}+\frac{Z_1\cdot Z_4}{Z_3} \\ \frac{1}{Z_2}+\frac{1}{Z_3} & 1+\frac{Z_4}{Z_2}+\frac{Z_4}{Z_3} \end{bmatrix}.$$

The output impedance of the discharge system (Z_{out}) is calculated as /5/:

$$Z_{out}=\frac{A_{2,2}\cdot Z_0+A_{1,2}}{A_{2,1}\cdot Z_0+A_{1,1}}, \quad (1)$$

where $A_{1,1}$, $A_{1,2}$, $A_{2,1}$, $A_{2,2}$ – the elements of the transmission matrix.

Assuming a typical discharge impedance (resistive component: tens of ohms; capacitive component: ~100 pF), approximate component values are: C_1 =30-1000 pF, C_2 = 30-500 pF, L_1 = 1.5 uH, L_2 = 2.6 uH.

Using Equation (1) in Wolfram Mathematica®, impedance matching ranges were computed for 2.64 MHz and 13.56 MHz (Figure 2), along with the region of simultaneous matching at both frequencies (Figure 3).

SimNEC® simulations yielded the frequency-dependent standing wave ratio (SWR) (Figure 4), confirming effective matching: SWR = 1.031 at 2.64 MHz and SWR = 1.015 at 13.56 MHz.

The matching procedure comprises two stages:

1) Low-frequency (LF) matching (2.64 MHz): Adjust the series capacitor (C_1) and parallel inductor (L_2), primarily affecting the LF path.

2) High-frequency (HF) adjustment (13.56 MHz): Tune the parallel capacitor (C_2) and series inductor (L_1), optimizing the HF path without perturbing the established LF match.

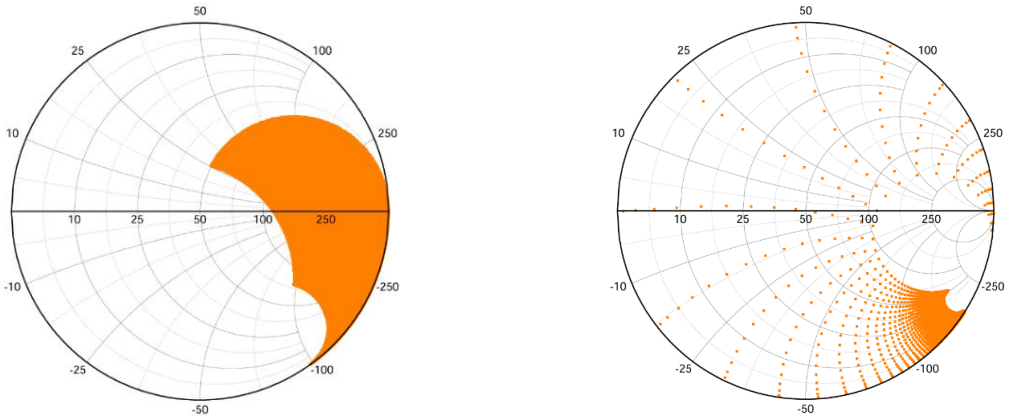

Fig. 2 Matching range at 2.64 MHz (a) 13.56 MHz (b)

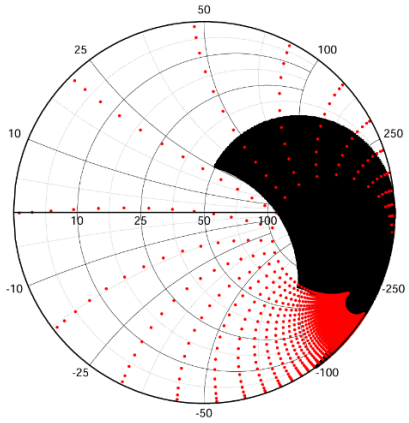

Fig 3 Simultaneous matching range

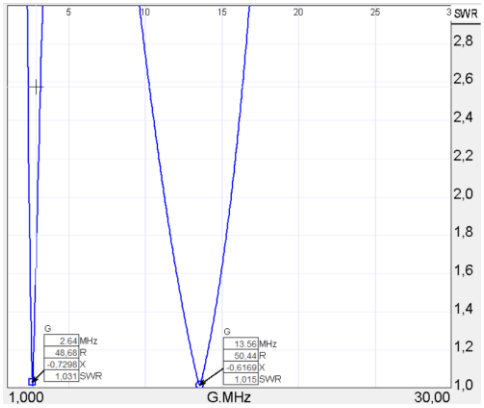

Fig 4 SWR vs. Frequency

The proposed dual-frequency matching network provides: broad simultaneous matching for reactive loads at 2.64 MHz and 13.56 MHz; SWR

values close to 1 at operating frequencies, which meets the requirements for stable operation of a dual-frequency plasma reactor power supply system; low power loss in the generator-to-discharge system circuit, due to minimal attenuation in the matching network.

References

1. **Baklykov D., Andronic M., Sorokina O., Avdeev S., Buzaverov K., Ryzhikov I. and Rodionov I.** Self-controlled cleaving method for silicon drie process cross-section characterization, Micromachines 2021, 12, 534, 1-2.
2. **Ishchuk V., Volland B., Hauguth M., Cooke M. And Rangelow I.** Charging effect simulation model used in simulations of plasma etching of silicon (2012) 084308-1-4.
3. **Curley G.** The dynamics of the charged particles in a dual frequency capacitively coupled dielectric etch reactor (2008) 18-23.
4. **Wenchang H., Jiaqi L., Shuai W., Yan H., Xiangxin L., Zhitian S. and Yaoyao C.** Dual-frequency impedance matching network design using genetic algorithm for power ultrasound transducer, Micromachines 2024, 15, 344, 3-5.
5. **Fusco F.** Analysis and computer-aided design (1990) 194-196.

COMPETING ELECTRON EMISSION MECHANISMS IN A LOW-PRESSURE ARC-BASED GRIDDED PLASMA EMITTER

R. A. Kartavtsov, M. S. Vorobyov, A. A. Grishkov, N. N. Koval,
M. A. Mokeev, S. Y. Doroshkevich, P. V. Moskvin, D. A. Gorkovskaya

Institute of High Current Electronics, Siberian Branch of the Russian Academy of Sciences, Russia, 634055, Tomsk, Akademichesky avenue, 2/3, kartavtsov@opee.hcei.tsc.ru, vorobyovms@yandex.ru, grishkov@to.hcei.tsc.ru, koval@opee.hcei.tsc.ru, maks_mok@mail.ru, doroshkevich@opee.hcei.tsc.ru, pavelmoskvin@mail.ru, diana191@inbox.ru

At present, electron sources with gridded plasma emitters (GPEs) are widely used in various scientific and technological fields. Electron beams generated by such devices can achieve high energy densities (up to 100 J/cm²) while operating at relatively low accelerating voltages (up to 30 kV), and their use does not require stringent radiation safety measures [1]. In addition, these sources feature a simple design without heating elements and are capable of operating at elevated pressures (up to 100 Pa), which makes them particularly effective for addressing a range of problems in the field of materials science [2, 3].

The current flowing through the acceleration gap in such electron sources with GPEs generally satisfies the following equation [4]:

$$I_0 = \alpha \cdot I_d + I_i + I_i \cdot (1 - \Gamma) \cdot \gamma_2 + I_i \cdot \Gamma \cdot \gamma_p, \quad (1)$$

where I_0 – current in the acceleration gap; α – electron extraction coefficient from the GPE; I_d – current measured in the power supply circuit of the GPE; I_i – current of accelerated ions extracted from the anode plasma; Γ – effective geometrical transparency of the emission electrode, which depends on the beam current density distribution function; γ_2 – ion-electron emission coefficient from the surface of the emission electrode; γ_p – ion-electron emission coefficient from the emission plasma.

The coefficient α can be considered constant. However, experimental observations revealed a slight increase relative to its steady-state value during the first 30 μs of the pulse. Furthermore, calorimetric measurements did not show any significant change in the sum $(1 - \Gamma)\gamma_2 + \Gamma\gamma_p$. Therefore, one of the factors that may compromise the stability of such an electron source is the flux of accelerated ions I_i, extracted by the accelerating field from the anode plasma. This plasma is formed as a result of ionization of the residual gas in the drift region by accelerated electrons. In [5], the effect of enhanced electron emission caused by ion bombardment of the surface of the gridded emission electrode was investigated. It was shown that the current in the acceleration gap is strongly dependent on the type of working gas, the energy of the ions, and the material

from which the electrode is made. These results point to a significant contribution of ion-electron processes – induced by the action of accelerated ions – to the energy of the generated electron beam.

Since a fine-structured thin mesh is used as the emission electrode, a portion of the accelerated ions – determined by the mesh's geometrical transparency – can penetrate into the GPE region. As a result of the incoming accelerated ions and ion bombardment of the GPE electrodes, both the spatial distribution of the emission plasma density and its potential may change. The combined effect of these factors can significantly influence the electron current extracted from the GPE. However, to date, the scientific literature lacks experimental data on the mechanisms by which accelerated ions affect the parameters of the generated electron beam.

The aim of the present work is to experimentally investigate the influence of accelerated ion bombardment from the anode plasma on the processes of emission plasma generation and electron extraction from it in an electron source with an arc-based gridded plasma emitter.

The schematic of the experimental setup is shown in Fig. 1. A detailed description of the operating principle of this electron source can be found in [5, 6]. In the configuration under consideration, additional aluminum cathode electrodes *4* and *5* were introduced to serve as collectors of the accelerated ion flux *9* entering the GPE. This design enables spatial separation of the emission regions: thermofield emission, associated with the operation of the cathode spot, occurs on the magnesium cathode *3*, whereas ion-electron emission, initiated by accelerated ion bombardment, takes place on electrodes *4* and *5*.

The influence of accelerated ions, as well as neutral particles formed as a result of charge exchange, is primarily manifested through bombardment of the cathode electrodes. These processes are expected to cause a redistribution of currents within the GPE region, provided that the total arc discharge current remains constant ($I_d = const$):

$$I_d\,(U_0 > 0) = I_{cs} + I_{iee} \qquad (2)$$

где U_0 – accelerating voltage; I_{cs} – current of the cathode spot; I_{iee} – ion-electron emission current from the surfaces of cathodes *4* and *5*.

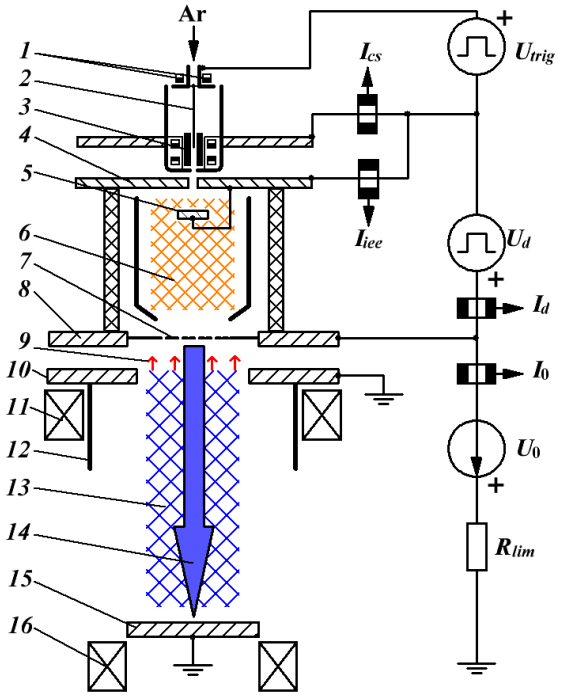

Fig. 1 – Schematic diagram of the modernized electron source «СОЛО»: *1* – permanent magnets; *2* – igniting electrode; *3* – magnesium cathode of the arc discharge; *4*, *5* – electrodes for measuring ion-electron emission current; *6* – emission plasma; *7* – emission grid; *8* – emission electrode; *9* – accelerated ion flux; *10* – extraction electrode; *11*, *16* – solenoids; *12* – drift tube; *13* – anode/beam plasma, *14* – electron beam, *15* – collector

Typical current oscillograms obtained during the experiment are shown in Fig. 2*a*. The oscillogram shows that during the first 5 μs of the arc discharge pulse (I_d), while the anode plasma is being formed, nearly the entire current flowing through the GPE is due to the operation of the cathode spot (I_{cs}). As the anode plasma develops, an increase in the current in the acceleration gap (I_0) is observed. Simultaneously, an accelerated ion flux *9* appears, bombarding the surfaces of cathodes *4* and *5*. This is reflected on the oscillograms as a rise in the ion-electron emission current (I_{iee}). At the same time, the current from the cathode spot decreases, while the arc discharge current (I_d) remains quasi-constant.

Under intense ion flux in the presented beam generation mode (Fig. 2a), ion-electron emission becomes the dominant current transport mechanism in the GPE, and the cathode spot current decreases to a value close to zero.

Fig. 2*b* shows the dependence of the ratio of the cathode spot current to the arc discharge current I_{cs}/I_d on the operating pressure p and the accelerating voltage U_0, constructed under the condition of the maximum current in the acceleration gap (70–100 μs from the pulse onset). The graph indicates that with increasing ion energy (due to the rise in U_0) and with increasing anode plasma

concentration (due to higher pressure), the contribution of the cathode spot current to the operation of the GPE becomes progressively less significant. These results confirm the above analysis of the operation of the electron source with a GPE.

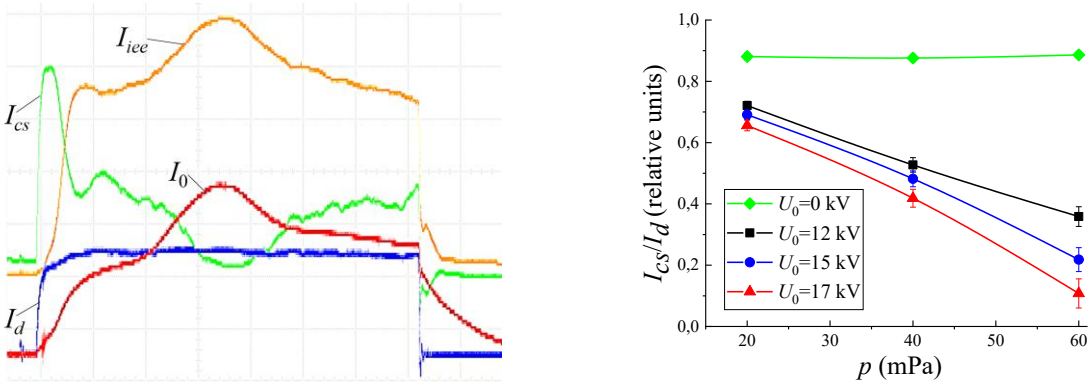

(*a*) (*b*)

Fig. 2 – Typical current oscillograms for the regime: p = 60 mPa, U_0 = 17 kV, $I_d \approx$ 20 A (scale: I_d – 10 A/div; I_0 – 40 A/div; I_{cs}, I_{iee} – 4 A/div; τ – 20 μs/div) – (*a*), dependence of the ratio I_{cs}/I_d on the gas pressure at various accelerating voltages, with current $I_d \approx$ 20 A – (*b*)

Thus, in the electron source with a GPE based on a low-pressure arc discharge, competition between two types of emission has been demonstrated: emission from the cathode spot and ion-electron emission. The possibility of such a current flow regime should be taken into account when implementing technological processes using electron sources with plasma cathodes and when analyzing current stabilization mechanisms in these systems.

Acknowledgements. The work was supported by the Ministry of Science and Higher Education of the Russian Federation (Number: FWRM-2021-0006)

References

1. **Koval N.N., Oks E.M., Protasov Y.S., Semashko N.N.** Emission Electronics. Moscow: Bauman Moscow State Technical University (2009).
2. **Burdovitsin V.A., Klimov A.S., Medovnik A.V., Oks E.M., Yushkov Y.G.** Forvacuum plasma sources of electrons. Tomsk: Tomsk University (2014).
3. **Gromov V.E., Ivanov Y.F., Vorobiev S.V., Konovalov S.V.** Fatigue of Steels Modified by High Intensity Electron Beams. Cambridge (2015).
4. **Kartavtsov R.A., Mokeev M.A., Vorobyov M.S., Moskvin P.V., Doroshkevich S.Y., Koval N.N., Grishkov A.A., Devyatkov V.N., Torba** M.S., Technical Physics Letters, 51 (4), 15 (2025).
5. **Grigoriev S.V., Devyatkov V.N., Koval N.N., Teresov A.D.** Technical Physics Letters, 36 (4), 23 (2009).

3. ATMOSPHERIC PRESSURE PLASMAS, PLASMA IN AND IN CONTACT WITH LIQUID, PLASMA-LIQUID INTERACTIONS

MICROWAVE DISCHARGE IN LIQUIDS: PHYSICS AND APPLICATION

T.S. Batukaev[1], I.V. Bilera[1], G.V. Krashevskaya[1,2], Yu.A. Lebedev[1]

[1] Topchiev Institute of Petrochemical Synthesis RAS, Leninsky Prospect, 29, Moscow, 11999,1 Russia, lebedev@ips.ac.ru
[2] National Research Nuclear University "MEPhI", Kashirskoe shosse, 31, Moscow, 115409, Russia, krashevskaya-gv@mail.ru

Electric discharges in the presence of a liquid phase are now one of the most important areas of research in plasma physics and its applications. Microwave discharge in liquids has been least studied. The main countries where research into this type of discharge is conducted are Japan, China and Russia (see reviews [1-3]). Here we will try to summarize the basic information about physical processes in the discharge, obtained in different laboratories of the indicated countries, paying special attention to the differences from traditional gas discharges. Applications of microwave discharge for solving various practical problems will be briefly considered.

Physical properties. Considering the known results, although usually talk about microwave discharges in a liquid, really these discharges is generated in a gas bubbles (a few millimeters in diameter) inside the liquid. The bubbles can be created in different ways: (a) by evaporation of the liquid in the vicinity of the microwave antenna tip heated by the microwave field, (b) creation of artificial bubbling by introduce of additional gases (argon is most often used), (c) by action of ultrasonic waves. The surface of the bubbles is located near the high-temperature plasma zone, which ensures a high rate input of evaporated molecules of fluids to the bubble. This bubble can be considered as mini plasma chemical reactor. Because of the intense flow of molecules into the bubble, high concentrations of active particles (atoms, radicals, charged particles) are created in the plasma. Therefore, the efficiency of physical and chemical processes in this reactor is high. Accordingly, the rate of formation of products is also high. These features are the major differences from conventional gas phase microwave plasma processing.

The microwave discharge at powers up to 2.5 kW is usually created at the end of a metal antenna immersed in a liquid (a wide range of liquids are tested: different hydrocarbons, water and aqueous solutions of different alcohols, etc.).

The properties of discharge are studied using gas chromatography, light emission spectroscopy, high-speed photo recording, schlieren and shadow photography.

It was shown that the microwave discharge is non-stationary even in the continuous mode of microwave generation. It consists of a sequence of solitary discharges randomly distributed in time [4, 5]. Lifetime of solitary discharge is determined by the lifetime of the gas bubble with plasma in the region of a strong microwave field at the end of the antenna until it breaks away and the discharge transitions to the decaying plasma mode. The duration of a solitary discharge decreases with increasing microwave power, but at the same time the frequency of occurrence of such discharges increases. This leads to the fact that, unlike gas discharges, the composition of the products depends weakly on the power, while the rate of their production increases linearly with power. This was shown by the results of experiments.

The formation of a solitary discharge is accompanied by a shock wave, which causes damped sound oscillations in the discharge volume.

The latter is not a surprise, since the breakdown of any discharge is accompanied by a shock wave. However, in the case of a microwave discharge in a liquid generation of shock waves is repeated with each breakdown. This situation is similar to the pulse gas discharges.

The oscillation frequency is determined by the natural frequencies of the reactor volume above the liquid surface and has a kilohertz scale.

These oscillations lead to effective mixing of the reactants. In addition, these frequencies coincide with the characteristic frequencies of chemical processes. This means that by selecting the geometry and dimensions of the reactor, it is possible to influence the course of chemical reactions.

Let us note one more important feature of the discharge under consideration, which is important for the implementation of chemical processes at high temperatures. It is known that any technological chemical process must contain a quenching stage, in which the temperature of the reagents is sharply reduced to suppress the flow of reverse reactions. Under the conditions of a microwave discharge in liquids, this stage is implemented automatically, since when the gas bubble is torn away from the antenna and the discharge into it is extinguished, the evaporation of the liquid surrounding the bubble continues. This leads to a rapid decrease in temperature in the gas bubble. This was verified during the implementation of the steam reforming process in a microwave discharge in water, where it was shown that the evaporation of water into the volume of the gas bubble leads to a decrease in temperature at a rate of 10^7 degrees/sec [6].

The obtained rate of quenching by evaporating water gives a value that is in good agreement with the value known for this method, but implemented by a special stage of the chemical process. Once again, we note that in discharges in liquids this process is natural and occurs immediately after the end of the active phase of the discharge.

Application. Considering the areas of application of microwave discharges in liquids, we will consider only several areas that are most intensively developing now, namely the obtaining of hydrogen and CO_2 destruction.

Various hydrocarbons are often used as liquids in the production of hydrogen [7-12]. It was shown that hydrogen is the main component (60-80 %) of exhaust gases of microwave discharge in any liquid hydrocarbons. Increase of the molecular weight of alkanes is accompanied by increase in the yield of acetylene and decrease in the yield of hydrogen (in the series C7–C16, including cycloalkanes). Hydrogen and acetylene are predominantly formed in aromatic compounds. Gas products of microwave discharge in liquid cycloalkanes and aromatic compounds without radical groups practically do not contain methane or ethylene. As the number of radical groups increases, the composition approaches the composition of the discharge products in alkanes.

Alcohol solutions are promising liquids for obtaining hydrogen in microwave discharge for a number of reasons (safety and ease of transportation and storage, a wide range of starting materials for ethanol production, a high hydrogen content compared to other fuels, low biotoxicity, etc.) [13-15]. For example, it was shown that in the case of ethanol aqueous solutions the composition of the reaction products at atmospheric pressure is practically independent the incident power, but the total output flow rate of gas products increases with an increase in the incident power. This is, as it was mentioned above, a distinctive feature of a microwave discharge in a liquid. Concentration of hydrogen in gas mixture on the discharge outlet was of 60 vol. %, It should also be noted that simultaneously with hydrogen production the carbon monoxide is also produced.

The process of steam methane reforming is implemented in [6]. A microwave discharge was created in the water near the antenna, and methane was bubbled through a channel in the antenna. The main component of the gas mixture at the outlet of the reactor is hydrogen, and its concentration reaches 75%. Energy consumption for hydrogen formation reaches 25 l/kWh. The remaining gas components at the reactor outlet are methane, CO, and CO_2.

Bubbling CO_2 through a microwave discharge region in liquid hydrocarbons has shown promise for this method of CO_2 destruction [16]. It was shown that simultaneously with the decomposition of CO_2 (decomposition degree was of 60 %), hydrogen is generated in the discharge. The hydrogen content in the gas mixture at the reactor outlet was 50-60%,

Another unusual application of microwave discharge in liquid hydrocarbons is demonstrated by the example of extracting valuable metals from crude oil by creating a microwave discharge in its volume at atmospheric pressure. It was shown for the first time that the content of metals Al, Co, Cu, Fe, Mo, Ni, V, Zn in a tree-like structure applied to a microwave antenna is up to 10 times higher than their content in the original substance [17].

A generalization of known experimental and calculated results shows the high potential of using microwave discharge in liquids to solve various applied problems.

Acknowledgements. The work was carried out within the framework of the State Plan of the A.V.Topchiev Institute of Petrochemical Synthesis, RAS.

References

1. **Lebedev Yu.A.** Plasma Phys. Reports, 43 (2017) 685–695.
2. **Lebedev Yu.A**. High Temperature, 56 (2018) 811–820.
3. **Lebedev Yu.A.** Polymers, 13 (2021) 1678–1706.
4. **Lebedev Yu.A., Krashevskaya G.V., Batukaev T.S., Epstein I.L.,** Plasma Proc. Polym.**,** 18, (2021), e2100051.
5. **Lebedev Yu.A., Krashevskaya G.V., Batukaev T.S, Mikhaylyuk A.V.,** Plasma Proc. Polym., 19, (2022), e2100215.
6. **Batukaev T. S., Bilera I. V., Krashevskaya G. V., Epstein I. L., Lebedev Yu. A., Tatarinov A. V., Titov A. Yu.,** Plasma. Process Polym., 21 (2024), e2400139.
7. **Nomura S., Toyota H., Mukasa S., Yamashita H., Maehara T., Kawashima A.,** J. Appl. Phys., 106 (2009) 073306.
8. **Nomura S., Toyota H., Tawara M., Yamashita H., Matsumoto K.,** Appl. Phys. Lett. 88 (2006) 231502.
9. **Averin K.A., Bilera I.V., Lebedev Yu. A., Shakhatov V.A., Epstein I.L.** , Plasma Proc. Polym., 16 (2019), e1800198.
10. **Lebedev Yu.A., Averin K.A., Tatarinov A.V.,** High Energy Chem., 54 (2019), 331-335.
11. **Batukaev T.S., Bilera I.V., Krashevskaya G.V., Lebedev Yu.A.,** Processes 11, (2023), 2292–2314.
12. **Yu Z., Sun B., Ding G., Liu J., Zhu X., Xin Y**, J. of Anal. & App. Pyrolysis, 190 (2025) 107119.
13. **Zhu T., Sun B., Zhu X., Wang L., Xin Y., Liu J.,** J. Anal. Appl. Pyrolysis, 156 (2021) 105111.
14. **Sun B. Zhao X, Xin Y., Zhu X.,** Int. J. Hydrogen. Energy, 42 (2017) 24047-24054.
15. **Batukaev T.S., Bilera I.V., Krashevskaya G.V., Lebedev Yu.A., Epstein I.L.,** Plasma Proc. Polym., 20, (2023), e2300015.
16. **Batukaev T.S., Bilera I.V., Krashevskaya G.V., Lebedev Yu.A., Nazarov N.A.,** Plasma, *6* (2023), 115–126.
17. **Lebedev Yu.A., Averin K.A.,** J. Phys. D: Appl. Phys., 51 (2018), 214005.

LONG-LIVED REACTIVE OXYGEN AND NITROGEN SPECIES IN LIQUIDS TREATED WITH CAPILLARY DISCHARGE

V. Gudkova[1,2], A. Davydov[1], M. Zimina[1,2], V. Borzosekov[1,2], I. Naumova[3], N. Gusein-zade[1], V. Titov[4]

[1]Prokhorov General Physics Institute of the Russian Academy of Sciences, Vavilova St 38, 119991, Moscow, Russian Federation, gudkova-vi@fpl.gpi.ru
[2]RUDN University, Miklukho-Maklaya St 6, 117198, Moscow, Russian Federation, gudkova-vv@rudn.ru
[3]Ivanovo State University, Yermaka St 39, 153025, Ivanovo, Russian Federation, irinauma@mail.ru
[4]G.A. Krestov Institute of Solution Chemistry of the Russian Academy of Sciences, Akademicheskaya St 1, 153045, Ivanovo, Russian Federation, titov25@gmail.com

Currently, research is being widely developed on the use of low-temperature plasma at atmospheric pressure to solve problems in medicine and agriculture /1/.

When gas discharges affect water or aqueous solutions, reactive oxygen and nitrogen species are formed, which are useful for the solving many biological problems - treatment of skin diseases, antibacterial effects, antitumor therapy, etc. /2/. One of the points is related to the use of plasma to obtain growth stimulants for agricultural crops by processing natural raw materials, such as chitosan /3/. The use of low-molecular water-soluble chitosan, which has fungicidal and phytostimulating properties, seems very promising /4/. Low temperature plasma can be used to depolymerize chitin-derived raw materials to reduce the molecular weight of chitosan in reactions with hydroxyl radicals.

The aim of this work was to evaluate the possibility of using a capillary microwave discharge at atmospheric pressure for the production of hydrogen peroxide and nitrogen compounds by acting on water and an aqueous suspension of chitosan. The capillary microwave discharge /5/ was excited using a magnetron with a frequency of f = 2.45 GHz. A high-voltage rectangular pulse generator, which is the power source for the magnetron, allows varying the pulse microwave power of the magnetron (P), the pulse duration (t_p), and their repetition frequency (f_p). The following mode was used in the experiment: t_p = 50 μs, f_p = 200 Hz, pulse microwave power P = 2800 W. Breakdown occurs at the metal-dielectric interface due to the interaction of the internal metal electrode, which removes microwave energy, and the external dielectric capillary. The internal electrode is hollow and simultaneously serves as a gas pipeline.

In the experiments, deionized water was treated (pH_0 5.6-5.8, σ ~ 0.033 μS/cm). Two plasma-forming gases were used – argon and air – at the same

volume flow rate of 300 cm^3/min. The duration of the discharge action on deionized water was 5 minutes, the volume of liquid was 30 ml. In separate experiments, an aqueous suspension of chitosan with a concentration of 1 wt.% was subjected to discharge treatment. Chitosan with a molecular weight of 400 kDa produced by Bioprogress Ltd. was used.

Figure 1 shows photographs of the discharge for different options of water treatment using an argon or air flow.

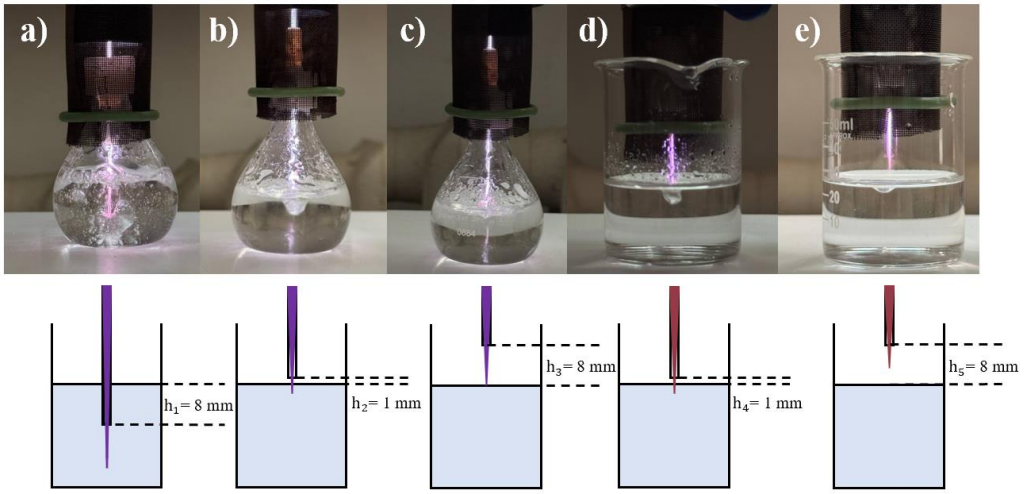

Figure 1. The effect of capillary microwave discharge on deionized water: a, b, c – in argon flow, d, e – in air flow.

The concentration of hydrogen peroxide (H_2O_2) and nitrite ions (NO_2^-) in water was measured spectrophotometrically (HACH LANGE DR-5000 spectrophotometer) using chemical probes. To measure the concentration of hydrogen peroxide, the interaction of H_2O_2 with Ti_4^+ ions in sulfuric acid was used to form a complex compound that gives the solution a yellow color /6/:

$$Ti(SO_4)_2 + H_2O_2 + 2H_2O \rightarrow [TiO(H_2O_2)]^{2+} + H_2SO_4^- + 2H^+.$$

The optical density of the solution after adding the titanium (IV) sulfate solution was recorded at a wavelength of 410 nm.

The Griess method was used to measure the concentrations of nitrite ions, based on the reaction of nitrite ions in an acidic medium with sulfanilic acid to form a diazo compound, which then reacts with α-naphthylamine to form an azo dye /7/. It should be noted that this method gives the total concentration of NO_2^- and HNO_2.

The concentration of NO_3^- ions was measured by potentiometric titration using an ELIS-121NO3 ion-selective electrode together with a reference electrode. The measurement results for different water treatment methods are presented in Table 1.

Table 1. Concentrations of long-lived reactive oxygen and nitrogen species after plasma treatment of deionized water.

Configuration (Fig. 1)	**Gas**	***C*(H_2O_2), µM**	***C*(NO_2^-), µM**	***C*(NO_3^-), µM**
a	Ar	950 ± 135	< 3	< 15
b		1650 ± 100	10.6 ± 3.1	37.6 ± 11.3
c		300 ± 40	68.0 ± 21.5	42.7 ± 8.4
d	Air	< 80	460 ± 35	106.9 ± 2.3
e		< 15	564 ± 43	67.5 ± 4.0

The highest concentrations of hydrogen peroxide were obtained when a distance between the capillary and the liquid surface was 1 mm, indicating the predominant formation of H_2O_2 in the liquid phase due to the dissociation of water under the action of plasma.

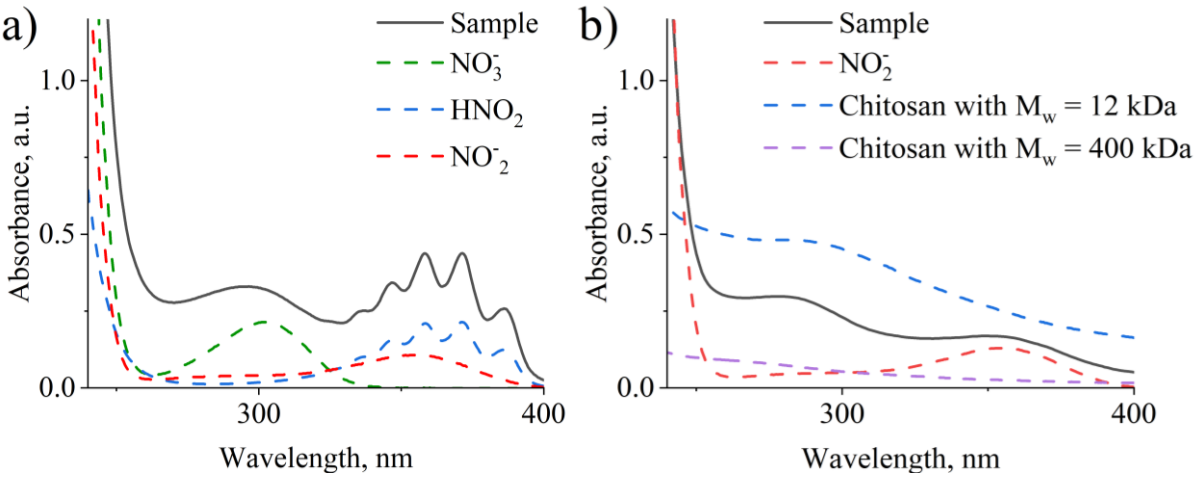

Figure 2. Electronic absorption spectra of deionized water (a) and solution of chitosan derivatives (b) after treatment with a capillary microwave discharge in air at *d*=1 mm and *t*=2.5 hours.

When exposed to a discharge in an air flow, the highest concentrations of nitrite- and nitrate ions were observed, which is due to the dissolution of nitrogen oxides formed in the air plasma. It is worth noting that even in the absence of direct contact of the discharge with the liquid surface, nitrites and nitrates enter the water with the gas flow. With direct plasma-liquid contact (*d*~1 mm), hydrogen peroxide was also formed, which promotes the oxidation of nitrite ions to nitrate ions. The accumulation of nitrogen-containing products in the liquid phase is confirmed by the corresponding bands in the electronic absorption spectra of the treated liquid (Fig. 2a). To have more precise identification of bands in the complex experimental spectra we have measured electronic absorption spectra of single chemically pure compound solutions (NO_3^-, HNO_2^-, NO_2^-).

Experiments on the effect of a capillary microwave discharge on an aqueous suspension of chitosan (M_w=400 kDa) showed that partial depolymerization of chitosan occurs with the formation of water-soluble products. After treatment with a discharge in an air flow, the appearance of a band at 280 nm was observed in the electronic absorption spectra of the liquid phase (Fig. 2b). This band corresponds to the terminal carbonyl groups that are formed as a result of the cleavage of glycosidic bonds in chitosan /3, 8/.

Acknowledgements. This work was supported by the Russian Science Foundation (project No. 25-19-00930).

References

1. **Adamovich I. et al.** Journal of Physics D: Applied Physics, 55(2022).
2. **Laroussi M. et al.** IEEE Transactions on Radiation and Plasma Medical Sciences, 6(2022).
3. **Titov V.A. et al.** High Energy Chemistry, 50(2016).
4. **Titov V.A. et al.** High Energy Chemistry, 57(2023).
5. **Gritsinin S.I. et al.** Plasma Physics Reports, 39(2013).
6. **Shutov D.A. et al.** Plasma Chemistry and Plasma Processing, 43(2023).
7. **Gudkova V.V. et al.** Plasma Chemistry and Plasma Processing, 44(2024).
8. **Chokradjaroen C. et al.** Carbohydrate Polymers (2017).

MODIFICATION OF THE SURFACE OF ELECTRODES IN A BARRIER DISCHARGE IN AIR

I. Selivonin[1], A. Lazukin[2], I. Moralev[1]

[1]Joint Institute for High Temperatures RAS, Moscow, Russia, inock691@ya.ru
[2]National Research University "Moscow Power Engineering Institute", Moscow, Russia

Dielectric barrier discharge (DBD) is a high-pressure discharge initiated in a system of two or more electrodes separated by a dielectric barrier. This type of discharge can be used to solve numerous technological problems in the field of plasma chemistry, processing of biological objects, plasma aerodynamics, plasma processing of metal and polymer surfaces.

The service life of discharge systems based on DBD in most cases is associated with the degradation of the dielectric barrier. Initiation of a discharge on dielectrics made of polymers and other organic materials leads to intense local melting and evaporation of the material, which ultimately leads to a breakdown of the barrier and the transition of a low-current discharge to a spark form. When using dielectric barriers made of materials resistant to discharge, the service life of the system is determined by the degradation of the electrodes.

The purpose of this work is to study the processes of electrode degradation in DBDs and devices based on them: ozonizers, plasma chemical reactors, systems for processing biological samples. For this purpose, a study was undertaken of the structure and electrical characteristics of the discharge in air on electrodes made of metals whose oxides have significantly different properties — oxide resistance to cathode sputtering and its electrical conductivity.

In this work, a DBD in a volumetric asymmetric configuration was studied (Fig. 1a). The high-voltage electrode 1 was made of a copper rod with a diameter of 15 mm. A 0.5 mm thick plate of alumina ceramics 3 was glued to the electrode with silicone compound 2, which acted as a dielectric barrier. The modified metal sample 4 was a 25x10x1 mm plate. It worked as a counter electrode and was placed on a plate of foil-clad heat-conducting ceramics 5, the central section of which was insulated and connected to the ground through ceramic SMD capacitors 7 with a total rating of 2.2 nF. This was done to measure the amount of charge that transferred in DBD. The plate was placed on a flow-through heat exchanger 8, which was connected to ground. Cooling was carried out by flowing a dielectric liquid.

All studies were conducted in synthetic air at a pressure of 1 and 0.4 atm and room temperature. To control the composition and pressure of the working medium, the discharge system was installed in a sealed gas chamber.

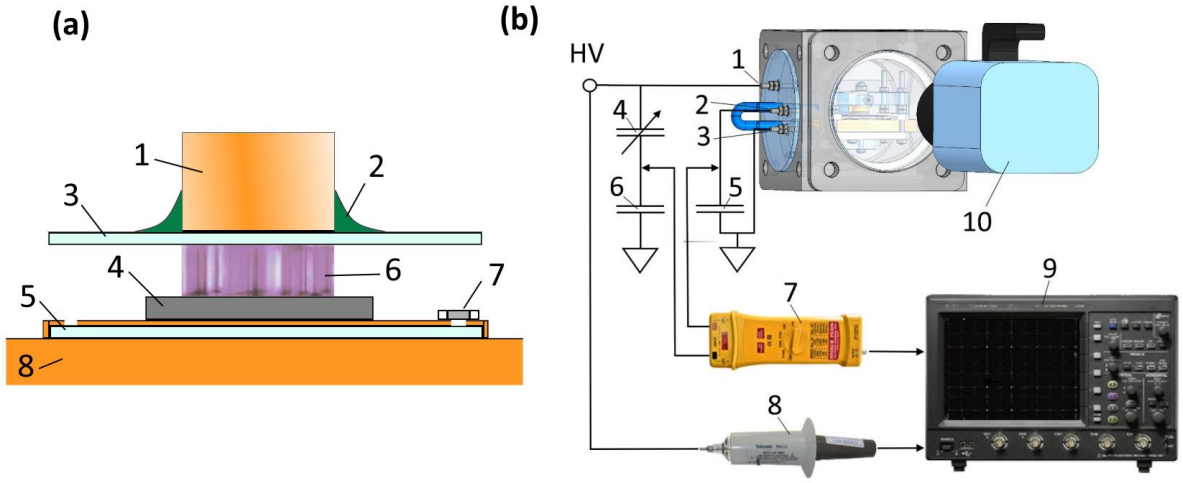

Fig. 1. (a) design of the discharge cell: 1 - high-voltage electrode, 2 - heat-conducting compound, 3 - ceramic plate, 4 - metal sample, 5 - foil-clad ceramics, 6 - DBD, 7 - measuring capacitors, 8 - flow-through heat exchanger; (b) installation diagram: 1 - high-voltage input, 2 - measuring terminal, 3 - grounding, 4 - variable high-voltage capacitor, 5, 6 - measuring capacitors, 7 - differential probe, 8 - high-voltage probe, 9 - oscilloscope, 8 - CMOS camera.

The discharge was fed with AC voltage with an amplitude of 3.4 kV and a frequency 100 kHz. During the experiment, the amplitude of the supply voltage was maintained constant. Exposure was carried out continuously for 300 minutes. During the first and last minutes of operation, the discharge glow was recorded on a Nikon EOS 250D CMOS camera. In addition to the supply voltage, oscillograms of the charge transferred through the measuring capacitor were registered, for which a differential probe was used. To increase the accuracy of the measurements, a circuit for analog compensation of the charge transferred through the parasitic capacitance of the cell was used (Fig. 1b). The DBD power dissipation was calculated by integrating volt-coulomb cyclograms (VCC).

Figure 2 shows the dynamics of the discharge power on electrodes made of different materials. In the first 10-15 minutes, some increase in the discharge power is observed on all electrodes. At lower pressures (at higher power), this phenomenon is not observed, so its causes are primary changes in the morphology and properties of the surface of the metal electrode, and not heating of the system. Then, a gradual increase in power is observed on the copper electrode and a drop on the aluminum one. Noticeable changes occur over a period of about 120-130 minutes, then the values reach a stationary state. Titanium expectedly demonstrates behavior similar to aluminum, since its

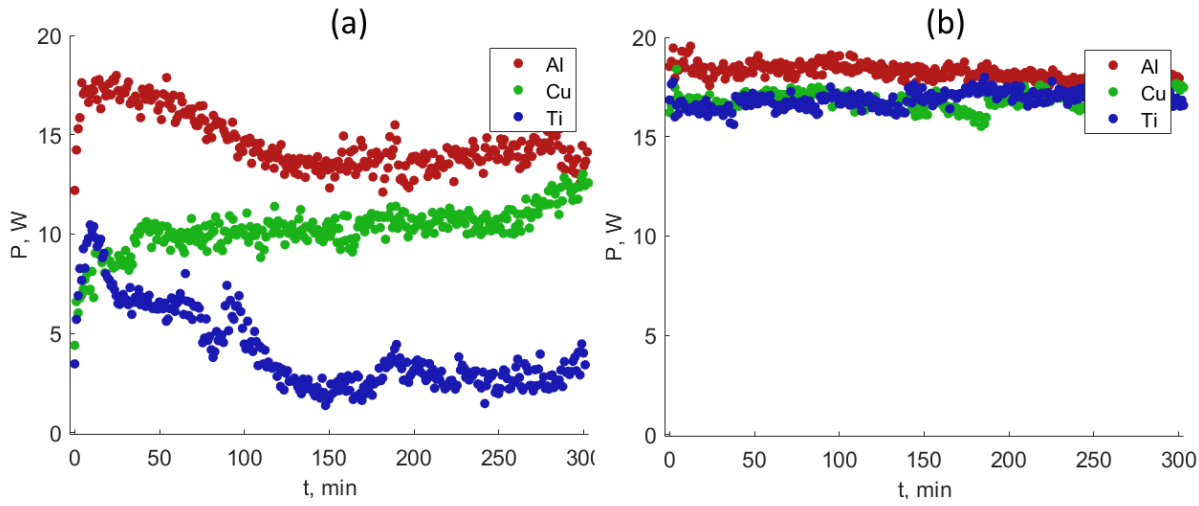

Fig. 2. Dynamics of the power dissipated in the discharge on electrodes made of different materials at 3.4 kV 100 kHz. (a) 1 atm, (b) 0.4 atm

oxides have a high enthalpy of formation. At lower pressure, noticeable power dynamics are not observed. In the photographs, the discharge looks almost the same on all electrodes during the entire discharge exposure.

An analysis of the discharge VCC shape and its distortions during long-term discharge operation was also conducted. Based on this, it can be stated that as a result of surface modification, the discharge operation mode can change due to the chaotization of microdischarges on the aluminum and titanium electrode, or the occurrence of the effect of synchronous start of microdischarges from the entire area of the copper electrode.

Analysis of the morphology of discharge-modified surfaces shows that, depending on the electrode material and the pressure of the plasma-forming gas, degradation can occur in fundamentally different ways.

On the copper electrode after the action of the discharge at a pressure of 1 atm, the formation of many craters with a regular structure is observed, the sizes of which, however, are much smaller than the expected size of the cathode spots of microdischarges, which indicates the absence of stable bindings of the discharge channels. When the pressure decreases to 0.4 atm, the formation of large craters with sizes approximately corresponding to the sizes of the cathode spots of microdischarges is observed on the electrode surface. This indicates the localization of the cathode spots in these areas.

On an aluminum electrode at atmospheric pressure, the electrode material on the surface is replaced by oxide, similar to the observed effects in the surface discharge configuration described in the numerous works. When the pressure decreases, the formation of a regular structure with the same characteristic scales

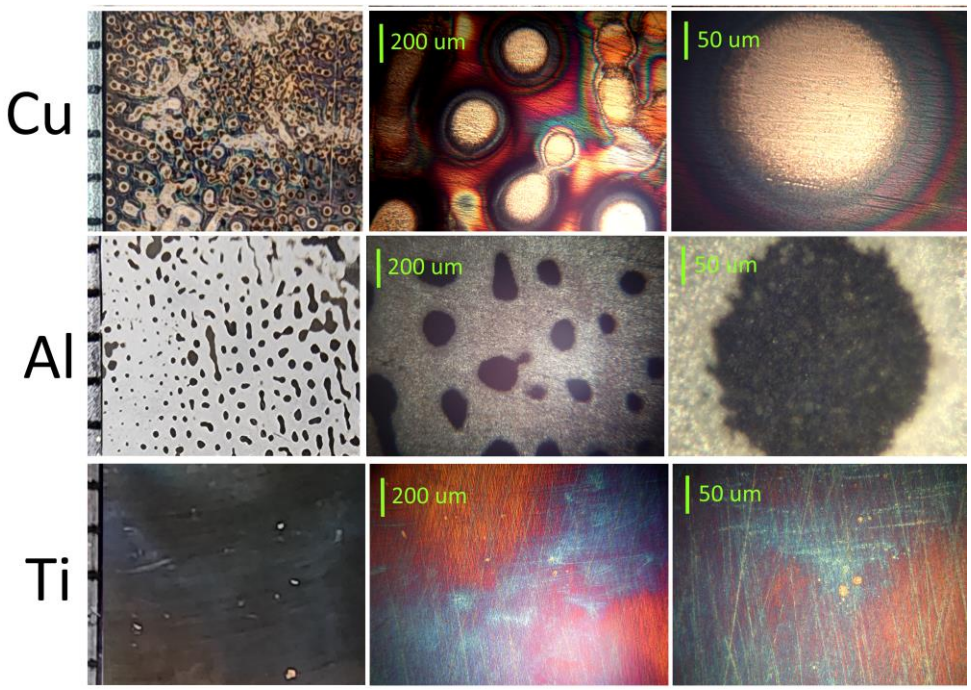

Fig. 3. Images of the surface of samples after modification in a barrier discharge for 300 minutes at a supply voltage amplitude of 3.4 kV and a frequency of 100 kHz at a pressure of 0.4 atm.

as on the copper electrode is observed. However, on the aluminum electrode, the craters are not metal purified from oxide, but oxide in a different phase state (and, presumably, with a different layer thickness). On the surface of the titanium electrode, during modification, a TiO2 layer is formed, which, depending on the local value of the fluence of incoming ions, can be replaced by Ti2O3. As a result, on the modified surface, one can see a structure with alternating oxides of different oxidation states with a spatial scale dependent on the pressure of the working environment, i.e. on the scale of spatial self-organization of microdischarges.

Acknowledgements. The was supported by Russian Science Foundation according to the research project No. 24-79-00168.

PLASMA-LIQUID SYNTHESIS OF MXENES AND THEIR PHOTOCATALYTIC PROPERTIES

N. Sirotkin, A. Khlyustova

G. A. Krestov Institute of Solution Chemistry, Academicheskaja, str., 1, Ivanovo, Russia 153045, e-mail: alexsad8@yandex.ru

The growing demand for environmental remediation has driven research into advanced materials like two-dimensional (2D) nanomaterials. Among these, MXenes—transition metal carbides, nitrides, and carbonitrides—have gained attention due to their high conductivity, tunable band gaps, and chemical stability, making them ideal for energy storage, sensing, and photocatalysis [1]. Photocatalysis offers sustainable solutions for water purification, hydrogen production, and CO_2 reduction. However, traditional photocatalysts like TiO_2 and ZnO face limitations, including poor visible-light absorption and rapid electron-hole recombination. MXenes ($M_{n+1}X_nT_x$, where M = Ti, V, Mo; X = C/N; T = surface groups) address these issues through tunable composition and functionalization [2]. For example, $Ti_3C_2T_x$ effectively degrades pollutants like methylene blue and diclofenac under visible light [3], while MXene/g-C_3N_4 composites enhance phenolic compound removal [4]. Conventional MXene synthesis relies on hazardous hydrofluoric acid (HF), posing environmental risks. Alternative methods (e.g., LiF/HCl etching, electrochemical etching, molten salt etching) improve safety but face scalability or quality challenges. In contrast, plasma–liquid synthesis offers a precursor-free, one-step approach under ambient conditions, avoiding toxic etchants. Previous studies show plasma in contact with liquid can synthesize oxide nanoparticles in water and non-aqueous solvents [5, 6]. For MXene production, we propose a pulsed discharge in tetrachloromethane (CCl_4), an oxygen-free, non-flammable solvent, to synthesize Ti-, Mo-, and Ti-Mo-MXenes in one step.

A 10 kV DC power supply with 1000 Ω ballast resistor generated plasma discharges. Emission spectra were recorded using an AvaSpec-3648 spectrometer. The average discharge current was 0.3 A. Voltage/current waveforms were monitored with an ADS-2072 oscilloscope. The experiments were carried out in a sealed glass cell with a fixed volume of 180 mL. Titanium and molybdenum wires (purity 99.99%), each with a diameter of 1.0 mm, served as electrodes and were used without any pre-treatment. The electrodes were enclosed within a refractory ceramic mullite tube to maintain a consistent inter-electrode gap of 1.0 mm. Carbon tetrachloride (JSC Ekos-1, Moscow, Russia; purity 99.99%) was employed as the dielectric medium for pulsed discharge. It is important to note that after synthesis, the solvent was separated via centrifugation and subsequently reused. The synthesized materials were

characterized using a range of analytical techniques: scanning electron microscopy (Quattro S, Thermo Fisher Scientific, Praha, Czech Republic), X-ray diffraction analysis (D2 Advance diffractometer with CuKα radiation, Bruker, USA), energy-dispersive X-ray spectroscopy (EDS, Thermo Fisher Scientific, Praha, Czech Republic), and Raman spectroscopy (Confotec NR500 Raman microscope with 532 nm excitation, SOL instruments, Minsk, Belarus). Specific surface area and pore size distribution were analyzed using the Brunauer–Emmett–Teller (BET) and Barrett–Joyner–Halenda (BJH) methods, respectively, on a NOVAtouch NT LX-1 Quantachrome analyzer at 77 K (Quantachrome Instruments, Boynton Beach, FL, USA). The photocatalytic performance of the synthesized MXene powders was evaluated by monitoring the degradation rate of organic dyes in aqueous solution under both dark and UV irradiation conditions. A mixture of three model dyes was used: Reactive Red 6C (RR6C, anionic dye, λmax = 533 nm), rhodamine B (RhB, zwitterionic xanthene, λmax = 554 nm), and methylene blue (MB, cationic thiazine, λmax = 667 nm), each at an initial concentration of 1.2 mg/L.

In carbon tetrachloride (ε = 2.24), the pulsed discharge develops differently than in water. It begins as a thin streamer from the anode to the cathode, followed by explosive breakdown and a bright flash, leading to localized overheating and bubble formation. Previous studies suggest plasma temperatures in this environment can reach several thousand degrees [6]. Since material synthesis occurs at the plasma–solution interface, emission spectra of the discharge were analyzed to better understand the process. The spectrum reveals Cl atoms and C_2 molecular bands, including the Swan bands at $\Delta v = 1$ (461–481 nm), $\Delta v = 0$ (501–517 nm), and $\Delta v = -1$ (545–560 nm). Emission lines from Ti and Mo atoms, including ionized Ti, indicate electrode erosion and participation of these species in plasma reactions. This suggests that MXene layers form sequentially at the plasma–liquid interface, differing from conventional etching-based methods. Voltage peaks reached up to 2500 V during discharge pulses, with a peak current of 0.65 A. Pulses occurred at ~20 Hz with a 10% duty cycle. Current and voltage waveforms reflect distinct discharge stages—sharp current rises indicate increased conductive species, while secondary sparks may result from solution overheating facilitating inter-electrode breakdown. The absorption edge in the UV-Vis absorption spectra of MXene appears at ~400 nm, indicating a small bandgap. Plasmon peaks are not clearly visible, likely due to variations in composition and flake thickness-thinner flakes tend to exhibit weaker plasmonic responses. All samples show indirect bandgaps consistent with reported DFT calculations for similar MXenes. Ti_2CT_x has the largest bandgap at 1.71 eV, followed by $Mo_2TiC_2T_x$ - 1.42 eV, and Mo_2CT_x, - 1.07 eV. These values align with previous findings for Ti_2CT_x (~1 eV). On XRD patterns Sample 1 exhibits peaks corresponding to Ti_2CT_x and TiC, with no detectable

oxides, confirming high purity. Sample 2 shows reflections from Mo_2CT_x and α-Mo_2C, characteristic of this MXene type. Sample 3 displays peaks from both Ti_2C and Mo_2C phases. Crystallite sizes were estimated using Scherrer's equation (Table 1). Raman spectroscopy reveals distinct vibrational modes that confirm MXene structure and surface terminations. SEM images reveal an "accordion-like" morphology typical of exfoliated MXenes, confirming layered structures. EDS analysis detected Ti, Mo, C, and Cl, with Cl as surface termination. No impurities like Al, O, S, or Cu were found, highlighting the purity of the plasma–liquid synthesis method. Elemental mapping showed uniform distribution, with Cl slightly enriched at flake edges. Combined Raman and SEM data suggest the formation of the Mo_2TiC_2 MXene phase rather than a simple mixture of Ti_2C and Mo_2C. BET and BJH analyses indicate an average mesopore size of ~12 nm, consistent with a layered MXene structure.

Table 1 presents data on the photocatalytic degradation of a dye mixture consisting of Reactive Red 6C, rhodamine B, and methylene blue, utilizing MXenes as catalysts. The removal efficiencies varied between 65% and 98%, with the highest activity observed for methylene blue (MB). This enhanced activity is attributed to the electrostatic attraction between the negatively charged MXene surface (due to -Cl groups) and the cationic MB molecules, which facilitates both adsorption and degradation. Under light irradiation, electrons are excited from the valence band to the conduction band, generating electron–hole pairs. Surface functional groups and structural defects assist in the separation of these charges, thereby reducing recombination. Electrons reduce oxygen to form reactive oxygen species (e.g., $O_2^{-}\cdot$, H_2O_2), while holes oxidize water to produce hydroxyl radicals (·OH). These radicals subsequently degrade the dyes into harmless byproducts such as CO_2 and H_2O. Adsorption prior to irradiation contributed 20–25% to the total dye removal, except for MB with Sample 2, where it reached approximately 35%, likely due to its higher surface area. The reaction rate constants indicate that degradation rates follow the order: MB > RhB > RR6C. This trend reflects both the structural characteristics of the dyes and the properties of the MXenes - MB's planar shape and positive charge enhance its interaction with MXenes, while the complex structure of RR6C slows its degradation. These findings underscore the significant influence of MXene composition, surface chemistry, and band structure on photocatalytic efficiency. This study successfully demonstrated the one-step synthesis of MXenes containing titanium (Ti), molybdenum (Mo), and Ti-Mo composites through pulsed discharges in carbon tetrachloride. By employing titanium and molybdenum electrodes in various configurations, three distinct samples of MXenes were synthesized. This study highlights the potential of plasma-assisted synthesis as a safe, efficient, and scalable method for producing tunable MXenes. The synthesized MXenes exhibit promising applications in

environmental remediation, particularly in the removal of organic pollutants from aqueous solutions. Future research could concentrate on optimizing the synthesis conditions and investigating the use of these materials in other advanced applications.

Table 1. Sample properties, rate constants and efficiency of dye decomposition.

Name	Chemical composition	E_g, eV	S_{BET}, m^2/g	Crystallite size, nm	Dye	Rate constants, min^{-1}	Efficiency of degradation, %
Sample 1	Ti_2CCl_x	1.71	4.45	21.5	MB	0.03191	89
					RR6C	0.01013	73
					RhB	0.01613	65
Sample 2	Mo_2CCl_x	1.07	7.22	16.7	MB	0.01985	83
					RR6C	0.01313	66
					RhB	0.01071	65
Sample 3	$Mo_2TiC_2Cl_x$	1.42	6.89	19.1	MB	0.03177	98
					RR6C	0.01413	69
					RhB	0.01609	66

Acknowledgements. The authors express their gratitude to the Center for the collective use of scientific equipment at the "Upper Volga Regional Center for Physical–Chemical Research". This study was supported by the Russian Science Foundation under grant 24-23-00146.

References

1. **Anasori B. Gogotsi Y.** Graphene 2D Mater, 7 (2022) 75–79.
2. **Naguib M., Mochalin V.N., Barsoum M.W., Gogotsi Y.** Adv. Mater. 26 (2014) 992–1005.
3. **Qu J., Teng D., Zhang X., Yang Q., Li P., Cao Y.** Ceram. Int. 48 (2022) 14451–14459.
4. **Kim S., Nam S.-N., Park C.M., Jang M., Taheri-Qazvini N., Yoon Y.** J. Hazard. Mater. 426 (2022) 128120.
5. **Agafonov A.V., Sirotkin N.A., Titov V.A., Khlyustova A.V.** Russ. J. Inorg. Chem. 67 (2022) 253–261.
6. **Sirotkin N., Khlyustova A., Agafonov A.** Plasma Chem. Plasma Process. 44 (2024) 1853–1866.

SIZE PROPERTIES OF NANOPARTICLES FORMED IN PLASMA OF ELECTRIC EXPLOSION IN DISTILLED WATER

A. Zelianko

State University of Grodno, Ozheshko Street 22, 230023, Grodno, Belarus,
zelenko_AV@grsu.by

At present, much attention is paid to the production of nanoparticles and their application. This is due to the fact that they have unique physicochemical properties that differ from the properties of these substances in the macrophase state. Various methods are used to produce nanoparticles /1, 2/. An effective and widely used method of obtaining nanoparticles in recent years is their synthesis from plasma /3, 4/. For this, at the first stage, the macrophase material is converted into plasma. At the second stage, nanoparticles are synthesized from the plasma. Of the plasma methods, the most widely used are pulsed laser ablation /5-7/ and electrical explosion /8, 9/ of macrophase materials in liquids or dense gases.

Pulsed laser ablation has been actively studied in recent decades. Interest in this is due to the rapid development of laser technologies for precision processing of parts and products /10, 11/ and the development of laser emission spectral analysis /12, 13/. Under the action of focused laser radiation, a glowing erosive plasma torch containing atoms and ions of the original substance is formed on the surface of the substance. After the laser radiation ceases to act, as the erosive torch cools, nanoparticles are synthesized in it. The synthesis of nanoparticles in electric explosion plasma is significantly more productive, but less controllable, compared to laser ablation. High pulse voltage is applied to the ends of a thin conductor. Under the action of the electric current flowing through it, it heats up, melts, evaporates and ionizes, i.e. turns into plasma. Nanoparticles are synthesized in the plasma at the stage of its recombination after the electric current ceases /14 - 16/. Although the processes occurring during the electric explosion of conductors and the synthesis of nanoparticles in electric explosion plasma have been studied relatively well, a number of phenomena occurring in this case have not yet received due justification. The aim of this work is to study the dimensional characteristics of nanoparticles synthesized in the plasma of an electrical explosion of copper and aluminum in distilled water.

An experimental setup for electrical explosion of conductors in liquids was created on the conceptual basis of excitation systems for electric-discharge lamps and excimer lasers /17, 18/. The prototype of the setup, on which the experimental studies were carried out, is described in /15, 16/. High-current electrical pulses for electrical explosion of conductors in liquids were formed using a high-voltage LC generator by switching storage capacitors pre-charged to high voltage on a load, which was an exploded conductor. The exploded conductor was located in a

reactor, in distilled water. Conductors made of M1 copper with a diameter of 0.4 mm and a length of 80 mm and AD0 aluminum conductors with a diameter of 0.8 mm and a length of 80 mm were subjected to electrical explosion. The experiments were carried out in equal volumes of distilled water amounting to 500 cm^3. The dimensional characteristics of the obtained nanoparticles were studied on an NT-206 atomic force microscope in an air atmosphere at room temperature. Fig. 1(a, b) illustrate histograms showing the dependence of the distribution of the dimensional characteristics of nanoparticles obtained in the electroexplosive plasma of copper and aluminum on the number of conductors exploded in the same volume of distilled water.

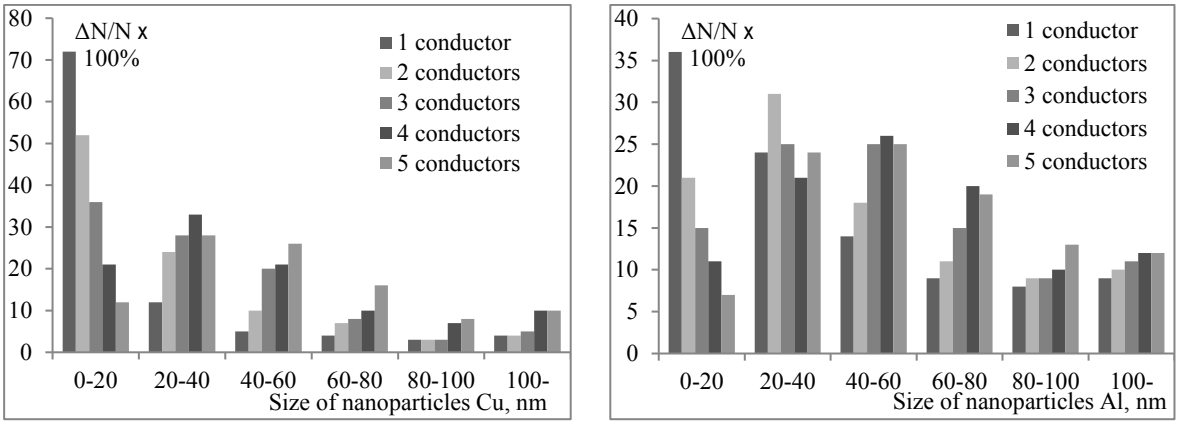

(a) (b)

Fig.1. Size distribution of copper (a) and aluminum (b) nanoparticles synthesized by electroexplosive plasma in distilled water as a functions of the number of exploded conductors

An increase in the number of exploded conductors in the same volume of water leads to a decrease in the proportion of small-sized nanoparticles and an increase in the number of large-sized nanoparticles. The proportion of nanoparticles larger than 100 nm did not exceed 10%. The location of the maxima of the size distributions of the obtained copper and aluminum nanoparticles depends on the number of conductors exploded in the same volume of distilled water. An increase in their number leads to an increase in the sizes of the obtained nanoparticles and a shift in the maxima of the size distributions to a larger side.

Fig. 2(a, b) show the dependences of the "arithmetic mean" d_{ca} and "volume average" d_{co} of the size (diameter) of copper and aluminum nanoparticles on the number of conductors exploded (dispersed) in the same volume of distilled water. It is evident that with the growth of the number of conductors exploded in the same volume of distilled water, both the "arithmetic mean" and "volume average" sizes of the obtained nanoparticles increase almost linearly for both copper and aluminum.

Fig. 3a shows the dependences of the concentration C of copper and aluminum nanoparticles on the number of exploded conductors in the same

volume of distilled water. With the growth of the number of exploded conductors, an increase in the concentration of aluminum nanoparticles is observed. The situation with the concentration of copper nanoparticles is somewhat different. It is evident that the dependence of the concentration of copper nanoparticles has a maximum. This indicates that with the growth of the number of exploded copper conductors in the same volume of water, larger copper nanoparticles are formed.

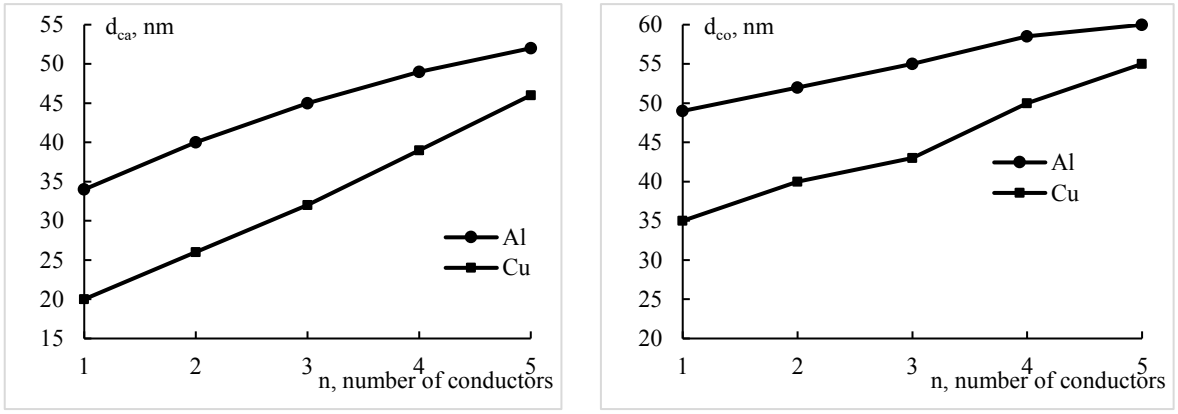

(a) (b)

Fig. 2. The arithmetic mean (d_{ca}) and volume average (d_{co}) diameter of copper (a) and aluminum (b) nanoparticles as a functions of the number of exploded conductors

Fig. 3b shows the dependences of the specific surface area of copper and aluminum nanoparticles on the number of exploded conductors in the same volume of distilled water. It is evident that for both copper and aluminum, the specific surface area of the obtained nanoparticles increases with the number of exploded conductors in the same volume of distilled water.

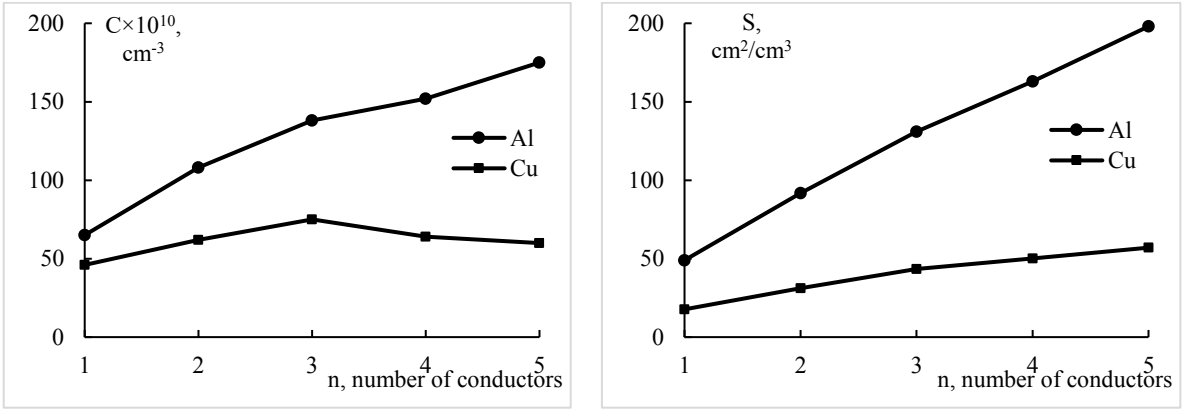

(a) (b)

Fig. 3. Copper and aluminum nanoparticle concentration (a) and specific surface area (b) as a functions of the number of exploded conductors (in the same volume of distilled water)

The effect of intense ultraviolet radiation from subsequent explosions of conductors leads to the ionization of surface atoms of nanoparticles and the appearance of electric charges on their surface. Due to the Coulomb interaction,

nanoparticles will attract oppositely charged ions, clusters and other nanoparticles. In this case, they will become larger after each subsequent explosion of the conductor. Thus, the Coulomb interaction inside the nanosuspension is apparently the main reason for the enlargement of nanoparticles with an increase in the number of exploded conductors in the same volume of water.

The work was carried out within the framework of task 2.2.05 of the State Scientific Research Program “Convergence - 2025”, subprogram “Microworld, Plasma and the Universe”.

References

1. **Maier G.G.** Volumetric nanostructured materials: modern methods of creation and research. Tomsk: IFPM SO RAN (2013).
2. **Ilyin A.P. Mostovshchikov A.V., Korshunov A.V., Root L.O.** Features of the physicochemical properties of nanopowders and nanomaterials. Tomsk: Tomsk. PTU (2017).
3. **Burakov V.S. Tarasenko N.V., Butsen A.V. [et al.]**. Problems of physics, mathematics and technology, No.2 (2011) 22-25.
4. **Orlov A.M., Yavtushkenko I.O., Bodnarski D.S.** Journal of Technical Physics, 85 (2015) 81-87.
5. **Gusakov G.A., PuzyrevM.V., Gorudko I.V. [et al.]**. Journal of the Belarusian State University. Physics, No. 2 (2022) 39-49.
6. **Leshchik S.D., Znosko K.F., Kalugin Y.K.** Vesnik of Brest State Technical University. Series: Mechanical Engineering, No.4 (2014) 6-10.
7. **Leshchik S. D., Znosko K.F., Sergienko I.G., [et al.]** Fundamental problems of radioengineering and device construction, 14 (2014) 84-87.
8. **Nazarenko O.B.** Electrospray nanopowders: production, application, properties. Ed. by Ilyin A.P.. Tomsk: PTU (2005).
9. **Ilyin A.P., Nazarenko O.B.**, **Shuvalov G.V. [et al.]**. Oproelectronics and Advanced Materials - Rapid Communication, 4 (2010) 834-837.
10. **Znosko K.F. and Leshchyk S.D.** Vesnik of Yanka Kupala State University of Grodno. Series 6. Engineering Science, 11, (2021) 45-58.
11. **Znosko K.F.** Vesnik of Yanka Kupala State University of Grodno. Series 2. Mathematics. Physics…, 13 (2023) 116-132.
12. **Kuriyan N.N., Znosko K.F., Grigut V.V.** Vesnik of Yanka Kupala State University of Grodno. Series 2. Mathematics. Physics…, 8 (2018) 101-110.
13. **Anufrik S.S., Kurian N.N., Znosko K.F. [et al.]**. Vesnik of Yanka Kupala State University of Grodno. Series 2. Mathematics.Physics… 6 (2016) 57-63.
14. **Burakov V.S., Butsen A.V., Bruser V. [et al.]**. Journal of Nanoparticle Research, 10 (2008) 881-886.
15. **Sergienko I.G., Znosko K F., Leshchik S D.** Vesnik of Yanka Kupala State University of Grodno. Series 6. Engineering Science, 7 (2017) 47-57.
16. **Znosko K.F.** Vesnik of Yanka Kupala State University of Grodno. Series 2. Mathematics. Physics…, 14 (2024) 81-92.
17. **Znosko K.F., Belash V.Ch.** Vesnik of Yanka Kupala State University of Grodno. Series 6. Engineering Science, 9 (2019) 28-39.
18. **Znosko K.F., Belash V.Ch.** Vesnik of Yanka Kupala State University of Grodno. Series 2. Mathematics. Physics…, 9 (2019) 74-85.

EFFECT OF THE PLASMA-FORMING GAS ON THE GENERATION OF LONG-LIVED REACTIVE OXYGEN AND NITROGEN SPECIES IN LIQUID IN THE PRESENCE OF COPPER ELECTRODE EROSION

M. Zimina[1,2], V. Gudkova[1,2], I. Moryakov[1], V. Borzosekov[1,2]

[1]Prokhorov General Physics Institute of the Russian Academy of Sciences, 38, Vavilova St., 119991, Moscow, Russian Federation, office@gpi.ru
[2]RUDN University, 6, Miklukho-Maklaya St, Moscow, 117198, Russian Federation, science@rudn.ru

The generation of reactive particles using low-temperature gas discharge plasma is an intensively developing field of research that allows solving a wide range of problems /1/. Of particular interest are multiphase systems (liquid – gas – plasma) in which, due to a variety of physico-chemical processes at the interface of phases, long-lived reactive species of nitrogen and oxygen (ROS and RNS) with pronounced antimicrobial properties are formed /2/. The key factors determining the efficiency of plasma chemical processes in such systems, in addition to the parameters of the discharge itself, are the nature of the plasma-forming gas, as well as the properties of the liquids under study /3/. Metal particles and ions in liquids can contribute to the formation of reactive species. Formed as a result of electrode erosion, they are capable of exhibiting high catalytic activity /4/. In this paper, a comparative study of two types of injected gases, air and oxygen, was carried out, and their effect on the formation of ROS and RNS in deionized water was analyzed depending on the time of treatment with a plasma source, as well as the erosion of a multi–spark ring discharge in a liquid was quantitatively and qualitatively investigated depending on the plasma-forming gas. The results obtained will make it possible to establish the relationship between the composition of the injected gas and plasma chemical reactions in liquids, as well as optimize processes for the successful implementation of plasma-activated liquids and the resulting nanoparticles in applied problems.

The concentrations of hydrogen peroxide, nitrite and nitrate ions, as well as the mass concentration of copper (II) ions were determined by the spectrophotometric method with the addition of chemical probes. For hydrogen peroxide – FOX reagent, for nitrite ions - Griess, divalent copper ions – sodium diethyldithiocarbamate (Russian GOST 4388). The concentration of nitrate ions was determined using an ion-selective electrode ELICE-121NO3. X-ray phase analysis was used for a qualitative analysis of the composition of particles formed during electrode erosion. The results were obtained in Bragg-Brentano geometry using a Rigaku Smartlab SE diffractometer using Cu $K_{a1,2}$ radiation (λ_1 = 1.54059 Å, λ_2 = 1.54441 Å, K_{a1}/K_{a2} ratio – 0.497, 50 kV, 40 mA) and a D/TeX

Ultra 250 detector. The samples were recorded with a diffraction angle of 2° in the range of 5-100°, with a step width of 0.02°, and at a speed of 10°/min. The rate of electrode erosion was estimated by gravimetric method.

The work uses a high–voltage pulse generator U = 20 kV with a storage capacity of C = 10^{-8} F. The energy input into the spark channel for each pulse is less than ≤ 1 J. Four pairs of copper (grade M1T, copper content up to 99.9%) electrodes measuring 8×14×2 mm each are coated on top with an electrical insulating material and mounted on the inner wall of a plexiglass dielectric chamber with a volume of 120 cm^3. A working gas is injected into the interelectrode spaces through a hole with a diameter of 2 mm – oxygen and air with a flow rate of 6 l/min. The working fluid is deionized water with a conductivity of 0.1 μS/cm, and the exposure time of the plasma source to the liquid is 2, 4, 6, 8 and 10 minutes. This experimental stand was developed at the Prokhorov General Physics Institute of the Russian Academy of Sciences /5/.

Table 1 shows the concentrations of ROS and RNS, as well as the mass concentration of copper (II) ions in deionized water during injection of air and oxygen into the interelectrode space. During oxygen bubbling, nitrogen oxides in deionized water are not observed within the sensitivity range of our instruments.

Injected gas: **air**				
Exposure time, min	Concentration of H_2O_2, μmol/l	Concentration of NO_2^-, μmol/l	Concentration of NO_3^-, μmol/l	Concentration of Cu^{2+}, μg/ml
2	200 ± 8	75 ± 6	36 ± 3	21 ± 4
4	240 ± 15	158 ± 20	60 ± 5	39 ± 5
6	172 ± 30	231 ± 18	79 ± 5	63 ± 5
8	116 ± 19	318 ± 17	95 ± 6	90 ± 2
10	108 ± 20	392 ± 30	116 ± 9	105 ± 2
Injected gas: **oxygen**				
Exposure time, min	Concentration of H_2O_2, μmol/l	Concentration of NO_2^-, μmol/l	Concentration of NO_3^-, μmol/l	Concentration of Cu^{2+}, μg/ml
2	42 ± 9	-	-	22 ± 3
4	56 ± 9	-	-	39 ± 2
6	67 ± 9	-	-	63 ± 3
8	74 ± 5	-	-	88 ± 6
10	87 ± 8	-	-	107 ± 13

Tab. 1. Concentrations of ROS, RNS and Cu^{2+} in deionized water depending on the exposure time of the plasma source for two types of plasma-forming gas.

The result obtained, indicating high concentrations of hydrogen peroxide

during air injection, unlike oxygen, can be explained by the influence of reactive forms of nitrogen, which are also involved in reactions of peroxide formation in the volume of liquid, and contribute to the creation of additional radical generation pathways. The observed decrease in ROS concentration after 4 minutes of exposure to a multi-spark discharge in the atmospheric air may be due to the achievement of a critical concentration of copper (II) ions in solution, which exhibit high catalytic activity with respect to H_2O_2 by the Fenton mechanism /6/ (1,2):

$$Cu^{2+} + H_2O_2 \rightarrow Cu^{+} + HO_2\cdot + H^{+} \quad (1)$$

$$Cu^{+} + H_2O_2 \rightarrow Cu^{2+} + OH\cdot + OH^{-} \quad (2)$$

In turn, when oxygen is injected, there is no intensive flow of reactive nitrogen species.

The determination of divalent copper ions in solutions is of interest from the point of view of studying the mechanisms of electrode erosion, as well as studying processes in a multiphase medium. At the moment, the scientific community doesn`t have a clear version of what affects the ratio of particles and ions in a liquid during plasma chemical synthesis. Thus, the non-trivial results indicating the same formation of Cu^{2+} during oxygen and air injection can be interpreted as the predominance of the influence of the liquid phase and other discharge parameters on electrode erosion compared with the gas phase.

This hypothesis is consistent with the data of gravimetric measurements of the erosion rate, which in both cases amounted to 2.3 mg/min from 4 spark channels. Additionally, the sludge mass was measured after centrifugation and drying. Taking into account the mass concentration of copper, the following values were obtained: 2.0 mg/min for air and 1.9 mg/min for oxygen. Thus, it can be assumed that the difference in comparison with gravimetric measurements of the mass of the electrodes before and after the experiments is due to the presence of copper in other oxidation states, as well as losses during particle centrifugation and drying.

X-ray phase analysis of the particles confirms the presence of crystalline Cu, CuO, and Cu_2O for both types of plasma-forming gases, as well as the presence of $Cu_4(NO_3)_2(OH)_6$ copper nitrate during air injection (Fig. 1). Using the Scherrer equation, the average particle sizes were calculated based on the broadening of diffraction reflection peaks. For oxygen, this value was 63 ± 3 nm, for air – 84 ± 2 nm.

As a result of the work, the role of plasma-forming gas on the formation of reactive species of nitrogen and oxygen in water, as well as on the rate of erosion of electrodes and on the massive formation of divalent copper (II) ions in solutions was revealed. The injection of air into the interelectrode space of a multi-spark ring discharge leads to the effective generation of nitrogen reactive

species, which subsequently contribute to the formation of hydrogen peroxide, which explains the higher concentration of H_2O_2 compared to oxygen injection. In the system under consideration, the type of plasma-forming gas doesn`t affect the rate of erosion of copper electrodes, but it does affect the phase composition of the resulting nano- and microparticles. Thus, controlling the composition of the plasma-forming gas makes it possible to adjust the balance between the generation of active forms, electrode erosion, and the morphology of nanostructures in plasma-liquid systems.

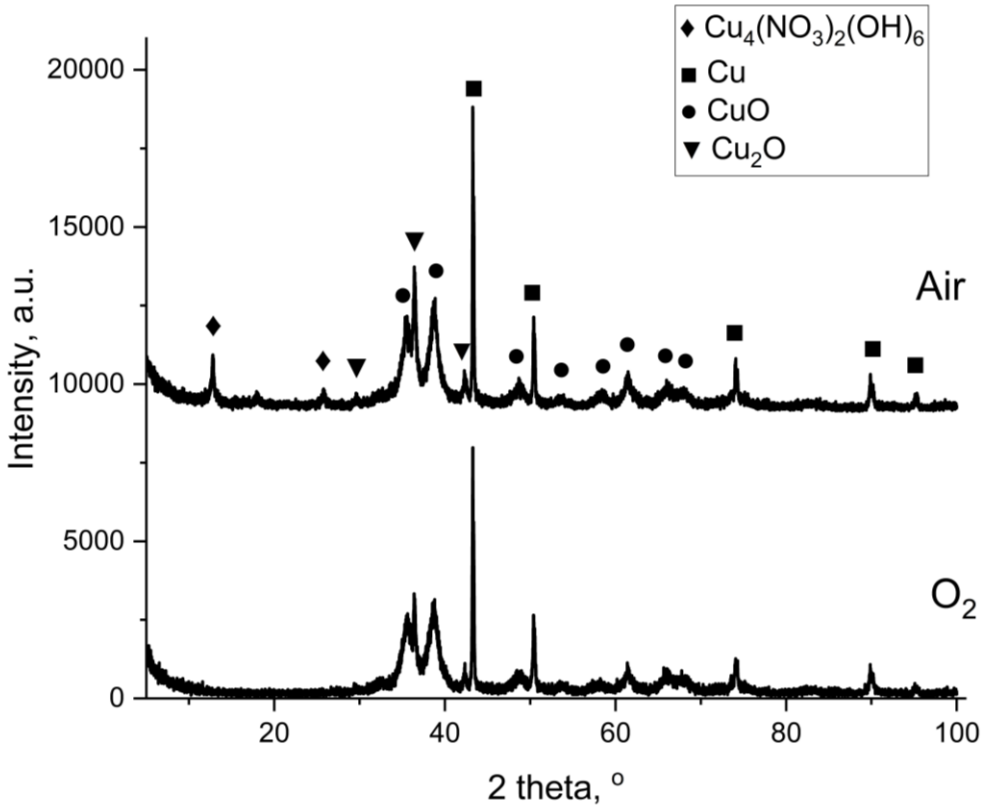

Fig. 1. X-ray diffractogram of dried particles obtained in an atmosphere of air and oxygen after exposure to a multi-spark discharge.

Acknowledgements. This study was conducted within the framework of the Russian Science Foundation Grant No. 24-29-00736 at the GPI RAS.

References

1. **Konchekov E.M.** et al. Biomolecules, 14(2024) 181.
2. **Darmanin M.** et al. Food Control, 113(2020) 107168.
3. **Du C.M.** et al. Plasma Chem Plasma Process, 28(2008) 523–533.
4. **Chen Q., Li J., Li Y.** J. Phys. D: Appl. Phys, 48(2015) 424005.
5. **Gudkova V.V.** et al. Plasma Phys. Rep, 49(2023) 1341–1349.
6. **Pham A.N.** et al. Journal of Catalysis, 301(2013) 54–64.

4. NON-IDEAL AND DUSTY PLASMAS, EXTREME PLASMA REGIMES, FUSION AND ASTROPHYSICAL PLASMAS

ENERGETICS AND EVOLUTION OF ACTIVE BROWNIAN MOTORS IN COULOMB SYSTEMS IN PLASMA, VISCOUS LIQUID AND SUPERFLUID HELIUM

O. Petrov, M. Vasiliev

Joint Institute for High Temperatures of the Russian Academy of Sciences (JIHT RAS)
125412, Izhorskaya st. 13 Bd.2,Moscow, vasiliev@ihed.ras.ru

In recent decades, the study of Brownian motion—particularly in systems far from thermodynamic equilibrium—has become a subject of intense scientific interest. Special attention has been given to the phenomenon of active Brownian motion, where particles are capable of harnessing energy from their surroundings to drive self-propulsion. This is in contrast to passive Brownian particles, which remain in thermal equilibrium with their environment and whose motion arises solely from random thermal fluctuations. Active Brownian particles operate outside this equilibrium, making them a compelling subject for the study of non-equilibrium statistical physics and complex systems [1–3].

In our research, we investigate the dynamics of charged grains with metal coatings, which are suspended in a low-pressure gas discharge environment. These grains are exposed to focused laser radiation, leading to localized heating effects and complex interactions that drive the system far from thermodynamic equilibrium. Specifically, we examine how the monolayer of these metallic grains undergoes a melting transition when subjected to varying intensities of laser light [1]. Through a series of carefully controlled experiments, we observe that the motion of these grains does not conform to classical Brownian behavior. Instead, they exhibit active Brownian dynamics, wherein the grains exhibit self-driven movement under the influence of external energy input.

This self-propulsion is attributed to a mechanism known as photophoresis. When laser radiation is absorbed by the metal-coated surface of a grain, a temperature gradient is established across the grain's surface. This temperature differential generates a radiometric (photophoretic) force, which propels the grain through the surrounding medium. As a result, both the kinetic energy and diffusion coefficient of the grains are significantly enhanced—by several orders of magnitude—compared to their values under conditions of passive Brownian motion. This remarkable increase underscores the influence of externally supplied energy in generation particle dynamics within plasma environments.

Beyond this, we extended our investigation to study the behavior of complex emulsion droplets containing magnetic nanoparticles. In a separate series of experiments, we examined charged oil-in-water emulsions, where the oil droplets (approximately 65 micrometers in diameter) encapsulate magnetite (Fe_3O_4) nanoparticles around 10 nanometers in size. The emulsion was stabilized

using a surfactant solution to ensure uniform droplet size and prevent coalescence [2]. When exposed to laser irradiation, the droplets exhibited pronounced active Brownian motion, which we determined to originate from the internal motion of magnetite nanoparticles within each droplet. These nanoparticles, upon absorbing the laser energy, initiate localized heating and generate internal thermal gradients, which in turn drive convective flows and internal forces within the droplet. This internal activity translates into net motion of the droplet as a whole, again highlighting a form of energy conversion from absorbed radiation to directed kinetic motion.

Finally, we present experimental findings on the motion of superconducting ceramic grains—with diameters reaching up to 60 micrometers and carrying electric charges as high as 10^5 elementary charges—levitating in a static magnetic trap immersed in superfluid helium. This system can be classified as a cryogenic colloid, operating at temperatures ranging from 1.7 K to 2.18 K. Here, the grains are suspended in a quantum fluid environment and are exposed to laser irradiation with a power density of up to approximately 2 W/cm². Under these extreme cryogenic conditions, we observe that increasing the laser power significantly affects the grains' motion: both their kinetic energy and diffusion coefficients rise dramatically—by 6 to 7 orders of magnitude—compared to the equilibrium values at the same temperature.

These experimental results confirm that the grains undergo active Brownian motion driven by the external laser energy input and modulated by strong Coulomb interactions (due to their electric charges) as well as magnetic interactions with the trapping field. Moreover, we observe the formation and evolution of grain assemblies, which initially exist in disordered configurations far from equilibrium. Over time, these structures undergo self-organization, forming more ordered and complex patterns of motion and structures. This spontaneous reduction in entropy—under conditions where classical thermodynamics would predict disorder—is attributed to export entropy mechanisms in superfluid helium media [3]. Such behavior provides important insights into the nature of self-organization in quantum fluids and demonstrates the potential for engineered colloidal systems to model complex, emergent behavior in soft matter and condensed matter physics.

In summary, our multifaceted study provides compelling experimental evidence of active Brownian motion across a range of systems—from dusty plasmas to emulsions and cryogenic colloids. In each case, the introduction of external energy, particularly in the form of laser radiation, drives the particles far from equilibrium and enables the exploration of novel physical regimes characterized by enhanced mobility, non-linear interactions, and emergent dynamical and structural self-organization. We define our active Brownian particles as Brownian motors because they possess three properties

simultaneously: the ability to obtain energy from outside sources, the ability to accumulate it, and the ability to subsequently convert and use it for their own active motion. And in our experiments, we we have the possibility to control these active Brownian motors.

Acknowledgements. This work was supported by the Russian Science Foundation (RSF) with grant № 25-12-00406.

References

1. **Petrov O.F., Statsenko K.B., Vasiliev M.M.** Active Brownian motion of strongly coupled charged grains driven by laser radiation in plasma. Scientific Reports, 12, 1, (2022) 8618.
2. **Kononov E.A., Senoshenko R.V., Vasiliev M.M., Petrov O.F.** Active Brownian motion of emulsion droplets driven by nanoscale effects under laser irradiation. Physics of Fluids, 36, (2024) 117145.
3. **Petrov O.F., Boltnev R.E., Vasiliev M.M.** Experimental evolution of active Brownian grains driven by quantum effects in superfluid helium, Scientific Reports, 12, 1, (2022) 6085.

ELECTROMAGNETIC RADIATION IN PLASMAS: NON-PLANCKIAN THERMAL EMISSION AND ASYMPTOTIC TUNNELING

S. V. Gaponenko, D. V. Novitsky, L. V. Simonchik, and M. S. Usachonak

B. I. Stepanov Institute of Physics of NAS Belarus, 68-2 Nezavisimosti Ave., Minsk 220072 Belarus, e-mail: s.gaponenko@ifanbel.bas-net.by

We consider two general properties of electromagnetic (EM) radiation in plasmas which seem to have been overlooked in the mainstream research. These are photon density of states effect on thermal emission and tunneling of EM-radiation.

Thermal emission spectrum is typically believed to obey the known Planck formula which is widely used, e. g., to estimate plasma temperature. However, the genuine Planck formula is strictly valid for vacuum only since it includes the photon density of states (DOS) factor ω^2/π^2c^3 derived for the free space. This factor is to be replaced by the explicitly calculated DOS in every case /1,2/. Since plasma features dielectric permittivity $\varepsilon(\omega) < 1$ everywhere and $\varepsilon(\omega) < 0$ at $\omega < \omega_p$ where ω_p is plasma frequency, photon DOS in plasmas is always less than in vacuum tending to 0 for $\omega \to \omega_p$ and being indefinite for $\omega < \omega_p$. These properties give rise to lower thermal emission intensity for frequencies close to ω_p, and to zero thermal emission for $\omega < \omega_p$. We showed that the genuine formula for equilibrium thermal radiation spectral density in vacuum

$$u(\omega) = \hbar\omega \frac{\omega^2}{\pi^2 c^3} \left(\exp\frac{\hbar\omega}{k_B T} - 1\right)^{-1} \tag{1}$$

takes for plasma the modified form /3/,

$$u_{plasma}(\omega) = \hbar\omega \frac{\omega}{\pi^2 c^3} \sqrt{\omega^2 - \omega_p^2} \left(\exp\frac{\hbar\omega}{k_B T} - 1\right)^{-1} . \tag{2}$$

In terms of radiation wavelength in vacuum λ_0, it reads

$$u_{plasma}(\lambda_0) = \frac{8\pi hc}{\lambda_0^5} \sqrt{1 - \frac{\lambda_0^2}{\lambda_p^2}} \left(\exp\frac{hc}{\lambda_0 k_B T} - 1\right)^{-1} \tag{3}$$

where $\lambda_p = 2\pi c / \omega_p$. One can see that plasma inhibits thermal emission at the long-wave wing of the spectrum disabling emissivity completely for $\lambda_0 > \lambda_p$. (Fig. 1).

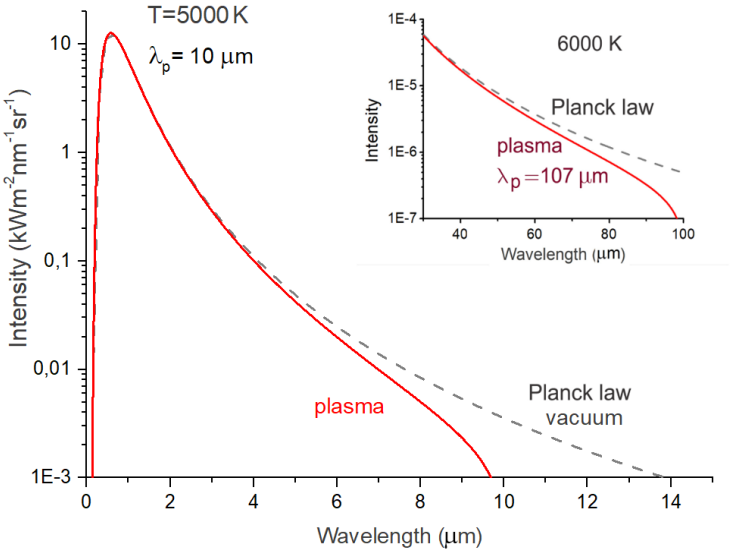

Fig. 1. Thermal emission spectra for 5000 K in vacuum (Planck law, dashes) and in plasma for λ_p = 10 μm (solid line). The insert shows a portion of thermal spectrum for 6000 K relevant to solar radiation and its modification for λ_p = 107 μm (corresponds to plasma density about 10^{17} cm^{-3} (solar photosphere)

In the case of solar radiation plasma density is supposed to be about 10^{17} cm^{-3} resulting in λ_p = 100 μm thus defining the spectral range where deviation from Planck law are expected (Fig. 1). Lower photon DOS in plasmas have also other physical manifestations, namely subnatural spectral linewidths and smaller Lamb shift. These effected though being less pronounced and hard to be detected experimental represent nevertheless the basic physical phenomena relevant to plasmas owing to its genuine ε(ω) < 1 dielectric pertmittivity.

EM radiation tunneling resembles a direct classical analog to quantum mechanical ones, the negative ε(ω) being an analog of $E < U$ in quantum mechanics with E being a particle energy and U being a barrier height. Electromagnetic tunneling has become the subject of extensive research (see, e.g. Ref 4 and Refs. therein) however tunneling dynamics in plasmas has not been systematically examined. Note, that radiation tunneling is important in astrophysics as possible emission from black holes and is known as Hawking radiation /4/.

For the case of normal radiation incidence at a plane plasma layer with Drude permittivity, $\varepsilon = 1 - \frac{\omega_p^2}{\omega(\omega+i\gamma)}$, the phase (Wigner) time $\tau_\varphi = \frac{d\varphi_t}{d\omega}$ can be derived analytically. Here φ_t is the phase of complex transmission coefficient $t = |t|e^{i\varphi_t}$. In the limit of weak transmission /6/ it reads

$$\tau_\varphi \approx \frac{2}{\sqrt{\omega_p^2 - \omega^2}} - \frac{\gamma}{2\omega^2}\frac{\omega_p^4 + 2\omega^4 - \omega_p^2\omega^2}{\left(\omega_p^2 - \omega^2\right)^2} \tag{4}$$

and is principally independent on layer thickness. Length-independent time allows for superluminal tunneling time. This is a direct classical electromagnetic analog of the known Hartman effect in quantum mechanics. In the limit of $\gamma \to 0$ (lossless plasma) Wigner time asymptotically tends to $2/\omega_p$. This plasma property notably differs from the cases of EM-tunneling through dielectric structures where a trend to $\tau_\varphi \to 1/\omega$ has been found /7/. Thus Wigner time for EM-tunneling through a plasma layer is defined exclusively by plasma properties and show no dependence on radiation frequency. Since $1/\omega_p$ is known to define the ultimate reaction rate of a plasma layer to external EM-perturbation we have suggested that tunneling can probably be viewed as a kind prompt burst or flinching thus returning to the original meaning of Wigner phase time as scattering time and avoiding the problem of superluminal propagation velocity since no propagation does actually occur.

The asymptotic behavior was found to be generally valid for the more realistic problems including losses and time-dependent consideration instead of the Wigner time approach /8/. We perform numerical simulations of EM pulses propagating through the plasma layer under normal incidence solving the scalar wave equation for the electric field E

$$\frac{\partial^2 E}{\partial z^2} - \frac{1}{c^2}\frac{\partial^2 E}{\partial t^2} = \frac{1}{c^2}\frac{\partial^2 P}{\partial t^2} \tag{5}$$

with the medium polarization P governed by the oscillation equation

$$\frac{\partial^2 P_i}{\partial t^2} + \gamma\frac{\partial P_i}{\partial t} = \omega_p^2 E_i \tag{6}$$

Using the numerical approach described in Ref. 9. We use the integrated value of "EM-pulse center of gravity" as a more stable measure, $\tau_c = \int I(t)t dt \,/\, \int I(t) dt$, where $I(t)$ is the radiation intensity. Fig. 2a shows asymptotic behavior of both Wigner time, τ_φ and τ_c. Fig. 2b shows the Hartman effect, i.e. saturation of tunneling time with growing barrier length, L.

These findings have been supported by experiments in the microwave range. We used gas discharge plasma with the effective permittivity which can be tuned by changing electron density and made negative. To reach effective negative permittivity, he electron density should be above 0.65×10^{13} cm^{-3} at 8 GHz. To determine the phase time τ_φ (group delay) as a function of frequency, the scattering parameters and the phase spectra were measured with the vector network analyzer N9918A Keysight. The derivative

of phase with respect to frequency allows us to obtain the spectrum of phase time (group delay). It is plotted in Fig. 2c. One can see that it can indeed be fitted as $\tau_\varphi \sim n_e^{-1/2}$ in accordance with the expected relation $\tau_\varphi \sim 1/\omega_p \sim n_e^{-1/2}$.

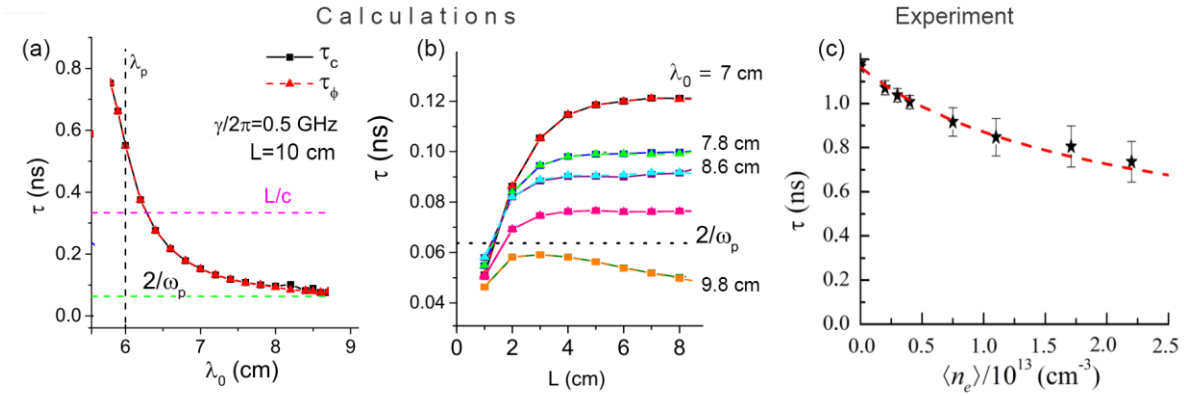

Fig. 2. (a), (b) Calculated and (c) measured tunneling time for EM radiation in plasma for microwave spectral range. (a) Center of gravity time τ_c and phase time τ_φ versus EM pulse central wavelength λ_0 for plasma wavelength $\lambda_p = 6$ cm and plasma layer thickness $L = 10$ cm. (b) Delay time versus plasma layer thickness for $\lambda_p = 6$ cm and various λ_0 values. (c) Measured phase time on electron density n_e at the frequency of 8 GHz; the dashed line shows the relation $\tau_\varphi \sim n_e^{-1/2}$

In conclusion, we have highlighted the two basic properties of plasmas with respect to emission and propagation of electromagnetic radiation, namely sub-Planckian thermal emission and asymptotic tunneling time. These basic features result directly from the specific dielectric permittivity of plasmas. Our findings not only complement the current knowledge of electromagnetic properties of plasma but can be also used in plasma diagnostics.

Acknowledgement. The work was supported by the BRFFR grant F23ICR- 002.

References

1. **Gaponenko S. V.** Introduction to Nanophotonics. Cambridge Uni. Press (2010).
2. **Gaponenko S. V.** Journal of Nanophotonics 8 (2014) 087599-087599.
3. **Gaponenko S., Novitsky D., Guzatov D.** Physica Scripta 98 (2023) 045614.
4. **Vanzo L., Acquaviva G., Di Criscienzo R.** (2011). Classical and Quantum Gravity 28(2011)183001.
5. **Dumont R., Rivlin T., Pollak E.** New Journal of Physics 22(2020) 093060.
6. **Gaponenko S. V. and Novitsky D. V.** Physical Review A 106 (2022) 023502.
7. **Esposito S.** Physical Review E 64 (2002) 026609.
8. **Novitsky D. V., Usachonak M.S., Simonchik L.V., Gaponenko S. V.** Physical Review A 111 (2025) 033529-033529.
9. **Novitsky D. V., Tuz V. R., Prosvirnin S. L., Lavrinenko A. V., Novitsky A. V.,** Physical Review B 96 (2017) 235129.

AB INITIO PSEUDOPOTENTIALS AND YUKAWA LIKE SCRENING IN MODERATE DENITIES PLASMA, INITIAL RESULTS

N. M. Sakan[1], Z. Simić[2], V. A. Srećković[1], M. Dechev[3], and B. Stankov[1]

[1]University of Belgrade, Institute of Physics, PO Box 57, 11001 Belgrade, Serbia, nsakan@ipb.ac.rs
[2]Astronomical Observatory, Volgina 7, 11060 Belgrade, Serbia
[3]Institute of Astronomy and National Astronomical Observatory, Bulgarian Academy of Sciences, 72, Tsarigradsko chaussee Blvd. Sofia, Bulgaria

Abstract

We present a computational approach for modelling collective phenomena in moderately dense plasmas using ab initio pseudo-potentials with Yukawa-like screening. Our code calculates the influence of plasma environment on emitter pseudo-potentials, enabling quantum-mechanical predictions of optical properties. Initial results demonstrate how ion-electron correlations and screening effects modify electronic states, providing a foundation for first-principles optical diagnostics in dense plasmas.

Introduction

In dense plasma, the inter-particle Coulomb interaction becomes dominant over the thermal kinetic energy [1]. Under such conditions, the coupled system of particles exhibits behaviour reminiscent of a crystalline solid. For the case of hydrogen, a simplified form of the non-ideality parameter Γ and Wigner-Seitz radius are given by

$$\Gamma=\frac{E_p}{E_k}=\frac{e^2}{\mathrm{kTr_{WS}}}\sim \mathrm{e}^2 N_e^{1/3}\beta, \qquad \beta=1/\mathrm{kT}, \quad r_{\mathrm{WS}}=\left(\frac{3}{4\pi \mathrm{N}_e}\right)^{1/3}.$$

At high Γ values ($\Gamma \gg 1$), the ions arrange themselves in a structured, nearly crystalline configuration to minimize Coulomb energy. In particular, the system tends toward a locally ordered state resembling a face-centred cubic (FCC) lattice, which is one of the most efficient packing arrangements for spheres in three dimensions. The FCC structure, found in many solid metals, maximizes the nearest neighbour distance while minimizing the free energy of the system. Similarly, in strongly coupled plasmas, the ions adopt configurations where their mutual repulsion is optimized, leading to short-range order analogous to that of an FCC crystal. Inside such a dense-packed, crystal-like structure, screening mechanisms become crucial in determining the effective local pseudo-potential. Up until now the interaction in plasma has been successfully modeled using a cut-off Coulomb potential, and the usage of ab-initio potentials has been introduced in order to have more applicable model that covers multiple atoms in plasma. It was demonstrated in [2], [3], and [4]. It is known that the electron cloud

surrounding ions modifies the bare Coulomb interaction, leading to screened potentials such as the Yukawa or Debye-Hückel form, which significantly influence the stability and dynamics of the ion lattice. This screening effect must be accounted for when describing the optical, thermodynamic and transport properties of strongly coupled plasmas.

The Debye radius (λ_D) is a characteristic length in plasma that describes the screening distance of electrostatic potential from a charge. Its definition differs depending on the degree of plasma non-ideality Γ, leading to factors of 2π or 4π in the expression. In ideal plasma (low density, high temperature), and in high densities plasma the Debye radius is defined as:

$$\lambda_D = \sqrt{\frac{\epsilon_0 k_B T_e}{n_e e^2}}, \text{ or modified } \lambda_D = \sqrt{\frac{\epsilon_0 k_B T_e}{4\pi n_e e^2}}.$$

where ϵ_0 is the vacuum permittivity, k_B is the Boltzmann constant, T_e is the electron temperature, n_e is the electron number density, and e is the elementary charge. The difference in the factor of 4π (or 2π in some sources) arises from different approaches in screening theory, in **ideal plasma**, screening is described by **Debye-Hückel theory**, where the potential of a single charge in plasma is:

$$\phi(r) \propto \frac{e^{-r/\lambda_D}}{r}$$

Yukawa-like Screening in Coupled Plasmas

The screening behavior in plasmas undergoes significant changes across different coupling regimes, Weak Coupling Regime ($\Gamma \ll 1$), here in the Debye-Hückel limit, the screening is characterized by the Debye length in SI as well as atomic units:

$$\lambda_D = \sqrt{\frac{k_B T}{4\pi n_e e^2}} = \sqrt{\frac{T}{4\pi n_e}},$$

where the screened potential follows the classical Yukawa form.

Intermediate Coupling Regime ($0.3 \lesssim \Gamma \lesssim 3.0$), here coupling increases, and nonlinear effects become important. A modified Yukawa screening is implemented by λ_{eff}, with the corresponding screened potential:

$$\lambda_{\text{eff}} = \frac{\lambda_D}{1+\alpha\Gamma^{3/2}}, \alpha \approx 0.2, \quad V(r) = -\frac{Z}{r} e^{-r/\lambda_{\text{eff}}}.$$

This modification accounts for correlated ion motion and electron polarization effects .

Generalized Screening Approach

For arbitrary base potentials $V_{\text{base}}(r)$, the screening can be incorporated through $V_{\text{screen}}(r)=\text{V}_{\text{base}}(r)e^{-r/\lambda_{\text{eff}}}$, where λ_{eff} may be determined self-consistently.

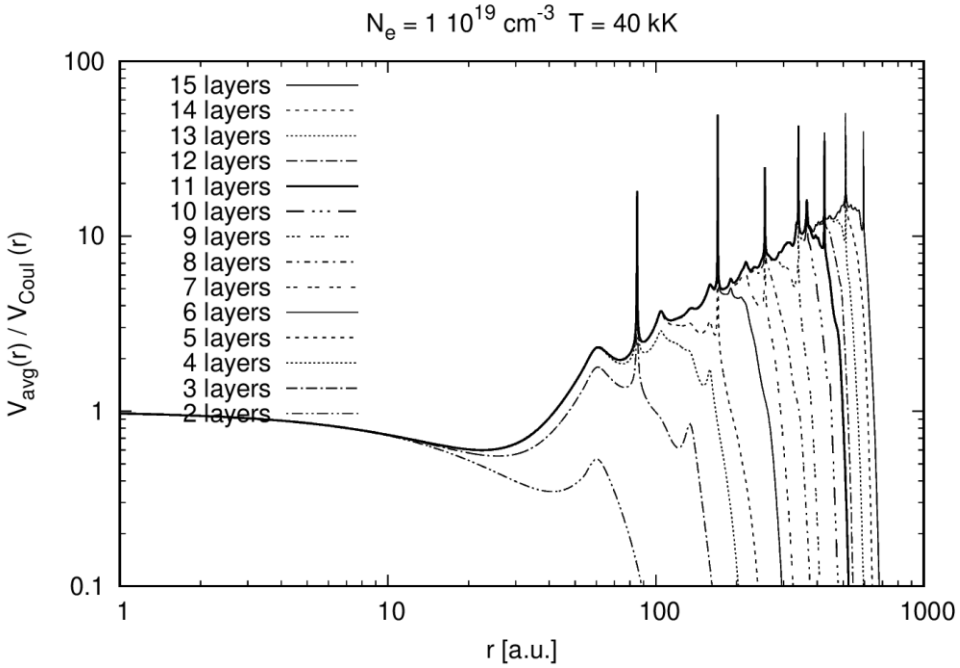

Fig. 1. Effect of number of layers onto the form of potential

Results and Discussion

The screening behaviour in moderately coupled plasmas exhibits characteristic features that depend on both the number of ionic layer shells considered in calculation, the system temperature, as well as the inter-ionic distance related to Wiegner-Seitz radius r_{WS}. For the purpose of the simplified analysis on figure a behaviour of the ratio of the calculated potential over a Coulomb potential, $V_{\text{avg}}(r)/V_{\text{Coul}}(r)$, is considered. The number of shells indicate how many shells with ions on roughly another layer of FCC are taken into account. They roughly assemble a shell like structure, like onion shells around a emitter, central ion, considered into calculation. The Fig. 1 shows the systematic convergence of the potential towards the long range averaged plasma potential as more ion shells are included. With the increasing of layers a ions count in a calculation of a averaged potential arises rapidly, so it was needed to estimate a optimal one. The characteristic slope change at $r \approx 50$ a.u. marks the transition from local ionic

structure to collective plasma screening. It could be seen that no more than couple of layers should not be considered, for hydrogen 8 layers is enough.

Conclusions

Our analysis of screening in moderately coupled plasmas ($0.3 \leq \Gamma \leq 3$) yields three principal findings. As first the modified Yukawa screening represents a improvement over conventional approaches in matching ab initio potentials with pure Debye screening, particularly for $1 \leq \Gamma \leq 2$ where correlation effects are strongest. This method is promising in obtaining a calculation intensity relaxed model that is capable producing a pseudo-potentials for describing a plasma behaviour by the means of optical as well as transport cross sections. The method's accuracy could be further improved by incorporating temperature effect of the ions.

Acknowledgements. This research was supported by the Ministry of Science, Technological Development and Innovation of the Republic of Serbia (MSTDIRS) through 2025. contract with Astronomical Observatory (Belgrade), and with Institute of physics and with the financial support from the Bulgarian Academy of Sciences (Bilateral grant agreement between BAS and Astronomical Observatory, Belgrade), that is gratefully acknowledged.

References

1. **Fortov, V.**, I. Iakubov, and A. Khrapak. 2006. Physics of Strongly Coupled Plasma. International Series of Monographs on Physics. OUP Oxford.
2. **Dimitrijevic, M. S.**, and S. Sahal-Bréchot. 2018. "Stark Broadening Models for Plasma Diagnostics." Astron. Astrophys. 612: A93. https://doi.org/10.1051/0004-6361/201732026.
3. **Ignjatović, L. M.**, A. A. Mihajlov, and N. M. Sakan. 2009. "Cutoff Coulomb Potential and Its Applications to Atomic Processes in Plasmas." Phys. Rev. E 79: 036401. https://doi.org/10.1103/PhysRevE.79.036401.
4. **Mihajlov, A. A.**, N. M. Sakan, and V. A. Srećković. 2015. "Influence of Ion Dynamics on the Width and Shift of Spectral Lines in Dense Plasmas." Phys. Rev. E 91: 033104. https://doi.org/10.1103/PhysRevE.91.033104.

SAGDEEV'S ION-ACOUSTIC SOLITON WITH TRAPPED ELECTRONS

S. Kuznetsov

Joint Institute for High Temperatures of RAS
Izhorskayast. 13 Bd.2, Moscow, Russia 125412
svk-IVTAN@yandex.ru

The nonlinear motion of collisionless nonisothermal ($T_e >> T_i$) plasma in the form of an ion-acoustic soliton is investigated in one-dimensional geometry based on two different approaches to describe the motion of the electron component of the plasma. The results of a more general kinetic method for studying the motion of nonisothermal plasma using the Vlasov equation for electrons are compared with the results of the classical approach /1/, in which the dependence of the electron concentration on the scalar potential of the longitudinal field of the ion-acoustic soliton is determined by the Boltzmann energy distribution for electrons in the potential field of the soliton. The motion of plasma ions in both cases is described by the equations of cold hydrodynamics.

It has been found that in the kinetic description of the motion of the electronic component of a plasma, which takes into account the movement of the soliton, the shape and velocity of the soliton propagation are determined by the following factors related to electrons: the total charge and shape of the velocity distribution function of electrons trapped in the potential well of the soliton, the asymmetry of the distribution function of passing electrons and the gap in its domain of definition caused by the presence of a potential well. It is shown that for low-amplitude solitons, when the electron energy in the potential well of the soliton is much less than the characteristic thermal energy of the electrons, the dependence of the concentration of passing electrons on the scalar potential can be represented as a series expansion containing fractional powers of the scalar potential, multiples of ½. This type of decomposition is a consequence of a gap in the domain of determining the velocity distribution function of passing electrons.

The velocity distribution of electrons trapped in the soliton potential well is a function of the characteristics of the Vlasov equation, and when decomposing the concentration of trapped electrons into a series of degrees of scalar potential, it also leads to fractional powers, multiples of ½, of the scalar potential.

The complex nature of the dependence on the scalar potential of the electron concentration in an ion-acoustic soliton in the kinetic description of the electronic component of a plasma and the permissible arbitrariness /2/ in choosing the shape of the velocity distribution function of trapped electrons

leads to a greater variety of the ion-acoustic soliton family than in the case of using the Boltzmann distribution for electrons /1/. However, if the shape of the velocity distribution function of trapped electrons is such that the terms with fractional powers in the decomposition of the concentration of trapped electrons cancel each other with similar terms in the decomposition of the concentration of passing electrons, then the resulting soliton solution of the Poisson equation, up to small corrections proportional to the square of the ratio of the velocity of the soliton to the velocity of ion sound, coincides with the soliton obtained in the classical approach.

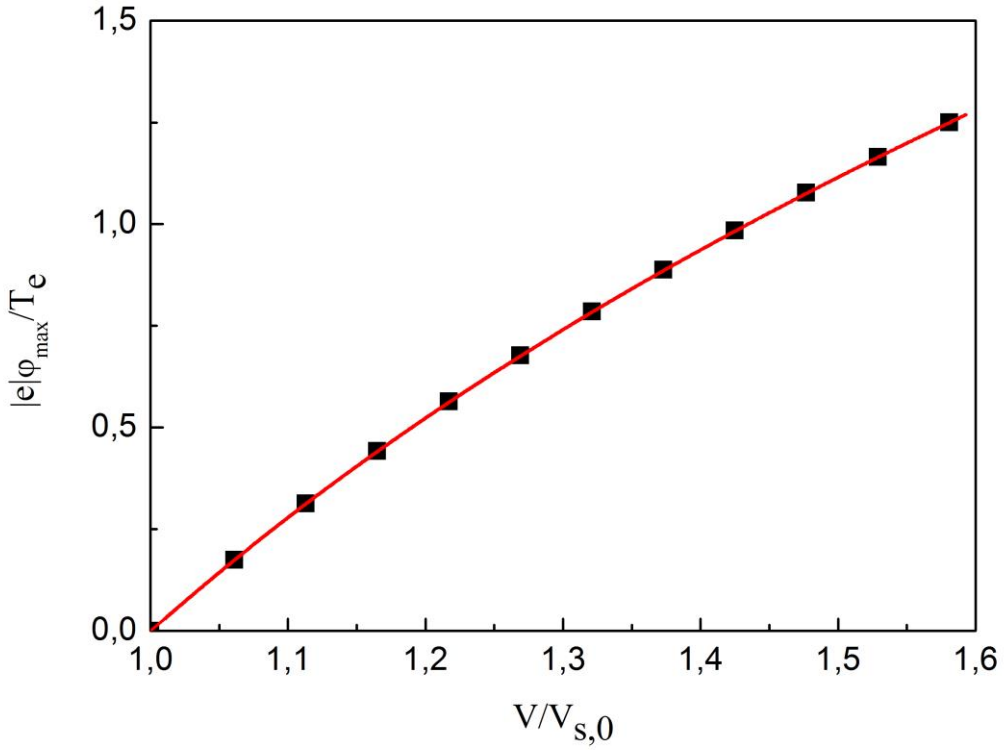

Fig. 1 – Dependence of the maximum potential $\varphi_{\max}$ of a soliton on its velocity $\hat{V} = V / V_{s,0}$, where $V_{s,0}$ is the velocity of ion sound in the Sagdeev model: squares are the soliton in the Sagdeev formulation, the red line is the soliton in the kinetic approach

Calculations show that for solitons with an amplitude of the scalar potential $\hat{\varphi} = |e\varphi|/T_e \approx 1$, it is sufficient to take into account the compensating terms up to $\hat{\varphi}^{7/2}$ for almost exact coincidence of such characteristics of the soliton as the dependence of the soliton amplitude on its velocity V (Fig. 1), the distribution along the length of the soliton of the scalar potential, the concentration of ions and electrons (Fig. 2), as well as the ion current (Fig. 3).

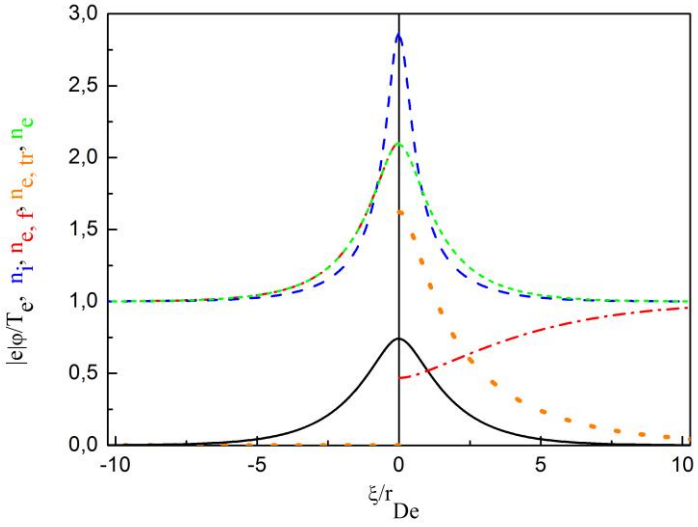

Fig. 2 – The profile of the soliton $|e|\varphi / T_e$ (solid black line) in the wave reference frame, the distribution of ion concentrations n_i in it (long blue dotted line), passing $n_{e,f}$ (red dash dot line), trapped $n_{e,tr}$ (orange dotted line) electrons and the total n_e (short green dotted line) electron concentration, normalized to the electron concentration n_0 of the undisturbed plasma, at the value of the soliton velocity $\hat{V}$ =1.3

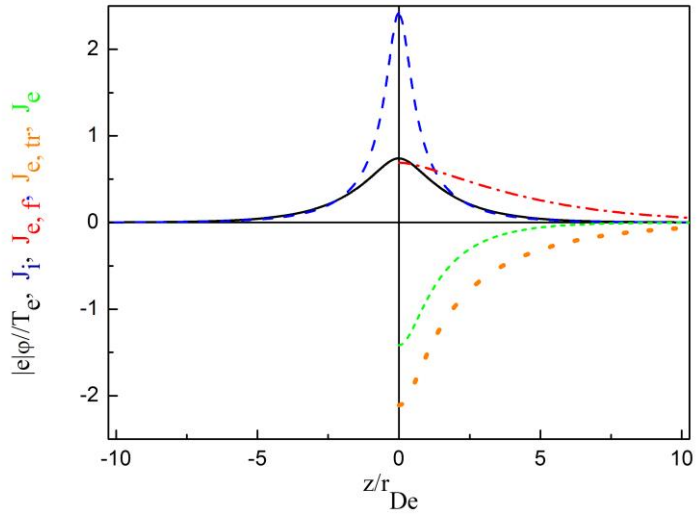

Fig. 3 – The profile of the soliton $|e|\varphi / T_e$ (solid black line), the distribution of ion current in it J_i (long blue dotted line), the currents of passing $J_{e,f}$ (red dash dot line) and trapped $J_{e,tr}$ (orange dotted line) electrons and the total electron current J_e (short green dotted line), normalized to $|e|n_0 V_{s,0}$, in the laboratory coordinate system at the value of the soliton velocity $\hat{V}$ =1.3

Since the ion-acoustic soliton and all its characteristics are symmetrical relative to its center, Figures 2 and 3 show both solitons for clarity: the left half of the figure is the Sagdeev soliton, the right half is its analogue in the kinetic approach. There is practically no visual difference between the right and left halves, except that the right half shows concentrations and currents of passing and trapped electrons, which cannot be determined in Sagdeev's formulation. The current of the passing electrons is comparable in magnitude to the current of trapped electrons, but opposite to it in sign (Fig. 4).

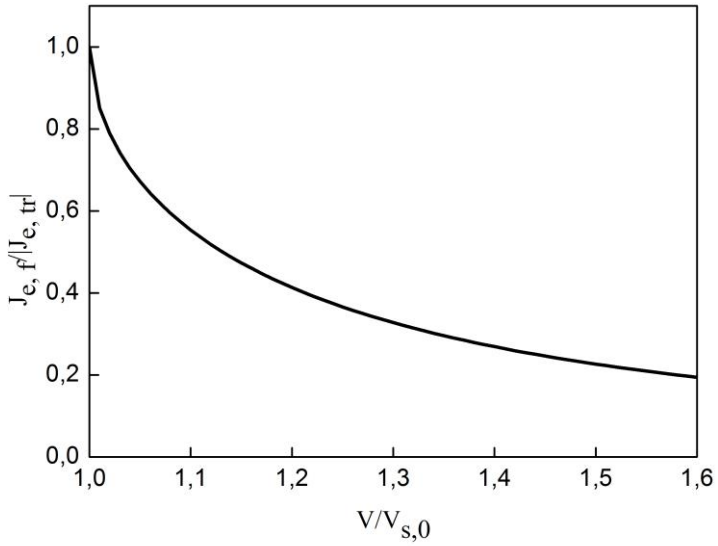

Fig. 4 – The ratio of the current of passing electrons $J_{e,f}$ to the current of trapped electrons $\left|J_{e,tr}\right|$, depending on the velocity of the soliton $\hat{V}$

Thus, the kinetic approach to the study of the Sagdeev ion-acoustic soliton provides a qualitatively different picture of electronic currents in the soliton region. The model using the Boltzmann distribution to describe the electronic component of a plasma is incomplete and limited for studying nonlinear motions of collisionless nonisothermal plasma.

Acknowledgements.The work was carried out at the expense of the federal budget, state assignment No. 075-00269-25-00 dated 12/26/2024.

References

1. **Vedenov A A, Velikhov E. P. Sagdeev R. Z.** Nuclear Fusion 1 (1961) 82–100.
2. **Bernstein I.B., Green J.M., Kruskal M.D.** Phys. Rev. 108 (1957) 546–550.

FEATURES OF ROTATION OF PLASMA-DUST STRUCTURES IN DIFFERENT PHASES OF A STRIATION IN A UNIFORM AND NON-UNIFORM MAGNETIC FIELD

S. Pavlov, E. Dzlieva, M. Morozova, L. Novikov, S. Tarasov, V. Karasev

Saint Petersburg State University, 199034, Universitetskaya emb., 7/9, St. Petersburg, Russia, E-mail: s.i.pavlov@spbu.ru

Abstract. The work is devoted to the study of the behavior of plasma-dust structures, simultaneously levitating in different phases of the glow discharge striation. The dynamics of the structures in the case of superposition of both a uniform and non-uniform magnetic field on the discharge is studied. The dependence of the angular velocity of rotation for each of the structures on the magnetic field induction is obtained. The spatial characteristics of dust structures such as longitudinal and radial interparticle distances, the position of structures in the strata phases are determined.

Introduction. Volumetric plasma-dust structures formed in a standing striation are formed from particles of different fractions levitating in different phases of the striation, i.e. at different vertical coordinates in the discharge tube /1/. The kinetics of electrons in a low-pressure and low-current discharge is non-local /2/. Its features determine the dynamics of dusty plasma /3-4/, which in a glow discharge turns out to be incredibly rich, which manifests itself when a longitudinal magnetic field is applied to the positive column of the discharge /5-8/. When forming dust structures in two or three phases of a striation simultaneously, a distortion of dust traps and an influence of the behavior of one dust structure on another are observed /1/. These changes in the structure, in the distribution of electron parameters and in the geometry of the striation are an addition to the change in the properties of the striation when an uniform longitudinal magnetic field is applied. In this paper, the dynamics (dependence of the angular velocity of rotation in a magnetic field) observed in experiments in a uniform and non-uniform magnetic field are compared. Changes that appear in the presence of weak inhomogeneity for double plasma-dust structures created at different vertical coordinates in the magnetic field range where the dominant rotation mechanism is the ion drag force are recorded.

Experiment. The experiment is described in detail in the work /1/. Fig. 1 shows the experimental setup. The studies were conducted in neon in the pressure range from 0.3 to 0.45 Torr, at a discharge current of 1.5 mA. To create dust structures, particles were used dust particles of melamine formaldehyde (MF) with a diameter of 5.19 μm and silicon dioxide (SiO_2) with a diameter of

1.1 μm. A uniform magnetic field was created by a split system of magnetic coils. To create a non-uniform magnetic field, the upper coil was switched off, and the structure under study was placed near the upper end of the lower magnetic coil. Fig. 2 shows a vertical section of a double dust structure. Figures 3 and 4 demonstrate the obtained dependences of the angular velocities of rotation of dust structures in uniform and non-uniform magnetic fields, respectively.

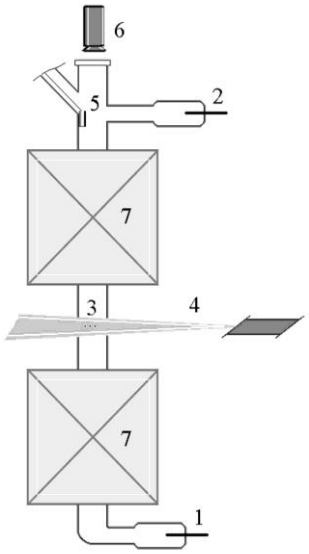

Fig. 1. Layout of the experimental setup: (1) cathode, (2) anode, (3) dusty structure, (4) laser illumination, (5) container with particles, (6) video camera, and (7) magnetic coils

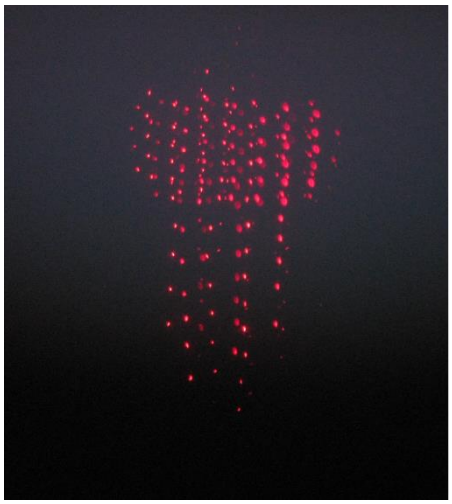

Fig. 2. Image of vertical cross-section of double dust structure without magnetic field. Conditions: Ne, P= 0.4 Torr, I=1.5 mA. Lower dust structure-MF 5.19 μm, upper structure-SiO_2 1.1 μm. Image width is 6 mm

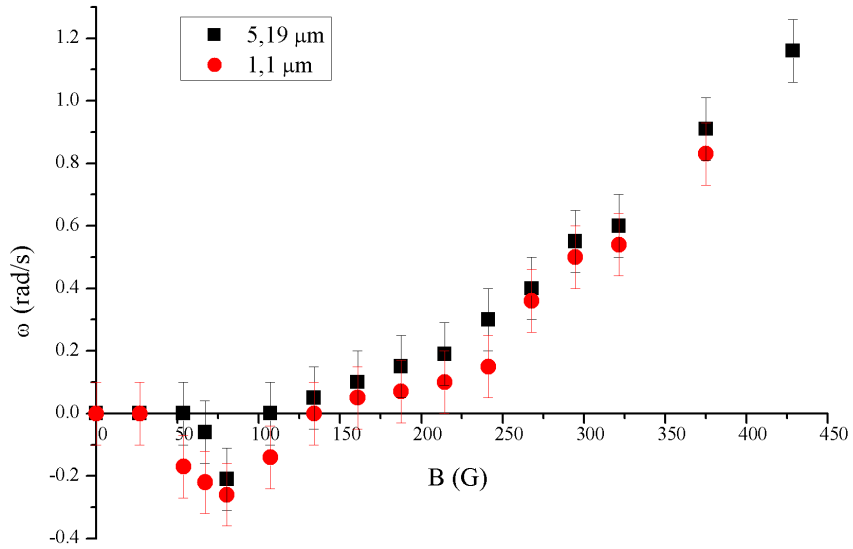

Fig. 3. Dependence of the angular velocity of dust structures on the magnetic induction B in a uniform magnetic field. Conditions: Ne, P= 0.33 Torr, I=1.5 mA. ■-lower dust structure (MF 5.19 μm), ●- upper structure (SiO_2 1.1 μm)

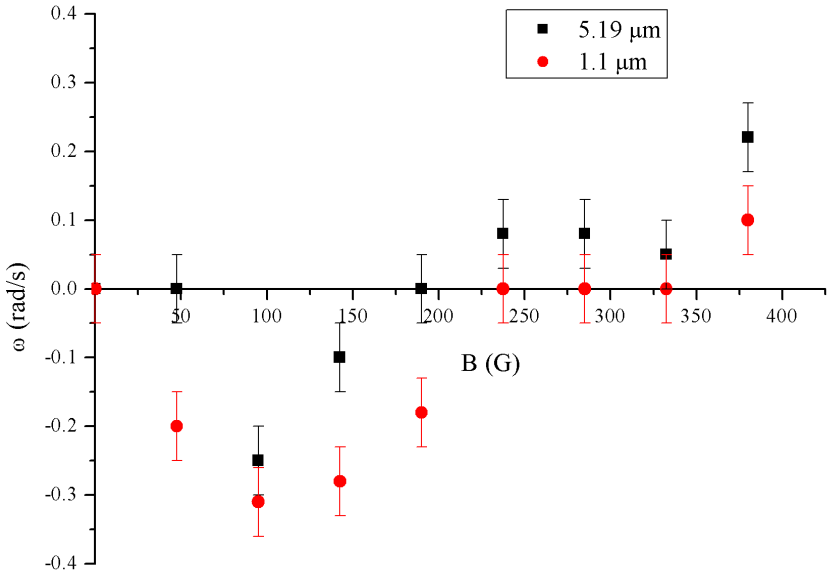

Fig. 4. Dependence of the angular velocity of dust structures on the magnetic induction B in a nonuniform magnetic field. Conditions: Ne, P= 0.4 Torr, I=1.5 mA. ■-lower dust structure (MF 5.19 μm), ●- upper structure (SiO_2 1.1 μm)

Results. From Fig. 4 it is evident that in the dependences obtained in a non-uniform magnetic field, the maxima and zero-crossing points are shifted to the region of large magnetic fields compared to the case of Fig. 3 (uniform field).

This is probably caused by mechanisms associated with the radial component of the magnetic field /9/.

Acknowledgements. This work was supported by the RSF (grant No 22-72-10004 П).

References

1. **Pavlov S.I., Dzlieva E.S., D'yachkov L.G., Novikov L.A., Balabas M.V., Karasev V.Y. P**lasma Phys. Rep., 49 (2023) 1199–1206.
2. **Golubovskii Yu.B., Skoblo A.Yu., Kozakov R.V., Nekuchaev V.O.** J. Phys. D: Appl. Phys., 41 (2008) 105205.
3. **Fortov V.E., and Morfill G.E.** Complex and Dusty Plasmas: From Laboratory to Space. New York: Taylor and Francis (2010).
4. **Bonitz M., Horing N. and Ludwig P.** Introduction to Complex Plasma. Berlin: Springer (2010).
5. **Dzlieva E.S., Dyachkov L.G, Novikov L.A., Pavlov S.I., Karasev V.Y.,** PSST, 29 (2020) 085020,.
6. **Dzlieva E.S., Dyachkov L.G, Novikov L.A., Pavlov S.I., Karasev V.Y.,** Plasma Phys. Rep., 49 (2023) 10-14.
7. **Dzlieva E. S., D'yachkov L. G., Novikov L. A., Pavlov S. I., and Karasev V. Y.** PSST, 28 (2019) 085020.
8. **Dzlieva E.S., Novikov L.A., Pavlov S.I., Karasev V.Y., Dyachkov L.G.** EPL, 123 (2018) 15001.
9. **Dzlieva E.S., Novikov L.A., Pavlov S.I., Karasev V.Y., D'yachkov L.G.,** Molecules, 26.(2021) № 13.

DYNAMICS OF AN ACTIVE BROWNIAN PARTICLE WITH A CENTRE-OF-MASS SHIFT IN A HARMONIC TRAP

E.A. Sametov, E.A. Lisin

Joint Institute for High Temperatures of the Russian Academy of Sciences,
Izhorskaya 13 Bldg 2, Moscow 125412, Russia

The displacement of the centre of mass in active Brownian particles, particularly in the case of Janus particles, is attributable to the presence of a light-absorbing coating. Consequently, this results in inhomogeneous heating of the Janus particle surface, which in turn gives rise to the phenomenon of photophoretic force. This is defined as the force exerted on an inhomogeneous object surrounded by a neutral gas when their temperatures are not equal /1/. It is hypothesised that the surface of the particle that is covered will have a higher temperature than the opposite surface. The photophoretic force exerted on the Janus particle can be estimated using the following formula /2/:

$$F_{\mathrm{ph}} = \pi R^2 nT \left[\alpha_1 \left(\frac{T_1}{T} - 1\right) - \alpha_2 \left(\frac{T_2}{T} - 1\right)\right], \qquad (1)$$

where R is the radius of the particle, n and T are the concentration and temperature of the neutral gas, and α_i and T_i are the thermal accommodation coefficients and temperatures of two different halves of the particle. Using expression (1), we can obtain the dependence of the ratio of the eigenvelocity of the active particle V_0 and its thermal velocity V_T on the ratio T_1/T_2 of the particle surface temperatures. The value of the velocity V_0 determines the effective driving force $F_{\mathrm{act}} = \nu_{\mathrm{fr}} m V_0$ and is an important characteristic of the motion of an active Brownian particle. For example, it is sufficient to warm up the light-absorbing coating by 5% relative to the uncovered part for the ratio V_0/V_T to exceed 1000. This shows how sensitive the Janus particles are to a very small temperature difference on their surface.

Let us consider the motion of a discoid particle of mass m consisting of two halves with masses m_1 and m_2 ($m_1 > m_2$) in the presence of a confinement force field of a trap in the framework of the ALP model /3/ (ALP – Active Langevin particle). The difference in the masses of the halves is related to the light-absorbing coating of one of the halves, the heavier one corresponds to the Janus half of the particle with a higher surface temperature. The active force is directed from the heavier half to the less heavy half. The inhomogeneous mass distribution leads to the displacement of the centre of mass by the distance $a_g = 2a(m_1 - m_2)/3\pi m$ from the geometrical centre along the direction of the active force, where $a = 2R$ is the particle size. The motion of such a particle is described by the following system of equations:

$$\ddot{x}(t) = -\nu_{\mathrm{fr}}\dot{x}(t) - \omega_{\mathrm{t}}^2 x(t) + \nu_{\mathrm{fr}} V_0 \cos\varphi(t) + \nu_{\mathrm{fr}}\sqrt{2D_{\mathrm{T}}}\,\xi^{(X)}(t), \qquad (2)$$

$$\ddot{y}(t) = -\nu_{\mathrm{fr}}\dot{y}(t) - \omega_{\mathrm{t}}^2 y(t) + \nu_{\mathrm{fr}} V_0 \sin\varphi(t) + \nu_{\mathrm{fr}}\sqrt{2D_{\mathrm{T}}}\,\xi^{(Y)}(t), \qquad (3)$$

$$\ddot{\varphi}(t) = -\nu_{\mathrm{rot}}\dot{\varphi}(t) + \frac{ma_g}{J}(\cos\varphi(t), \sin\varphi(t)) \times \left(\ddot{x}(t), \ddot{y}(t)\right) + \nu_{\mathrm{rot}}\sqrt{2D_{\mathrm{R}}}\xi^{(\Phi)}(t), \qquad (4)$$

where $\omega_t = \sqrt{(\beta q/m)}$ is the trap frequency, q is the particle charge, β is the gradient of the trap field, $\nu_{fr} = T/(mD_T)$ and $\nu_{rot} = T_R/(JD_R)$ are the coefficients of translational and rotational friction, D_T and D_R are the coefficients of translational and rotational diffusion, $J = \alpha mR^2$ is the moment of inertia of the particle, and $T_R = T$ if the source of rotational noise is thermal fluctuations, $\xi^{(X)}$, $\xi^{(Y)}$, $\xi^{(\Phi)}$ are random variables with standard normal distribution.

The proposed model of a composite particle was employed for numerical simulations across a broad spectrum of parameters. The numerical modelling of stochastic processes was performed by means of the molecular dynamics method. The particle parameters employed in the simulation are as follows: a = 1 μm, $m = 7.9 \cdot 10^{-13}$ g. It should be noted that the calculations were performed both for a particle without centre-of-mass displacement ($a_g = 0$, $m_1/m_2 = 1$, α = 0.5) and at $a_g = 0.25R$ ($m_1/m_2 = 3.87$, $\alpha = 7/16$). The simulations were performed for T = 0.0247 eV (≈ 286 K), V_0/V_T ratio from 0 to 1000, which is consistent with the observed values in experiments /4/, trap parameters $k_{trap} = \omega_t/\sqrt{(\nu_{fr}D_R)}$ = 0.1, 1, and 10 and three ratios of characteristic frequencies ν_{fr}/D_R = 0.01, 1, and 100 corresponding to underdamped, transient, and overdamped modes.

As demonstrated in Figure 1, which presents examples of particle trajectories at varying V_0/V_T in the case of $\nu_{fr}/D_R = 100$ and $k_{trap} = 10$, the nature of particle motion without displacement of the centre of mass remains constant, with particles rotating chaotically around the trap centre (see Fig. 1(a)). In the case of particles with displacement, different modes of motion are observed. Chaotic rotation around the trap centre is evident (see Figs. 1(b) and 1(c) in the case of $V_0/V_T = 10$), directed rotation around the trap centre is also apparent (see Figs. 1(b) and 1(c) in the case of $V_0/V_T = 100$), and complex motion resembling a hypocycloid is observed (see Fig. 1(b) in the case of V_0/V_T = 300). Furthermore, different modes of motion are evident at other values of k_{trap} and are reflected in motion characteristics, such as kinetic energy and mean squared displacement (MSD), as illustrated in Figure 2, where jump-like changes corresponding to transitions between modes are observed.

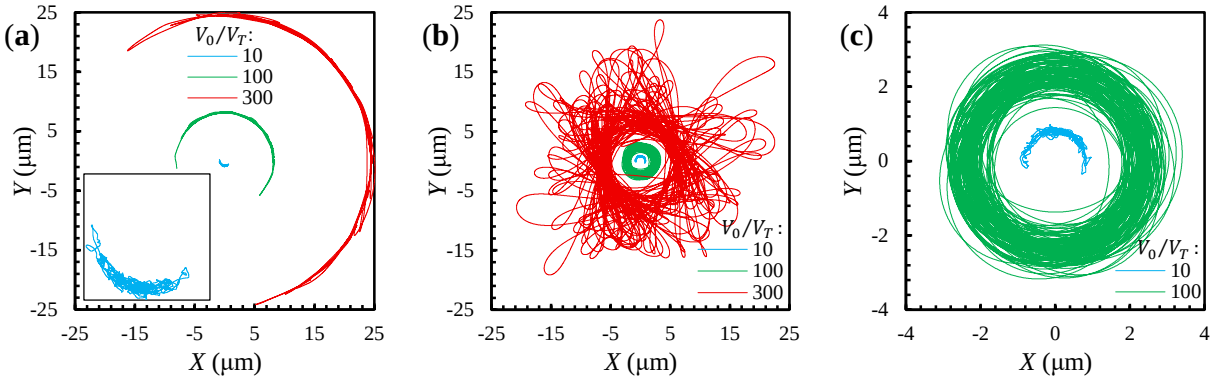

Figure 1. Particle trajectories in time 0.01 s for the case $\nu_{fr}/D_R = 100$ and $k_{trap} = 10$ with $V_0/V_T = 10$, 100 and 300 for particles (**a**) without centre-of-mass displacement and ((**b**) and (**c**)) for 0.25R displacement

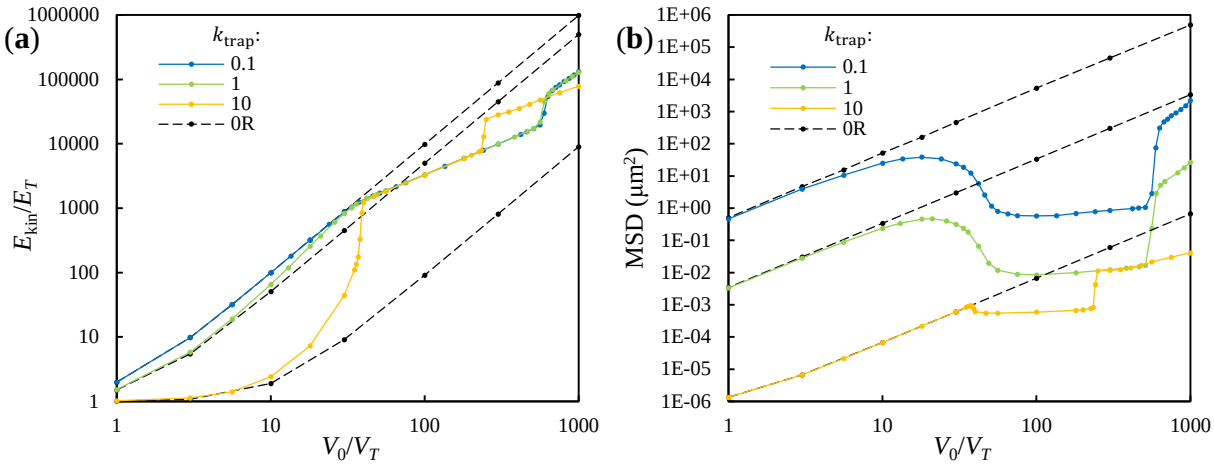

Figure 2. (**a**) Ratio of particle kinetic energy to thermal energy E_{kin}/E_T and (**b**) mean square displacement (MSD) for particles with no centre-of-mass displacement (0R – black dashed lines) and with displacement (coloured lines) for the case $\nu_{fr}/D_R = 100$ and $k_{trap} = 0.1$, 1 and 10 as a function of V_0/V_T. Dots indicate the results of numerical simulations

Thus, a mathematical model has been developed to describe the dynamics of active Brownian particles in rarefied gases and complex plasmas. The model incorporates the primary features, namely the existence of an active force associated with non-uniform heating of the particle surface, translational and rotational inertia, and the non-uniform distribution of the particle mass due to the presence of a light-absorbing coating on one of the particle's Janus halves. The dynamics of an active Brownian particle with a displacement of the centre of mass in the confinement force field of the trap are simulated numerically. It is evident that inhomogeneous heating of the surface exerts a substantial influence on the motion of an active Brownian particle in the free-molecular regime.

Acknowledgements. This work was supported by the Russian Science Foundation under grant № 24-12-00345.

References

1. **Du C.-R., Nosenko V., Thomas H.M., Müller A., Lipaev A.M., Molotkov V.I., Fortov V.E., Ivlev A.V.** New J. Phys. 19, 073015 (2017).
2. **Nosenko V., Luoni F., Kaouk A., Rubin-Zuzic M., and Thomas H.** Phys. Rev. Research 2, 033226 (2020).
3. **Lisin E.A., Vaulina O.S., Lisina I.I., and Petrov O.F.** Phys. Chem. Chem. Phys. 24, 14150 (2022).
4. **Koss K.G., Lisina I.I., Vasiliev M.M., Alekseevskaya A.A., Kononov E.A., and Petrov O.F.** Plasma Phys. Rep. 49, 57 (2023).

ELECTRIC CURRENTS IN VYSIKAYLO'S CUMULATIVE-DISSIPATIVE STRUCTURES OF THE UNIVERSE

P.I.Vysikaylo

Moscow Institute of Physics and Technology, Russia, E-mail filvys@yandex.ru

Actually, life is simple,
but we persistently complicate it.

Historians believe that China was the first civilization to create a magnetic compass that could be used for navigation. They knew 2,000 years ago that rubbing an iron needle against a natural magnet would temporarily magnetize the needle and it would point north and south. The Europeans adopted the invention of the compass from the Chinese in the late 12th century. This is reported in the 8th grade physics textbook in the Russian Federation, A. V. Peryshkin, § 61/https://gdz.tutoronline.ru/fizika/8-klass/fizika-8-klass-a-vperysh kin/61-magnitnoe-pole-zemli/. The compass is a very important practical application of the Earth's magnetic field for navigation. Based on this paradigm, scientists have not yet been able to determine the cause of the generation of solar and cosmic winds and the energies of positive ions in these rays. It is believed that magnetic storms come from the Sun, affecting the well-being of weather-sensitive people, and technologies for «treating» magnetic fields have appeared. At the same time, the influence of the arrival of a huge number of protons (during magnetic storms) on negatively charged leukocytes is ignored by representatives of this paradigm.

The author shares and explores the second paradigm in his works. It consists in the special importance of electrical forces compared to magnetic forces. In this paradigm, electric fields acting on charged particles cause their flows, and the currents, according to Maxwell's equations, form magnetic fields. (The smallness of magnetic forces compared to electrical forces is determined by the parameter v/c /1/). In this paradigm, it is believed that Coulomb's law is true for any objects with an electric charge, from electrons to galaxies (at characteristic sizes of their interactions from 10^{-15} to 10^{26} m) /1/. This paradigm is not properly accepted in astrophysics. We have applied this second paradigm to describe phenomena in the heliosphere /1/. Before we list our achievements, we will dwell on the history of the development of this paradigm in physics.

The study of the interference of gravitational and electric potentials on the Earth's surface began with the work of William Gilbert in 1600 (long before the discovery of Coulomb forces in 1785). He found that the petals of his electroscope levitated near a candle flame. We now know that free electrons are

born in the candle plasma. They have a small mass and are therefore very mobile. They penetrate into the petals of the electroscope and charge them with a negative charge. The petals, charged with like charges, repel each other and they levitate in the Earth's gravitational field. Perhaps viruses have learned to levitate in negatively charged water droplets above the surface of the negatively charged Earth. Based on the first paradigm about the importance of only magnetic fields, all these phenomena cannot be explained! Polarization effects (interference of Coulomb and gravitational forces) have not been studied well enough even in the heliosphere. Many works have been devoted to this problem.

If the negative charge of the Earth was known to Lomonosov, then Pannekoek, Rosseland and Eddington guessed about the positive charge of the Sun due to the difference in the masses of free electrons and positive ions (protons, etc.). The electric field that arises due to this charge of the Sun (or stars) is called the Pannekoek-Rosseland's field. It was already clear to them that the ***Sun is positively charged***. Eddington estimated the charge of the Sun at +300 C. Eddington considered these fields to be insignificant, see /1/. This charge is sufficient to form a solar wind of protons and alpha particles. This was noted only in see /1/. Astrophysicists still do not accept this model of the solar wind due to the volume charge of the Sun and the heliosphere. They are trying to switch to the magnetic field as the main mechanism of phenomena in the heliosphere. The Pannekoek-Rosseland-Eddington's model took into account the difference in the masses of electrons and positive ions (protons), but did not take into account the important role of high-energy electrons running away (from the Sun) and, accordingly, the duality of electron flows in the heliosphere (from the Sun and to the Sun due to its positive charge).

The Pannekoek-Rosseland-Eddington's model took into account the difference in the masses of electrons and positive ions (protons), but did not take into account the important role of high-energy runaway (from the Sun) electrons and, accordingly, the duality of electron flows in the heliosphere (from the Sun and to the Sun due to its positive charge). According to the alternative model we have formulated, high-energy electrons (emitted from the positively charged Sun with energy greater than 18 keV) leave the Sun and the heliosphere, while low-energy electrons, unable to leave the Coulomb potential hole – the positively charged Sun and the heliosphere, return to the positively charged Sun. The small difference between the opposite currents of high-energy electrons (emitted from the Sun) and low-energy electrons (returned to the Sun) is compensated by the current of positive ions and protons from the Sun. This is how the solar wind (SW) is formed (**Figure 1**) /1/. All positively charged Vysikaylo's cumulative-dissipative structures /1/ with sizes from 10^{-15} to 10^{26} m are formed in a similar manner. In the presence of an uncompensated effective charge of the Sun, according to this model, positively charged ions are selected by the magnitude

of their charge. As our analysis of experimental observations of positively charged iron ions showed, ions with a charge of Fe5+ are not recorded, while ions with a charge of Fe6+ and more are observed in the SW. In this case, lighter positive ions with a charge of C4+, O5+ are recorded. This phenomenon of selection of positive ions allows us to estimate the dynamic charge of the Sun at a level of 1400 C (all the way to the Earth's orbit and possibly further). At the same time, the quasi-neutrality of the Sun and the heliosphere is well maintained up to $\alpha \sim 7.2 \cdot 10^{-36}$ ($\alpha = (n_i - n_e)/N \ll 1$, N is the density of the number of nucleons) /1/. In this case, the ratio of the charge number Z to the mass number of nucleons M in positive ions flying in the SW $Z/M > 0.107$. Stellar winds of protons are observed even for black holes at $\alpha_0 \sim 0.8 \cdot 10^{-36}$. Apparently, intergalactic lightning, like the jet from the galaxy M 87 (1781), is formed at $\alpha > \alpha_0$ (for the black hole at its center).

Within the framework of the second paradigm, we have explained all the parameters of the weak (constant) solar wind (proton velocities, electron temperature profiles throughout the heliosphere, components of positive ions with $Z/M > 0.107$ flying in the SW). Originating on the Sun, the SW (protons and positive ions with $Z/M > 0.107$) rushes past the Earth at a speed of 400 km/sec (about 1 400,000 km/hour), reaches distant planets and goes into interstellar space due to the positive charge of the Sun /1/.

The presence of a negative charge of 500,000 C on the Earth and a charge of 1,400 C on the Sun allows us to substantiate the hypothesis about the possibility of a global non-uniform nonequilibrium discharge between the Sun and the Earth /1/. The positively charged Sun acts as an anode, and the negatively charged Earth acts as a cathode. This hypothesis was put forward in 1896 by the Norwegian physicist Olaf K. Birkeland. He suggested that the aurora borealis could be created by electrically charged "corpuscular rays" ejected from the Sun and "drawn" by the Earth's magnetic field near the poles. He came to this conclusion based on the fact that the aurora borealis are very similar to an electrical discharge in the then recently invented tubes generating streams of charged particles ("cathode rays").

Within the framework of a detailed development of this second paradigm, the following becomes clear /1/: 1) the parameters of SW; 2) discharges in the upper layers of the Earth's atmosphere (at altitudes above 30 km); 3) charge characteristics on the day and night sides of the Moon (during the day, protons flow to the Moon, and at night, only electrons return to the Sun), which causes longer levitation of dust on the dark side of the Moon.

The presence of intergalactic lightning, for example, in the region of the galaxy M 87 and the above considerations about electric currents in the heliosphere, allow us to assert the presence of global currents in the Universe at all sizes (from 10^{-15} to 10^{26} m) of Vysikaylo's cumulative-dissipative structures

/1/, and not only in the Earth's atmosphere.

We have proposed an original method for determining the effective charge of the Sun and the inner heliosphere by the types of positive ions in the SW /1/. This method must be used in all solar, planetary and satellite probes such as the Parker probe.

To this day, the Physics of Plasmas writes that the Sun may be charged with a huge negative charge.

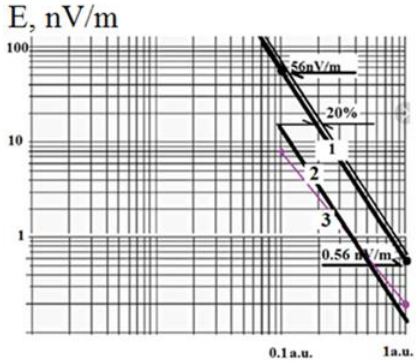

Figure 1. Calculations of electric fields E_r in the heliosphere: 1- according to the spectrum of positive ions in the SW /1/. (Q_S = 1,420 C; error less than 20%); 2 - according to the Eddington's calculations; 3 - according to the calculations of the electric field based on experimental observations of the electron distribution function using the Parker solar probe (Q_S = 200 ÷ 500 C, the 3 is built by J.S. Halekas).

The description of transport processes in collisional plasma with current in the heliosphere can be carried out according to Vysikaylo's perturbation theory. In ***zero*** approximation, the drift velocity of electrons and ions is described by the relations: $\boldsymbol{V}_{e0} = \mu_{e0}\boldsymbol{E}_0$, $\boldsymbol{V}_{i0} = \mu_{i0}\boldsymbol{E}_0 + \boldsymbol{U}$. Here the mobilities of electrons– μ_{e0} и ионов – μ_{i0} are presented respectively. In zero approximation ($\mu_{j0}n_e\nabla\boldsymbol{E}_0 = -\boldsymbol{E}_0\nabla(\mu_{J0}n_e)$) we obtain a non-stationary 3D equation for simple plasma /1/:

$$\partial n_e/\partial t - \partial[(\boldsymbol{l}_{E0}/\mu_{e0})\nabla](\mu_{e0}n_e)/\partial t + (\boldsymbol{j}/e)\nabla(\mu_{i0}/\mu_{e0}) + \boldsymbol{U}\nabla n_e - \nabla(\boldsymbol{U}(\boldsymbol{l}_{E0}/\mu_{e0})\nabla(\mu_{e0}n_e)) - \nabla\{\boldsymbol{l}_{E0}(\mu_{i0}\boldsymbol{E}_0/\mu_{e0}\nabla)(\mu_{e0}n_e)\} - \beta n_e(\boldsymbol{l}_{E0}/\mu_{e0})\nabla(\mu_{e0}n_e) + \mu_i m_i(\boldsymbol{g}/z_i e)\nabla n_i - (\mu_i\mu_e[\boldsymbol{E}\mathrm{x}\boldsymbol{H}]/c)\nabla n = I_{i0} - R_{i0}; \quad \boldsymbol{l}_{E0} = \boldsymbol{E}_0/(4\pi e n_e). \qquad (1)$$

The four-dimensional Vysikaylo's equation (1) is derived by modifying the ion concentration n_i by n_e-$(\boldsymbol{l}_{E0}\nabla)(n_e\mu_{e0})/\mu_{e0}$. ***Equation (1) is the Navier-Stokes equation modified by Vysikaylo to account for the violation of plasma electroneutrality***. The terms with the vector $\boldsymbol{l}_{e0}$ in (1) arise due to the violation of electroneutrality.

References

1. **Vysikaylo P.I.**: (2022) Quantitative Investigation Nonequilibrium Inhomogeneous Plasma of the Heliosphere With Runaway Electrons // IEEE Transactions on Plasma Science (V 50, № 4) P. 810 - 816 DOI: 10.1109/TPS.2022.3160189 https://ieeexplore.ieee.org/document/9745462

FEATURES OF PLASMA FORMATION DURING THE EXPLOSION OF FLAT CONDUCTORS IN MEGAGAUSS MAGNETIC FIELDS

I. Datsko[1], S. Chaikovsky[2], V. Van'kevich[1], N. Labetskaya[1], V. Oreshkin[1], N. Ratakhin[1]

[1]Institute of High Current Electronics of the Siberian Branch of the Russian Academy of Sciences, Akademichesky Avenue 2/3, Tomsk 634055, Russia, datsko@ovpe.hcei.tsc.ru
[2]Institute of Electrophysics of the Ural Branch of the Russian Academy of Sciences, Amundsen 106, Yekaterinburg 620016, Russia, stas-chaikovsky@yandex.ru

Interest in the physical processes during electrical explosion of flat conductors or foils in vacuum arose in connection with the advent of the MagLIF (Magnetized Liner Inertial Fusion) project /1/, aimed at obtaining high-density high-temperature plasma by compressing a magnetic field with a liner made of light metal. Although a cylindrical shell is used in the MagLIF scheme, the ratio of its thickness to the radius is so small that a segment of this shell can be considered as a current-carrying plane. However, the number of publications devoted to the explosion of foils in vacuum is relatively small /2-8/. They present the results of the explosion of foils up to 10 μm thick /2-5/, or discuss issues related to the development of thermal instabilities during their explosion /6-8/. The process of skin explosion of flat conductors and cylindrical foils, the thickness of which is close to the thickness of the loads in the MagLIF experiments, has not been systematically studied. The experiments were carried out on a high-current MIG generator /9-10/ at a current level of up to 2.5 MA with a rise time of 100 ns. Rogowski coils, magnetic probes, voltage dividers, a four-frame optical camera HSFC Pro, and vacuum X-ray diodes (XRD) were used for diagnostics. Time-resolved spectral measurements were performed using a Hamamatsu Photonics Universal streak camera C10910-05. Plasma on the surface of the conductor under study was recorded by its glow in the visible range using a four-frame optical camera with an exposure time of 3 ns for each frame. The camera allowed setting any required time interval between frames. The load was flat conductors (plates) with a length in the direction of current flow of about 1.5 cm (z axis) with different widths (x axis) and thicknesses (y axis).

A characteristic feature of a flat conductor with a current pulse flowing along its surface is a multiple amplification of the magnetic field at the plate edges compared to the magnetic field in its center. For the loads used in our experiments, the magnetic field amplification factor at the edges is $\beta \sim 1.8$. This means that the magnetic field pressure at the conductor edge is approximately 3.2 times greater than on the surface in the conductor center. Such pressure distribution causes the suppression of plasma expansion along the x-axis in

width and the conductor expands along the *y*-axis in thickness. And the field amplification at the edges leads to an earlier explosion of the end faces of the flat conductor (faces in the YZ plane) with the formation of plasma glowing in the optical range. The glow of this plasma is recorded significantly earlier than the glow of the wide surface of the conductor (its core) - at 20-30 nanoseconds from the beginning of the current in experiments conducted on the MIG generator, while the glow of the wide face (in the XZ plane) is observed after 70 ns. This is demonstrated by the images shown in Fig. 1.

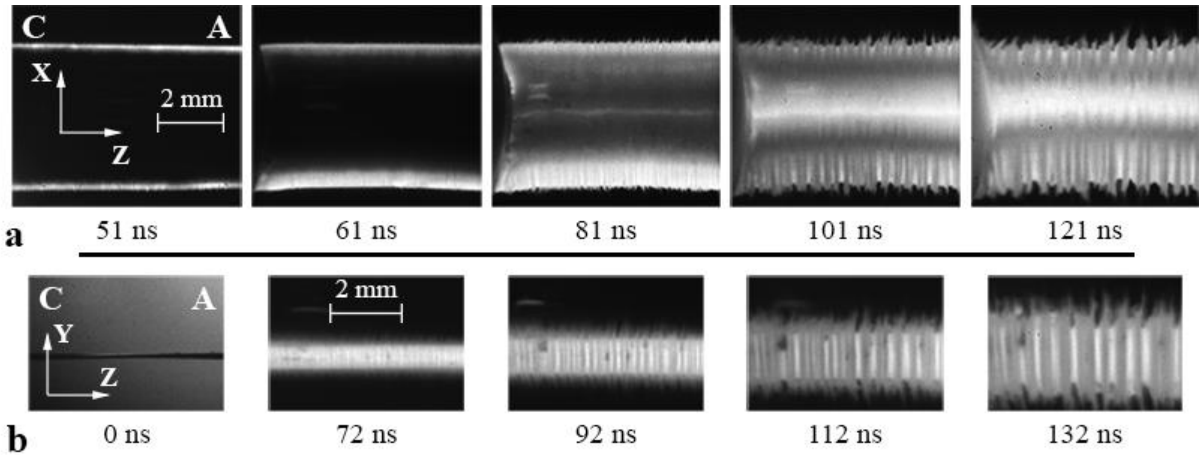

Fig. 1. Images in the optical range of the wide face (a) and from the end face (b) of a flat copper conductor 90 μm thick, 4.4 mm wide in its own glow at different moments in time from the start of the flow of the MIG generator current

Based on such images of flat conductor explosions in the optical range of the spectrum obtained from different directions, it can be stated that the plasma from the exploded end faces flies apart not in the direction of conductor expansion in the XZ plane, as in the case of cylindrical load geometry. The plasma from the end faces moves along the magnetic field lines above the surfaces of the wide faces on both sides of the conductor toward the center of symmetry of these wide faces. When these plasma flows, formed on the end faces of the exploded conductor, collide, a plasma channel with a sufficiently high (several electron volts) temperature is formed in the region of the conductor's symmetry axis. The density of the substance in this channel is low, it is determined by the density of the incident plasma flows. Therefore, the conductivity of this low-density plasma is small compared to the conductivity of the core of the main conductor /11/. Apparently, the presence of this plasma channel has little effect on the redistribution of the current flowing through the core of the main conductor. Note that at the initial stage, plasma from light substances from the surface, such as carbon and hydrogen, can accumulate on the symmetry axis of the wide XZ face. This was shown by spectral

measurements with time resolution of the glow of the axial region of the wide face of the conductor. The obtained spectra contained hydrogen and carbon lines. Moreover, in work /3/, during the explosion of flat conductors by a current with a front of more than 500 ns, the carbon lines began to be recorded 50-100 ns earlier than the lines of the conductor material. This mechanism determines the characteristic feature of the explosion of flat conductors, i.e. the presence of a pronounced glow in the central part of the plate along its longitudinal *z* axis on the XZ plane, as shown in Fig. 1. This glow always began around the seventieth nanosecond in the cathode region and developed toward the anode. In this case, a clear dependence of the onset time of glow in the axis region on the width *x* (the distance from the axis to the edges) of the conductor and its thickness *y* was observed. It should be noted that the glow in the axis region in experiments with flat conductors was also observed by other researchers and even in the ultraviolet region of the spectrum /2-4/. We also note the possibility of another mechanism for the formation of a plasma channel on the axis of the exploded conductor. This mechanism was considered in the work /12/, it is connected with the dynamics of propagation of the nonlinear diffusion wave of the magnetic field and the accompanying pressure wave. For a more detailed study of the nanosecond explosion of flat conductors and clarification of the mechanism of formation of the plasma channel on the axis of the exploded conductor, studies of the explosion of aluminum plates with perforation in the form of round holes were conducted (see Fig. 2b). In these experiments, a luminous halo was registered around the hole from the side faces. Moreover, the halo begins to form approximately in the middle of the distance from the boundary of the hole to the end (side) face, taking into account the speed of movement of plasma flows and the earlier in time, the closer the hole is to this face. This is demonstrated by the images presented in Fig. 2. Optical images of an exploded perforated conductor show that, apparently, the main mechanism for the formation of a plasma channel on the axis of the exploded conductor is the collision of plasma flows formed on the end faces of the exploded conductor.

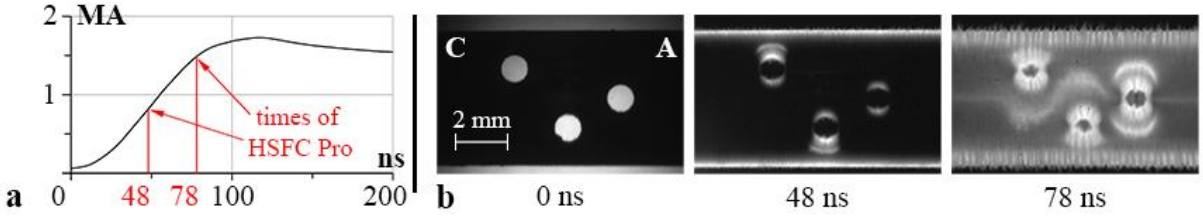

Fig.2. a – Oscillogram of the current through the load with the times of the obtained images; b – optical images of the explosion of a flat Al conductor 100 μm thick, 5 mm wide with three holes Ø1 mm at different times from the beginning of current flowing through it. The holes are distributed across the width of the plate at different distances from the axis

Acknowledgements. This work was supported by the Russian Scientific Foundation (Grant No. 25-19-00352).

References

1. **Gomez M.R., Slutz S.A., Sefkow A.B., Hahn K.D., Hansen S.B., Knapp P.F., Schmit P.F., Ruiz C.L., Sinars D.B., Harding E.C., Jennings C.A., Awe T.J., Geissel M., Rovang D.C., Smith I.C., Chandler G.A., Cooper G.W., Cuneo M.E., Harvey-Thompson A.J., Herrmann M.C., Martin M.R., Peterson K.J., Schroen D.G., Stygar W.A., and Vesey R.A.** Physics of Plasmas. 2015. V. 22. P. 056306.
2. **Shelkovenko T.A., Tilikin I.N., Pikuz S.A., Mingaleev A.R., Romanova V.M., Hammer D.A.** Journal of Applied Physics. 2020. V. 128. P. 205902
3. **Baksht R.B., Zhigalin A.S., Rousskikh A.G., Oreshkin V.I.** Physics of Plasmas. 2020. V. 27. P. 043510.
4. **Shelkovenko T.A., Tilikin I.N., Pikuz S.A., Mingaleev A.R., Romanova V.M., Atoyan L., Hammer D.A.** Matter and Radiation at Extremes. 2022. V. 7. P. 055901.
5. **Tilikin I.N., Shelkovenko T.A., Pikuz S.A., Oginov A.V., Mingaleev A.R., Romanova V.M., Ter-Oganesyan A.E.** Journal of Applied Physics. 2023. V. 134. P. 033302
6. **Awe T. J., Peterson K. J., Yu E. P., McBride R. D., Sinars D. B., Gomez M. R., Jennings C. A., Martin M. R., Rosenthal S. E., Schroen D. G., Sefkow A. B., Slutz S. A., Tomlinson K., and Vesey R. A.** Physical Review Letters. 2016. V. 116. P. 065001.
7. **Baksht R.B., Rousskikh A.G., Zhigalin A.S., Oreshkin V.I., and Artyomov A.P.** Physics of Plasmas. 2015. V. 22. P. 103521.
8. **Steiner A.M., Campbell P.C., Yager-Elorriaga D.A., Cochrane K.R., Mattsson T.R., Jordan N.M., McBride R.D., Lau Y.Y., and Gilgenbach R.M.** Physics of Plasmas. 2018. V. 25. P. 032701.
9. **Luchinsky A.V., Ratakhin N.A., Feduschak V.F. and Shepelev A.N.** Izv. Vyssh. Uchebn. Zaved. Fiz. 1997. V. 40. P. 67.
10. **Petin V.K., Shljakhtun S.V., Oreshkin V.I., and Ratakhin N.A.** Technical Physics. 2008. V. 53 (6). P.776.
11. **Chaikovsky S.A., Datsko I.M., Labetskaya N.A., Oreshkin E.V., Oreshkin V.I., Ratakhin N.A., Rousskikh A.G., Vankevich V.A., Zhigalin A.S., Baksht R.B.** Physics of Plasmas. 2022. V.29. P.103501.
12. **Chaikovsky S.A., Oreshkin V.I., Labetskaya N.A., Datsko I.M., Rybka D.V., Vankevich V.A., Ratakhin N.A.** Russian Physics Journal (Izv. Vyssh. Uchebn. Zaved. Fizika). 2019. V.62. P. 1235.

DUSTY PLASMA IN A GLOW DISCHARGE IN HELIUM IN A STRONG MAGNETIC FIELD

L. Dyachkov[1], E. Dzlieva[2], L. Novikov[2], S. Pavlov[2], V. Karasev[2]

[1]Joint Institute for High Temperatures of RAS, Izhorskaya st. 13, bld. 2, 125412, Moscow, Russia, dyachk@mail.ru
[2]Saint-Petersburg State University, Universitetskaya nab. 7/9, 199034, Saint-Petersburg, Russia, plasmadust@yandex.ru

Research into dusty plasma has been conducted for about 30 years. Particular attention is paid to various methods of influencing it, for example, with a magnetic field, as this can be important in various technological processes. Research is conducted both in high-frequency discharges /1, 2/ and in stratified direct current discharges /3, 4/. Dust particles can be retained in a non-uniform electric field, such as a striation. The rotation of the dust structure in the striation under the application of a magnetic field B was considered in our works /5, 6/. In fields $B \sim 0.01$ T, as a result of ion drag, the rotation of dust particles in the striation occurs counterclockwise when viewed in the direction of **B**. But as the field increases, the direction of rotation changes, since the main rotation mechanism changes, and neutral gas drag begins to predominate.

In /7, 8/ we have shown that the hanging of dust particles and the formation of a dust structure can occur not only in the striation, but also in the region of narrowing of the current channel inside the insert, which serves to stabilize the striation. The position of the insert is shown in Fig. 1. Here the possibility of the existence of a trap for dust particles is apparently connected with the double electric layer in the region of the change in the cross-section of the current channel.

Inside the insert, the dust structure can exist in magnetic fields significantly greater than in the striation. We observed the emergence of a dust structure in helium inside the insert in fields up to 1.5 T, while in the striation it is possible to create a dust structure only in fields several times smaller. The magnetic field, as in other gases, causes the dust structure to rotate. But inside the insert, unlike the rotation in the striation, there is no change in the direction of rotation when the magnetic field increases. In the striation, rotation inversion is associated with a change in the direction of the radial current as a result of an increase in the intensity of eddy currents with an increase in the magnetic field. At low fields, the radial current in the striation is directed from the axis to the wall; with an increase in the field, its direction changes to the opposite /4/. We explain the absence of rotation inversion inside the insert by the fact that there are no eddy currents here, and below the insert throat the current channel expands and a radial current component appears.

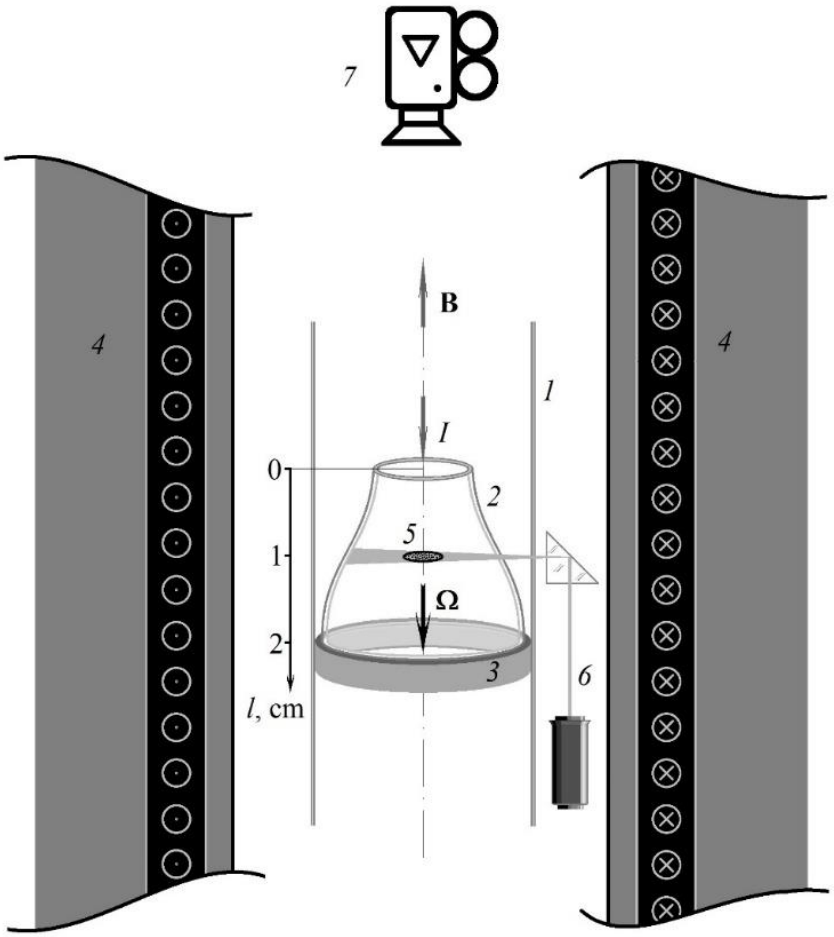

Fig. 1. Position of the insert in the discharge tube: *1* discharge tube with a diameter 22 mm and distance between electrodes 115 cm, *2* glass insert with upper inner diameter 4 mm, *3* teflon support for insert, *4* solenoid in warm hole of a cryostat, *5* dust structure, *6* laser illumination, *7* video camera

In helium, a very interesting dependence of the rotation velocity of the dust structure on the magnetic field is observed. It is shown in Fig. 2. A high rotation velocity is observed at relatively small fields $B \sim 0.1$ T and large fields $B > 1$ T. There is no complete explanation for this dependence yet. There are two mechanisms of the dust structure rotation as in the striation – ion drag and neutral gas drag. However, in the striation at high magnetic fields, they work in the opposite direction, but inside the insert – in the same direction. The ion drag contribution is /7/

$$\Omega_1 = -\frac{2.9 n_i}{R_x^2 n_a} \frac{T_i z^2 \tau^3 \nu_e \omega_{iB}}{m_i \nu_e (\nu_i^2 + 4\omega_{iB}^2) + 2 m_e \nu_i (\nu_e^2 + \omega_{eB}^2)},$$

where ω_{iB} and ω_{eB} are the ion and electron cyclotron frequencies, ν_i and ν_e are the ion-atom and electron-atom collision frequency, $\tau = T_e / T_i \sim 10^2$, $z = |Z_d| e^2 / aT_e$, eZ_d and a are the dust particle charge and radius. R_x is the radius of the discharge tube, but in this case, we must take the average between the radii of the tube R and the insert neck R_0.

The neutral gas drag contribution may be given as

$$\Omega_2 = -\frac{BI}{6\pi\eta} \frac{k(B)\left[(R_0 + k(B)H)^2 - r^2\right]}{(R_0 + k(B)H)^3},$$

where I is the discharge current, η is the dynamic viscosity of the gas, H is the distance between the insert throat and the dust structure, $k(B)$ is the fitting parameter:

$$k(B) = -26.1B^2 + 5.31B - 0.13, \quad B < 0.2 \text{ T},$$
$$k(B) = 0.0282B^2 - 0.0427B + 0.0164, \quad B > 0.2 \text{ T}.$$

Results of our calculations are presented in Fig. 2. Red solid curve shows the total velocity $\Omega = \Omega_1 + \Omega_2$ in comparison with experimental data, blue dashed curve shows the ion drag contribution Ω_1.

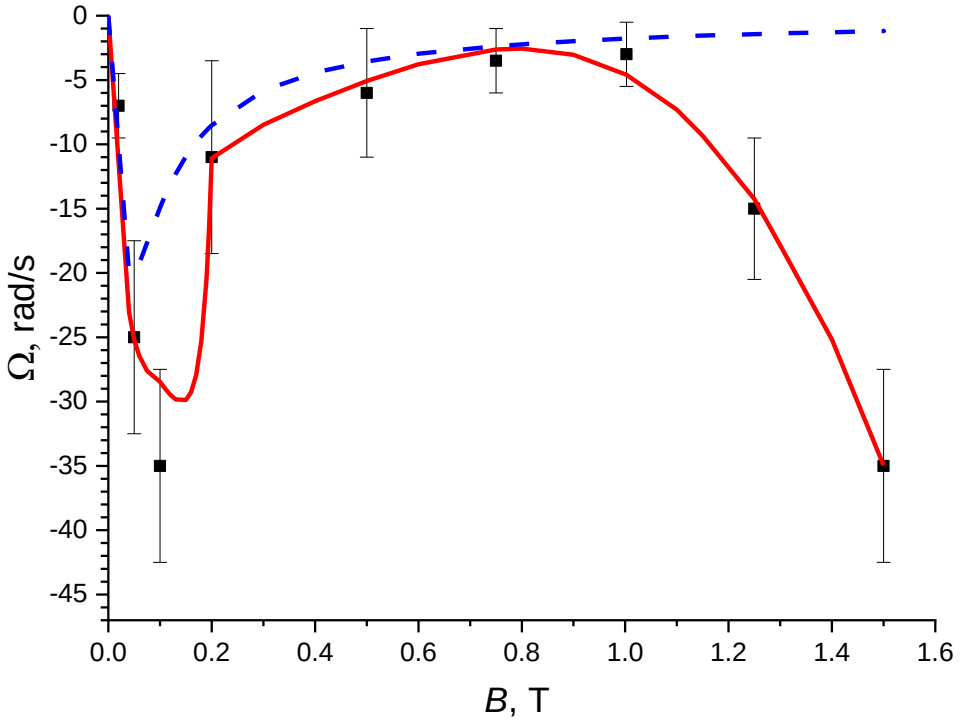

Fig. 2. Dependence of the angular velocity of a dust structure inside the dielectric insert on the magnetic field in helium at $p = 0.6$ Torr, $I = 1.5$ mA. Experimental data are given by black squares; curves show the calculation results, solid curve is the total result $\Omega_1 + \Omega_2$, dashed curve is the ion drag contribution Ω_1

Acknowledgements. The work was supported by the Russian Science Foundation (the grant No 22-72-10004) in the part of experiments and by the Ministry of Science and Higher Education of the Russian Federation (State Assignment No 075-00269-25-00) in the part of theoretical calculations.

References

1. **Melzer A., Kruger H., Schutt S. and Mulsow M.** Phys. Plasmas 26 (2019) 093702.
2. **Choundhary M.**, **Bergert R., Mitich S. and Thoma M.H.** Phys. Plasmas 27 (2020) 063701.
3. **Vasiliev M.M., Dyachkov L.G., Antipov S.N., Huijink R., Petrov O.F. and Fortov V.E.** Europhys. Lett. 93 (2011) 15001.
4. **Nedospasov A.V.** Europhys. Lett.103 (2013) 25001.
5. **Dzlieva E.S., Dyachkov L.G., Novikov L.A., Pavlov S.I. and Karasev V.Yu.** Europhys. Lett., 123 (2018) 15001.
6. **Dzlieva E.S., Dyachkov L.G., Novikov L.A., Pavlov S.I. and Karasev V.Yu.** Plasma Sources Sci. Technol. 29 (2020) 085020.
7. **Dzlieva E.S., Dyachkov L.G., Novikov L.A., Pavlov S.I. and Karasev V.Yu.** Plasma Sources Sci. Technol. 28 (2019) 085020.
8. **Dyachkov L.G., Dzlieva E.S., Novikov L.A., Pavlov S.I. and Karasev V.Yu.** High Temperature 62 (2024) 279 – 282.

ON THE DYNAMICS AND CHARGE OF A DUST PARTICLE IN A STRONG MAGNETIC FIELD

V. Karasev, E. Dzlieva, L. Novikov, M. Gasilov, D. Janitsin, M. Golubev, S. Pavlov

Saint Petersburg State University, 199034, Universitetskaya nab., 7/9,
St. Petersburg, Russia
E-mails: plasmadust@yandex.ru, v.karasev@spbu.ru

Abstract. The experimental dependence of the dust structure rotation in DC discharge in magnetic field of 2 T is presented. According to the probe theory, under experimental conditions one should expect a decrease in the charge of the dust particle and a change in the rotation speed. The analysis of the rotation dynamics shows an inverse trend, interpreted as the absence of a change in the dust particle charge. The obtained data are confirmed by independent experiments in RF discharge in field of 6 T.

Frontal studies of dusty plasma in a strong magnetic field, which began in the last decade, lead to verification of ideas about the dynamics and diffusion of magnetized plasma particles /1-9/. Elementary and widely used in dusty plasma models about the diffusion and drift of electrons and ions in the vicinity of a dust particle are borrowed from the probe theory /10-11/. A dust particle is considered as a spherical probe with a radius usually from 1 to 10 μm. For magnetic fields with induction up to 6 T used today, the cyclotron radius of electrons becomes smaller than the radius of the dust particle. According to the probe theory for moderate magnetic fields (when an electron is "magnetized" relative to the probe, but an ion is not "magnetized" relative to the probe), such conditions should lead to a change (initially to a decrease) in the charge of the dust particle /12/. This should be reflected in experiments on the dynamics of particles: their retention in dust traps, features of rotational motion in a magnetic field, features of oscillation frequencies. The results presented in the work, as well as the available literature data, seem to refute the existing theoretical ideas about the charge of dust particles in a magnetic field.

In the experiment dusty plasma was created in a neon glow discharge in stratum in a magnetic field above 1 T. A fragment of the dependence of the angular velocity on the magnetic induction is shown in Fig. 1. The conditions of the experiment described in detail in /4/ are as follows: gas neon, pressure p = 0.66 Torr, discharge current i=1.5 mA, discharge tube radius R = 1 cm, the size of the studied quartz particles with a density of 2.4 g/cm^3 is equal to a = 2 μm.

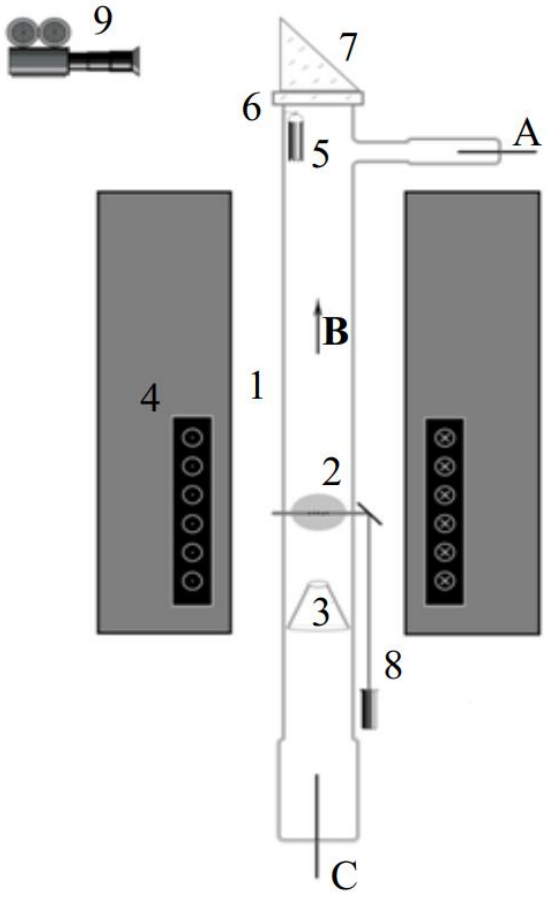

Fig. 1. Experimental setup: (1) discharge tube, (2) dust structure in striation, (3) dielectric insert, (4) superconducting solenoid, (5) container with dust particles, (6) end window, (7) turning prism, (8) laser illumination system, (9) video camera, (A) anode, (C) cathode

Let us present numerical estimates of the plasma magnetization existing at the maximum applied magnetic field B=2.2 T. The first Hall parameter is expressed as $h=w_e\tau_e=eB/(m\upsilon_e)$, where υ_e is the frequency of electron collisions with neon atoms, equal to about 600. The second and most important magnetization parameter for this problem is the ratio of the cyclotron radius to the radius of the dust particle (polydisperse, but close to spherical in shape) is expressed as $r_{ce}/a=(m_e v_{e\perp})/Ba$, where $v_{e\perp}$ is the electron velocity in the plane perpendicular to the magnetic induction, equal to 0.5.

Thus, in the magnetic field range of 1.6-2.2 T, one can expect a change in the charge of the dust particle, which should be reflected in a change in the nature of the angular velocity dependence. Fig. 2 shows that within the measurement error, the angular velocity of rotation does not change.

Under the experimental conditions the rotation of the dust plasma in the stratum occurs due to eddy electric currents in the magnetic field, i.e. it weakly depends on the charge of the dust particle. Taking into account the charge dependence by taking into account the ion drag force acting in the opposite direction should lead to a decrease in the rotation speed, which is quadratically dependent on the charge. According to the work /12/ on the probe theory, as well as estimates and modeling of the charge of a dust particle in a magnetic field /13/, the decrease in the particle charge can be by a factor of 1.5-2. However, no corresponding increase in the angular velocity is observed in Fig. 2. According to independent studies in the argon discharge in a field of up to 5.8 T, the authors did not detect a change in the charge for particles 10 μm in size, using an analysis of the dust structure.

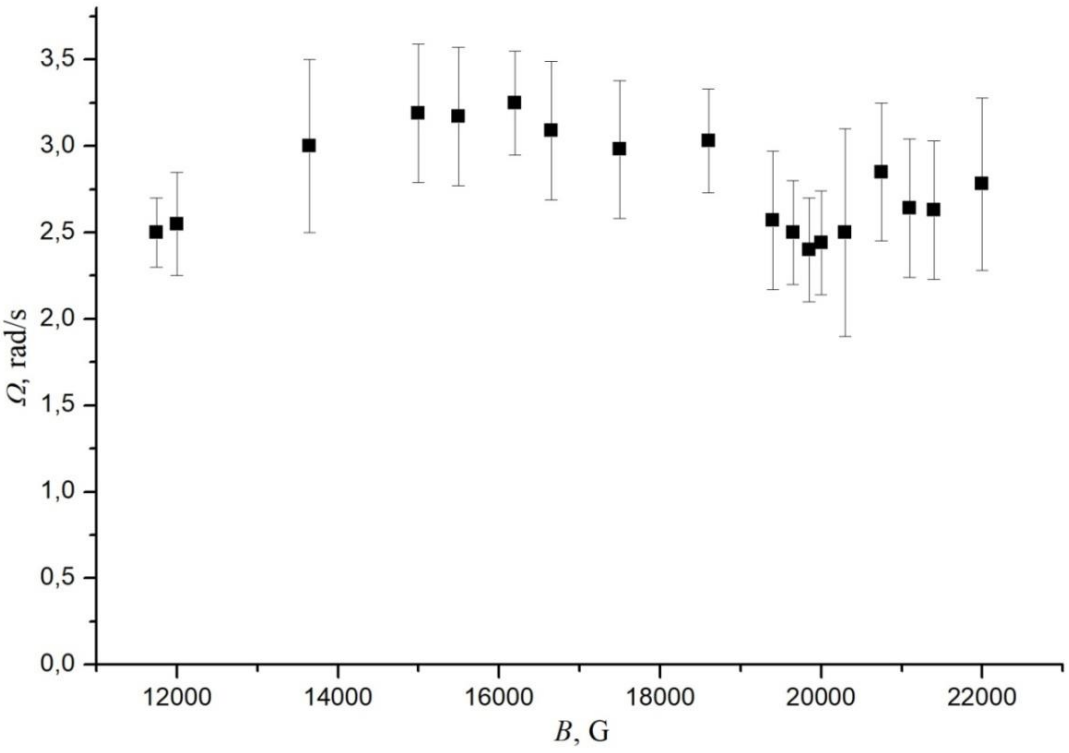

Fig. 2. Dependence of the angular velocity of the dust structure (the widest cross section) in a striation of a glow discharge on the magnetic field in neon at p = 0.66 Torr and I = 1.5 mA

Thus, despite the expected change in the charge of the dust particle, when the cyclotron radius of the electron reaches the radius of the dust particle, the experiments conducted do not confirm the expected change in charge.

Acknowledgements. This work was supported by the RSF (grant No 22-72-10004 П).

References

1. **Schwabe M., Konopka U., Bandyopadhyay P., and Morfill G. E**., Phys. Rev. Lett, vol. 106, p. 215004, 2011.
2. **Melzer A., Krüger H., Schütt S., Mulsow M.,** Phys. Plasmas, vol. 26, p. 093702, 2019.
3. **Thomas E.J., Lynch B., Konopka U., Merlino R.L., and Rosenberg M**., Phys. Plasmas, vol. 22, p. 030701, 2015.
4. **Dzlieva E.S., Dyachkov L.G, Novikov L.A., Pavlov S.I., Karasev V.Y.,** PSST, vol. 29, p. 085020, 2020.
5. **Dzlieva E.S., Dyachkov L.G, Novikov L.A., Pavlov S.I., Karasev V.Y.,** Plasma Phys. Rep., vol. 49, no. 1, 2023 p.10-14.
6. **Dzlieva E. S., D'yachkov L. G., Novikov L. A., Pavlov S. I., and Karasev V. Y.,** PSST, 28, 085020 (2019).
7. **Dzlieva E.S., Novikov L.A., Pavlov S.I., Karasev V.Y., Dyachkov L.G.,** , EPL, vol. 123, no. 1, p. 15001, 2018.
8. **Ishihara O., Kamimura T., Hirose K.I., Sato N.,** Phys. Rev. E, vol. 66, p. 0464061, 2002.
9. **Sato N.,** AIP Conf. Proc, vol. 649, pp. 66-73, 2002.
10. **Bonitz M., Horing N., and Ludwig P.,** Introduction to Complex Plasma. Berlin: Springer, 2010.
11. **Fortov V.E., and Morfill G.E.,** Complex and Dusty Plasmas: From Laboratory to Space, New York: Taylor and Francis, 2010.
12. **Chen F.,** Introduction to Plasma Physics and Controlled Fusion. London: Plenum press, 1983.
13. **Kodanova S. K., Bastykova N. K., Ramazanov T. S., Moldabekov Z. A., Nigmetova G. N., and Maiorov S. A.,** IEEE Trans. Plasma Sci., 47, 3052-3056 (2019).

5. LASER AND PLASMA INTERACTIONS WITH MATERIALS, LASER ABLATION, MODIFICATION OF MATERIALS BY PLASMA AND LASER TREATMENT, SPUTTERING AND DEPOSITION

OPTOPLASTIC EFFECT OBSERVED IN METALS EXPOSED TO NANOSECOND ULTRAVIOLET LASER PULSES

V.E. Rogalin, T.V. Malinskiy, S.I. Mikolutskiy, Yu.V. Khomich, V.A. Yamshchikov

Institute for Electrophysics and Electric Power RAS, St. Petersburg, Russia
v-rogalin@mail.ru

Optical breakdown under the influence of pulsed laser radiation on the surface of condensed media was studied long ago and described in many monographs /1/. However, the behavior of condensed media in a pre-melting state under intense pulsed thermal action has been significantly less studied. Until recently, scattered works appeared, for example, /2/, which did not receive a theoretical explanation. Subsequently, interesting theoretical studies by F. Mirzoev appeared /3/, unfortunately, at that time they did not find experimental justification.

It turned out that the properties of metals in this case can largely model the behavior of these materials during the operation of devices experiencing significant cyclic thermomechanical loads.

Since 2019, our team has conducted a series of experimental studies devoted to the study of thermocyclic fast-flowing processes in polished samples of copper and a number of its low-alloy bronze alloys Cu – Cr, Cu – Zr and Cu – Cr – Zr, as well as brass /4–9/, when exposed to intense laser UV radiation of nanosecond duration. Copper is the main electrical engineering material, as it has high electrical and thermal conductivity. Therefore, copper alloys are actively used in various fields of science and technology. In particular, copper mirrors are used in powerful CO_2 and CO lasers.

Heating was carried out by focused pulses of UV laser radiation (355 nm, 10 ns, up to 100 Hz, laser spot size ~ 200 μm, energy density $W_E \sim 0.1–1.0$ J/cm^2, slightly below the optical breakdown threshold, so that the processes under study occurred in a condensed state). The transfer of photon energy of the electron component of the skin layer of ~ 15 nm in metals occurs within ~ 2–3 ps. During the pulse (10 ns), the surface (layer of ~ 2 μm) was heated to a temperature close to melting; the phase transition was not overcome. Complete cooling of this layer occurs at $f < 50$ MHz, which is significantly higher than the $f = 10–100$ Hz used in the work.

The sharp heating of the local irradiated volume of the initially cold sample caused its thermal expansion. It occurred mainly in the direction of the free surface. And the subsequent rapid cooling fixed the resulting structure. Thus, an irreversible rise occurred on the surface of the metal, and a micro-protrusion was formed, similar to the shape of the distribution of laser radiation in the spot. The

sharp increase in roughness is apparently due to the thermal activation of structural defects in the metal (point defects, dislocations, grain boundaries, etc.), which caused them to move towards the free surface, which ultimately led to plastic deformation. Changes in surface shape are stable. The profilograms of the sample after keeping in the laboratory for six months turned out to be completely identical to those obtained immediately after irradiation.

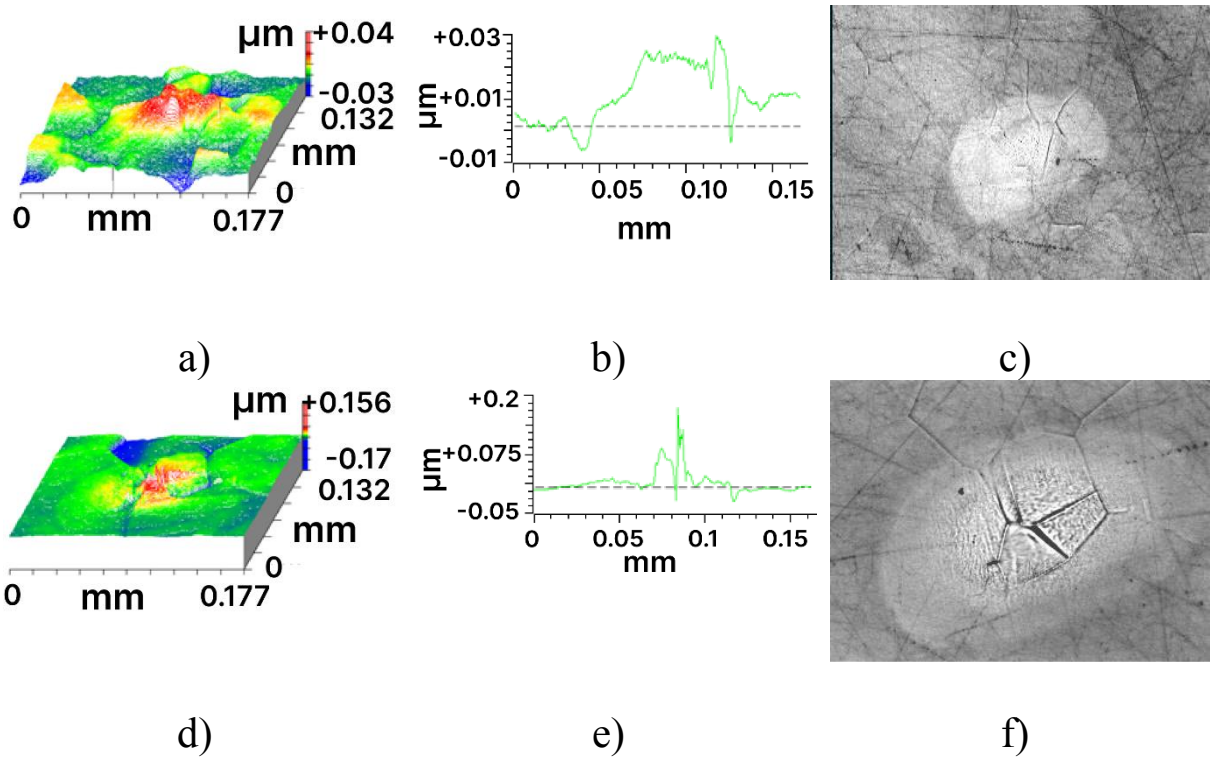

Fig. 1. Surface profile of copper sample after exposure to UV laser pulse (355 nm, 10 ns, up to 100 Hz, $W_E \sim 0.6$ J/cm^2).
a, b, c – one pulse; d, e, f – 20 pulses (10 Hz); a) and d) – 3D profilograms; b) and e) – 2D profilograms; c) and f) – micrographs of laser spot

High-precision optical profilometry revealed residual traces of high-temperature deformation – a previously unobserved effect of uneven irreversible raising of the metal surface in the irradiation zone. Sliding and cracking were observed along grain boundaries, within which traces of crystallographic slip appeared (Fig. 1). This effect was called optoplastic. As W_E and the number of impacting pulses increase, damage accumulates.

Previously, subthreshold damage on the metal surface, if it was detected, was quite rightly considered insignificant compared to superthreshold craters. However, modern methods of studying the structure of irradiated samples allow us to examine these defects more closely.

It turned out that:
– the main mechanism of relief development is dislocation relaxation of stresses associated with the anisotropy of thermal expansion of differently oriented grains;
– thermomechanical stresses in the surface layer exceed the yield strength of the material.

The obtained data are outwardly similar to the well-known phenomenon of radiation swelling of metals under the influence of prolonged exposure to radiation and are in many ways similar to the studied acoustoplastic, electroplastic and magnetoplastic effects.

The obtained experimental data allowed us to deepen our understanding of a number of fundamental phenomena that arise in metals during alternating thermocyclic fast-flowing processes, and also to obtain practical results, consisting in identifying the grain boundary structure of metal blanks without using traditional chemical etching, and without noticeable crater formation that worsens the quality of the surface /10/.

Acknowledgements. This work was supported by the Russian Science Foundation, grant no. 24-19-00727. https://rscf.ru/project/24-19-00727/.

References

1. **Anisimov S.I., Imas YA.A., Romanov G.S. and Hodyko YU.V.** Dejstvie izlucheniya bol'shoj moshchnosti na metally. Moskva: Nauka (1970).
2. **Rovinskij R.E., et. al.** Fizika i himiya obrabotki materialov, 3 (1980) 7-11.
3. **Mirzoev F.** Technical Physics. 47(10) (2002) 1258-1262.
4. **Malinskiy T.V., et. al.** Technical Physics Letters, 46(8) (2020) 831-834.
5. **Khomich Yu. V., et. al.** Acta Astronautica, 194 (2022) 434-441.
6. **Malinskiy N.V., Rogalin V.E.** Technical Physics, 67(2) (2022) 211-215.
7. **Malinskiy T.V., Rogalin V.E., Yamshchikov V.A.** Physics of Metals and Metallography, 123(2) (2022) 178-185.
8. **Malinskiy T.V., et. al.** Physics of Metals and Metallography, 124(7) (2023) 728-733.
9. **Nelasov I.V., et. al.** ZHurnal eksperimental'noj i teoreticheskoj fiziki, 167(6) 2025 782-797.
10. **Zheleznov V.YU., et. al.** Sposob obrabotki poverhnosti cvetnogo metalla putem formirovaniya mikrorel'efa, Patent RF № 2764777 ot 21.01.2022.

XPS STUDY OF PLASMA-MODIFIED POLYMER SURFACES: FUNCTIONALIZATION AND DEPOSITION USING GLOW DISCHARGE IN A GAS FLOW

D. Zuza[1,2], V. Nekhoroshev[1], A. Korzhova[2], A. Bryuzgina[2]

[1]Institute of High Current Electronics SB RAS, Akademicheskiy Ave 2/3, 634055, Tomsk, Russia, zzdnl@yandex.ru
[2]National Research Tomsk State University, Lenin Ave 36, 634050, Tomsk, Russia

Introduction

Currently, there exists a thorough understanding of glow discharge /1/, and it has numerous applications /2/. However, glow discharge within a gas flow remains a poorly studied tool for materials science due to the complex interaction of gas-dynamic and plasma processes, which currently limits its practical implementation.

One promising application of beam-plasma surface engineering is the modification of biocompatible materials, particularly polymers for biomedical applications /3/, and the deposition of biocompatible coatings /4/. For a biomedical material, it is essential that cells attach to its surface without compromising their functionality /4/. This requires enhancing the material's surface energy /3/, for instance, by generating polar nitrogen-containing and oxygen-containing groups on its surface. This increases the polar component contribution and improves the material's wettability.

The aim of the present work is to investigate the chemical state of material surfaces processed using glow discharge plasma within a flow of various gas mixtures.

Experimental part

The materials were processed using a plasma-chemical system with a low-pressure DC glow discharge in a gas flow, the schematic of which is shown in Fig. 1. The gas-discharge system was placed inside a vacuum chamber evacuated down to a residual pressure of 1×10^{-3} Pa. The glow discharge was powered by a direct current source and maintained between two hollow electrodes. The plasma-forming gas was injected into the hollow cathode. Depending on the experiment, admixture vapors were introduced into the gas-discharge system (into the positive column region).

Three distinct materials were produced under the following conditions:

1. *Silicon-based layer.* Deposition was performed by injecting hexamethyldisiloxane (HMDSO) into the discharge maintained in an argon

flow. The argon flow rate was 130 sccm, and the HMDSO flow rate was 0.13 sccm. The discharge current was set to 40 mA. Deposition was carried out at a chamber pressure of 1 Pa for 10 minutes.

2. *Modified polylactic acid (PLA).* Modification was performed by injecting diethylamine (DEA) into the glow discharge within an argon flow. The argon flow rate was 130 sccm, and the DEA flow rate was 2.6 sccm. The discharge current was set to 60 mA. Modification was carried out at a chamber pressure of 1 Pa for 5 minutes.

3. *Modified polycaprolactone (PCL)*. Modification was performed using a glow discharge maintained in a nitrogen flow. The nitrogen flow rate was 90 sccm. The discharge current was set to 40 mA. Modification was carried out at a chamber pressure of 0.7 Pa for 5 minutes.

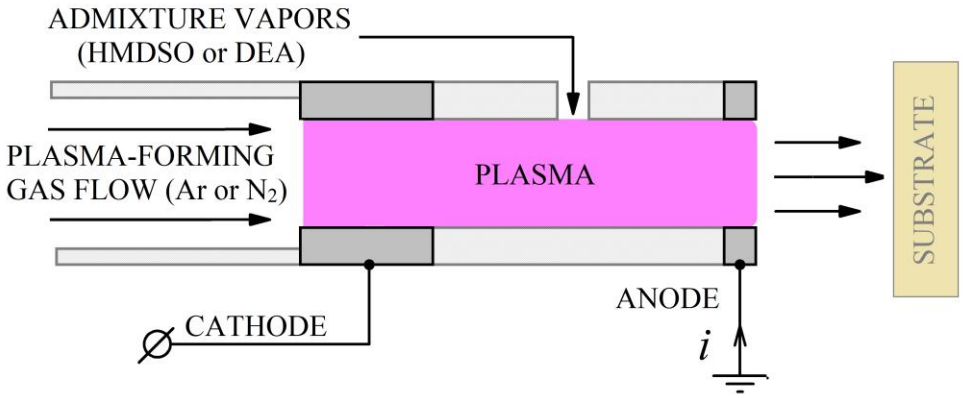

Fig. 1. The scheme of the gas-discharge system

Following deposition or modification, the material surface was investigated using X-ray photoelectron spectroscopy (XPS). Spectra of unmodified polylactide (PLA) and polycaprolactone (PCL) samples were also recorded. The photoelectron spectra were acquired on a PHI5000 VersaProbe II spectrometer using Al Kα radiation (1486.6 eV). The CasaXPS software package was used for spectral analysis.

Results and discussion

Analysis of the silicon-based layer. Fig. 2 presents the survey spectrum for the deposited silicon-based layer sample. The survey spectrum exhibits peaks corresponding to carbon (C1s), oxygen (O1s), and silicon (Si2p and Si2s) atoms. Based on quantification using relative sensitivity factors, the atomic composition of the coating (excluding hydrogen atoms) comprises 43% carbon, 30% oxygen, and 27% silicon. This atomic composition corresponds to a polydimethylsiloxane (PDMS) with a high degree of substitution of methyl groups by polar oxygen-containing groups. The above finding supports the

justified inference that the surface energy of the silicon-based layer is higher than that of typical PDMS, due to the contribution of the polar component.

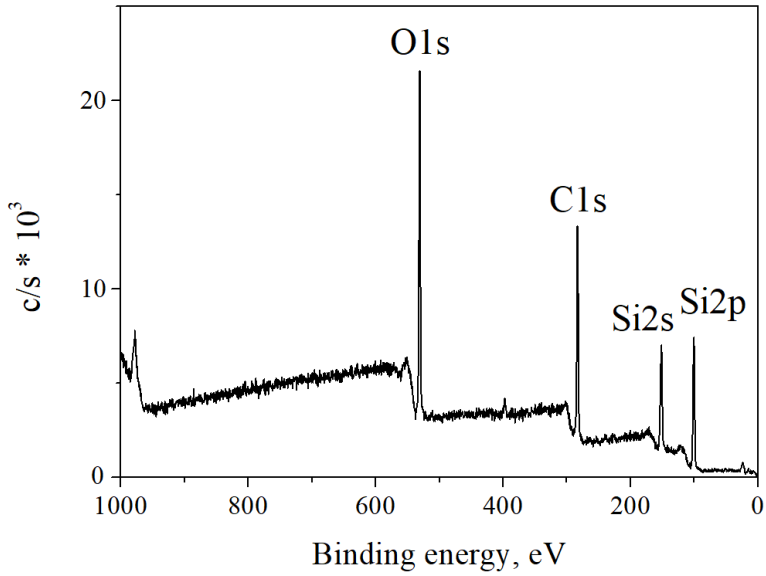

Fig. 2. X-ray photoelectron spectrum of the silicon-based layer

Analysis of modified PLA. Fig. 3 presents the X-ray photoelectron spectra of unmodified and modified PLA. Calculation shows that the atomic composition of unmodified PLA (70% carbon and 30% oxygen) deviates somewhat from the theoretical composition, likely due to the presence of adventitious carbon. In the spectrum of the modified PLA sample, an N1s peak appears, and the atomic concentration is redistributed as 77% carbon, 15% oxygen, and 7% nitrogen. The increased carbon concentration and appearance of nitrogen indicate successful grafting of amine groups onto the PLA surface.

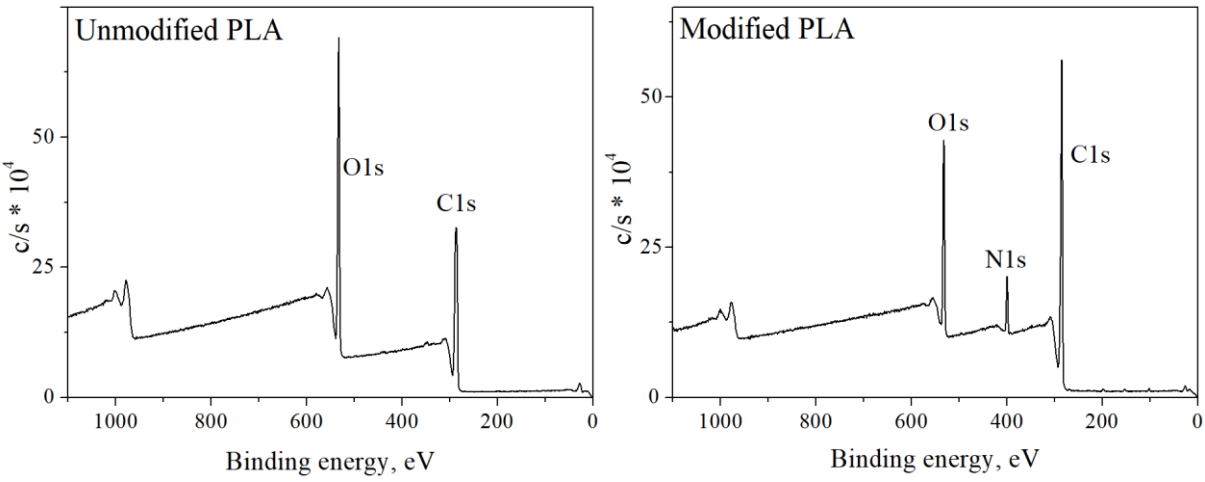

Fig. 3. X-ray photoelectron spectra of the PLA samples

Analysis of modified PCL. Fig. 4 displays the spectra of the PCL samples. For the initial material, the experimentally determined surface composition was 78% carbon and 22% oxygen. As a result of modification by glow discharge in a nitrogen flow, nitrogen-containing functional groups appear on the polymer surface. The nitrogen concentration in this case is 6%.

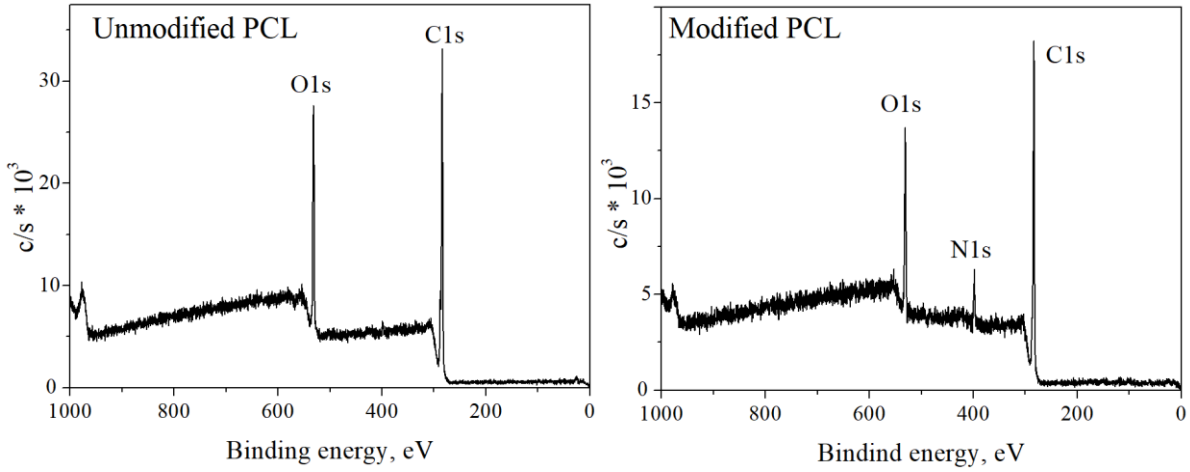

Fig. 4. X-ray photoelectron spectra of the PLA samples

Conclusion

It has been established that glow discharge in a gas flow is a suitable tool for material surface modification. This modification can be performed in various gas environments: An Ar/HMDSO mixture is well-suited for depositing a silicon-based layer containing oxygen-containing groups; An Ar/DEA mixture is effective for grafting amine groups onto the surface of polymers; Pure N_2 also facilitates the formation of nitrogen-containing functional groups on polymer surfaces.

Acknowledgements. The work was supported by the Ministry of Science and Higher Education of the Russian Federation (№ FWRM-2021-0007).

References

1. **Anders A.** Applied Physics Reviews, 11(2024) 031310.
2. **Gudmundsson J.T. and Hecimovic A.** Plasma Sources Science and Technology, 26(2017) 123001.
3. **Booth J.-P., Mozetič M., Nikiforov A. and Oehr C.** Plasma Sources Science and Technology, 31(2022) 103001.
4. **Coad B.R., Favia P., Vasilev K., Griesser H.J.** Plasma Processes and Polymers, 19(2022) e2200121.

PREPARATION AND CHARACTERIZATION OF LASER NANO-HYDROXYAPATITE CLADDED ON TI6AL4V SUBSTRATES FOR BIOMEDICAL APPLICATIONS

Man. Ganjali[1,*], Mo. Ganjali[2], A. Rasouli Azad[3]

[1]NoureZoha Materials Engineering Research Group, P.O. Box: 14566-55945, Tehran, Iran, ganjali.m@gmail.com

[2]Bioengineering Research Group, Nanotechnology and Advanced Materials Department, Materials and Energy Research Center, P.O. Box: 14155-4777, Alborz, Iran, monireh.gan@gmail.com

[3]Department of material Science and Engineering, Science and Research Branch, Islamic Azad University of Sirjan, P.O. Box: 78185-577, Sirjan, Iran, en_andishe_azad@yahoo.com

Abstract: This study fabricates nano-hydroxyapatite (HA) coatings on Ti6Al4V via laser cladding method, analysing the impact of process parameters on microstructure and properties. SEM/EDS and microhardness tests confirmed optimal Ca/P ratios and mechanical performance. Apatite formation after SBF immersion suggests strong bioactivity, supporting potential use in dental and orthopedic implants.

Introduction: Metallic implants (e.g., cobalt-chromium alloys, stainless steels, titanium alloys) offer high mechanical strength and corrosion resistance but often lack bioactive surfaces, limiting osteo-integration and posing risks of metal ion release. Bioactive coatings, such as nano-hydroxyapatite (HA), improve bone healing due to their structural similarity to bone mineral, enhanced resorb-ability, and superior cellular interactions /1,2/. The present study includes: a) Nano-HA was synthesized via co-precipitation and deposited on Ti6Al4V using laser cladding method (LCM), varying laser scanning speeds and output powers. b) Coating microstructure was analyzed via SEM, before and after immersion in simulated body fluid (SBF). c) Morphology, Ca/P ratio, and hardness were systematically evaluated. And key findings consist of a) Nano-HA coatings exhibit accelerated calcium ion release, mimicking biological apatite. b) LCM provides strong mechanical bonding, high precision, and production efficiency. c) Post-SBF immersion analysis confirms coating stability and bioactivity. This study was significantly demonstrated laser-cladded nano-HA coatings enhancing implant bioactivity, osteo-integration, and durability, addressing limitations of traditional metallic implants /3/.

Experimental procedures: In preparation and characterization of hydroxyapatite (HA)-coated Ti6Al4V alloy for biomedical applications, there are key findings as:
a) substrate preparation: Ti6Al4V alloy (10 × 10 × 2 mm) was verified via quantometry (Ti-6Al-4V purchased consisting in percentage of 90 Ti, 4.24 V, 0.152 O, 0.16 Fe, 0.017 C, 0.008 N and 0.0006 H and of standard one of 90 Ti, 3.5-4.5 V, <0.2 O, <0.3 Fe, <0.08 C, <0.05 N and <0.015 H), cleaned ultrasonically, and treated with NaOH to form sodium titanate for improved HA nucleation.
b) nano-HA synthesis /4/,
c) coating & laser treatment: HA-PVA slurry was dip-coated (0.8 mm thick), dried, and laser-treated (CO_2 laser, 20–30 W, 1–3 mm/s) to enhance adhesion. The specimens coding with S0 cod to S6 cod, the utilized laser treatment power: 0, 20, 20, 20, 30, 30, 30W, the laser scanning speed: 0, 1, 2 , and 3 mm/s was considered.
d) Characterization:
   a) SEM-EDS analyzed microstructure, Ca/P ratios, and SBF immersion effects.
   b) Vickers microhardness (100gf, 15s) assessed mechanical properties.
e) Results: optimized laser parameters improved HA coating integrity, with post-treatment microstructural analysis revealing uniform layers and biocompatible Ca/P ratios. This work demonstrated a potent method for producing HA-coated Ti6Al4V implants with enhanced bioactivity and mechanical properties for biomedical applications.

Result and discussion: LC and coating analysis: Laser-cladding HA coatings exhibited three distinct zones: clad zone (A), heat-affected zone (HAZ) (B), and base metal (C). And Vickers micro-hardness of the starting and laser treated specimens (from S0 until S5) were measured 220, 1428, 1783, 1550, 1558 and 1873 VHN respectively. Consequently, laser-clad HA coatings, particularly S2**,** exhibit superior biocompatibility and mechanical stability, making them promising for biomedical implants. The study highlights the importance of processing parameters in optimizing coating performance (See Fig. 1).
Higher scanning speeds reduced microcracks by minimizing thermal gradients and impurities, ensuring dense, well-adhered coatings. Ca/P ratio and biocompatibility: initial Ca/P ratios were higher than natural bone (1.67) due to phosphorus loss during laser processing. a) Specimen S2 demonstrated optimal bioactivity, achieving a Ca/P ratio of 1.6 after 21 days in SBF, along with high micro-hardness and uniform particle distribution. b) Other specimens showed varying dissolution and re-precipitation behaviours, with S2 outperforming prior studies (e.g., Ca/P = 6.34 in Chann et al. /5/) (See Fig. 2. (a), (b)).

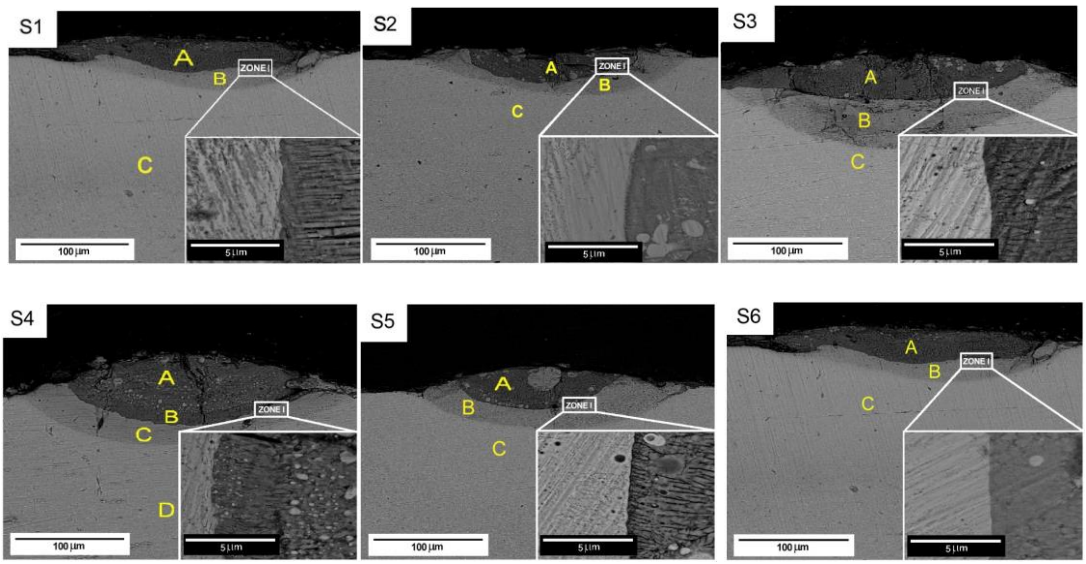

Fig. 1. Cross-sectional SEM micrographs of coated samples and zoomed zone I

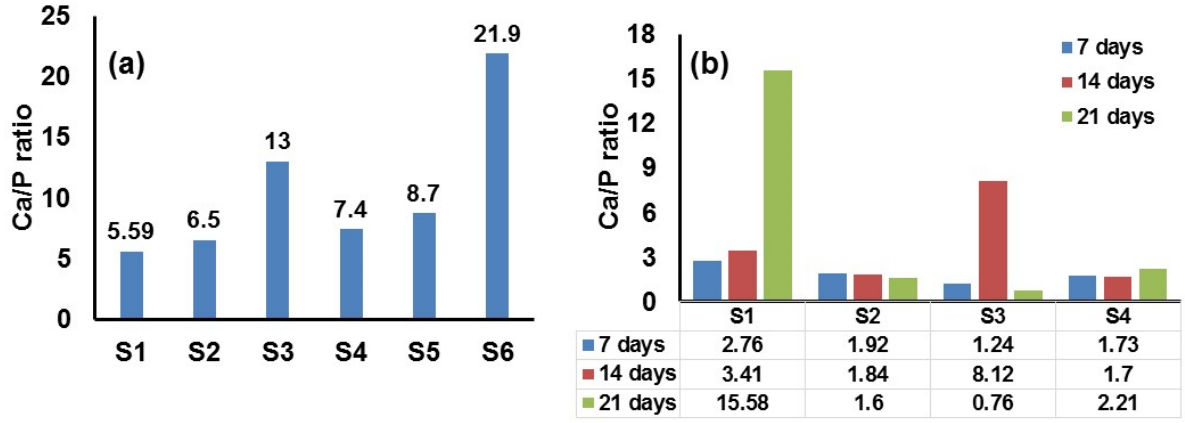

	S1	S2	S3	S4
7 days	2.76	1.92	1.24	1.73
14 days	3.41	1.84	8.12	1.7
21 days	15.58	1.6	0.76	2.21

Fig. 2. Comparison of Ca/P ratio in zone (a) before immersion and (b) after three weeks immersion in SBF

Fig. 3 presents SEM images of specimens (S1–S3, S5) after 7, 14, and 21 days in SBF. S1 exhibited early precipitation of Ca/P-rich particles (Zone B), with ionic interactions in SBF influencing apatite formation. Stable Ca/P ratios were observed in Zones A–F over three weeks. By Week 3, dissolution in Zone E led to needle-like crystal formation, replacing smaller particles. These findings highlight the dynamic dissolution-precipitation process and bioactive apatite growth in SBF, critical for biomaterial performance.

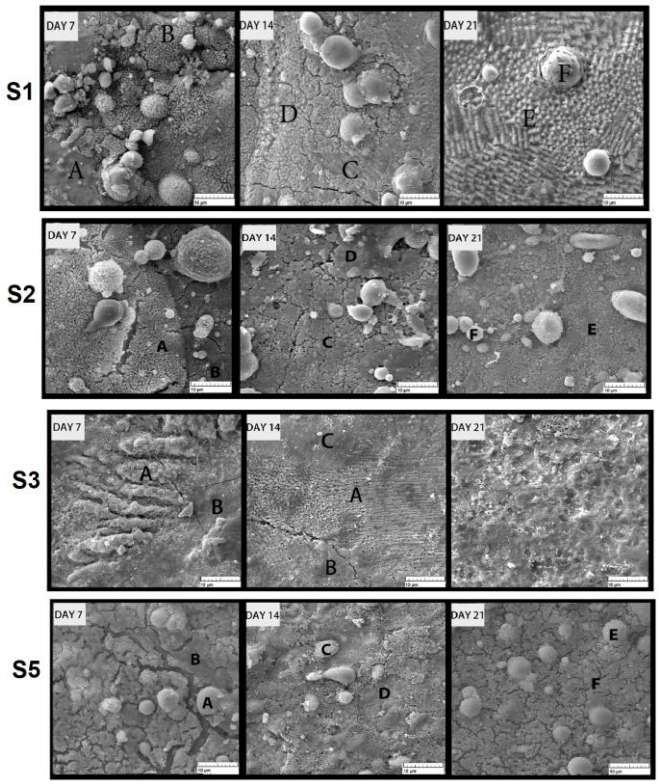

Fig. 3.Cross sectional SEM micrographs of the fabricated coating during 3 weeks immersion in SBF

Conclusion: Laser-cladded nano-HA coatings demonstrated: a) Dense, crack-free layers with enhanced structural integrity**.** b) Higher scanning rates minimized microcracks via improved cooling and impurity removal. c) Ca/P ratio shifted from >1.67 to ~1.63 post-SBF immersion (optimal in S2**).** d) S2 coating achieved peak hardness **(**1873 VHN**)** due to denser microstructure.

References:

1. **Mediaswanti K., Wen C., Ivanova E. P., et al.** A review on bioactive porous metallic biomaterials. J. Biomim. Biomater. Tissue Eng., 18 (1), (2013).
2. **Habraken W., Habibovic P., Epple M., et al.** Calcium phosphates in biomedical applications: materials for the future. Mater. Today, 19(2), (2016).
3. **Ganjali Mo., Ganjali Man., Sadrnejad SK. and Pakzad Y.** Laser cladding of Ti alloys for biomedical applications. Book, Springer, (2020).
4. **Hajinaebi, M., Ganjali, M. and Nasab, N. A.** Antibacterial activity and drug release of ciprofloxacin loaded PVA-nHAp nanocomposite coating on Ti-6Al-4 V. Journal of Inorganic and Organometallic Polymers and Materials. 32(9), (2022).
5. **Chien C. S., Liao T. Y., Hong T. F., et al.** Surface microstructure and bioactivity of hydroxyapatite and fluorapatite coatings deposited onTi-6Al-4V substrates using Nd-YAG laser. J. Med. Biol. Eng. 34 (2), (2014).

ENHANCEMENT OF TI-6AL-4V SURFACE PROPERTIES THROUGH GRAPHENE-REINFORCED HYDROXYAPATITE COATINGS: HARDNESS AND WEAR RESISTANCE EVALUATION

A. Sohrabi[1], Mo. Ganjali[1], F. Torknik[1], Ma. Ganjali[2]

[1]Materials and Energy Reasearch Center, Karaj, Iran, monireh.gan@gmail.com, a.sohrabijam@gmail.com, fstorknik@gmail.com
[2]Nour zoha materials engineering research group, Tehran, Iran, ganjali.m@gmail.com

Abstract. The Ti-6Al-4V alloy, while widely used in medical implants, suffers from poor wear resistance. This study enhanced its properties through laser cladding with a hydroxyapatite/graphene nanocomposite coating. The results of the hardness test show that due to the presence of graphene, the hardness of the samples has increased by 9, 15 and 27 percent, respectively, for the samples with 1, 3 and 5 percent graphene compared to the sample without graphene. Also, the abrasion properties of the coating have improved by 6, 29 and 36 percent for the samples with 1, 3 and 5 percent graphene due to the presence of graphene.

Introduction. Titanium alloys are widely used in aerospace, medical, and industrial applications due to their biocompatibility, strength-to-weight ratio, and corrosion resistance. In medical implants, Ti-6Al-4V is favored for its fatigue resistance (~2×10^6 cycles/year) but suffers from wear in joint applications. To address this, surface modifications like hydroxyapatite (HA) coatings are employed, as HA mimics bone mineral composition and enhances osseointegration. However, HA coatings face mechanical instability at the metal-ceramic interface over time. Recent studies propose graphene-reinforced HA coatings to improve mechanical properties. Graphene enhances osteoblast adhesion, offers superior crack resistance compared to carbon nanotubes, and exhibits low cytotoxicity. Various coating techniques including electrophoretic deposition, plasma spray, and laser treatments are being explored to optimize implant performance. These advancements aim to combine HA's bioactivity with graphene's mechanical strength for longer-lasting implants. Researchers have successfully synthesized hydroxyapatite/graphene (HA/G) composites using spark plasma sintering (SPS) /1/. Raman spectroscopy confirmed that graphene nanosheets (GNS) maintain structural integrity under SPS conditions. Hydroxyapatite (HA) nanocomposites reinforced with graphite nanosheets (GNs, 0.5-2 wt%) and multi-walled carbon nanotubes (MWNTs) were fabricated via spark plasma sintering /2/. Mechanical testing revealed that MWNT/HA composites showed progressive strength improvement with increasing MWNT content, while GN/HA composites peaked at 0.5 wt% GN before declining. Baheti and et al. /3/ modified Ti implant surfaces, which was

coated with graphene oxide (GO), HA, HA-2wt%GO and HA-5wt%GO via electrophoresis deposition. HA-2wt%GO coatings demonstrate strong potential for dental implant applications due to their dual optimization of surface characteristics and biological activity. All of the investigations on laser cladding of graphene/hydroxyapatite coatings focused on Ti and especially Ti-6Al-4V as deposition substrate and to our knowledge, there is not any report on laser cladding of graphene/hydroxyapatite coatings on Ti-6Al-4V substrates. In this work, we investigated the deposition of nanohydroxyapatite and its graphene composite (HA/G) on Ti-6Al-4V substrates using laser cladding.

Experimental procedure.

In order to prepare the samples, the alloy sheet was first cut into dimensions of 20×30×30 mm. The percentage of elements in the substrate alloy was tested by optical emission spectrometry (Foundery Master Quantmeter, Germany), the results of which are shown in Table 1. The substrates were then polished using 800, 1200 and 2500 grit silicon carbide plates and in order to clean the surfaces of the polished samples from suspended particles of surface contaminants, they were placed in an ultrasonic bath (Wiseclean WUC-D10H) for 10 minutes in a stove, ethanol and distilled water and then dried in a greenhouse at 60 °C. The coating operation of the hydroxyapatite/polyvinyl alcohol/graphene nanocomposite samples was first carried out by immersion method. For this purpose, first, an 8% by weight polyvinyl alcohol (PVA, C_2H_4O, 99.5%, Merck) solution was synthesized in deionized water at a temperature of 70-80 °C. Nano-hydroxyapatite powder (nHAp) synthesized according to the method by Ganjali et al. /4/. Then, 5 wt% of the synthetic nHAp was gradually added to the PVA solution while stirring. After that, to prepare nHA/PVA nanocomposites with different percentages of nanographene, first, 1, 3 and 5 percent by weight of graphene (G, 99.5%, 2-18 nm thickness, US NANO) (relative to the composite) were poured into a certain amount of deionized water and then placed in an ultrasonic bath for 45 minutes to disperse it and added to the PVA solution. After the composite reached the appropriate viscosity, it was used as a coating applied to the surface and dried.

Table 1: Chemical composition of TI-6AL-4V alloy used as substrate.

Element	**Al**	**V**	**C**	**Fe**	**O**	**N**	**H**	**Ti**
wt%	6.3	4	0.006	0.17	0.166	0.006	0.002	Bal.

In this study, a fiber laser with a wavelength of 1064 nm a maximum average power of 500 W, a laser beam diameter of 2 mm, a laser focal length of 14 mm, was used. Argon gas was used to protect the molten pool on the sample surface during laser irradiation.

Characterization. Scanning electron microscopy (SEM, Mira3 TESCAN, Czech Republic) equipped with an energy dispersive X-ray detector (EDX) was used for the microstructural and elemental analysis of HA/G nanocomposite coatings after laser treatment. Wear testing evaluated the tribological performance of engineering materials under specified operating conditions. The experiments employed an Iranian-manufactured pin-on-disk apparatus, with a fixed sliding distance of 500 meters. The test utilized a pin with a Rockwell hardness of 64 HRC. Vickers hardness measurements were performed on the as-coated and laser-treated samples using a microhardness tester (Koopa Pazhoohesh, KM2/01-92123, Iran, power rating 220–240 V, 1 A, at 1 kg load for 15 s).

Results and discussion. SEM analysis (200-300×) shows that the laser-treated HA coating retains its nanostructure with uniform surface distribution. Limited microcracking (Fig. 1 (a-f)) occurs due to: (1) thermal stresses from rapid cooling (thermal gradient/expansion mismatch) and (2) PVA burnout defects /4/. These microcracks do not significantly affect coating integrity.

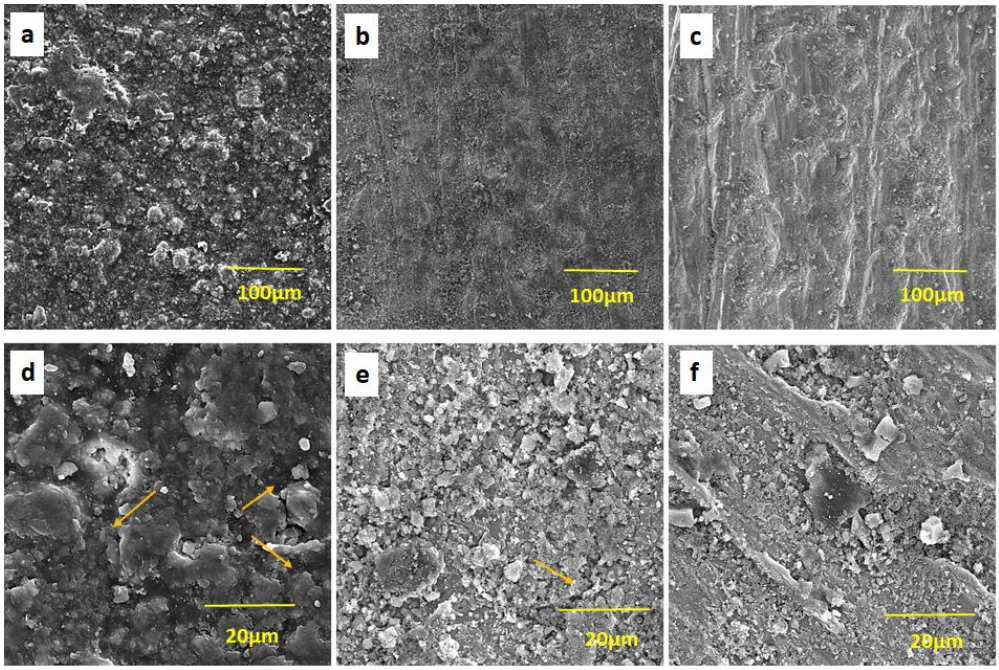

Fig. 1. SEM images of coated samples with (a-c) 1-5% graphene at 300× and (d-f) 200× magnification

Vickers hardness tests showed that graphene enhances coating hardness (Fig. 2a). The baseline (0% graphene) measured 269 HV. Hardness increased by 9% (1% graphene), 15% (3%), and 27% (5%). Wear tests revealed three phases (Fig. 2b):

Initial (0–100 m): high wear (soft surface layer);

Mid (~300 m): low wear and (hardened HAZ contact);
Final: increased wear (softer substrate interaction).
Microhardness gradients (surface < HAZ > substrate) explain this behavior /5/. Higher graphene content (5 wt%) improved wear resistance (Fig. 2b).

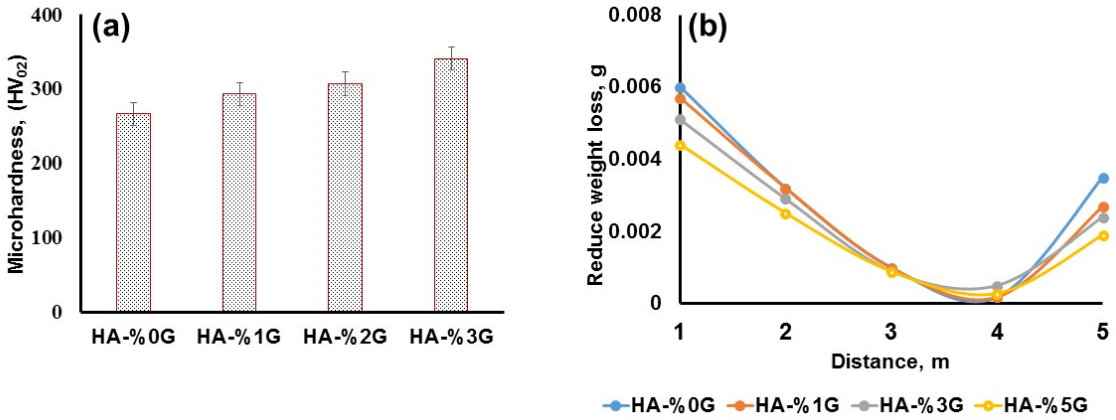

Fig. 2. Microhardness (a) and weight loss (b) of samples through 500 m under 50 N loads

Conclusion. This study employed laser cladding to deposit HA/graphene nanocomposite coatings on Ti-6Al-4V substrates. SEM analysis revealed the formation of uniform, dense coatings with excellent substrate adhesion. The coating process significantly enhanced surface microhardness, increasing from 269 HV (uncoated substrate) to 346 HV. Notably, coatings containing 5 wt% graphene demonstrated optimal wear resistance performance.

Acknowledgments. This work was supported by the Materials and Energy Research Center (MERC) for Fundamental Research (grant No. 7713950730).

References

1. **Zhang, L., Liu, W., Yue, C., Zhang, T., Li, P., Xing, Z., & Chen, Y.** Carbon, 61(2013), 105-115.
2. **Zhu, J., Wong, H. M., Yeung, K. W. K., & Tjong, S. C**. Advanced Engineering Materials, 13(2011), 336-341.
3. **Baheti, W., Lv, S., Mila, Ma, L., Amantai, D., Sun, H., & He, H.** Journal of Applied Biomaterials & Functional Materials, 21 (2023), 22808000221148104.
4. **Hajinaebi, M., Ganjali, M., & Nasab, N. A.** Journal of Inorganic and Organometallic Polymers and Materials, 32(2022), 3521-3532.
5. **Tlotleng, M., Akinlabi, E., Shukla, M., & Pityana, S.** Materials Science and Engineering: C, 43 (2014), 189-198.

PLASMA LINEAR MULTICUSP MAGNETIC TRAP FOR MATERIAL TESTING AND PLASMA PHYSICS APPLICATIONS

D.I. Kavyrshin[1,2*], S.D. Fedorovich[1], V.P. Budaev[1], Quang Vinh Tran[1], M.V. Lukashevsky[1], A.V. Karpov[1]

[1]National Research University, «MPEI», Moscow, Russia
[2]Joint Institute for High Temperatures of the Russian Academy of Sciences, Moscow, Russia
*dimakav@rambler.ru

To support the construction of a fusion neutron source (FNS) based on a tokamak reactor in Russia, research and development of cooled thermal protection linings for the divertor and first wall are being conducted. The interaction of plasma with plasma-facing materials in the tokamak will largely determine the reactor's performance and service life [1]. In a thermonuclear reactor, the expected plasma-thermal loads (based on calculations for ITER [2]) in an ITER-scale tokamak during the stationary phase of DT-discharge will reach ~10-15 MW/m^2 on the divertor plates, causing average material surface temperature increase up to ~1100 °C. The average plasma-thermal load on the first wall be more than 1 MW/m^2. Such powerful loads can lead to surface overheating, crack formation, and even melting of tungsten, which is intended to be used as the material for the divertor and first wall in ITER [1]. Therefore, it is necessary to evaluate the consequences of possible tungsten melting and cracking, recrystallization, formation of heterogeneous and porous layers on the surface of tungsten plates under critical and subcritical thermal loads, as well as the formation of dust particles after the destruction of such layers.

Studies from previous years [1,3,4] have demonstrated the promising application of linear devices with magnetized plasma as divertor simulators for testing in-chamber reactor components. For these purposes, the plasma linear multicusp magnetic (PLM-M) installation was constructed in 2021-2023 based on the PLM installation [5]. The PLM-M installation has no analogues in Russia, with parameters comparable to several of the most powerful installations in the world. The installation is a linear magnetic trap with a multicusp magnetic plasma confinement scheme. It utilizes a longitudinal magnetic field generated by a current-carrying coil and a system of radial magnetic fields formed by permanent neodymium magnets. This creates a magnetic field configuration known as an octupole multicusp. A distinctive feature of this facility is its steady-state operation mode with plasma confinement lasting multiple hours, which provides an advantage for testing candidate fusion reactor materials, studying turbulent plasma physics, and developing plasma technologies. The powerful plasma flow in PLM-M is used for testing materials and structures for fusion reactor walls, as well as for irradiating materials to modify them and

achieve new physicochemical properties.

The main components of the PLM-M experimental installation are shown in Fig. 1. A stationary discharge is sustained in a discharge chamber equipped with systems for working gas injection, vacuum pumping, and magnetic stabilization of plasma. The discharge current is generated and maintained by a digitally controlled DC power supply system. The setup also includes plasma diagnostics tools, such as optical emission spectroscopy and probe diagnostics.

The discharge chamber of the installation is water-cooled, has cylindrical shape with a diameter of 0.16 m and length of 0.72 m, and is fabricated from non-magnetic stainless steel. Its output flange is connected to a large-volume receiver chamber (1 m diameter and 1 m length), also constructed from non-magnetic stainless steel.

A longitudinal magnetic field of up to 0.03 T in the vacuum discharge chamber is generated by a solenoid coil mounted around the discharge chamber (Fig. 2). The solenoid coil is powered by an external stabilized power supply. To create a multicusp magnetic configuration, permanent N45H-grade neodymium magnets with size 45 × 15 × 15 mm and magnetic induction 1.32–1.38 T are used instead of the classical Ioffe bar (current-carrying conductor) approach. These magnets are housed within eight non-magnetic steel cassettes fixed along the discharge chamber. Near the chamber walls, where the radial component of the magnetic field reaches its maximum, the magnetic induction is predominantly governed by the azimuthal component of the magnetic fields generated by the permanent magnets of the octupole system. Measurements have shown that the magnetic induction near the vacuum chamber walls reaches a peak value of 0.2 T.

A tantalum cathode is mounted on the output flange of the discharge chamber. The plasma flow exits the discharge gap through a 3.5 cm diameter aperture in the copper anode, forming a cylindrical jet of corresponding dimensions. The discharge chamber is equipped with five diagnostic ports. The receiver chamber, connected to the discharge chamber, captures plasma flow leaving the magnetic trap. This configuration simulates plasma streams in gradient magnetic fields, such as those in a tokamak divertor, as well as conditions for testing plasma-based electric propulsion technology. The residual gas pressure in the discharge chamber does not exceed 1×10^{-6} Torr, and is below 6×10^{-7} Torr in the receiving chamber, ensuring high-performance plasma discharge during experiments.

The plasma-forming gas is helium, which is supplied through automatically regulated valves into the cathode region at a flow rate of 0.15 g/cm^3. A throttling valve at the vacuum chamber outlet to the pumping system is used to maintain a constant flow rate. The pressure in the chamber during installation operation is maintained at $(2–4)\times10^{-2}$ Torr. The gas supply system of the installation includes

replaceable high-capacity gas cylinders and allows the use of different gases in experiments, such as argon, nitrogen, hydrogen, xenon, and krypton.

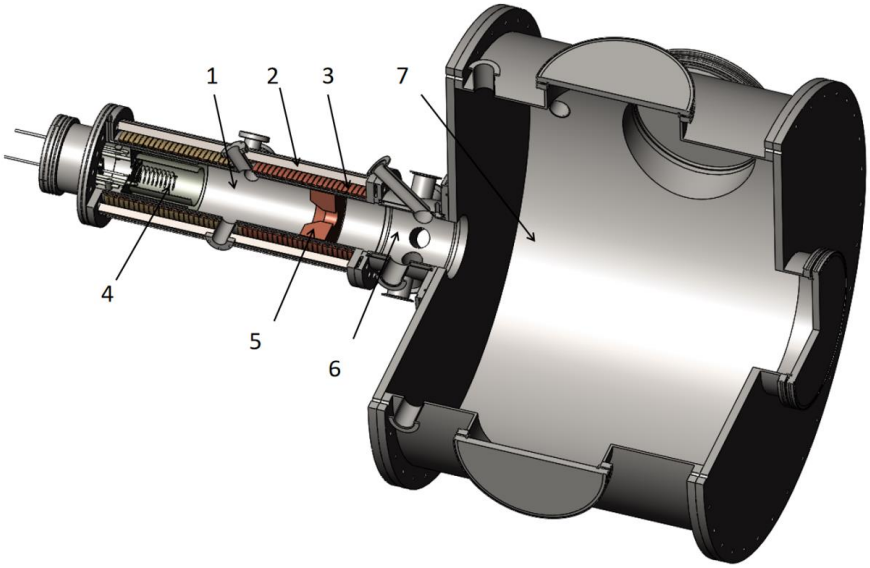

Fig. 1 — Basic components of PLM-M installation:
1 — discharge chamber, 2 — permanent magnets, 3 — longitudinal magnetic field solenoid coil, 4 — cathode, 5 — anode, 6 — high-frequency plasma heating section, 7 — receiver chamber

In the PLM-M discharge chamber, plasma is generated via electron impact stepwise ionization of the plasma-forming gas atoms (which was helium in reactor material tests). The gas is fed into the discharge vacuum chamber through a regulated valve. The electron current density required for stepwise ionization is provided by thermionic emission from the cathode made of tantalum. Plasma is heated by electric current in the plasma discharge in the electric field between the cathode and the grounded anode. The power supply system and cathode design are able to provide plasma discharge current of up to 50 A, resulting in discharge energy input power of approximately ~5 kW.

The end section of the discharge chamber is designed to accommodate a high-frequency (HF) plasma heating system. A water-cooled helicon antenna, powered by a generator with 13 MHz frequency and 4 kW output power, enables supplying extra power to the plasma flow exiting the discharge chamber. The utilization of ion cyclotron resonance heating (ICRH) also facilitates the testing of plasma thruster technologies, including components of the established design proposed for electrodeless plasma jet engines.

Plasma diagnostics on PLM-M employ optical emission spectroscopy in the 200–1100 nm range and movable Langmuir probes assembled into arrays. Probe measurement data enables determining electron concentration distribution across the discharge radius, while the ratio of measured spectral line intensities of helium atom He I and the single observed helium ion line He II 468.5 nm are

used to determine electron temperature. Measurements obtained via probe and optical diagnostics allowed us to determine following plasma parameters in the discharge during tests, their values depending on discharge modes:

- electron temperature 1 eV – 10 eV,
- electron density from $0{,}5 \cdot 10^{19}$ m^{-3} to $3 \cdot 10^{19}$ m^{-3}.

Such high-power plasma flows can be utilized for testing materials and structures of in-chamber components of fusion reactors [6], as well as for advancing plasma technologies and electric propulsion engine technologies for space applications [7].

Acknowledgements. This work was supported by the Ministry of Science and Higher Education of the Russian Federation (State Assignment No. FSWF-2025-0001 and 075-00269-25-00).

References

1. **Budaev, V.P.** Results of high heat flux tests of tungsten divertor targets under plasma heat loads expected in ITER and tokamaks (review). Phys. Atom. Nuclei 79, 1137–1162 (2016). https://doi.org/10.1134/S106377881607005X
2. **PittsR.A. et.al.** A full tungsten divertor for ITER: physics issues and design status. — J. Nucl. Mater., 2013, vol. 438, p. 48—56.
3. **Ueda Y., Coenen J.W., De Temmerman G., Doerner R.P., Linke J., Philipps V., Tsitrone E.** Research status and issues of tungsten plasma facing materials for ITER and beyond. — Fusion Eng. Des., 2014, vol. 89, p. 901—906.
4. **Budaev V.P., MartynenkoYu.V., KarpovA.V. et al.** Tungsten recrystalization and cracking under iter-relevant heat loads. — J. Nucl. Mater., 2015, vol. 463, p. 237—240.
5. **Budaev, V.P., Fedorovich, S.D., Dedov, A.V. et al.** Testing of Tungsten Plasma-Facing Components of a Divertor in PLM Plasma Device. Phys. Atom. Nuclei 87 (Suppl 1), S91–S98 (2024). https://doi.org/10.1134/S1063778824130143
6. **Van Oost, G., Dedov, A.V. & Budaev, V.P.** The Plasma-Facing Materials of Tokamak Thermonuclear Reactors: Requirements, Thermal Stabilization, and Tests (a Review). Therm. Eng. 68, 185–200 (2021). https://doi.org/10.1134/S0040601521030095
7. **Budaev V.P., Fedorovich S.D., Frick P.G. et al.** Plasma magnetic trap of linear multi-cusp configuration – the component of a plasma propulsion rocket engine. —Magnetohydrodynamics, 2019, vol. 55 (1-2), p. 31-38. https://doi.org/10.22364/mhd.55.1-2.4

SYNTHESIS OF SILICON-TIN ALLOYED NANOPARTICLES BY LASER ABLATION OF SILICON COVERED BY TIN FILM IN LIQUID

V. Kornev[1], N. Tarasenka[1,2], M. Nedelko[1], A. Manshina[3], A. Kuchmizhak[4], N. Tarasenko[1]

[1] B.I. Stepanov Institute of Physics, National Academy of Sciences of Belarus,
[2] University of Strathclyde, Glasgow, UK
[3] Saint Petersburg State University, Institute of Chemistry
[4] Institute of Automation and Control Processes, Russian Academy of Sciences

Silicon-tin alloyed nanoparticles (NPs) are of particular interest because they remain compatible with the existing silicon technology. Doping silicon with tin allows not only reducing the bandgap, but also changing it from indirect to direct /1/. According to estimations, $Si_{1-x}Sn_x$ alloys become direct band gap materials at tin content of about 18-23% /2/. Sn has a significantly narrower bandgap than silicon with the same crystal structure. The similarity of crystalline structures allows mitigating typical problems upon alloying and doping such as lattice mismatches, dislocations and defects at interfaces /3/. As photovoltaic materials, silicon-tin alloys can improve the performance of solar cells by expanding the spectral range and increasing absorption in the wavelength range of 1.0–1.6 μm. In particular, in /4/, Si and Sn were deposited on n-type Si (100) substrates to form a $Si_{1-x}Sn_x$ layer, thus enabling to achieve a Sn content in the alloy of up to 18 ± 4%. The authors in /4/ also determined the values of the direct and indirect band gaps of the obtained nanostructures using the Fourier transform infrared spectroscopy method, which were equal to 0.83 and 1.05 eV, respectively. The band gap width depends on the alloy composition: a number of works have demonstrated that the band gap width of the $Si_{1-x}Sn_x$ alloy decreases with increasing tin concentration. In /5/, the radio frequency magnetron sputtering method was used to deposit a film of the amorphous $Si_{1-x}Sn_x$ alloy. An analysis of the conductivity and band gap width showed that the film can be used as a material for the sensitive layer of near infrared sensors. The synthesis of $Si_{1-x}Sn_x$ alloy nanocrystals with an optical band gap of 0.81 eV by laser ablation in liquid media was reported in /6/. The authors of /7/ used the molecular beam epitaxy method to grow a $Ge_{0,85}Sn_{0,15}$ buffer layer on Si (100) and then deposit a $Si_{1-x}Sn_x$ film. Band gap measurements showed that $Si_{1-x}Sn_x$ alloy in the Sn content range from 15% to 24% can be converted to a direct band gap material. Some research report estimations of the $Si_{1-x}Sn_x$ band structure using simulations /2, 8/, but the predicted tin contents vary greatly and thus the effect of Sn doping concentration on the band structure of SiSn alloy is

controversial. Furthermore, the studies of the effect of Sn concentration on the optical properties are very few. Despite some progress in synthesis of $Si_{1-x}Sn_x$ structures, the development of new approaches to the controlled synthesis of silicon-based alloyed NPs remains an urgent task. As has been demonstrated recently /9/, plasmas generated in liquids, both by lasers and by electrical discharges have a high potential in the field of nanomaterial fabrication, since they provide the required synthesis conditions and the level of control of the characteristics of the resulting NPs by adjusting the experimental parameters.

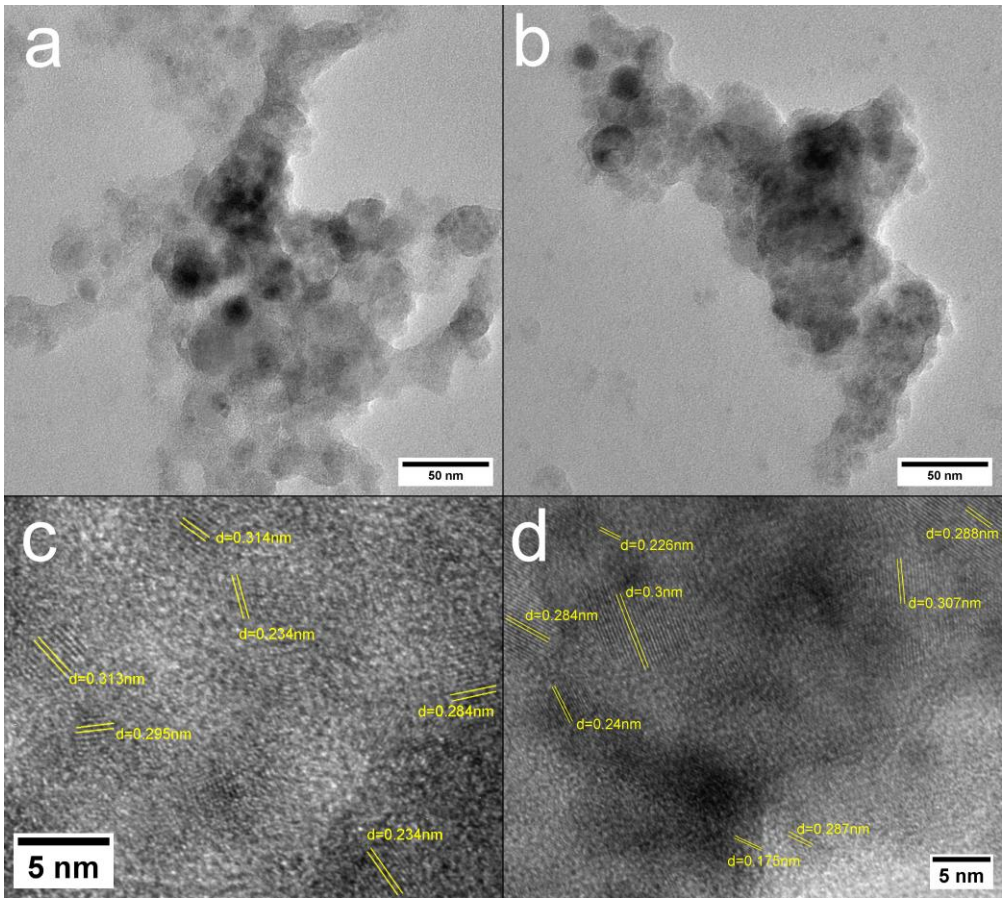

Fig. 1. Transmission electron microscopy (TEM) images with low (a, b) and high resolution (c, d) of silicon-tin NPs formed in the solution after laser ablation of tin-covered silicon target with a Bessel (a, c) and annular (b, d) beam profiles

In this work, the synthesis of $Si_{1-x}Sn_x$ alloyed NPs were performed by laser processing of a silicon wafer with a tin thin film deposited on its surface with a variation in the spatial profile of the incident laser beam. The synthesis procedure includes scanning of focused Nd:YAG laser radiation (1064 nm) in the ablation mode over the surface of a Si-Sn target immersed in a cuvette with a liquid (ethanol). Optimum scanning parameters for forming $Si_{1-x}Sn_x$ NPs were determined (scanning speed of 2.5-3 mm/s, laser spot diameter of 1.1-1.2 mm,

scanning step of 0.3 mm, laser pulse energy of 60 mJ/pulse at a pulse repetition rate of 10 Hz, duration of individual pulses of 10 ns). The main mechanisms of nanostructure formation are assumed to be laser-induced processes of rapid heating, subsequent joint melting and recrystallization at high cooling rates.

The formation of composite silicon-tin NPs was observed in the solution above the processed substrate, especially in the multiple scanning mode with complete removal of the tin film from the substrate. The obtained hybrid NPs had a diameter in the range of 5-50 nm, while the average diameter was about 17 nm (Fig. 1a, b) after laser ablation with a Bessel and annular beam profiles. The observed composition of the hybrid NPs and the corresponding structural changes are confirmed by the results of their study using high-resolution transmission electron microscopy (Fig. 1) with mapping of the elemental composition by the energy-dispersive X-Ray spectroscopy method (Fig. 2). As it is followed from (Fig. 1c, d) NPs with various atomic planes (d-spacing) are formed including hybrid $Si_{1-x}Sn_x$ NPs. The formation of hybrid NPs can be evidenced by nanocrystals with d-spacing in the range of 0.307–0.314 nm, which correspond to the silicon lattice deformed due to the introduction of tin atoms. As it follows from EDX analysis, the tin content in the synthesized NPs ranges from 1.4 to 4.2 at.% and it is determined by the laser exposure parameters (the energy of the incident radiation and the ablation time of the tin-covered silicon target).

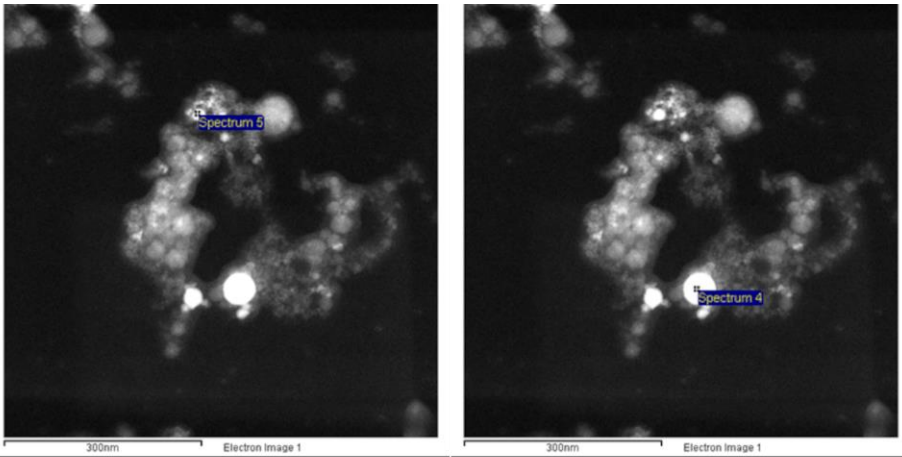

Element	Weight%	Atomic%
C K	66.01	84.85
O K	10.34	9.98
Si K	1.97	1.09
Cu K	11.22	2.73
Sn L	10.46	1.36
Totals	100.00	

Element	Weight%	Atomic%
C K	48.63	77.65
O K	10.00	11.99
Si K	4.12	2.82
Cu K	10.87	3.28
Sn L	26.37	4.26
Totals	100.00	

Fig. 2. Results of EDX analysis at a selected point of NPs formed as a result of laser ablation of Si wafer covered with Sn film by annular beam profile

The obtained particles have an optical band gap in the range of 0.72 - 0.73 eV, which is consistent with the literature data for the $Si_{1-x}Sn_x$ semiconductor alloy with a direct band gap. A correlation was found between the properties of NPs and the laser irradiation conditions. It was shown that the beam profile is an important factor affecting not only the ablation efficiency, but also the composition and morphology of the resulting nanostructures.

Acknowledgements. The work was supported by the Belarusian Foundation for Fundamental Researches under Grant F23RNF-156. Part of this work related to the NP characterization was supported by the Russian Science Foundation (grant No. 23-49-10044).

References

1. **Bürkle M., et al.** Adv. Funct. Mater., 30, 1907210 (2020).
2. **Tolle J., et al.** Appl. Phys. Lett., 89, 231924 (2006).
3. **Geisz J. F., et al.** Nat. Energy, 5, 326–335 (2020).
4. **Kurosawa M., et al.** Appl. Phys. Lett., 106, 171908 (2015).
5. **Timofeev V.A., et al.** Nanotechnology, 29, 154002 (2018).
6. **Lozac M., et al.** Materials today Energy, 7, 87-97, (2018).
7. **Jiang X.D., et al.** Mater., 12, 4076–4079 (2019).
8. **Lozac'h M., et al.** Scientific Reports, 13, 7958 (2023).
9. **Zhang D., et al.** Journal of Physics: Photonics, 3(4), 042002 (2021).

EFFECT OF PLASMA AND ION-BEAM TREATMENT ON GLASS SURFACE MORPHOLOGY

K.T. Logunov, D.A. Kotov, A.V. Aksiuchyts

Belarusian State University of Informatics and Radioelectronics, 6 P. Brovki Street, 220013, Minsk, Belarus, k.logunov@bsuir.by

Surface preparation of substrates plays a key role in surface modification technology and formation of functional coatings and layers. An important stage of surface preparation is the removal of contaminants and modification of its morphology to control adhesion properties. A number of chemical and physical methods are used for this purpose /1/. These include approaches such as mechanical treatment, ultrasonic cleaning, wet etching in acidic or alkaline solutions, and treatment with organic solvents. However, these approaches are often associated with a risk of recontamination, insufficient treatment uniformity or limited effectiveness in removing persistent impurities. In this regard, plasma and ion beam cleaning methods are of particular interest, as they provide a high degree of contaminant removal, precise effects on surface structure, and the ability to fine-tune process parameters /2, 3/. Various plasma and ion beam cleaning methods are currently regarded as some of the most effective and controllable surface preparation methods in high-tech manufacturing.

The present work is aimed at a comparative analysis of the influence of ion-beam cleaning, cleaning in inductively coupled plasma at reduced pressure and dielectric barrier discharge plasma at atmospheric pressure on the surface morphology of glass substrates by AFM methods.

The substrates made of optical glass of K8 grade with thickness of 0.7 mm and area of about 400 mm^2 were used as objects of research. Ion-beam cleaning and cleaning in high-density inductively coupled plasma were carried out in an experimental complex based on a modified equipment BY-1. The system was pumped to a base pressure of about 8×10^{-3} Pa.

Ion-beam cleaning was carried out in vacuum at a pressure of $2\text{-}4 \times 10^{-2}$ Pa by anode-layer ion source. Ion energy was 350-750 eV, treatment time was 1-2 min in stationary mode. The source-substrate distance was 200 mm, the discharge voltage was 800-2500 V and the discharge current was 50-100 mA. The generated ion beam has a conical shape, so its cross-section varies depending on the distance. In our experiments, the uniform treatment area was a 40 mm in diameter.

Cleaning in high-density inductively coupled plasma (ICP) was carried out at a chamber pressure of $7\text{-}8 \times 10^{-2}$ Pa. The power of the RF source was varied in the range of 300-1000 W, the treatment time was up to 5 min, and the frequency of the supply voltage was 13.56 MHz.

A coaxial system of plasma generation at atmospheric pressure developed at BGUIR /4/, Republic of Belarus, was used for substrate surface cleaning by dielectric-barrier discharge plasma at atmospheric pressure. The samples were processed for 1 min by low-temperature plasma of dielectric barrier discharge (DBD). Plasma source power 50 W. Flow rate was 143 L/h. The distance from the source to the sample was 10 mm.

Atomic force microscopy (AFM), in contact scanning mode, was used to analyze changes in surface morphology. Scanning was performed on area of 5×5 μm^2. The area in the center of the samples was selected for the studies. The obtained images were analyzed using specialized software to calculate roughness parameters including arithmetic mean height deviation (R_a), root mean square deviation (RMS), and 3D relief visualization.

Surface images were obtained for initial (untreated) samples as well as for samples after ion-beam cleaning, treatment in high-density inductively coupled plasma and exposure to dielectric barrier discharge plasma at atmospheric pressure. The main attention was given to the change of roughness parameters (R_a and RMS), the character of microrelief and the presence of structural defects resulting from different processing modes.

The experimental results are presented in the form of images of the surface of the treated samples and the original substrate in Fig. 1.

Ion cleaning leads to a noticeable increase in adhesion parameters, which is due to both the achievement of atomic surface purity and its activation, and the creation of a sufficiently developed micro- and nano-relief of the surface. R_a increases with increasing treatment time.

Unlike ion beam cleaning, where high-energy ions can damage the surface (causing amorphization, sputtering or even heating), atmospheric plasma generates metastable atoms, radicals and low-energy electrons (mainly due to active radicals rather than ions). This is especially important for glass, as its structure can be disrupted by aggressive processing, impairing film morphology. In addition, atmospheric plasma generates active forms of oxygen and nitrogen that oxidize organic contaminants (fats, adsorbed hydrocarbons), turning them into volatile compounds (CO_2, H_2O). Also, the creation of polar groups (-OH, -$COOH_2$=O) on the glass surface improves the wettability and adhesion of the film /4/. In fact, the treatment increases hydrophilicity /5/, but does not lead to a significant change in nanoscale topography.

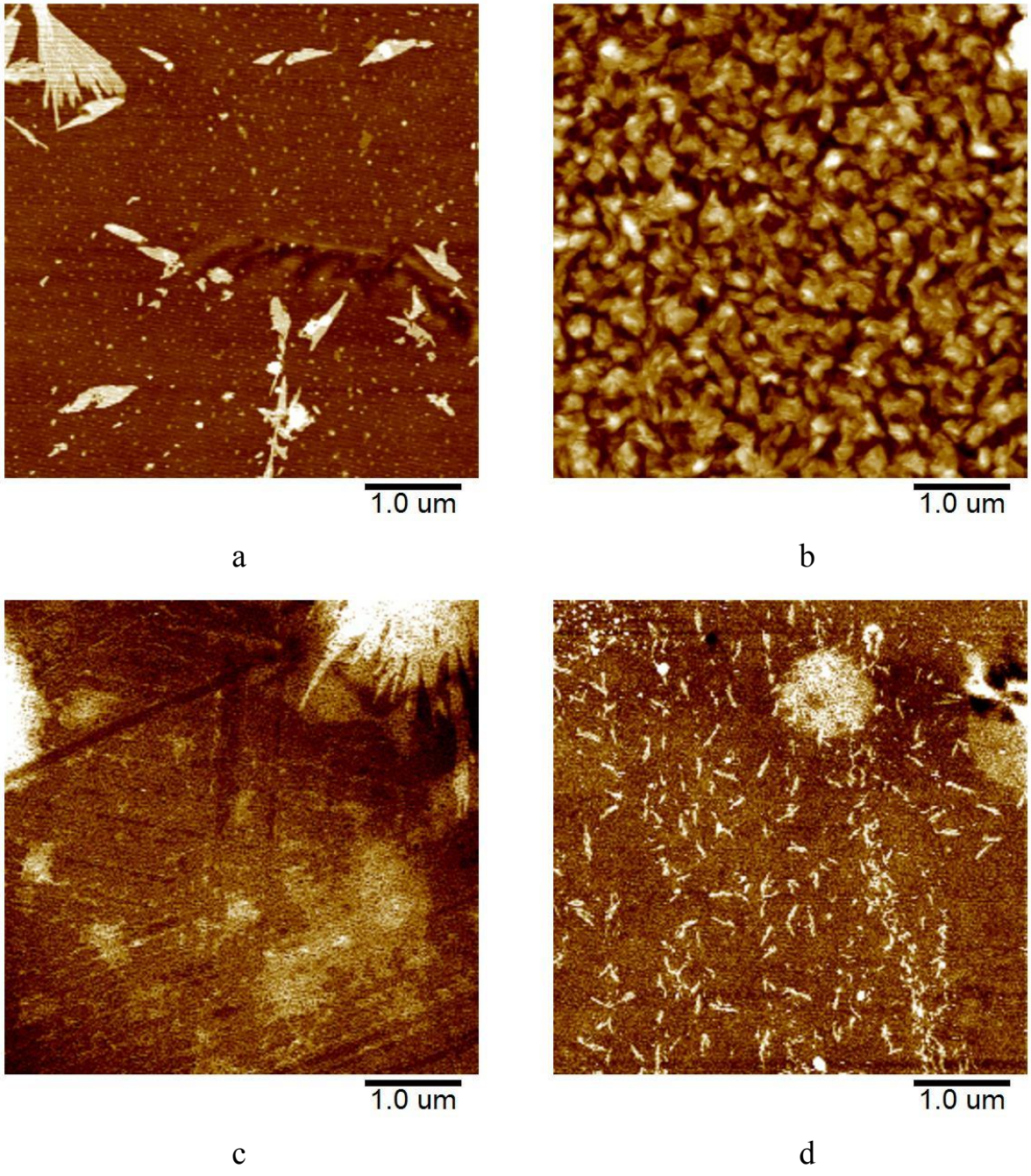

Fig. 1. AFM images of the surface of glass substrates: a) before treatment, b) after ion-beam cleaning c) after cleaning by atmospheric plasma d) after cleaning in high-density plasma

Cleaning in ICP plasma provides uniform cleaning and activation of the surface with a precise impact on the surface. This is due to the lower particle energy (electrons: 10-25 eV, ions: 5-15 eV) compared to ion-beam methods and the absence of undesirable influence from the external environment, as in the case of treatment in atmospheric plasma. There is an increase in surface energy and a slight increase in roughness.

The average roughness of the original glass surface was 1.0 nm. Comparative analysis shows that ion beam cleaning has a rather strong influence on the morphology of the treated surface (R_a=5,56), while high-density inductively coupled plasma (R_a=0,749) and dielectric barrier discharge plasma at atmospheric pressure (R_a=2,14) allow precision cleaning and modification of the surface of glass substrates without significant changes in their morphology.

Different methods of plasma and ion beam treatment have different effects on the morphology of glass substrate. Ion beam cleaning can be used for intensive contaminant removal, but requires precise parameter control as it significantly alters the surface morphology and structure of the near-surface layers. Atmospheric plasma is a promising method for fast and gentle treatment. ICP plasma provides the most effective combination of cleaning and surface activation effects. The obtained data can be used to optimize the processes of substrate cleaning for ultrathin film deposition technology, bonding, etc.

References

1. Luchkin, A. G. Surface cleaning of substrates for coating by vacuum-plasma methods / A. G. Luchkin, G. S. Luchkin // Bulletin of Kazan Technological University. - 2012. - № 15. - C. 208-210.
2. J. Sun, Y. Yu, J. Tang, Y. Zeng and J. Chen, "Plasma Cleaning Technology: Mechanisms, Influencing Factors, and Applications," in IEEE Access, vol. 13, pp. 37221-37242, 2025
3. Rauschenbach, B. (2022). Ion Beam Deposition and Cleaning. In: Low-Energy Ion Irradiation of Materials. Springer Series in Materials Science, vol 324. Springer, Cham.
4. A. Aksyuchits, D. Kotov, K. Logunov, A. Osipov / Research characteristics of plasma jet generated by coaxial dielectric barrier discharge at atmospheric pressure / Plasma Physics and Plasma Technology: IX International conference (Minsk, 12-16 september, 2022) / B.I. Stepanov Institute of Physics Netional Academy of Sciences of Belarus - Minsk, 2022. - 87 - 90 p.
5. Y. V. Zaporozhchanka, A. V. Aksiuchyts, K. T. Logunov, D. A. Kotov / Concentration of aeroions, charged and excited particles in plasma at atmospheric pressure / Youth in Science - 2023 : abstracts of the XX International Scientific Conference of Young Scientists (Minsk, September 20-22, 2023): agrarian, biological, humanities and arts, medical, physical, mathematical, physical-technical, chemistry and earth sciences / National Academy of Sciences of Belarus, Council of Young Scientists ; editor: V. G. Gusakov (chief editor) [and others]. - Minsk : Belaruskaya navuka, 2023. - 589 - 592 с.

MODIFICATION OF CR-VN COATINGS ON SILICON BY LOW INTENCITY NANOSECOND BICHROMATIC IRRADIATION

V. Lychkouski, A. Chumakov, I. Nikonchuk, V. Aniskevich

B.I. Stepanov Institute of Physics of the NAS of Belarus, Minsk, Belarus,
e-mail: v.luchkouski@dragon.bas-net.by

Abstract. *Action of series of low intensity (~10^1 MW/cm^2) bichromatic laser pulses with wavelengths 355 and 532 nm on Cr-VN coating on silicon substrate was carried out. Dependencies on interpulse time interval and order in which pulses follow of irradiated spots morphology changes on investigated coating, as well as visual look and change in atomic composition of surrounding aureoles was established. Significant change of aureoles coloring was observed for different regimes of laser bichromatic irradiation. Change in atomic composition of O, N and C was approximately several weight %.*

Introduction. Deposited coatings can possess different properties (roughness and porosity, different values of adhesion and microhardness) depending on method and means of its production, for example pulsed laser or magnetron deposition. Properties of such coatings not always suffice requirements depending on area. Needed enhancement or correction of properties of deposited coatings can be achieved by laser irradiation or plasma flows in different conditions, such as all kinds of liquid or gas mediums /1-3/. Laser modification of materials and deposited coatings seems particularly promising, thanks to possibility to strictly control parameters of acting laser radiation, as well as result of performed modification. Understanding of main principles and research for optimal regimes for laser modification materials is of great importance. Use of bichromatic laser radiation can allow its utilization even more effectively.

Experimental. The installation is based on two Nd: YAG lasers and synchronization system which provide generation of combined nanosecond laser pulses with wavelengths 355 and 532 nm and pulse duration of 18 and 15 ns respectively. Pulses follow in controlled order and time interval between them. The coaxial beam from both lasers was formed with spectral splitter and focused on sample's surface in calculated spot diameter of 172 μm (λ = 355 nm) and 223 μm (λ = 532 nm). Surface of irradiated 400 μm thick silicon samples with Cr-VN coatings studied using optical microscope as well as TESCAN VEGA 3 (TESCAN, Czech Republic) scanning electron microscope (SEM) fitted with power dispersive X-ray spectroscopy (EDS) devise.

Results and discussion. Investigated Cr-VN coatings on silicon substrate was irradiated by series of 10 combined bichromatic laser pulses with intensities q_{355} = 17,3 MW/cm^2 и q_{532} = 18,6 MW/cm^2 and interpulse time interval ranged

from −12 до +12 μs (negative value of interpulse time interval corresponds to leading action of 355 nm laser pulses). Since spots irradiated by 355 and 532 nm laser pulses were partially overlapped, both optical and SEM images of irradiated samples clearly show areas of monochromatic as well as bichromatic laser action (fig. 1). Laser irradiated areas surrounded with crater rim and deepening can be clearly seen inside irradiated spot. Optical microscopy images of Cr-VN coatings (*a-d*) show presence of colored aureole around irradiated spots. It is possible to distinguished following areas for all regimes of laser action: laser irradiated area, "middle" blue and "far" dark-brown areas of aureole. Laser irradiation with 355 nm leading action formed additional "close" bright-brown area.

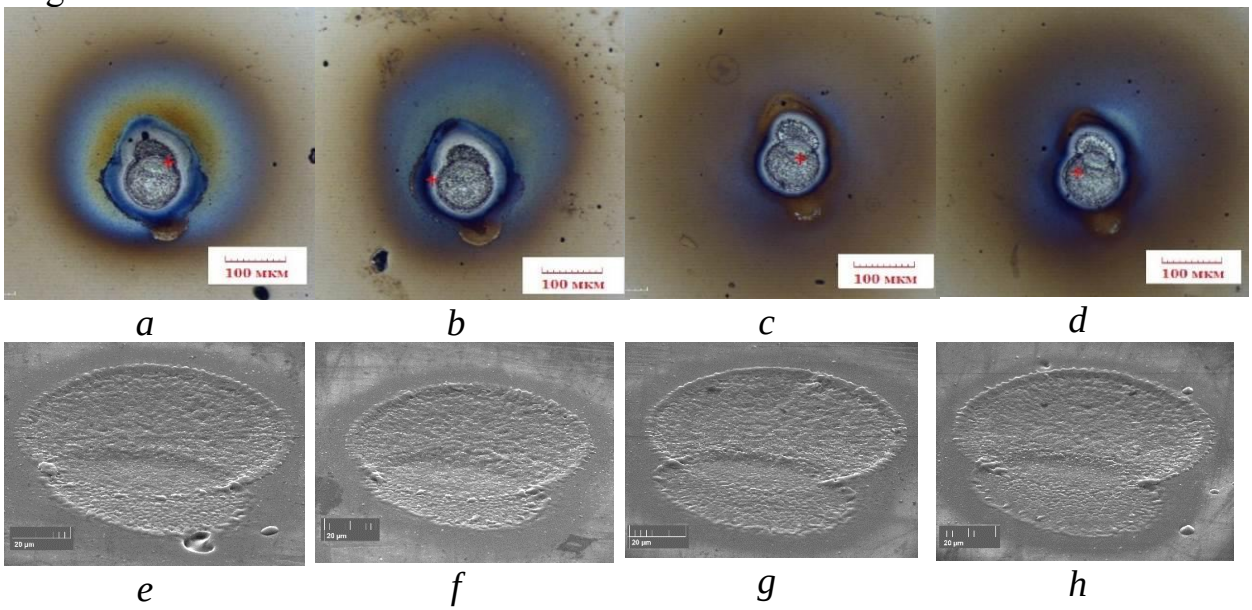

Figure 1. Optical and SEM images of Cr-VN coatings on silicon substrate, irradiated by bichromatic laser pulses with λ = 355 and 532 nm and q_{355} = 17,3 MW/cm^2 и q_{532} = 18,6 MW/cm^2 (interpulse time interval $\Delta\tau$ = −12 μs (*a*, *e*), −1,4 μs (*b*, *f*), +1,4 μs (*c*, *g*), + 12 μs (*d*, *h*), negative value of interpulse interval corresponds to leading action of 355 nm laser pulses)

SEM images of irradiated spots on treated coatings shows grain-like microstructure surrounded with crater rim on edge of 355 and 532 nm laser spots (fig. 1 *e-h*) and its overlapping (area of bichromatic action). Thanks to SEM images been taken with 75° angle it is clearly seen that removal of material is bigger inside bichromatic irradiated area. Composition of laser modified Cr-VN coatings on silicon substrate within laser irradiated spots and different areas of aureole (fig. 2) was studied by means of electron microscopy with EDS spectrometry.

Analysis of presented results demonstrate that bichromatic laser action with wavelengths 355 and 532 nm and power density ~ 18 MW/cm^2 lead to change in dynamics of atomic composition when changing interpulse time interval and order in which pulses follow. Change in presence of Oxygen correlate with such

for Carbon and inversely correlate for Nitrogen. Which means intensification of oxidation and carbonization processes due to mitigation of nitrification. Maximum nitrification of coatings within irradiated spot achieved for 1.4 to 4 μs leading action of 532 nm laser pulses, while in most aureole areas nitrification maximum is observed for 1.4 μs leading action of 355 nm laser pulses.

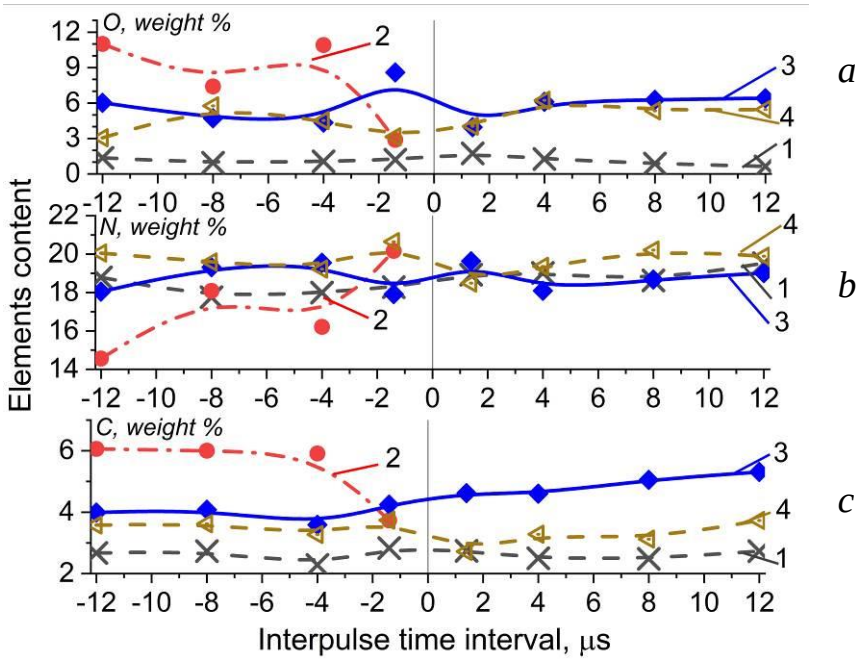

Figure 2. Relative composition of O (*a*), N (*b*), and C (*c*) on surface of laser irradiated Cr-VN coating on silicon substrate in areas of: partial overlapping (*1*) of laser spots with wavelengths 355 and 532 nm (q_{355} = 17,3 MW/cm^2 и q_{532} = 18,6 MW/cm^2), in "close" brown (*2*), "middle" blue (*3*) and "far" brown area of aureole (*4*). Composition measured by means of EDS.

Conclusions. Action of bichromatic laser pulses with λ = 355 and 532 nm on Cr-VN films on silicon substrate was investigated. Was shows forming of colored aureoles around irradiated spots and formation of grain-like microstructure inside laser craters. Dependance of size and coloring of aureoles on time interval and order in which laser pulses follow take place.

Results of colored aureoles EDS spectroscopy show that dynamics (when changing interpulse time interval and order in which pulses follow) of change in content of Oxygen correlate for content of Carbon and inversely correlate for Nitrogen. Relative composition of this elements is nonlinear dependent of interpulse time interval and order in which they follow, what suggest plasma-chemical nature of this phenomenon. Maximum nitrification of coating inside irradiated laser spot was observed for 1.4 – 4 μs leading action of 532 nm pulses and on most areas of aureoles for 1.4 μs leading action of 355 nm laser pulses.

Acknowledgements. The work was supported by the Belarusian Republican Foundation for Fundamental Research (Grant No. F22SRBG-003).

The authors are grateful to D.S. Milovanović for providing samples with Cr-VN coatings.

References

1. **Chumakov, A. N. et al.** Physica Scripta. 162, 014016 (4pp) (2014).

2. **Munther, M. et al.** Engineering Research Expresss. 2, 022001 (2020). doi:10.1088/2631-8695/ab9b16

3. **Osonkie V. et al.** J. Chem. Phys. 153, 144709 (2020). https://doi.org/10.1063/5.0027996

MORPHOLOGY CHANGE OF CR-VN COATINGS ON SILICON USING LOW INTENCITY NANOSECOND LASER IRRADIATION

V. Lychkouski, A. Chumakov, I. Nikonchuk, V. Aniskevich

B.I. Stepanov Institute of Physics of the NAS of Belarus, Minsk, Belarus,
e-mail: v.luchkouski@dragon.bas-net.by

Abstract. *Changes of surface morphology due to action of series from 1 to 30 laser pulses of low intensity (~10^1 MW/cm^2) and wavelengths 355 and 532 nm on Cr-VN coatings on silicon was carried out. Cracking of coating surface that with increasing number of pulses transformed into grain like microstructure was revealed, as well as forming of "raise" in ring area surrounding irradiated spot.*

Introduction. Deposited coatings can possess different properties (roughness and porosity, different values of adhesion and microhardness) depending on method and means of its production, for example pulsed laser or magnetron deposition. Properties of such coatings not always suffice requirements depending on area. Needed enhancement or correction of properties of deposited coatings can be achieved by laser irradiation or plasma flows in different conditions, such as all kinds of liquid or gas mediums /1-3/. Laser modification of materials and deposited coatings seems particularly promising, thanks to possibility to strictly control parameters of acting laser radiation, as well as result of performed modification. Understanding of main principles and research for optimal regimes for laser modification materials is of great importance.

Experimental. The installation is based on two Nd: YAG lasers and synchronization system which provide generation of combined nanosecond laser pulses with wavelengths 355 and 532 nm and pulse duration of 18 and 15 ns respectively. Pulses follow in controlled order and time interval between them. The coaxial beam from both lasers was formed with spectral splitter and focused on sample's surface in calculated spot diameter of 172 μm (λ = 355 nm) and 223 μm (λ = 532 nm). Surface of irradiated 400 μm thick silicon samples with CrVN coatings studied using optical microscope as well as TESCAN VEGA 3 (TESCAN, Czech Republic) scanning electron microscope (SEM) fitted with energy dispersive X-ray spectroscopy (EDS) devise.

Results and discussion. Irradiation of Cr-VN coatings on silicon substrate was carried out in ambient air with energy densities of ≈ 31 and 18 MW/cm^2 for laser emission λ=355 and 532 nm respectively. Each experiment varied number of laser pulses in series (1, 5, 10 and 30 pulses) (fig. 1, 2). Experiments show that Cr-VN coatings on silicon are subjected to significant structural modification inside irradiated spot even after action of single laser pulses with

wavelength 355 nm and power density 31 MW/cm^2 (fig. 1 *a, e*), and action of laser pulses with wavelength 532 nm with even smaller power density of 18 MW/cm^2 (fig. 2 *a, e*).

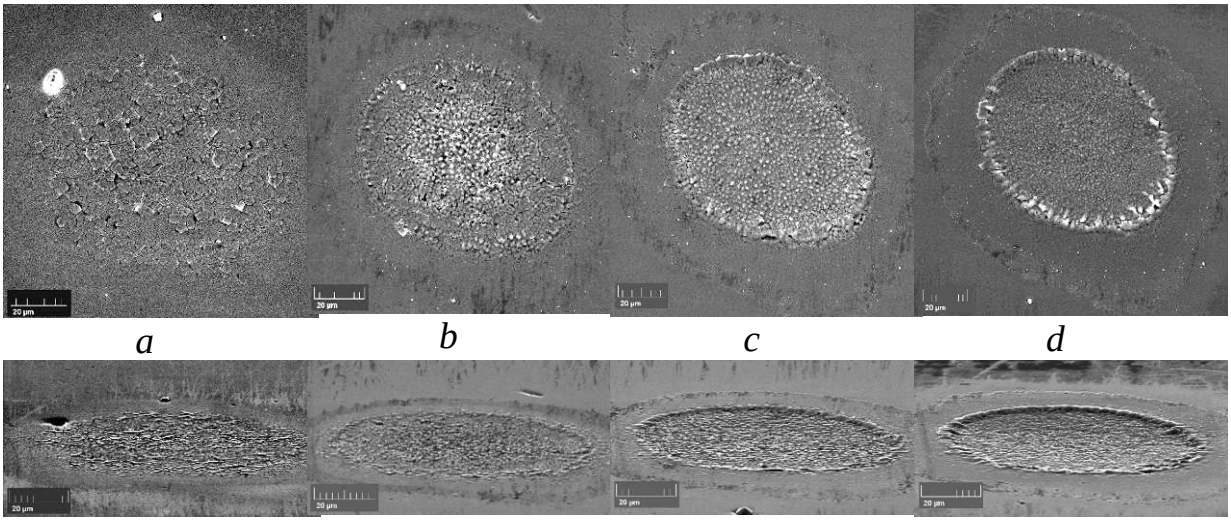

a *b* *c* *d*

e *f* *g* *h*

Figure 1. SEM images of Cr-VN coatings on silicon substrate after action of 1 (*a, e*), 5 (*b, f*), 10 (*c, g*) and 30 (*d, h*) laser pulses with λ = 355 nm и q_{355} = 31 MW/cm^2. Images *e-h* made with 75° to surface normal.

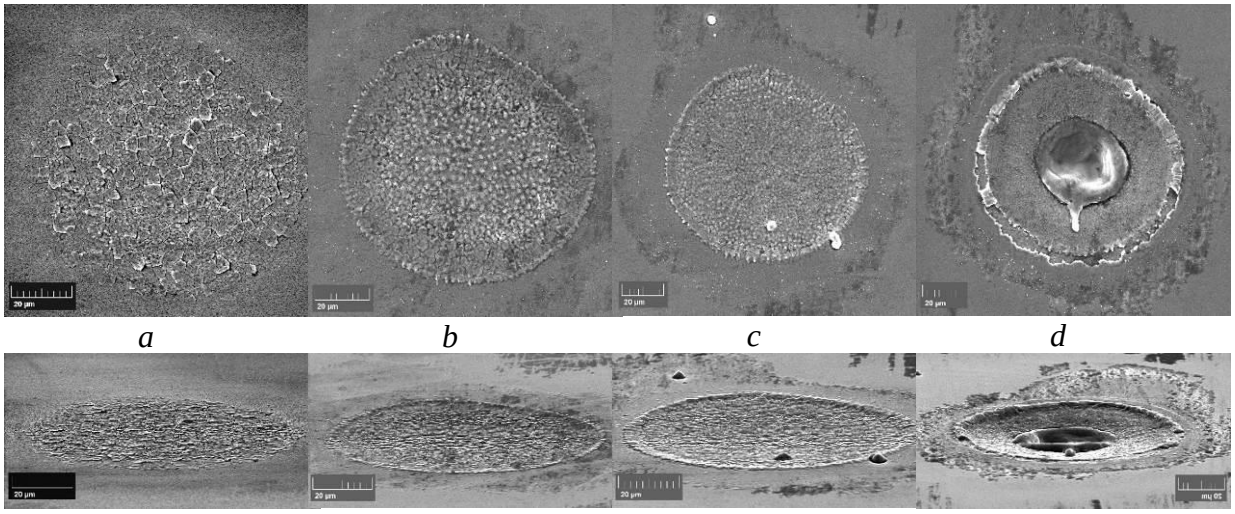

a *b* *c* *d*

e *f* *g* *h*

Figure 2. SEM images of Cr-VN coatings on silicon substrate after action of 1 (*a, e*), 5 (*b, f*), 10 (*c, g*) and 30 (*d, h*) laser pulses with λ = 532 nm и q_{355} = 18 MW/cm^2. Images *e-h* made with 75° to surface normal.

It is seen that action of a single laser pulse with both wavelengths lead to abundant cracking of coating surface (fig. 1 *a, e,* 2 *a, e*). Magnified version of figure 1 *d* and 2 *d* allows us approximate thickness of "scales" as of no more than 1 μm, which is less than thickness of coating (≈3 μm). This mean

delamination of coating itself take place by inner mechanical stress, not its separation from substrate.

Increase in number of laser pulses in series for laser irradiation using both wavelengths lead to melting of "flaking" surface and formation of distinct grain-like microstructure (fig. 1 *b-d*, fig.2 *b-c*), while some minor traces of cracking remain on the outer edge of formed laser crater's rim. Grain-like microstructure, produced by melting of mentioned "flakes", start to form closer to center (fig. 1, 2 *b, f*). With raise of laser pulses number in series this area grows to overall irradiated spot size and distribution of "grains" become more and more even (fig. 1 *d, h*, 2 *c, g*). Along with formation of grain-like structure, removal of film's material take place, which can be clearly seen on figures 1 (*e-g*) and 2(*e-g*) that are made with 75° angle to surface normal.

Results of EDS spectroscopy demonstrate change of relative composition of O and N atoms with change of laser irradiation regimes. Laser irradiation of sample with both wavelengths lead to increase of O atoms content from ≈ 1 weight % for case of single laser pulse action to saturation with value of ≈ 2 weight % for case of 5 and more laser pulses action. 355 nm laser irradiation led to opposite change of N atoms content: fall from 21 weight % for case of single pulse action to 20 weight % for case of 5 and more laser pulses. 532 nm laser irradiation led to somewhat similar dynamics of N content. But for case of 30 pulses action a raise to 22 weight % in N content was observed, which can be result of melting all the way through coating to material of substrate.

It is worth noting presence of destruction caused by absorption of laser emission on defects of Cr-VN coating scattered all around surface. Also, formation of more significant destruction caused by 532 nm laser pulses take place despite lower power density of laser emission than for case of 355 nm laser irradiation (q_{532} = 18 MW/cm^2 against q_{355} = 31 MW/cm^2). Action of single 532 nm laser pulse caused more developed cracked structure on coating surface (fig. 2 *a, e*), while series of 30 laser pulses cause melting through Cr-VN film at the center of laser irradiated spot and start of substrate material melting and removal (fig. *d, h*). It is especially worth noting that initial destruction of Cr-VN coating in laser spot's center followed by a little "raise" of irradiated and small surrounding area (~20 μm) for cases of laser action with both wavelengths.

Conclusions. Action of 355 and 532 nm nanosecond laser pulses on Cr-VN films on silicon substrate was investigated. Revealed cracking formation of film's surface after action of single laser pulses, that followed by change in surface morphology and formation of grain-like microstructure with increase of laser pulses number in series from 1 to 30. Increase in number of laser pulses in series also caused decrease of microstructure grain's size, increase and saturation of O content with corresponding decrease of N content (with

exception of 30 pulses 532 nm laser irradiation case, when raise of N content was observed).

Acknowledgements. The work was supported by the Belarusian Republican Foundation for Fundamental Research (Grant No. F22SRBG-003).

The authors are grateful to D.S. Milovanović for providing samples with Cr-VN coatings.

References

1. **Chumakov, A. N. et al.** Physica Scripta. 162, 014016 (4pp) (2014).

2. **Munther, M. et al.** Engineering Research Expresss. 2, 022001 (2020). doi:10.1088/2631-8695/ab9b16

3. **Osonkie V. et al.** J. Chem. Phys. 153, 144709 (2020). https://doi.org/10.1063/5.0027996

LASER MODIFICATION OF CR-VN COATING ON STEEL IN LIQUID

V. Lychkouski, A. Chumakov, I. Nikonchuk, V. Aniskevich

B.I. Stepanov Institute of Physics of the NAS of Belarus, Minsk, Belarus; e-mail: v.luchkouski@dragon.bas-net.by

Abstract. *Laser action of paired nanosecond laser pulses (λ = 355 and 532 nm) on Cr-VN coating on steel substrate in 20% alcohol solution was investigated in comparison with laser action in air. Established change in visual look of modified area and their atomic composition after switching from air to liquid medium. Spots irradiated by series of 10 pulses showed absence of oxygen atoms and up to 1.5 times more carbon (in weight %), while aureole demonstrate significant presence of oxygen after same laser irradiation.*

Introduction. Processing of materials by short laser pulses with nanosecond length gives wide possibilities for modification of its properties /1, 2/. Development of laser methods for the formation of wear-resistant iron-based coatings is of significant interest /3/. Given its good chemical, mechanical and tribological properties, a nitrides of transition metals can be used as such hard wear-resistant coatings, applied on surface of tools and machinery parts. Coatings made from chromium nitride (CrN) form hard, chemically inert layer, resistant to aggressive environments, but such coatings have high friction coefficient which makes difficulties for its wide use. CrVN coatings considered as more promising, due to its high hardness, chemical inertness and relatively low friction coefficient of vanadium nitride /4-6/.

Current work devoted to search for possibilities of laser modification of structure and composition of CrVN coatings on steel in liquid by action of nanosecond laser radiation (LR) pulses with wavelengths λ = 355 and 532 nm.

Experimental. The installation is based on two Nd: YAG lasers and synchronization system which provide generation of combined nanosecond laser pulses with wavelengths 355 and 532 nm and pulse duration of 18 and 15 ns respectively. Pulses follow in controlled order and time interval between them. The coaxial beam from both lasers was formed with spectral splitter and focused on sample's surface in calculated spot diameter of 172 μm (λ = 355 nm) and 223 μm (λ = 532 nm). Sample was placed under ~1.5 cm of 20% C_2H_5OH solution in distillated water. Alcohol used to inhibit formation of oxides but higher concentration of alcohol increase chance of open fire. Surface of irradiated samples with CrVN coatings studied using optical microscope as well as TESCAN VEGA 3 (TESCAN, Czech Republic) scanning electron microscope (SEM) fitted with energy dispersive X-ray spectroscopy (EDS) devise.

Results and discussion. Irradiation of CrVN in liquid by 1 and 10 bichromatic laser pulses ($q_{355} = q_{532} = 120$ MW/cm^2) does not induce formation

of vast colored areas around laser crater what is visible on Fig.1 (*b-c, e-f*) unlike situation of laser action in ambient air Fig.1 (*a, d*). Only continued action of 10 pulses led to notable transformation within laser crater (Fig. 1 *c*, *f*).

Laser action in liquid caused intensive formation of bubbles in laser irradiated area that traveled to liquid's surface. These bubbles interacted and scattered LR significantly, up to absence of laser ablation. Overall flow of bubbles continued for ~1-2 second. Another ~1 second took bubbles to dissipate on liquid's surface and travel away from LR path.

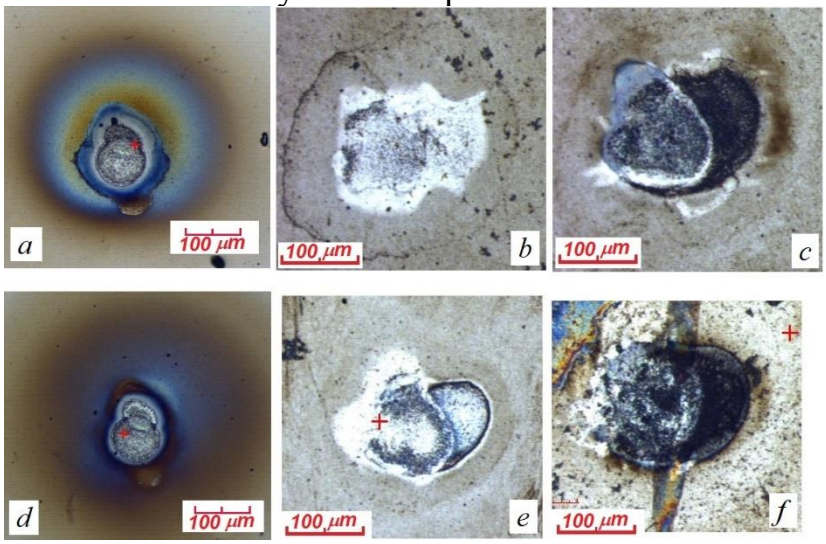

Fig. 1. Optical images of spots irradiated by 355 and 532 nm bichromatic laser pulses in air (*a, d*) with $q_{355} = q_{532} \approx 120$ MW/cm^2 and liquid (*b-c, e-f*) with $q_{355} = q_{532} \approx 18$ MW/cm^2. Irradiation regimes: *a* – 10 pulses in air, interpulse time interval $\Delta\tau = -12$ μs; *b* – 1 pulse in liquid, $\Delta\tau = -12$ μs; *c* – 10 pulse in liquid, $\Delta\tau = -12$ μs; *d* – 10 pulses in air, interpulse time interval $\Delta\tau = +12$ μs; *e* – 1 pulse in liquid, $\Delta\tau = +12$ μs; *f* – 10 pulses in liquid, $\Delta\tau = +12$ μs. (negative value of time interval corresponds to leading action of 355 nm pulses)

Area of coating's surface modified by scanning with bichromatic laser pulses ($q_{355}=q_{532}\approx450$ MW/cm^2) shows both structured surface morphology (Fig.2 *a*, *b*) and coloring of irradiated scanned area (Fig. 2 *c*, *d*) with almost absent aureole around. Structuring of morphology was influenced by two major factors. Increased pressure, induced by laser ablation in liquid and interaction with flow of bubbles mentioned above. In order to neglect influence of bubbles, laser pulses repetition rate was set to lowest possible of 1 Hz, but even so, part of pulses didn't ablated material because of scattering on these bubbles. Laser irradiation with leading action of 355 nm pulses caused such "misfires" about ~1.5 times more often. Coloring of surface areas scanned by laser pulse with leading action of 355 nm consist of more bright, even white, colors. While case of 532 nm leading action induces dark blue and brown colored areas, which presumably caused by more intensive plasma chemical processes. Presumably, white areas have such color because of induced surface roughness and dark ones – because of carbonization.

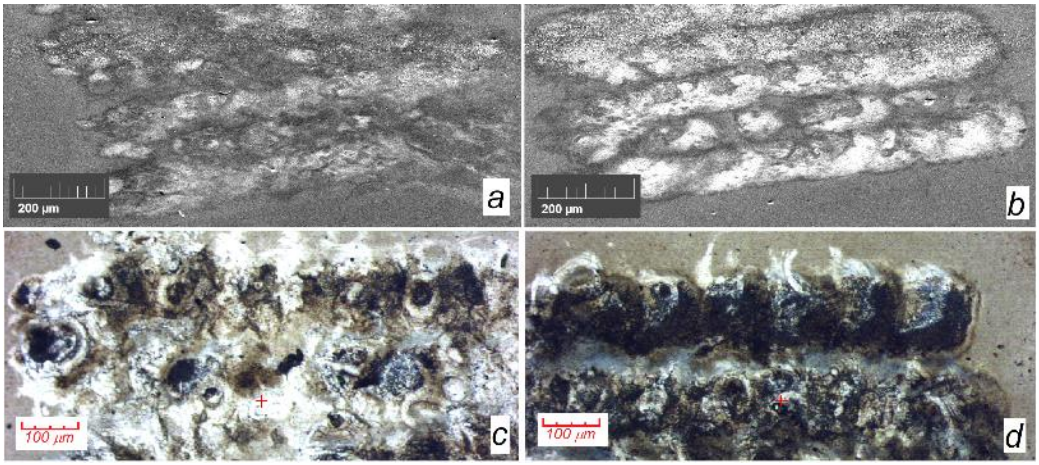

Fig. 2. Sample's area scanned by action of bichromatic laser pulses with λ = 355 and 532 nm (q_{355}=q_{532}=450 MW/cm^2) and interpulse time intervals Δτ = −8 μs (*a*, *c*) and + 8 μs (*b*, *d*). Laser pulse repetition rate 1 Hz

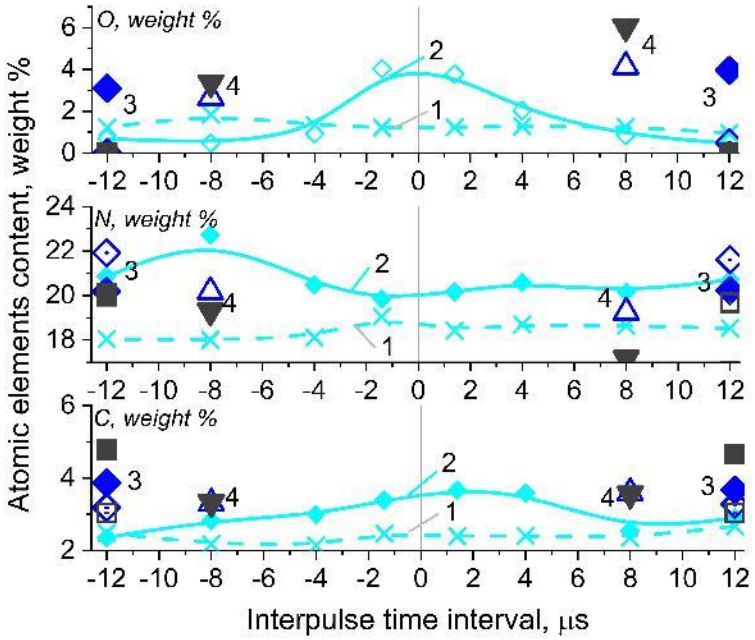

Fig. 3. Atomic elements composition for different bichromatic (λ = 355 and 532 nm) laser irradiation regimes in air (*1*, *2*) with $q_{355} = q_{532} \approx 120$ MW/cm^2 and liquid (*3*, *4*) with $q_{355} = q_{532} \approx 18$ MW/cm^2. 1 – irradiated spot area, 2 – aureole area, 3 – irradiated spot (*black marks*) and surrounding area (*blue marks*) for 1 (*hollow marks*) and 10 (*filled marks*) bichromatic laser pulses, *4* – inside of area scanned (*black filled marks*) by $q_{355} = q_{532} \approx 450$ MW/cm^2 bichromatic laser pulses and its surrounding (*blue hollow marks*)

Atomic composition of irradiated areas due to formation of oxides, nitrides and carbides of coating's material was studied by mean of EDS (Fig. 3).

It shows absence of oxygen in areas irradiated by 1 and 10 bichromatic laser pulses ($q_{355} = q_{532} \approx 120$ MW/cm^2) both for leading action of 355 and 532 nm laser pulses. But oxygen content for surroundings of laser crater increased from 0.2 to 3-4 weight %. Concentration of nitrogen decreased from

~23 to ~20 weight % with exception for case of 10 bichromatic pulses action with interpulse time interval $\Delta\tau = +12$ μs, where decrease was down to ~16.5 weight %. Carbon content decreased by ~0.2 weight % for single bichromatic action and increased from ~3.2 to 4.7 weight % after irradiation by 10 laser pulses both for cases of 355 and 532 nm leading action. Increase of iron contents at cost of chrome and vanadium was observed as long as count of bichromatic pulses in series increased, with leading action of 355 nm being more effective at removing coating's material. Area scanned by bichromatic LR ($q_{355} = q_{532} \approx$ 450 MW/cm^2) showed atomic composition with greatly increased oxygen content. Increase was from 0.2 to 3.4 weight % for −8μs leading action of 355 nm laser pulses and from 0.2 to 6 weight % for +8μs leading action of 532 nm laser pulses, which corresponds to colors of laser scanned areas pictured in Fig. 2 *e*, *f*.

Conclusions. Laser modification of CrVN coating on steel in 20% alcohol liquid medium by bichromatic laser pulses was studied. Irradiation in liquid with $q_{355} = q_{532} \approx 120$ MW/cm^2 bichromatic LR led to absence of colored areas around laser crater. With EDS analysis showing absence of oxygen in irradiated crater, but increase from 0.2 to 3-4 weight % in surrounding area. Continues action of at least 10 combined laser pulses also caused increase of carbon content in irradiated crater from 3.2 to 4.7 weight %. Bichromatic laser action caused bubbles flow formation, that interacted and scattered LR up to absence of laser ablation. Scanning bichromatic laser action formed developed surface morphology caused by increased pressure in liquid and by interaction with mentioned bubbles flow, which can be excluded when organizing laminar fluid flow.

Acknowledgements. The work was supported by the Belarusian Republican Foundation for Fundamental Research (Grant No. F22SRBG-003).

The authors are grateful to D.S. Milovanović for providing samples with CrVN coatings.

References

1. **Chumakov A.N., et al.** Physica Scripta, **162**, (2014) 014016.
2. **Chumakov A., Luchkouski V., et al**. Techn. Physics, **67**, (2022) 16–24.
3. **Devoino O.G., et al.** *Technology of wear-resistant iron-based coatings formation using laser processing methods*. Misnk; BNTU, 2020. (in Russian).
4. **Petrović S., et al.** Opt Quant Electron., **50**(208), (2018)
5. **Aissani L., et al.** *Thin Solid Films*, **732**, (2021), 138782.
6. **Kuprin A.S., et al.** *Tribology International*, **165**, (2022), 107246.

COMPOSITE MATERIAL BASED ON NATURAL HIGH MOLECULAR WEIGHT COMPOUND FILLED WITH ACRYLIC EMULSIONS MODIFIED BY LOW ENERGY ION FLOW

K. I. Maksimova[1], I. I. Latfullin[1], G. R. Rakhmatullina[1], R.R. Kayumov [2]

[1] Kazan National Research Technological University, 68 Karl Marx Str., Kazan, Russia, lilatfullin@gmail.com

[2] Kazan National Research Technical University named after A.N. Tupolev-KAI, 10 Karl Marx Str., Kazan, Russia

Polymers are hold special positions in fur production. Leather tissue of fur is a natural high molecular weight compound, which have capillary-porous structure. Filled by polymers leather tissue of fur is similar to composite materials. Acrylic polymers are widely used to increase softness, fullness and the physical and mechanical performances of leather tissue of fur. The disadvantage of polymers used as fillers for capillary-porous structure materials is their limited diffusion and nonequilibrium distribution in the bulk. Thus, leather tissue of fur may have uneven properties across its area, which leads to a decrease in quality as a whole. In this regard, it is important to modify the polymers characteristics to ensure conditions for their uniform diffusion.

To regulate the polymers characteristics is known using low-energy ion flow (LEIF) generated in plasma of gas flow RF discharges at intermediate-pressure /1-5/.

In order to change the particle sizes of the filling polymers the influence of capacitively coupled and induction coupled RF discharges on the distribution of LP and TX acrylic emulsions particles was studied in this work. The particles size distribution was analyzed by the dynamic light scattering method /6-8/. The scattering angle was 173°. Particle size measurement errors are ±2%.

The LP acrylic emulsion modification carried out in two types of RF discharges at intermediate pressure.

Modification of LP acrylic emulsion by a low-energy ions flow generated in a capacitively coupled radio frequency discharge plasma jet (LEIF CCRF) was carried out in the mode: discharge power (W_{cd}) 700 W, treatment duration (τ_{cd}) 10 minutes, argon plasma-forming gas flow rate (G_{Ar}) 0.04 g/s, vacuum chamber pressure (p) 55 Pa.

Modification of LP acrylic emulsion by a low-energy ions flow generated in induction coupled radio frequency discharge plasma jet (LEIF ICRF) was carried out in the mode: discharge power (W_{id}) 0,1 kW, treatment duration (τ_{id}) 20 minutes, vacuum chamber pressure (p) 5 kPa.

Fig. 1 shows the particle size distribution of LP acrylic emulsion depending on the type of discharge.

It is known /9/ a polymerization process occurs in plasma, which is characterized by significant fragmentation and (or) redistribution of structural units or atoms in the original compound. At the same time, reactions occur involving particles of different chemical nature.

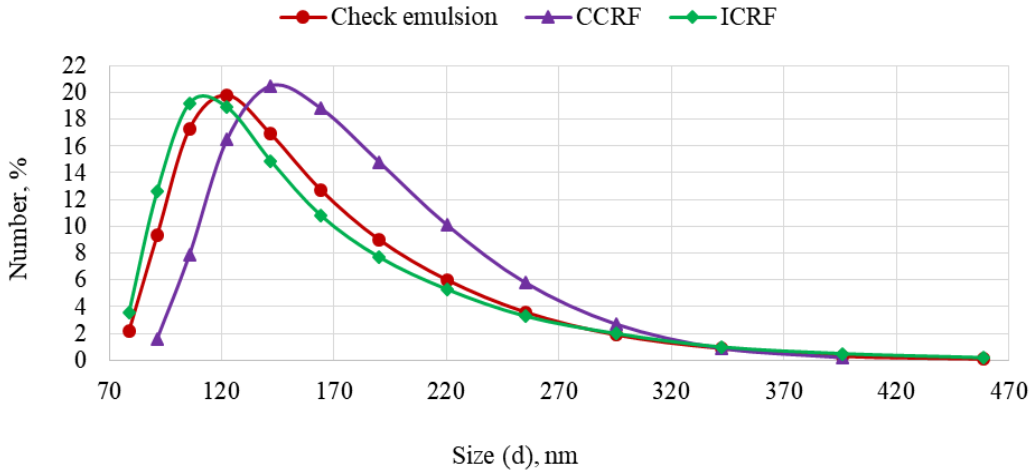

Fig. 1 – Particle size distribution of LP acrylic emulsion depending on the type of discharge

According to the presented Fig., it can be conclude that the particles fragmentation of LP acrylic emulsion occurs by the effect of the LEIF ICRF. As a result, the intensification of acrylic resin diffusion into the leather tissue and its uniform distribution in the bulk is expected.

The TX emulsion has a wider range of particle size distribution compared to the LP emulsion – from 58.77 nm to 825 nm. In this regard, the ICRF discharge used for modifying the TX emulsion. Thus, the TX emulsion particle size change occurs in the range of 58.77 nm-458.7 nm by LEIF ICRF effect. Fig. 2 shows the particle size distribution of TX acrylic emulsion.

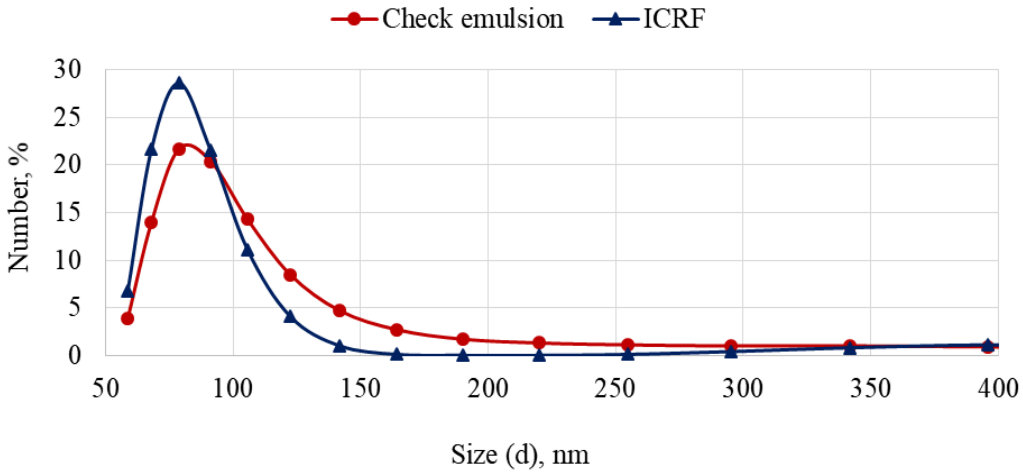

Fig. 2 – TX acrylic emulsion particles size distribution

Tables 1 and 2 provide summary data characteristics of acrylic emulsions.

Table 1 – LP acrylic emulsion characteristics

Emulsion	Polydispersity index	Polydispersity		Z-verage size, nm
		nm	%	
Check emulsion LP	0.124	65.4	35.2	185.5
Emulsion modified by LEIF CCRF	0.049	42.6	22.1	192.4
Emulsion modified by LEIF ICRF	0.147	74.3	38.3	194.1

Table 2 – TX acrylic emulsion characteristics

Emulsion	Polydispersity index	Polydispersity		Z-Average size, nm
		nm	%	
Check emulsion TX	0.510	456.9	71.4	639.9
Emulsion modified by LEIF ICRF	0.516	209.3	71.8	291.5

The concentration of acrylic emulsions was 10 g/dm^3. Physical and mechanical performances tested according to the following indicators: grain layer strength (σ_{gl}), grain layer elongation (ε_{gl}), tensile strength (σ), tensile elongation (ε) and module of elasticity. The module of elasticity indicator studied in the range of 2-5 MPa, since according to All-Union state standard fur materials must withstand a stretching of 4.9 MPa. Table 3 shows the results of physical and mechanical tests of fur sheepskin.

Table 3 – Physical and mechanical performances of fur sheepskin

Indicator	Check sample	LP check emulsion	LP LEIF ICRF	TX check emulsion	TX LEIF ICRF
σ_{gl}, MPa	6.6	9.3	7.4	12.2	12.8
ε_{gl}, %	62.7	82.9	69.0	72.5	75.5
σ, MPa	11.9	9.6	12.6	13.0	13.0
ε, %	105.8	90.0	107.0	85.1	79.0
Module of elasticity, MPa	12.3	11.0	15.4	14.0	15.3

According to the obtained results, the σ_{gl} increases by 12.1 %-93.9 % compared to the control sample in the case of modified emulsions LP and TX respectively. The tensile strength increases by 0.7 MPa-1.1 MPa in the case of filling the fur sheepskin with modified emulsions LP and TX respectively. The module of elasticity of samples filled with TX and LP modified emulsions increases by 24.4 %-25.3 % respectively. Thus, acrylic emulsions exhibit low structure formation ability, but show themselves as lubricating reagents in general.

References

1. **Shapoval G.S., Gorodysky A.V.** Uspekhi khimii, 42, 5 (1973) 854–880.

2. **Ponomarenko A.T., Tameev A.R., Shevchenko V.G.** Uspekhi Chemii, 87, 10 (2018) 923–949.

3. **Oulet R., Barbier M., Cheremisinoff P. et al**. Technological application of low-temperature plasma: Translated from English. Moscow: Energoatomizdat (1983).

4. **John R. Hollahan, Alexis T. Bell**. Techniques and applications of plasma chemistry. A Wiley-Interscience publication (1974)

5. **G. Blasek, G. Brauner et al**. Vakuum. Plasma. Technologien. Beschichtung und Modifizierung von Oberflachen. Teil 1

6. **Sultanova N.M., Belova I.A., Shabanova N.A., Popov K.I.** Advances in Chemistry and Chemical Technology, 25, 2 (2011) 45–50.

7. **Elizalde O., Leal G.P., Leiza J.R.** Particle & Particle Systems Characterization: Measurement and Description of Particle Properties and Behavior in Powders and Other Disperse Systems, 17,5-6 (2000) 236–243.

8. **Pivovarov A.A., Kravchenko A.V., Tishchenko A.P. et al**. Russian Chemical Journal, 57, 3-4 (2013) 134–145.

9. **Yasuda H.** Polymerization in plasma: Trans. from English. M: Mir (1988)

THE EFFECT OF THE LOW-ENERGY ION FLUX OF A LOW-PRESSURE HF PLASMA OF ARGON WITH AN ADMIXTURE OF NITROGEN AND OXYGEN ON THE MECHANICAL CHARACTERISTICS OF METALS AND ALLOYS

I. S. Abdullin[1], K. S. Mastyukov[2], S. V. Mironov[3], A. V. Shestov[4]

[1]LLC "Plazma VST" Russia 420081, Kazan, Kurskaya st. 27;
[2]Kazan National Research Technical University named after A. N. Tupolev – KAI, Russia, Kazan, Karl Marx St., 10
[3]Kazan (Volga region) Federal University, Russia, Kazan, Kremlevskaya St., 18, building 1
[4]Moscow Automobile and Road Construction State Technical University, Russia, Moscow, Leningradsky Ave. 64

Abstract: studies of changes in the physical and mechanical characteristics like residual stress of samples from materials have been carried out BT-1, BT-3, BT-6, BT-8, BT-9, 20X13, 40X13, 12X18H9T, 08X18, steel 45, steel 30.

The service life of products is often determined by the quality of the surface layer. Therefore, there is a need to improve the physical and mechanical characteristics of the surface layers of the products. One of the most effective ways to increase the durability of parts is to modify them with a stream of charged particles, which can reduce surface roughness, increase wear resistance, and remove residual stresses.

Samples from materials BT-1, BT-3, BT-6, BT-8, BT-9, 20X13, 40X13, 12X18H9T, 08X18, steel 45, steel 30 were used for the study. The use of these materials is due to the fact that they are widely used in most industries, including aircraft engine building, mechanical engineering and in the manufacture of medical instruments.

To obtain a low-pressure HF discharge, study its characteristics and treat the surfaces of solids with an HF plasma flow, an upgraded HF-plasma installation was used, the functional scheme of which is shown in Fig.1.

The microhardness of the surface was measured with a z ПМТ-3 microhardness meter at various loads at three points with ten measurements for each load. The hardness of the samples was measured with a ТП-2 «Виккерс» instrument. The mechanical properties were determined in the initial state and after exposure for 500 hours at 450°C on the PM-5 machine. Photographs of the microstructure of the surface were obtained using an Olympus OLS LEXT 4100 laser microscope (Fig. 2). Residual stresses in the subsurface layer were studied on a ПИОН-2 device by electrochemical etching of the studied layers with simultaneous measurement of sample deflections and subsequent calculation.

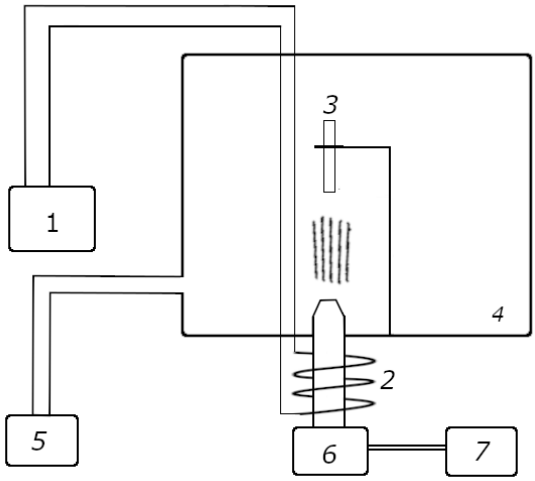

Fig.1. Functional diagram of an HF plasma installation: 1 – HF generator, 2 – inductor, 3 – processed product, 4 – vacuum chamber, 5 – pumping system, 6 – gas flow regulator changer, 7 – gas supply system

In order to consider the possibility of maximizing the cost of the HF plasma polishing and hardening process, as well as the possibility of plasma chemical reactions, the effect of gas impurities in argon on the nature of plasma treatment was investigated. Titanium alloys, carbon structural and corrosion-resistant steels were processed at different nitrogen and oxygen contents in plasma-forming argon.

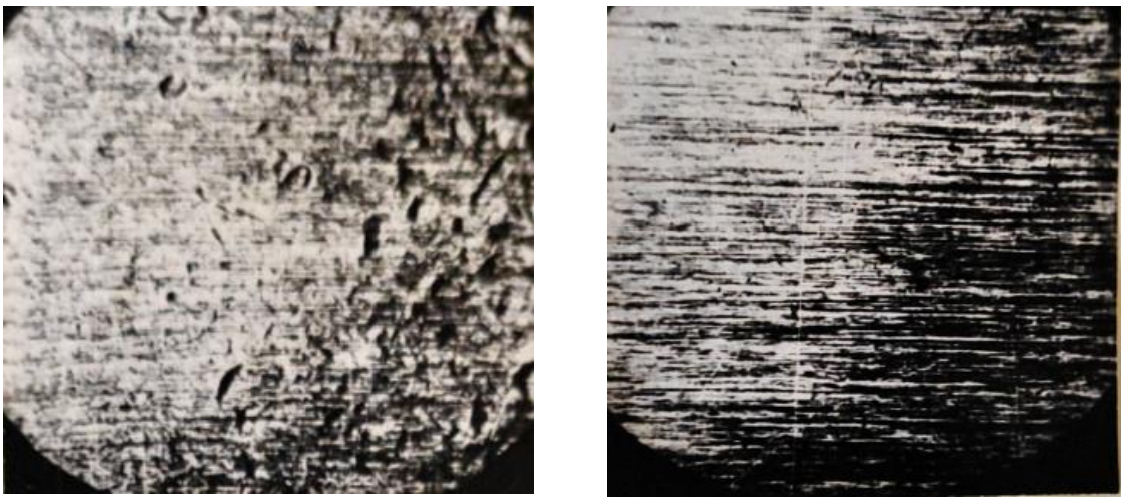

a b

Fig. 2. Sample surface: a) after plastic surface deformation, b) after treatment with HF plasma W_p=2.5 kW, G = 0.08g/s, t = 300 s

When carbon structures were treated with oxygen-containing plasma, the surface color changed depending on the oxygen content from light yellow to dark yellow, brown, blue, dark blue and almost black. The films are uniformly colored

over the entire treated surface. The color and intensity of the coloring also depend on the temperature of the part during processing and on the processing mode. The resulting films have high strength and wear resistance /1/. They can be used as protective and decorative coatings on carbon structural steels.

The introduction of nitrogen impurities during the processing of carbonaceous structural and corrosion-resistant steels also leads to intense surface staining /2/. The microhardness of the surface increases by 2-3 times (Fig.3). Saturation of the surface layer with nitrogen is also observed, leading to an increase in the hardness of the surface layer material. This processing method can be used to increase the hardness and wear resistance of steel parts.

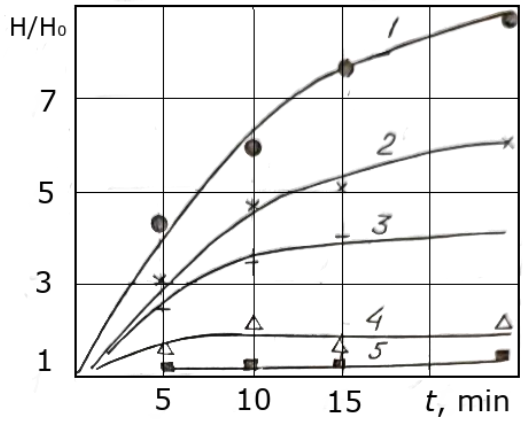

Fig. 3. Relative change of surface microhardness during processing W_p=2.5 kW, G = 0.08g/s, t = 300 s: 1 – content N_2 – 30%, Ar – 70%; 2 - N_2 – 5%; 3 - N_2 – 1%; 4 - N_2 – 0.1%; 5 - N_2 – $5 \cdot 10^{-3}$%, O_2 - $7 \cdot 10^{-4}$%

After grinding, compressive residual stresses of -150...400 MPa are deposited in the surface layer of the samples with a sublayer maximum up to -350...-750 MPa at a depth of 20...35 microns with a change in sign at a depth of 120 microns (Fig. 4).

After hardening by HF plasma treatment, compressive residual stresses of -50...-650 MPa are formed in the surface layer with a sublayer maximum of -350...-800 MPa at a depth of up to 20 microns with a change of sign at a depth of 145...270 microns. The diagrams of residual stresses after hardening by plastic surface deformation (PSD) and HF plasma are smoother than after grinding, up to the investigated depth of 40...80 microns, the amount of compressive residual stresses decreases to a lesser extent than in the case of ground samples without hardening.

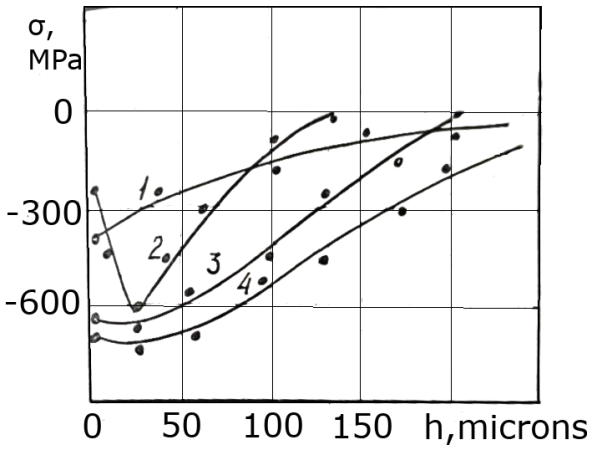

Fig. 4. Generalized diagrams of residual stresses in the surface layer after treatment: 1, 4 – HF plasma treatment W_p=2.5 kW, G = 0.08g/s, t = 300 s, 2 – manual polishing, 3 – hydroblasting + vibrating dressing

After grinding and manual polishing, both tensile stresses with a maximum of +100 MPa at a depth of 20 microns with a change of sign at a depth of 50 microns and compressive residual stresses with a maximum of -500 MPa at a depth of up to 10 microns with a change of sign at a depth of 130 microns were observed in the samples. Compressive residual stresses with a maximum of -300...-350 MPa are observed in samples manufactured using full factory technology (grinding, polishing, hydroblasting and vibration grinding) at a depth of 50...70 microns with a further decrease and a change of sign at a depth of 120 microns or more /3/.

The process of surface modification with HF plasma is considered, the characteristics of residual stresses after HF plasma treatment, manual polishing and PSD are compared, it is shown that after HF plasma, the amount of compressive residual stresses is greater than with other types of surface treatment, resulting in increased microhardness. The dependence of microhardness on the amount of introduced nitrogen and oxygen impurities in plasma is also shown.

References

1. Abdullin I.S., Nekrasov I.K., Sagitova F.R., Mironov S.V. Characteristics of a jet high-frequency low-pressure induction discharge in product modification processes. Engineering and Physics Journal, vol. 98, № 2, 2025.
2. Abdullin I.S., Vdovin D.A., Sharifullin S.N., Shcherbakov V.D. Treatment of thin aluminum films with high-frequency induction plasma. – Phys. and chem. processing materials. 1979 №4 c. 74-77.
3. Gainutdinov I.S. and others. Cleaning and polishing of substrate surfaces with low-pressure high-frequency induction plasma. – Phys. and chem. processing materials. 1977 №6 c. 150-152.

EFFECT OF PULSE BICHROMATIC IRRADIATION OF OXYGEN-FREE COPPER SURFACE

S.I. Mikolutskiy[1], A.N. Chumakov[2], V.V. Lychkovsky[2], Yu.V. Khomich[1], V.E. Rogalin[1], V.Yu. Zheleznov[1]

[1]Institute for Electrophysics and Electric Power RAS, Saint Petersburg, Russia, E-mail: mikolserg@mail.ru
[2]B.I. Stepanov Institute of Physics of the NAS of Belarus, Minsk, Belarus, E-mail: a.chumakov@dragon.bas-net.by

The effect of laser plasma generated by nanosecond pulses on various materials used in industry has been the subject of many works /1-3/. It is known that at laser pulse repetition rates above 5 kHz and relatively high radiation intensities, the efficiency of material ablation increases sharply, and the possibilities of their laser processing expand /4, 5/. Even when irradiated with two nanosecond laser pulses following with a time interval of several microseconds, an increase in the ablation of the irradiated material and the heating of the forming plasma is observed /6-8/. It is obvious that the use of two-pulse bichromatic laser action will provide more degrees of freedom for controlling the processes of laser modification and ablation of materials, which is the subject of this work.

It was decided to use oxygen-free copper as the main material to be processed; its structure and properties have been well studied, and due to its high electrical and thermal conductivity, it is widely used in various areas of mechanical engineering. The experiments were performed on polished (average roughness was 25 nm) cylindrical samples of oxygen-free copper with a diameter of 40 mm and a height of 8 mm.

An experimental setup based on two nanosecond Nd:YAG lasers with wavelengths of 532 and 355 nm and pulse durations of 15 and 18 ns, respectively, was used to process the samples. The synchronization system provided the generation of paired nanosecond pulses with a controlled time interval between them and the order of their sequence, which is important due to the difference in the reflection coefficient, that for most metals drops noticeably with decreasing of wavelength.

The experiment investigated the formation of erosion plasma in air with various combinations of acting pulses and interpulse time intervals between them. The ablation laser plume was recorded by a video camera based on an ICX415AL CCD matrix with an I-90U 4/75 lens (f = 75 mm). The exposure of an individual frame was about 3 ms. The frame series were recorded with synchronization from the second pulse of bichromatic laser radiation (LR).

The laser spot diameter was ~125 μm and was formed on the sample surface by a spectrum splitter and an achromatic objective. The peak energy density (W_p) from each pulse was about 200 J/cm^2. During the experiment, it was possible to vary the number of double pulses, as well as interpulse time interval Δτ from 1 to 10 microseconds. After laser processing, changes in the surface structure were studied using an optical profilometer (NewView 7300).

Fig. 1 shows the crater profiles on the copper surface after exposure to one pair of bichromatic pulses with Δτ = ±4 μs. A negative time interval value means the leading action of 355 nm pulses, and a positive interval value means the leading action of 532 nm pulses. It is evident that the crater depth is greater when the laser pulse with a wavelength of 532 nm comes first, and reaches 7 μm. With the reverse order of laser pulses, the crater depth is near 5 μm.

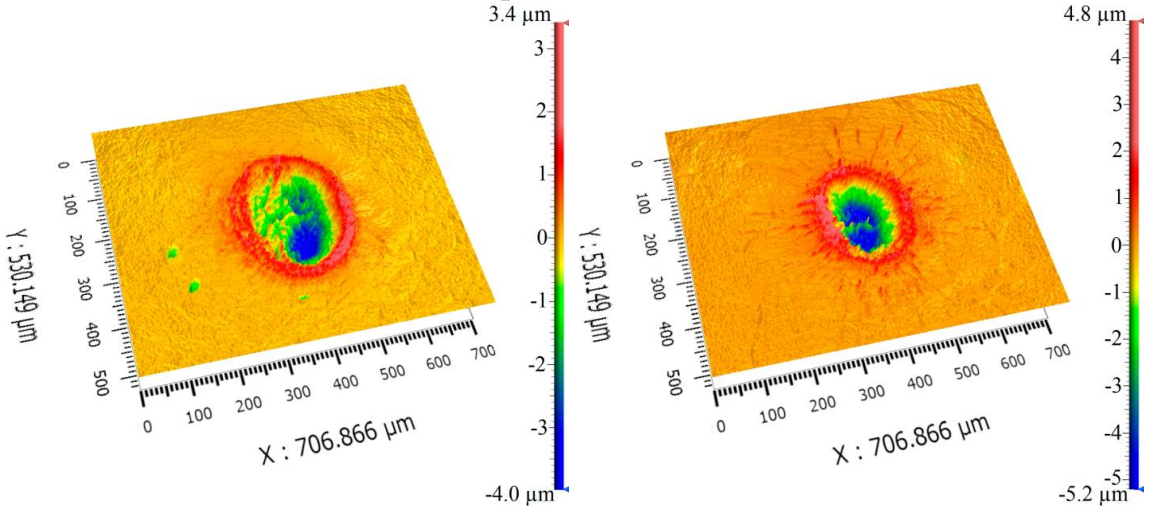

a) b)

Fig. 1. Surface profilometry data for oxygen-free copper treated in air with bichromatic pulses with interpulse time interval of 4 μs: a) λ = 355+532 nm; b) λ = 532+355 nm

The results of this study for three different time intervals are presented in more detail in Table 1. As can be seen, the depth of the craters in the case of interpulse time interval Δτ > 0 is significantly greater, which can be used for choosing the optimal mode for processing materials with bichromatic pulses.

With the leading action of pulses with a wavelength of 355 nm (Fig. 2a-c), the formation of a near-surface plasma plume with a vertically elongated shape was observed. This is probably due to plasma shielding and the displacement of the plasma plume focus from the irradiated surface. This elongated structure was already formed at laser irradiation modes for Δτ = –1.4 μs in the form of a structure with a small “offshoot” (Fig. 2a) and quickly reached its maximum size already at modes for Δτ = –4 μs. With the leading action of pulses with a wavelength of 532 nm (Fig. 2d-f), the torch dynamics change in a similar way,

but in a wider range. With the laser irradiation mode $\Delta\tau$ = +1.4 μs, the torch of the surface plasma has the form of a hemisphere, at $\Delta\tau$ = +4 μs, an "offshoot" is already visible, as in the previous case for $\Delta\tau$ = –1.4 μs, and for $\Delta\tau$ = +6 μs, the elongated structure reaches its maximum size.

Table 1. Crater depth values obtained after irradiation by bichromatic laser pulses depending on their number, sequence and interpulse time interval

Number of double pulses / Pulse delay Δτ, μs	1	2	3	5	7	10
+1.4	7.3	12.5	18.8	29.2	38.9	50.8
–1.4	4.1	8.4	12.2	17.7	25.5	32.4
+4.0	7.0	12.5	19.0	27.9	37.9	50.8
–4.0	4.9	8.4	11.7	18.1	24.2	31.3
+6.0	10.5	13.8	17.8	28.8	39.0	50.1
–6.0	4.9	8.3	12.3	18.3	26.4	32.4

The images of the near-surface plasma from bichromatic laser pulses have some differences for different pulse sequences (see Fig. 2).

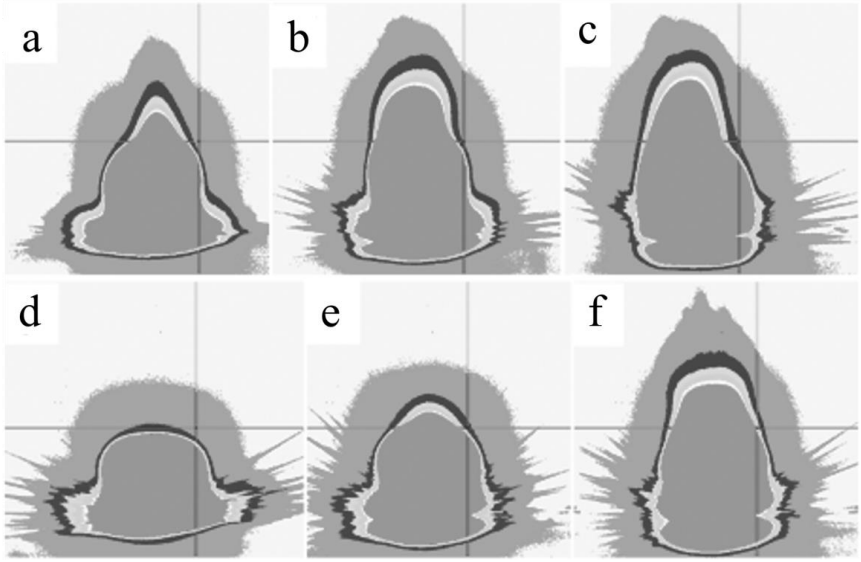

Fig. 2. Images of the near-surface plasma induced by bichromatic laser pulses with wavelengths of 355 and 532 nm (W_p ~ 200 J/cm^2, q_{355} = 12 GW/cm^2, q_{532} = 13.8 GW/cm^2) in the irradiation modes with interpulse time intervals $\Delta\tau$: a) –1.4 μs; b) –4 μs; c) –6 μs; d) +1.4 μs; e) +4 μs; f) +6 μs

At high intensities, part of radiation with a wavelength of 355 nm that manages to reach irradiated surface is capable of noticeably "heating" the resulting plasma along the entire path of its passage to the irradiated surface. With bichromatic irradiation, this effect is enhanced, since there is a laser action

on the ablation products from the first pulse (532 nm), which, during the time interval between the acting pulses, manage to occupy some volume due to thermal expansion. However, additional studies of the dynamics of laser ablation are necessary to confirm these assumptions.

Thus, as a result of experiments with different numbers of bichromatic nanosecond laser pulses, it was found that in the case of 532 nm leading action, craters of a significantly greater depth are formed on oxygen-free copper samples than with the leading action of a pulse with a wavelength of 355 nm. The identification of such a synergetic effect facilitates the selection of the optimal mode for processing materials with bichromatic pulses (for example, drilling metal foils), and in the future will allow to obtain fundamental results in the field of laser plasma formation.

Acknowledgements. This work was carried out within the framework of the state assignment of the Ministry of Education and Science of Russia (FFGR-2025-0001), as well as the State Scientific Research Program of the Republic of Belarus "Convergence-2025" (task 2.2.02).

References

1. **Khomich V.Yu., Shmakov V.A.** Doklady Physics, 56 (6) (2011) 309–313.
2. **Zheleznov V.Yu., Malinskiy T.V., Rogalin V.E., Khasaya R.R., Khomich Yu.V., Isakov V.V., Kozlov A.L., Novikov I.A., Nozhnitskiy Yu.A. and Shibayev S.A**. Uspekhi Prikladnoy Fiziki, 11(2023) 340–355.
3. **Zheleznov V.Yu., Malinskiy T.V., Rogalin V.E., Khomich Yu.V., Ashkinazi E.E., Sovyk D.N., Zavedeev E.V., Fedorov S.V. and Litvinov A.P.** Fizika Tverdogo Tela, 65(2023) 2181–2183.
4. **Min'ko L.Ya., Chumakou A.N., and Bosak N.A.** Sov J Quantum Electronics, **20** (11) (1990) 1389–1392.
5. **Klimentov S. M., Pivovarov P. A., Konov V. I., Breitling D. and Dausinger F.** Quantum Electronics, **34** (6) (2004) 537–540.
6. **Minko L. Ya., Chumakov A. N. and Bakanovich G. I.** J. Appl. Spectrosc., **61** (5–6) (1994) 805–811.
7. **Chumakov A.N., Bosak N.A. & Panina, A.V**. J Appl Spectrosc **84** (4) (2017) 620–626.
8. **Chumakov A.N., Lychkovsky V.V., Nikonchuk I.S., Matsukovich A.S.** J. Tech. Phys., 67 (1) (2022) 16–24.

MEASUREMENT OF OPTICAL NONLINEARITY COEFFICIENTS OF INTEGRATED MICRORESONATORS

D. Morozov[1,2], A. Vorobyev[1,2], V. Pavlov[1], I. Stepanov[1,2], N. Dmitriev[1,2], D. Chermoshentsev[1,2], I. Bilenko[1,3]

[1]Russian Quantum Center, Skolkovo Innovation Center, Bolshoi Boulevard, Building 30, Moscow, Russia e-mail: morozov.dv@phystech.edu
[2]Moscow Institute of Physics and Technology, 9 Institutskiy Per., Dolgoprudniy, Russia
[3]Faculty of Physics, Lomonosov Moscow State University, Leninskie gory, GSP-1, Moscow, Russia

Integrated optical silicon nitride (Si_3N_4) microresonators (MR) are widely used in nonlinear photonics due to their high quality factors ($Q \sim 10^5$–10^7) and small mode volumes combined with Kerr nonlinearity [1, 2]. Importantly, nonlinear dynamics of light in a MR is significantly affected by thermal heating processes with a characteristic time $\tau_{thermal} \geq 1$ μs [2, 3]. In fact, the nonlinear dependence of the refractive index on the light intensity in a MR is determined by both Kerr and thermal nonlinearity coefficients:

$$\delta n = (n_2 + n_{2T})I, \quad (1)$$

where δn is the refractive index change, I is the light intensity, n_2 and n_{2T} are Kerr and thermal nonlinearity coefficients respectively.

For fast intensity variations with characteristic time $\tau \ll \tau_{thermal}$, the thermal nonlinearity may be neglected ($n_{2T} \to 0$). Thus, the coefficients n_2 and n_{2T} can be independently determined in experiments using slow ($\tau \gg \tau_{thermal}$) and fast ($\tau \ll \tau_{thermal}$) modulation of the intensity in a MR.

The experimental setup for measuring n_2 and n_{2T} coefficients consists of continuous wave laser, MR and Mach-Zehnder interferometer. The laser wavelength is scanned with period τ near the MR resonant mode ($\lambda_0 \approx 1540$ nm). For different light intensities, the spectral shift of the resonant frequency $\delta\omega_0$ is measured using a reference Mach-Zehnder interferometer. The corresponding refractive index change is determined by:

$$\frac{\delta\omega_0}{\omega_0} = -\frac{\delta n}{n_g}, \quad (2)$$

where ω_0 is the resonant frequency, $\delta\omega_0$ is the spectral shift of the resonant frequency, and ng is the group refractive index.

We study the MR with following parameters: R = 50 μm, $Q = 0.6 \times 10^6$ (linewidth 268 MHz). Two series of measurements using slow ($\tau \gg \tau_{thermal}$) and fast ($\tau \ll \tau_{thermal}$) laser frequency tuning yield the following optical nonlinearity

coefficients: $n_2 = 2.0 \times 10^{-19}$ m^2/W; $n_{2T} = 17.0 \times 10^{-19}$ m^2/W.

Thus, measured value of thermal nonlinearity significantly exceeds the magnitude of Kerr nonlinearity. Our study

highlights that thermal nonlinearity should be taken into account when nonlinear phenomena in MRs are examined either numerically or experimentally. We also collect measurement data for other eigenmodes of the MR under study and show that thermal nonlinearity strongly depends on resonance linewidth. Moreover, we thoroughly compare the results for MRs with different geometries and reveal that geometrical properties of a MR significantly influence its thermal properties.

Acknowledgements

This work was supported by the Russian Science Foundation (Project No. 23-42-00111).

References

1. **Kippenberg T.J. et al.** Science 361 (2018).
2. **Gao M. et al.** Nat. Commun. 13, 3323 (2022).
3. **Lobanov V.E.** J. Exp. Theor. Phys. 137, 603–614 (2023).

IMPACT OF LASER IRRADIATION AND TRANSITION METALS DOPING ON THE PHOTO-ACTIVATED CONDUCTIVITY OF COPPER OXIDE-BASED NANOSTRUCTURES

S. T. Pashayan[1], V.G. Kornev[2], N. V. Tarasenko[2],
S. V. Zlotski[3], S.V. Husakova[3], V.M. Anishchik[3]

[1]Institute for physical research of NAS of Armenia, Ashtrak-2, 0204, Armenia, stpashayan@gmail.com
[2]B.I. Stepanov Institute of Physics, NAS of Belarus,220072, Nezalezhnasti Ave. 68-2, Minsk, Belarus
[3]Belarusian State University, Nezalezhnasti Ave. 4, 220030, Minsk, Belarus

Metal oxide (MO) nanostructures have been proposed as novel functional materials for various smart and specialized applications /1/. The interest in transition metal oxide nanomaterials such as copper and zinc oxides is mainly associated with the possibilities of the creation of various types of detectors, photo- and optoelectronic devices /2/. In this work, properties of CuO, Cu_2O and ZnO nanoparticles (NPs) and thin films prepared by laser ablation in liquid are studied and discussed. The main attention is focused on the influence of laser irradiation conditions and transition metal doping on the properties of the produced NPs and thin films which can be obtained more stable and with improved photo-activated conductivity.

Zinc oxide (ZnO) is a direct-gap n-type semiconductor with a band gap of about 3.37 eV and a high exciton binding energy (about 60 meV) at room temperature. Copper oxides exist in two crystalline phases, namely cuprite or copper oxide (Cu_2O), and tenorite or copper oxide (CuO) which is also called cupric oxide and used as a precursor in many copper products. CuO has a monoclinic structure and a band gap of 1.2–1.9 eV /3/, while Cu_2O has a cubic crystal structure and a band gap of 2.1–2.6 eV /4/. In addition, both copper oxides have a high optical absorption coefficient in the visible and near infrared regions and are relatively inexpensive materials. Thus, copper and zinc oxides form an important pair for making heterojunctions for photodetectors and solar cells.

In our work NPs were obtained by laser ablation in ethanol of a pressed targets made from pure (99.9%) powders of copper and zinc oxides (Cu_2O and ZnO) and of hybrid ZnO/Cu_2O mixture (50/50) followed by annealing at the temperatures 270°C. By deposition of these NPs on the surface of glass, silicon and ITO substrates thin-film nanostructures were formed. The characteristics of samples obtained were studied by SEM, XRD measurements, Raman and absorption spectroscopy. In addition the photoactivity of the ZnO/Cu_2O structure on the surface of the ITO substrate was studied.

Fig. 1 shows the results of a study of the absorption characteristics of ZnO/Cu_2O nanoparticles obtained by laser ablation in ethanol.

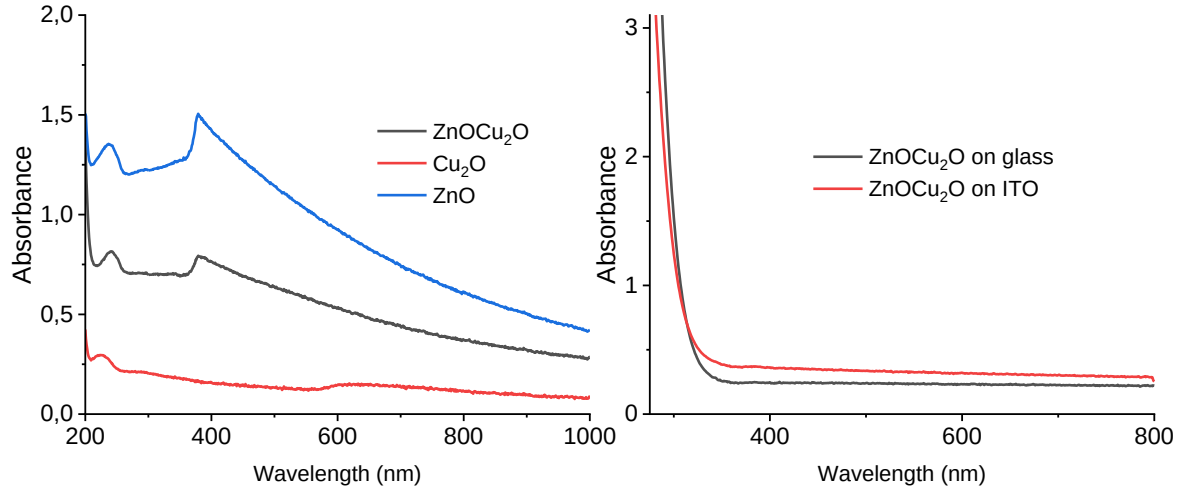

Fig. 1. Extinction spectra of ZnO, Cu_2O and hybrid ZnO/Cu_2O nanoparticles obtained by laser ablation in ethanol of a target made of a mixture (50/50) of pressed copper and zinc oxide powders (a) and structures formed by deposition of hybrid ZnO/Cu_2O nanoparticles on the surface of glass and ITO substrates

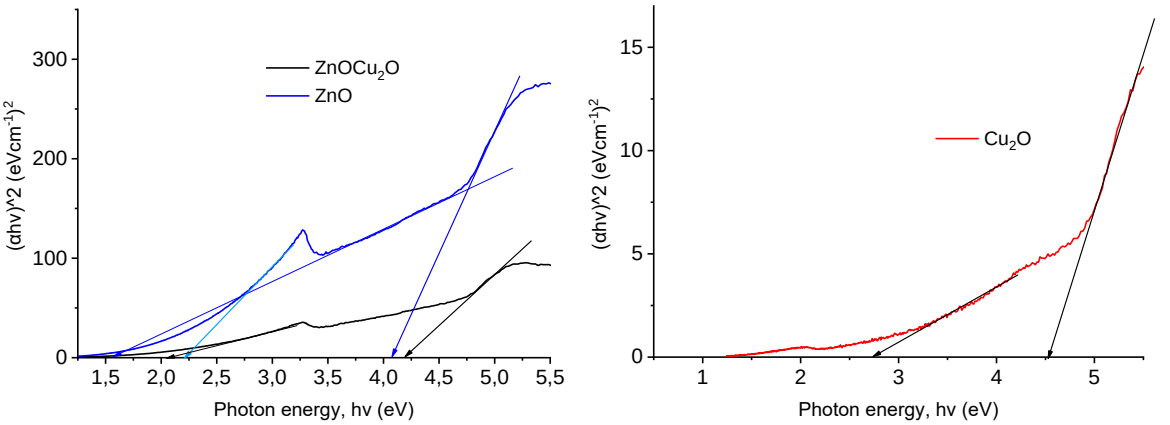

Fig. 2. Results of determining the optical band gap width of the synthesized nanoparticles

The absorption spectra were analyzed to estimate the optical band gap of the synthesized nanoparticles. The optical band gaps were estimated using the Tauc plot, $(\alpha h\nu)^2$ as a function of the radiation energy hν in eV, where α is the absorption coefficient, h is Planck's constant, and υ is the frequency. The optical bandgap energies were found to be 2.1 and 4.1eV, which are in accordance with the band gap of Cu_2O and ZnO, respectively.

The morphology of the deposited structures is represented by their SEM images, shown in Fig. 3. The phase composition of the obtained nanoparticles was studied on an Ultima IV X-ray diffractometer in parallel beam geometry using CuKα radiation with a wavelength of 0.154179 nm. X-ray diffraction patterns of the ZnO/Cu_2O sample in the form of nanoparticles deposited on a glass plate and after annealing at a temperature of 270°C are shown in Fig. 4.

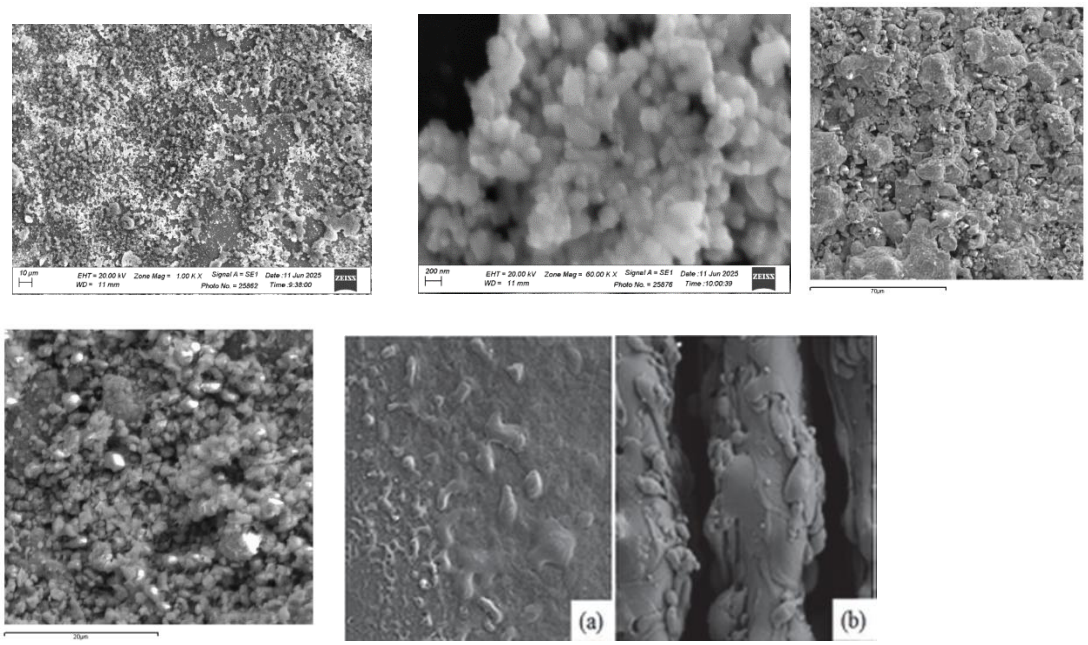

Fig. 3. SEM images of surface structures with deposited zinc oxide (top) and copper oxide (down) nanoparticles under different magnifications

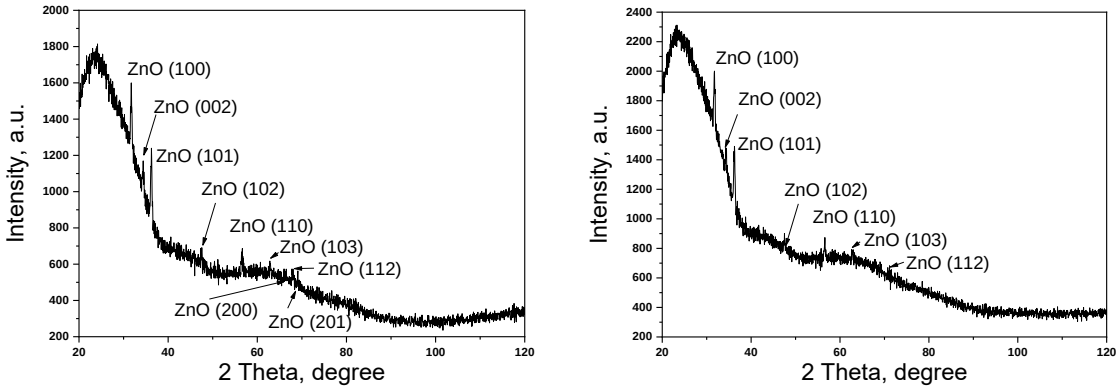

Fig. 4. X-ray diffraction patterns of ZnO/Cu_2O sample before and after annealing at 270°C

Analysis of the X-ray diffraction pattern showed the formation of a ZnO phase with a hexagonal lattice structure (wurtzite-P63mc type). The lattice parameters are a=0.324710±0.000018, c=0.52006±0.00006, which correspond to the parameters of the hexagonal ZnO lattice. The size of the coherent scattering region (CSR) is (29±6) nm, the microstrain of the ZnO lattice is (-0.20±0.07) %. It should be noted that the X-ray diffraction pattern does not reveal diffraction peaks corresponding to the Cu_2O phase, which may indicate the X-ray amorphism of this phase. The amorphous halo present in the X-ray diffraction pattern corresponds to reflection from the substrate (amorphous glass). Analysis of the X-ray diffraction pattern of the ZnO/Cu_2O sample after annealing for 20 min at 270°C (Fig. 4b) showed that annealing does not change the phase composition of the sample. Annealing also does not change the lattice

parameter *a* of the crystalline phase, while the lattice parameter *c* increases slightly (by 0.063%).

The results of scanning electron microscopy (SEM) and X-ray EDX - analysis show that the surface morphology and chemical composition of the surface layer changes under the influence of laser radiation. Depending on laser parameters and the surrounding environment laser-induced copper oxides surface involve both reduction and oxidation processes. In our experiments, using the LA method in various liquid-phase media copper and its oxides NPs were obtained by changing of laser irradiation parameters. Specifically, additional laser treatment can induce the formation of cuprous oxide (Cu_2O) and even metallic copper from cupric oxide (CuO) /5/.

Another example is the drastically changes in the surface microstructure and elemental composition of copper oxide samples coated by transition metals Cu or Ag films before and after laser radiation treatment with increasing in energy density of laser radiation, which were observed (SEM image on Fig. 3), F = 1, 9 J/sm^2 (a) and F = 30 J/ sm^2 (b), Magnification - 1000x) /6/.

Modification of copper oxides properties by the laser irradiation influence can be used to improve the activation energy and the band gap of copper oxides which is in the optimal range /3, 4/ and is in good accordance with solar spectra.

Further studies will be directed to laser processing aiming to modify the morphology and cristallinity of copper oxide based nanostructures that can result in changes their conductivity and alter their electrical and optical properties. In addition, doping by atoms of transition metals can alter the bandgap of CuO and improve its light absorption, change grain size, porosity and create oxygen vacancies. Thus, both laser irradiation and transition metals doping are expected to play crucial roles in improving photo-activated conductivity of copper oxide-based nanostructures and in optimizing CuO NPs for applications in optoelectronics and other fields.

References

1. K. Iqbal et al. Materials for Renewable and Sustainable Energy (2018) 7:4.
2. H. M. Zabed , M. Kumar et al. Renewable and Sustainable Energy Reviews. V. 168, 2022, 112887.
3. Pedram Ghamgosar, Federica Rigoni, Shujie You, et al. Nano Energy, 51, 2018, 308-316.
4. Min-Jyun Hong, Yong-Chen Lin et al. Applied Surface Science 346, 2015, 18-23.
5. N.N. Tarasenka et al. Applied Surf. Sci. 2021, 554, 149570
6. S. T. Pashayan, N. V. Tarasenko et al. Journal of Contemporary Physics (Armenian Academy of Sciences), 50(4), 2015, 367-374.

THE INFLUENCE OF PLASMA ASSISTANCE IN THE APPLICATION OF TITANIUM DIOXIDE BY THE VACUUM ARC METHOD

N.A. Prokopenko, Yu.F. Ivanov, E.A. Petrikova, N.N. Koval, M.S. Vorobyov, M.A. Mokeev, I.I. Azhazha

Institute of High Current Electronics SB RAS, Russia, Tomsk, Akademichesky Avenue 2/3, 634055, nick08_phantom@mail.ru

There are several forms of titanium dioxide. Crystals with tetragonal (anatase and rutile) and rhombic (brukite) syngonics can be found in nature /1/. In addition, two more high-pressure forms were created in laboratory conditions: rhombic IV and hexagonal V /2/.

Despite the active use of titanium dioxide films and nanoparticles in various industries and in medicine, methods for the directed synthesis of nanoparticles with a given modification of the atomic structure, such as amorphous structure, anatase or rutile, have not been formed at present. Moreover, methods for the directed synthesis of titanium dioxide with a given size and shape of nanoparticles have not been developed /3/.

The aim of this work is to synthesise titanium dioxide coatings by vacuum-arc plasma-assisted method and to reveal the influence of plasma assisted modes on the structure, composition and properties of the formed coatings.

Titanium dioxide was sputtered on the "QUINTA" unit (Fig. 1) used for vacuum-arc plasma-assisted sputtering of thin films and coatings /4/. The unit is equipped with an electric arc evaporator with a cathode Ø 80 mm and an extended source of gas plasma "PINK-P" based on a non-self-standing arc discharge with incandescent and hollow cathodes /5/. Technically pure titanium of Grade2 was used as the material of the vaporised cathode. The coatings were applied to samples of titanium grade Grade5, for the study of elemental composition and defective substructure, and hard alloy WC, for the study of elemental composition by micro-X-ray spectral analysis and phase composition by X-ray phase analysis.

Coating was carried out at a total gas mixture pressure of 0.3 Pa. The gas mixture consisted of 5% oxygen and 95% argon. The arc discharge current of the electric arc evaporator I_{Ti} = 70 A, bias voltage U_b = -35 V, gas discharge current of the plasma generator "PINK-P" I_p = 0, 30, 60, 90, 130 and 160 A. Time of coating sputtering is 15 min. All parameters except the discharge current of the gas plasma source were kept constant for all deposition modes.

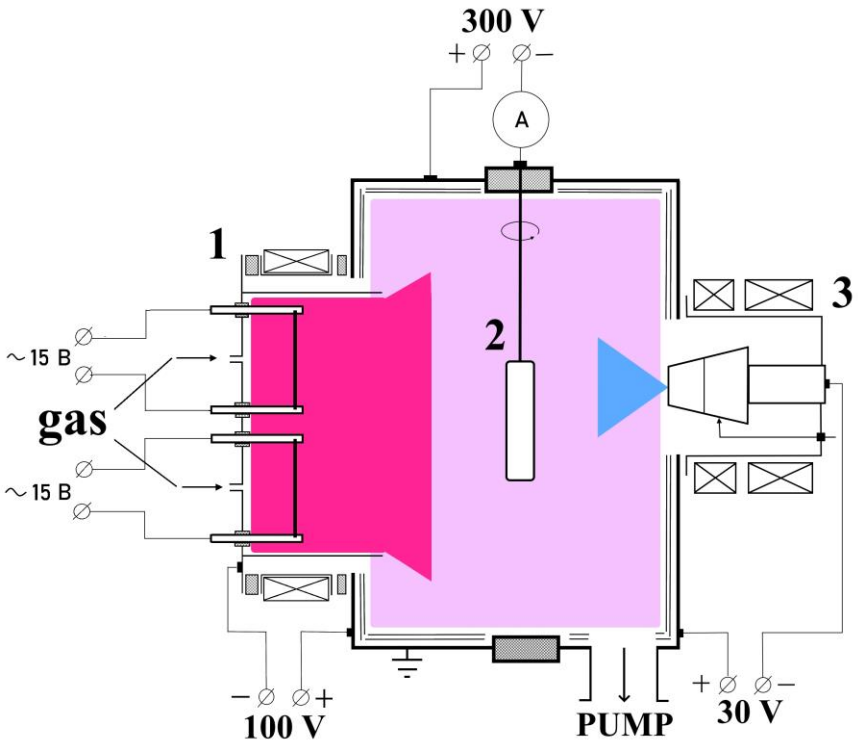

Fig. 1. Block diagram of the discharge system of the "QUINTA" unit. Where 1- "PINK-P" gas plasma generator, 2- collector for ion current density measurement or substrate holder, 3- DI-80 arc evaporator

To evaluate the influence of the plasma generators when working together, the azimuthal characteristics of the ion current density on the collector (S_k = 200 cm^2) were taken. For this purpose, the collector was placed on the satellite of a planetary rotating table, the same one on which the tooling with samples is placed, and passed a full circle around the chamber. During the experiments, the discharge current of the "PINK-P" gas plasma generator was varied, while the current of the metal plasma generator remained unchanged at 70 A. The ion current to the collector (I_k) was recorded using a milliammeter. The bias voltage U_b, at which saturation from the plasma occurs, i.e. at U_b= - 300 V, was applied to the collector. The saturation ion current density from the plasma was calculated by the well-known formula $j = I_k/S_k$.

Figure 2, shows plots of the azimuthal distribution of the ion current density on the collector for different gas mixtures and plasma generator discharge currents. As can be seen in the figure, the ion current densities monotonically increase with increasing discharge current, and decrease with increasing oxygen fraction in the working gas mixture.

From the obtained results it is clear that joint operation of plasma generators increases the uniformity of plasma distribution in the chamber volume. Thus, if we compare the sum of ion current densities at separate operation of generators, the ion current density at joint operation can be up to 2

times higher. At joint operation of plasma generators ion current density in argon medium varies from 5.25 mA/cm^2 to 16.5 mA/cm^2, at equal argon/oxygen ratio from 3.75 mA/cm^2 to 15.5 mA/cm^2, at argon/oxygen ratio Ar/O2=5/95 % from 2.2 mA/cm^2 to 12.5 mA/cm^2.

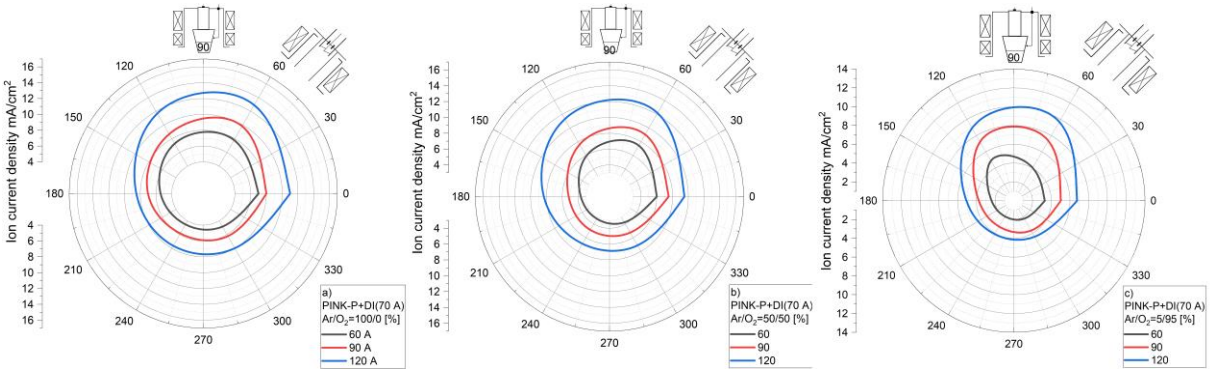

Fig. 2. Azimuthal distribution of ion current density of the plasma generators when working together. Parameters: a) in argon atmosphere, b) in equal ratio of argon and oxygen, c) 5% argon and 95% oxygen

The thickness of the coatings varied within (2-2.5) μm. The coating growth rate was in the range of (7-10) μm/h depending on the plasma assisted mode. As the discharge current of the gas plasma source I_p increased, the substrate temperature at the end of the deposition process increased from 250 ºC (Ip = 0 A) to 400 ºC (I_p = 160 A). It is worth noting that the ratio of the ion current density on the substrate of the gas plasma source to the ion current density of the metal plasma source varied linearly from $j_p/j_d = 0$ at $I_p = 0$ A to $j_p/j_d = 8.7$ at I_p = 160 A.

The results of measuring the elemental composition of titanium dioxide coatings, performed by methods of micro-X-ray spectral analysis, indicate a non-monotonic change in the relative content of oxygen atoms in the coating. The highest concentration of oxygen atoms (δ (O_2) = 63.8 at.%) is observed in the coating formed at the maximum discharge current of the gas plasma source.

X-ray diffraction analysis methods show that the main phase of the formed oxide coatings is titanium dioxide (TiO_2) (Fig. 3).

In a small amount (10-15 wt%) titanium oxide of TiO composition was found in the coatings. Titanium dioxide in the coating is present in two polymorphic modifications: rutile and anatase (Fig. 3). It was found that the relative content of rutile and anatase in the film depends on the discharge current of the gas plasma source (I_p). Namely, the maximum content of rutile (R/A = 5.86) is observed in the coating formed at the discharge current $I_p = 0$ A (i.e., with the plasma generator switched off); the maximum content of anatase (A/R = 6.88) - at I_p = 90 A.

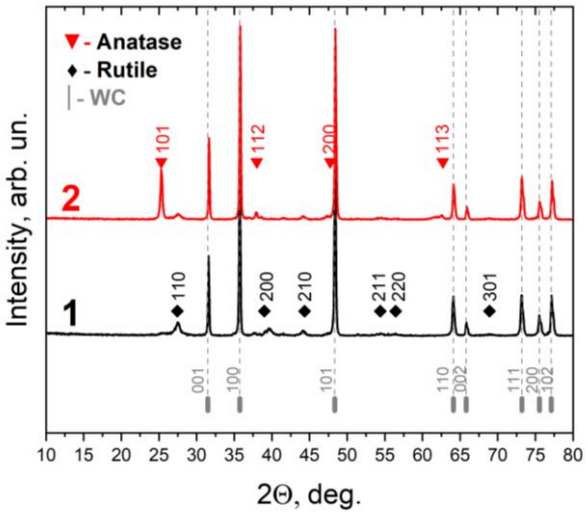

Fig. 3. Fragments of X-ray radiographs of titanium oxide coating: 1 - I_p = 0 A; 2 - I_p = 90 A. R - rutile; A - anatase; WC - tungsten carbide (main phase of substrate WC)

Thus vacuum-arc plasma-assisted method synthesised titanium dioxide coatings at variation of discharge current values of gas plasma source. The influence of joint operation of gas and metal plasma generators has been studied. It is shown that the main phase of the formed oxide coatings is titanium dioxide (TiO_2) represented by polymorphic modifications of rutile and anatase. The relative content of rutile and anatase in the film depends on the discharge current of the "PINK" source. The maximum content of anatase is observed at discharge current "PINK" I_p = 90 A; the maximum content of rutile - at discharge current "PINK" I_p = 0 A.

Acknowledgements. This work was supported by a grant from the Russian Science Foundation (Grant No. 24-69-00074).

References

1. **Etacheri V., Di Valentin C., Schneider J., Bahnemann D. W., Pillai S. C.** Journal of Photochemistry and Photobiology C: Photochemistry Reviews. 25(2015) 1-29.
2. **Muhammad Ali, H. (Ed.)** IntechOpen. J.W. Titanium Dioxide - Advances and Applications (2022).
3. **Rempel, A.A., Valeeva, A.A.** Russ Chem Bull 68(2019) 2163–2171.
4. **Vintizenko, L.G., Grigoriev, S.V., Koval, N.N. et al.** Russian Physics Journal 44(2001) 927–936.
5. **Shugurov V. V., Koval N., Krysina O., Prokopenko N. A.** Journal of Physics: Conference Series 1393(2019) 12131.

FINISH CLEANING OF THE SUBSTRATE SURFACE DUE TO SECONDARY EMISSION IN A LASER EROSION PLASMA ION SOURCE FOR THE FORMATION OF NANOSTRUCTURES.

V.K. Goncharov, M.V.Puzyrev
[1]A.N.Sevchenko Institute of Applied Physics Problems, Belarusian State University, 7 Kurchatova Street, Minsk 220045, Belarus

Abstract. It has been experimentally determined that during the deposition of nanostructures using ion flows, obtained from laser erosion plasma, there is a regime of secondary emission of ions of the substrate material due to the bombardment of the laser target material by ions. This effect can be used for the final cleaning of the substrate surface before deposition the laser target material.

The laser-plasma method of forming nanostructures is the most promising. The laser-plasma method of forming nanostructures is quite simple. An erosive plasma plume is formed due to the gas-kinetic pressure from the target surface at laser radiation action on a target. It moves at a velocity of 10 km/s. The direction of the plume movement is orthogonal to the target surface. If a substrate is placed at some distance from the laser target, various nanostructures can be formed on it. These can be either uniform homogeneous nanofilms or nanostructures with different surface topography /1-3/. It is necessary to smoothly change the power density of the acting laser radiation to obtain various the conditions for the formation of nanostructures from different materials. This is achieved by changing the radiation energy in the laser pulse and changing the radiation focusing. However, the energy change has a small dynamic range in modern technological lasers. Devices for smoothly changing the focusing are complicated, expensive and unreliable.

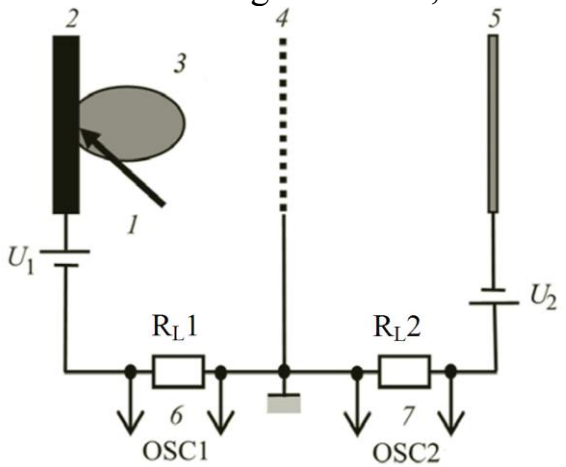

Fig. 1. Scheme of the experiment: 1 - laser radiation; 2 - laser target; 3 - erosion plume; 4 - grid; 5 – substrate; 6 and 7 signals to the first and second beam of oscillograph; U_1 and U_2 - independent power supplies

A scheme of a laser-plasma source for deposition nanocoatings using ion flows from a laser plasma was proposed to eliminate this drawback /4/. A grid is located between the laser target and the substrate in this source. The charged particles flow is formed after the grid when a negative electric field potential is applied to the grid relative to the target, It consist mainly of ions. It is possible to smoothly change the electric field in the grid-substrate interval at the same time

smoothly changing the kinetic energy of ions in a large dynamic range if a positive potential is applied to the grid relative to the substrate. The grid was grounded in order to the potential sources in the target-grid and grid-substrate intervals to be independent.

The electrical scheme is shown in Fig. 1.

The experimental equipment

The target was irradiated by the LOTIS-TII pulsed YAG:Nd^{3+} laser with a wavelength λ = 1064 nm and a pulse duration τ = 20 ns (FWHM) and a laser pulse repetition rate of 5 Hz. The target was made of technically pure tin. The target was mounted at 45° with respect to the laser beam. The experiments were carried out in a vacuum chamber under pressure of $2.6 \cdot 10^{-3}$ Pa. The target was rotated with a velocity of 2 rev/min to prevent formation of a deep crater on the target surface which can affect the spatial shape of the erosion plume.

The substrate was positioned parallel to the target surface and was made of SDB 7.5 silicon. The distance between the substrate and the target was 12 cm. The grid was located at a distance of 6 cm from the target surface. The grid transparency was 90%. The change in currents over time was monitored using a Tektronix TDS 2022B oscilloscope. The power density of the laser radiation affecting the target was $3.8 \cdot 10^8$ W/cm^2.

Discussion of results

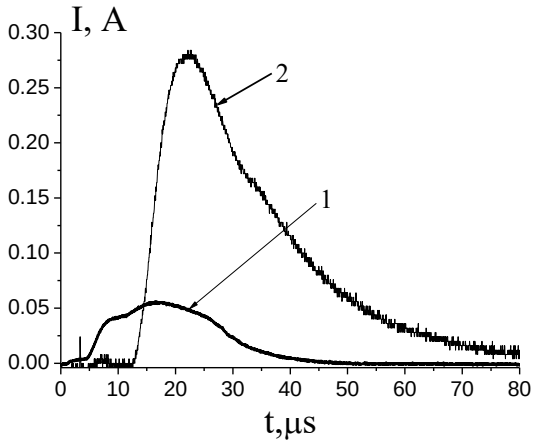

Fig. 2. Change in currents over time in the target-grid (1) and grid-substrate (2) intervals

Fig. 2 shows typical changes currents over time in the target-grid interval (curve 1) and grid-substrate (curve 2). The ion current pulse in the grid-substrate interval is an asymmetric curve (like the plasma glow pulse of the laser target). The change in current over time in the target-grid interval has a more complicated curve consisting of several "humps". At the leading edge, an electron current is observed towards the target (the first "hump"), and then the second "hump" is the sum of the electron current to the target and the ion current to the grid. The reverse electron current is recorded on the oscilloscope as a positive signal. Fig. 2 shows the curves at a potential in the grid-substrate interval of 100 V.

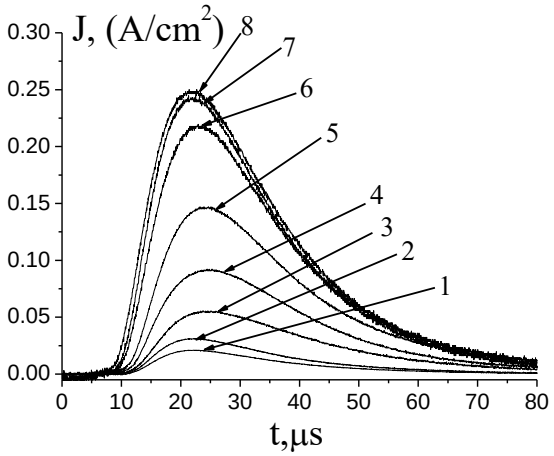

Fig. 3. Change in current density in the grid-substrate gap at different potentials: 1- 0V, 2-25 V, 3-50V, 4-75 V, 5-100V, 6-125 V, 7-150V, 8-200 V

Measurements of the ion current density in the grid-substrate interval were carried out at different accelerating potentials in this interval. These results are presented in Fig. 3.

The initial increase in the accelerating potential in the grid-substrate interval due to the acceleration of ions in the electric field at increase potential in up to 2 times. Current due to the increase in the ion velocity based on the relationship $E=m\boldsymbol{v}^2/2$ of increase up to $\sqrt{2}\approx1.4$. In the experiment, a greater is observed (see Fig. 3).

This is due to the fact that the cross section of the ion flow some lager substrate size. An increase in the accelerating potential connected with the ion beam is subfocused and some of the peripheral ions also hit the substrate /5/. However, at accelerating potentials above 100 V, a significant decrease in the growth of ion current occurs (current increase by 1.1 times). This can be explained by the appearance of a reverse current of silicon ions due to secondary emission from the substrate surface. This phenomenon can be estimated using the Zigmund theory in the primary knockout mode. In /6/, a formula for determining the sputtering coefficient is proposed:

$$Y = \frac{3}{4\pi^2}\alpha\frac{4M_1M_2}{(M_1+M_2)^2}\frac{E}{U_0},$$

α- is a coefficient depending on the ratio $\frac{M_2}{M_1}$, in our case M_1 is the mass of a tin atom, M_2 is the mass of a silicon atom, E - the energy of the incident ion, U_0 is the surface potential barrier. The value α-0.18 was taken by us from /7/, and the value of U_0 equal to 7.8 eV from /8/. The energy of the incident ion E in our case is determined by the sum of the energies: the kinetic energy E_{kin} of the tin ion due to the gas-kinetic pressure in the erosion laser plume, the energy of the tin ion due to its by the electric potential in the target-grid interval (E_{tg}) and the energy at acceleration in the electric field in the grid-substrate gap (E_{gs}). $E = E_{kin} + E_{tg} + E_{gs}$. In our experiments E_{tg}=30 eV, and Egs varies from 0 to 200 eV. E_{kin} can be calculated from the experimental data and the power density of the laser radiation acting on the tin target ($3.8\cdot10^8$ W/cm^2). It is 50 eV. Substituting

all the necessary data into the Zygmund formula at E_{gs}=100 eV, we obtain the sputtering coefficient Y=0.17 or 17%, and at an accelerating potential of 200 V, the sputtering coefficient reaches 25%. Thus, the decrease in the current growth on the substrate (see Fig. 3) after 100 V can be explained by the secondary emission of silicon ions from the substrate surface when bombarded with accelerated tin ions. This effect can be used for final cleaning of the substrate surface due to the accelerated ions of the target material.

References

1. Eason R. (Ed.). Pulsed Laser Deposition of Thin Films: Applications Led Gnowth of Functional Materials. Hoboken,New Jersey: John Wiley & Sons, Inc., 2007.
2. **Goncharov V. K., Gusakov G. A., Puzyrev M. V,** Journal of Engineering Physics and Thermophysics. 86 (2013) 1020–1026.
3, **Goncharov V.K. Kozadaev K.V., Shchegrikovich D.V.** Journal of Engineering Physics and Thermophysics, 86 (2013) 798 – 804.
4. **Goncharov V.K., Puzyrev M.V., Stupakevich V.Yu.** Device for controlling the parameters of an erosive laser plume in a vacuum for depositing nanostructured coatings on various materials: patent BY 12575. – publ. 30.04.2021.
5. **Goncharov V.K., Puzyrev M.V., a and Stupakevich V.Yu.** Journal of Engineering Physics and Thermophysics. – 91 (2018) 1056-1062.
7. **Zigm P.** Spraying by ion bombardment, in: *Spraying of Solids by Ion Bombardment*, Mir, Moscow (1984), p. 55, 75.
8. **Komarov F.F. and Komarov A. F.**, Physical Processes on Ionic Implantation into Solid Bodies [in Russian], UP "Tekhnoprint," Minsk (2001).

FABRICATION OF LEAD ZIRCONATE TITANATE FILMS BY COMBINED LASER ABLATION/ LASER MODIFICATION TECHNIQUE

A.O. Radomtsev, A.A. Nevar, M.I. Nedelko, N.V. Tarasenko

B.I. Stepanov Institute of Physics NAS of Belarus, Nezalezhnasti Ave 68-2, 220072, Minsk, a.radomtseu@gmail.com

Recently, there has been a resurgence of interest in complex oxides having ferroelectric and ferromagnetic properties. Although these properties were discovered decades ago, the renewed interest for these materials is connected to a progress in modern deposition techniques that allow the production of high-quality thin films and the creation of promising devices based on them. Ferroelectrics are dielectric materials that have spontaneous polarization in a certain temperature range and exhibit a nonlinear dependence of polarization on the electric field, called a hysteresis loop. These properties of ferroelectrics are due to the non-centrosymmetric crystal structure that arises from a slight distortion of their cubic perovskite structure.

Ferroelectric materials are ferroelastic in the sense that changing the shape results in a change in the electric polarization (and hence the electric field) developed in the crystal, and vice versa. They can therefore be used to convert acoustic waves into an electrical signal in sonar detectors and to convert an electric field into motion in actuators and mechanical scanners that require precise control. More generally, ferroelectric materials can be used for pyroelectric and piezoelectric sensors, voltage-controlled capacitors, infrared detectors, surface acoustic wave (SAW) devices, microactuators, and non-volatile random access memories (NVRAM), including the potential production of single-transistor memory cells and applications requiring nonlinear optical components.

One of such ferroelectric compounds is lead zirconate titanate $PbZr_{1-x}Ti_xO_3$ (PZT). PZT is an actively studied perovskite-like functional material that exhibits both ferroelectric and antiferroelectric properties depending on the titanium concentration. Ferroelectric PZT is popular due to its high piezoelectric coefficients, making it one of the leaders in the piezoelectric materials market /1/. For the creation of promising PZT based devices the production of high quality material of required stoichiometry is needed. However, preparation of PZT structures with attaining a composition control poses a persistent challenge.

Various methods for obtaining PZT structures are discussed in the literature /2-5/. The main ones are: sol-gel method, hydrothermal method, pulsed laser deposition, metal-organic chemical vapor deposition, molecular beam epitaxy.

In the present work, a novel approach based on laser ablation in liquid in combination with additional laser modification has been developed for PZT nanostructures fabrication.

A schematic representation of the setup for laser ablation synthesis of the colloidal solution of nanoparticles is shown in Fig. 1. First metal plates of Pb, Zr and

Ti were subjected to laser ablation in ethanol (Nd:YAG laser, wavelength of 1064 nm, energy 80 mJ/pulse, repetition rate 10 Hz, pulse duration 10 ns), then the obtained colloidal solutions were mixed. To achieve the stoichiometric composition of the final PZT product, the production time, as well as the ratio of the concentrations of Pb, Zr and Ti in the mixture, were controlled. After that the obtained mixture was irradiated with the fourth harmonic of the Nd:YAG laser (wavelength of 266 nm, energy 45 mJ/pulse, repetition rate 10 Hz, pulse duration 8 ns, exposure time 30 min).

Besides, laser ablation of PZT target (a tablet of pressed PZT powder) was performed under similar experimental conditions.

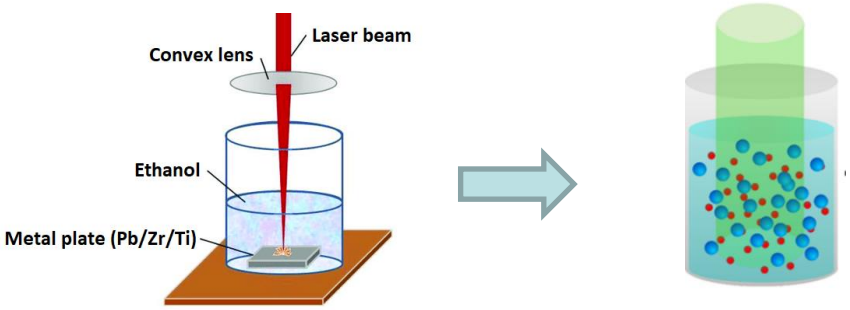

Fig. 1 - Setup for synthesis of nanoparticle colloidal solutions

The colloidal solution obtained after laser treatment was deposited on a copper plate to form a film on its surface. Characterization of the obtained sample was carried out using Raman spectroscopy, scanning electron microscopy in combination with energy-dispersive X-ray elemental microanalysis. The results of the sample characterization are presented below.

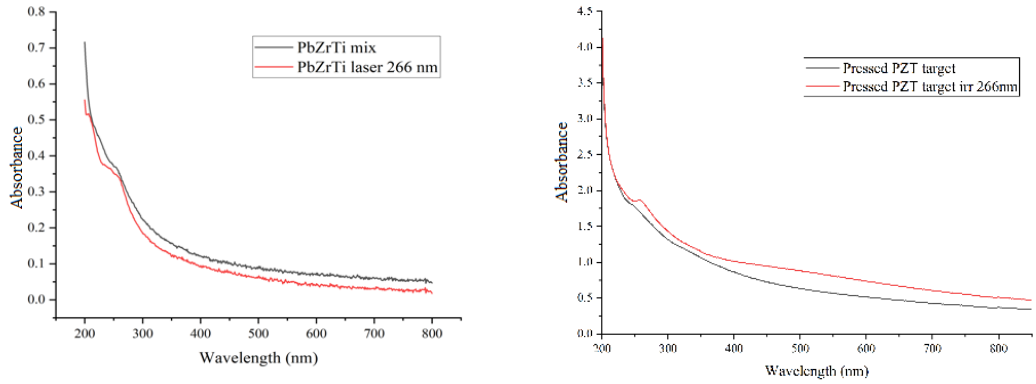

Fig. 2 –Absorbance of PbZrTi colloidal solutions prepared as a mixture of individual Pb, Zr and Ti solutions (left) and by laser ablation of the pressed PZT target (right) before (black) and after (red) 266 nm laser irradiation

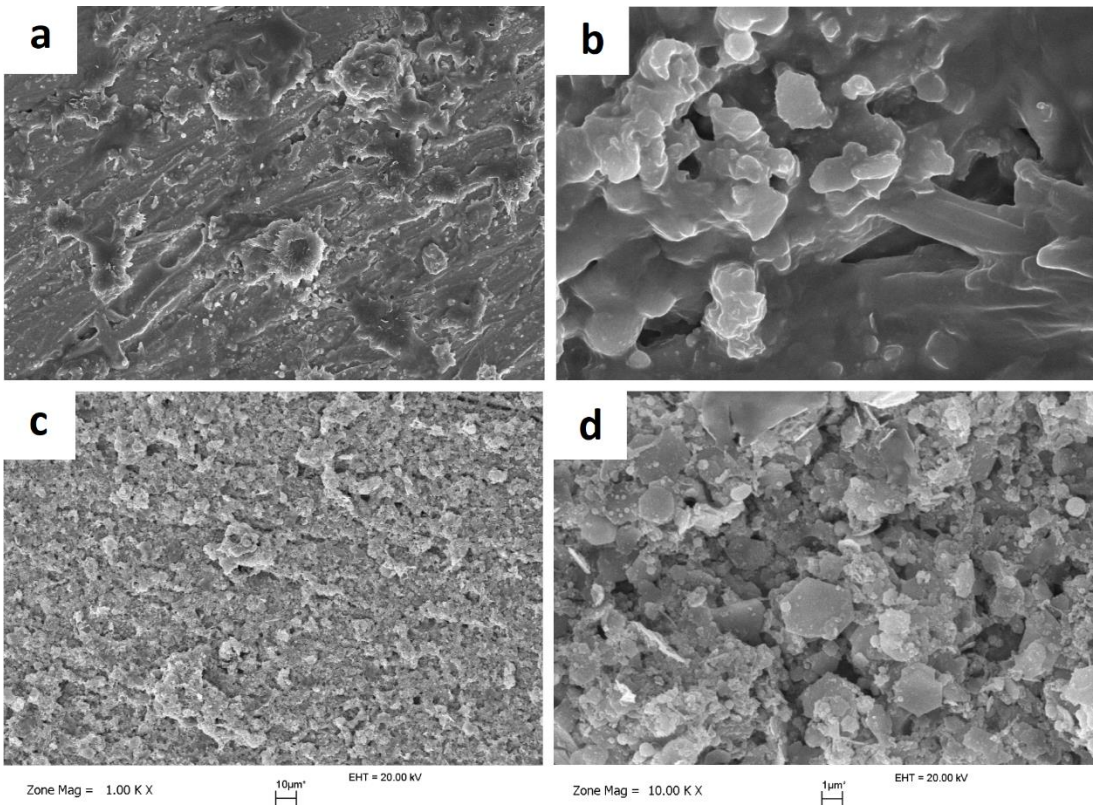

a,b – PZT samples before 266 nm laser irradiation; c,d – PZT samples after laser irradiation

Fig. 3 – SEM images of PZT samples prepared as a mixture of individual Pb, Zr and Ti solutions

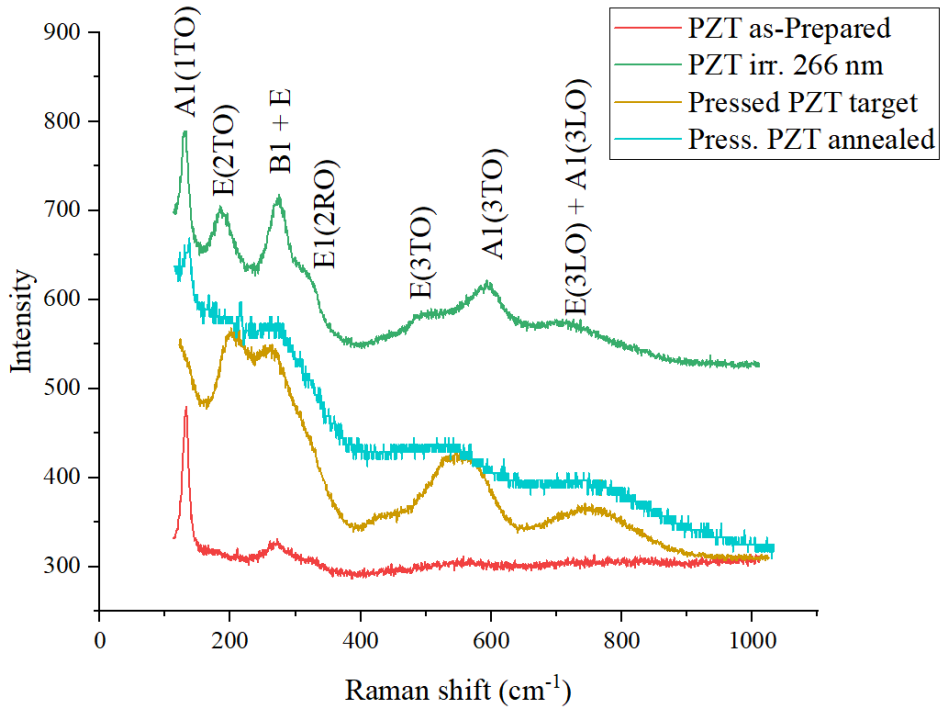

Fig. 4 – Raman spectrum of PZT sample prepared as a mixture of individual Pb, Zr and Ti solutions before (red) and after (green) 266 nm laser irradiation as well as Raman spectra of the PZT target (color) and of the sample prepared by PZT target laser ablation with an additional thermal annealing at 700°C during 30 min.

The Raman spectrum of the obtained sample at room temperature is shown in Fig. 4. Intense bands with maxima near 130, 196, 274, 328, 493, 600 and 719 cm^{-1}, identified as the modes A1(1TO), E(2TO), B1+E, A1(2TO), E(3TO), A1(3TO) and E(3LO)+A1(3LO), can be a good indicator of the crystallinity of the perovskite phase and can be attributed to the tetragonal phase of PZT, according to the results of papers /4, 5/.

The results of studies of the morphology, structure as well as composition of the formed nanocomposites confirmed the formation of lead zirconate titanate with tetragonal inner structure. In order to check the ferroelectric nature of the in situ deposited PZT films, the P–E hysteresis loops of the samples should be measured using a standard ferroelectric test system. The resulting PZT films will be tested in near future as piezoelectric sensor material in Micro-Electro-Mechanical Systems (MEMS).

This preliminary results of the study of the obtained sample by the methods of energy-dispersive elemental and X-ray structural analysis, allow us to hope for the optimization of the developed combined approach for the reliable synthesis of lead zirconate titanate films.

The work was partially financed by the National Academy of Sciences of Belarus under project Convergence 2.2.05.

References

1. **Andronikova D.A.** Physics of the Solid State, **61** (2019) 1772-1778
2. **Anderson P.S.** Sixteenth IEEE International Symposium on the Applications of Ferroelectrics, (2007) 159-162
3. **Traianidis M.** Journal of the European Ceramic Society, **19** (1999) 1023-1026
4. **Burns, G.** Physical Review Letters, **25** (1997) 1191-1194
5. **Meng, J.F.** Physica Status Solidi A, **164** (1997) 851-862

DEPOSITION AND CHARACTERIZATION OF TITANIUM NITRIDE THIN FILMS AS COATINGS FOR PACEMAKER ELECTRODE PROTOTYPES

Yu. Rukina, O. Obrezkov, Yu. Martynenko, S. Shevchuk

National Research Centre «Kurchatov institute»

Introduction

The properties of the deposited thin films, which are principal in a wide range of applications, are significantly affected by the deposition modes. A large effective surface is required for efficient operation of supercapacitors, catalysts and pacemaker electrodes. Pacemaker electrodes in particular require a high specific capacitance of their contact with myocardial tissue /1/.

This work aims to explore the impact of substrate preparation before deposition and platinum implantation on the functional properties of titanium nitride thin films. The characteristics of the coatings were studied using electron microscopy and by analyzing the properties of the double electric layer (DEL), which were measured using impedance spectroscopy.

The material used for implantable cardiac electrodes should be biocompatible, capable of transmitting electricity, and stable enough to continue operating throughout the device's lifespan. Titanium nitride films were chosen for the study because this material is widely used /1/ as coatings for implantable devices, and titanium nitride with a high effective surface is used in pacemakers and neurostimulator electrodes /2/.

Experimental setup

Titanium nitride films were deposited on a titanium substrate using magnetron sputtering of titanium in the presence of reactive nitrogen gas. Pulsed vacuum arc evaporation was used for platinum implantation.

The coated samples to be analyzed were flat titanium discs. Impedance spectroscopy was carried out in a two-electrode electrochemical cell with 0.9 % NaCl solution used as the electrolyte. The anode was a titanium plate with a porous titanium nitride coating with a large area significantly exceeding the working area of the cathode (4 mm^2) with a thin film to be examined. This was done to minimize the impact of the anode's capacitance on the measurement of the cathodes' double-layer capacitance.

The biocompatible functional coatings being investigated consist of several layers. The first adhesive layer of titanium has a thickness around 0.15

micrometer. The second layer, consisting of densely packed columnar grains of titanium nitride with a thickness of 0.2-0.5 microns is for a corrosion protection of the substrate from electrochemical corrosion. It will prevent the penetration of active ions from the blood, which react chemically with the electrode material. The final functional layer consists of porous titanium nitride in the form of tapered crystallites separated by voids. The extensive surface area of this layer enhances the electrode's engraftment in the human body and increases its capacitance of the DEL.

The deposition of thin-film coatings for pacemaker electrodes is carried out using the “Micromed” vacuum installation designed in the Laboratory of coating technologies at NRC «Kurchatov institute», equipped with a planar magnetron, 3 pulsed arc evaporators and a source of metal ions named “Sokol-Mini”. The sample holder with planetary rotation allows to apply coatings simultaneously on 1000 cardiostimulator electrodes. It is equipped with a heater, a thermocouple and an electric bias source to regulate ion energy during deposition.

Results and discussion

The addition of platinum to the coating is due to the need to improve the biocompatibility of the coating without compromising its electrophysical properties. In order to investigate the effect of platinum deposition methods on the electrophysical properties of coatings, various methods of applying the platinum layer were used: platinum layer deposited after the titanium nitride layer with a developed structure, layered deposition of platinum and titanium nitride.

Table 1 – The electron microscopy images and DEL capacitance of multilayer coating of titanium nitride thin film (№1), multilayer coating of titanium nitride with a platinum layer of 150 nm (№2), layer-by-layer deposition of titanium nitride and platinum of 10 nm (№3), layer-by-layer deposition of titanium nitride and platinum of 1 nm (№4)

№1	№2	№3	№4
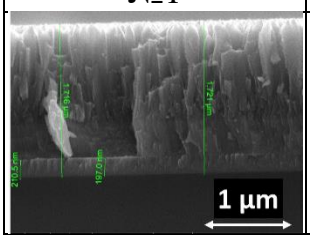	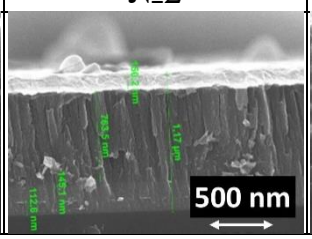	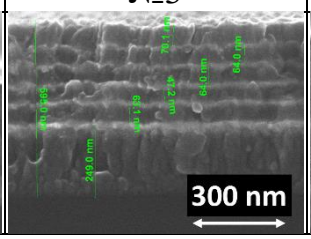	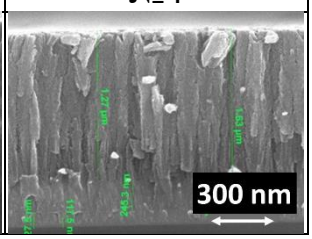

The DEL capacitances of these samples are: for №1 - 380 µF, №2 – 250 µF, №3 – 50 µF, №4 – 340 µF. A dense layer of platinum, deposited using a pulsed vacuum arc evaporation, has covered the developed titanium nitride structure, reducing the DEL capacitance. When platinum layers with a thickness of about 1

nm (№ 4) are deposited, there is no disruption in the growth of titanium nitride columns (unlike №3) and the capacity decreases within the measurement error. The impact of platinum on the biocompatibility of the coatings will be investigated in the future.

To increase the effective area of the cardiac electrode coating, the substrates can be sandblasted or plasma treated to obtain structures similar to fluff or laser treated to increase the geometric area of the substrate before deposition of titanium nitride.

The characteristic size of the straight furrows produced by laser treatment of substrates with a fiber laser (6-12 W with a wavelength of 1064 nm) is approximately 50 microns. Electron microscopy has established (see Table 2) that the specific surface area of the substrate after laser treatment is significantly higher than after sandblasting, which is confirmed by impedance spectroscopy results.

Table 2 – The electron microscopy images and cyclic voltammograms (CV) of samples with titanium nitride coatings on substrates treated in different ways: polished (№1), laser-treated (№2), treated with a laser beam in mutually perpendicular directions (№3), sandblasted (№4)

№1	№2	№3	№4
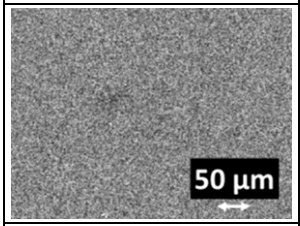	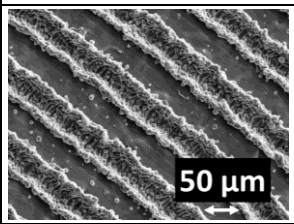	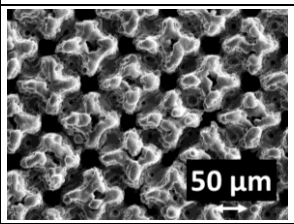	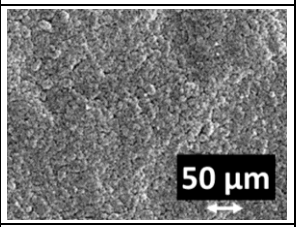
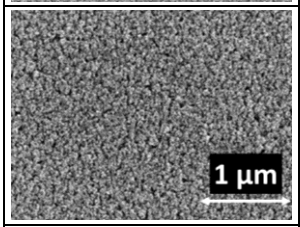	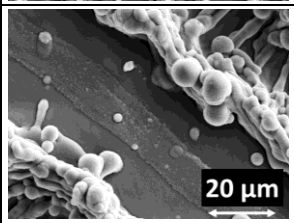	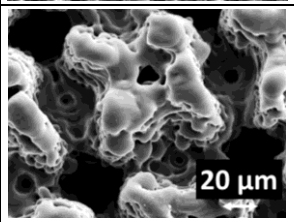	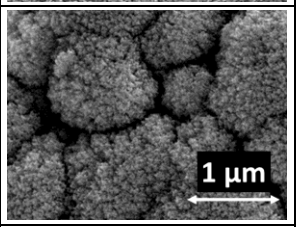
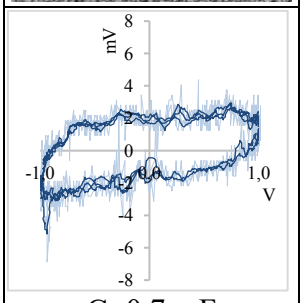	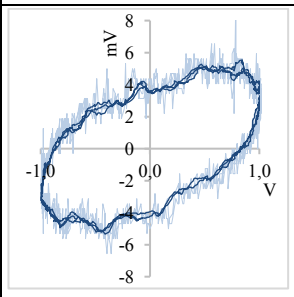	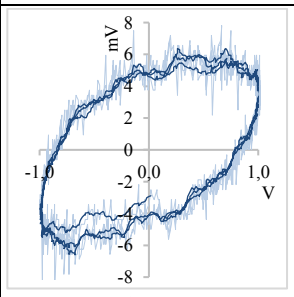	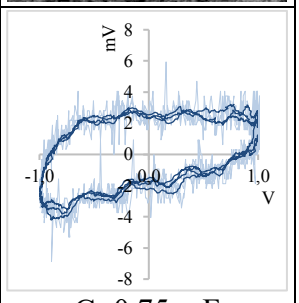
C=0,7 mF	C=1,2 mF	C=1,7 mF	C=0,75 mF

The resistance of the coating samples to electrochemical influences and their DEL capacitance were assessed through the analysis of the shape of the cyclic

voltammogram (CV) based on a sinusoidal potential waveform.

A significant difference between the DEL capacitances calculated by the CV shape is noted only at low scan speeds. The cyclic voltammograms scanned at 40 mV/sec are shown in Table 2. The sample, whose surface was treated with a laser beam in mutually perpendicular directions, has cyclic voltammetric curves of the DEL with more elliptical shape than other samples. This indicates a better resistance of the sample to electrochemical reactions. A larger span along the current response axis indicates a higher DEL capacitance. However, significant increase in DEL capacitance was only noted at low scan rates, this does not fully correspond to cardiac pacing pulses. The positive effect of laser treatment on increasing the surface area of a substrate can be used to develop electrodes for energy storage devices, such as supercapacitors.

Conclusion

The method of platinum implantation into a titanium nitride structure with a high surface area that do not significantly degrade the electrochemical properties has been found. Future work will investigate the impact of platinum on the biocompatibility of these coatings. Cytotoxicological and antibacterial studies of electrodes with titanium nitride coatings with platinum implantation are planned at the Bakulev Scientific Center for Cardiovascular Surgery. Laser beam treatment of the substrate prior to deposition of TiN coating results in a significant increase in the DEL capacitance particularly at low frequencies, which could be useful for energy storage devices such as supercapacitors.

Acknowledgements. The work was carried out as a part of the Federal project "Development of technologies for controlled thermonuclear fusion and innovative plasma technologies". We would like to thank E.V. Kukueva, Scientific Researcher at the Kurchatov Institute, for conducting a study on electron microscopy.

References

1. **Schaldach M.** Electrocardiotherapy (Technical aspects of electrocardiostimulation). Saint Petersburg.(In Russ)] (1992).
2. **Sun N. et al.** Journal of Power Sources. – 2021. – T. 489. – C. 229406.

SYNTHESIS OF NANOPARTICLES BY LASER ABLATION OF COPPER TARGET IN A SURFACTANT SOLUTION FOLLOWING PHOTOINDUCED COALESCENCE

N.A. Savastenko[1], N.V. Tarasenko[2], A.V. Butsen[3], A.A. Nevar[2], O. M. Tursunkulov[4]

[1] Belarusian State University,International Sakharov Environmental Institute of Belarussian State University, 23 Dolgobrodskaya Str., 220070, Minsk, Belarus, nataliesavastenko@iseu.by

[2] B.I. Stepanov Institute of Physics NAS of Belarus, Nezalezhnasti Ave 68-2, 220072, Minsk, Belarus, a.nevar@ifanbel.bas-net.by, n.tarasenko@ifanbel.bas-net.by

[3] Belarusian State Technological University, Sverdlov str., 13a, 220006, Minsk, Belarus, a.butsen@belstu.by

[4] Center for Advanced Technologies, Talabalar shaxarchasi 3a, 100174, Tashkent, Almazar district, Uzbekistan, oybtmuz@gmail.com

Copper and copper-based nanoparticles (NPs) have attracted considerable interest because of their optical, catalytic, and electronic properties [1-3]. Cu- and Cu-based NPs can be synthesized by various techniques including both top-down and bottom-up approaches. As unique properties of NPs are size-dependent, the size-controllable preparation methods are preferable. Pulsed laser ablation in liquid (PLAL) is proved to be a versatile technique for NPs generation with controlled properties. In PLAL, NPs with a wide range of sizes can be create by only changing the laser's parameters [1, 4]. The postprocessing steps are often required to tune the physical and chemical NPs properties. Laser irradiation techniques have also been used as a powerful tool for the post-synthesis control of NPs structure. The laser irradiation of metal colloids can cause fragmentation or fusion through the photo-thermal melting of the nanoparticles [5, 6].

The present work describes the synthesis and characterization of Cu-based NPs produced by PLAL and morphological changes of NPs induced by laser irradiation.

Cu-based nanoparticles were prepared by laser ablation of a copper metal plate in an aqueous sodium dodecyl sulpate (SDS) solution (0.01 M). Experiments were carried out by using 25 Hz pulsed Nd:YAG laser (LTI 402), operating at the fundamental (1064 nm) wavelength. The laser fluence was 12 J cm^{-2}. The metal plate was placed on the cuvette filled with 60 ml aqueous solution of SDS. The laser-assisted modification of the nanoparticles was performed immediately after synthesis was completed. The synthesized colloid irradiated with the unfocused 532 nm output form Nd:YAG laser (LOTIS TII, LS2134). The laser irradiation fluence was 0.3 J cm^{-2}. The laser-induced morphology changes of nanoparticles were investigated by the UV-Vis

spectroscopy (Cary 5000 UV-Vis-NIR spectrophotometer) and transmission electron microscope TEM (LEO 906E).

Fig.1 shows the absorption spectra of freshly prepared nanoparticles. The spectra were measured before (curve 1) and immediately after (curve 2) irradiation. The freshly prepared colloids featured an absorption band peaked around 600 nm. No characteristic absorption band for copper oxide (CuO) around 800 nm was observed [7]. A peak of absorbance around 600 nm can be attributed either to Cu or to Cu_2O nanoparticles [7]. Though emerald color of colloidal solution indicates the formation of copper oxide particles, absorption spectra suggest the possible presence of copper metallic nanoparticles. Thus, our results imply that both copper and copper oxide particles may exist in solution.

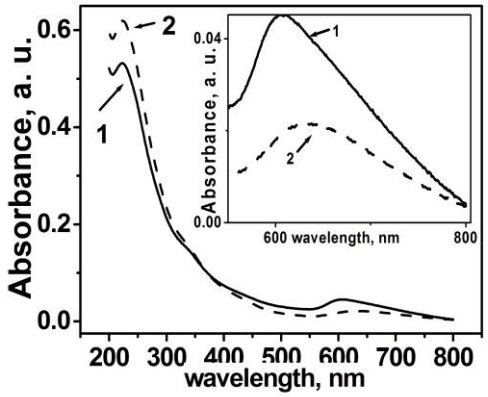

FIG. 1. Absorption spectra of freshly prepared nanoparticles before (1) and immediately after (2) irradiation. Inset: enlarged optical spectra around 600 nm

As it is clearly seen in Fig. 1, the absorbance at the wavelength of 240 nm increased by the laser irradiation. The height of the peak centring around 600 nm was found to be lowered by the laser irradiation. The comparison of the absorption spectra for irradiated and non-irradiated colloids indicates that 605 nm peak was redshifted to 630 nm after irradiation. It may be explained by the increase of the nanoparticle size as a result of coalescence [8, 9].

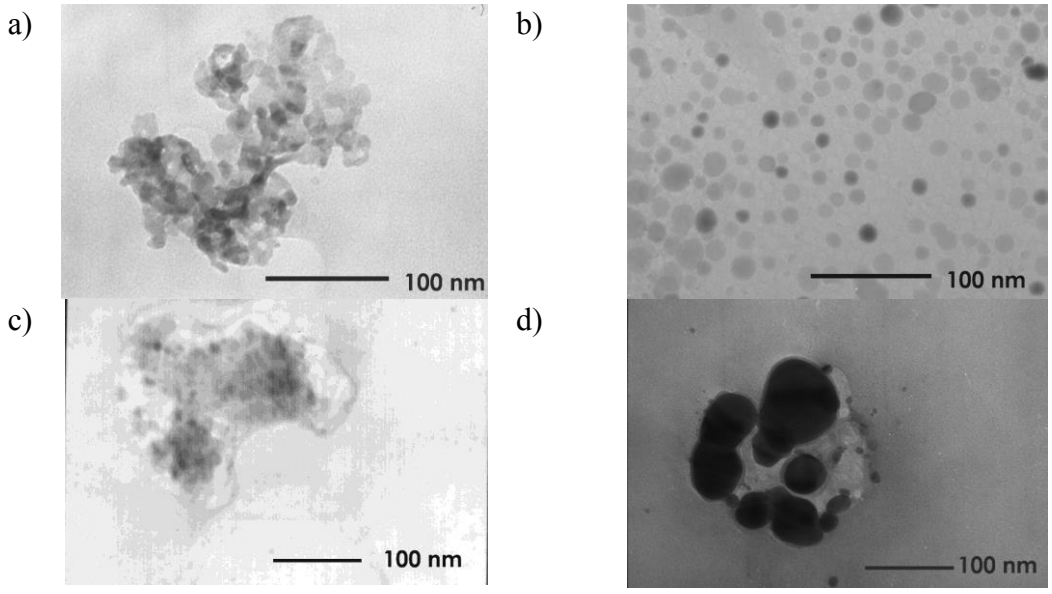

FIG. 2. TEM images of NPs from as-prepared (a, c) and irradiated (b,d) suspensions immediately after synthesis (a, b) and in 60 min after synthesis completion (c, d)

Fig.2 shows TEM images of as-prepared and irradiated NPs immediately after synthesis and in 60 min after synthesis completion. The as-prepared specimens consisted of small spherical particles (Fig.2a) Though irradiated nanoparticles were good separated in fresh, the coalescence processes was observed one hour later (Fig. 2d).

Fig.3 shows the particles size distribution (PSD) of as-prepared and irradiated NPs immediately after synthesis and in 60 min, 24 h, 1 week after synthesis was completed. As it shown in Fig.4, the as-prepared specimens consisted of spherical particles with mean diameter of 8 – 10 nm Irradiation of nanoparticles in aqueous solution by a pulsed Nd:YAG laser at 532 nm was found to cause the coalescence of nanoparticles. The multimodal dispersion was identified using TEM for irradiated NPs (Fig. 4 b, d, f, i, k) and nonmodified NPs after 1 week after synthesis.

(a)

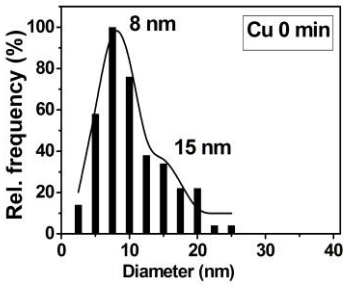

(b)

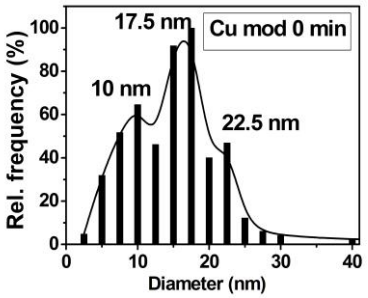

(c)

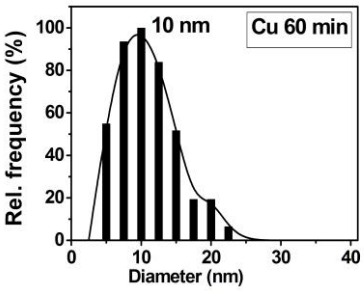

(d)

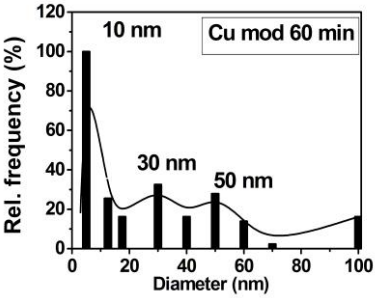

(e)

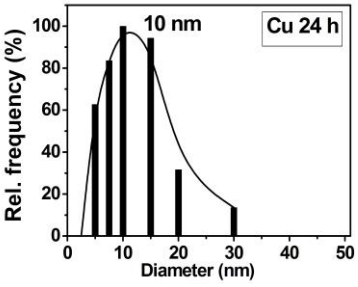

(f)

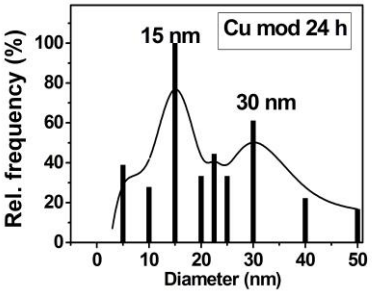

(j) (k)

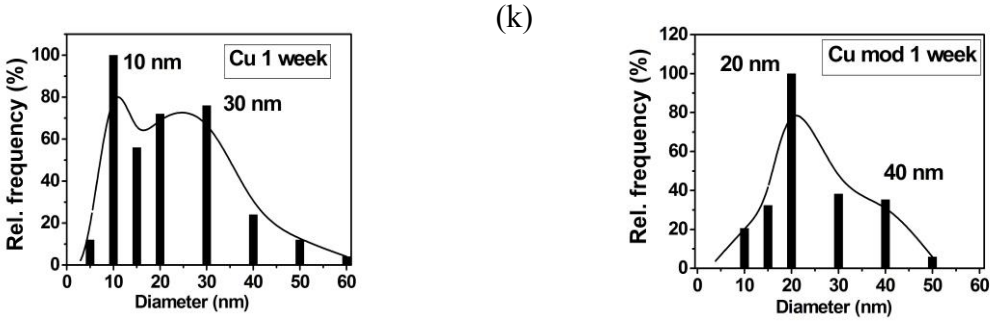

FIG. 3. Size distribution of as-prepared (Cu) and irradiated (Cu mod) NPs immediately after synthesis and in 60 min, 24 h, 1 week after synthesis was completed

The obtained data on the evolution of PSD allows to estimate the period of time in which the NPs remain stable to integrate them into other functional materials (e.g. composite catalysts).

Acknowledgements. This work was partially financially supported by the State Research Program Convergence 2025. 2.2.02. NIR 8, the State Research Program Convergence 2025. 2.2.05 and by KOICA, in collaboration with the Korea Research Institute of Chemical Technology (KRICT) and the Center for Advanced Technology (CAT).

References

1. **Quintero M., Manrique-Moreno M., Riascos H., Torres-Palma A., Castro-Narvaez S. and Ávila-Torres, Y.P**. Int. J. Mol. Sci., **25 (2024)** 6817-1–6817-19.
2. **Xu V.W., Nizami M.Z.I., YinI.X., Yu O.Y., Lung C.Y.K. and Chu C.H.** Nanomaterials, 12(2022) 805-1−805-15.
3. **Deng D., Cheng Y., Jin Y., Qia T. and Xiao F.** Journal of Materials Chemistry, 22(2012) 23989-23995.
4. **Attallah A.H., Abdulwahid F.A. Yasir A.A., Haider A.J.** Plasmonics, 20(2023) 1491-1521.
5. **Tarasenko N. V., Butsen A. V., Nevar E. A.** Appl. Surf. Sci., 247(2005) 418-422.
6. **Resta V., Siegel J., Bonse J., Gonzalo, J., Afonso C.N., Piscopiello E., Tenedeloo G.** Journal of Applied Physics, 100(2006) 084311.
7. **Yanase A. and Komiyama H.** Surf. Sci., **248**(1991) 20-26.
8. **Kamat P. J.** Phys. Chem. B **106**(2002) 7729-7744
9. **Wang Z.L**. (ed.) Characterization of Nanophase Materials, Weinheim: Wiley (2000).

VORTEX MOTION IN A SYSTEM OF ACTIVE BROWNIAN PARTICLES UNDER LASER IRRADIATION

R.V. Senoshenko[1,2], E.A. Kononov[1], M.M. Vasiliev[1,2], O.F. Petrov[1]

[1] Joint Institute for High Temperatures of the Russian Academy of Sciences, Izhorskaya 13 Bldg 2, Moscow, 125412, Russia
[2] Moscow Institute of Physics and Technology, Institutskiy Pereulok 9, Dolgoprudny, 141701, Russia

The phenomenon of activity, in which external energy is converted into kinetic energy, can occur in non-equilibrium systems containing colloidal particles that absorb energy and are distributed in a liquid or gas medium /1/. Particles with these properties are known as active Brownian particles. Depending on their own properties and the type of external influence, various collective phenomena and changes in the type of motion are possible in systems of active Brownian particles. Transition to vortex motion has been observed in both living active systems /2/ and artificial systems of active Brownian particles under the influence of laser radiation /3/. It is possible to maintain the previous characteristics of motion in such systems during subsequent changes and evolution.

Experimentally observed the formation of vortices in a monodisperse suspension under the influence of laser radiation, as well as their subsequent evolution. Spherical particles with a diameter of 2.05 μm, made of melamine-formaldehyde and partially copper-coated, were surface-stabilised with a surfactant to prevent coagulation. The liquid phase medium was an inert mixture of limited hydrocarbons, i.e. mineral oil, with a viscosity of 0.4 Pa·s. A system containing approximately 3,000 particles was exposed to a uniform beam of laser radiation. It was observed initially that the structure came into motion and formed a closed unidirectional flow. It was observed that at prolonged exposure to the laser beam, flow separation into two differently directed vortices occurred.

Using the collected experimental video data, the coordinates of particle motion in time were determined and their trajectories were reconstructed. The particle velocities were also calculated and the dependence of the mean-square displacement (MSD) on time was plotted for each observed mode of motion. The mean kinetic energies and diffusion coefficients for each mode were also calculated. The results demonstrate that the observed motion is active Brownian motion due to the thermophoresis effect /4/.

References

1. **Ramaswamy S.** J. Stat. Mech. Theory Exp., (2017), 054002.

2. **Vincenti B. and Ramos G. and Cordero M.L. and Douarche C. and Soto R. and Clement E.** Nat. Commun. 10 (2019), 5082.
3. **Madden I.P. and Wang L. and Simmchen J. and Luijten E.** Small 18 (2022), 2107023.
4. **Сеношенко Р. В. and Кононов Е. А. and Васильев М. М. and Петров О. Ф.** ЖЭТФ 167 (2025), 594.

DEVELOPMENT OF VAPOR-PLASMA FORMATION UNDER LASER ACTION ON A SAMPLE LOCATED IN A LIQUID

S. Vasiliev, A. Sitkevich

Yanka Kupala State University of Grodno, Belarus, Grodno, 230023, 22 Ozheshko str.,
rotkevich_al@grsu.by

The aim of this work is to investigate the processes occurring near a target when exposed to radiation from a pulsed laser with a power density of ~ 10^6 W/cm² on a metallic sample located in water.

Fig. 1 shows the schematic of the experimental setup used to study the dynamics of vapor-gas formation. The impacting laser, labeled as 1, was a GOR-100M laser operating in free-running mode, which allowed for the generation of laser radiation (LR) pulses with a duration of approximately 1.2 ms and energy E varying from 5 to 60 J, with a wavelength of 0.694 μm. The focusing system 2 formed an image of the diaphragm 4 on the surface of the studied sample 3. The diameter D of the resulting radiation spot with sharp edges varied during the experiments from 1 to 2 mm.

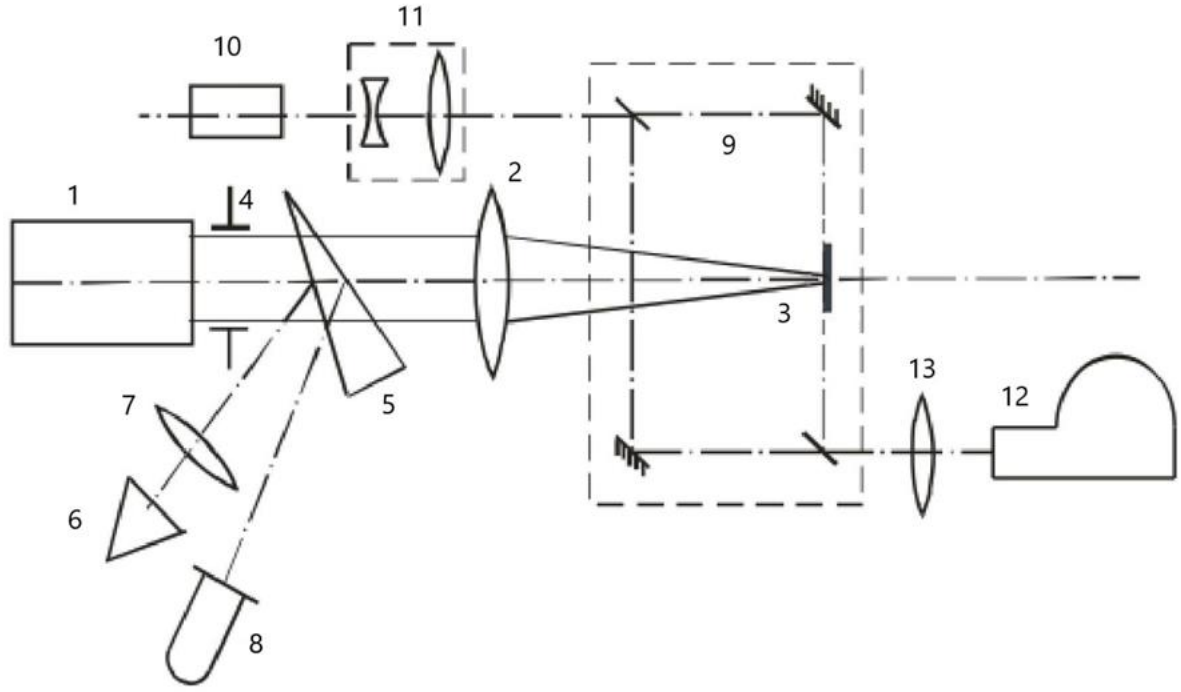

1 – impacting laser; 2 – focusing system; 3 – studied sample; 4 – diaphragm;
5 – beam splitter; 6 – energy meter; 7 – lens; 8 – coaxial element;
9 – Mach-Zehnder interferometer; 10 – probing laser; 11 – telescopic system;
12 – camera; 13 – objective of the photorecorder

Fig.1 – Schematic of the experimental setup

Experimental studies have shown that the topography of the crater formed by laser radiation on a lead sample submerged in water (Fig. 2) significantly differs from the shape of the crater formed by a laser pulse with the same parameters on a similar sample surrounded by air at normal pressure (10^5 Pa).

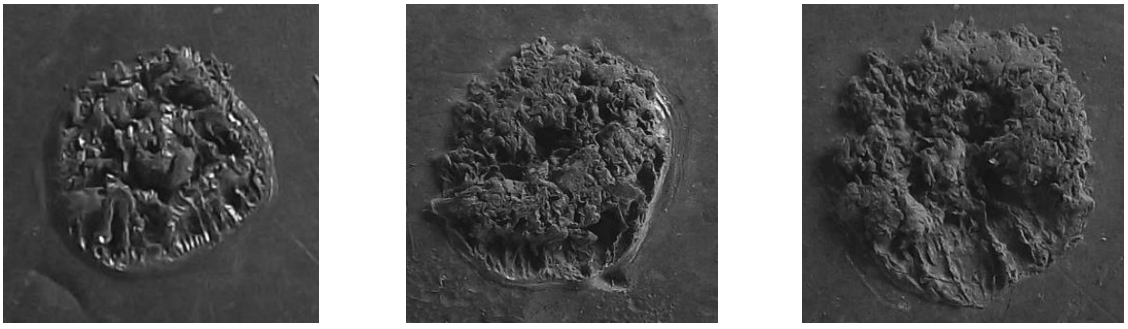

a) b) c)

The energy of the laser pulses is 10 J (a), 20 J (b), and 40 J (c).
Fig. 2 – Photographs of the craters formed by laser pulses on the lead sample submerged in water

Time-resolved shadow images of the growth and collapse of the vapor-gas bubble were studied to clarify the possible reasons for this difference. Fig. 3 presents snapshots of the vapor-gas formation development at 50, 500, 1000, 1500, 1600, and 2000 μs after the onset of laser exposure on the lead sample submerged in water. It was observed that approximately 1550 μs after the start of laser exposure, the growth of the bubble ceases. Following 2000 μs, its collapse is noted.

Analysis of the shadow images of the vapor-gas formation yielded linear dimensions of the bubble. Fig. 4 shows graphs of the radius of the vapor-gas formation as a function of the duration of laser exposure on the lead sample. It was established that in the initial growth phase, the radius along the laser beam (R_{laser}) and the radius along the surface ($R_{surface}$) are nearly identical. However, after approximately 400 μs, these values exhibit different trends depending on the duration of laser exposure.

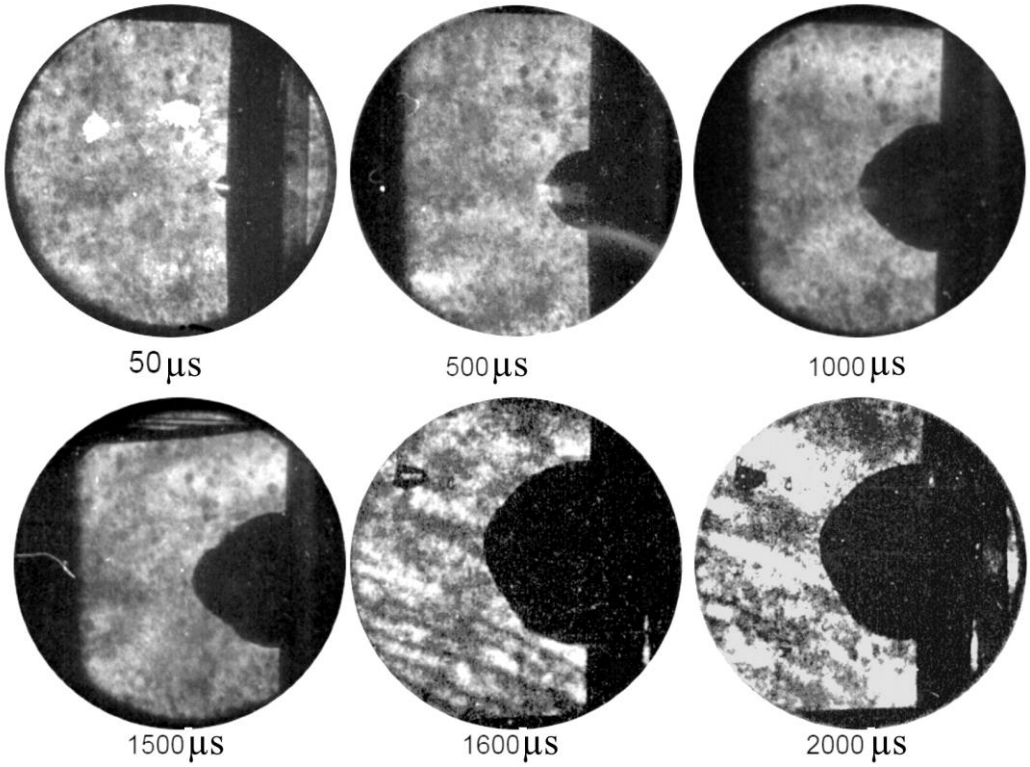

The diameter of the field of view is 4 centimeters

Fig. 3 – Shadow images of vapor-gas formation recorded at various time intervals after the onset of laser exposure on the lead sample

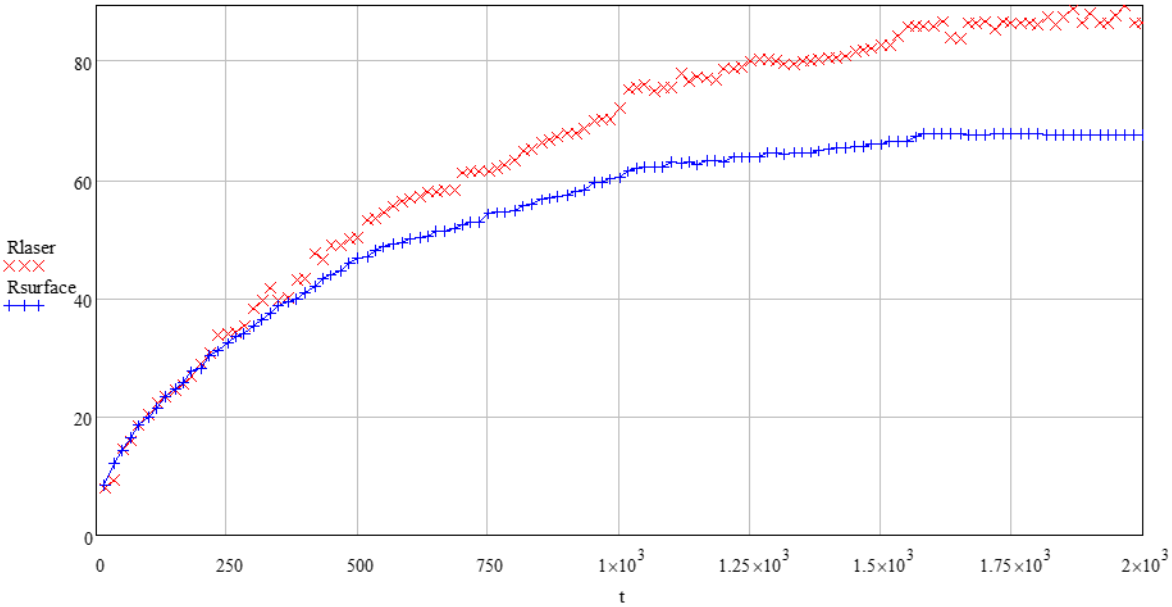

The red line (upper) represents the bubble radius along the laser beam, while the blue line (lower) represents the bubble radius along the surface of the plate

Fig. 4 – Change in linear dimensions of the bubble as a function of the duration of laser exposure

However, despite the differences in the magnitude of the radius changes over time, they exhibit a similar form of this dependence:

$$\begin{cases} R = at^3 - bt^2 + ct + d, \text{ if } t \le 1550\ \mu s \\ R = \text{const}, \text{ if } t > 1550\ \mu s \end{cases}$$

The observed differences can be attributed to several factors. The emergence of a temperature gradient due to uneven heating may lead to varying growth rates of the vapor-gas formation along the laser beam and across the surface of the irradiated sample /1, 2/. Additionally, changes in pressure can affect the size of the bubble.

The dynamics of vapor-gas formation growth near the surface of the metal submerged in water during its destruction by laser radiation was studied to provide a more detailed description of the reasons for this discrepancy.

Thus, the significant difference in the shape of the crater formed by laser pulses with identical parameters on similar samples surrounded by air and water is determined by the fundamentally different nature of the plasma and vapor-gas flow in these cases.

It is known that when laser radiation with parameters corresponding to the described experiment is applied to a sample, a vapor-plasma formation is created at the surface of the target. When laser radiation is applied to a metal surrounded by gas at a pressure of 10^5 Pa, the plasma formation can reach several centimeters in size. In contrast, when the sample is surrounded by water, the luminous area of the laser jet is significantly smaller – about 1 mm. This difference is attributed to the intense heating and evaporation of water, which leads to the formation of a vapor-gas "bubble." The contents of the "bubble" consist of two components: products of erosion from the irradiated sample (in our case, lead vapor) and water vapor.

References

1. **Bosak N.A., Vasiliev S.V., Ivanov A.Yu., Minko L.Ya., Nedolugov V.I., Chumakov A.N.** Features of crater formation on the surface of metal irradiated by repeated laser pulses: Quantum Electronics, 27(1999) 69 – 72.
2. **Butsen A., Burakov V., Kiris V., Tarasenko N.** Spectroscopic characterization of laser ablation in liquids: PPPT-VII, 1(2012) 220-223.

ROLE OF CHARGES IN WETTABILITY OF PLASMA-TREATED POLYTETRAFLUOROETHYLENE

M.Yu., Yablokov, A.A. Kuznetsov
Enikolopov Institute of Synthetic Polymeric Materials RAS, Moskow, Russia
yablokov@ispm.ru

Introduction

Modification of polymers by low-temperature plasma is a very effective method for improving wettability and adhesive strength /1/. However, aging of plasma-treated polymers leads to partial loss of hydrophilicity. This kind of instability of wetting is very undesirable for many industrial applications of polymeric materials. Determining the mechanism of hydrophobic recovery of polymers, as well as finding ways to overcome it, is an important scientific and practical task. To solve this problem, it is necessary to understand the mechanism of hydrophilization of polymers during their treatment in plasma. We used polytetrafluoroethylene (PTFE) to study the effects of plasma-treatment. Processing of PTFE by direct current (DC) glow discharge leads to significant hydrophilization and improvement of adhesive properties. Previously we showed the existence of a correlation between wetting, adhesive, and electret properties of PTFE films, modified by DC glow discharge /2/. It was shown, that the aging of plasma-treated PTFE films in the air with high relative humidity results in accelerated charge decay and loss of wettability, compared to the aging in dry air. We proposed to consider the hydrophobic recovery as a consequence of the surface charge relaxation of polymer electrets /3/. The reason for charge leakage in a humid atmosphere is the increase in surface conductivity due to the adsorption of water molecules /4/. Our interpretation of the obtained results is that the initially hydrophobic polymer surface during plasma treatment acquires an electric charge, which attracts polar water molecules due to charge-dipole interaction. Thus, the polymer surface becomes hydrophilic. Currently, the prevailing opinion is that the hydrophilicity of plasma-treated polymers is due to the appearance of oxygen-containing polar groups on their surface – carbonyl, carboxyl and hydroxyl, which attract water molecules due to dipole-dipole interaction /1/.
The aim of this study is to investigate the role of charges and surface chemistry in wettability modification of PTFE films treated by low-temperature plasma.

Experimental

The procedure for film modification by DC discharge is detailed in /5/. Two parallel plate aluminum electrodes of 13,5 cm in diameter with 4 cm distance between electrodes were used. PTFE samples with a thickness of 40 μm ("Plastpolymer", St. Petersburg, Russia) were placed on the bottom electrode.

The working plasma-forming gas was air, the pressure was 10 Pa, the discharge current was 50 mA, and the processing time was 40 s. The surface properties were characterized by water contact angle (WCA) values measured using an Easy Drop DSA100 instrument (KRUSS, Germany). Surface potential was measured using custom-made noncontact "dynamic capacitor" technique. The chemical composition of the surface was studied by X-ray photoelectron spectroscopy (XPS) using a LAS-3000 instrument (Riber, France).

Results and discussion

The experimental data on WCA measurement of PTFE films subjected to DC glow discharge on the anode and the cathode are shown on Fig.1.

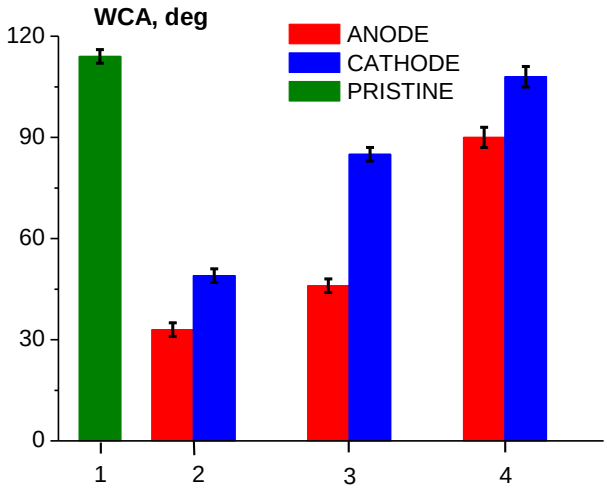

Fig.1. Wettability of PTFE films treated by DC discharge at the anode and at the cathode: water contact angle (WCA) values for (*1*) the pristine film, (*2*) the plasma-modified film, (*3*) the plasma-modified film aged for 14 days under ambient conditions, (*4*) the plasma-modified film heated at 150°C for 30 min

Film treatment on the anode (Fig.1, red columns) is more effective than on the cathode. Aging of PTFE film for 14 days leads to an increase in the WCA values. Heating of the film at 150^0C results in a much more pronounced hydrophobic recovery than 14-day aging. If the wettability of plasma-treated polymers is due to the appearance of oxygen-containing chemical groups on the surface, then the phenomenon of hydrophobic recovery should be accompanied by a decrease in the oxygen concentration on the surface. However, in a number of publications, devoted to the study of hydrophobic recovery of plasma-treated polymers, for example /6/, it is reported that the aging of polymer films after plasma treatment is not accompanied by a decrease in the surface concentration of oxygen. This result contradicts the interpretation of hydrophilicity a result of the appearance of polar chemical groups on the surface after plasma treatment.

Treatment of polymers by DC glow discharge at the cathode results in a positive charging of the surface, while treatment at the anode results in negative charging. Surface charges are deposited directly from the plasma during the treatment process and can also be the result of ionization of polymer by UV-radiation. The values of WCA, effective surface charge density and surface oxygen concentration measured for the PTFE film treated at the anode by DC discharge are shown in Fig.2. Plasma treatment results in an increase of surface charge, a significant reduction in WCA and appearance of oxygen on the surface. It is also known that free radicals are produced in plasma-irradiated PTFE /7/. Aging of plasma-treated PTFE film results in an increase in WCA value and a decrease in surface charge. Aging of plasma-treated PTFE film results in an increase in WCA value and a decrease in surface charge.

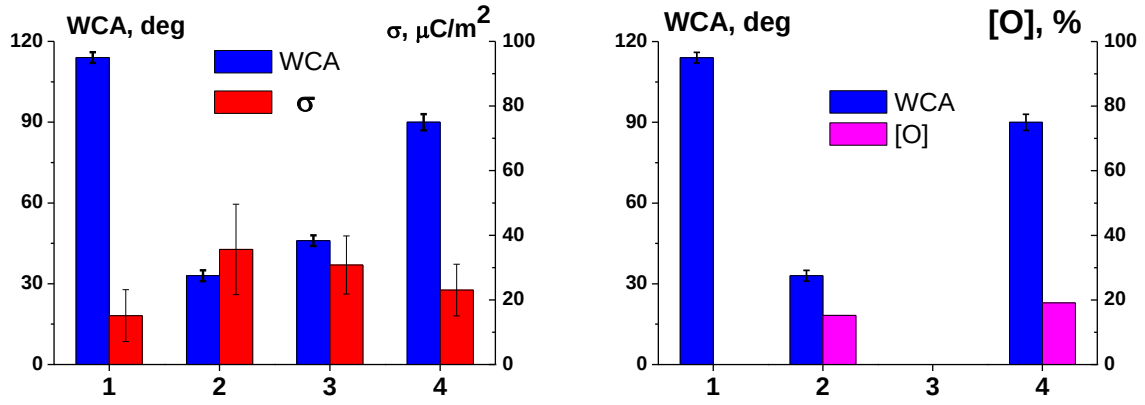

a. b.

Fig.2. Properties of PTFE film treated at the anode by DC discharge: a) water contact angle (WCA) and effective surface charge density σ; b)WCA and surface oxygen concentration [O]: (*1*) the pristine film, (*2*) plasma-modified film, (*3*) plasma-modified film aged for 14 days under ambient conditions, (*4*) plasma-modified film heated at 150°C for 30 min

Heating of the film also results in an increase in WCA and a decrease of surface charge, but the hydrophobic recovery under heating is higher, than that under aging. The atomic concentration of oxygen, determined using XPS, remains unchanged upon heating (Fig.2b). This result shows that the hydrophobic recovery of plasma-treated polymers is not directly related to surface oxygen, and therefore the wettability cannot be explained solely by the presence of oxygen-containing polar groups. To explain the hydrophobic recovery, it is necessary to take into account the decay of surface electrets charges. During plasma treatment, electric charges – ions and electrons – are deposited in the surface layer of polymers. The charges are stabilized in the surface layer of

polymers by oxygen-containing groups and free radicals that appear on the surface as a result of plasma treatment. One of the main factors of charge stabilization in plasma-treated PTFE is the very high electron affinity of fluorine-containing radicals /8/. In particular, the electron affinity of the CFO radical is about 3.3 eV, which is comparable to the dissociation energy of C-C bond. Aging of plasma-treated films in a humid atmosphere results in increased surface conductivity and leakage of surface charges. Heating increases the mobility of electric charges and empties surface traps. The existence of a wide energy distribution of charge traps leads to a partial hydrophobic recovery: the WCA value after aging or heating does not return to the WCA value of the pristine PTFE film /3/. Our interpretation of the change in wettability of plasma-treated polymers is based on the simultaneous consideration of three processes: free radicals formation, oxygen-containing group formation and surface charging. None of these processes alone can explain wettability improvement.

Conclusions

Based on the results of the study of PTFE films treated by DC glow discharge, it can be concluded that charges play an important role in improving wettability of plasma-treated polymers. Increased wettability after plasma treatment is achieved by the interaction of polar water molecules with surface charges via charge-dipole forces. Stabilization of charges in the surface layer of polymers is achieved by oxygen-containing groups and free radicals.

Acknowledgements

This work was supported by the Ministry of Science and Higher Education of Russian Federation, contract № FFSM-2024-0002.

References

1. **Wu S.** Polymer interface and adhesion. New York: M. DEKKER (1982).
2. **Yablokov M., Piskarev M., Gilman A., Kechek'yan A., Kuznetsov, A.** Journal of Physics: Conference Series, 982(2018) 012012 (1-4).
3. **Yablokov M., Kuznetsov A.** Physics of Complex Systems, 5(2024)202-204.
4. **Shuvayev V., Turyshev B., Romanovskaya O. Lobanov A., Vorobyev V., Myasnikov G., Kuznetsova O.** Polymer Science USSR, 19(1977) 698–703.
5. **Rychkov D., Yablokov M., Rychkov A.** Applied Physics A, 107 (2012) 589–596.
6. **Xie X., Gengenbach T., Griesser H.** Journal of adhesion science and technology, *6*(1992) 1411-1431.
7. **Kuzuya M., Ito H., Kondo S., Noda N., Noguchi A.** Macromolecules, 24 (1991) 6612-6617.
8. **Harland P., Thynne J.** Journal of Physical Chemistry, *74*(1970) 52-59.

DIGITAL UPGRADE OF ANALOG OPTICAL DEVICES IN LASER SURFACE PROCESSING APPLICATIONS

V. Zheleznov

Institute for Electrophysics and Electric Power of the Russian Academy of Sciences, 18 Dvortsovaya Nab., St. Petersburg, 191181, Russia, vyuzheleznov@ieeras.ru

Due to its high accuracy and efficiency, lasers have become an integral part of modern technologies. They are used for cutting, welding, diagnostics, hardening, and high-precision material processing /1-3/.

In the era of import substitution, it is essential to focus on domestic equipment that demonstrates outstanding technical characteristics, although often based on analog components. Attention should also be paid to novel metrological methods. The development of proprietary technological solutions will help reduce dependence on imported equipment.

The registering part of the analogue equipment can have good technical characteristics, however, the absence of digital methods of processing the information received sharply reduces their information capabilities, and requires a large time cost of calculations and register the obtained measurement results. This is especially noticeable when measuring the energy of the package of laser pulses with a high track frequency.

In this paper, the possibility of extending the operation of well-proven analog measuring devices is considered, a method for measuring the energy density/power of the focused bundle of impulse laser radiation is presented. The possibility of measuring the reflection coefficients is shown, due to synergy of digital modernization and the measurement method.

Experimental setup and methods. A solid-state Nd:YAG laser operating at a wavelength of 355 nm was employed as the radiation source. The laser produced pulses with a duration of 10 ns and pulse energies up to 8 mJ, at a repetition rate of up to 100 Hz. The laser beam had a diameter of approximately 3 mm and a divergence of 1–2 mrad.

The ILD-2M laser dosimetry meter (Fig. 1) was upgraded and automated using the Arduino UNO controller and calibrated using a portable laser power and energy meter the Nova II /4/. ILD-2M characteristics: spectral range 0,49-1,15 microns; The range of energy measurement and radiation power 10^{-8}-1 J, 10^{-6}-10 watts; The frequency of pulses is up to 500 Hz /5/.

The connection diagram of the devices to the Arduino Uno controller is presented in /4/. The ILD-2M CRU was connected to the controller through an inverting operational amplifier, which reversed the polarity of the signal at the CRU output. Then the positive signal came to the analog input of the controller. The Nova II /6-9/ meter was connected to the analog input and ground of the

controller. A photodiode connected to the digital output of the controller was used to synchronize measurements and control the optical shutter controlling the number of laser pulses.

Fig. 1 - Conversion and registration unit (CRU) and measuring head of ILD – 2M

In the study of the optical resistance of metals and semiconductors, it became clear that reliable measurement of the laser spot size is a big problem. In many ways, the measured size of the spot depends on the physicochemical properties of the material under study and the focus of the lens.

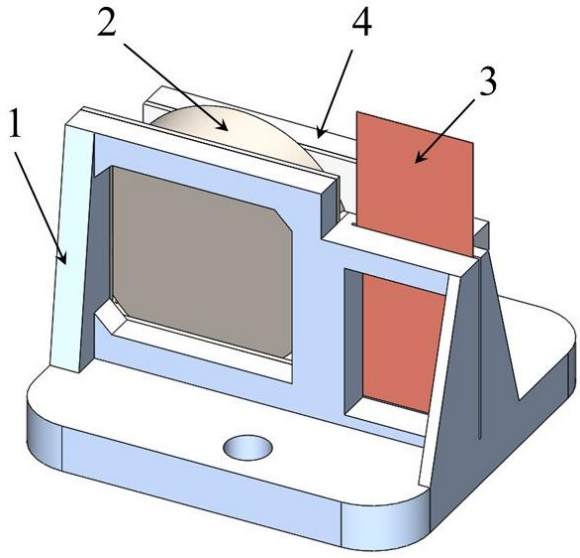

Fig. 3 – Sample mounting device: 1 – base; 2 – sample; 3 – standard; 4 – pressure plate /10/

To eliminate their influence the 3D printed device was developed to measure the spot size of a laser beam (Fig. 2). Its purpose is to ensure that the examined surfaces of the sample and the standard are positioned in the same plane, thereby minimizing the influence of their physical, chemical, and optical properties during interaction with the laser beam. Copper foil with a thickness of 0.1 mm was chosen as a standard.

The measurements were conducted as follows. The sample and the standard (calibration) target were fixed in the mounting device, after which the standard was irradiated with laser pulses at a specified energy. The standard was then

removed, and the dimensions of the irradiation spots on its surface were measured. The laser beam dimensions were calculated from the spot measurements using the methodology described in references /10,11/. Subsequently, the test sample was irradiated at specified energy densities. The measured laser beam area was 1 mm².

Results and discussion. Monocrystalline silicon and germanium samples with a surface roughness of approximately 5–6 nm were utilised. The scheme of the setup employed for measuring the reflection coefficient is presented in /4, 12/.

The reflection coefficient R was determined in accordance with the standard procedure as the ratio of the reflected to incident energy flux. Measurements were conducted over a laser pulse energy density range of 0.01–0.2 J/cm².The plots of the reflectivity of Si and Ge are demonstrated in Fig. 3.

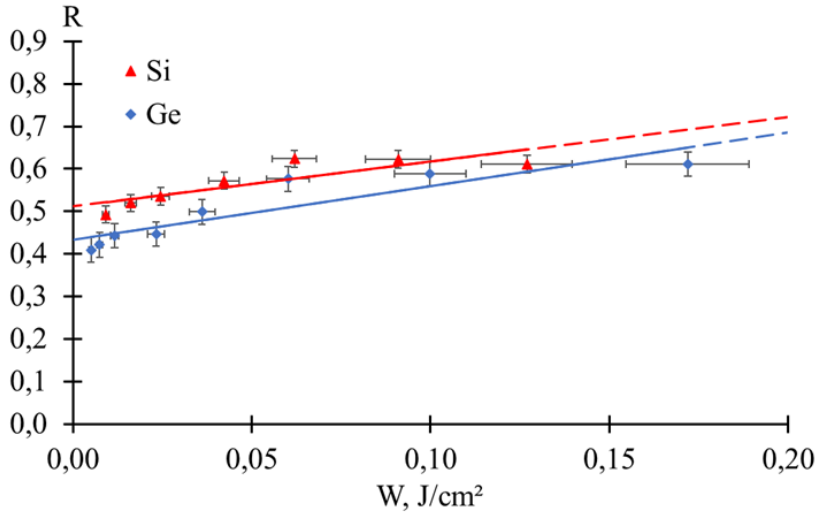

Fig. 3 – Experimental plots of the reflection coefficients of monocrystalline Si and Ge as functions of the incident 355 nm Nd:YAG laser energy density

Reflectivity increased with rising pulse energy density, as expected. Experimental reflectance values could not be obtained for energy densities ≥ 0.13 J/cm² (Si) and ≥ 0.17 J/cm² (Ge) due to surface degradation and increased scattering.

Based on the experimental dependencies, the following analytical expressions were derived, enabling the calculation of the reflection coefficients for germanium and silicon as functions of the laser energy density:

$$R_{Si} = 0{,}49 * e^{0{,}14*w}, \quad (1)$$

$$R_{Ge} = 0{,}36 * e^{0{,}174*w}, \quad (2)$$

where w denotes the energy density of the laser radiation.

It is anticipated that, within the 0.1–1.0 J/cm² interval, this relationship persists, as surface degradation remains confined to the condensed phase. In contrast, at 1.0–2.0 J/cm², optical breakdown induces phase transitions, resulting in melting and vaporization of the material.

Conclusion. This work presents a method for measuring the energy density of laser radiation using a reference standard, thereby eliminating the influence of the physicochemical properties of the samples under investigation. An analog ILD-2M device was upgraded to a digital version based on an Arduino Uno controller and successfully employed to measure the reflection coefficients of Si and Ge under UV nanosecond laser pulses. The dependences of reflectivity on energy density in the range of 0.01–0.2 J/cm² were obtained.

Acknowledgements. This work was supported by the Russian Science Foundation, grant no. 24-19-00727.

References

1. **Ganin D.V., Mikolutskiy S.I., Tokarev V.N., Khomich V.Y., Shmakov V.A., Yamshchikov V.A.** Quantum Electronics, 44(2014) 317–321.
2. **Zheleznov V.Yu., Malinskiy T.V., Rogalin V.E., Khasaya R.R., Khomich Yu.V., Isakov V.V., Kozlov A.L., Novikov I.A., Nozhnitskiy Yu.A., Shibayev S.A**. Uspekhi Prikladnoy Fiziki, 11(2023) 340–355. (in Russian)
3. **Tokarev V. N., Cheshev E. A., Bezotosnyi V. V., Khomich V. Y., Mikolutskiy S. I., Vasil'yeva N. V.** Laser Physics, 25(2015) 056003.
4. **Zheleznov V.Yu., Malinskiy T.V., Rogalin V.E., Filin S.A.** Prikladnaya Fizika, 2(2023) 90–96. (in Russian)
5. **Rakhmanov B.N., Kibovskiy V.T.** Bezopasnost' v Tekhnosfere, 2(2013) 3–13. (in Russian)
6. **Zheleznov V.Y., Malinskii T.V., Mikolutskii S.I., Khomich Y.V.** *Journal of Communications Technology and Electronics*, 68(2023) 1061–1066.
7. **Zheleznov V.Yu., Malinskiy T.V., Mikolutskiy S.I., Rogalin V.E., Khomich Yu.V., Kaplunov I.A., Ivanova A.I., Ashkinazi E.E.** Materialovedenie, 2(2025) 16–20.
8. **Zheleznov V.Yu., Malinskiy T.V., Rogalin V.E., Khomich Yu.V., Ashkinazi E.E., Sovyk D.N., Zavedeev E.V., Fedorov S.V., Litvinov A.P.** Fizika Tverdogo Tela, 65(2023) 2181–2183.
9. **Khomich Y.V., Malinskiy T.V., Rogalin V.E., Shakhmatov E.V., Yamshchikov V.A., Zheleznov V.Yu.** Acta Astronautica, 225(2024) 556–564.
10. **Zheleznov V.Yu., Malinskiy T.V., Mikolutskiy S.I., Rogalin V.E., Filin S.A.** *Prikladnaya Fizika*, 1(2024) 38–42. (in Russian)
11. **Byskov-Nielsen J., Savolainen J. M., Christensen M. S., Balling P.** *Applied Physics A*, 101(2010) 97–101.
12. **Malinskiy T.V., Zheleznov V.Y., Rogalin V.E., Kaplunov I.A.** Journal of Physics: Conference Series, 2103(2021) 012154.

LASER POLISHING OF NATURAL LEATHER

A. G. Anisovich[1], M. I. Markevich[2], V. I. Zhuravleva[3],
T. Zh. Kodirov[4], U. O. Khudanov[4]

[1] Institute of Applied Physics of the National Academy of Sciences of Belarus,
Akademicheskaya St., 16, 220085, Minsk, Republic of Belarus,
anna-anisovich@yandex.ru
[2]Physical-Technical Institute of the National Academy of Sciences of Belarus, st. Kuprevich,
10, 220141, Minsk, Republic of Belarus,
a.chaplanov@gmail.com
[3]Military Academy of the Republic of Belarus, Nezavisimosti Ave. 220, 2200057,
Minsk, Republic of Belarus
[4]Tashkent Institute of Textile and Light Industry, 100100,
Tashkent, Republic of Uzbekistan

Introduction

Natural leather products continue to enjoy significant popularity and demand, even in the face of advanced synthetic alternatives. This enduring preference is largely attributed to natural leather's superior hygroscopic properties, exceptional durability, and inherent biocompatibility with the human body /1−3/.

During the growth and development of animals, various factors may lead to the formation of scars on their skin. These scars, characterized by dense collagen-rich tissue, detract from the aesthetic quality of the leather. Laser resurfacing, however, offers a promising solution by effectively smoothing the leather surface and eliminating scars and imperfections.

Despite substantial advancements in our understanding of the physical processes underlying leather tanning, the specific effects of laser treatment on natural leather – particularly the morphological changes induced by dual-pulse processing – remain insufficiently explored.

Key advantages of laser processing of natural leather include:
– Rapid processing speeds;
– No deformation of material outside the targeted area;
– Precise treatment of minute surface areas (approximately 10–20 μm);
– Non-contact processing that prevents material distortion;
– Sterile treatment conditions.

This study aims to investigate the surface morphology of natural leather and to elucidate the unique characteristics of laser resurfacing on both the grain (outer) and flesh (inner) sides when processed in a dual-pulse mode.

Materials and methods

The study was conducted using uncolored chromium-tanned leather waste sourced from Uzbekistan. The samples exhibited the following physicochemical properties: moisture content – 52.4%, total ash – 4.8%, fat content – 3.2%, proteinaceous matter – 76.83%, chromium oxide – 5.2%, and hydrothermal degradation threshold – 92.0 °C. The thickness of the leather samples was approximately 1.2 mm.

Laser treatment of the natural leather samples was performed in a dual-pulse mode using an LS-2134D Nd:YAG laser (LOTIS, Belarus) with a wavelength of 1064 nm. The laser operated in a dual-pulse regime, where the pulses were separated by a 3 μs interval and had a pulse duration of 10 ns /3-5/. The samples were subjected to laser irradiation at energy levels ranging from 30 to 240 J, with exposure times varying between 30 and 240 seconds. The treatment was applied to both the grain (outer) and flesh (inner) sides of the leather.

Surface morphology analysis was conducted using a MIRA-3 scanning electron microscope (Czech Republic) equipped with an Oxford Instruments microanalysis system (United Kingdom). This equipment enabled simultaneous investigation of surface morphology, elemental composition distribution, and high-resolution imaging across a broad magnification range /2,5/.

Results

Fig. 1 presents the surface morphology of the grain side of the natural leather sample before and after laser resurfacing. The image reveals that the laser ablation process significantly alters the grain surface, smoothing out the texture and effectively polishing the leather.

Fig. 2 displays the morphology of the flesh side of the natural leather sample before and after laser treatment. The findings indicate that the energy required to initiate the polishing process on the flesh side is higher than that needed for the grain side.

In Fig. 2b, individual fibrils with an approximate thickness of ~0.5 μm can be observed. Notably, the fibrous structure of the flesh side exhibits a well-developed internal surface with numerous empty spaces of varying shapes and sizes, ranging from 7 to 40 μm. This structural complexity distinguishes the flesh side from the grain side and influences its response to laser processing.

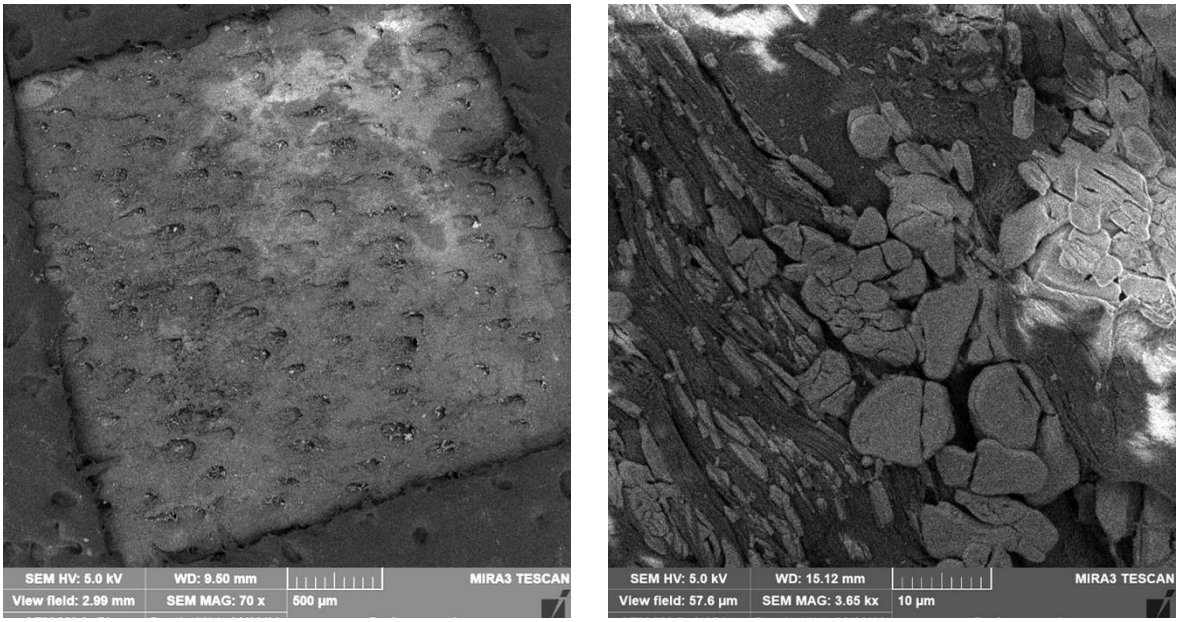

a b

Fig. 1. Morphology of the surface of the front side of the skin: a – without exposure, b – after exposure (input energy 30 J, exposure time 30 s)

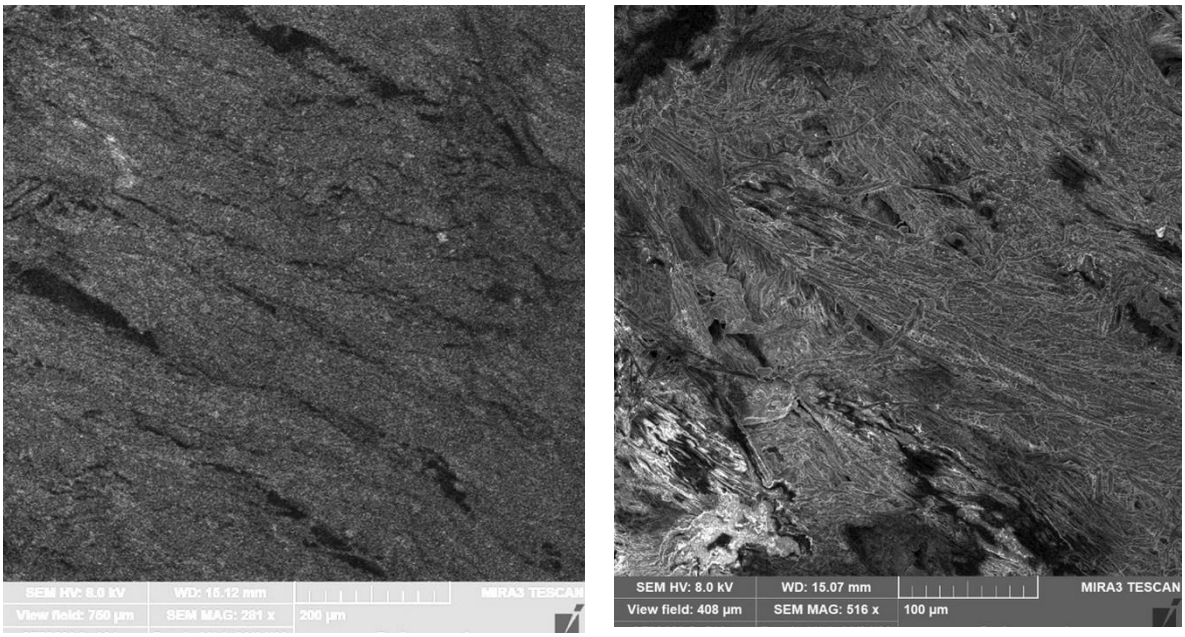

a b

Fig. 2. Surface morphology of the reverse side of the leather: a – without exposure, b – after exposure (input energy 60 J, exposure time 60 s)

Conclusions

For the first time, we have investigated the laser resurfacing of natural sheepskin leather by applying laser treatment to both the grain (outer) and flesh (inner) sides using a laser operating in a dual-pulse mode. The study established that laser exposure effectively polishes the leather surface on both sides.

Our findings demonstrate that the initiation of laser resurfacing on the grain and flesh sides occurs at different threshold energy levels, with the process beginning at 30 J for the grain side and 40 J for the flesh side. This difference is likely attributed to the looser fibrous structure of the flesh side, which results in lower absorption of laser radiation compared to the grain side.

References

1. **Voznesensky E.F., Khasanshin R.R., Krasina I.V., Abdullin I.Sh., Safin R.R., Aminov L.I.** General principles of modification of natural fibrous materials of various origins in low–pressure RF discharge plasma. Bulletin of Kazan Technological University. –2009.– No.1/5.– P.304–307.
2. **Anisovich A.G., Markevich M.I., Zhuravleva V.I., Shcherbakova E.N., Shapovalov S.V.** Surface morphology of natural leather after laser exposure. Electronica plus.–2021.–No.2.–P.49–51.
3. **Kodirov T.J., Markevich M.I., Malyshko A.N., Zhuravleva V.I., Sodikov N.A.** Researches of Morphological Structure, Element Composition And Natural Leather Adsorption By Exposure to Laser Radiation International Journal of Resent Technology and Engineering.–2020.–V.8.–I.6.– P.4880–4884.
4. **Sodikov N.A., Markevich M.I., Kodirov T.Zh., Abdirashidov H.A.** Study of water adsorption of natural leather tanned with guz–pai tannide under laser radiation exposure. Proceedings of the conference "Nature management and current issues of ecology and safety of human life in the 21st century".– Kazakhstan.–Taraz.–2021.– P.131–133.
5. **Anisovich A., Kodirov T., Khudanov U, Markevich M., Zhuravleva V.** Morphology of the surface of natural lamb leather after tannide tanning and laser exposure. Plasma Physics and Plasma Technology.–Contributed papers. – Minsk.–Belarus.–12–16 September.–2022.– P.165–168.

SURFACE MORPHOLOGY, OPTICAL AND ELECTROPHYSICAL PROPERTIES OF FILMS $La_{0.82}Sr_{0.18}Co_{0.9}Ni_{0.1}O_{3-d}$

N.A. Bosak[1], M.V. Bushinsky[2], L.V. Baran[3], V.V. Malyutina-Bronskaya[4], O.S. Mantytskaya[2], A.S. Kuzmitskaya[4], N.V. Podvitsky[1]

[1]B.I. Stepanov Institute of Physics, National Academy of Sciences of Belarus, 68-2 Nezavisimosti Ave., 220072 Minsk, Belarus, n.bosak@ifanbel.bas-net.by
[2]GO "Scientific and Practical Center of the National Academy of Sciences of Belarus for Materials Science", st. Petrusya Brovki 19, 220072 Minsk, Belarus, bushinsky@physics.by
[3]Belarusian State University, 4 Nezavisimosti Ave., 220030 Minsk, Belarus, baran@bsu.by
[4]SSPA "Optics, Optoelectronics and Laser Technology", 68 Nezavisimosti Ave., 220072 Minsk, Belarus, malyutina@oelt.basnet.by

Introduction. Currently, cobaltite-based materials are gaining popularity in the field of materials science due to their exceptional optical, magnetic and electrical properties. The study of epitaxial $LaCoO_3$ films showed that below 85 K they are ferromagnetically ordered, while bulk samples of the same composition are diamagnetic at temperatures below 30 K /1/. In /2/, a comparison of the magnetic properties of a bulk sample and a film of rare-earth cobaltite $Pr_{0.5}Sr_{0.5}CoO_3$ was carried out, which showed the absence of a second magnetic transition in the film upon cooling.

In this paper, studies of thin films of $La_{0.82}Sr_{0.18}Co_{0.9}Ni_{0.1}O_{3-d}$ on a silicon substrate obtained by multi-pulse high-frequency laser deposition in vacuum were carried out /3/. The morphology of the obtained thin films was studied using atomic force microscopy, the features of the transmission spectra in the near and middle IR regions and the reflection spectra in the visible and near IR regions were revealed, and the current-voltage (CVC) and capacitance-voltage (CV) characteristics were investigated.

Experimental setup. $La_{0.82}Sr_{0.18}Co_{0.9}Ni_{0.1}O_{3-d}$ films were deposited by high-frequency laser sputtering of ceramic targets in vacuum (p = 1.7 Pa). The experimental laser setup (λ = 1.06 μm) with an adjustable laser pulse repetition rate from 5 to 50 kHz contained a laser radiation source, an optical system for transporting laser radiation to the sputtered target, a vacuum chamber, and a measuring and diagnostic module. The laser pulse repetition rate was changed by varying the laser pumping level and the optical density of the shutter made of radiation-irradiated crystalline lithium fluoride LiF with F_2^- color centers; the laser pulse duration at half maximum was $\tau \sim 85$ ns. Deposition of macroscopically homogeneous thin films was achieved at a laser power density of q = 21.4 MW/cm^2 and a pulse repetition rate of $f \sim 10–12$ kHz. The surface morphology of the samples was studied using a Solver P47-Pro scanning probe microscope (NT-MDT, Russia) in the semi-contact mode. The optical

transmission of thin films in the near infrared (IR) range of the spectrum was measured on a Carry 500 Scan spectrophotometer. Transmission spectra in the mid-infrared region were recorded using a NEXUS IR Fourier spectrometer (Thermo Nicolet) in the range of 400-4000 cm^{-1}. The *I–V* characteristics of the dark and laser radiation with different wavelengths were measured at room temperature on an automated basic laser test complex with a multispectral laser radiation source (a set of laser diodes with wavelengths of 405, 450, 520, 660, 780, 808, 905, 980 and 1064 nm with a common fiber optic output and calibrated radiation power). The *C–V* characteristics were measured on an E7-20 immittance meter at a signal frequency of 100 kHz, 500 kHz and 1 MHz.

Experimental results and their analysis. AFM images of the surface morphology of $La_{0.82}Sr_{0.18}Co_{0.9}Ni_{0.1}O_{3-d}$ films on a silicon substrate are shown in Fig. 1. Atomic force microscopy showed that high-frequency laser deposition results in the formation of finely dispersed films. A small number of large droplets up to 450 nm high with a lateral size ranging from 0.5 to 2.5 μm and a large number of small formations with a lateral size of 100–200 nm are observed on the film surface. The average height of the surface relief of the film

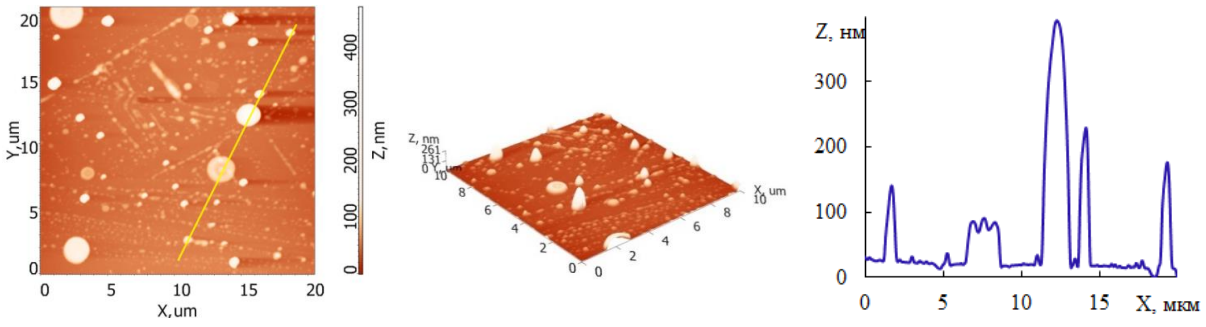

a b c

Fig. 1. Surface morphology of the $La_{0.82}Sr_{0.18}Co_{0.9}Ni_{0.1}O_{3-d}$ film on a silicon substrate: a – two-dimensional AFM image, b – three-dimensional AFM image, c – cross-section profile along the selected line

deposited on a silicon substrate, which was determined by five different scanning areas of 20x20 μm, is 66 nm with a root-mean-square roughness of 31.5 nm. The transmittance of the laser-deposited $La_{0.82}Sr_{0.18}Co_{0.9}Ni_{0.1}O_{3-d}$ film on a silicon substrate in the visible and near-IR spectral regions are shown in Fig. 2, a. The transmittance spectrum shows a plateau of T = 5.9% in the wavelength region of λ = 840 nm and a sharp increase in the transmittance in the wavelength region of λ = 1050 nm, reaching a constant transmittance value of T = 64.2% at λ = 2811 nm. In the transmission spectrum of the film on the silicon substrate in the mid-IR region (Fig. 2, b), two absorption bands are observed in the frequency range ν_1 = 609 cm^{-1} and ν_2 = 1093 cm^{-1} with a smooth increase in the transmittance to T_{max} = 68.5% at ν = 3714 cm^{-1}. In the reflection

spectrum R of the film (Fig. 2, c), an oscillating behavior of the reflectivity is observed from R_{min} = 2.5% at λ = 795 nm to R_{max} = 37.6% at λ = 1098 nm.

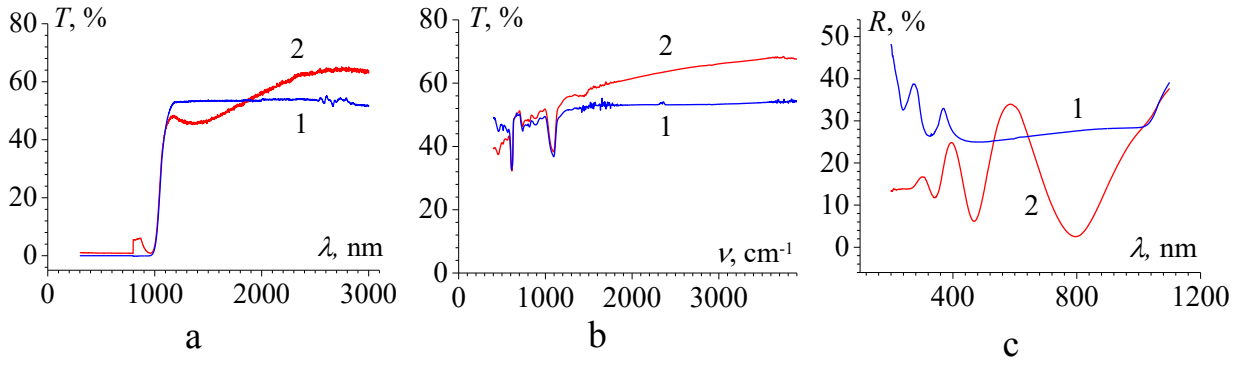

Fig. 2. Transmission spectra of silicon substrate (1) and laser-deposited $La_{0.82}Sr_{0.18}Co_{0.9}Ni_{0.1}O_{3-d}$ film on silicon substrate (2) in the visible, near-IR (a) and mid-IR (b) regions. Reflectance spectra of silicon substrate (1) and laser-deposited film on silicon substrate (2) in the visible and near-IR regions (c)

Fig. 3, a shows the asymmetric CVC measured across the $La_{0.82}Sr_{0.18}Co_{0.9}Ni_{0.1}O_{3-d}$ structure on silicon substrate irradiated with laser radiation of different wavelengths. As can be seen from the figure, the photoelectric effect is not very pronounced. Fig. 3, b shows the transverse CVC

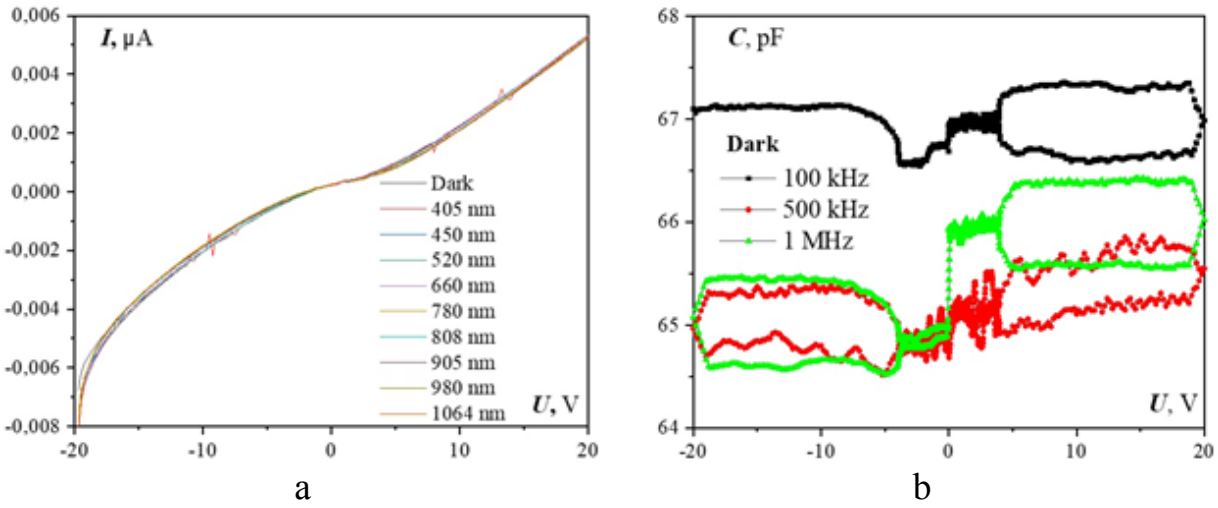

Fig. 3. Current-voltage (a) and capacitance-voltage (b) characteristics measured across the oxide film of the $La_{0.82}Sr_{0.18}Co_{0.9}Ni_{0.1}O_{3-d}$/Si structure when illuminated by laser sources with different wavelengths

of the film obtained, which exhibit hysteresis, especially at both voltage polarities at frequencies of 500 kHz and 1 MHz. The nature of the hysteresis

loops indicates nonlinearity with the applied electric field of the dielectric properties of the film. However, the shape of the CVC is not typical for the ferroelectric properties of films /4/, and is characteristic of the composition with a lower lanthanum content $La_{0.82}Sr_{0.18}Co_{0.9}Ni_{0.1}O_{3-d}$.

Conclusions. Nanostructured $La_{0.82}Sr_{0.18}Co_{0.9}Ni_{0.1}O_{3-d}$ films with an average roughness of 66 nm were obtained by the method of multi-pulse high-frequency laser deposition in vacuum, on the surface of which an insignificant number of droplets with a lateral size of 0.5–2.5 μm are observed. The transmittance of the film on the silicon substrate increases compared to the transmittance of the substrate itself in the near IR region in the wavelength range from λ = 1911 nm to λ = 2997 nm and in the mid IR region in the frequency range from ν = 1120 cm^{-1} to ν = 3898 cm^{-1}. Analysis of the electrophysical properties showed that the films did not exhibit ferroelectric properties and photoelectric effect, which may be due to the composition of the film and the presence of a high density of states at the interface, acting as traps for charge carriers.

Acknowledgements. This work was supported by the Belarusian Republican Foundation for Fundamental Research (grant № Ф23МЭ-029).

References

1. **Fuchs D., Pinta C., Schwarz T., Schweiss P., Nagel P., Schuppler S., Schneider R., Merz M., Roth G. and Löhneysen H. v.** Phys. Rev. B, 75(2007) 144402.
2. **Padilla-Pantoja J., Herrero-Martın J., Torrelles X., Bozzo B., Blasco J., Ritter C. and Garcıa-Munoz J.L.** Journal of Applied Physics, 115(2014) 17D721.
3. **Чумаков А.Н., Авраменко В.Б., Босак Н.А.** Журнал прикладной спектроскопии, Т.79, №2 (2012) 279-287.
4. **Thomas R., Dube D.C., Kamalasanan M.N., Chandra S.** Thin Solid Films, 346 (1-2) (1999) 212–225.

LASER ABLATION IN LIQUID FOR PREPARATION OF MULTIELEMENT NANOPARTICLES: STOICHIOMETRY PRESERVATION

N. Tarasenko[1], A. Butsen[2]

[1]Institute of Physics of National Academy of Sciences of Belarus,
220072 Belarus, Minsk, Nezalezhnasti Ave. 68-2
[2]Belarusian State Technological University, 220006 Belarus, Minsk, Sverdlov str. 13a

To solve the problems of laser spectral analysis, as well as to obtain nanosized particles by laser ablation /1,2/, the use of double laser pulses has proven to be very effective. In particular, it has been shown that in the double-pulse mode, the particle production rate is higher than in the single-pulse ablation mode for the same number of laser pulses. The time interval between double pulses is determined by the lifetime of the gas bubble and usually lies in the range from 5 to 100 μs.

In this paper, the studies were concentrated at clarifying the features of the development of a plasma plume formed under the influence of double laser pulses in a liquid (distilled water) using a zinc alloy as a target. Based on the experimentally established values of the plasma parameters (temperature and electron concentration) using the laser emission spectral calibration-free analysis method, the issue of the correspondence of the stoichiometry of the plasma and target compositions, determined using the LIBS method, was considered.

Experimental setup. The target material was ablated and excited by a double pulsed Q-switched Nd: YAG laser (model LS 2131D, LOTIS TII). The duration and energy of each pulse were 10 ns and ≤100 mJ, respectively. The delay between pulses could be varied from 0 to 120 μs. The laser radiation was focused by a quartz condenser onto a target located in a liquid-filled cuvette with quartz windows. The orthogonal cross section of the plasma formed near the target surface was projected onto the slit of a GMS-850 spectrograph (focal length 850 mm, grating 600 lines/mm, slit 50 μm). A zinc alloy sample with known composition (wt. %) was used as a target: Zn (83.4%), Cu (8.19%), Al (7.78%), Mg (0.76%), Fe (0.14%). Diagnostics of plasma generated by laser radiation on a target immersed in liquid was carried out using a combination of methods. The electron concentration Ne was determined using the magnesium line (Mg I 518.4 nm), which is broadened due to the quadratic Stark effect. The temperature was estimated from the Boltzmann plot for the spectral lines of copper in the range of 510.5 – 529.2 nm, as well as from the intensity ratio of two spectral lines with a low reabsorption probability (Zn I 307.2 and Zn I 307.6 nm). The experimentally established values of the electron concentration and plasma temperature served as the basis for estimating the concentration of the

target material components using the calibration-free LIBS method.

Emission spectra of laser plasma in water. The time-integrated spectrum of plasma formed when a target is exposed to laser radiation in the double-pulse mode depends on the duration of the interval τ between pulses. When the target was placed underwater, the experiments were carried out with delay times τ equal to 10, 25, 40, 50, 60, 75, 100 and 120 μs. At the first two specified values of τ, a very intense spectrum of continuous radiation was observed, which made it difficult to measure the intensity of spectral lines. For this reason, the analysis of the plasma spectra was carried out with time delays between pulses from 40 to 120 μs

Fig. 1 shows fragments of spectra for the ultraviolet range obtained by laser ablation of the zinc alloy target immersed in water; the spectra are given for three values of the time interval τ between the second and first pulses (50, 75 and 100 μs). The spectrum reveals lines of all chemical elements included in the target; the intensity of the spectral lines increases with increasing delay between pulses.

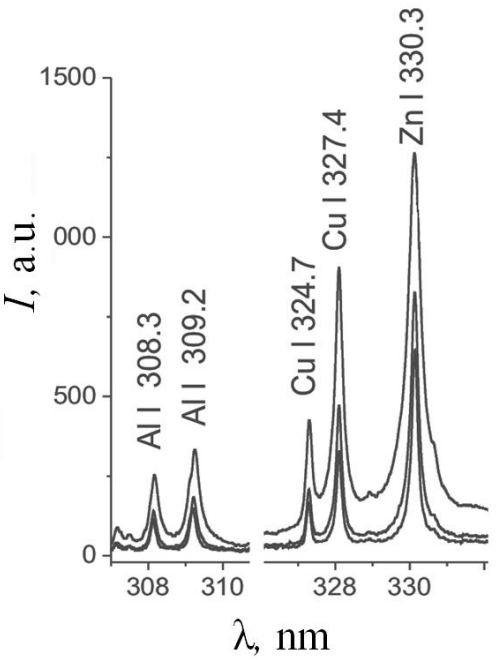

Fig. 1. Emission spectrum of plasma (fragment) produced by the action of pused laser radiation on the zinc alloy target in water

Determination of plasma parameters. The quantitative characteristics of plasma properties (depending on τ) are the temperature and electron concentration. These parameters were determined based on the analysis of the intensity and width of spectral lines measured integrally without taking into account their changes during the evolution of the pulsed plasma plume.

The plasma parameters (temperature and electron concentration) obtained using the above indicated diagnostic methods are given in Table 1. It should be noted that the temperature values determined by the group of copper lines are practically unchanged with variation of τ. The discrepancies between the temperature values calculated by the zinc lines Zn I 307.2 nm and Zn I 307.6 nm are somewhat larger, which can be explained to a certain extent by the greater measurement error due to the comparatively low intensity of these lines. Nevertheless, it should be recognized that the agreement between the temperature values established by the atomic lines of two different elements is quite satisfactory.

Table 1. Values of temperature and electron concentration in plasma during double-pulse ablation of the zinc alloy target in water

	Spectral lines, nm	Time delay, μs					
		40	50	60	75	100	120
Te, eV	Copper lines (510,5 – 529,2 nm)	0.73	0.73	0.71	0.69	0.71	0.70
	Zn I 307,2 / Zn I 307,6	0.66	0.67	0.72	0.72	0.70	–
Ne, 10^{17} cm^{-3}	H_α (FWHM)	6.7	5.8	4.4	3.6	2.6	2.5
	Mg I 518,4 (FWHM)	–	1.0	0.85	0.73	0.77	–

Note that the electron concentration values determined from the H_α line width are significantly overestimated due to self-absorption and can serve as a guide. Therefore, the N_e values calculated from the Mg I 518.4 nm line width were taken into account.

Estimation of the stoichiometry of the composition of laser-induced plasma in water. The LIBS method is based on the known dependence of the intensity I of the spectral line

$$I = \frac{hc}{\lambda_0} A_{ij} g_i \frac{FC_z}{U_z} \exp\left(-\frac{E_i}{kT}\right), \quad (1)$$

where h is Planck's constant, c is the speed of light, λ_0 is the wavelength of the line center, A_{ij} is the probability of a spontaneous transition from the upper level i; g_i and E_i are the statistical weight and energy of the i-th level, k is the Boltzmann constant, T is the plasma temperature; Cz is the concentration of atoms of the z component (chemical element) in the plasma, U is the sum over the states for the atoms of the z component, F is a dimensionless coefficient that takes into account: the plasma volume, the solid angle of radiation collection, the radiation registration time, light losses during registration, and the efficiency of the detector of the registration system.

The obtained values of the intensities of the spectral lines of atoms, as well as the temperature determined by the group of copper lines in the green region of the spectrum, and the electron concentration estimated by the magnesium line, were used to check the possibility of maintaining the stoichiometry of the material entering the plasma that occurs when laser radiation impacts a target immersed in water. The concentration of the ionic component (for elements whose ion lines are not recorded in the plasma) was

calculated using the Saha equation taking into account the FCz value, i.e. the concentration Nz of the z-component atoms. The established FCz values of the atoms and ions of all sample components are reduced to wt. values and their sum is equal to 1.0 (100%) /3/.

The analytical lines and the obtained concentration values are given in Table 2 for four time intervals between double pulses. The zinc concentration values obtained by the specified lines of this element coincided with a relative error not exceeding 3%.

Table 2. Content (wt.%) of elements (Zn, Cu, Al) in laser plasma in water for different delays between laser pulses

Element (element content, wt. %)	τ, μs			
	50	60	75	100
Cu (8.19%)	7.9	8.9	9.8	12.5
Zn (83.4%)	85.1	84.1	83.3	82.2
Al (7.78%)	5.9	6.9	7.6	7.2

With increasing delay between the second and first pulses, a tendency for the concentration of the alloying element (copper, aluminum) to increase is evident. Although in essence the ratios of components in the sample and plasma do not have sharply expressed differences, nevertheless, it should be noted that the fractional nature of the alloying additives entering the plasma increases with increasing delay. Such a manifestation of fractionalization processes with increasing delay between double pulses is most likely explained by the transition from the explosive to the thermal mechanism of substance entry into plasma.

Acknowledgements. This work was supported by the by the National Academy of Sciences of Belarus under project Convergence 2.2.05.

References

1. **V. S. Burakov, N. V. Tarasenko, A. V. Butsen, V. A. Rozantsev and M. I. Nedel'ko** Eur. Phys. J. Appl. Phys. 30 (2005) 107–11.
2. **V.S. Burakov (et al.).** Spectrochimica Acta B, 64/2 (2009) 141–146.
3. **A. Ciucci [et al.]**. Appl. Spectroscopy. 53/8 (1999) 960–964.

NONLINEAR MULTIVARIATE CALIBRATION OF LOW-ALLOY STEEL COMPOSITION BY APPLYING SUPPORT VECTOR REGRESSION TO LOW-RESOLUTION SPECTRA OF COMPACT LIBS SETUP

M.V. Belkov, K.Yu. Catsalap, M.A. Khodasevich

Institute of Physics of the National Academy of Sciences of Belarus, Minsk, Belarus

Introduction. Express measurement of the elemental composition of steels is an actual need for any construction or engineering enterprises. Laser-induced breakdown spectroscopy (LIBS) can be used to solve this problem. A fast measurement procedure, negligible mass of target erosion products, minimal sample preparation and acceptable measurement accuracy make LIBS methods suitable for characterizing the elemental composition of steels.

The industry requires compact analyzers for rapid measurements in industrial conditions. Size limitations force an analyzer developer to abandon large-sized spectral devices with high resolution and use compact spectrometers with low resolution. Machine learning methods, such as neural networks and multivariate analysis, are used to process the signal in these analyzers /1-2/.

Previously, we demonstrated the successful application of a linear multivariate partial least squares method to create calibrations of the C, Si, Mn, Cu, Ni, Cr content of low-alloy steel standards from low-resolution emission spectra /3/. This paper demonstrates the advantage of using a nonlinear method to calibrate the concentration of the same elements under optically dense plasma emission conditions.

Experiment. At Fig. 1 the overview (a) and sketch (b) of the experimental setup are shown. The compact setup was used to excite laser-erosion plasma based on the diode-pumped erbium glass laser *1* generating packets of 8-9 pulses with a total energy of 40-45 mJ at a wavelength of 1535 nm with a packet repetition rate of 5 Hz. The laser pulse was focused by optical unit *2* on sample surface *4*, which was put on a sample table *3*. Erosion plasma emission was supplied to spectrometer by the same optical unit *2*. Spectra were recorded by a compact FireFly 4000 spectrometer *5* in the wavelength range of 172-507 nm with spectral resolution of 0.5 nm and wavelength step of 0.1 nm by CCD array *6*. Laser power source and spectrometer CCD were controlled by PC *7*. A total of 65 standard (reference) samples of low-alloy steel (vendors: IMZ, Poland and ISO, Russia) were used to create calibration models for 8 elements.

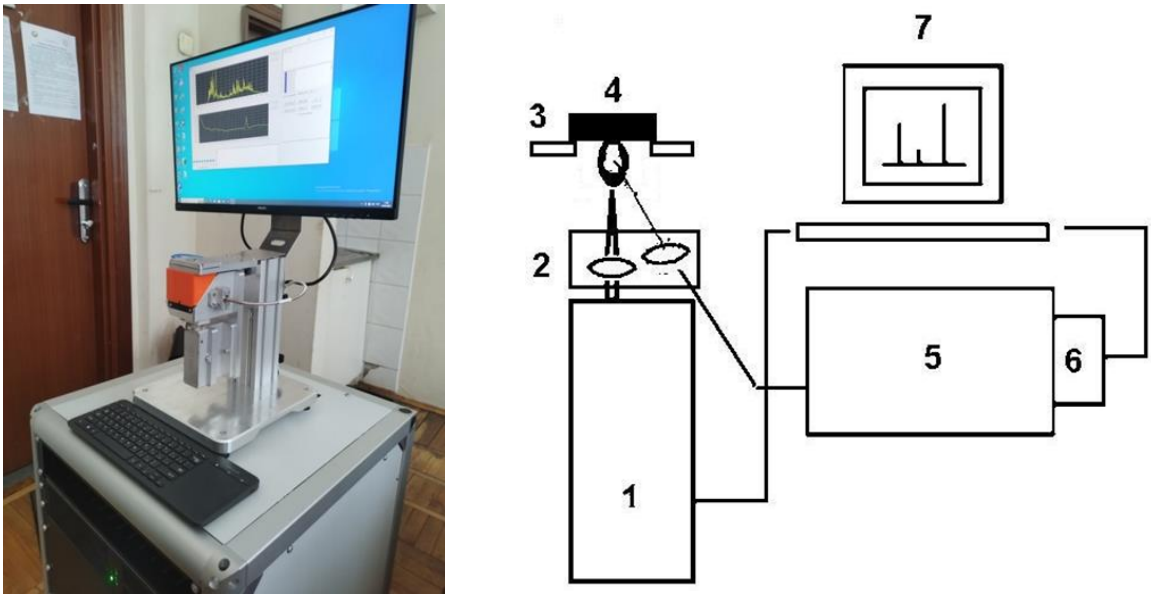

(a) (b)

Fig. 1. Experimental setup: overview (a) and sketch (b)

Calibration. The calibration of the concentration of chemical elements based on the emission spectra was divided into two stages. At the first stage, the linear method using searching combination moving window interval partial least squares (scmwiPLS) was used to reduce the multicollinearity of spectral counts at different wavelengths and to select spectral variables /4/. At the second stage, the nonlinear support vector regression (SVR) method was applied to the selected spectral variables /5/. SVR is a variation of the support vector machine (SVM), used to solve classification problems, which aims to find the optimal hyperplane that best separates two classes of input data. The method maximizes the margin, which is the distance between the hyperplane and the closest data points from each class, called support vectors. SVR also uses the concept of a hyperplane and a margin, which in this method is defined as the model error tolerance. The margin is also called the ε-insensitivity tube and in this case describes the permissible deviation of concentration estimates from the diagonal line on a plot of predicted versus measured values. SVR can be used for both linear and nonlinear regression problems using kernel functions such as polynomial, radial, etc. for preprocessing spectral data. Using the nonlinear SVR method at the stage of selecting spectral variables leads to excessive computer time costs, so we chose the compromise option scmwiPLS+SVR.

Results. Conventional LIBS methods are based on the dependence of the spectral line intensity on the element concentration in the sample material. One of the limitations of classical models and the partial least squares method is the linear dependence between the spectral signal and the element concentration. For optically thin plasma, the spectral line intensity is proportional to the

element atom concentration in the plasma. With increasing optical density, the self-absorption effect increases and the linear dependence is distorted. Thus, the use of a linear approximation leads to significant deviations in estimated element concentrations from the reference values. Self-absorption is most pronounced for lines whose lower level of the radiative transition is close to or is the ground state of the atom (resonance line). Fig. 2 shows the root mean square errors (RMSE) and residual predictive deviations (RPD) of linear and nonlinear calibration of elements concentration for reference steel samples. Under self-absorption conditions, the dependence of intensity on concentration changes from linear (~C) to power-law (~$C^{1/2}$). Due to the consideration of this dependence for the lines' optical thickness, the standard deviation RMSE decreased, and the correlation coefficient R^2 increased. Similar results were obtained for other elements.

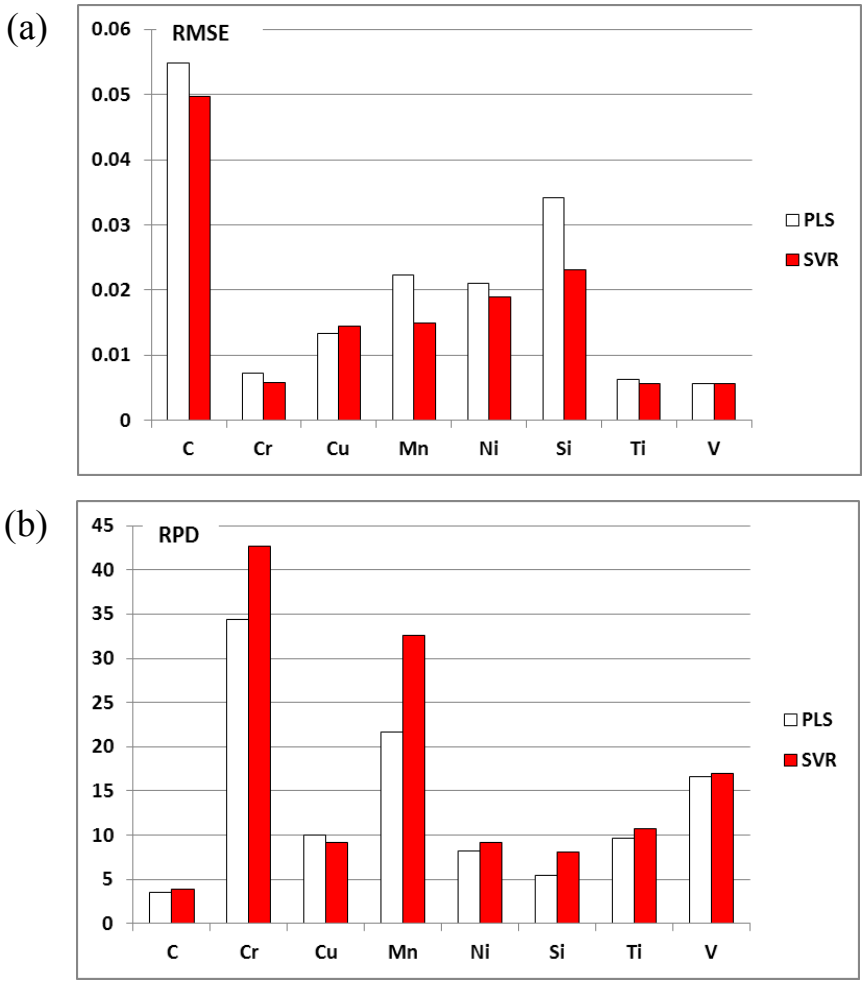

Fig. 2. RMSE (a) and RPD (b) values of calibration dependencies for C, Cr, Cu, Mn, Ni, Si, Ti and V concentration in laser plasma of steel samples (PLS - regression by the linear partial least squares method, SVR - nonlinear support vector regression)

As it can be seen from the values, the elements considered mostly show significant improvement. Thus, the advantage of using calibration methods that take into account the nonlinear dependence of the line intensity on the element concentration under conditions of excitation of optically dense laser-erosion plasma is demonstrated.

Conclusion. A numerical model of elemental analysis has been developed, including nonlinear calibration algorithms. The model has been tested on a low-resolution laser spectral analyzer and a set of spectral data from 65 standard samples of low-alloy steel. Calibration algorithms based on scmwiPLS+SVR successfully describe the nonlinear dependence of intensity on the measured concentration, which allows expanding the range of measured concentrations and significantly increases the accuracy of the models (Fig. 2).

Acknowledgements. This work was supported by the State program of scientific research “Photonics and electronics for innovation”, sub-program “Photonics and its applications” № 1.5.

References

1. **Quackatz L., Griesche A., and Kannengiesser T.**, Forces Mech. 6, 100063 (2022) https://doi.org/10.1016/j.finmec.2021.100063.
2. **Wang Z., Sher M. Afgan, Gu W., Song Y., Wang Y., Hou Z., Song W., and Li Z.**, Trends Anal. Chem. (2021) 143–151 https://doi.org/10.1016/j.trac.2021.116385.
3. **Belkov M. V., Borisevich D. A., Katsalap K. Yu. and Khodasevich M. A.** Selection of Spectral Variables in Multivariate Calibration of C, Mn, Si, Cr, Ni, and Cu Concentrations in Low-Alloy Steels by Laser-Induced Breakdown Spectroscopy. Optics and Spectroscopy, Vol. 130, No. 8, (2022) 488–494.
4. **Khodasevich M.A. Saskevich N.A.** Methods for constructing a training set for calibration using fluorescence spectroscopy of small samples // Весці НАН Беларусі, сер. фіз.-мат. навук.[in Russian] No. 1. (2018) 77-83.
5. **Guenther N., Schonlau M.** Support Vector Machines // The Stata Journal: Promoting Communications on Statistics and Stata. Vol. 16, No. 4 (2016) 917–937.

STRUCTURE AND HIGH-TEMPERATURE OXIDATION RESISTANCE OF AUSTENITIC STAINLESS STEEL SURFACE LAYER ALLOYED BY COMPRESSION PLASMA FLOWS IMPACT

N.N. Cherenda[1], D.A. Bronov[1], V.M. Astashynski[2], A.M. Kuzmitski[2]

[1]Belarusian State University, Nezavisimosty Ave. 4, 220030 Minsk, Belarus, cherenda@bsu.by
[2]A.V. Lyikov Heat and Mass Transfer Institute NAS of Belarus, P. Brovki str. 15, 220072 Minsk, Belarus, ast@hmti.ac.by

Steels of this type have found application in conditions of high temperatures, irradiation and aggressive environments due to their high corrosion resistance and comparatively high heat resistance. Therefore, the research of the behavior of this class of steels under such conditions is an actual task. Austenitic steels can be alloyed with additional elements just to increase their mechanical strength. Preliminary deposition of film containing alloying elements and following treatment of film-substrate system by high energy particles or plasma flows can be used to alloy the surface layer of substrate material. Formation of the alloyed layer occurred due to surface layer melting and convective mass transfer in the liquid /1, 2/. Structure, phase and elemental composition, mechanical and corrosion properties of austenitic stainless steel AISI 321 (18% Cr, 10% Ni) surface layer alloyed with Ti and Al atoms during annealing in air at 600 ^{o}C were investigated in this work.

Alloying was carried out by cathodic arc vacuum deposition of Ti-Al coating (40 at.% Ti, 60 at.% Al) on the steel surface and the following treatment with compression plasma flows. The treatment was carried out with three pulses of compression plasma flows with duration of ~ 100 μs at the energy density absorbed by the surface layer of 10 and 22 J/cm^2. Nitrogen was used as a gas-discharge gas. The annealing was carried out at 600 °C at the time duration of 1-3 hours. X-ray diffraction analysis (XRD) was carried out using a Rigaku Ultima IV diffractometer. Elemental composition was investigated by energy dispersive analysis using LEO1455VP electron microscope. Microhardness was measured on a Wilson Instruments MVD402 microhardness tester at a load of 100 grams using the Vickers method.

During annealing in air structural and phase changes occurred in the surface layer. Fig. 1 shows the XRD patterns of initial steel sample before and after annealing. One can see that diffraction peaks of the ferrite phase are visible, which is due to the heterogeneous distribution of chromium and nickel in the surface layer of steel and appearance of ferrite areas inside austenite structure. Annealing led to more a homogeneous redistribution of chromium and nickel in the surface layer and decrease in ferrite content in the analyzed layer.

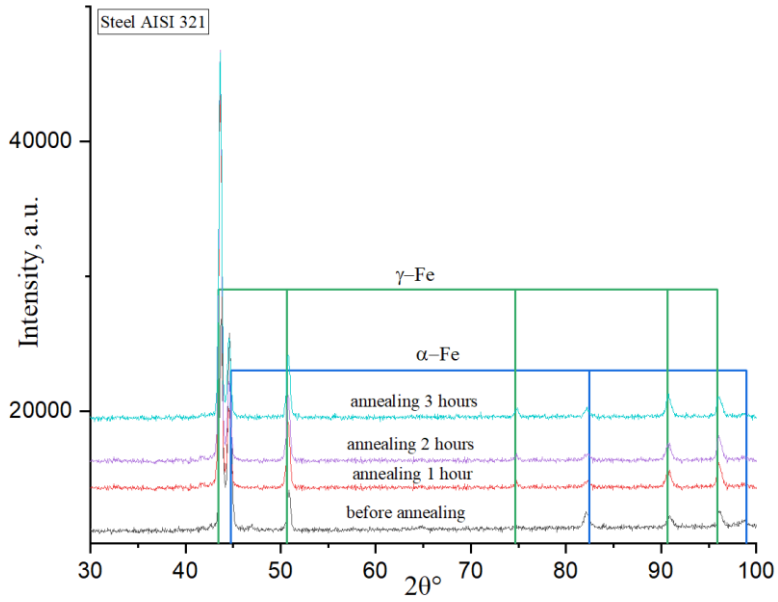

Fig. 1. XRD patterns of initial steel sample before and after annealing

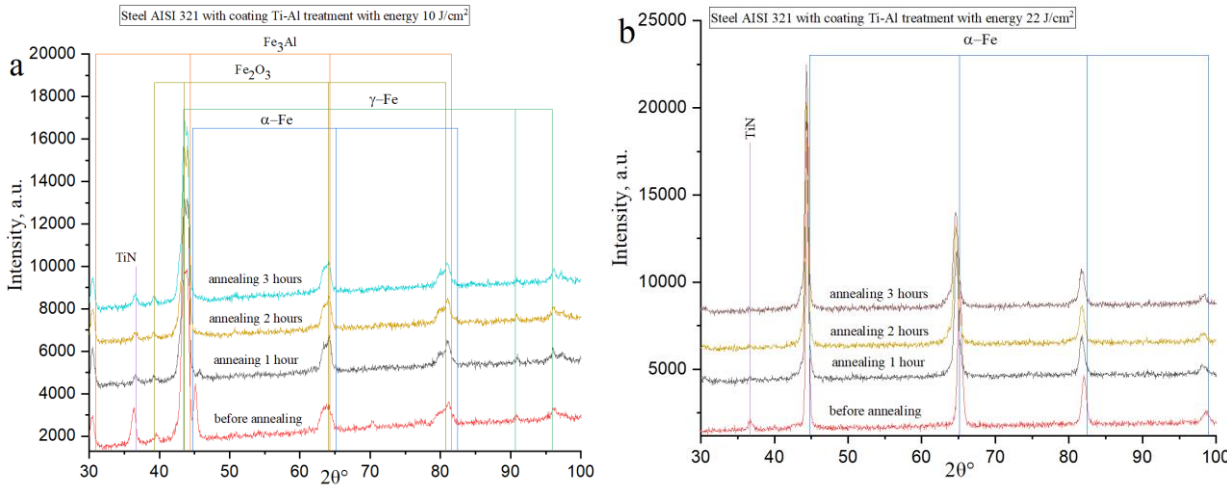

Fig. 2. XRD patterns of samples treated with energy density of 10 J/cm^2 (a) and 22 J/cm^2 (b) before and after annealing

XRD patterns of samples treated with energy density of 10 J/cm^2 and 22 J/cm^2 (b) before and after annealing are shown in Fig. 2. The findings showed that alloying led to the formation of surface layer with the thickness of ~ 10 μm containing supersaturated solid solutions on the basis of ferrite containing Ti and Al atoms. Interaction with atoms of plasma forming gas resulted in TiN film growth at the surface of the alloyed layer. Change of the absorbed energy density led to the diminishing of alloying elements concentrations in the surface layer: from 30 at.% Al and 17 at.% Ti at 10 J/cm^2 to 7 at.% Al and 6 at.% Ti at 22 J/cm^2. Increase of the energy density also led to more homogeneous distribution of Ti and Al inside the alloying layer. As one

can see from the Fig. 2 the ferrite diffraction peaks have a larger width in the sample treated at 10 J/cm^2, which is associated with the non-uniform distribution of alloying elements and the formation of solid solutions with different concentrations of Ti and Al atoms. An increase in the density of absorbed energy up to 22 J/cm^2 led to the formation of a surface layer containing ferrite only. The surface layer phase composition formed after plasma impact remained stable during annealing. At the same time increase of annealing duration resulted in formation of "shoulders" at the left side of ferrite diffraction peaks indicating formation of a new solid solution on the basis of ferrite with increased lattice parameter (Fig. 2b). Oxygen penetration into the surface layer during annealing could be the reason of this effect. Annealing resulted also in partial dissolution of TiN phase in the surface layer.

Structural-phase transformations led to changes of the surface layer mechanical properties. Fig. 3 shows that annealing resulted in the growth of microhardnes of plasma treated samples. The microhardness increase can be explained by formation of a new phase based on α-Fe with a larger lattice parameter and possible interaction of alloying elements and formation of Ti-Al intermetallides in the modified layer.

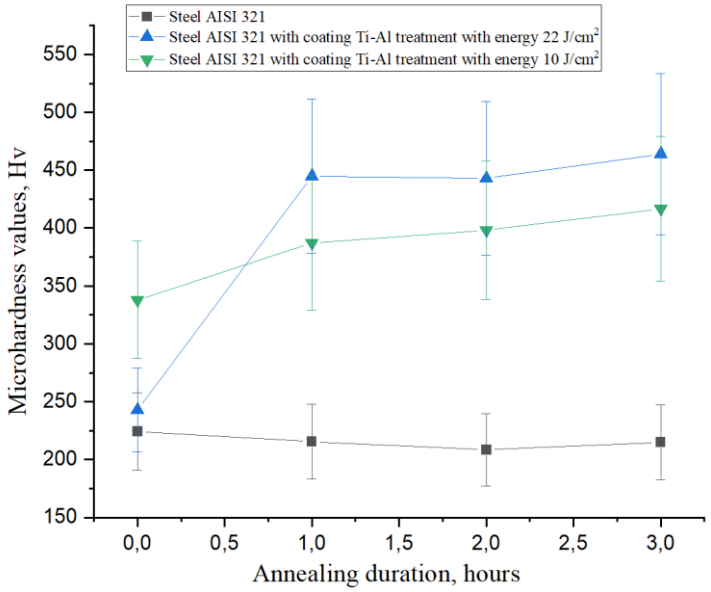

Fig. 3. Dependence of samples microhardness on annealing duration

The annealing in air can lead to oxygen penetration into the surface layer and oxides formation resulting in samples mass gain. The value and rate of mass gain can be used to characterize the corrosion resistance of steel. From Fig. 4 one can see that the sample treated with plasma at the energy density of 22 J/cm^2 possessed the lowest value of mass gain and hence the highest oxidation resistance. Formation of the thin dense titanium or aluminum oxide films

decelerating oxygen penetration into the surface layer could be the reason of such a behavior.

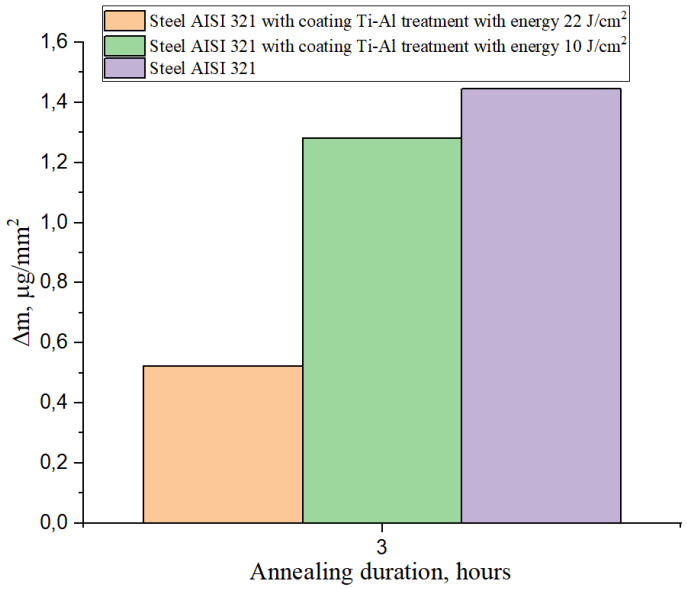

Fig. 4. Samples mass gain after 3 hours of annealing.

The findings showed that alloying of austenitic steel with Ti and Al atoms led to the formation of surface layer containing solid solution on the basis of ferrite that remained stable under following annealing. Interaction with atoms of plasma forming gas resulted in TiN film growth on the surface of the alloyed layer. Alloying and following annealing allow increasing microhardness of the surface layer. Plasma alloying provided oxidation resistance increase of AISI 321 steel.

References

1. **Uglov V.V., Cherenda N.N., Anischchik V.M., Astashynski V.M., Kvasov N.T.** Modification of materials by compression plasma flows. Minsk: Belarusian State University (2013), (in Russian).
2. **Beskorovainy N.M., Belomytsev Y.S., Abramovich M.D., Ivanov V.K., Shulepov V.I.** Constructions materials of nuclear reactors. In 2 parts. Part 2. Moscow: Atomizdat (1977), (in Russian).

6. PLASMA SPECTROSCOPY AND OTHER DIAGNOSTIC METHODS, PLASMA CHEMISTRY

DIAGNOSTICS OF ATMOSPHERIC PRESSURE DISCHARGES VIA SPECTRAL LINE SHAPE ANALYSIS

B. Obradović[1], G. Sretenović[1], N. Cvetanović[2], S. Ivković[1], V. Kovačević[1], I. Krstić[1] and M. Kuraica[1]

[1]University of Belgrade, Faculty of Physics, Stud. Trg 12, 11001 Belgrade, Serbia
[2]University of Belgrade, Faculty of Transport and Traffic Engineering, Vojvode Stepe 305, 11000 Belgrade, Serbia, obrat@ff.bg.ac.rs

Optical emission spectroscopy (OES) remains a fundamental diagnostic technique for characterizing electrical gas discharges under various conditions. The analysis of atomic line shape modifications, resulting from different physical broadening mechanisms, enables the determination of crucial plasma parameters, including gas temperature, electron number density, and electric field strength. The broadening mechanisms of the atomic line shapes are often mutually related and their influences strongly depend of the discharge condition. For example, in low-pressure discharges, the resolution of Doppler broadening—attributable to the thermal motion of radiating species—permits precise measurement of gas temperature while, for atmospheric-pressure low-temperature discharges, Doppler effects are typically negligible, and pressure broadening mechanisms predominate. Specifically, the assessment of resonant and van der Waals broadening not only provides gas temperature estimations but also facilitates the determination of partial pressures of perturbing gas species.

At elevated charged particle densities, microscopic electric fields induce Stark broadening, which serves as a diagnostic tool for electron number density and temperature estimation. Additionally, macroscopic electric fields—such as those present in the cathode regions of glow discharges or within streamer heads—result in Stark splitting, spectral line shifts, and, in some cases, the manifestation of electric field-dependent forbidden transitions. These spectral modifications provide a means to quantify local electric field strengths.

This lecture explores the application of spectral line shape analysis in diagnosing atmospheric-pressure discharges, including dielectric barrier discharges, RF discharges, free-expanding plasma jets, plasma jets interacting with solid targets, pulsed discharges with liquid electrodes, and pulsed discharges in liquid media. Representative experimental case studies are reviewed, accompanied by methodological guidelines for implementing these diagnostic techniques. For example, the Balmer H_α and H_β emission lines were used to determine the average electron number density (N_e) in the plasma of an underwater discharge, see Fig.1. Particularly, several experiments that will be presented here give an insight to the various manifestations of Stark spectral line shifts in atmospheric pressure plasma. The important difference between the

Stark shift caused by the micro field of charged particles, and the Stark shift caused by macroscopic electric field occurring in plasma sheaths is pointed out /1/.

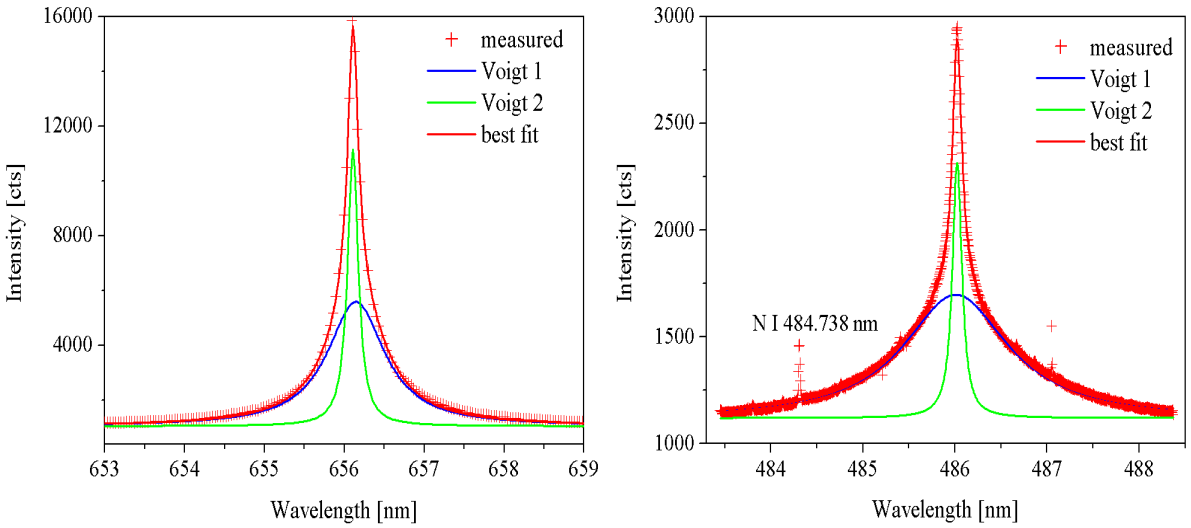

Figure 1. Fitting of H_α (left) and $H\beta$ (right) line profiles by two Voigt functions.

Acknowledgements. This work was supported by the Ministry of Science, Technological Development, and Innovation of Republic of Serbia (Contract No. 451-03-65/2024-03/200162).

References

1. **Ivković M., Ivković S.S., Cvetanović N., Sretenović G.B., Kovačević V.V., Krstić I.B., Kuraica M.M.**, Astrophysics and Space Science, 361 (1) (2016) 42, 01-06

APPLICATION OF SPECTRAL PYROMETRY TO DETERMINE DISCHARGE TEMPERATURE IN THE LIQUID ANODE METHOD

Yu.S. Baryshnikov, R.O. Kurakin, F.A. Orlov, S.A. Ponyaev

Ioffe Physical-Technical Institute of the RAS, Saint-Petersburg, Russia,
iulianbaryshnikov@ya.ru

Temperature diagnostics of plasma during discharge on a liquid electrode is presented in works /1-4/ researchers use the method of emission spectroscopy, where the availability of data on atomic or ion lines is important. In the publication /4/ the authors point out the complexity of such a method for determining the temperature: "Determining the electron temperature from the above spectra is difficult, since there is insufficient data on atomic (and) or ion lines". For temperature diagnostics of discharge during discharge on a liquid anode we have chosen a relatively new method of "Spectral pyrometry" widely studied by the group of doctor of physical and mathematical sciences A.N. Magunov /5, 6/, the method is notable for the fact that to determine the temperature, data on the emissivity of the discharge under study are not needed, which simplifies obtaining the temperature, where data on emissivity is problematic to obtain or they are variable.

The spectral pyrometry method is a method that allows one to derive the temperature of the discharge being studied using the obtained spectrum of thermal radiation of the discharge being studied in comparison with the spectrum of a black/gray body and the transformed Planck formula (1).

$$\varepsilon_\lambda(\lambda, T) = \frac{2\pi hc^2}{\lambda} \frac{1}{e^{\frac{hc}{\lambda kT}} - 1} \quad (1)$$

$$I = \frac{C_1 \lambda^{-5}}{\exp\left(\frac{C_2}{\lambda T}\right) - 1} \quad (2)$$

(2) - Spectral intensity according to Planck's formula, where

$C_1 = 1{,}91 \cdot 10^{-16}\ W \cdot m^2 \cdot sr^{-1}$ C_2 =143,88 m $\cdot$ K - constants that are derived from Planck's formula.

Wien model ($C_2/\lambda T \gg 1$) coincides with Planck's formula up to wavelengths 3–4 times shorter than $\lambda = C_2/T$, that is, you can use such wavelengths to calculate temperature (for example, for a temperature of 4800K, the long-wave limit will be 750 μm).

$$\ln(\varepsilon C_1) - C_2/(\lambda T) = \ln(\lambda^5 I) \quad (3)$$

$$\ln(\lambda^5 I) - \ln(\varepsilon C_1) = -C_2/(\lambda T) \quad (4)$$

For a gray body, the emissivity is ε – const, where can you plot a straight line graph, where $y = \ln(\lambda^5 I)$ и $x = C_2/\lambda$. C_2 =143,88 m·K. Based on the nature of

the straightening of the straight line in Fig. 1, it is possible to determine the temperature using formula (12) of the discharge being studied or the heated surface, using the Excel package in which the discharge spectrogram being studied is displayed.

$$\ln(\lambda_2^5 I) - \ln(\varepsilon C_1) = -C_2/(\lambda_2 T) \quad (5)$$

$$\ln(\lambda_1^5 I) - \ln(\varepsilon C_1) = -C_2/(\lambda_1 T) \quad (6)$$

$$\ln(\varepsilon C_1) = C_2/(\lambda_1 T) + \ln(\lambda_1^5 I) \quad (7)$$

$$\ln(\lambda_2^5 I) - (C_2/(\lambda_1 T) + \ln(\lambda_1^5 I)) = -C_2/(\lambda_2 T) \quad (8)$$

$$\ln(\lambda_2^5 I) - \ln(\lambda_1^5 I) = -\frac{1}{T}\left(\frac{C_2}{\lambda_2} - \frac{C_2}{\lambda_1}\right) \quad (9)$$

$$y_1 = \ln(\lambda_1^5 I);\ y_2 = \ln(\lambda_2^5 I);\ x_1 = \frac{C_2}{\lambda_1};\ x_2 = \frac{C_2}{\lambda_2}; \quad (10)$$

$$y_2 - y_1 = -\frac{1}{T}(x_1 - x_2) \quad (11)$$

$$T = \frac{x_2 - x_1}{y_2 - y_1} \quad (12)$$

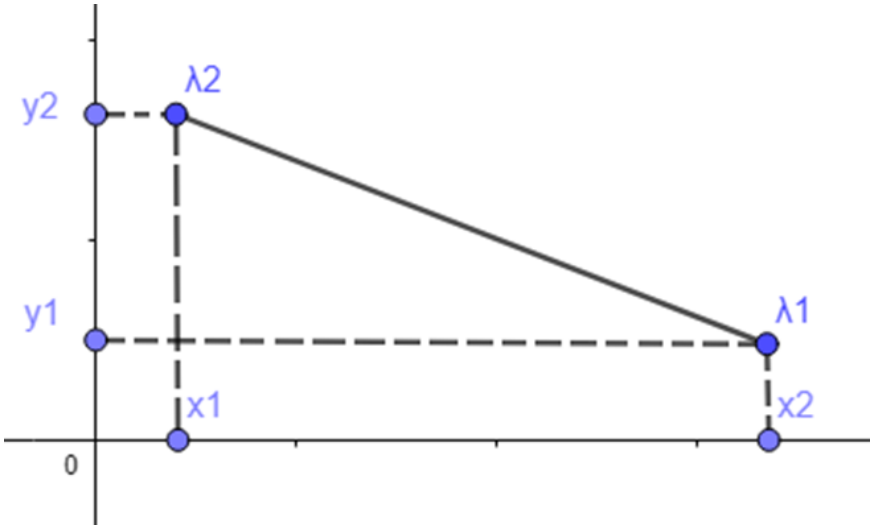

Fig. 1 Example of the dependence y = $\ln(\lambda^5 I)$ и x=C_2/λ determine the nature of the straightening of the line to determine the temperature

To test the method, comparative calculations were made of the temperature obtained by the spectral pyrometry method for a black body and the known parameters of the black body temperature. The data were identical and had a slight discrepancy.

Next, the spectrum of the heated tungsten filament SI8-200 was measured on a calibration lamp with known data on the heating temperature depending on the current. It was needed to calibrate our spectrometer (a spectrometer developed by the Saint Petersburg State Electrotechnical University "LETI" named after V.I. Ulyanov (Lenin)). The calculated temperature by the method of spectral

pyrometry of the heated tungsten filament practically coincided with the known values. The difference was 23 Kelvin.

Then the discharge spectra of galvanized steel wire with a diameter of 1 mm on a liquid anode were measured, with the experimental parameters: 300-320 V, 2-3 A, 31.85 mS/cm (electrical conductivity of the liquid anode). And calculations were carried out using the method of spectral pyrometry formula (12) on the nature of rectification.

By means of calculations, by straightening the transformed spectrograms according to formula (12) in the Excel package, the following data on the discharge temperature on the liquid anode of galvanized iron were obtained: 2529 K, 2668 K, 2538 K.

The region on the initial discharge spectrum selected for temperature calculation is shown in Fig. 2. It corresponded to wavelengths from 700 nm to 900 nm.

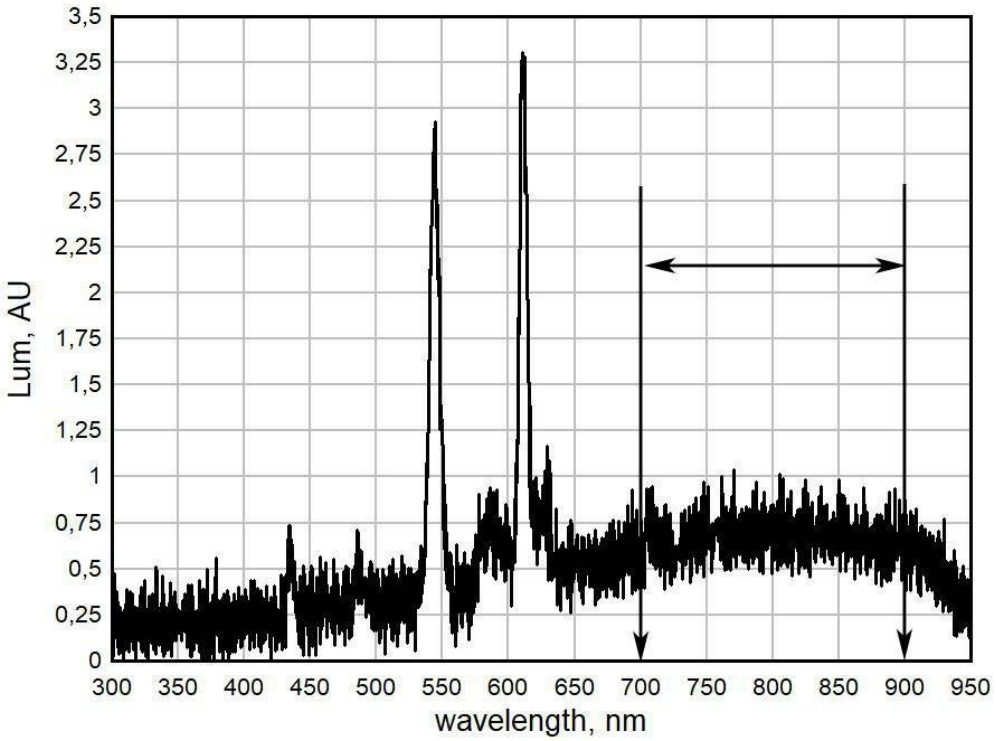

Fig. 2. The original (not transformed) spectrum of the discharge of galvanized iron on a liquid anode with the highlighted region used to calculate the temperature using the spectral pyrometry method

Conclusions

The spectral pyrometry method can be used to determine the discharge temperature of metals on a liquid anode. The temperature data obtained by the spectral pyrometry method were correlated with a calibration lamp. And the melting of galvanized iron cathodes corresponded to the melting temperature of

iron or when, with the same experimental parameters (electrical conductivity of the liquid anode, volt-ampere characteristics of the discharge), but a tungsten cathode was used, such a cathode did not melt in this case. In the future, it is planned to measure the temperature by the spectral pyrometry method with other metals and electrical characteristics of the discharge, which will help to derive a formula for the dependence of temperature on the characteristics of the discharge with a liquid anode.

References

1. **Гайсин А.Ф., Гайсин Ф.М., Басыров Р.Ш., Каюмов Р.Р., Мирханов Д.Н., Петряков С.Ю.**, Теплофизика высоких температур. 61 (4), 481, (2023). DOI: 10.31857/S004036442304004X
2. **Каюмов Р.Р., Купутдинова А.И., Мирханов Д.Н., Гайсин А.Ф.**, Физика плазмы. 50 (1), 102, (2024). DOI: 10.31857/S0367292124010096
3. **Чистолинов А.В., Якушин Р.В., Лубин А.А., Угрюмов А.В.** Прикладная физика. 6, 17, (2024). DOI: 10.51368/1996-0948-2024-6-17-23
4. **Gaisin Al.F., Gaisin F.M., Zheltukhin V.S., Son E.E.**, Plasma Phys. Rep., 48 (1), 48 (2022). DOI: 10.31857/S0367292122010061
5. **Магунов А. Н.**, Журнал технической физики, 80(7), 78 (2010)
6. **Магунов А. Н.**, Спектральная пирометрия. (М.: ФИЗМАТЛИТ, 2012)

MODELING OF THE FORMATION OF BACTERICIDAL COMPONENTS OF AIR GLOW DISCHARGE PLASMA JETS

A.V. Kazak, A.A. Kirillov, L.V. Simonchik, V.M. Chukhalionak

B.I. Stepanov Institute of Physics of NAS of Belarus, Ave. Nezavisimosti 68-2, 220072 Minsk, Belarus, Email: a.kirillov@ifanbel.bas-net.by

1. Introduction

Cold atmospheric pressure plasma jets have become the most widely used plasma source for biomedical applications due to their ability to provide spatially uncoupled electrodeless plasma with a low gas temperature /1/. Air plasma jets of atmospheric pressure glow discharge (APGD) are a promising tool for biomedical applications due to the generation of reactive oxygen- and nitrogen-containing compounds (RONS), including NO, NO_2, HNO_2/2/. Due to the formation of bactericidal components directly in the discharge chamber, air plasma jets have a strong inactivation effect /3/. The paper investigates the formation of bactericidal components in a discharge chamber using a model based on a system of chemical kinetics equations in the form of ordinary differential equations (ODE).

2. Experimental

The air plasma jet generated by the APGD /4/ is formed in a two-electrode gas-discharge chamber consisting of a cylindrical quartz tube of diameter of 8 mm, inside which a copper rod cathode of diameter of 6 mm is coaxially placed and a flat copper anode with a thickness of 4 mm with a central hole with a diameter of 1.5 mm, located at the end of the tube (Fig. 1). The discharge current was 30 mA. Air at a flow through the channel in the cathode was fed into the discharge chamber, passed through the APGD with an interelectrode gap of ~1 mm, and exited through the hole in the anode to form a plasma jet.

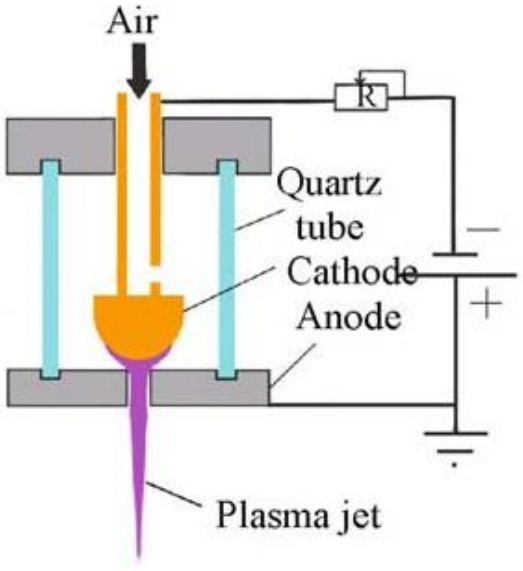

Fig. 1. Diagrams of discharge chambers of air plasma jets of APGD

Since the gas temperature at the outlet of the discharge chamber is ~200 C, biological objects are treated with a jet at a distance of 4 cm from the discharge chamber, where the gas temperature does not exceed 40 C.

Emission and absorption spectroscopy methods were used to identify and diagnose the bactericidal components of the plasma jet. Using the diffraction monochromator MDD 500x2, the emission spectra of the discharge of the APGD and the spectrum of the part of the jet located 1 cm below the anode edge were recorded. In the spectrum of the APGD, bands of molecules of NO, OH and the second positive system of N_2 are observed. In the spectrum of the jet, an intensive band of NO_2 in the range of 400 – 800 nm additionally appears.

The mole fractions of the main bactericidal components of the APGD plasma jet NO, NO_2, HNO_2 were determined by UV and IR absorption spectroscopy methods /5/. The recorded IR (700–3000 cm^{-1}) and UV (200–350 nm) absorption spectra of the jet were used to determine the mole fractions of the jet components in the case of IR spectra using the spectral database /6/ and in the case of UV spectra using the standard method using the Beer – Lambert law and the spectral absorption cross sections of nitrogen dioxide molecules, nitrous acid and ozone available in the literature.

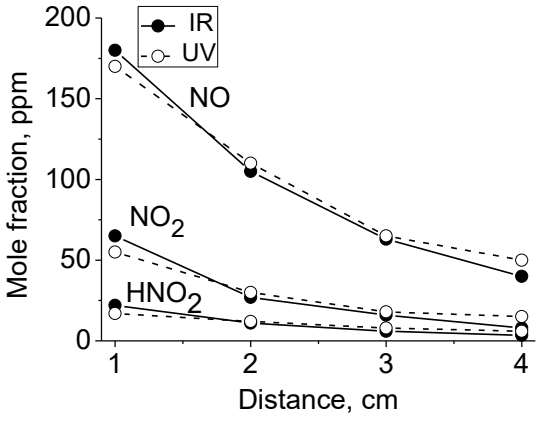

Fig.2. Axial distribution of mole fractions of bactericidal components

Good agreement is observed between the mole fractions of the bactericidal components determined by UV and IR spectroscopy (Fig. 2). The absence of a significant change in the ratio between the mole fractions of the main bactericidal components with increasing distance from the discharge chamber indicates an insignificant impact on them outside the chamber of chemical reactions.

3. Result and discussion

Numerical modeling of the formation of bactericidal components of an air glow discharge plasma jet in a discharge chamber was carried out. The model, containing 32 reactions for 13 gas components, is based on a system of chemical kinetics equations in the form of ordinary differential equations (ODE). At this stage of the study, the plasma–chemical reactions taken into account in the model were only the dissociation of N_2, O_2, H_2O and NO molecules by electron impact.

Fig. 3 shows the results of the calculation of gas components formed in the air during the passage of a glow discharge region with a gas temperature of 2000 K and a length of 0.1 cm and subsequent flow with a linear decrease in temperature to 570 K over a section of 0.4 cm in length. In the discharge region, the electron density is $5.0 \cdot 10^{12}$ cm^{-3} and the electron energy is 1 eV, typical for a discharge in molecular gases at a current of 30 mA /7/.The initial composition of the air is 78% N_2, 21% O_2 and 1% H_2O. The calculations were performed using reaction rate constants from the NIST Chemical Kinetics Database /8/.

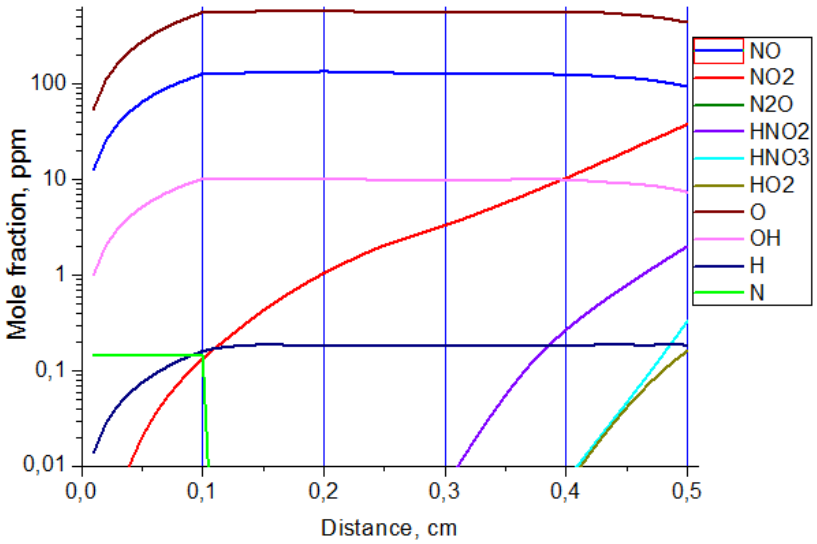

Fig.3. Evolution of the mole fractions of formed gas components during flow in the discharge chamber

Thermal NO is formed from oxidation of atmospheric nitrogen at high temperatures and has a strong temperature dependence. This process is described by the widely accepted Zeldovich two-step mechanism

$$N_2 + O = NO + N, \quad (1)$$
$$N + O_2 = NO + O, \quad (2)$$

An additional elementary reaction is added to the thermal NO mechanism in what is referred to as the modified or extended Zeldovich mechanism

$$N + OH = NO + H. \quad (3)$$

The components O, N and OH participating in reactions (1-3) are formed in a hot gas due to thermal dissociation of molecules.

In the plasma of the APGD, the dissociation of air molecules is carried out much more effectively by electron impact. It is this mechanism that ensures the growth of the amount of O, OH and N, which leads to a rapid increase in the molar fraction of NO in the glow discharge zone. The practical cessation of the dissociation of molecules outside the discharge and the decrease in the gas temperature when moving along the channel leads to a slowdown in the increase

in the molar fraction of NO, and then a decrease, due to the formation of NO_2, HNO_2 and other components.

Since high temperatures provide conditions for thermal dissociation of NO_2 and HNO_2 molecules, a significant increase in their concentrations begins with a decrease in temperature downstream. The equilibrium constant for the oxidation reaction of nitrogen monoxide to nitrogen dioxide exceeds 1 at temperatures below 800 K. The formation of NO_2 occurs in a three-particle chemiluminescent reaction

$$NO+O+M = NO_2+M+h\upsilon \quad (4)$$

and is accompanied by intense emission of a jet in the spectral range of 400–800 nm, which indicates the presence of atomic oxygen also outside the discharge chamber.

Molecules of nitrous acid are formed in the reaction

$$OH + NO + M = HNO_2 + M. \quad (5)$$

As follows from the dissociation rates, nitrous acid is less thermally stable than nitrogen dioxide. Therefore, the formation of nitrous acid occurs at lower temperatures than nitrogen dioxide.

Thus, this kinetic model of the formation of bactericidal components of the air stream in the discharge chamber allows us to correctly describe the sequence of formation and the ratio of mole fractions of the main bactericidal components. To ensure a more correct calculation of the values of mole fractions of bactericidal components, the set of components should be expanded and plasma-chemical reactions should be taken into account.

References

1. **Winter J., Brandenburg R. and Weltmann K.-D.** Plasma Sources Sci. Technol., 24 (2015) 064001.
2. **Kirillov A.A., Paulava A.V., Safronau Y.A., Simonchik L.V. and Dudchik N.V.** Appl. Phys., 5 (2013) 52–55.
3. **Kazak A.V., Kirillov A.A., Simonchik L.V., Nezhvinskaya O.E. and Dudchik N.V.** Plasma Med., 7 (2017) 109–115.
4. **Arkhipenko V.I., Kirillov A.A., Safronau Y.A. and Simonchik L.V.** Eur. Phys. J. D, 60 (2010) 455–463.
5. **Kazak A.V., Kirillov A.A., Simonchik L.V., Kuraica M.M. and Obradovic B. M., Sretenovic G. B.** J. Appl. Spectrosc., 91 **(**2024) 511–518.
6. http://www.cfa.harvard.edu/HITRAN/
7. **Arkhipenko V.I., Kirillov A.A., Safronau Y.A., Simonchik L.V. and Zgirouski S.M.** Eur. Phys. J. D, 66 (2012) 252.
8. https://kinetics.nist.gov/kinetics/

SPATIAL DISTRIBUTION OF ELECTRIC FIELD STRENGTH IN A GLOW DISCHARGE AT ATMOSPHERIC PRESSURE IN HELIUM WITH NON-PLANAR ELECTRODES

P.A. Ivanova[1], A.V. Kazak[1], L.V. Simonchik[1], I. Rafatov[2], V.V. Shkurko[3]

[1]B.I. Stepanov Institute of Physics of NAS of Belarus, Ave. Nezavisimostsi 68-2, 220072 Minsk, Belarus, p.ivanova@ifanbel.bas-net.by
[2]Department of Physics, Middle East Technical University, Ankara 06800, Türkiye
[3]University of NAS of Belarus, Kalinina Lane 10, Minsk, Belarus

Atmospheric pressure glow discharges (APGD) are used in many technological applications /1, 2/, since they simplify the operation of the installations and reduce their cost. A normal glow discharge has a special property of self-organization, in which the voltage of the cathode region practically does not change with an increase in current /3, 4/. When the cathode surface is completely filled, a further increase in current will be possible only due to an increase in the intensity of gas ionization, which is possible only with an increase in voltage. In our paper, the cathode potential fall layer parameters of the self-sustained normal APGDs in helium with different cathode shapes are under investigation.

Experiment. A self-sustained normal glow discharge at atmospheric pressure was ignited in an air-locked chamber, similar to /3/. In the experiments, we used cathodes with different shapes (fig. 1), namely, the planar, rod cathodes and a planar cathode with a hole. The first planar copper cathode is of a disk shape 30 mm in diameter and 8 mm in thickness, the second planar cathode has a 2 mm central hole. The third one is a rod copper cathode of a cylindrical shape with a diameter of 10 mm. We used a copper thin planar cathode 40

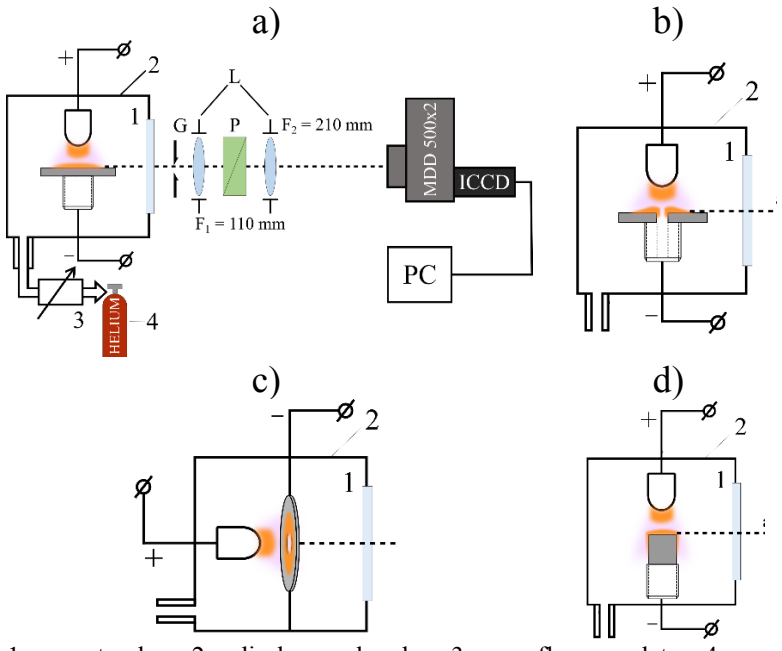

1 – quartz glass, 2 – discharge chamber, 3 – gas flow regulator, 4 – gas cylinder, G – gap, L – lens, P – polarizer, MDD 500x2 – monochromator, ICCD – camera Andor, PC – personal computer

Fig. 1. Sketch of the experiment with a) planar, b) planar with 2 mm hole, c) thin planar cathode with 2 mm hole and d) rod cathodes

mm in diameter and 0.4 mm in thickness with the 2 mm central hole, as well. A slightly rounded copper rod with a diameter of 6 mm used as an anode. As a plasma-forming gas helium was used with a flow rate of about 1 l/min and provided through the chamber in all cases. The discharge gap was 5 mm. The discharge was powered by a direct current source with a voltage of 1.5 kV.

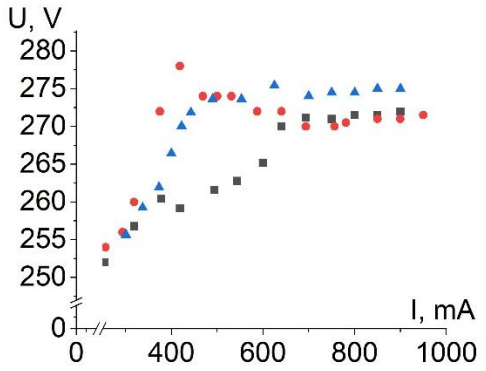

triangles – planar cathode, circles – rod cathode and squares – planar cathode with hole,

Fig. 2. V-I characteristics of the planar, planar with 2 mm hole and rod cathodes

The V-I characteristics for glow discharges with different cathodes shapes are shown in Fig. 2. It can be seen in case of planar cathode, the interelectrode voltage is rised with a current increase up to 0.4 A and then practically does not change with an increase in current larger 0.4 A. The voltage growth at currents less than 0.4 A is due to cathode heating /3, 4/. In case of the rod cathode, we observe the voltage growth too at currents less than 0.4 A. After that, the voltage reaches the maximum value of about 280 V at the current of 0.4 A and then is deacreased on 8-10 V. The presence of this little voltage maximum on a V-I characteristic points on sligth abnormality of discharge. It occures just before spred of cathode layer on lateral surface of rod cathode. In the case of planar cathode with a hole, the voltage increases without significant peculiarities up to 0.65 A and is about 270 V at larger currents.

The electric field strength in the cathode layer was determined using the spectropolarization method /5/ based on the broadening of the hydrogen H_β 486.13 nm line and helium HeI 492.2 nm line profiles formed by the Stark π- or σ-components. The optical scheme is shown in Fig. 1, a. The profiles of hydrogen H_β and helium HeI 492.2 nm lines formed by Stark π-components were recorded at side-on observation along cathode surface.

At the line profile registration on the lateral surface of rod cathode, the view line of optical system was perpendicular to the surface in the observation points. In this case, the registered profiles are formed by Stark σ-components. It will be noticed, that in this case the registered radiation will be integral over the entire thickness of the cathode layer including the emission of the negative glow. Therefore, the numerical simulation of registered profiles took into account the summation over the thickness of the cathode layer. The profiles were calculated using the dependences of the π- and σ-component intensities and shifts on the electric field strength taken from /7/.

The radial distribution of the electric field strength along planar uncooled cathode surface at the discharge current of 1 A is shown in Fig. 3. It can be seen

that the field strength decreases with the distance from discharge axis from about 60 kV/cm up to 20 kV/cm at the edge of cathode layer at about 9 mm.

Unfortunately, we could not to determine a magnitude of electric filed in the center of rod cathode, since the light intensities close to edge of rod are significant high than on the axis and it is problematic to receive the local intensities on the discharge axis. The maximum value of the electrical field strength, which is 26 kV/cm, takes place near the edge of the cathode surface at the distance of 0.35-0.4 cm from the discharge axis. The value of the electric field strength on the lateral surface slightly decreases from 25 kV/cm up to about 15 kV/cm at the distance of 8 mm from the end of the rod. These magnitudes of electric field strength are very close to magnitudes at the edge of cathode regions in case of planar cathode. It allows to suppose that cathode layer on the lateral surface of rod cathode is continue of cathode layer on the anode facing surface.

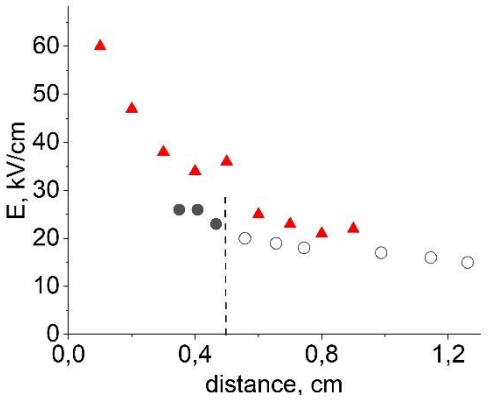

triangles – planar cathode, filled and open circles – rod cathode, dashed line – the edge of the rod cathode

Fig. 3. Spatial distribution of electric field strength in case of the rod cathode

The spread of cathode fall layer through hole on the back side of cathode is observed in case of thin planar cathode with the 2 mm hole. The corresponding spatial electric field strength distribution at the discharge current of 0.55 A is shown on the Fig. 4. As it's seen, the electric field strength decreases from about 25 kV/cm close to the hole edge to 12 kV/cm at the distance of a few mm from edge.

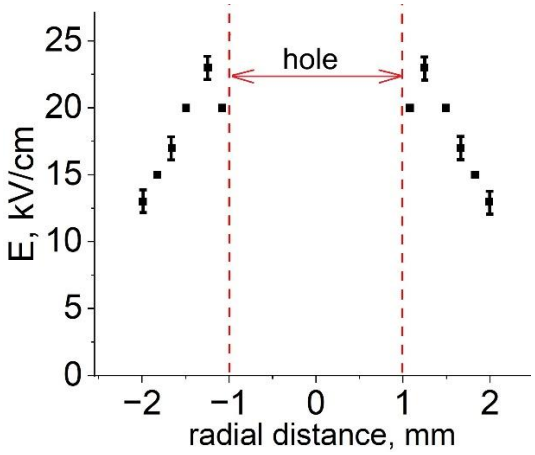

dashed line – the edge of the hole

Fig. 4. Radial electric field distribution on the back surface of thin planar cathode

The simulation of cathode fall layer parameters was performed within the framework of the 2D model presented in /4/. The model assumed cylindrical symmetry. The cathode temperature in the calculation was set at 300 K for a current of 0.1 A and increased up to 800 K with an increase in the discharge current to 4 A.

Fig. 5 shows the calculated distributions of the electric field strength on the surface of the flat and rod cathodes at different discharge currents.

The main patterns of spreading of the cathode layer with increasing discharge current and outflow to the lateral surface of the cathode can be observed. Thus, at discharge currents up to the moment of the cathode layer outflow onto the lateral surface, the parameters of the cathode layer on the planar and rod cathodes are the same (fig. 5). Electric field strength on the surface of the cathode that is faced to anode slightly increase, which apparently indicates a slightly anomalous discharge mode observed experimentally (fig. 2).

Conclusion. A comprehensive study of a direct current glow discharge in helium with the rod and planar with hole cathodes was carried out. Spatial distributions of the electric field strength were obtained and the work regimes of the glow discharge were studied in cases of different cathodes. It was shown that the main regularities of the physical processes of the numerical model correspond to the experimental picture.

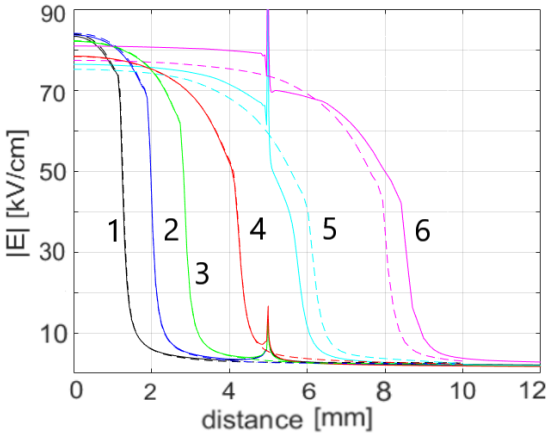

Current strength: 1 – 0.1 A; 2 – 0.25 A; 3 – 0.5 A; 4 – 1 A; 5 – 2 A; 6 – 4 A
Solid curves – rod cathode, dashed – flat

Figure 5 – Distribution of electric field strength on the cathode surface at different discharge currents

Acknowledgements. The work was carried out with partial financial support from BRFFR (grant F24MP-017) and TUBITAK (grant 221N363).

References

1. **Bogaerts A.** Journal of Analytical Atomic Spectrometry, 1999, **14**, №9. P. 1375.
2. **Becker K, Schoenbach K and Eden J** 2006 J. Phys. D: Appl. Phys. 39 R55.
3. **Arkhipenko V.I. [et al.]** 2008 Plasma Sources Sci. Technol. 2008, 17, 045017.
4. **Simonchik L.V. [et al.]** Plasma Sources Sci. Technol. 2024, **33**, 025014.
5. **Arkhipenko V.I. [et al.]** Appl. Spectrosc. 2000. **60**, №5. P. 910.
6. **Ivanova P.A. [et al.]** Memoirs of the Faculty of Physics Lomonosov MSU, 2024, №4, 2441114.
7. **Kuraica M.M. [et al.]** Spectrochim. Acta. Pt. B. 1997. **52**, №6, P. 745.

PLASMA VELOCITY IN MPK-A40 FOR DIFFERENT ENERGIES

Ivan B. Krstić, Nora Trklja Boca, Goran B Sretenović, Vesna V Kovačević, Bratislav B. Obradović, Milorad M. Kuraica

Faculty of Physics, University of Belgrade, PO Box 44, Belgrade 11001, Serbia

Abstract: The modified version, MPC-A40, is more compact than conventional MPC, but retains the same capability to generate a compressed plasma flow. The MPC-A40 is placed in a dielectric cylindrical chamber, which allows side-on plasma diagnostics. Plasma flow velocity was measured using four capacitive probes positioned in the axial direction, at equal distances. Measurements were conducted over a wide range of energies.

Introduction. The beginning of intensive research in the field of plasma physics, also in the field of plasma acceleration, is related to the 60s years of the last century. Initial theoretical work of A. I. Morozov predicted of two regimes of operation of plasma dynamic devices in which extreme plasma parameters are obtained: In the first regime (acceleration regime) high plasma velocities are obtained (several hundred kilometers per second), while in the second regime (compression regime) large values of particle density are obtained [1, 2]. Morozov's first works showed the perspective that initiated further experimental and theoretical research. The basic requirements in the design of quasi-stationary dynamic plasma devices are formulated as the results of many years of experimental work and theoretical modelling of plasma flow in profiled accelerating channels. In short, the following important conclusions and requirements in the construction were reached: a) it is necessary to switch to the regime of ionic transport of charges in the inter-electrode space, which implies radical changes in the design of the electrode system; b) all solid structural elements of the electrode system should be protected by their own magnetic field.

The magnetoplasma compressor (MPC) is a quasi-stationary plasma accelerator whose work is based on the theory developed by Morozov [1, 2, 3]. MPC electrode system consists of a central cone-shaped copper cathode and copper anode rods symmetrically positioned around the cathode [4]. Plasma is accelerated due to the interaction of the radial discharge current with the azimuthal magnetic field. Accelerated plasma is compressed due to the interaction of the longitudinal (output) current with its own azimuthal magnetic field (pinch effect).

The ability of high plasma parameters achievement makes MPC a device

of interest for fundamental magneto-hydrodynamic research, material modification and improvement of material characteristics.

In the present research, the modified version of the magnetoplasma compressor device [5], MPC-A40, has been constructed. It is more compact than conventional device, but retains the same capability. The aim of this research is to examine the fundamental operating principles of the device and to verify the basic laws using a scaled-down version of the MPC. This analysis would serve as an initial investigation leading to the next step, which involves studying an experiment in which two MPC sources are configured to launch accelerated, confined plasma toward each other, creating two colliding plasma flows, a setup that is supported by the current experimental configuration.

Experimental setup. The electrode system of MPC-A40 consists of the conically shaped copper central electrode (cathode) with radius 24 mm and 5 mm, 35 mm in length, with divertor on the top. Outer electrode (anode) is made of 8 copper rods (6 mm in diameter and 80 mm in length), symmetrically positioned along the circle of 40 mm in diameter. Conically shaped cathode of MPC defines the profile of the acceleration channel. The cathode is slightly recessed with respect to the anode to improve plasma focusing and discharge uniformity. This electrode system of MPC is positioned in a cylindrical plexiglass vacuum chamber filled with hydrogen 5.0 as a working gas (Fig. 1). Results presented here are recorded under the residual gas regime (p = 10 mbar).

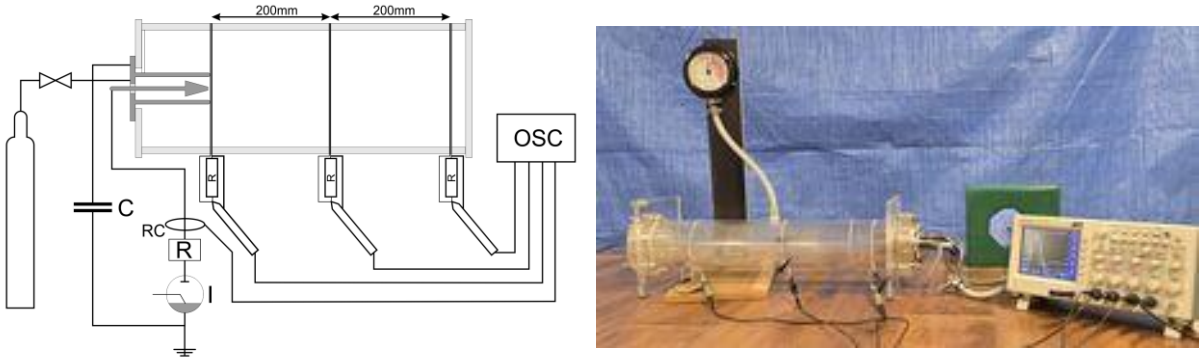

Fig. 1. Schema and picture of experimental setup

The electrode system is connected through an ignitron (I) and resistor (R=0.183Ω) with 94 μF capacitor banks (C). Discharge current was measured using the Rogowski coil (RC). Capacitive ring-shaped probes were placed around the outside diameter of the vacuum dielectric chamber, perpendicular to the path of the accelerated plasma. The probes were positioned at distances of 0 cm, 20 cm, and 40 cm from the end of the anode rods (Fig. 1). The purpose of this setup is to registers the moments of time when the plasma front intersects the plane of the ring capacitive probes and induces a voltage signal in them and

calculates the plasma velocity based on. The signals were simultaneously recorded by four-channel Tektronics oscilloscope 2024C (OSC).

Results and Discussion. Measurements were conducted for 5 operating voltage values (voltage to which the capacitor is charged): U_1=4.25 kV, U_2=5 kV, U_3=6 kV, U_4=7 kV and U_5=8 kV, which corresponds to the energies stored in the capacitors before discharging: W_1= 0.85 kJ, W_2= 1.18 kJ, W_3=1.69 kJ, W_4=2.30 kJ and W_5=3 kJ.

Fig. 2 present one current signal at operating voltage U_1=4.25kV and Capacitive ring-shaped probe signals recorded in time at described distances. On the figure, we can see that maximum from ring probes is shifted, which corresponds to the plasma flight time Δt. In order to determine the position of the maximum more precisely, the voltage signals from the ring capacitive probes were fitted. Based on the thus obtained flight times Δt and the mutual distance between the probes, the plasma velocities (plasma fronts) were calculated and presented in Fig. 4. Fig. 3 just shows current signals in time for different applied voltages. Here we can see that maximum current at 8kV is around 23kA.

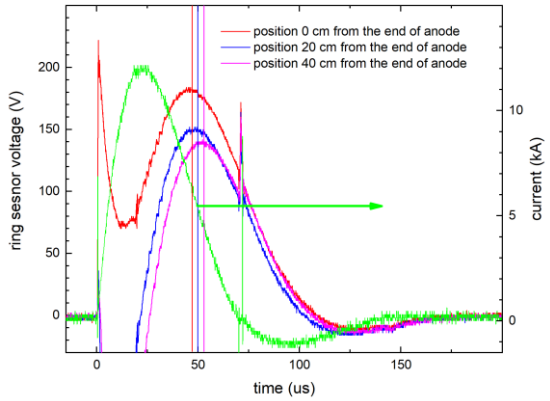

Fig. 2. Current signal at operating voltages 4.25kV in time, and voltage signals recorded on ring probes in time

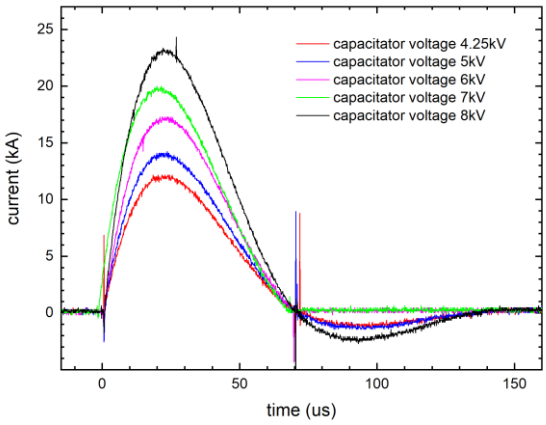

Fig. 3. Current value in time under different operating voltages

On Fig. 4 one can see that velocity of the plasma rises, from 33 to 56 km/s, with applied current (higher operating voltages). That change is more prominent at higher currents, and especial in the region of the first 20 cm, from 71 to 215 km/s. The decrease in velocity in the region from 20 cm to 40 cm is probably because of higher scattering rate of plasma particles and residual gas, and maybe because of the reflection from back wall of chamber what still needs to be determined.

Conclusions The modified version of the magnetoplasma compressor device, MPC-A40, has been constructed and unlike conventional metal vacuum chambers mounted on a dielectric, optically clear chamber in the form of a tube with an inner diameter of 77 mm. Preliminary measurements described in this

work were carried out in the residual gas regime at initial capacitor voltages of 4.25 to 8 kV. The discharge current was measured using a Rogowski coil. The goal of these studies is to test the reliability of the miniature MPC design at higher voltages and to measure the dependence of the plasma discharge velocity on the voltage (energy) of the capacitor and the discharge current. An unexpectedly high plasma velocity was measured at distances of 200 mm from the end of the anode. Further systematic measurements using capacitive, optical and Hall probes, as well as the Doppler effect, at voltages up to 20kV will be continued.

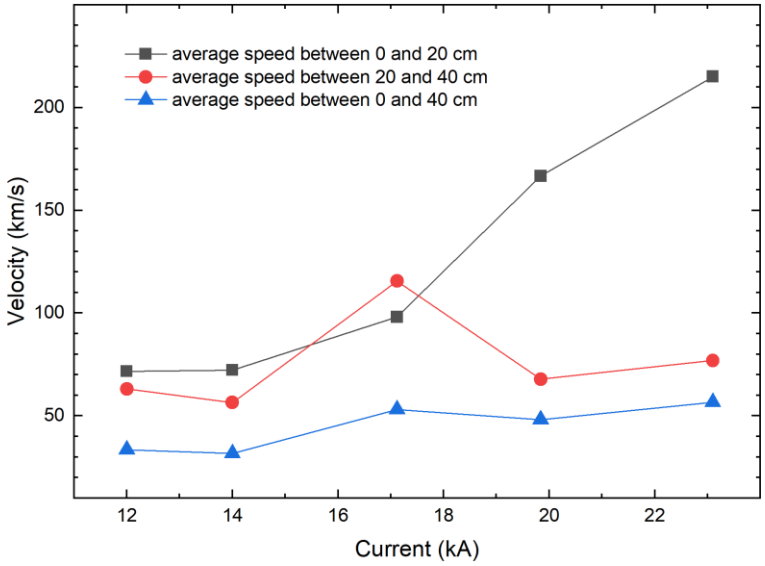

Fig. 4. Average velocity of the plasma in different segments for different currents (operating voltages)

Acknowledgements This work was supported by the Ministry of Science, Technological Development, and Innovation of Republic of Serbia (Contract No. 451-03-136/2025-03/200162)**.**

References

1. Morozov A. The acceleration of a plasma by a magnetic field, Soviet Phys. JETP, vol. 5 (1957)
2. Vinogradova A. and Morozov A. Physics and application of plasma accelerators, Minsk: Nauka i tekhnika (1974)
3. Morozov A. and Solov'ev L. Steady-state plasma flow in a magnetic field, Reviews of Plasma Physics (1980) pp. 1–103
4. Purić, J. et al. Diagnostic of magnetoplasma compressor of compact geometry, Obs. Astron. Belgrade (2003)

USING THE TM_{110} MODE OF A CYLINDRICAL CAVITY TO DIAGNOSTIC THE PLASMA DENSITY IN A GAS DISCHARGE TUBE

N.N. Bogachev[1], V. P. Stepin[1], V.I. Zhukov[1], S.E. Andreev[1], D.M. Karfidov[1], M.S. Usachonak[2]

[1]Prokhorov General Physics Institute of the Russian Academy of Sciences, Moscow, Russia, bgniknik@yandex.ru
[2]B.I. Stepanov Institute of Physics of the National Academy of Sciences of Belarus, Minsk, Belarus

Plasma diagnostic methods based on microwave resonators hold an important place in modern experimental plasma physics due to their non-invasiveness and sufficiently high measurement accuracy. The principle of these methods is based on analyzing the interaction between the resonator's electromagnetic fields and the plasma, which allows determining such important parameters as dielectric permittivity, electron density, plasma oscillation frequency, and electron collision frequency. The key advantage of resonator methods lies in the absence of direct contact with the plasma, making them indispensable in conditions where traditional probe measurements are impossible or severely hindered.

Among various types of resonators used in plasma diagnostics, cylindrical resonators, particularly those operating in the TM_{010} mode, have gained the most widespread use. Their popularity is due to axial symmetry, which significantly simplifies both experimental procedures and theoretical descriptions of interaction processes. However, traditional modes of cylindrical resonators, including TM_{010}, TM_{020}, and TE_{010}, have a significant limitation — they cannot be used for measuring plasma density at $n_e > 10n_0$, where n_0 is the critical plasma density corresponding to the resonant frequency of the empty resonator. This limitation is associated with the nonlinear dependence of the resonant frequency shift $\Delta\omega$ on plasma density n_e at such density values, as well as with possible broadening and noise contamination of the resonance peak [1-4].

This work proposes the use of the TM_{110} mode of a cylindrical resonator as an alternative to traditional approaches. This choice is motivated by the fact that this mode reduces the nonlinearity of the $\Delta\omega(n_e)$ dependence at $n_e > 10n_0$ and provides stable resonance peaks even at high plasma densities. At the same time, the method maintains implementation simplicity compared to multimode models of rectangular resonators, which require complex calculations accounting for a large number of harmonics.

The theoretical basis of the applied method is the analysis of the dielectric permittivity of gas-discharge plasma, which according to the Drude model is a

function of the electromagnetic wave frequency ω, plasma frequency ω_p, and electron collision frequency with neutral particles ν. To relate the average volume electron concentration to the resonant frequency shift, a relationship was used that accounts for the plasma and resonator volumes, as well as the form factor Cv, which determines the relationship between the electric field in the resonator volume and electron concentration.

Experimental studies were conducted using a cylindrical resonator with a radius of 45 mm and height of 30 mm (Fig. 1). For this resonator, the resonant frequencies of available modes in the 2-4 GHz range were determined: TM_{010} with a frequency of 2.53 GHz (critical plasma density $n_0 = 8 \cdot 10^{10}$ cm^{-3}) and TM_{110} with a frequency of 3.79 GHz ($n_0 = 1.77 \cdot 10^{11}$ cm^{-3}). Calculations of the $C_v(n_e)$ coefficient showed an important advantage of the TM_{110} mode—its C_v coefficient changes weakly and linearly in the range from $n_e = 10^{11}$ cm^{-3} to $n_e = 10^{12}$ cm^{-3}, unlike the TM_{010} mode, for which C_v changes threefold over the same plasma density range.

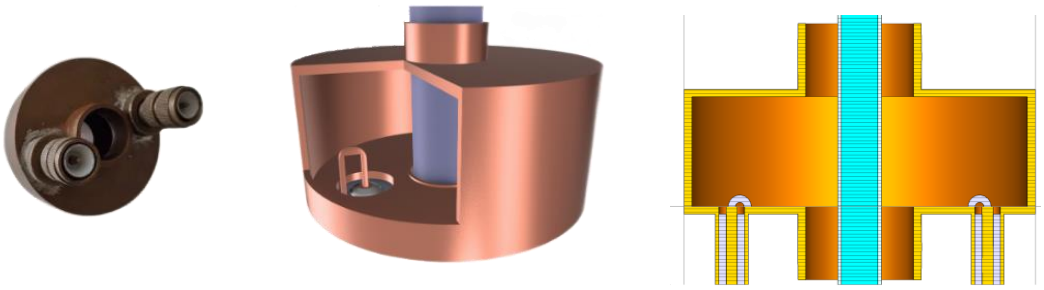

a) b) c)

Fig. 1. Cylindrical resonator (cavity): a) photograph; b) 3-D model in section; c) model with a gas discharge tube in the COMSOL Multiphysics software package

The experimental setup included an RF signal generator with an initial power of 45 W, a feeding device (surfatron), a gas-discharge tube with plasma, and a measurement complex based on a vector network analyzer. Plasma was formed in a transparent bactericidal glass lamp 700 mm long filled with argon at 1-3 Torr and mercury vapor at about 10^{-2} Torr. A surface electromagnetic wave was used to excite the discharge. Measurements were performed using the transmission coefficient S21, from which the resonant frequency was determined. Simultaneously, plasma luminosity measurements were conducted using two photodetectors optically aligned with the emitting zone of the gas-discharge tube.

To analyze the dependence of resonator parameters on plasma concentration, a numerical model was developed in the COMSOL Multiphysics

software environment. Electromagnetic wave propagation modeling was performed using the finite element method with a tetrahedral mesh. Plasma in the gas-discharge tube was described as a medium with complex dielectric permittivity according to the Drude model, assuming uniform filling of the entire tube volume. The model geometry precisely corresponded to the experimental resonator, accounting for coaxial waveguides and the opening for installing the gas-discharge tube.

The numerical modeling results showed electric field distributions in the transverse section of the resonator for different electron concentrations. For the TM_{010} mode, as the concentration increased to $5 \cdot 10^{11}$ cm^{-3}, field compression toward the axis was observed, and with further increase to $n_e = 1 \cdot 10^{12}$ cm^{-3} - a sharp decrease in field amplitude and loss of the characteristic mode structure. In contrast, the TM_{110} mode demonstrated significantly greater stability against concentration increase, maintaining its shape even at high n_e values.

Experimental measurements confirmed the numerical modeling results. For the TM_{010} mode at plasma concentrations above $7 \cdot 10^{11}$ cm^{-3}, resonance peak broadening and level reduction were observed, up to complete suppression near the excitation zone. Meanwhile, the TM_{110} mode maintained a clear symmetric resonance along the entire length of the discharge tube, demonstrating a linear dependence of frequency shift on position.

Comparison of electron density measurement results by various methods showed good agreement between data obtained using the TM_{110} mode and independent measurements by the passing wave method (Fig. 2). Characteristic for surface wave discharges, a decrease in plasma density from $\sim 4-5 \cdot 10^{11}$ cm^{-3} near the excitation point to $\sim 1-2 \cdot 10^{10}$ cm^{-3} at the remote end of the tube was observed. The advantage of the TM_{110} mode was confirmed by its stability against spatial plasma inhomogeneities and maintenance of resonance peak clarity even under high density conditions.

An important result of the work is the establishment of a linear dependence of the relative frequency shift on normalized plasma density for the TM_{110} mode, in contrast to the nonlinear dependence for the TM_{010} mode. This property significantly improves measurement accuracy in the density range of 10^{11}-10^{12} cm^{-3} and reduces the error in determining electron concentration.

Thus, the conducted research demonstrates the high effectiveness of using the TM_{110} mode of a cylindrical resonator for non-invasive diagnostics of longitudinal electron density distribution in gas-discharge plasma. The obtained results are important for optimizing parameters of RF discharges maintained by surface waves and can be used for diagnostics of various plasma devices, including plasma antennas.

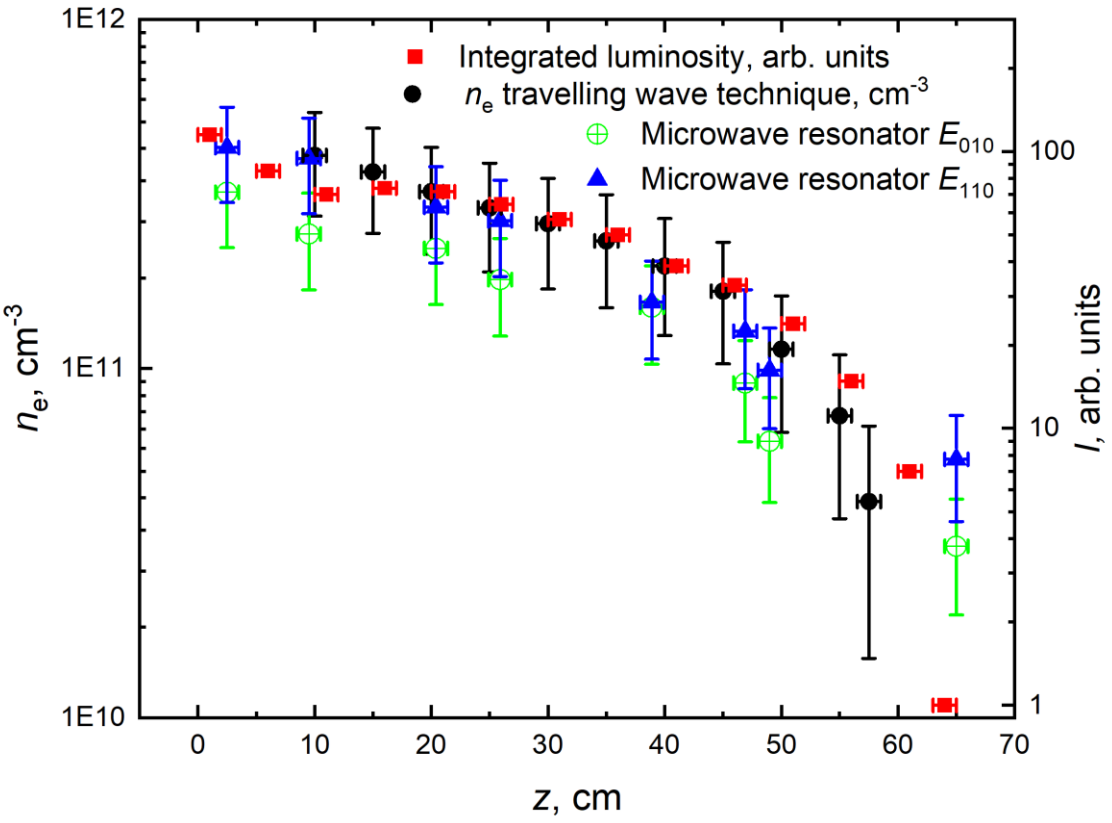

Fig. 2. Experimentally measured axial distribution of electron density and integrated luminosity of plasma in a gas discharge tube

Acknowledgements. The authors express their gratitude to PhD K.F. Sergeychev, DSc L.V. Simonchik, DSc, Associate Professor S.N. Zaumruev, and DSc, Professor N.G. Guseyn-zade for their assistance in organizing the experiment, valuable discussions, suggestions, and comments.

References

1. **Heald M.A., Wharton C.B., Furth H.P.** Plasma diagnostics with microwaves. New York: Wiley John Wiley & Sons Inc. (1965).
2. **Golant V.E.** Microwave methods of plasma research. Moscow: Nauka (1968) (in Russian).
3. **Li J., et. al.** IEEE Transactions on Plasma Science, 49, 3, (2021) 1001-1008.
4. **Dorbin M.R., et. al.** IEEE Access, 11, (2023), 120721-120727.

INFLUENCE OF INITIAL COMPOSITION OF THE Cl_2/HBr/Ar MIXTURE ON PLASMA CHARACTERISTICS AND ETCHING PROFILE EVOLUTION

F. Oksanichenko[1], A. Efremov[2]

[1]JSC MERI st. Academika Valieva, Zelenograd, 6/1, Moscow, 124460, Russia, foksanichenko@niime.ru
[2]JSC MERI st. Academika Valieva, Zelenograd, 6/1, Moscow, 124460, Russia, aefremov@niime.ru

Nowadays, plasma etching (PE) is one of the key technological processes in the production of ultra-large integrated circuits [1]. This process applies a wide range of operations, which include cleaning, surface structuring and the formation of functional layers. The transition to more comprehensive device technologies places increasing demands on parameters of the etching profile, which means that the issue of optimizing this technological process is urgent. The key feature of PEs is the complicated relationship between adjustable control parameters and output characteristics. Such situation means, in fact, that purely experimental approaches are no longer sufficient to determine the optimal set of control parameters. That is why, the significant attention is attracted to plasma modeling methods providing the self-consistent description of both gas-phase chemistry and heterogeneous process kinetics.

One of key operations in manufacturing of integrated field-effect transistors is the etching of polysilicon to produce the gate area, and the widely used etching environment is the Cl_2/HBr/Ar plasma. Most of the existing studies related to this issue are focused on two aspects, such as the modeling of plasma itself as a source of active species without the connection to etching kinetics [2,3] as well as the modeling of etching profiles without the connection to gas-phase chemistry [4]. Obviously, both types suffer from limited values, as the description of whole etching process is not provided. The purpose of our work is to combine above approaches into one complex model which is able to predict the etched profile evolution based on known processing conditions, such as initial composition of gas mixture, pressure, input power, etc.

To describe plasma physics and chemistry, we developed the self-consistent 0-dimensional model. The kinetic scheme (the set of reactions with corresponding rate coefficients) was composed with accountion for previous works dealt with modeling of Cl_2/Ar, HBr/Ar and HBr/Cl_2 plasmas. As a result, the model took into account ten types of neutral ground-state species (Cl, Cl_2, HBr, HCl, BrCl, Br, Br_2, H, H_2, Ar), corresponding positive ions, two types of negative ions (Cl^-, Br^-) and electrons. General model assumptions were similar to those repeatedly used for low-pressure high-density inductive plasmas. These

are as follows:

1) The electron energy distribution function is close to Maxvellian one. The reason is the sufficient impact of equilibrium electron-electron collisions in the overall electron energy balance.
2) The loss of atoms on chamber wall follows the first-order kinetics with nearly constant recombination probabilities.
3) The reactor operates in well-mixed mode that assumes the dominant role of chemical process in formation of steady-state plasma composition.

The modeling algorithm was based on the simultaneous solution of several equations, such as:

1. Equations determining the rate constants of plasma chemical reactions.
2. Equations of chemical kinetics for each type of particle, which were used to determine the particle constants.
3. Charged particle balance equations, which were used to determine the electron temperature (T_e) by binary search method.
4. Power input balance equation, which was used to determine the electron concentration (n_e).

Each of them was described in more detail in our previous article [5]. The calculation scheme is shown in Fig. 1.

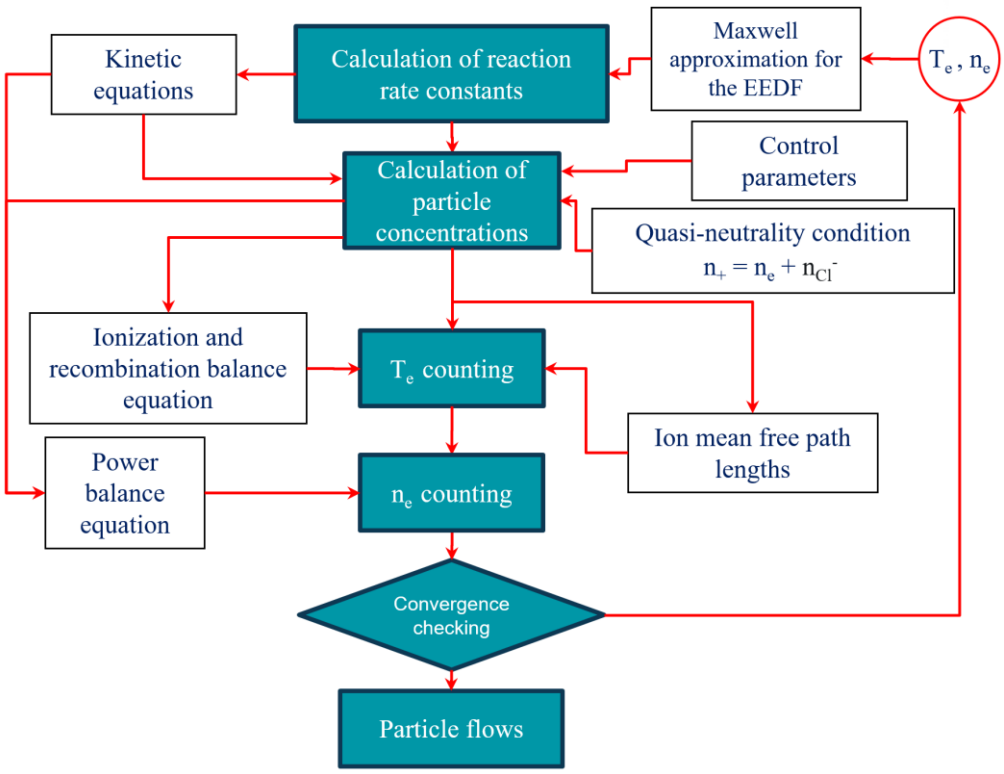

Fig. 1. Plasma module scheme

As control parameters of these module were taken: power supplied to plasma, composition of mixture, and pressure. The output parameters were fluxes of ions and chemically active particles onto the plate surface.

A 2D module of heterogeneous processes was developed to calculate the etching profile. A cellular automaton model to describe evolution of the profile was used. The scheme of this process is described in Fig. 2.

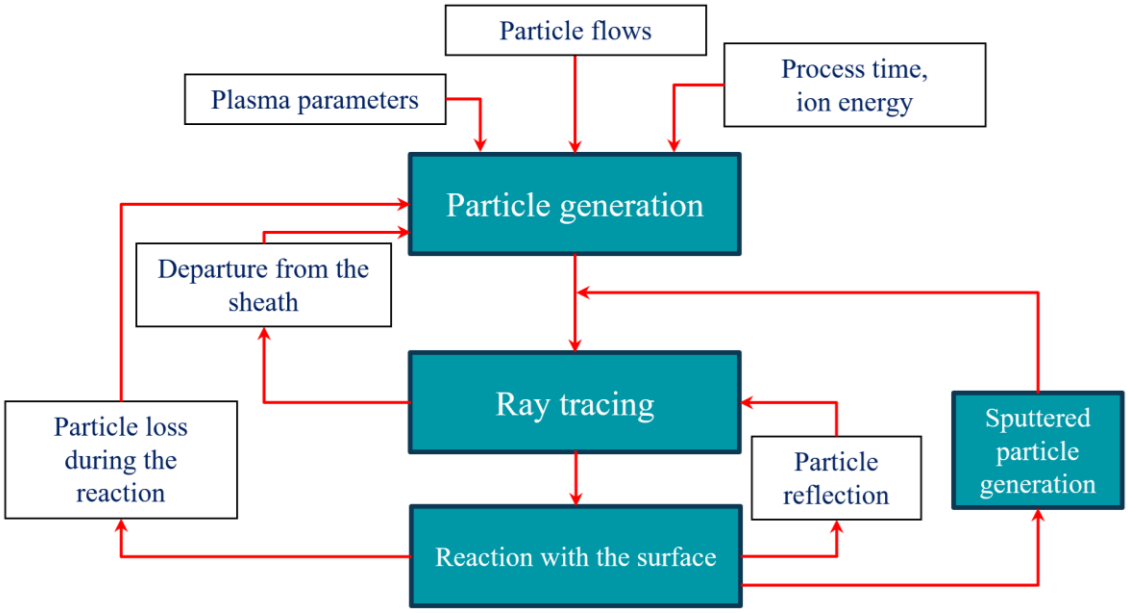

Fig. 2. Heterogeneous processes module scheme

The two-dimensional space was divided into square cells with a side of 2.5 nm, which could take on 3 different states:

1. Void. The cell contains nothing and the particles in question fly through it.
2. Mask. In our model, it was assumed to be indestructible and the particles were reflected from it.
3. Polysilicon. Each cell of this kind contains a series of counters containing information about surface composition within that cell. Particles coming from the plasma interact with this type of cell.

The Monte Carlo method was used to calculate the flows for each element to wafer. Particles were generated above the surface. The amount of each type, angle of incidence and energy distributions were determined based on the fluxes calculated in the previous module, etching time, and bias, which determined energy of positive ions. To determine the point of incidence of particles on the surface of the plate, the ray tracing method was used based on Bounding Volume Hierarchy method[6]. When a particle hits a polysilicon cell, 5

processes were considered based on the ray tracing method: chemical etching (chemically active particles), physical sputtering (positively charged ions), ion-stimulated etching (positively charged ions), redeposition of products of previous reactions, as well as particle reflection if all previous reactions did not occur. The output characteristics of this process were the etching rate, anisotropy, and the shape of the result profile.

References

1. **Krasnikov. G. Ya.** Konstruktivno-tekhnologicheskie osobennosti submikronnykh MOP tranzistorov. Moscow: TEKhNOSFERA (2011).
2. **Efremov. A. M. [et al.].** Plasma Chemistry and Plasma Processing 31(2011) 259-271
3. **Chung. S.-Y.[et al.].** Physics of Plasma. 31(2024) 053502
4. **Mahorowala A. P. and Sawin H. H.** Journal of Vacuum Science & Technology B: Microelectronics and Nanometer Structures 20(2002) 1064
5. **Oksanichenko F. V.** Uchenye zapiski fizicheskogo fakul'teta moskovskogo universiteta 1(2024) 2431401
6. **Gu Y.[et al.]** Conference: Proceedings of the 5th High-Performance Graphics Conference (2013)

A COMPARISON OF PARAMETERS OF STARK BROADENING OBTAINED UNDER DIFFERENT PRESSURES IN LASER PLASMA

A.M. Popov, S.M. Zaytsev, B.S. Chilikin

Lomonosov Moscow State University, Department of Chemistry, Leninskie Gory, 1-3, 119234, Moscow, Russian Federation, popov@laser.chem.msu.ru

Parameters of Stark broadening are of interest for plasma diagnostics in different fields ranging from astrophysics to analytical chemistry. It is because that electron density calculation by Stark broadening is a remote and non-contact technique even in non-equilibrium plasma, which is widely used for characterization of the glow discharge, the discharge in a hollow cathode, high-density star plasma and others. On the other hand, the knowledge of Stark parameters is crucial point for spectra modeling in astrophysical and analytical applications. However, Stark parameters can be reliably calculated by numerical methods for hydrogen-like atoms and ions only (see, for example, the paper by Gigosos et al /1/). Nevertheless, there are many calculations performed by Griem /2/ or, more recently, by Dimitrijević and Sahal-Bréchot (Stark-B Database /3/). Unfortunately, the data calculated by the different methods are often non-consistent. Experimental estimation of Stark parameters is seriously hampered by a heterogeneity of plasma sources and self-absorption /4/. In case of laser-induced plasmas it is necessary short time gating due to their fast temporal evolution. Sparse experimental data on Stark broadening (shifts and widths) are critically evaluated and collected in several comprehensive reviews by Konjević with colleagues (see, for example, recent review /5/).

To determine the Stark parameters, characterization of the radiation source is a crucial point. Therefore, diagnostics of laser-induced plasma was carried out both in air for two pressures (<10 Torr, 760 Torr) and the evolution of plasma temperature and electron density were studied for different plasma observation times from 0.1 to 10 μs. Diagnostics of laser plasma will also help to evaluate the possible contribution of other mechanisms of line broadening, namely Doppler, van der Waals, and resonance. Electron density was estimated by Stark broadening of both H_α line and Na I at 616 nm, while plasma temperature was estimated by Fe I multiplets around 372 and 382 nm.

For alkali metals (Na and K, especially), experimental estimation of Stark broadening was previously performed for strong resonance lines of Na I and K I /6/. In present work we have experimentally investigated Stark broadening for a series of transitions from high-lying doublet states [nd] ^{2}D and [ns] ^{2}S to the first excited state [3p] ^{2}P° Na I/[4p] ^{2}P° K I and a series of doublet transitions from [np] ^{2}P° to the ground state [3s] ^{2}S Na I/[4s] ^{2}S K I with the exception of the resonant transitions 3p-3s Na I and 4p-4s K I. There are no any experimental

estimates of the Stark parameters for many of these transitions for alkali metals. Specially synthesized samples of the Na3AlF6-KF-NaF system with a high content of both alkali metals will be used as targets for laser evaporation. We have compared Stark broadening parameters obtained under atmospheric pressure and low-pressure conditions. We have obtained a large discrepancy between theoretical Stark parameters retrieved from Stark-B Database and experimental ones for several high excitation lines of Na I and K I. We discussed possible reasons for such a discrepancy.

Acknowledgements. This work was supported by Russian Science Foundation (grant No. 25-22-00173).

References

1. **Gigosos M.A., Cardeñoso V.** Journal of Physics B 29 (1996) 4795-4838.
2. **Griem H.R.** Spectral Line Broadening by Plasmas, Academic Press, 1974.
3. **Sahal-Bréchot S., Dimitrijević M.S., Moreau N.** 2025. STARK-B database http://stark-b.obspm.fr/
4. **Konjević N.** Physics Reports 316 (1999) 339–401.
5. **Djurović S., Blagojević B., Konjević N.** Journal of Physical and Chemical Reference Data 52 (2023) 031503.
6. **Purić J., Labat J., Ćirković Lj., Lakićević I., Djeniže S.** Journal of Physics B 10 (1977) 2375- 2380.

VACUUM DISCHARGE WITH STRIP LINE CURRENT DRIVER AS EUV RADIATION SOURCE

L. Stepanov[1,2], N. Matyukhin[1,3], P. Antsiferov[1,2]

[1]Institute of Spectroscopy of Russian Academy of Science, Moscow, Russia, isan@isan.troitsk.ru
[2]National Research University Higher School of Economics, Moscow, Russia, hse@hse.ru
[3]Moscow Institute of Physics and Technology (National Research University), Dolgoprudny, Russia, info@mipt.ru

Investigations of the extreme ultraviolet (EUV, λ = 8 - 25 nm) radiation sources are actual now due to their potential applications in EUV lithography /1,2/. Electrical discharge plasma is one of the most technically simple sources of such radiation. However, the practical use of gas-discharge radiation sources faces some challenges. One of these challenges is decreasing of debris, generated during such source operation.

One of the difficulties with investigations of high-current spark discharges is related to poor reproducibility of their spatial structure and temporal dynamics. Detection of radiation by means of the microchannel-plate (MCP) detectors, that exhibit spatial (50 μm) and temporal (few ns) resolution, makes it possible to reveal the features of plasma dynamics that cannot be noticed using averaging techniques (see, e.g., /3/). In previous works, where methodology of simultaneous registration of plasma spatial distribution and its EUV spectra was used, it was found that spectral lines of multicharged Fe ions have been emitted at the initial stage of discharge evolution /4/. Discharge current is relatively low in this stage, so there is no pinching.

The main idea of this work was creating vacuum discharge with time limited current pulse. This would make it possible to cut off the discharge after the stage with detected EUV radiation, avoid the subsequent erosion of electrodes and obtain discharge with lower debris level comparing to classical vacuum discharge. There is a standard way of generating nanosecond high voltage electrical pulses – strip line generator. Due to the usage of strip line as a current driver, current pulse duration was decreased from ~10 μs /4/ to ~0.4 μs. The stage with radiation of multicharged Fe ions spectral lines took place without notable changes with comparing previous work. It was shown also, that intensity of EUV radiation depends on discharge current value, which is defined by resistance of strip line.

Experiments with anodes made from different materials were made with this type of discharge. It was shown, that discharge plasma consists mostly of anode material. So, it is possible to generate different types of spectra in this discharge. It could be line spectra (using Al (Fig.1a), Mg or Li anode), spectra with bands of radiation (like Sn spectrum (Fig1.b)), or quasi-continuous spectra (from heavy metals (Fig.1c)). It is worth to note presence of radiation band in 13.5 nm range in tin spectra, that is actively used in EUV lithography.

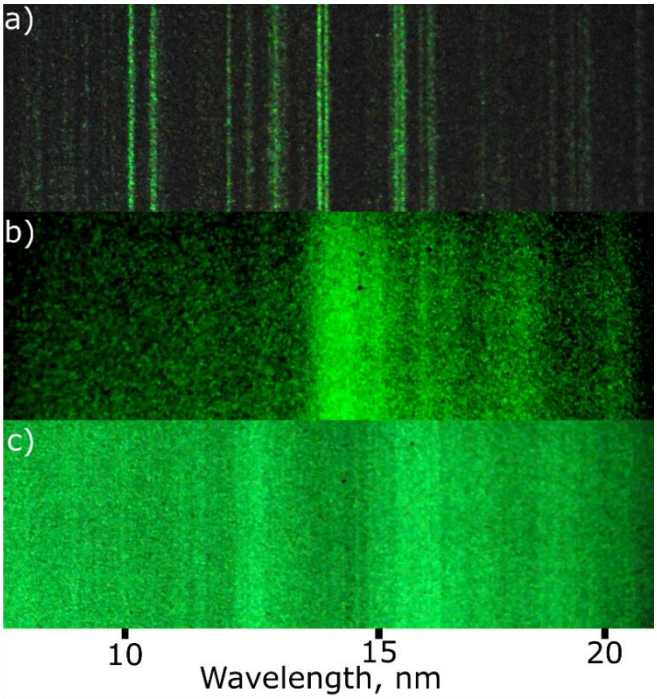

Fig.1. Spectra, emitted from vacuum discharge with strip line current driver: a) Al spectrum b) Sn spectrum c) Pb spectrum

References

1. **Beckers J., van de Ven T., van der Horst R., Astakhov D., Banine V.** Appl. Sci. 2019, 9, 2827.
2. **Banine V. Y., Koshelev K. N., and Swinkels G. H. P. M.** J. Phys. D: Appl. Phys. 44, 253001 (2011).
3. **Antsiferov P.S. and Dorokhin L.A.** Plasma Physics Reports, 2022, Vol. 48, No. 11, pp. 1246–1253.
4. **Antsiferov P.S., Stepanov L.V., and Matyukhin N.D**. Plasma Physics Reports, 2024, Vol. 50, No. 6, pp. 742–748.

STUDIES OF ERROR BUDGET IN CF-LIBS IN CONNECTION WITH TEMPERATURE BEHAVIOUR OF PARTITION FUNCTION

N. Sushkov, A. Popov

M.V. Lomonosov Moscow State University, Department of Chemistry,
Leninskie gory ul.1 str. 3, 119234, Moscow, Russia, nikolaisushkov@laser.chem.msu.ru

Traditional calibration-based elemental analysis by laser-induced breakdown spectroscopy (LIBS) is hampered by lack of calibration standards, suitable in terms of matrix composition and concentration ranges of elements to be measured. In order to tackle this problem, calibration-free LIBS (CF–LIBS) was proposed in 1999 /1/. This method assumes that plasma and sample composition are the same, plasma is optically thin and in local thermodynamic equilibrium (LTE). Then, standard equations can be used:

$$I = \alpha\Phi\left(\frac{hcg_kAN}{4\pi\lambda Z(T)}\right)\exp\left(\frac{-E_k}{kT}\right). \quad (1)$$

Here I is emission intensity for a transition of a given chemical element, Φ dimensionless coefficient related to setup geometry, h Planck's constant, c the velocity of light, g_k and E_k upper level degeneracy and energy, A transition probability, N number density of all forms of the element, λ transition wavelength, Z partition function (**PF**), k Boltzmann constant, T temperature, and α the proportion of emitting species relative to all other forms of the corresponding element (e.g., $\alpha_{\mathrm{Ca\,I}} = n(\mathrm{Ca\,I})/(n(\mathrm{Ca\,I}) + n(\mathrm{Ca\,II}) + \cdots)$), which can be derived on the basis of the Saha–Eggert equation:

$$\frac{n_{q+1}n_e}{n_q} = \left(\frac{2Z_{q+1}}{Z_q}\right)\left(\frac{(2\pi m_e k)^{\frac{1}{2}}}{h}\right)^3 T^{\frac{3}{2}}\exp\left(\frac{-E_{ion}}{kT}\right), \quad (2)$$

where n is number density of particles with specified charge (q or q+1), n_e electron number density, E_{ion} ionisation energy, m_e electron mass.

CF–LIBS provides estimates of plasma composition (N_i or their ratios) through solving a system of equations (1) written for a number of transitions of elements composing the sample. As it can be seen from the equations (1) and (2), there are at least four sources for the uncertainty of plasma composition, namely, the uncertainties of T, N_e, gA (according to databases such as NIST), and signal intensities (I). Contributions of these factors vary depending on experimental parameters and choice of analytical lines, and can be assessed using the conventional uncertainty propagation law.

Table 1 shows contributions of the four error sources in CF–LIBS experiments with biological and metallic alloy samples. Uncertainties of gA

values (dgA) and line intensities (dI) appear to be the principal error sources. Conversely, electron number density makes a negligible contribution. The role of temperature can be different depending on plasma conditions, species and transitions in question. In easily ionisable elements such as K or when ionic lines (such as Sr II line at 407.77 nm) are considered, T fluctuations severely affect the ionisation equilibrium (see Eq. (2)). On the other hand, there are cases when the derivatives of temperature-related terms in Equations (1) and (2) are so balanced that dT introduces only a slight error (see results for the Mg alloy). Such cases are particularly favourable for practical applications.

Table 1. Contributions of error sources in different CF–LIBS experiments

Element ratio	Analytical lines (λ in nm)	Experiment		Error sources (in % of the overall variance)				Ratio RSEM†
				dT	dN_e	dI	d(gA)	
K/C	K I 404.41, C I 247.86	Zooplankton*		35.4	0.090	55.8	8.7	0.62
P/C	P I 253.56, “ ”			19.3	0.026	32.0	48.7	0.44
Sr/C	Sr II 407.77, “ ”			27.8	0.0028	48.8	23.4	0.37
Mn/Li	Mn I 403.08, Li I 413.26	Mg alloy**	d/g 1.5 µs	2.2	0.55	35.5	61.7	0.089
			3 µs	0.0023	0.42	58.5	41.1	0.11
			5 µs	2.0	0.25	39.8	58.0	0.092

RSEM = relative standard error of mean. “D/g” = acquisition delay/gate.
*Kara Sea *Thysanoessa raschii*, Nd:YAG laser, 266 nm, 25 mJ, d/g 0.75/0.08 µs.
**MA21–325 alloy, Nd:YAG laser, 532 nm, 7 mJ.
†As calculated on the basis on the uncertainty propagation law.

An important part of temperature contribution to overall uncertainty is related to partition function, $Z(T)$. Formerly, it was usually supposed that $(\partial Z/\partial T)\times \mathrm{d}T$ is a negligible value of an order of 0.1 % /2/, but this is not always true. For example, for Ca I, the values of Z at temperatures of 0.9, 1.0 and 1.1 eV are 6.79, 10.56, and 15.82, respectively. Since temperature uncertainty of 0.1 eV is typical of LIBS, the resulting uncertainty of Z will severely affect CF–LIBS results. Let us introduce the η parameter:

$$\eta = \frac{\Delta Z/Z}{\Delta T/T} \tag{3}$$

The parameter shows how much the uncertainty of Z is larger than the uncertainty of T. It can also be shown that

$$\eta = \left(\frac{\Delta Z}{\Delta T}\right)\frac{T}{Z} = \frac{T}{Z}\frac{dZ}{dT} = \frac{1}{T}\frac{W}{Z}, \text{where } W = \sum_{n=2}^{N} g_n E_n \exp\left(-\frac{E_n}{T}\right). \tag{4}$$

Thus, the physical sense of η is the ratio of internal and kinetic energy of a species. The $\eta(T)$ graph is a non-monotonous dependence showing a fast growth in the low-temperature region, a maximum, and a slow decrease at high temperatures. In Figure 1, the graph is shown for the elements of the 2nd group of the Periodic table. It can be seen that the position of maximum depends on atomic number, shifting from *approx.* 2 eV for Be I to 0.9 eV for Ra I. The maximum itself becomes sharper for heavier elements. Conversely, the maximum of $\eta(T)$ shifts to higher temperatures in going across a period, e.g., from 1 eV for Na I to 2.8 eV for Cl I, jumping back to 2.5 eV for Ar I.

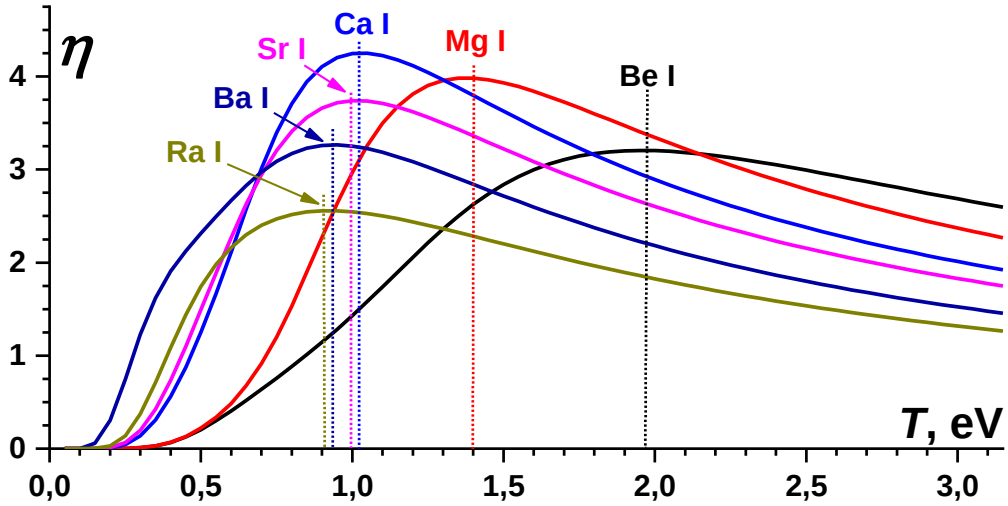

Figure 1. Dependence of η *versus* T as plotted for the elements of the 2nd group of the Periodic table

It is also interesting that the position of the $\eta(T)$ maximum strongly correlates with the energy of the second excited term of the species. In Figure 2, this correlation is shown in bilogarithmic coordinates. The exact causes of the described η(T) behaviour are not yet completely clear. Nonetheless, the η parameter already appears to be very promising for planning analytical works in the field of plasma spectroscopy, because it will help to find T regions where the uncertainty of PF will be the lowest. More specifically, if a ratio of two elements A and B is to be determined, we can express the relative uncertainty of Z_A/Z_B as

$$\Delta\left(\frac{Z_A}{Z_B}\right)\Big/\left(\frac{Z_A}{Z_B}\right) = |\eta_A - \eta_B|(\Delta T/T). \tag{5}$$

Accordingly, Figure 3 shows the values of $|\eta_A - \eta_B|$ for several pairs of species, plotted *versus* T. From this diagram, it is evident that Ca I/C I ratio should not be measured at temperatures below ~ 1.8 eV to avoid severe errors. In contrast with this, the Sr I – Ca I pair shows favourable behaviour in a broad range of temperatures.

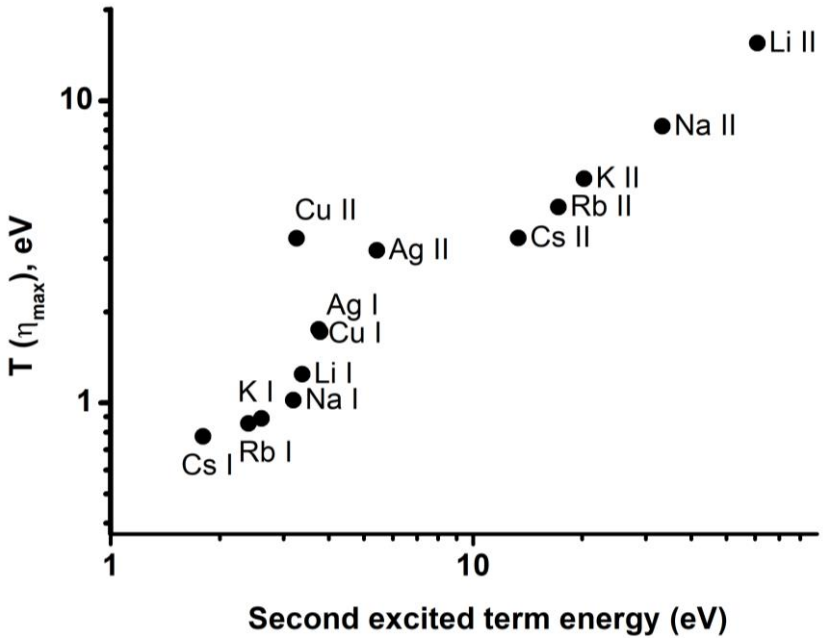

Figure 2. Position of the maximum of η(T) versus second excited term energy as plotted for the elements of the 1st group of the Periodic table

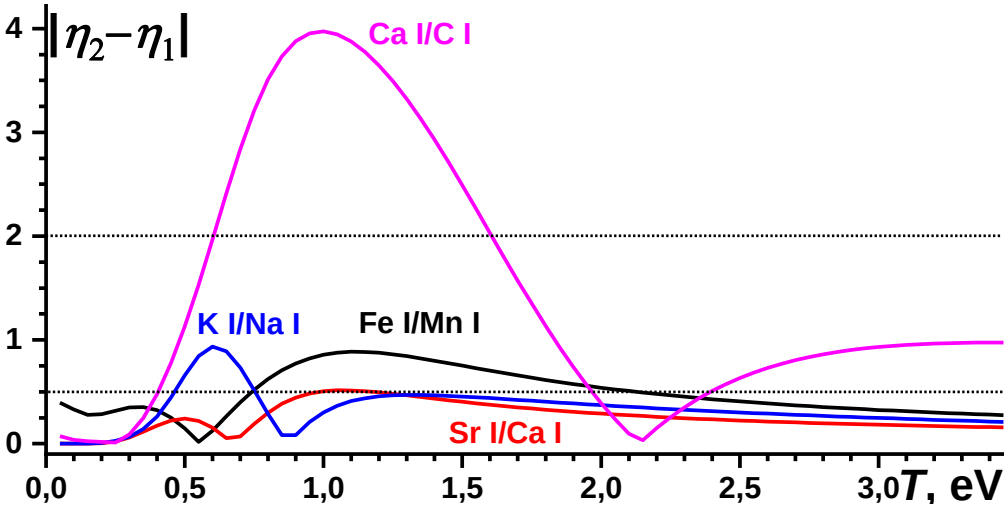

Figure 3. Values of $|\eta_A - \eta_B|$ for several pairs of species *versus* T

Acknowledgements. The authors are grateful to Dr. Nikolay V. Lobus (IPP RAS) for providing zooplankton samples, and to Dr. Timur A. Labutin for valuable advice. This work was supported by the Russian Science Foundation (grant No. 25-22-00173).

References

1. **Ciucci A. et al.** Applied Spectroscopy, 53(1999) 960–964.
2. **Griem H.R.** Physical Review, 128(1962) 997–1003.

PLASMA DIAGNOSTICS DURING A SKIN EXPLOSION OF CONDUCTORS IN MEGAGAUSS MAGNETIC FIELDS

V. Van'kevich, I. Datsko, N. Labetskaya, A. Rousskikh, A. Zhigalin, A. Kuzminykh, V. Oreshkin

Institute of High Current Electronics of the Siberian Branch of the Russian Academy of Sciences, Akademichesky Avenue 2/3, Tomsk 634055, Russia

Interest in physical processes during electrical explosion of conductors (EEC) or foils in vacuum arose in connection with various applications. Firstly, the generation of strong magnetic fields, both by compression of metal shells /1,2/ and by means of single-turn solenoids /3/. Secondly, compression in Z-pinch geometry of heavy metal liners, inside which extreme states with pressures of 1-100 Mbar can be realized /2,4/. Another EEC research area is related to the MAGO/MTF (Magnetized Target Fusion) /5,6/ and MagLIF (Magnetized Liner Inertial Fusion) /7,8/) concepts.

Experiments on electrical explosion of conductors were carried out on a high-current generator MIG /9,10/ at a current level of up to 2.5 MA with a rise time of 100 ns. Cylindrical conductors with a diameter of 1-5 mm were used as loads, allowing them to explode in magnetic fields of up to 700 T. The HSFC Pro optical camera, vacuum X-ray diodes (XRD's) with different cathodes and filters, the integral spectrometer and the spectrometer with a time resolution in the optical range were used for diagnostics of the resulting plasma. Plasma on the surface of the conductor was recorded by its glow in the visible range using a four-frame optical camera with an exposure time of each frame of 3 ns. The camera allowed setting any (up to 5 ns) required time interval between frames. Figure 1c shows the current waveform at the load and the XRD signal.

Time-integrated spectra in the range of 200 – 1100 nm were recorded by a VISIO2GO VISNIR spectrometer with a spectral resolution of 2 nm and an adjustable exposure time of 10 μs – 4000 ms. Time-resolved spectral measurements were performed using a Universal streak camera C10910-05 Hamamatsu Photonics synchronized with the MIG setup. An Action Spectra PRO SP-2300 Princeton Instruments spectrograph was installed in this camera. The spectrometer was calibrated by wavelengths using the hydrogen lines H_α and H_β obtained using a spark discharge in a hydrogen atmosphere in the same geometry. In the time-integrated spectrum of plasma radiation in the optical range during the skin explosion of a Cu conductor with a diameter of 2 mm with a spectrometer exposure of 10 μs, against the background of the continuous spectrum of thermal radiation of the load surface, the lines of copper of the second degree of ionization were clearly recorded. Figure 1 shows optical images of exploding copper conductor with a diameter of 2 mm at different

moments in time (a) and the behavior of the emission spectrum of the same conductor over time in the range of 340 – 650 nm (b) /11/. In this range, the highest emission intensity was recorded on the integral spectrum. As can be seen from Fig. 1(b), with a time resolution of 15 ns/mm, line emission is not recorded in this range of wavelengths.

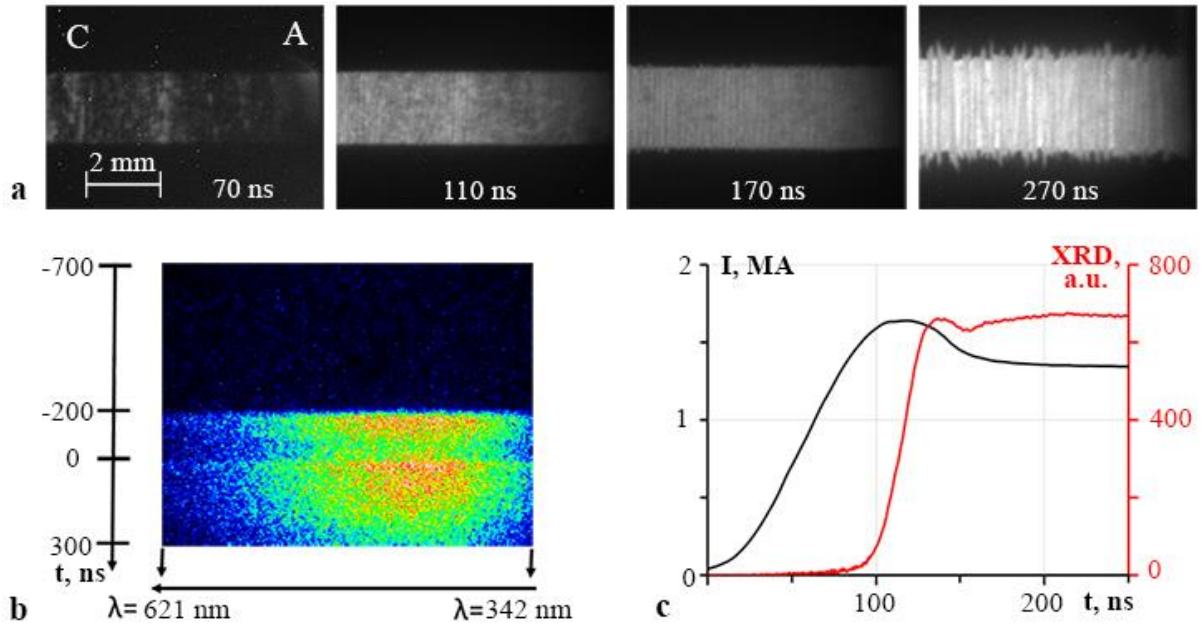

Fig. 1. Optical images of exploding copper conductor (∅ 2 mm) in its own glow at different moments in time from the start of the flow of the MIG generator current (a) /11/; change in the emission spectrum of the same conductor over time in the range of 340 – 650 nm (b) /11/; the vacuum X-ray diode (XRD) signal and the current waveform at the load (c).

To correctly determine the role of the near-surface substance in the current transfer during the skin explosion of conductors, it is necessary to know the distribution of its density along the radius of the plasma column. Such a distribution can be obtained from X-ray images obtained by radiation with $h\nu > 0.8$ keV, which is formed in the "hot spot" of the X-pinch. A calculation code was developed using the inverse Abel transform to solve the problem of reconstructing the substance distribution profile from X-ray data on the electrical explosion of conductors in a vacuum numerically. Thus, according to the Bouguer-Lambert-Beer law (1), to determine the density of the probed substance, it is necessary to know its absorption coefficient μ.

$$I = I_0 e^{-\mu \rho d} \quad (1)$$

where: μ is the mass absorption coefficient; ρ is the density of the substance being studied; *d* is the thickness of the probed object.

The value of the mass absorption coefficient of radiation μ was determined from the X-ray images of transmission of stepped filters of known thickness made of the same substance as the load. In each experiment, X-ray images of the load and the stepped attenuator were obtained simultaneously on one image. Thus, for this load and attenuator substance, the absorption coefficient of the probing radiation is identical.

In the experiments, the image of the exploding conductor was recorded on X-ray films. The films were then scanned, and the resulting image was inverted and processed in accordance with the requirements of the numerical code, as shown in Figure 2a /12/.

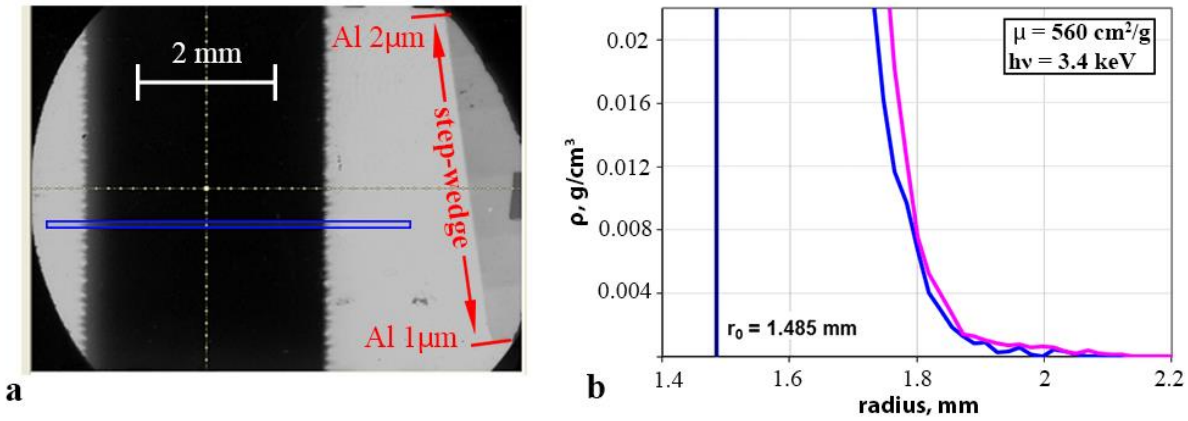

Fig. 2. a - Inverted X-ray images of the explosion of a cylindrical aluminum conductor with a diameter of 2.97 mm, obtained at 216 ns from the start of current flow. The location of the step attenuator (step-wedge) is marked on the right. b - Dependences of the substance density on the radius ρ(r) for a cylindrical aluminum load with a diameter of 2.97 mm, corresponding to the left (blue curve) and right (pink curve) boundaries of the conductor in Figure 2a. /12/.

It shows an inverted X-ray images of the explosion of a cylindrical aluminum conductor with a diameter of 2.97 mm, obtained at 216 ns from the start of current flow, prepared for use in numerical calculations. The calculation was carried out in the rectangular section highlighted in blue. The results of calculating the distribution of the substance density from the radius ρ(r) for this load in this section are shown in Figure 2b /12/. The absorption coefficient of the probed radiation by the substance was determined using a six-step Al attenuator with thicknesses of 1-2 μm (with a step of 0.2 μm). For this spectrum of the probed radiation, it averaged ~560 cm^2/g.

From Figure 2b it is evident that the aluminum conductor has expanded by 400 μm in radius. The density of the substance at a diameter of 3.5 mm is 0.02 g/cm^3. With such a density of the substance in the surface layer, the proportion of the current carried in it is small.

Acknowledgments. This work was supported by the Russian Science Foundation (grant no. 25-19-00352).

References

1. **Sakharov A.D.** Physics-Uspekhi 9 (2), 294-299 (1966).
2. **Knoepfel H.** Pulsed high magnetic fields. (North-Holland, Amsterdam, 1970).
3. **Krivosheev S., Titkov V. and Shneerson G.** Technical Physics 42 (4), 352-366 (1997).
4. **Oreshkin V.I., Chaikovskii S.A., Labetskaya N.A., Ivanova Y.F., Khishchenko K.V., Levashov P.R., Kuskova N.I. and Rud A.D.** Technical Physics 57 (2), 198-202 (2012).
5. **Mokhov V., Burenkov O., Buyko A., Garanin S., Kuznetsov S., Mamyshev V., Startsev A. and Yakubov V.** Fusion engineering and design 70 (1), 35-43 (2004).
6. **Lindemuth I.R.** Physics of Plasmas 22 (12), 122712 (2015).
7. **Gomez M.R., Slutz S.A., Sefkow A.B., Sinars D.B., Hahn K.D., Hansen S.B., Harding E.C., Knapp P.F., Schmit P.F. and Jennings C.A.** Physical Review Letters 113 (15), 155003 (2014).
8. **Slutz S., Herrmann M., Vesey R., Sefkow A., Sinars D., Rovang D., Peterson K. and Cuneo M.** Physics of Plasmas 17 (5), 056303 (2010).
9. **Luchinsky A.V., Ratakhin N.A., Feduschak V.F. and Shepelev A.N.** Izv. Vyssh. Uchebn. Zaved. Fiz. 1997. V. 40. P. 67.
10. **Petin V.K., Shljakhtun S.V., Oreshkin V.I., and Ratakhin N.A.** Technical Physics. 2008. V. 53 (6). P.776.
11. **Datsko I.M., Chaikovsky S.A., Rousskikh A.G., Van'kevich V.A., Zhigalin A.S., Oreshkin V.I., Kuzminykh A.M.** Proceedings of 9th International Congress on Energy Fluxes and Radiation Effects (EFRE-2024). Tomsk, Russia, 2024. PP.155-159.
12. **Datsko I.M., Labetskaya N.A., Vankevich V.A.** Journal of Physics: Conference Series. 2021. V.2064. P.012011

EXPERIMENTAL DETERMINATION OF THE STARK BROADENING PARAMETERS OF THE NA I AND K I LINES IN LASER PLASMA

B. Chilikin, S. Zaytsev, A. Popov

Lomonosov Moscow State University, Department of Chemistry, Leninskie Gory, 1-3, 119234, Moscow, Russia,
etothmask@gmail.com, sergz@laser.chem.msu.ru, popov@laser.chem.msu.ru

The Stark broadening parameters are an important characteristic of plasma irradiation and are widely used for plasma diagnostics, including in the absence of local thermodynamic equilibrium (LTE). The use of knowledge of the Stark parameters of plasma significantly expands the list of objects available for study, both laboratory plasmas (plasma discharge, inductively coupled plasma, laser plasma) and astrophysical objects (plasma of stars, meteors entering the atmosphere of planets, etc.). Unfortunately, there's not much of experimental data on the Stark parameters of various lines; it's mainly collected in reviews by Konjevic et al. /1/. At present, a large theoretical base of Stark line parameters has been collected (Griem, H.R. /2/; Stark-B database /3/), but sometimes has low trust factor and the lack of experimental data is still a problem. Thus, the aim of this work was to determine the widths and shifts of lines caused by the quadratic Stark effect for the spectral series of 3p-nd/ns Na I and 4p-nd/ns K I observed in the visible and near IR ranges.

Since the Stark effect does not depend on plasma generation method, but only on the parameters of the line and electron density in the plasma, laser plasma is a good object for laboratory research, the parameters of which can be set by changing the parameters of the laser radiation used for ablation and excitation. While using laser in a pulse mode, it is possible to set a gate and delay of the recording device, recording spectra for the same object at different levels of electron density and temperature.

For determination of Stark parameters, it is necessary to characterize the studied plasma by electron density and temperature. In the present work, electron density was acquired by examining the change of Stark broadening effect on spectral lines of H I (H_α, 656.3 nm) and Na I (3p-5s, 616 nm); it was changing in range of $N_e=(3*10^{15}\div4*10^{16})$ cm^{-3}. The temperature was determined by Boltzmann plot method, using the Fe I multiplets around 372 and 382 nm. The temperature range was 4000÷7500 K.

As the object of study, we chose cryolite (Na_3AlF_6) with potassium fluoride (KF) added during fusion. This choice was made due to the chemical stability of the object, sufficient adhesiveness (compressibility), that allows to increase the strength of powder tablets prepared for analysis and reduce the risk of sample burning and crumbling.

Conditions for obtaining the spectra, such as accumulation time for each recording delay, the energy of the excitation radiation, etc., were selected by the signal-to-noise ratio and the rate of the electron density and temperature changes. A large error in determining the Stark parameters can be introduced by not taking self-absorption into account, which can occur in samples with a significant concentration of emitting particles. To detect self-absorption for multiplet transitions that allows application of the LS coupling, one can check the observance of the corresponding intensity ratio of the multiplet components, since this ratio is violated during self-absorption /4/. The fulfillment of the "intensity rule" for such transitions indicates the absence of a significant contribution of self-absorption to the emission spectra.

Often the obtained values of Stark parameters differ significantly from the calculated ones, which indicates the imperfection of theoretical approximations.

Acknowledgements. This work was supported by Russian Science Foundation (grant No. 25-22-00173).

References

1. **Djurović S., Blagojević B., Konjević N.** Journal of Physical and Chemical Reference Data 52 (2023) 031503.
2. **Griem H.R.** Spectral Line Broadening by Plasmas, Academic Press, 1974.
3. **Sahal-Bréchot S., Dimitrijević M.S., Moreau N.** 2025. STARK-B database http://stark-b.obspm.fr/
4. **Popov A. M. et al.** Spectrochimica Acta Part B 125 (2016) 43–51.

MODEL-BASED APPROACH TO CHARACTERIZE PLASMA COMPOSITION AND ETCHING/POLYMERIZATION KINETICS IN VARIOUS FLUOROCARBON GASES MIXED WITH ARGON AND/OR OXYGEN

A. Efremov[1], K.-H. Kwon[2]

[1]Molecular Electronics Research Institute (MERI), 6/1 Academic Valiev st., 124460 Zelenograd, Moscow, Russia, aefremov@niime.ru
[2]Department of Control and Instrumentation Engineering, Korea University, Sejong, 30019, Republic of Korea, kwonkh@korea.ac.kr

Gaseous fluorocarbons with a general formula of $C_xH_yF_z$ are frequently used plasma-forming environments for the "dry" patterning of silicon and silicon-based materials during the production of integrated electronic devices. The most comprehensive tool here is the reactive-ion etching (RIE) process in inductively-coupled plasma (ICP) reactors. Such a combination provides two parallels etching pathways (the gasification of surface atoms in a form of volatile fluorides and the physical sputtering of treated surface) as well as allows one to obtain the wide range of output process characteristics due to the independent adjustment of ion flux and ion bombardment energy.

The specific feature of all fluorocarbon gas plasmas is the surface polymerization effect provided by non-saturated CF_x radicals. This causes the formation of continuous fluorocarbon polymer film on the etched while the film thickness influences etching kinetics and output RIE characteristics, such as etching rate, etching selectivity in respect to over- and under-layer materials and etching profile. It is known that a) the polymerizing ability of any fluorocarbon gas plasma strongly depends on the z/x ratio in the original molecule; and b) various fluorocarbon gases being exposed to one and the same plasma excitation conditions exhibit very different properties in respect to RIE of Si and SiO_2. The effective method to adjust the etching/polymerization balance is to combine high- or low-polymerizing fluorocarbon gas with the additive component, such as other fluorocarbon, Ar and/or O_2. Obviously, the optimization of RIE regimes in multi-component gas assumes the complete understanding of plasma chemistry that allows one to control both neutral and charged fluxes on the etched surface. This complicated task cannot be solved by experimental methods only.

Previously, we have proposed the advanced research scheme which combines plasma diagnostics and plasma modeling techniques /1-4/. Such an approach directly connects variable processing parameters with gas-phase plasma characteristics as well as allows one to analyze both etching and polymerization phenomena based on model-predicted fluxes of plasma active species. Accordingly, the application of this method to several gas fluorocarbon-based

mixtures indicated the good agreement between measured and model-predicted plasma parameters as well as provided reasonable explanations and predictions for etching-rate-related effects. The main idea of this work was to summarize our data related to two- and three-component fluorocarbon gas plasmas excited under one and same operating conditions. The main focus was on such issues as a) to compare the influence of various gas mixing ratios on electrons- and ions related plasma parameters; b) to figure out peculiarities of fluorine atom kinetics in both non-oxygenated and oxygenated gas systems; and c) to analyze how differences in initial mixture composition influences the RIE process for silicon through gas-phase plasma parameters and densities of active species.

Both plasma diagnostics and etching experiments were carried out in the planar (with the top-side flat coil) ICP reactor /1-4/. Plasma was excited using the 13.56 MHz power supply while another RF generator produced the negative bias on the bottom electrode where the etched samples were placed. The subjects were CF_4-, CHF_3- and C_4F_8-based plasmas. The variable parameter was always the gas mixing ratio while gas pressure, input power and bias power were kept to be constant.

Electrons- and ions-related plasma characteristic were obtained using the double Langmuir probe tool (DLP2000, Plasmart Inc.) installed through the viewport on the chamber wall. In order to minimize experimental errors due to the deposition of fluorocarbon polymer on probe tips, these were conditioned in 50% Ar + 50% O_2 plasma before and after each measurement. As a result, we obtained the electron temperature (T_e) and the ion current density (J_+).

Steady-state densities of F atoms were determined using plasma diagnostics by the optical emission spectroscopy (AvaSpec-3648, JinYoung Tech) using the standard actinometrical approach. For this purpose, we introduced 2 sccm (~ 4.5%) of Ar in each gas mixture where it was originally absent and then, monitored emission intensities for widely used actinometrical lines, such as Ar 750.4 nm and F 703.8 nm.

In order to analyze the influence of gas mixing ratios on kinetics and densities of plasma active species, we used a simplified 0-dimensional (global) kinetic model. Sets of chemical reactions with corresponding rate coefficients were taken from our previous works. In fact, these are well-adjusted kinetic schemes which previously have been tested by several authors and demonstrated the good agreement of measured plasma parameters with their model-predicted counterparts. The basic assumptions were that a) The electron energy distribution function (EEDF) is close to Maxwellian one; b) The electronegativity of CF_4, CHF_3, C_4F_8 and O_2 plasmas at $p < 20$ mTorr is low enough to assume $n_e \approx n_+$, where n_e is the electron density; and c) The loss of atoms and radicals on chamber walls follows the first-order (Eley-Redeal) recombination kinetics with nearly-constant recombination probabilities.

Results for CF_4 + Ar, CHF_3 + Ar and C_4F_8 + Ar plasmas indicated that an increase in Ar faction in a feed gas always a) causes sufficient changes in electron temperature and plasma density (due to changes in both electron energy loss balance and total ionization rate); b) increases the intensity of ion bombardment; and c) leads to the lower-than-proportional decrease in F atom density. The last feature is due to either an increase in electron-impact dissociation frequencies for CF_x species (in the case of CF_4 + Ar) or a decrease in F atom loss frequencies in gas-phase reactions R1: $CHF_x + F \rightarrow CF_x + HF$ and R2: $C_2F_4 + F \rightarrow CF_2 + CF_3$, (in the case of CHF_3 + Ar and C_4F_8 + Ar, respectively).

Results for $CF_4 + CHF_3$ + Ar and $CF_4 + C_4F_8$ + Ar plasmas indicated that the substitution of CF_4 by any second fluorocarbon component at constant 50% Ar a) causes moderate changes in electrons- and ions-related plasma characteristics; b) increases both formation rates and densities for polymerizing radicals; and c) lowers the density of F atoms. The last phenomenon contradicts with the change of total F atom formation rate and is connected with increasing F atom loss frequency in R1 and R2.

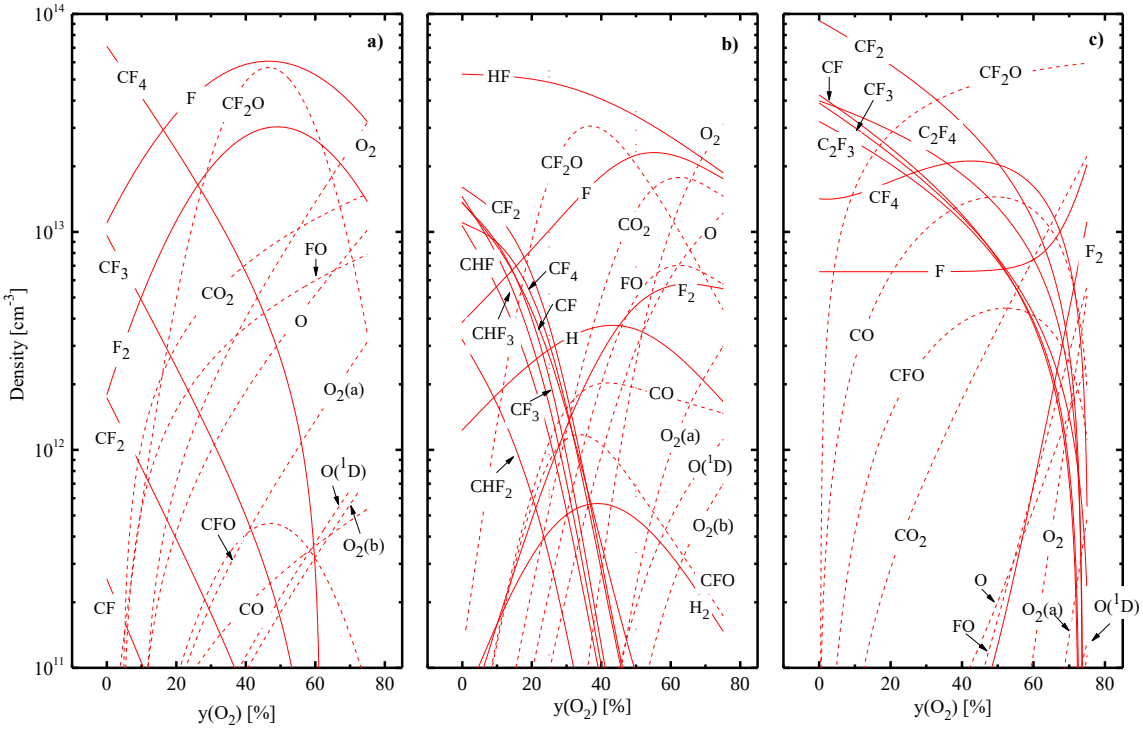

Fig. 1. Model-predicted densities of neutral species vs. fraction of O_2 in CF_4 + O_2 (a), CHF_3 + O_2 (b) and C_4F_8 + O_2 (c) plasmas. Processing conditions are: gas pressure of 6 mTorr, input power of 700 W and bias power of 200 W

Results for CF_4 + O_2, CHF_3 + O_2 and C_4F_8 + O_2 plasmas indicated that an increase in O_2 content in a feed gas a) always disturbs electrons- and ions-related plasma parameters (identically for plasma density and non-identically for electron

temperature, as follows from expected changes in total ionization rates and electron energy losses); b) results in faster, compared with the dilution effect, decrease in densities of fluorocarbon radicals due to their oxidation into CF_xO, FO and CO_x compounds; and c) sufficiently influences the kinetics of fluorine atoms. In particular, the non-monotonic (with a maximum at ~ 40-50% O_2, see Fig. 1) change in the F atom density in the $CF_4 + O_2$ plasma repeats behavior of their formation rate after the contribution of processes involving CF_xO и FO species. At the same time, corresponding effects for both $CHF_3 + O_2$ and $C_4F_8 + O_2$ plasmas contradict with changes in F atom formation rates, but results from decreasing decay frequency in gas-phase processes R1 and R2. From etching experiments, it was found that the nearly constant surface temperature does not mean the constant Si + F reaction probability. In fact, the latter depends on the polymerizing ability for the given fluorocarbon gas as well as appears to be sensitive to the O atom flux through both change in the thickness of fluorocarbon polymer film and oxidation of silicon surface. The domination of last mechanism lowers the Si + F reaction probability in O_2-rich $CF_4 + O_2$ plasmas while their competition produces non-monotonic behaviors of reaction probabilities in $CHF_3 + O_2$ (with the maximum at ~ 25–30% O_2) and $C_4F_8 + O_2$ (with the maximum at ~ 50% O_2) plasmas.

Results for $CF_4 + CHF_3 + O_2$ and $CF_4 + C_4F_8 + O_2$ plasmas indicated that the substitution of CF_4 by any second fluorocarbon component at constant 50% O_2 does not lead to principal changes in electron temperature and plasma density (due to no principal changes in electron energy loss channels and total ionization rate); b) causes an increase in plasma polymerizing ability (due to increasing densities and fluxes of polymerizing radicals); and c) reduces F atom density that was surely confirmed by actinometrical results. The last effect is mainly due to an increase in F atom loss frequency in gas-phase reactions R1 and R2. The analysis of Si etching kinetics allowed one to conclude that a) the dominant etching mechanisms are the ion-assisted chemical reaction that composes more than 70% of total etching rate; and b) the change in effective reaction probability does not correlate with increasing polymer deposition rate. In our opinion, such situation reflects the change in passivation of polymer-free surface by oxygen atoms.

References

1. **Efremov A., Murin D., Kwon K.-H.** Russian Microelectronics 49 (2020) 157-161.
2. **Efremov A., Son H. J., Choi G., Kwon K.-H.** Vacuum 206 (2022) 111518.
3. **Lim N., Efremov A., Kwon K.-H.** Plasma Chem. Plasma Process. 41 (2021) 1671-1688.
4. **Efremov A., Lee B. J., Kwon K.-H.** Materials 14 (2021) 1432-1446.

FEATURES OF THE FORMATION OF EROSIVE PLASMA IN THE TWO-PULSE CLAY ABLATION MODE

N. Kurian, S. Anufrik

Yanka Kupala State University of Grodno, Ozheshko 22, 230023, Grodno, Belarus

In modern ceramic production, materials processing and other industries, various methods of spectral analysis are widely used to determine the elemental composition [1]. Among them, a special place is occupied by laser emission spectral analysis (LESA) [2], which is distinguished by its accuracy, speed and high reproducibility of results.

The two-pulse laser mode allows to increase the accuracy of element concentration measurements by increasing the intensity of spectral lines and reducing the noise level. There are several theories in the literature explaining the mechanism of two-pulse plasma excitation.

According to [3], the first laser pulse creates an erosive plasma in the air. The second pulse additionally ionizes the plasma, which leads to an increase in the intensity of the radiation of excited atoms. According to [4], the main contribution to the formation of plasma under two-pulse action is made by the absorption of the second pulse at the boundary of the vapor-gas torch.

The works [5, 6] present theoretical models that consider the dynamics of plasma torches on a nanosecond scale and the interaction at the laser-solid body boundary. In [7] it is shown that the increase in the intensity of spectral lines in the two-pulse mode of plasma torch generation is associated with an increase in the number of excited atoms entering the plasma under the action of the second pulse. In [8] it is emphasized that preliminary hearing of the sample surface increases the efficiency of laser ablation.

Thus, a significant increase in the intensity of the analyzed spectral lines and an increase in the efficiency of material ablation are explained by various physical mechanisms. In this case, in the literature, various metals are mainly used as study samples. However, the mechanisms of interaction of a laser pulse with ceramic materials under various ablation modes have not yet been sufficiently studied.

The purpose of this work is to establish the physical mechanism for the formation of an erosion crater, an increase in the intensity of spectral lines of laser-emission plasma of technological clays during their heating and ablation by single and double laser pulses.

The object of the study is samples of technological clays used in the production of ceramic tiles at the enterprise OJSC "Keramin". The morphology of craters formed on clay samples was studied using an optical microscope with

a magnification of ×25. The study of the effect of the temperature of clay samples on the intensity of the analyzed spectral lines was carried out using a setup (Fig. 1) developed on the basis of previous versions [9].

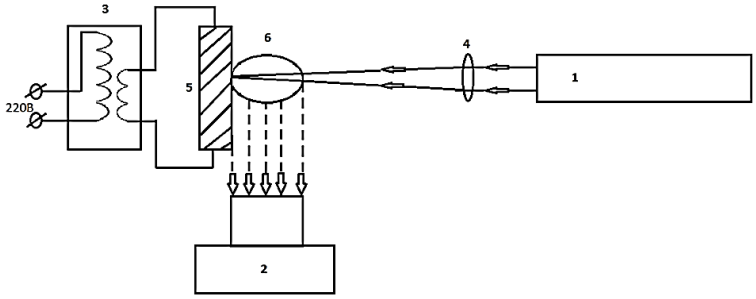

1. YAG:Nd^{3+} laser; 2. thermal imager (IT-3SM); 3. autotransformer; 4. lens; 5. test sample; 6. plasma torch

Fig. 1 – Experimental setup diagram

Initially, the clay tablet samples (4 cm in diameter) were baked for 4 h at a temperature of ~1300°C. Then, the baked samples were irradiated with laser radiation of 15 ns duration with an energy density of 10^9 W/cm^2, both in single- and double-pulse modes with a delay between pulses of 1 μs, followed by an examination of the morphology of the resulting craters. Figure 2 shows micrographs of erosion craters formed on red and white clay after laser irradiation with single (1) and double (2) laser pulses.

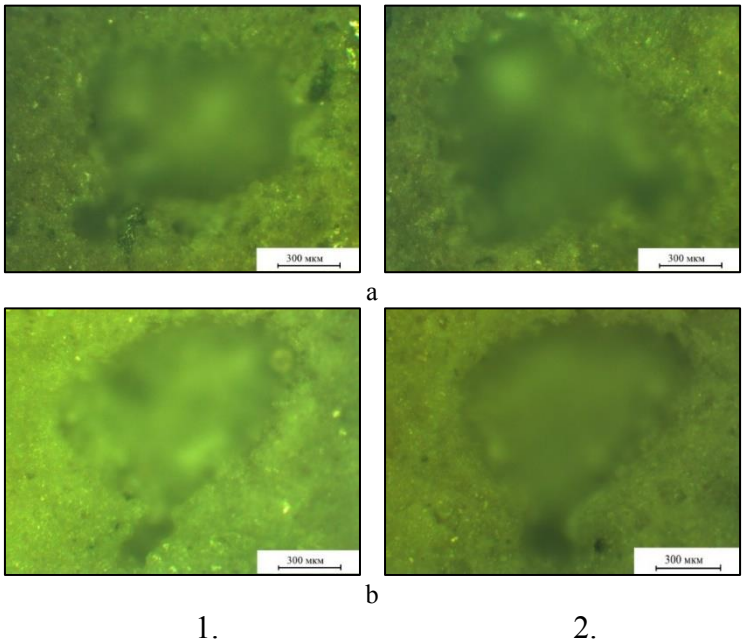

Fig. 2 – Microscopic images of laser craters on red (a) and white clay (b) with single- (1) and double-pulse (2) ablation

The typical size of the craters, determined by the largest diameter, was ≈1.7 mm. The study of the images of craters formed as a result of erosion did not reveal a heat-affected zone typical of metals. Microscopic examination of the bottom of the craters formed by double-pulse irradiation revealed the presence of ring-shaped tarnish colors, which is a sign of exposure to extreme temperatures (~1300 K). This, in turn, stimulated intense oxidation of the surface and changes in the structure of the material, which was confirmed by X-ray diffraction data. The heat-affected zone had dimensions from 3 to 6 times larger than the crater diameter. In the photographs, in the lower part of the craters, a depression is also noticeable, formed by the removal of the flow of steam-gas plasma of the molten substance. Consequently, the removal of material from the crater occurs not only due to evaporation, but also due to the displacement of the melt under the influence of vapor and plasma pressure.

Next, we studied how the temperature of the samples affected the intensity of the spectral lines of the main components of clays (Si, Al, Ca, Mg). Figure 3 shows the relationship between the intensity of the spectral lines of the main components of clays and the temperature of the sample, measured under the influence of single (1) and double laser pulses (2).

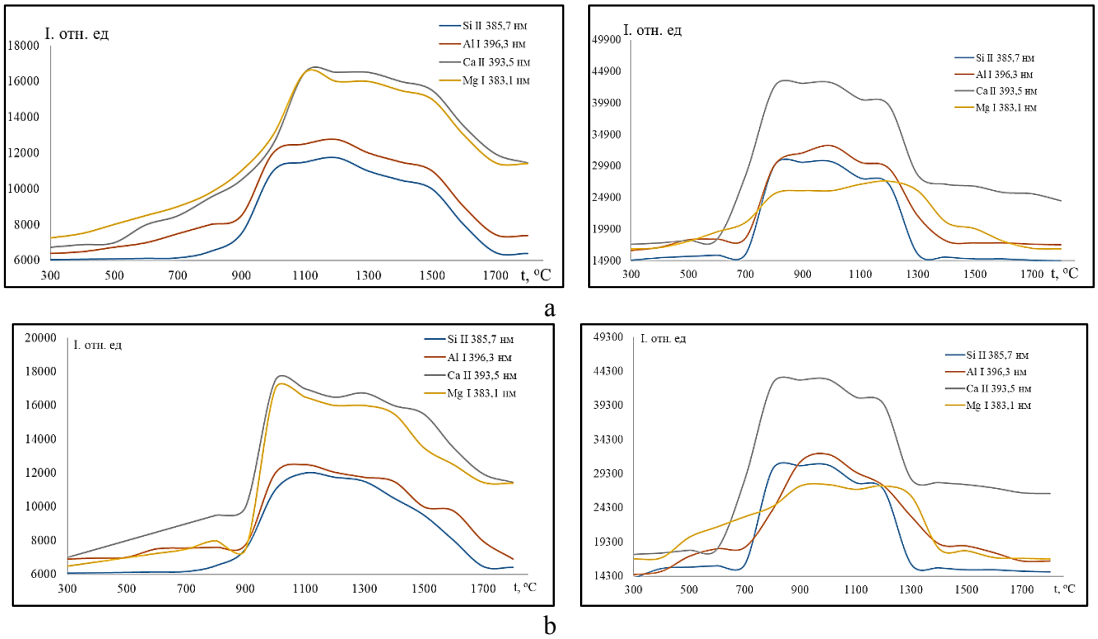

Fig. 3 – Dependences of the intensity of the spectral lines of the main components of red (a) and white technological clay (b) on temperature in single-pulse (1) and double-pulse ablation mode (2)

Analysis of the presented dependences (Fig. 3) demonstrates that the sample surface temperature has a significant effect both on the process of material removal from the erosion area and on the intensity of the emission of

spectral lines corresponding to the main elements included in the clay. The general tendency is that the intensity of spectral lines emitted by both neutral atoms and ions of the main clay components increases when the sample is heated to (800–900)°C (single) and to (600–700)°C (double pulses). The shift of the intensity maximum observed for all the studied elements with double-pulse excitation occurs toward lower temperatures (by approximately 200°C), which indicates preliminary hearing of the erosion area by the first pulse. In both cases, an increase in the clay sample temperature leads to an increase in the intensity of the spectral lines. When plasma is excited by single laser pulses, the maximum intensity of the studied spectral lines is achieved at a temperature of ~1000°C, while when using double pulses, it is ~800°C. In both cases, the intensity of the spectral lines increases by (2.0–2.5) times.

Analysis of the obtained data allows us to conclude that the key factor determining the increase in the mass of the material removed from the laser erosion zone, as well as the increase in the intensity of the spectral lines of the main components of clays, in the scheme with two nanosecond laser pulses, is the high temperature (600–700)°C of the crater bottom created by the first pulse and serving as a "target" for the second. When powerful laser radiation affects the heated lower area of the crater, a significant increase in the amount of evaporated substance is observed ($\approx 5.4\times10^{-6}$ g per one double pulse). The efficiency of this process is inversely proportional to the time interval between pulses: the shorter it is, the more effective the ablation and the higher the intensity of the spectral lines.

Thus, the results of the laser ablation experiments on clay materials preheated to high temperatures highlight the important role of the crater temperature, maintained after the first pulse, on the increase in the volume of the evaporated substance and the growth of the intensity of the analyzed spectral lines.

References

1. **Oracio S.**, **et. al.** Victor Ulises Lev Contreras Loera - Leon de los Aldama, (2013) 2-7 p., 19-27.
2. **Miller J.S., et. al.** Berlin: Springer Verlag, (1994) 187 p.
3. **Andrzej W., et. al.** Cambridge University Press (2008) 5-7.
4. **Pershin, S.M.** Quantum Electronics 16 (1989) 325-330.
5. **Ershov-Pavlov E.A.** Spectrochimica Acta, Part B. 63 (2008) 1024-1037.
6. **Babushok V.I.** Spectrochimica Acta, Part B. 61 (2006) 999–1014.
7. **Corsi M.** Spectrochimica Acta, Part B. 59 (2004) 723–735.
8. **Veiko V.P.** M.: Fizmatlit (2008) 312.
9. **Anufrik, S.S.** Bulletin of the Yanka Kupala Grodno State University 199 (2015) 83–92.

DYNAMICS OF SPECTRAL LINE INTENSITY ALONG THE AXIS OF THE EROSION PLASMA TORCH ON AN ALUMINUM TARGET

A. Liskovich

State University of Grodno, Ozheshko Street 22, 230023, Grodno, Belarus,
L30041997@mail.ru

A number of modern industries require monitoring of the chemical composition of materials, substances, semi-finished products and final products at different stages of technological cycles /1, 2/. This requires non-destructive express testing systems and devices. Laser emission spectroscopy (LIBS) is one of the promising methods of express analysis of the elemental composition of materials /3-5/. Its advantages include: minimal sampling, remoteness, the ability to analyze samples in various aggregate states, high analysis speed. The LIBS method is based on the analysis of plasma radiation generated by the action of a laser pulse on the surface of an object. The plasma temperature in the first microseconds can reach 10^5 K, which ensures the excitation and ionization of atoms and the formation of characteristic spectra. However, the accuracy and sensitivity of the method are limited by the non-stationarity of the plasma, which quickly cools and recombines, as well as background radiation and matrix effects. The non-stationarity of the plasma leads to a change in the intensity of spectral lines in time and space /6-8/. To overcome these difficulties, plasma stabilization methods are being actively studied /9, 10/, including the use of double laser pulses /11, 12/. The use of double pulses allows increasing the mass of the evaporated substance and stabilizing the plasma, but the intensity distribution along the height of the torch remains poorly understood. This paper presents the results of a study of the intensity distribution of aluminum spectral lines along the height of a plasma torch formed by double nanosecond laser pulses.

The experiments were carried out on a setup with a YAG:Nd^{3+} laser generating single and double pulses (wavelength 1.064 μm, duration ~15 ns, energy up to 32 mJ) /12, 13/. The plasma torch was formed on an aluminum target in air. The spectra were recorded from the orthogonal direction relative to the torch axis through slit diaphragms (slit width 1 mm). This allowed scanning the plasma torch radiation along its axis with a step of 0.5 mm. Both atomic and ionic lines of aluminum with different excitation energies were selected for the studies. The spectra were recorded in air in the wavelength range of 258–370 nm with interpulse intervals of 0 μs, 1 μs, 5 μs and 50 μs.

Below are shown the dependences of the intensity of the spectral lines of the plasma torch formed on the surface of the aluminum sample on the distance between the radiation detection zone and its surface (Fig.1). The formation of

flame torches by both single and double pulses was used. Lines with different characteristics were selected for the study: atomic lines of aluminum: Al I 305.7 nm and Al I 308.2 nm; lines of singly ionized aluminum atoms: Al II 263.16 nm, Al II 281.62 nm and Al II 358.66 nm; line of doubly ionized aluminum Al III 361.24 nm. The spectral lines Al II 358.66 nm and Al III 361.24 nm are lines with high excitation energy (15.3 and 17.8 eV, respectively), and the line Al I 308.2 nm is with low excitation energy (4 eV). The line Al I 308.2 nm is one of the most intense, and the lines Al II 263.16 nm and Al III 361.24 nm are relatively weak. This set of spectral lines was chosen in order to study the effect of the position of the radiation selection zone relative to the target on the intensity of lines with different properties.

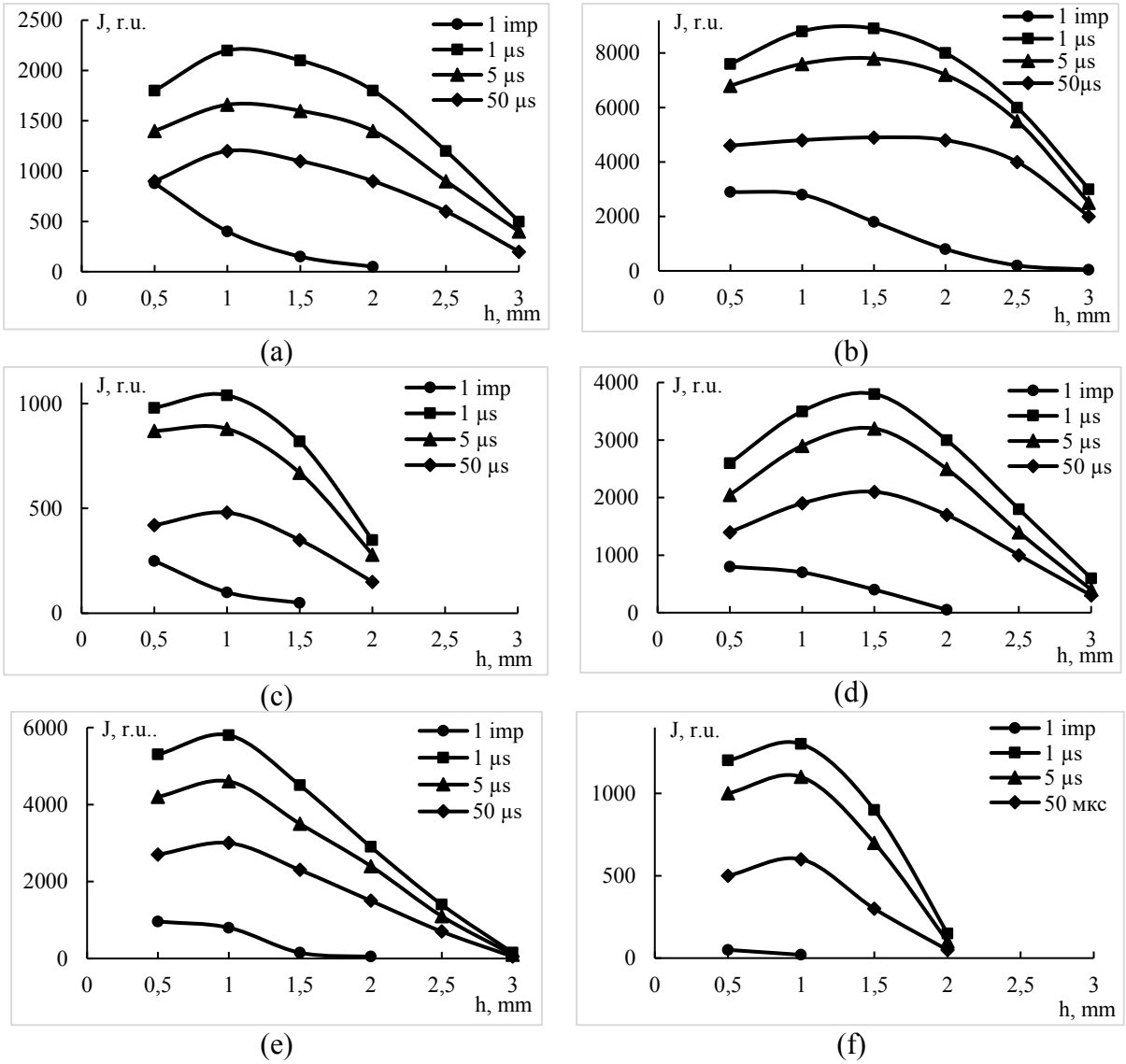

Fig. 1 – The intensity of spectral lines of the plasma torch formed on the surface of the aluminum sample, depending on the distance between the radiation recording zone and its surface: (a) Al I 305.7 nm; (b) Al I 308.2 nm; (c) Al II 263.16 nm; (d) Al II 281.62 nm; (e) Al II 358.66 nm; (f) - Al III 361.24 nm

When using single laser pulses, the maximum intensity of spectral lines was observed in the near-crater zone (0 – 1 mm from the sample surface), where the plasma temperature was maximum. However, background radiation in this region reduced the signal-to-noise ratio. When switching to double laser pulses, the intensity of spectral lines increased up to 6 times. The increase in intensity was greater for ion lines than for atomic lines. It also depended on the excitation energy of the line. The higher the excitation energy of the line, the greater its intensity increases when switching to plasma formation by double pulses.

Atomic lines Al I 305.7 nm and Al I 308.2 nm in this case are reliably recorded up to distances from the sample of 3 mm and more. Their maximum intensity is in the range of distances from the target of 0.5–2.5 mm. The plasma torch region from which the radiation emission is most intense shifted toward greater distances from the sample. This is due to the fact that the second laser pulse removes a significantly larger mass of the target substance from the crater than the first /13/. The second laser pulse interacts with the “hot” crater formed by the first pulse, which increases the ablation efficiency up to 10 times.

The plasma torch formed by the second laser pulse does not propagate into the air, but into the medium of the recombining plasma formed by the first laser pulse, the pressure of which is lower than atmospheric /14/. In this case, the medium will provide less resistance and the speed of its propagation into the first plasma torch will be greater. The injection of hot plasma formed by the second pulse into the first torch leads to repeated evaporation of nanoparticles and clusters /15-16/ formed from the substance of the first plasma torch, repeated excitation and ionization of its atoms. This leads to the fact that the plasma torch formed by double laser pulses will be larger, its emitting zone will be more voluminous /17/. The intensity of the spectral lines of plasma torches formed by double laser pulses depends on the time interval between them. The highest intensity of the spectral lines was observed at short interpulse intervals (~1 μs). At a delay of 50 μs, their intensity decreased by about half, since the second pulse interacts with already cooled plasma.

The most intense radiation of the continuous (background) spectrum comes from the near-crater zone /4, 6 8/, from the region where the plasma has a high temperature approaching 10^5 K. Therefore, the intensity of the spectral lines from the region of 0–1 mm from the target surface (in Fig. 1 (a-f), point h=0.5 mm) is not the highest. As the distance from the target increases, the plasma temperature decreases, and with it the intensity of the background radiation decreases, the intensity of the selective radiation increases, and the signal/noise ratio increases. From the above it follows that the selection of radiation from emission plasma plumes formed by double nanosecond laser pulses on the target, for the purposes of LIBS spectroscopy, should be performed by screening the near-crater zone of the plasma plumes.

Thus, the conducted studies have shown that the use of double laser pulses significantly increases the intensity of aluminum spectral lines, especially ionic ones, and expands the area of recording the analytical signal. The obtained results can be used to optimize the parameters of LIBS spectrometers and improve their analytical characteristics.

The work was carried out within the framework of task 1.5 of the State Scientific Research Program “Photonics and Electronics for Innovations-2025”, subprogram “Photonics and its Applications”.

References

1. **Anufrik S.S., Znosko K.F., Kuryan N.N.** Vesnik of Yanka Kupala State University of Grodno. Series 2. Mathem.Physics…No.3(199), (2015) 83-92.
2. **Anufrik S.S., Kurian N.N., Znosko K.F.,** [et al.]. Vesnik of Yanka Kupala State University of Grodno. Series 2. Mathematics…, 6 (2016) 57-63.
3. **Singh J., Thakur S.** Laser-Induced Breakdown Spectroscopy. Amsterdam: Elsevier (2007).
4. **Kremers D., Radiemski L.** Laser-Induced Breakdown. M.: Technosphere (2009).
5. **Voropay E., Ermalitskaia E.** European Physics Journ.D. 64 (2011) 453-458.
6. **Popov A.M., Labutin T.A., Zorov N.B.** Vesnik of Moscow University. Series 2. Chemistry, 50 (2009) 453-467.
7. **Kuriyan N.N., Znosko K.F., Grigut V.V.** Vesnik of Yanka Kupala State University of Grodno. Series 2. Mathematics…, 8 (2018) 101-110.
8. **Voropay E.S., Ermalitskaya K.F., Ermalitsky F.A.** Journal of Applied Spectroscopy. 86 (2019) 83-89.
9. **Kiris V.V., Tarasenko N.V., Nevar, E.A.,** [et al.]. Journal of Applied Spectroscopy. 86 (2019) 817-825.
10. **Znosko K.F.** Vesnik of Yanka Kupala State University of Grodno. Series 2. Mathematics. Physics… 11 (2021) 94-106.
11. **Pershin S.M.** Quantum Electronics. 39 (2009) 63-67.
12. **Znosko K.F.** Vesnik of Yanka Kupala State University of Grodno. Series 2. Mathematics. Physics… 10 (2020) 100-113.
13. **Znosko K.F., Leshchik S.D.** Vesnik of Yanka Kupala State University of Grodno. Series 6. Engineering Science. 11 (2021) 45-58.
14. **Znosko K.F.** Vesnik of Yanka Kupala State University of Grodno. Series 2. Mathematics. Physics…, 10 (2020) 103-115.
15. **Znosko K.F.** Vesnik of Yanka Kupala State University of Grodno. Series 2. Mathematics. Physics…, 14 (2024) 81-92.
16. **Goncharov V.K., Kozadaev K.V., Shchegrikovich D.V.** Journal of Engineering Physics and Thermophysics. 84 (2011) 723-728.

17. **Znosko K.F.** Vesnik of Yanka Kupala State University of Grodno. Series 2. Mathematics. Physics…, 13 (2023) 116-132.

OPTICAL EMISSION SPECTROSCOPY OF COAXIAL DBD PLASMA AT ATMOSPHERIC PRESSURE

K.T. Logunov, D.A. Kotov, A.V. Aksiuchyts

Belarusian State University of Informatics and Radioelectronics, 6 P. Brovki Street, 220013, Minsk, Belarus, k.logunov@bsuir.by

Nowadays, surface modifications and its activation are attracting great interest. It is possible to change surface properties using plasma technology, which is based on a simple physical principle: by supplying energy, aggregate states change (solid becomes liquid, liquid becomes gaseous). If additional energy sufficient for ionization is supplied to the gas, it will move to the fourth aggregate state - plasma. Plasma can be used to modify surface properties. The consequence of plasma pretreatment is a significant and precisely controlled increase in the adhesion and wettability of surfaces. This allows the use of new (including non-polar) materials in industry and production, as well as environmentally safe materials that do not contain solvents, varnishes and adhesives. Many pretreatment technologies today can be replaced by plasma treatment /1-4]/.

One of the most informative and non-destructive methods of plasma diagnostics is optical emission spectroscopy (OES), which allows analyzing qualitative and quantitative parameters of plasma by its spectral emission. The OES method is based on the registration and interpretation of atomic and molecular spectral lines arising from transitions of excited plasma particles to lower energy levels. This approach provides the determination of key characteristics such as electron temperature, density of charged and neutral particles, plasma composition, and identification of active forms (radicals, ions). This paper presents the results of the study of atmospheric plasma by the OES method aimed at establishing a correlation between discharge parameters and spectral features, which is necessary to optimize its practical use.

Figure 1 shows a schematic diagram of an experimental setup for studying cold atmospheric plasma by emission spectroscopy. The setup includes a discharge system generating plasma and control electronics: power supply, transformer, transistor key and a high-voltage probe for controlling discharge parameters. Optical emission from the plasma is transmitted through a light guide into the SOL Instruments S150-2-3648USB spectrometer, which records emission spectra for subsequent analysis. This measurement was performed along the flare jet at the distance 15mm with a spectral resolution of <0.15 nm in the range from 200 to 980 nm. Identification of spectral lines was performed using the NIST Atomic Spectra Database /5/.

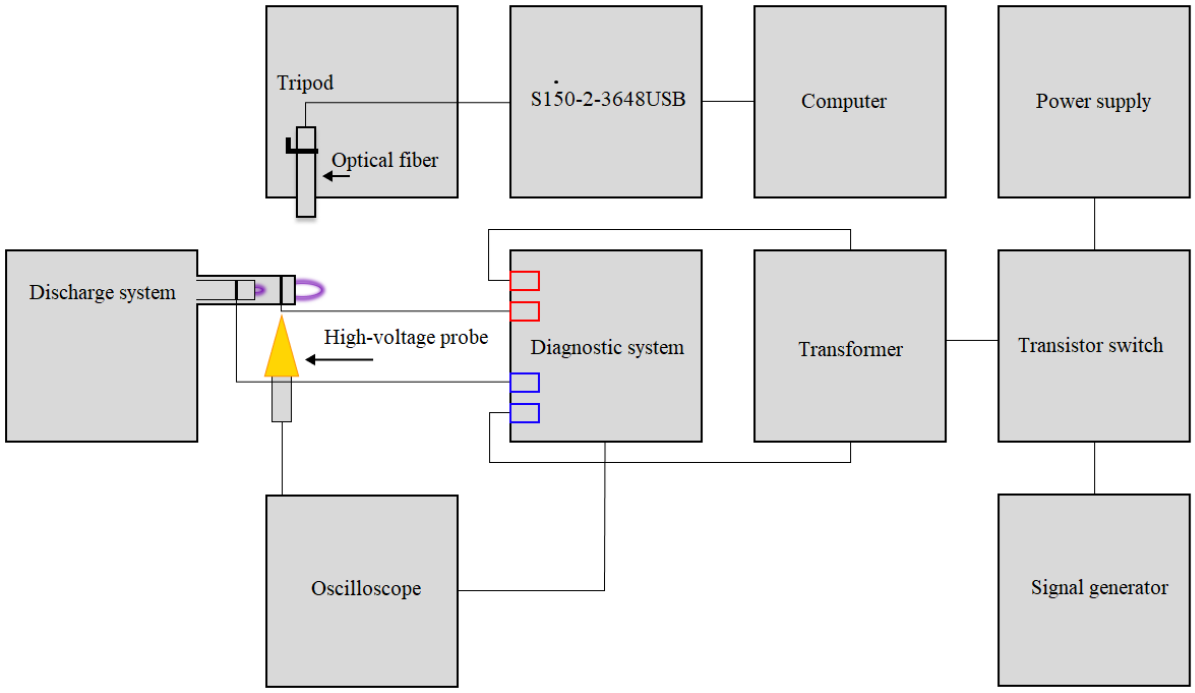

Figure 1 - Scheme of studies of qualitative and quantitative parameters of cold atmospheric plasma by the emission spectroscopy method

To ensure the accuracy of measurements, the circuit is supplemented with a signal generator, an oscilloscope and a computer that processes the obtained data. A tripod provides stability of the optical system. This configuration makes it possible to study in detail the qualitative and quantitative parameters of the plasma, including its chemical composition and energy characteristics, which is important for applications in biomedicine, nanotechnology and ecology.

Figure 2 shows the emission spectra of a coaxial plasma of a dielectric barrier discharge at atmospheric pressure. The spectra are recorded at different voltages on the electrode.

The obtained spectra show a set of intense lines characteristic of argon plasma in the region of 690-850 nm, corresponding to transitions of excited states of argon atoms (Ar I). An increase in the voltage leads to an increase in the intensity of most spectral lines, indicating an increase in the degree of gas excitation and an increase in the electron density and temperature of the electron component. In the region of 309-315 nm there are peaks corresponding to the emission of the OH hydroxyl radical resulting from the interaction of the plasma with the atmospheric medium. In the range of 330-380 nm there is the emission band of the second positive system (SPS) of molecular nitrogen N_2, which indicates the presence of air impurities and non-equilibrium discharge /6/.

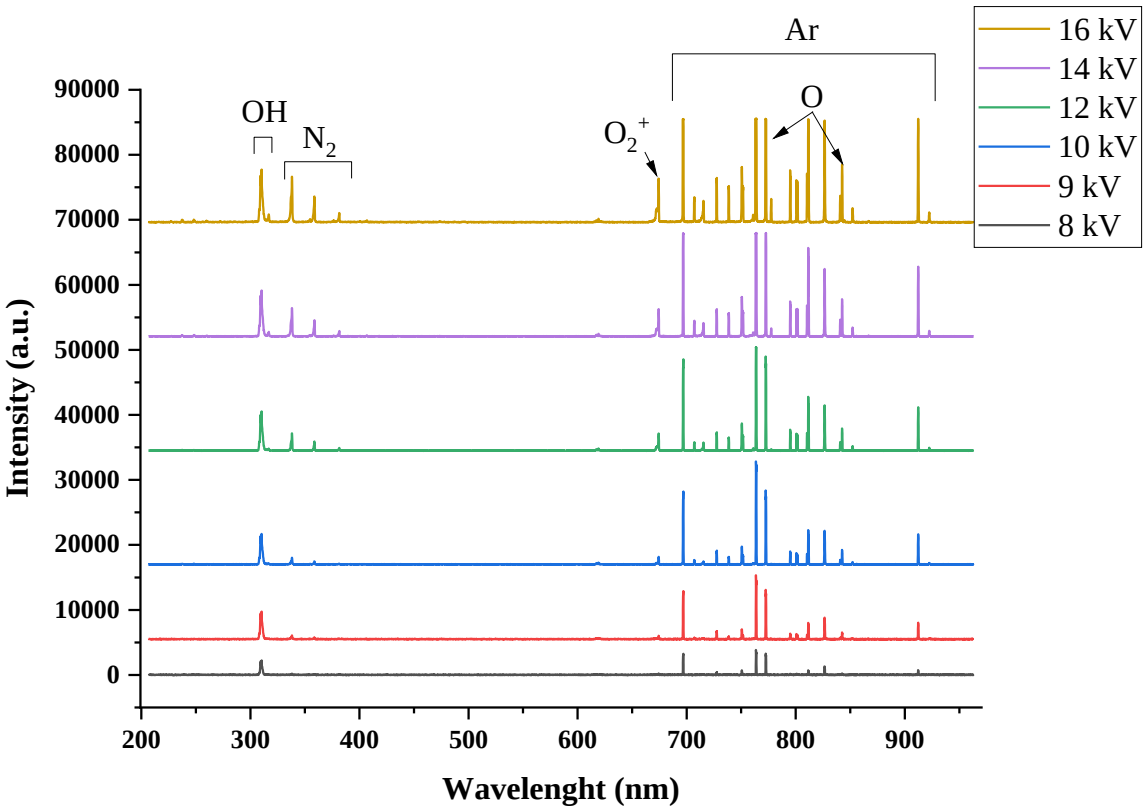

Figure 2 - Optical emission spectrum of atmospheric plasma at different electrode voltages

As the voltage at the electrode increases, a general increase in the intensity of spectral lines is observed, especially in the region from 700 nm and above. This indicates an increase in the discharge power, more active argon ionization and, accordingly, an increase in the number of excited atoms.

In addition, the number of weakly resolved lines in the 700-800 nm range increases, which also reflects an increase in the density of excited states. Such an increase in intensity can be used as an indirect indicator of the increase in the electron density and kinetic energy of particles.

The influence of the distance between the end of the discharge system and the sample to be treated was also investigated. The distances of 5, 10, 15, 20, 25 and 30 mm were investigated. They showed that with increasing distance the intensity of the spectrum decreases naturally, but the emission band of molecular nitrogen N_2 has a maximum at a distance of 15 mm, which indicates the maximum influence of the atmospheric medium at this distance.

Optical emission spectroscopy allowed us to establish that with increasing voltage in the coaxial plasma of a dielectric barrier discharge, a regular increase in the intensity of argon spectral lines is observed, as well as an increase in the

emission of impurity components such as OH and N_2. This indicates an increase in the density of excited states and confirms the non-equilibrium character of the plasma, potentially suitable for various applications: from the treatment of biological objects to the modification of the surface of materials.

References

1. M. M. M. Bilek, M. Vandrovcová, A. Shelemin, A. Kuzminova, O. Kylián, H. Biederman,L. Bačáková, A. S. Weiss. Appl. Surface Sci., 518 (2020) 146128.
2. K. Ollegott, P. Wirth, C. Oberste-Beulmann, P. Awakowic, M. Muhler. Chem. Ing. Tech., 92, N 10(2020) 1542—1558
3. S. H. Liu, M. Neiger. J. Phys. D: Appl. Phys., 34 (2001) 1632—1638
4. E. Wagenaars, R. Brandenburg, W. J. M. Brok, M. D. Bowden, H.-E. Wagner. J. Phys. D: Appl. Phys., 39, N 4 (2006) 700—711.
5. Kramida, A., Ralchenko, Yu., Reader, J., and NIST ASD Team. NIST Atomic Spectra Database (ver. 5.12). National Institute of Standards and Technology, Gaithersburg, MD, 2024. Available: https://physics.nist.gov/asd.
6. A.V. Aksyuchits, D.A. Kotov, K.T. Logunov, A.N. Osipov, / Research characteristics of plasma jet generated by coaxial dielectric barrier discharge at atmospheric pressure / Plasma Physics and Plasma Technology: IX International conference (Minsk, 12-16 september, 2022) /B.I. Stepanov Institute of Physics Netional Academy of Sciences of Belarus – Minsk, 2022. – 87 p.

RECOMBINATION RADIATION REGIME OF LASER PRODUCED LITHIUM PLASMA (Li)

N. Matiukhin[1,2], M. Krivokorytov[1], V. Gubarev[1], L. Stepanov[1,3]

[1]Institute of Spectroscopy of the Russian Academy of Sciences,
Moscow, Troitsk, Fizicheskaya str., 5, 108840, e-mail: isan@isan.troitsk.ru
[2]Moscow Institute of Physics and Technology (National Research University),
Moscow region, Dolgoprudny, Institutsky lane, 9, 141701,
e-mail: matiukhin.nd@phystech.edu
[3]Higher School of Economics Research University,
Moscow, Pokrovsky Boulevard, 11, 109028 e-mail: hse@hse.ru

Introduction

Over the past two decades (since the early 2000s), intensive technological advancement has been reached in the soft X-ray range ($\lambda \approx 10$ nm). This progress has been driven by the development of technologies utilizing soft X-ray radiation, such as water-window microscopy /1/, gas pinch imaging, and others. One of the key technologies employing soft X-rays is X-ray lithography /2/. Lithography is a crucial process in the fabrication of integrated circuits, where the minimum achievable feature size in such a process is proportional to the wavelength of the radiation used in the lithography tool. For this reason, modern lithography utilizes soft X-ray radiation with a wavelength of 13.5 nm, enabling the production of nanostructures with feature sizes below 10 nm /3/.

A major challenge in the operation of photolithography tools is the inspection of photomasks used for pattern formation /4/. This inspection must be performed using radiation at the same wavelength as the operational one /5/. Since conventional optics are inefficient in the soft X-ray range due to high absorption coefficients, inspection optical systems employ either multilayer interference mirrors or zone plates /6/. Among the available sources, laser-produced tin plasma sources are most widely used; however, their spectrum near 13.5 nm is not monochromatic but consists of overlapping spectral lines, making them incompatible with zone plates due to chromatic aberrations. Thus, there is a pressing need to develop 13.5 nm radiation sources with a spectral bandwidth narrow enough to fully exploit the capabilities of modern zone plates.

It is known that hydrogen-like lithium (Li^{2+}) produces an intense single emission line at 13.5 nm (Ly_α) /7/. An experimental radiation source based on laser produced lithium plasma was developed at the Laboratory of Atomic Spectroscopy of the Institute of Spectroscopy, Russian Academy of Sciences (ISAN).

In the experiment, a Nd:YAG laser operating at 1064 nm wavelength, with a pulse duration of 1.5 ns and pulse energy of 0.5 mJ, was used. The laser focal spot diameter was 50 μm, yielding a power density on the target of ~ 10^{10} W/cm². Spectra were recorded using a grazing-incidence spectrometer with shifted from the Rowland circle slit /8, achieving a resolving power of $\lambda/\Delta\lambda = 500$.

Additionally, measurements of the radiation source geometry were performed using a Schwarzschild objective.

Results

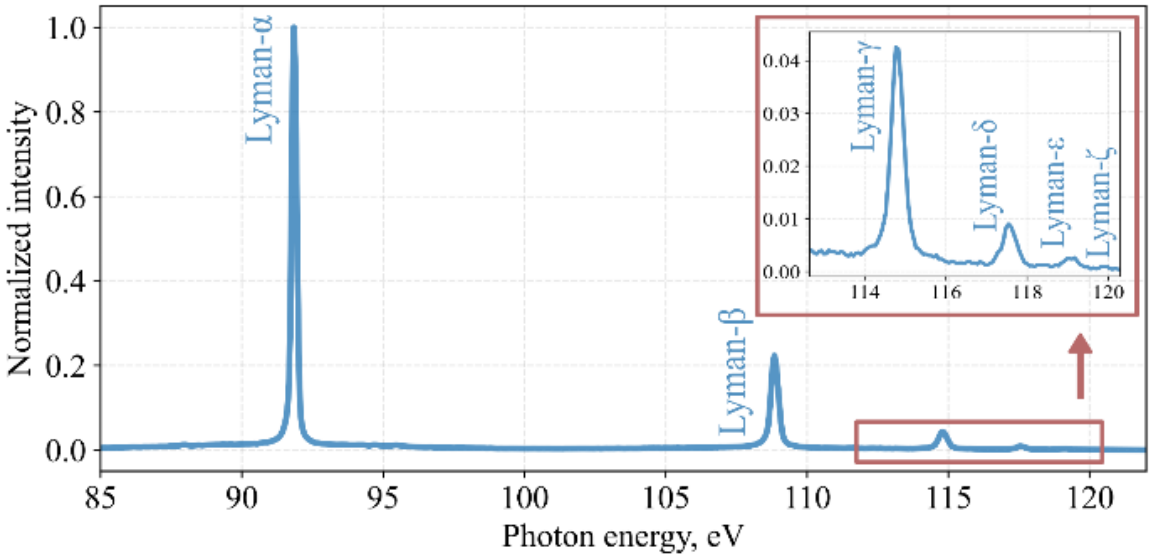

Fig. 1 The emission spectrum of hydrogen-like lithium in the range of soft X-rays

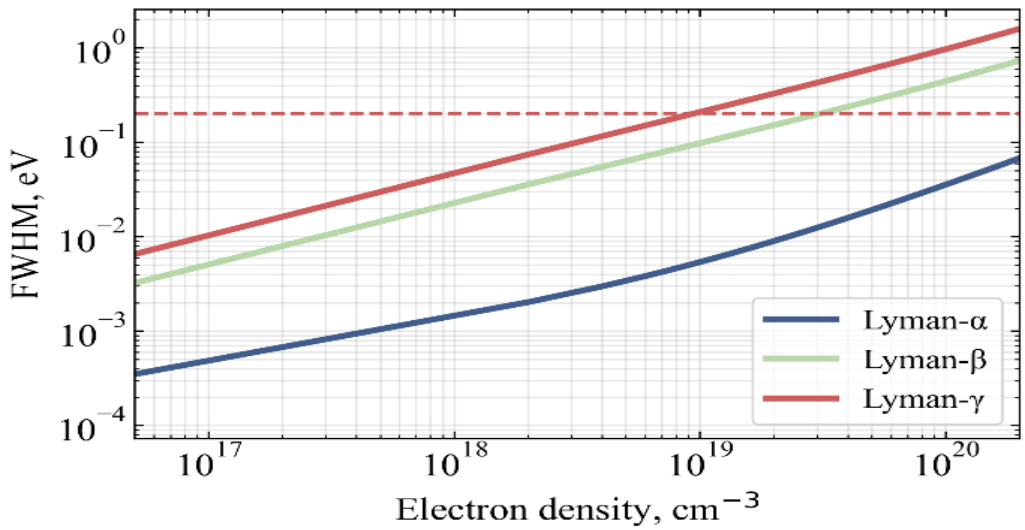

Fig. 2 The widths of the Lyman series lines corresponding to the electron density of the plasma

Fig.1 demonstrates the emission spectra of the source in range 80-120 eV. The spectral analysis revealed that the lower limit of the line monochromaticity $\lambda/\Delta\lambda$ is at least 500. This value is defined by the spectrometers resolving power. Based on Stark broadening calculations for the observed lines, the upper limit of the plasma density was estimated as $N_e < 10^{19}$ cm^{-3} (Fig. 2), while the line intensity ratios yielded a temperature estimate of T∼6 eV.

Images of the source obtained using the Schwarzschild objective demonstrate that the emitting plasma size is approximately ∼200 μm. Thus, the radiation in this source originates from a recombination regime in a cold, low-density plasma region, allowing the line monochromaticity to exceed $\lambda/\Delta\lambda$=500.

Conclusions

The presented laser-induced lithium plasma source provides radiation with a line monochromaticity of $\lambda/\Delta\lambda \geq 500$, achieved through operation in the recombination radiation regime. Owing to the high monochromaticity of its emission lines, this source can be employed as an inspection tool for X-ray lithography applications.

Acknowledgements

This work was carried out with the support of the Russian Science Foundation, grant № 25-22-00363. The authors are thankful to P. Antsiferov for useful discussions.

References

1. **M. Kördel, A. Dehlinger, C. Seim, U. Vogt, E.Fogelqvist, J. Sellberg, H. Stiel, and H. Hertz,** "Laboratory water-window x-ray microscopy," Optica 7, 658-674 (2020)

2. **C. Wagner and N. Harned**; “Euv lithography: Lithog-raphy gets extreme”. Nature Photonics, 4, 01 2010. DOI: 10.1038/nphoton.2009.251

3. **Päivänranta, Birgit & Langner, Andreas & Kirk, Eu-genie & David, Christian & Ekinci, Yasin.** (2011). Sub-10 nm patterning using EUV interference lithog-raphy. Nanotechnology. 22. 375302. 10.1088/0957-4484/22/37/375302.

4. **L. Juschkin and D. Wack.** Source performance metrics for EUV mask inspection. // J. Micro/Nanopattern. Mater. Metrol. Apr–Jun 2022 • Vol. 21(2). DOI: 10.1117/1.JMM.21.2.021204

5. **K. Seki, K. Badger, E. Gallagher, T. Konishi, G. McIntyre.** Shedding light on EUV mask inspection. // SPIE 8441, Photomask and Next-Generation

Lithography Mask Technology XIX, 844114 (June 1, 2012); DOI: 10.1117/12.976059
6. **Kenneth A. Goldberg et al.** An EUV Fresnel zoneplate mask-imaging microscope for lithography generations reaching 8 nm // Proc. of SPIE Vol. 7969 796910-12
7. **Kramida, A., Ralchenko, Yu., Reader, J. and NIST ASD Team** (2023). NIST Atomic Spectra Database (version 5.11), [Online]. Available: https://physics.nist.gov/asd [Thu Jun 13 2024]. Na-tional Institute of Standards and Technology, Gaithersburg, MD. DOI: doi: 10.18434/T4W30F
8. **P. Antsiferov, L. Dorokhin, P. Krainov.** Rev. Sci. Instrum.1 May 2016; 87 (5): 053106.

7. PLASMA APPLICATIONS AND ADVANCED PLASMA TECHNOLOGIES

THE ALOE – DEVICE FOR PLASMA MEDICINE

A.V. Kazak, L.V. Simonchik

B.I. Stepanov Institute of Physics of the National Academy of Sciences of Belarus,
220072, Nezavisimosti ave 68-2, Minsk, Belarus, Email: a.pavlova@ifanbel.bas-net.by

1. Introduction. The ability to produce “cold” plasma under atmospheric pressure conditions has been the basis for the rapid growth of plasma applications in biomedicine /1,2/. Plasma has a number of properties such as charged particles, electric current, ultraviolet radiation, temperature, active molecules, radicals, and metastable species that can act synergistically /3,4/.Antipruritic, antimicrobial, anti-inflammatory, tissue stimulating, blood flow enhancing, and pro-apoptotic effects have been demonstrated in vivo and in vitro experiments, and no pathogen resistance to plasma treatment has been observed to date /2,5,6/. The combination of various biologically active components and their wide range of positive effects on various diseases makes plasma as an attractive option for medical use.

This paper presents a description of the device "ALOE" for generation the air plasma jet and its characteristics.

2. The structure and operating principle of the device "ALOE". The ALOE air plasma jet generating device consists of a power source, a compressor, a discharge chamber, and a flexible metal hose, inside which there is an air supply tube and a high-voltage wire. The operating principle of the device consists of ignition and maintenance of the stable glow microdischarge between two electrodes in the discharge chamber through which air is continuously blown. The appearance of the device is shown in Figure 1. The control panel contains a display, buttons for decreasing/increasing the output current, buttons for decreasing/increasing the processing time, and a start/stop button. The output current can be selected from a range of 30, 35 and 40 mA. The operating time can be set from 1 to 20 minutes in 1 minute increments. A green bar is induced at the bottom of the display and shows the duration of the preheating or cooling time of the discharge chamber.

Figure 1 – Photo of the device “ALOE”

3. Plasma jet characteristics. The chemical composition of air plasma jets depends on the gas temperature in the discharge region [7]. Plasma jets generated by a glow microdischarge in air, characterized by an elevated temperature. As shown in [10], the flow and temperature distribution profiles vary greatly depending on whether the jet flows into open space or onto some barrier, such as a Petri dish.

Figure 2 shows the spatial temperature profiles for a jet flowing into open space (Figure 2, b) and onto the obstacle (Figure 2, c) at the same gas flow rate of 5 l/min.

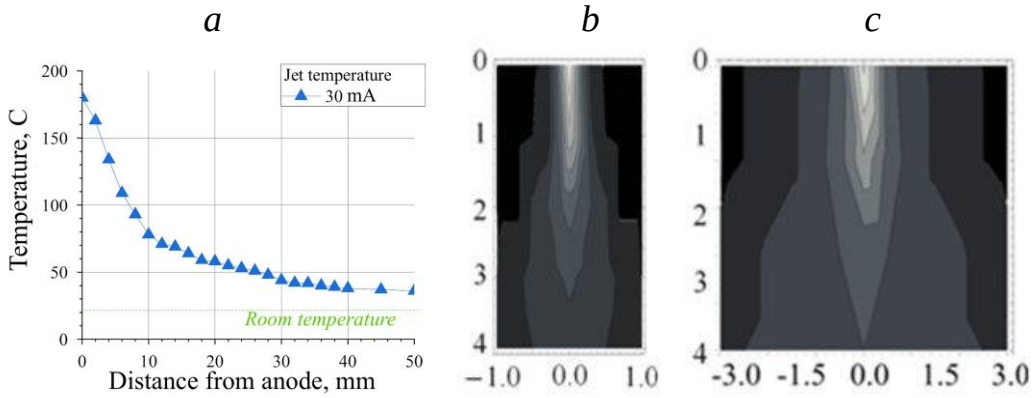

Figure 2 – Axial distribution of gas temperature in the jet which depends on the distance from the anode (a) and spatial temperature profiles in the case of jet flowing into open space –b and in the case of jet flowing onto a barrier –c at a flow rate of 5 l/min, current of 30 mA.

The profile of the gas temperature of the jet in the presence of an obstacle becomes 3 times wider, and the distribution of the gas temperature acquires a bell-shaped form. This bell-shaped distribution is likely associated with the spreading of the jet along the Petri dish surface, its heating, and the ascending hot flows, which necessitates additional gas temperature restrictions when working with living objects.

The concentration of bactericidal components of the air plasma jet was determined by the method of absorption IR spectroscopy. The absorption spectra were recorded using a Nexus IR Fourier spectrometer (Thermo-Nicolet) with a 186-0305 gas cell (Perkin-Elmer). The optical path of the gas cell was 135 cm.

The entire plasma jet from the hole in the anode was directed into the cuvette using a silicone tube. The absorption spectra were calculated using the HITRAN spectral database. [11] The mole fractions of the bactericidal components at the outlet of the hole in the anode of the discharge chamber under various conditions are given in Table 1.

Table 1. Parameters of the air plasma jet.

	Discharge parameters	NO, ppm	NO_2, ppm	HNO_2, ppm
1	Discharge gap 0.5 mm, Current strength 30 mA, Air flow 1.5 l/min, Outlet diameter 4.0 mm	500±25	250±25	50 ±5
2	Discharge gap 0.5 mm, Current 30 mA, Air flow 0.15 l/min, Outlet diameter 0.25 mm	335±25	140±25	15 ±5

The resulting molar fractions of NO, NO_2 and HNO_2 in the air plasma jet of a glow microdischarge at atmospheric pressure decrease exponentially with distance from the anode, and at the distance of 4 cm are approximately 40 ppm, 20 ppm, and 10 ppm, respectively.

4. Possible applications of the device

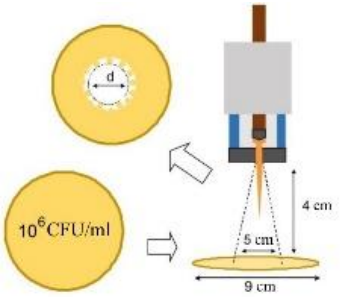

Figure 3 – Scheme of the experiment with the processing of Petri dishes

Processing of samples and surfaces in open atmosphere. The experimental setup using a Petri dish as an example is shown in Figure 3. The discharge chamber is fixed vertically on a laboratory stand (or other holder) so that the distance from the jet outlet to the surface is at least 4 cm. Place the Petri dish so that its central part is located opposite the jet outlet. Set the current to 30 mA and the required processing time on the display. Remove the lid from the Petri dish. Press the "Start-Stop" button to turn on the "ALOE" device. After the discharge has turned off (short sound), close the Petri dish and remove it for further examination.

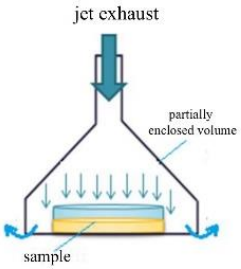

Figure 4 – Scheme of the experiment with processing products in a partially closed volume

Processing of products in a partially enclosed space. The scheme of the experiment with processing of products in a partially closed volume is shown in Figure 4. The product of a complex shape that needs to be processed should be placed on a flat surface and covered with a cap-shaped container. Direct the jet exhaust into the cap-volume from above. The gases will escape through the unevenness of the cap's contact with the surface.

Set the current to 30 mA and the required processing time on the display. Press the "Start-Stop" button to turn on the "ALOE" device. After the discharge has been turned off, remove the product for further examination.

Figure 5 – Photo of the discharge chamber in hand

Treatment of large surfaces or biological tissues/wounds.

Set the current to 30 mA and the required treatment time on the display. Press the «Start-Stop» button to turn on the ALOE device. After a short signal to turn on the main discharge, take the discharge chamber in your hand, as shown in Figure 5, and bring it to the

area of the body to be treated. Make sure that the distance from the jet exhaust hole to the object is at least 4 cm. The special made limiter can be used for this. Continuously move the discharge chamber over the surface to be treated. After the discharge is turned off (short sound), place the discharge chamber on a stand made of non-flammable material.

Treatment a local area using extended channels. This configuration is used to use the device in the treatment of dental diseases. Studies have shown that the loss of RNS concentration is several percent when using a channel up to 2 meters, while the use of long channels allows to reduce the gas temperature of the exhaust. The use of dental cannulas (Figure 6) at the second end of the tube allows delivering the exhaust to a locally selected area, for example, for the treatment of abscess or any other cavity, in addition, such treatment promotes disinfection in this area and accelerates healing.

Figure 6 – Photo of the discharge chamber with dental cannula

Thus, the development will be in demand in the field of healthcare, veterinary medicine, and cosmetology upon receipt of the relevant certificates and permits. The device can be used for effective sterilization and disinfection of surfaces, including heat-sensitive ones, such as living tissues, and also serve as the prototype in the development of various physiotherapeutic devices. Currently, the program and methodology for clinical trials for applications in dentistry and maxillofacial surgery have been prepared, clinical trials were conducted and a certificate No. IM-7.117470 was received.

References

1. **J.M. Sadowska et al.** Europhysics News 53,3 (2022) 20–23.
2. **M. Laroussi**, IEEE Trans., Plasma Sci.,30 (2002) 1409–15.
3. **Lu X. et al.** Plasma Sources Sci. Technol.21(2012) 034005.
4. **Winter J. et al.** Plasma Sources Sci. Technol. 24 (2015), 064001.
5. **Isbary G. et al.** Br. J. Dermatol, 163 (2010) 78.
6. **M. Laroussi**, Plasma Process. Polym. 11 (2014)1138–41.
7. **V.I. Arkhipenko et al.** HTMP, 22, 4, (2018) 273–278.
8. **Kazak, A.V. et al.** Journal of Applied Spectroscopy, 88 (2021)293–298.
9. **Kazak A.V. et al**. Plasma Medicine, 7,2 (2017)109-115.
10. **Stepanova, O.M. et al.** Tech. Phys. Lett. 44 (2018)841–843.
11. **Kazak A.V.et al.** Journal of Applied Spectroscopy, 91,3 (2024) 352-360.

ANTIMICROBIAL ACTIVITY OF AN ATMOSPHERIC PRESSURE GLOW DISCHARGE JET

Pashkova V.M.[1], Dudchik N.V.[2], Emelyanova O.A.[2], Simonchik L.V.[3], Kazak A.V.[3]

1. Faculty of Biology, Belarusian State University, 220030, Kurchatov St. 10, Minsk, Belarus, Email: post.varya@gmail.com
2. Research Institute of Hygiene, Toxicology, Epidemiology, Virology and Microbiology, State Institution "Republican Center for Hygiene, Epidemiology and Public Health", 220012, Akademicheskaya St. 8, Minsk, Belarus
3. B. I. Stepanov Institute of Physics, National Academy of Sciences of Belarus, 220072, Nezavisimosti ave 68-2, Minsk, Belarus,

The rapid emergence and spread of antibiotic-resistant bacteria pose a major threat to public health worldwide, challenging the effectiveness of conventional antimicrobial therapies and prompting the search for alternative strategies. Among the innovative approaches, non-thermal plasma technologies have attracted considerable attention due to their ability to inactivate a wide range of microorganisms through the generation of reactive oxygen and nitrogen species (RONS), ultraviolet radiation, and charged particles, without relying on chemical agents that can induce resistance [1]. Atmospheric pressure glow discharge (APGD) jets, in particular, offer a versatile and efficient platform for microbial inactivation, allowing localized treatment under ambient conditions [2]. While numerous studies have demonstrated the antimicrobial potential of APGD against standard laboratory strains, data on its effects against clinically relevant and wild-type pathogens remain limited.

In this study, we focus on two Gram-positive bacteria representing complementary experimental models: *Streptococcus pneumoniae*, a wild isolate associated with serious human infections such as pneumonia, meningitis, and sepsis, and *Staphylococcus aureus* (ATCC 25923), a well-characterized museum strain widely used as a reference in antimicrobial testing. This combination allows us to assess the plasma's efficacy in both real-world and controlled laboratory contexts, addressing the gap between experimental studies and clinical relevance. By quantifying the reduction in viable cell counts and exploring the potential mechanisms of plasma-induced microbial inactivation, we aim to evaluate the feasibility of APGD jets as a rapid, chemical-free approach for bacterial control. Ultimately, this work contributes to the broader effort of developing alternative antimicrobial strategies capable of overcoming the challenges posed by resistant pathogens, offering insights into practical applications in infection management, sterilization, and hygiene practices.

The main criterion for assessing antimicrobial potential is microbial survival rate, which is expressed as a percentage of the initial contamination and is calculated according to the formula:

$$I = \frac{N_t}{N_0} \text{ x } 100\ \% \qquad (1)$$

where I - survival rate in %;

N_0 - number of test strain cells before plasma exposure, CFU;

N_t - number of test strain cells after plasma exposure for t min, CFU.

In laboratory practice several methods are commonly used for assessing antimicrobial potential. One method is to apply low temperature plasma to a suspension of a test culture of a microorganism in a liquid medium. However, this method has limitations to the effectiveness of plasma exposure because plasma will mainly affect the surface layer of the bacterial suspension. In addition, water will screen the action of plasma, which affects the effectiveness of the procedure. The most adequate method of assessing antimicrobial potential is considered to be the exposure of a population of test microorganism models on the surface of agarose nutrient medium to plasma medium [3].

The experiments were carried out using the atmospheric pressure plasma jet generator **"ALOE"** (B.I. Stepanov Institute of Physics, NAS of Belarus) [4]. The device consists of a discharge chamber connected to a power supply and an air compressor, with a flexible hose containing a high-voltage electrode and air supply tube. A stable glow microdischarge is formed between two electrodes inside the chamber, while compressed air is continuously fed through the system, producing a directed plasma jet at the outlet. The operating parameters of the device can be adjusted via the control panel. The discharge current is selectable in the range of 30–40 mA, and the treatment time can be set from 1 to 20 minutes in 1-minute steps. In this study, the current was fixed at 30 mA with an air flow rate of 1.5 L/min and an outlet diameter of 4.0 mm., which was attached to the chamber to create a closed volume.

After exposure of the microorganisms to low-temperature plasma, clear evidence of antimicrobial activity was obtained for both tested strains. The reference strain *Staphylococcus aureus* (ATCC 25923) showed a gradual decline in viability during treatment. After 10 minutes of plasma exposure, the survival rate decreased to 8.2, which can be considered a satisfactory result for this organism (Figure 1). This demonstrates that *S. aureus* is susceptible to plasma treatment, although a longer exposure time is required to achieve pronounced antimicrobial effects compared to more sensitive pathogens.

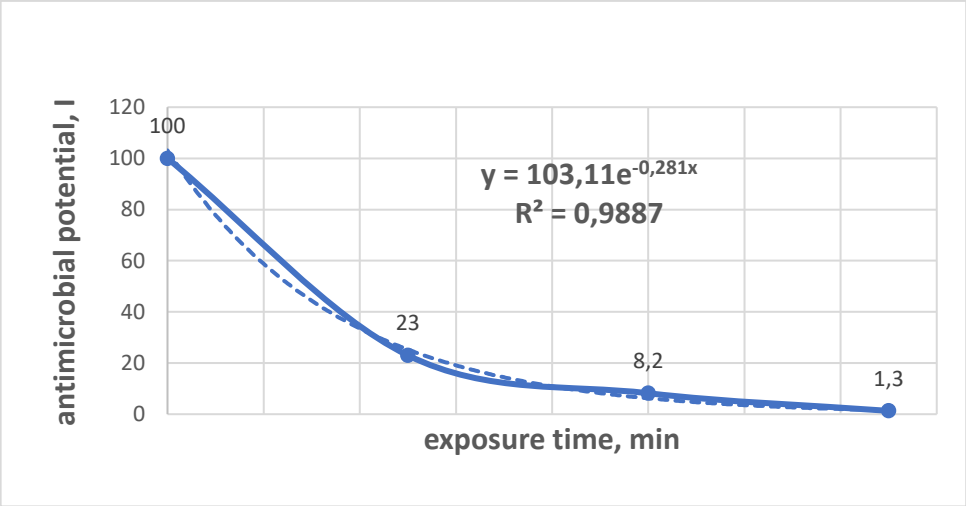

Figure 1 – Dependence of antimicrobial potential of plasma on time of exposure to *Staphylococcus aureus* population

The wild isolate *Streptococcus pneumoniae* exhibited a markedly different response. Already after 5 minutes of plasma treatment, the survival rate dropped to 0.3, indicating a near-complete inactivation of viable cells (Figure 2). This rapid reduction reflects the high sensitivity of pneumococci to plasma-generated reactive species and emphasizes the potential of low-temperature plasma as an effective tool against clinically relevant pathogens.

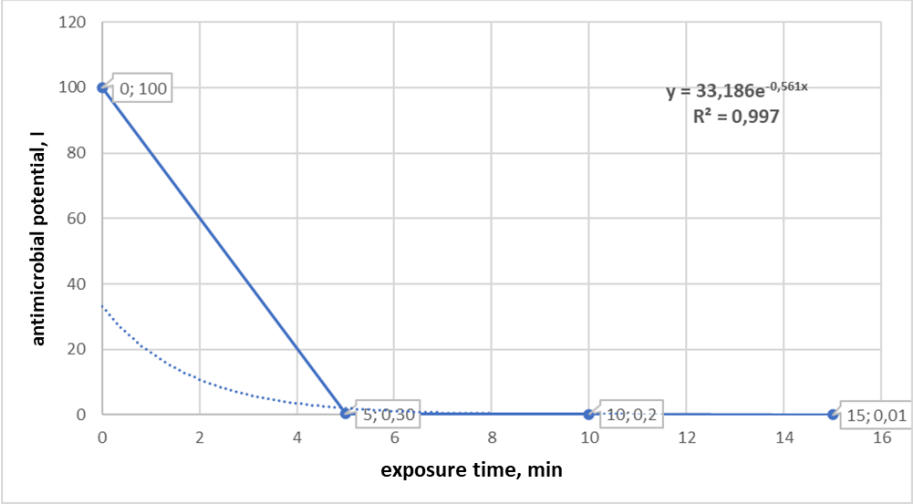

Figure 2 – Dependence of antimicrobial potential of plasma on time of exposure to *Streptococcus pneumoniae* population

A regular dependence of the efficiency of plasma exposure on the time of exposure to the population of test microorganisms *Staphylococcus aureus* and *Streptococcus pneumoniae* was obtained, which was described by an exponential

function. The high approximation coefficient allows one to conclude that the chosen mathematical model describes the obtained dependence with a high degree of reliability.

The results of the study clearly demonstrate the pronounced antimicrobial potential of low-temperature plasma against both reference and wild-type strains of pathogenic bacteria. The atmospheric pressure glow discharge jet effectively reduced the generation of the typical museum strain *Staphylococcus aureus*, as well as the wild isolate *Streptococcus pneumoniae*, with rapid and reproducible inactivation observed under the chosen experimental conditions. The fact that plasma treatment was effective against a standardized laboratory model and against a clinically relevant natural isolate as well highlights its broad applicability and robustness. These findings confirm that low-temperature plasma represents a powerful, universal, and non-chemical antimicrobial approach with potential for implementation in medical, sanitary, hygiene and biotechnological practice.

References

1. **Kazak A.V. et al.** Plasma Medicine, 7,2 (2017)109-115.
2. **Kazak, A.V. et al.** Journal of Applied Spectroscopy, 88 (2021)293–298.
3. **M.Y. Alkawareek et al.,** Int. J. Antimicrob. Agents 43,2 (2014) 154–160.
4. **A.V. Kazak, L.V. Simonchik,** Pribory i Metody Izmerenii 15,3 (2013) 186–194.

PLASMACHEMICAL SYNTHESIS OF MICRO- AND NANO-SIZED MATERIALS IN CHAIN REACTIONS INITIATED BY MICROWAVE PULSES OF THE POWERFUL GYROTRON IN POWDERS

N.N. Skvortsova[1], N.S. Akhmadullina[1,2], V.D. Borzosekov[1], N.G. Gusein-zade[1], E.M. Konchekov[1], D.V. Malakhov[1], E.A. Obraztsova[3], V.D. Stepakhin[1], N.K. Kharchev[1], O.N. Shishilov[1,4]

[1]Prokhorov General Physics Institute of the Russian Academy of Sciences, Moscow 119991, Russia, Vavilova st. 38, mukudori@mail.ru
[2]A.A. Baikov Institute of Metallurgy and Material Science of Russian Academy of Sciences, Moscow, 119991, Russia, Leninsky avenue 49, nakhmadullina@mail.ru
[3]Moscow Institute of Physics and Technology, Dolgoprudny, Moscow Region, 141700, Russia, Institutsky Per. 9, brenka@mail.ru
[4]MIREA – Russian Technological University, Institute of Fine Chemical Technologies, Moscow, Russia, Vernadskogo pr., 86, oshishilov@gmail.com

1. Introduction

Ceramic materials are widely used in modern technology and have attracted significant research attention due to their unique mechanical and physical properties /1,2/. Various discharge types, such as spark, arc, glow, high-frequency and other discharges have been employed in the synthesis of micro- and nanostructured ceramic materials. Many challenges in modern materials science related to the synthesis of such materials can be addressed using plasma-chemical microwave methods. However, gyrotrons, being one of the most powerful sources of microwave discharges, have long remained underutilized in these applications. Their use has primarily been limited to high-density ceramics sintering /3/. While existing review publications often focus on the synthesis of specific materials via different methods (see, e.g., /4,5/), a more promising approach for chemical technology is the synthesis of materials with varied composition within a single process type. The discovery of such processes is rare and typically well-documented, often pioneered by renowned scientists. Two notable examples are self-propagating high-temperature synthesis /6/ and chain reactions, discovered in the 20th century /7/.

The method described in this report - plasma-chemical synthesis of micro- and nanosized substances initiated in powder mixtures by powerful gyrotron radiation - can be viewed as an advancement of such processes for plasma-microwave /8,9/.

A plasma-chemical setup based on a gyrotron from the L-2M/MIG-3 stellarator thermonuclear complex was developed at the General Physics Institute of the Russian Academy of Sciences /10/. This setup demonstrated that, under specific conditions in the reactor, gyrotron pulses can initiate chain

reactions in mixtures of metal and dielectric powders, leading to the synthesis of microdispersed materials with controlled physicochemical properties. Experimental results confirmed the successful synthesis of materials suitable for micro- and nanostructured ceramics. The resulting materials exhibit properties with broad applicability, ranging from structured surface coatings /11,12/ to novel heterogeneous catalysts and luminescent materials /13,14/.

2. Experimental setup.

The experiments were carried out on a setup using a powerful pulsed gyrotron (power up to 0.8 MW, pulse duration up to 12 ms, frequency 75 GHz). The description of the experiment and different diagnostics (spectral, video, microwave) are described in detail in /10/. Powder mixtures that were used in experiments include metals (Al, Pt, Pd, Ti, Ag, Mg, est.), inorganic dielectrics (B, Al_2O_3, AlN, BN-cub, BN-hex, SiO_2, TiO_2, SiAlO, Al_5O_6N, est.), organic dielectrics ($Eu(acac)_3$, $Ce(acac)_3$, melamine) and catalytic additives ($C_2B_{10}H_{12}$, $NaBH_4$, H_3BO_3) in different proportions. The conditions of microwave breakdown of powder mixtures and chain plasma-chemical processes in the reactor are studied separately for each powder mixture used.

3. Plasma-chemical chain reaction

Plasma chemical chain reaction initiated by gyrotron radiation in mixtures of powders includes three stages of the classical chain process: initiation, development andtermination . The process is initiated by absorption of 1–3 kJ of microwave energy in a mixture of precursor powders in accordance with /15/. The synthesis time reaches several seconds and exceeds the microwave pulse length by 3–4 orders of magnitude. A generalized scheme of the plasma-chemical process initiated by a microwave pulse of a gyrotron in a mixture of metal and dielectric powders is shown in Table 1 /16/.

Table 1. Plasma chemical process main stages

Initiation Stage			Main Stage		Decay Stage	
MW Pulse	MW Absorption	Coulombic Expansion	Decomposition of Starting Materials	Oxidative Transformation	Irreversible Cooling	Deceleration of the Reactions
Dust particles, atoms, ions are formed in the reactor zone			Ensembles of charged particles, self-sustaining oscillating process		Condensation from the gas phase, deposition of the particles	

Under the conditions of our experiment, the first stage of the chain reaction is accompanied by the expansion of charged particles according to the Coulomb mechanism from the surface of the powder mixture into the reactor volume. These particles serve as additional centers of condensation of synthesized

secondary materials. The addition of catalysts to the mixture of powders makes it possible to lengthen the second stage of the chain process and transfer the reactions to a self-oscillatory mode /9/.

Optimization of all three stages of the chain process was carried out to increase the yield of synthesized substances. Currently, it is possible to obtain 10-100 grams of the final product in the experimental reactor. This allows us to study additional characteristics of the obtained and deposited materials: selectivity of heterogeneous catalysts, cathode and photoluminescence of luminescent materials, efficiency in depositing powders on solar panels, etc.

4. Examples of synthesized substances

To date, the synthesis of materials has been carried out in many experiments for various applied problems. In this report we will mainly focus on two tasks.

1. The synthesis of heterogeneous catalysts in the form of micro-particles from various dielectrics with nanoparticles of platinum, palladium, copper, silver, etc. deposited on them (Fig. 1 and 2) /17/. With the examples of their use in the reactions of methylcyclohexane dehydrogenation and olefin oxidation.

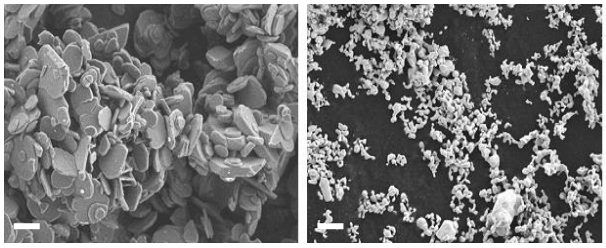

Fig. 1. Initial powders Al_2O_3 and Ag. Scale 10 μm.
SEM image of the initial aluminum oxide powder (left); SEM image of the silver powder (right).

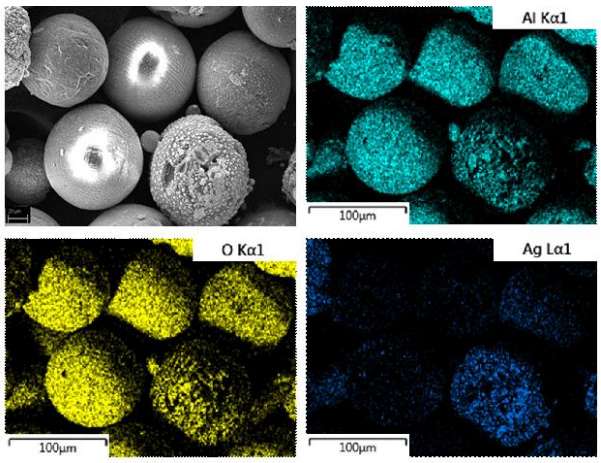

Fig. 2. SEM image and elemental mapping analysis for the particles after the treatment of Al_2O_3 + 5 w/w % Ag mixture.

2. The synthesis of oxide, nitride and oxonitride ceramic materials with the introduction of doping additives (rare earth metals) to impart luminescent properties in Al/Al_2O_3/melamine mixtures with the addition of europium acetylacetonates ($Eu(acac)_3$) and cerium ($Ce(acac)_3$). Intense bands are observed in the cathodoluminescence emission spectra (Fig. 3) /14/.

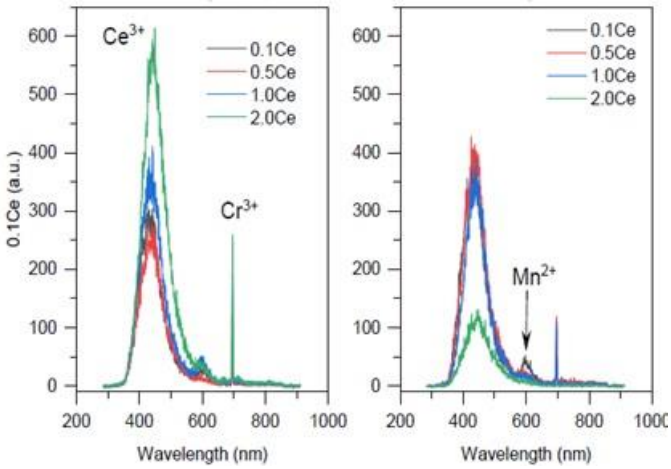

Fig/ 3. Cathodoluminescence emission spectra of materials syntheses in the mixtures Al/Al_2O_3/melamine/$Ce(acac)_3$ (left – 1:2:1, right – 2:2:1), poured on top of the powder AlN.

Acknowledgements. This work was supported by the Ministry of Science and Higher Education of the Russian Federation (State Assignment GZ BV10-2025) in the framework of the Federal project "Development of Fusion Technologies and Innovative Plasma Technologies".

References

1. **Bajraktarova-Valjakova E.** et al. J. Med. Sci. 6 (2018) 1742–1755**.**
2. **Kargin Yu.F.,** et al. Inorg. Mater. 50 (2014) 1325–1342.
3. **Bykov Y.V.,** et al. J. Phys. D: Appl. Phys. 34 (2001) R55–R75.
4. **Hosmane N. S.** Boron Science: New Technologies and Applications. CRC Press, Boca Raton, Florida (2012)
5. **Ivanovskii A. L.** Russ. Chem. Rev. 71(3) (2002) 175–194.
6. **Tavadze G. F. and Shteinberg A. S.** Production of Advanced Materials by Methods of Self-Propagating High-Temperature Synthesis, Springer, (2013).
7. **Semyonov N.N.** Physics-Uspekhi (Adv. in Phys. Sc.) 11 (1931) 250–275.
8. **Akhmadullina N.S.** et al. Chemical Physics 516 (2019) 63-70.
9. **Skvortsova N.N.** et. al. Ceramics International 47(3) (2021) 3978–3987.
10. **Sokolov A.S.** et.al. Radiophys. Quantum Electron. 65 (2023) 840–854.
11. **Skvortsova N. N.** et al. RF Patent No. 2727958 (July 28, 2020).
12. **Skvortsova N.N.** et al. Plasma Physics Reports 49(1) (2023) 120–128.
13. **Gusein-zade N.G.** et al. RF Patent No. 2772704 (May 24, 2022).
14. **Shishilov O.N.** et al. RF Patent No. 2826861 (May 30, 2024).
15. **G. M. Batanov**, et al., J. Nanophotonics 10 (2016). 012520.
16. **Skvortsova N.N.** et al. Fusion Science and Technology (2023) 882-892.
17. **Skvortsova N.N.** et al. Int. J. Mol. Sci. 25 (2024) 5326.

SUPPORT OF THE EXPERIMENT IN THE LABORATORY OF PLASMA AERODYNAMICS USING NUMERICAL MODELING: GAS DYNAMICS, COMBUSTION, ELECTRICAL DISCHARGES

A. Firsov

Joint Institute for High Temperatures of the Russian Academy of Sciences,
Moscow, Russia, firsov@jiht.ru

When researchers mention plasma aerodynamics, they usually associate it with the dielectric barrier discharge (DBD), which can create a directed low-speed gas jet (ion wind) and prevent the flow separation near wing at some conditions. Various geometric configurations of plasma actuators based on DBD are known, and recently there has been growing interest in extremely fast actuators based on nanosecond discharge. Other types of discharges, such as spark discharge, arc or DC discharge, are mentioned less frequently. The latter make a significant energy release to the flow, and therefore, in terms of the type of impact and the type of problems solved, are somewhat on the sidelines, more often mentioned in conjunction with the intensification of mixing or combustion in a supersonic flow.

On the other hand, it is this feature, when the main contribution from the discharge is realized in the form of volumetric heat release, that allowed us to start using numerical modeling more than 10 years ago in addition to the experiments performed in our laboratory. Calculations are performed using the industrial CFD software FlowVision 3.14, which allows modeling supersonic flows, shock waves, taking into account external sources of heat and combustion. Automatic grid generation with the ability to automatically adapt to the solution (e.g. density gradients or high temperature regions) allowed the use of 1-2 million cells and perform calculations on modern desktop multi-core computers.

1. Spark discharge

The studies of an extended (length much greater than diameter) spark (or pulse) discharge were motivated by interest in new methods of organizing the mixing of fuel with a supersonic air flow. The discharge was created by organizing an overvoltage of 100 kV over a gap of ~50 mm, the energy in the pulse was 1-3 J. The typical diameter of the discharge channel before its expansion was ~0.6 mm. After the discharge, an intense shock wave departed from the breakdown site, and later the decay of the thermal cavern was observed, which had a strongly disturbed turbulent structure. It was also shown that if a significant curvature of the discharge channel was created using an additional electrode, then a jet flow movement was observed inside the formed angle.

In order to clarify the nature of the turbulent structure and the resulting jet flow, additional experiments were performed in several configurations, and numerical modeling of the thermal chamber disintegration after rapid pulsed heating was carried out /1/. The modeling results had good qualitative agreement with the experimental results. From the modeling results, it became clear that the converging shock waves from parts of the discharge interact with each other and are amplified. Behind this region, a low-pressure zone is formed, into which part of the hot gas rushes and a jet flow is formed with a speed of more than 100 m/s (Fig. 1). It was also found that the cold gas from the electrodes is drawn into the thermal cavern, further disturbing it. Later, the conclusions made were confirmed experimentally using an 8-frame camera with 8 matrices with the ability to set any, including very small (severtal ns) delay between frames. It has been shown that even small bends lead to the formation of jet flows, and with a smoother channel, the drawing in of cold gas from the electrodes is clearly visible (Fig. 2) /2/.

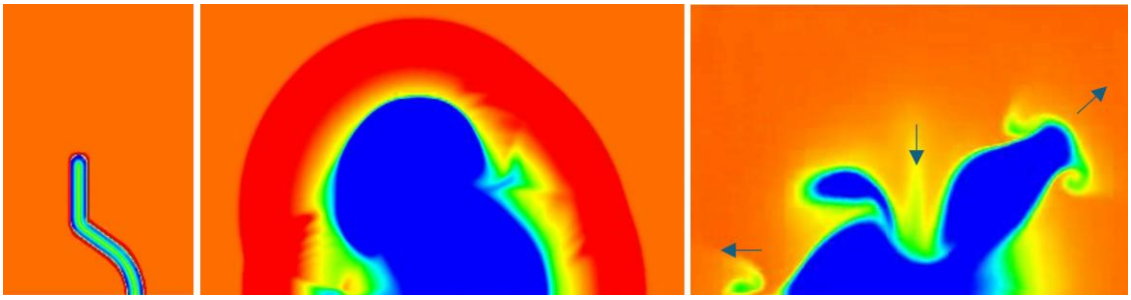

Fig.1. CFD simulation of thermal cavity decay, density field (0.1 μs, 15 μs, 140 μs)

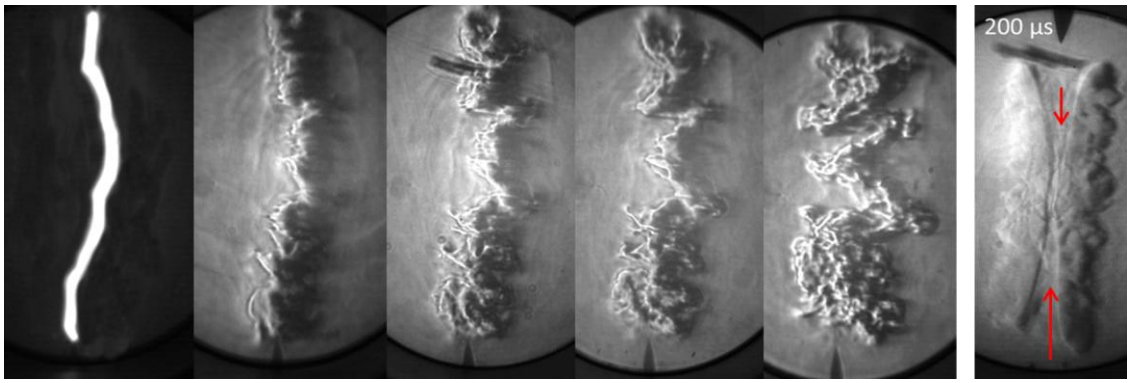

Fig. 2. Jet instabilities formation by the bends of the discharge filament and superposition of small disturbances with jets (delay after discharge 0 μs, 50 μs, 100 μs, 150 μs, 350 μs), and suction of cold gas into the thermal cavity for smooth discharge (200 μs)

In the first experiments, the pulsed discharge for ming was ignited across the flow and had a length equal to the channel height. However, a supersonic flow does not allow organizing a fuel jet across the entire cross-section; the jet is very quickly deflected and carried away by the flow. Therefore, a new approach to intensifying the mixing of fuel with a supersonic flow was implemented. It

was decided to place a shorter discharge (<15 mm) near the channel wall in the wake of the fuel jet supplied through a ⌀ 4 mm hole in the wall perpendicular to the flow /3/, and later, instead of placing it in the wake of the jet, a short discharge of ~3 mm in length was installed directly in front of the jet. This formulation of the problem made it possible to avoid the limitation on the jet flow rate observed for the previous geometry: at high flow rates, the jet broke away from the wall, and the discharge ended up outside the jet. In the new geometry, the shock wave from the discharge and the decay of the thermal cavern affects the separation zone in front of the jet and directly the jet at any gas flow rate of the jet. Numerical modeling of the discharge effect on the jet was performed for a wide frequency range of 10-60 kHz, as well as modeling of the jet without a discharge for the Jet-to-crossflow momentum flux ratio of 0.7, 1.0 and 1.3. It was found that the frequency of natural oscillations of the jet is ~40 kHz, and it is at this frequency of discharge operation that the best intensification of mixing of the jet with the oncoming flow is observed - an improvement of up to 20%. Due to technical limitations, the experimental study was carried out for a discharge with an operating frequency of no more than 10 kHz. However, as modeling showed, for some jet flow rates, for example for J = 0.7, the discharge operation at this frequency led to an effect that was slightly different from operation at a frequency of 40 kHz.

2. DC discharge

Fundamental studies of DC discharge in a supersonic flow began many years ago and are still ongoing, as new high-speed diagnostic and visualization methods appear. For example, to visualize the dynamics of a DC discharge in a supersonic flow, a video recording speed of more than 120,000 fps is required. In recent studies, the current-voltage characteristic of the discharge, the dependence of temperature on current were refined, and a direct comparison of modeling with experiment was carried out for a special longitudinal configuration /4/, excluding the influence of such factors as breakdown and boundary layer. It is important to note that in this case the discharge was modeled using an MHD model, and not as a volumetric heat source. At the same time, for a longitudinal-transverse discharge, which is more familiar in applied applications, the dependences of its properties on the interelectrode distance and discharge current were determined /5/.

One of our most popular works on supersonic flow control using a DC discharge is flow control in an air intake (Fig.3) /6/. A ceramic plate with electrodes was installed in the air intake in front of the compression surface to form 5 loops of a longitudinal-transverse discharge. For a flight Mach number exceeding the calculated Mach number for a given air intake, switching on the discharge led to a change in the flow profile around the compression surface, to an improvement in the shock wave configuration and a decrease in total pressure

losses. This work was accompanied by numerical modeling throughout – from experiments in an attached curved air duct simulating the compression surface to an experiment with an air intake model in a wind tunnel. Modeling was also used to assess the reproducibility of the effect for a model enlarged twice.

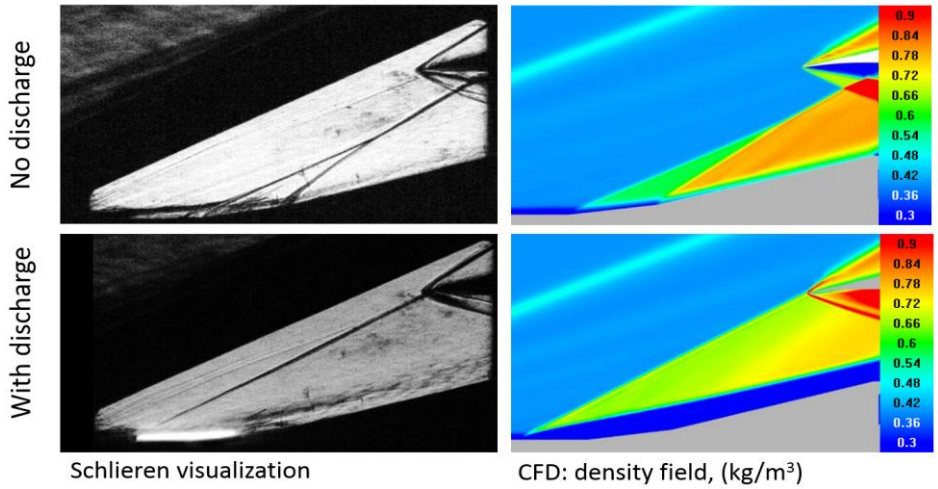

Fig 3. CFD result for longitudinal discharge at 3 A current: temperature distributions (top), density (bottom) and current density (bottom, in dashed contour); and fast visualization of longitudinal-transverse discharge in the experiment (right)

Acknowledgements. This review was supported by the Ministry of Science and Higher Education of the Russian Federation (State Assignment).

References

1. **Firsov AA, Shurupov MA, Yarantsev DA, Leonov SB, Shneider MN** Mixing actuation by unstable filamentary discharge. AIAA 2013-1188
2. **Firsov AA, Dolgov EV, Shurupov MA, Leonov SB** Mixing enhancement by electrical discharge in supersonic airflow. AIAA 2018-1195
3. **Dolgov E V., Kolosov NS, Firsov AA** (2019) The study of the discharge influence on mixing of gaseous fuel jet with the supersonic air flow. Computer Research and Modeling 11:849–860.
4. **Firsov A, Bityurin V, Tarasov D, Dobrovolskaya A, Troshkin R, Bocharov A** (2022) Longitudinal DC Discharge in a Supersonic Flow: Numerical Simulation and Experiment. Energies (Basel) 15:7015.
5. **Perevoshchikov EE, Firsov AA** (2023) Influence of current and interelectrode gap on characteristics of longitudinal-transverse discharge in a supersonic airflow. Plasma Physics Reports 49:634.
6. **Falempin F, Firsov AA, Yarantsev DA, Goldfeld MA, Timofeev K, Leonov SB** (2015) Plasma control of shock wave configuration in off-design mode of M = 2 inlet. Exp Fluids 56:54.

AMMONIA CONVERSION IN THE PLASMACHEMICAL REACTOR WITH A NON-SELF-SUSTAINED DC GLOW DISCHARGE AT ATMOSPHERIC PRESSURE

A.V. Kazak, A.A. Kirillov, L.V. Simonchik, M.U. Tomkavich

B.I. Stepanov Institute of Physics of NAS of Belarus,
Ave. Nezavisimosti 68-2, 220072 Minsk, Belarus, Email: m.tomkavich@ifanbel.bas-net.by

1. Introduction

Hydrogen is an efficient and clean alternative for energy produce to fossil fuels, which have a high carbon ecological footprint. However, there are a number of problems with using hydrogen as a fuel, including its storage and transportation, as well as its explosiveness /1/. Hydrogen has a very high energy density by mass, but it has a very low energy density by volume. In this regard, there is a temptation to store H_2 in the form of a hydrogen-containing compound, which is easily transported, and hydrogen is formed on site of usage as a result of a chemical reaction /2/. One of the promising compounds for this is ammonia /3, 4/. Ammonia has a high hydrogen content and can be liquefied at low pressure around 10 atm, so its transportation and storage are relatively simple /5/.

2. Experimental setup

The design of the plasma-chemical reactor is based on a three-electrode system developed in /6/ for generating stable large volume gas discharges. This three-electrode system was previously used by us for the conversion of ethanol-water mixture /7/ and biogas /8/. The photo and the schematic of the plasma-chemical reactor are shown in Fig. 1, a and b, correspondingly. The reactor consists of a two-section discharge chamber A and B (Fig.1, b).

a b

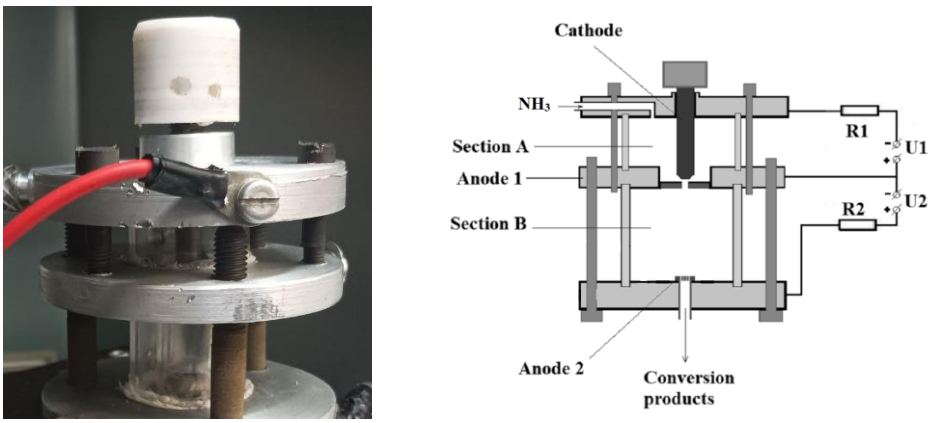

Fig. 1. Photo (a) and schematic (b) of the plasma–chemical reactor

The segments of cylindrical quartz tubes form sections of the chamber. In section A there is a cathode (a steel rod with a diameter of 8 mm). A 1 mm thick brass

insert in a duralumin disk 1 acts as the anode. The interelectrode gap is 1-2 mm. A flow of ammonia is provided through section A. Ammonia flows out from section A through a hole (diameter 2 mm) in the center of the brass plate into the section B.

In section A, a self-sustained normal Atmospheric Pressure Glow Discharge (APGD) is ignited by the power supply U1 (1500 V, R1 ~5 kΩ). This discharge serves as a plasma cathode for a non-self-sustained discharge in section B, which feeds from another DC power supply U2 (3000 V, R2 ~ 10 kΩ). Its voltage is applied between anode 1 and anode 2. The interelectrode gap in section B is fixed at ~16 mm. The discharge current of the non-self-sustained discharge is ~200 mA. The conversion products are removed from the plasma reactor through a hole in the center of anode 2 (Fig. 1b) and taken away by a curved tube for analyzing or burning in the form of a free flame (Fig. 2).

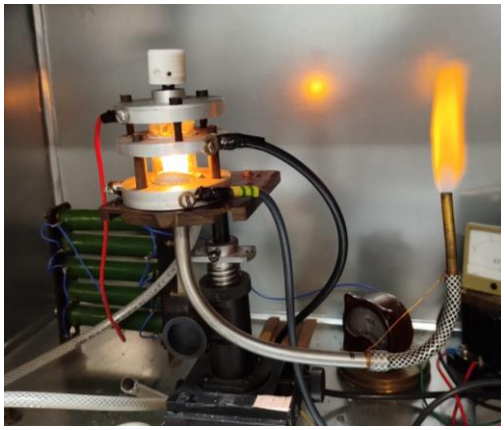

Fig. 2. Photo of operating reactor

3. Experimental results

The temperature of the gas of the non-self-sustaining APGD was determined by the vibrational-rotational (0,2) N_2 ($C^3\Pi_u$ – $B^3\Pi_g$) (λ = 380,49 nm) band of the second positive electron transition system of the neutral nitrogen molecule. The choice of this band was due to the fact that it is quite intense and free from the overlap of other spectral lines and bands. An example of an experimental spectrum of a rotational band is shown in Fig. 3, a (points). The spectrum calculation was carried out using the SpecAir 3.0 program /9/. We assume that the

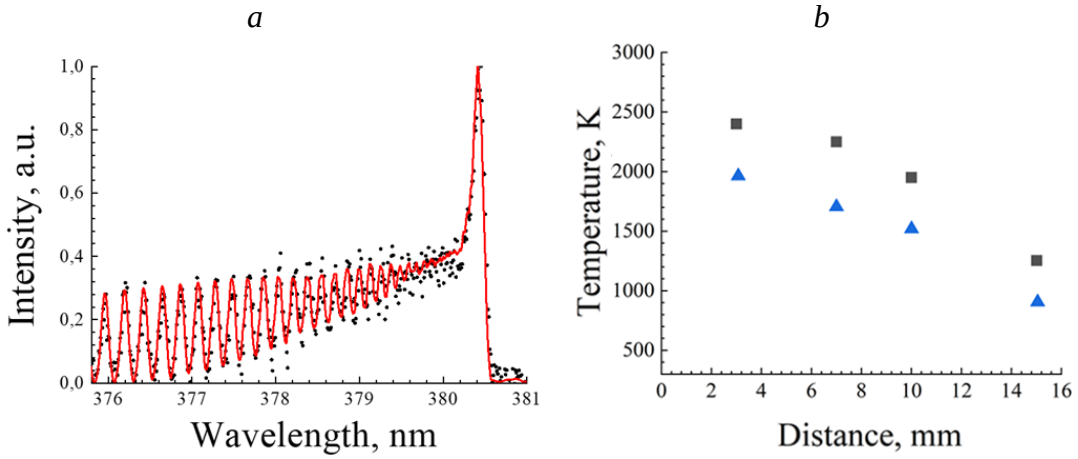

Fig. 3. Experimental and calculated spectra of second positive system of nitrogen (a) and axial gas temperature profiles for ammonia flow of 1l/min (squares) and 4 l/min (triangles)

rotational temperature corresponds to the temperature of the gas. The computational spectrum is represented in the same figure by a solid line.

Axial temperature distributions in the positive column of non-self-sustaining APGD at ammonia flow rates of 1 l/min (squares) and 4 l/min (triangles) are shown in Fig. 3 (b). Zero in this figure corresponds to the anode 1 surface. As can be seen, the gas temperature of 2000-2400 K is maximum at the surface of anode 1 and drops slightly towards anode 2 for both flows. The temperature difference for these flows is ~400 K at the surface of anode 1 and decreases to ~200 K at the surface of anode 2.

The composition of the conversion products of the ammonia at the outlet of the plasma–chemical reactor was observed by a diagnostic method based on absorption infrared (IR) spectroscopy, similarly to that used in /8/. In this experiment, a NEXUS (Thermo Nicolet, USA) IR spectrometer was used. The absorption spectra were recorded in the range of wavenumber 400–4000 cm^{-1} with a resolution of 2 cm^{-1}. A triangular apodization function was chosen, resulting in the diffractive contours of lines. For the spectroscopic analysis, exhaust gases from the plasma–chemical reactor were passed through a 5-cm cuvette with germanium windows.

First, the IR spectrum of an ammonia at the outlet of the reactor without discharges was recorded. It is shown in the Fig. 4 (a). Here we see three vibrational–rotational bands for NH_3 (500–1250, 1400–2000, and 3100-3600 cm^{-1}). The absorption spectra of the gas mixture at the outlet of the reactor is shown in the Fig. 4(b). It can be seen that the intensity of the ammonia bands in the IR spectrum has significantly decreased as a result of conversion. This indicates the progress of the conversion process and its high efficiency.

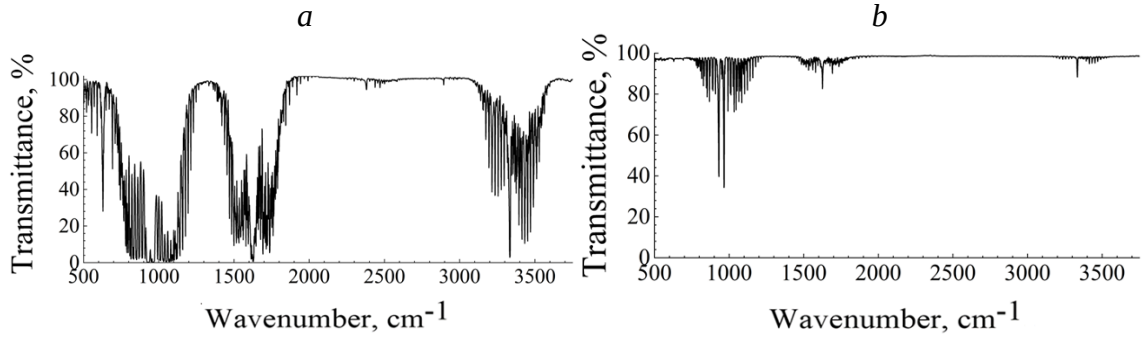

Fig. 4. Absorption spectra of ammonia (a) and ammonia conversion products (b)

The mole fractions of the IR active components of the ammonia and its conversion products were determined by comparing the experimental absorption spectra with those calculated using the HITRAN spectral database /10/. The mole fractions of ammonia were determined in the band of 3100-3600 cm^{-1}. Fig. 5 shows the experimental and calculated spectra of the band. The dots represent the

experimental spectrum, the line represents the calculated spectrum.

Table 1 shows conversion data for ammonia at four total flow rates of 4 l/min, 2 l/min, 1 l/min and 0.5 l/min. Analyzing the data in Table 1, we can conclude that with a decrease in ammonia flow from 4 l/min to 0.5 l/min, the amount of H_2 and N_2 increases, while the amount of NH_3 decreases.

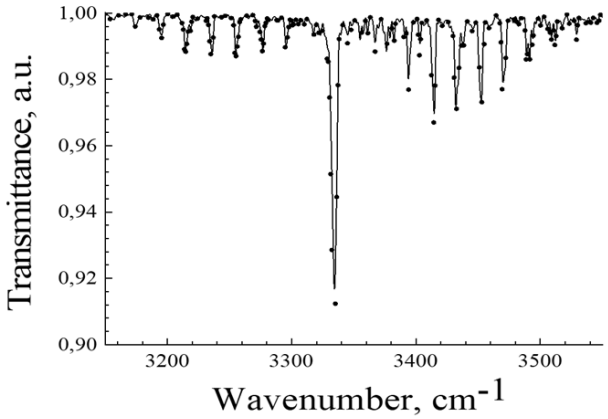

Fig. 5. Experimental (points) and calculated (line) spectra of ammonia conversion products

The conversion degrees of NH_3 are important characteristics of the conversion process, which can be defined as follows:

$$\eta(\mathrm{NH_3}) = \frac{\{\mathrm{NH_3}\}_{in} - \{\mathrm{NH_3}\}_{out}}{\{\mathrm{NH_3}\}_{in}} 100\%,$$

where $\{NH_3\}_{in}$ and $\{NH_3\}_{out}$ denote the number of molecules of the NH_3 at the input and output of the reactor, respectively.

Table 1 Conversion data of ammonia

Flow $(NH_3)_{in}$, l/min	0.5		1			2			4		
Discharge power, W	200	350	200	350	480	200	350	480	200	350	480
Conversion degrees, %	98	99	60	88	93	45	66	68	20	33	40

As a result, the degrees of conversion of NH_3 increase from ~20% to ~99%. The reasons for this increase in the productivity/conversion rate appear to be higher gas temperature and longer residence time of the reaction mixture in the reactor core at the lower flow rate.

References

1. **Abdalla [et al]** Energy Conversion and Management, **165** (2018) 602 – 627.
2. **Jensen [et al]** Journal of Alloys and Compounds., **446–447** (2007) 723–728.
3. **Chang, F. [et al]** Advanced Materials, **33** (2021) 2005721.
4. **Spatolisano, E. [et al]** Ind. Eng. Chem. Res., **62, 28** (2023) 10813–10827.
5. **Ojelade, O.A. [et al]** Chem. Papers, **75** (2021) 57–65.
6. **Arkhipenko [et al]** IEEE Trans. Plasma Sci., **37, 6** (2009) 740-749.
7. **Arkhipenko [et al]** Int. J. Hydrogen Energy, **41,41** (2016) 18320-18328.
8. **Arkhipenko [et al]** High Temp. Mat. Proc., **26, 4** (2022) 17–23.
9. http://www.specair-radiation.net/
10. https://lweb.cfa.harvard.edu/HITRAN/

COPPER–IRON ALLOY CONTACTS IN HIGH CURRENT PROTECTION DEVICES

M.E. Pinchuk, A.A. Bogomaz, V.A. Kolikov,
I.V. Bagriy, I.Yu. Pervashov, A.V. Budin

Institute for Electrophysics and Electric Power of Russian Academy of Sciences,
Dvortsovaya nab., 18, St.-Petersburg, 191186, Russia, pinchme@mail.ru

In electric power transmission networks, specialized switching and protective systems are responsible for ensuring reliable operation. During the process of breaking a circuit in the power switches or protective devises, electric arcs form between the electrodes or parting contacts. A huge energy flow on the contact surface in the area of an arc attachment causes erosion wear, while interacting with heated gas flows in the switching and lightning protection devices /1/.

One of the most effective components of lightning protection systems is the multi-chamber arrester, which consists of a series of two-electrode discharge chambers connected and mounted in a silicone rubber profile /2/. In the electrode system of a multi-chamber arrester, the quenching efficiency improves with current force-driven instabilities developing, leading to the acceleration of the arc channel and its movement away from the discharge chamber towards the outside. The optimal geometry of the discharge chamber and the electrode system in the arrester should be such as to provoke the development of force instability, leading to a more intense initial acceleration of the arc channel. Further when an arc passes through the chamber, the inner chamber walls and electrode materials are involved in the discharge zone, what accelerates the dissociation of an arc plasma. But an erosion of the electrode significantly affects the speed of the discharge channel, because the electrode material increases the density of the plasma channel /3/.

Composite electrode materials can provide the desired electrode properties due to the heterogeneity of their composition and the additive set of properties that are introduced into the material by the corresponding phase components /4/. Copper-based composite pseudoalloys, combining high electrical conductivity and erosion resistance, offer promising solutions. This material results in a lower additional average molecular weight relative to pure copper in the discharge plasma.

The emergence of a new type of layer-by-layer laser sintering for the production of such composite materials makes it possible to customize material design for targeted applications even more flexibly. But using a new production technology requires making sure of the advantages of the material compared to the same material produced using traditional powder metallurgy technologies.

This was the main motivation of this work. The erosion on operational conditions of fixed electrodes, opening contacts, with transverse and longitudinal gas blowing, and in puffer breaker geometry were investigated, see some previous results in /5–8/.

Electric erosion of the laser sintering material CuFe (85/15%) were compared with the erosion of CuW (25/75%) and CuFe (70/30%) produced by the traditional powder metallurgy methods. The erosion of the electrodes was measured for arcs in the range of current amplitudes up to 150 kA at an air and nitrogen pressure from 20 Pa to 2 MPa with different gas-puff systems and contact opening scheme. Research results indicates that CuFe (85/15%) electrodes produced via laser sintering achieve specific erosion rates of ~1 mg/C, comparable to powder metallurgy counterparts.

References

1. **Slade P. G.** Electrical Contacts: Principles and Applications. 2nd ed. CRC Press, (2017).
2. **Podporkin G. V., Enkin E. Y., Kalakutsky E. S., Pilshikov V. E., and Sivaev A. D.**, IEEE Trans. Power Delivery 26, 214 (2011).
3. **Bobashev S. V., Zhukov B. G., Kurakin R. O., Ponyaev S. A., and Reznikov B. I.**, Tech. Phys. Lett. 41, 964 (2015).
4. **Lebedev A. D. and Malevinskij K. V.** In Proceedings of the I All-Union Workshop on the Dynamics of High-Current Arc Discharges in a Magnetic Field, Novosibirsk: KIT SB RAS, 160–194 (1990).
5. **Budin A. V., Pinchuk M. E., Kuznetsov V. E., and Rutberg F. G.** Tech. Phys. Lett. 40, (2014).
6. **Pinchuk M. E., Budin A. V., Kumkova I. I., and Chusov A. N.**, Tech. Phys. Lett. 42, 395 (2016).
7. **Budin A. V., Pinchuk M. E., and Kurakina N. K.** Tech. Phys. Lett. 44, 808 (2018).
8. **Pinchuk M. E., Budin A. V., Kurakina N. K., and Leks A. G.**, PPT 6, 227 (2019).

TOWARDS IMPLEMENTING ATMOSPHERIC PRESSURE PLASMA JET FOR PAPER DOCUMENT RESTORATION

M.E. Pinchuk[1], E.A. Tileva[2], O.M. Stepanova[1],
I.V. Tseveleva[2], D.G. Grudkin[1], V.N. Snetov[1]

[1]Institute for Electrophysics and Electric Power of RAS, 18, Dvortsovaya nab., St. Petersburg, 191186, Russia, pinchme@mail.ru
[2]Library, Russian Academy of Sciences, St. Petersburg, 199034, Russia

Most historical documents are saved on paper and exposed to biological, organic, and inorganic contamination. The critical unresolved issue lies in safely eliminating such contaminants without damaging the documents. This makes the study of advanced cleaning techniques an urgent research priority. The scientific challenge of developing a novel, efficient, and safe method for removing contaminants from paper-based documents during their recovery or restoration is under consideration.

During the natural aging process, the molecular chains of paper polymers become shorter, causing the material to lose its strength /1/. When the cellulose polymer chain breaks, acids are released, leading to further autocatalytic destruction of the cellulose. This process can cause oxidation, discoloration, and discoloration of various dyes on the documents. The impurities that accumulate during the life of a document, such as stains, pencil marks, ink marks, finger grease, dust, and other contaminants, accelerate the destructive processes in paper, leading to an accelerated decline in its mechanical strength. In high humidity conditions and with poor air circulation, paper is at risk of mold growth. Paper can also serve as a substrate for bacterial and fungal biofilms /2/, causing biological damage that results in the destruction and discoloration of paper due to the activity of microorganisms, especially mold fungi. Most of this damage and contamination are localized. But even with local damage, mold fungi can penetrate paper to the entire thickness of the sheet, forming localized, through-colored spots (foxing). At the same time, mold fungi and some bacteria have an extraordinary ability to survive in harsh conditions, even in outer space /3/, which makes it challenging to remove them.

Currently, generally accepted practices of restoration, conservation, and renewal of documents have been formed. Traditional processing methods for restoring a paper document are quite laborious, as a rule, they are associated with wet chemistry, affecting the entire document in the process /4/. In some cases, a stationery eraser and household sponges are used to solve the problem, but for particularly valuable documents it is more important to develop non-contact gentle methods for removing local contamination. There are no such standards for general practice. Continuous work is being carried out to improve

the methods /5/. But, in most cases, when processing documents on canvas, paper and similar media, wet chemistry or contact processing techniques are still preferred.

There are several examples of using nonequilibrium low-temperature plasma to restore art objects /6/. For example, a lipstick stain on a painting "Bathtub" (Andy Warhol, 1961) was removed after it was damaged at an exhibition by processing with RF discharges in a rarefied oxygen atmosphere /7,8/. The issue of resistance of the ink layer, ink of the image, and the base paper to the action of discharges during the removal of impurities under certain processing conditions was considered satisfactory /9,10/.

We conducted preliminary tests to investigate the fungistatic effect of dielectric barrier discharge products in air on filter paper samples contaminated with a suspension of mold fungi /11/. Several tests were also performed to remove model contamination of an office paper by ball pen using an argon atmospheric pressure jet. One example of the testing process and a ball pen ink trace before and after 10 minutes treatment is shown in Figure 1.

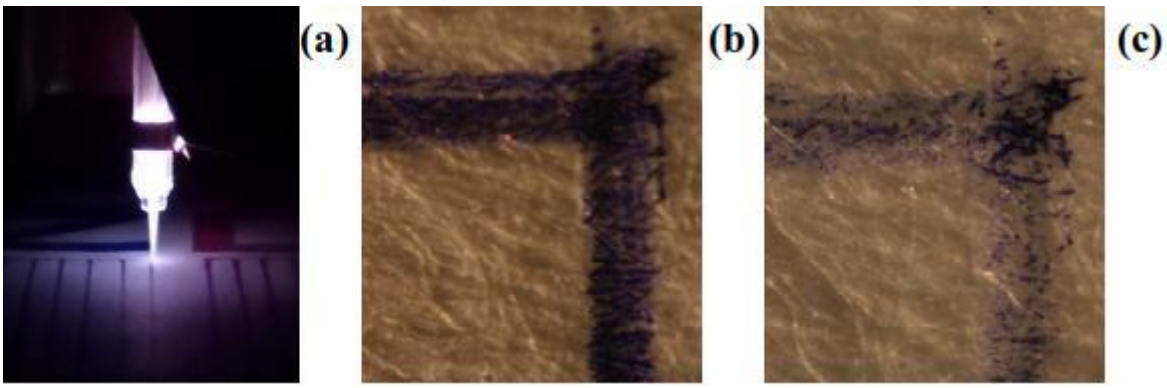

Fig. 1. Treatment of paper with ball pen ink traces by atmospheric pressure plasma jets (a); macrophoto of the traces before (b) and after (c) treatment.

For the effective future implementation of non-equilibrium plasma methods, it is essential to identify the key physicochemical factors of plasma actions to surface pollutants of biological, organic, and inorganic origin. Need to determine the permissible level of exposure on the base material and colorants.

Non-equilibrium atmospheric-pressure plasma jets are a promising solution. Moving forward, the study is planned to assess the feasibility, efficiency, and safety of this approach and to examine its potential for practical application in document restoration and scenarios define for optimal source design, plasma jet generation modes for paper cleaning.

Acknowledgements. The work was an initiative project partially supported by personal savings.

References

1. **Fljate D. M.** Paper properties. [Svojstva bumagi. Moskva: Lesnaja promyshlennost'] (1986). in Russian.
2. **Selow M. L. C., Rymovicz A. U. M., Ribas C. R., Saad R. S., Rosa R. T., and Rosa E. A. R.** Mycopathologia 180, 27 (2015).
3. **Deshevaya E. A., Fialkina S. V., Shubralova E. V., Tsygankov O. S., Khamidullina N. M., Vasilyak L. M., Pecherkin V. Ya., Shcherbakova V. A., Nosovsky A. M., and Orlov O. I.** Sci Rep 14, 334 (2024).
4. **Nikitin M. K. and Mel'nikova E. P.** Chemistry in restoration. Reference book. [Himija v restavracii. Spravochnoe posobie. Leningrad: Himija] (1990). in Russian.
5. **Tileva E. A., Krupin V. I., and Polovnikova E. V.** St.Petersburg Library School. [Peterburgskaja bibliotechnaja shkola] 80 (2017). in Russian.
6. **Jiao R., Sun F., Zeng S., and Li J.** Journal of Cultural Heritage 63, 240 (2023).
7. **Miller S., Banks B., and Waters D.**, MRS Proceedings 852 (2005).
8. **Markevicius T., Bonaduce I., Nikiforov A., Olsson N., Pastorelli G., and Suliga A.** 20th ICOM-CC Triennial Conference (2023).
9. **Ioanid E. G., Rusu D. E., Vlad A. M., Dunca S., Tănase C., Frunza V., Savin G., and Ursescu M. C.** IEEE Transactions on Plasma Science 44, 3037 (2016).
10. **Ioanid E. G., Frunză V., Rusu D. E., Vlad A. M., Savin G., and Popescu C.-M.** IEEE Transactions on Plasma Science 47, 81 (2019).
11. **Stepanova O. M., Kuzikova I. L., Snetov V. N., Grushko O. I., Medvedeva N. G., and Pinchuk M. E.** In Proceedings of XIII Conference in Physical Electronics FE-2024. [Fizicheskaja Elektronika] Mahachkala: DGU, 124–128 (2024). in Russian.

STRUCTURE OF TNTZ TITANIUM ALLOY WITH ZN NANOPARTICLES TREATED WITH COMPRESSIVE PLASMA FLOWS

V.V. Uglov, S.V. Zlotski

Belarusian State University, Nezavisimosty ave. 4, Minsk, 220030, Belarus, uglov@bsu.by

Engineering bionics, antibacterial property and surface osteogenic activity are three basic requirements for ideal oral bone implant materials. Currently, one of the promising oral bone implant materials is β-titanium alloy Ti-35Nb-2Ta-3Zr (TNTZ), which has high strength and low elastic modulus, effectively meeting the requirement of engineering bionics by reducing the elastic modulus to 50 GPa. However, achieving antibacterial property and surface osteogenic activity in the material design is a difficult task.

Surface modification becomes an important approach and an urgent task for the development of functional materials. Zinc (Zn) has good osteogenic induction and certain antibacterial property, and has great potential in promoting osseointegration /1/. The friction stir processing (FSP) can be used to coat zinc on the surface of titanium alloy. It has the advantages of low-temperature solid-phase bonding, good metallurgical compatibility between the coating and the substrate, small difference in the coefficient of thermal expansion and small interfacial thermal stress. It can uniformly embed the second-phase biofunctional metal particles into the titanium alloy substrate to obtain a solid metal matrix composite with the surface micro-nano-scale biocomposite topology /2, 3/.

Compressive plasma flows (CPF) can create micro-nano gradient materials on the surface of materials due to the high flow rate, density and temperature, long discharge time and high stability /4/, which will make it possible to modify the surface of titanium alloy after FSP to improve its strength and biological properties /5/.

Samples of titanium alloy Ti-35Nb-2Ta-3Zr were processed by compression plasma flows with the following modes: distance to the electrode - 12 cm, voltage on storage capacitors - 4.0 kV, pressure of plasma-forming gas (nitrogen) - 3 torr (400 Pa), number of pulses - 3. The results of the study of the elemental composition of samples obtained under different modes are presented in Table 1.

As can be seen from Table 1, the CPF treatment of Ti-35Nb-2Ta-3Zr alloy with Zn nanoparticles leads to a small (about 2 at.%) decrease in titanium concentration and an increase in concentration. The Zn concentration in the treated samples is up to 3.8 at.% (sample B). The zinc concentration in samples

C and E is less than 0.5 at.% and its detection is associated with the accuracy and features of the X-ray microanalysis method. Comparing the zinc concentration with the samples not treated with CPF, it can be said that the CPF treatment leads to an increase in the zinc concentration in the near-surface region.

Table 1. Concentration of elements in titanium alloy Ti-35Nb-2Ta-3Zr with Zn nanoparticles

Sample	Friction stir processing	Concentration of elements, at.%					
		Ti	Zr	Nb	Ta	Zn	Si
	Initial	77.4	1.8	20.1	0.7	-	-
A	Zn-0.5 mm, 300 rotations	75.1	1.9	22.3	0.7	-	-
B	Zn-1 mm, 300 rotations	71.9	1.6	21.4	-	3.8	1.3
C	Zn-2 mm, 300 rotations	75.0	1.8	22.5	0.7	-	-
D	Zn-1 mm, 225 rotations	74.1	1.8	22.4	0.7	1.0	-
E	Zn-1 mm, two treatments, 300 rotations	74.6	1.7	22.7	0.6	-	0.4

As can be seen from Table 1, the CPF treatment of Ti-35Nb-2Ta-3Zr alloy with Zn nanoparticles leads to a small (about 2 at.%) decrease in titanium concentration and an increase in concentration. The Zn concentration in the treated samples is up to 3.8 at.% (sample B). The zinc concentration in samples C and E is less than 0.5 at.% and its detection is associated with the accuracy and features of the X-ray microanalysis method. Comparing the zinc concentration with the samples not treated with CPP, it can be said that the CPF treatment leads to an increase in the zinc concentration in the near-surface region.

Let us consider the phase composition of the samples after CPF treatment. Fig. 1 shows the X-ray diffraction patterns of the Ti-35Nb-2Ta-3Zr titanium alloy samples with Zn nanoparticles treated with compression plasma flows.

Analysis with the initial X-ray diffraction pattern showed that the phase composition of the alloy does not change after CPP: the main phase remains the substitutional solid solution (Ti,Nb) with a bcc lattice and niobium oxide phases. It was revealed that the lattice parameter of the solid solution (Ti,Nb) changes after CPP and from the friction treatment modes.

Table 2 shows the results of determining the lattice parameter, the crystallite size and the lattice microstrain of the solid solution (Ti,Nb) in the Ti-35Nb-2Ta-3Zr titanium alloy with Zn nanoparticles. As can be seen from the table 2, CPF treatment leads to a significant decrease in the lattice parameter of the solid solution (Ti,Nb). At the same time, the size of the crystallite size decreases and microstrain increase, as can be seen from Table 2.

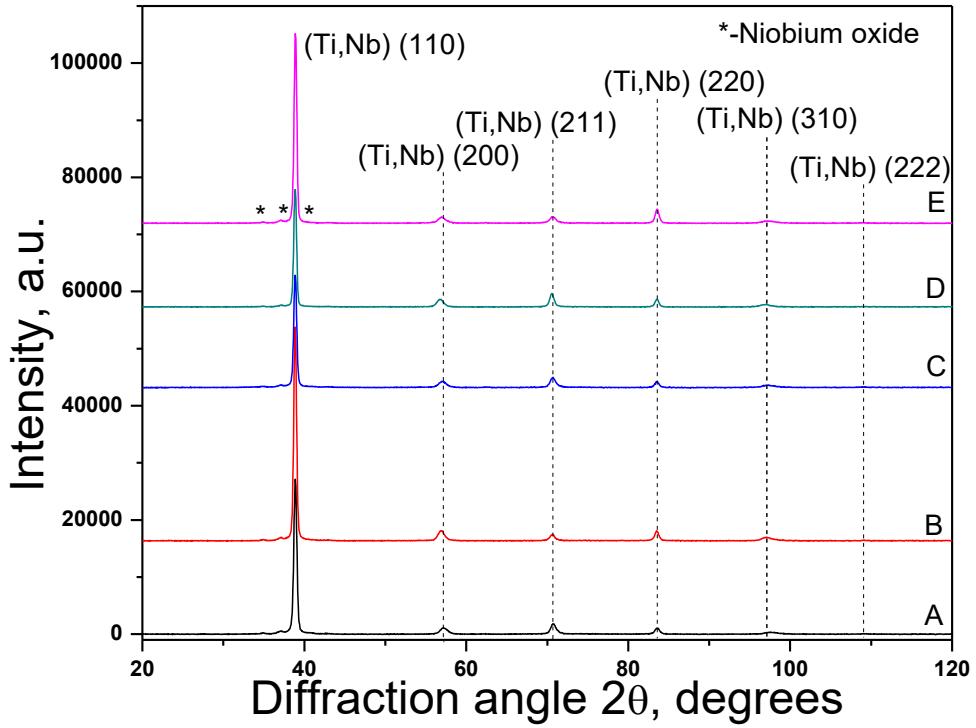

Fig. 2 – X-ray diffraction patterns of Ti-35Nb-2Ta-3Zr titanium alloy samples with Zn nanoparticles treated with compression plasma flows

Table 2. Lattice parameter, crystallite size and lattice microstrain of the solid solution (Ti,Nb) in titanium alloy TNTZ with Zn nanoparticles

Sample	Friction stir processing	Lattice parameter of (Ti,Nb), nm	Crystallite size, нм	Lattice microstrain, %
	Initial	3.29066±0.00018	59	-0.3
A	Zn-0.5 mm, 300 rotations	3.2562±0.0014	35	-1.3
B	Zn-1 mm, 300 rotations	3.2613±0.0010	39	-1.2
C	Zn-2 mm, 300 rotations	3.2589±0.0012	29	-1.8
D	Zn-1 mm, 225 rotations	3.2578±0.0004	36	-1.4
E	Zn-1 mm, two treatments, 300 rotations	3.2592±0.0010	25	-2.1

The largest lattice parameter was found for sample B, and the smallest for sample A. At the same time, the crystallite size and microstrains for these

samples are close. The lattice parameter of sample D coincides within the error with the value for sample A. At the same time, the crystallite size and microstrains for these samples are also close. A group of samples C and E is also distinguished. They have the same lattice parameter within the error, the values of the crystallite size and microstrains are also close. For these samples, the crystallite size values are the smallest, and the microstrains are the largest.

Thus, the elemental and phase composition of the titanium alloy TNTZ with Zn nanoparticles processed by compression plasma flows was investigated. It was shown that the CPF treatment leads to a decrease in the titanium concentration and an increase in the niobium concentration by 2 at.%. The phase composition of the alloy does not change after the CPF treatment, only a decrease in the lattice parameter of the solid solution (Ti, Nb) by 1% occurs. The patterns of the influence of friction treatment modes on the lattice parameter of the solid solution, the crystallite size and microstrain were revealed.

Acknowledgements. This work was supported by the Belarusian Republican Foundation for Fundamental Research (grant № T24KI-057).

References

1. **Gao C., Li C., Wang C. et al**. Journal of Alloys and Compounds, 726 (2017) P. 1072-1084.
2. **Fang Y., Wang Q., Yang Z. et al.** Materials & Design, 221 (2022) 110987.
3. **Wang Y., Shi H., Zhou P. et al.** Journal of Materials Research and Technology, 15 (2021) 6442-6452.
4. **Uglov V.V., Remnev G.E., Kuleshov A.K. et al.** Inorganic Materials: Applied Research, 2(2011) P.242-246.
5. **Gangwar K.K., Mamidala R.** Materials & Design, 141 (2018) 230-255.

TANTALUM DIBORIDE SURFACE AFTER TREATMENT WITH COMPRESSION PLASMA FLOWS

V.V. Uglov[1], I.V. Kondrus[1], M.O. Kovalenko[1], A.Ya. Pak[2], A.A. Svinukhova[2]

[1] Belarusian State University (BSU), 220030, Minsk, Independence ave. 4, Belarus, uglov@bsu.by
[2] National Research Tomsk Polytechnic University, 634050, Tomsk, Lenin Avenue 30, Russia

Metal diborides have proven themselves to be promising materials capable of withstanding extreme operating conditions while exhibiting excellent physical and mechanical properties /1-6/. A particularly interesting topic in modern materials science is the production of diborides of refractory metals such as hafnium, vanadium, tantalum, niobium and many others /3-6/. The tantalum diboride (TaB_2) considered in this paper exhibits outstanding thermophysical and mechanical properties: high melting point (>3000°) /1/, high hardness (~25 GPa) /4/, good chemical resistance at elevated temperatures /3-5/, which makes it extremely promising for use in the aerospace industry.

However, their post-synthetic processing remains a complex technological task due to the high melting point and low plasticity of these materials /4,5/. Common methods of post-synthetic sintering of refractory metal diboride powders, such as hot pressing (HP), spark plasma sintering (SPS) and mechanochemical activation combined with high-temperature sintering, have a number of disadvantages.

In this context, high-temperature plasma is considered as a promising method for modifying the structure and properties of diborides, allowing local changes in their morphology, composition and phase state /3,4/. To date, studies /7,8/ have shown that plasma treatment during synthesis leads to the formation of nanostructured layers, a decrease in porosity and an improvement in mechanical characteristics, which opens up new possibilities for the use of these materials in extreme conditions.

However, little is known about the results of treatment with directed high-temperature plasma flows on the structural and phase state of refractory metal diborides.

The starting materials for the preparation of TaB_2 samples were powders of tantalum and boron. The synthesis of tantalum diboride compounds was carried out in a laboratory electric arc reactor in an air atmosphere. A detailed description of the process for obtaining powdered compounds of metal diborides is presented in /2/.

After sintering, the massive tantalum diboride samples were placed in natural cooling conditions. The resulting samples were then processed by grinding and polishing.

The study on modification of surface properties was carried out using compression plasma flows (CPF) of medium energies generated by a compact geometry gas-discharge magnetoplasma compressor /7,8/. Samples in a chamber filled with a nitrogen atmosphere at a pressure of 3 Torr were located at a distance of 8 cm from the cut of the inner electrode. The initial voltage of the energy storage was 4 kV, with a total discharge duration of ~ 100 μs. Samples were exposed to 3 CPF pulses.

The phase composition of the samples was studied by X-ray diffractometry (XRD) on a Rigaku Ultima IV diffractometer using copper radiation, λ = 0.15418 nm.

Analysis of the elemental composition and study of the surface morphology of the samples were performed on a ZEISS LEO 1455 VP scanning electron microscope at an accelerating voltage of 20 kV.

The surface morphology of the samples was studied by atomic force microscopy (AFM) using a NEXT II scanning probe microscope. Standard contactless silicon cantilevers with a tip curvature radius of less than 10 nm were used. The surface morphology was studied in the amplitude-frequency modulation mode using the constant force method.

Fig. 1 shows X-ray diffraction patterns of tantalum diborides in the initial state and after exposure to compression plasma flows.

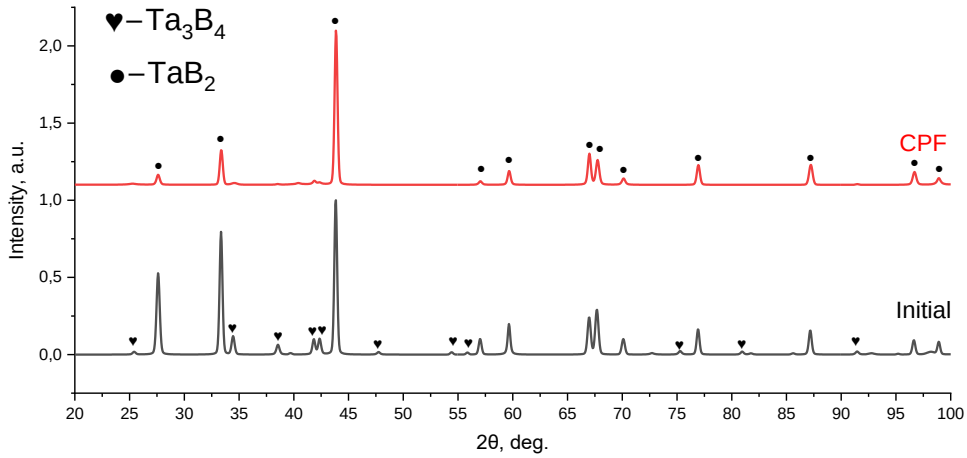

Fig. 1 – X-ray diffraction patterns of TaB_2, in the initial state and after CPF treatment

In the initial state of the tantalum diboride sample, phase analysis revealed the presence of two phases: Ta_3B_4 and TaB_2. As a result of the quantitative X-ray phase analysis, these phases were in a ratio of 17.6 and 82.4%, respectively.

The lattice parameters for the orthorhombic phase Ta_3B_4 were: a = 3.279±0.003 Å, b = 13.979±0.009 Å, c = 3.127±0.006 Å, and for the hexagonal phase TaB_2: a = 3.0953±0.0002 Å, c = 3.2253±0.003 Å. After the CPF treatment, the ratio of the orthorhombic phase Ta_3B_4 and the hexagonal phase TaB_2 was: 0.1 and 99.9%, respectively. The corresponding peritectic transformation $Ta_3B_4 + L \rightarrow TaB_2$ occurs through incongruent melting of the tetragonal phase, diffusion redistribution of components in the ultrafast cooling melt and crystallization in the form of a hexagonal phase /8/.

Fig. 2 shows images of the surface of TaB_2 samples in the initial state and after surface CPF treatment.

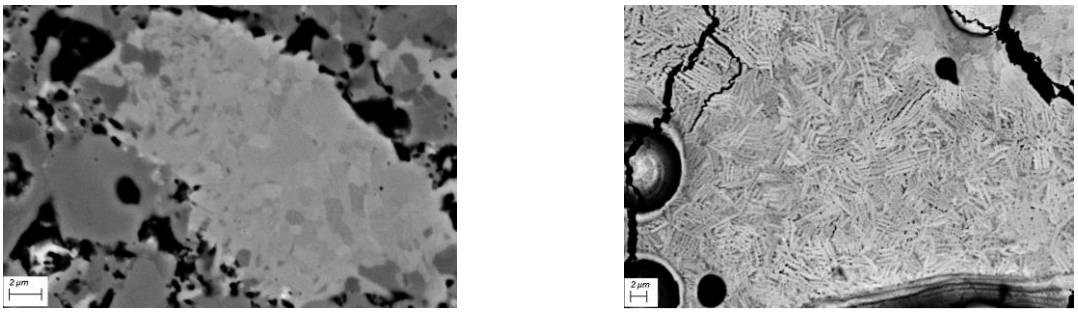

a b

Fig. 2 – Surface morphology of TaB_2 samples in the initial state (a) and after CPF treatment (b)

As the analysis of the surface morphology, carried out using a scanning electron microscope, showed, after the KPP treatment, the samples and TaB_2, which in the initial state had an equiaxed grain structure with a grain size of about 2-5 μm, acquired an ordered needle-like structure. The length of such a structure along the predominantly elongated direction is ~ 2 μm, and the width is 0.5 μm. Cracks also appeared on the surface, mainly due to a change in the density and porosity of the formed surface layer in comparison with the initial sintered state of the samples /7, 8/.

The surface reconstruction shown in Fig. 3 of a tantalum diboride sample after CPF treatment, performed using surface atomic force microscopy, showed that the needle-shaped structure formed as a result of CPF treatment has a complex articulated shape, where the length of one element is approximately 300-500 nm along the predominant direction of stretching. Also, on the surface of such a needle-shaped structure, the formation of spheroidal structures with a maximum diameter of about 80 nm was detected (highlighted by blue circles in Fig. 3). Such structures are clustered over the entire surface of the needle-shaped structure.

Thus, the treatment of tantalum diboride (TaB_2) with compression plasma flows leads to a decrease in the porosity of the sample and an increase in the

single-phase and homogeneity of the surface layer of the sample, therefore such treatment is generally positive and allows improving important operational parameters for the use of this material in the aerospace, nuclear and metallurgical fields.

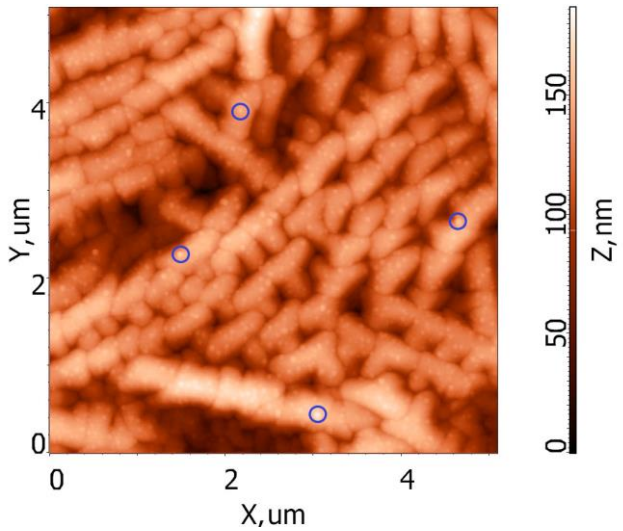

Fig. 3 – Surface of TaB_2 sample after CPF treatment (spherical particles with a diameter of ~ 60-80 nm are highlighted in blue)

Also of scientific interest is the formation of nanodispersed particles formed on the surface of complex periodic structures of tantalum diboride treated with compression plasma flows, since these studies can subsequently form the basis of the theory of the formation of needle-like structures of metal diborides from an ultra-rapidly cooled melt.

Acknowledgements. This work was supported by State Program of Scientific Research "Energy and Nuclear Processes and Technologies" (2.1.2).

References

1. **Lyakishev N. P.** State Diagrams of Binary Metal Systems: Handbook (1996).
2. **Pak A. Y.** International Journal of Refractory Metals and Hard Materials, 93 (2020) 105343.
3. **Sahoo S.** Ceramics International, 43 (2017)15561–15566.
4. **Demirskyi D.** Ceramics International, 42 (2016) 16674–16679.
5. **Zhang X.** Materials Letters, 62 (2008) 4251–4253.
6. **Ran S.** Journal of the European Ceramic Society, 30 (2010) 2633–2642.
7. **Shymanski V. I.** Applied Surface Science, 491 (2019) 43–52.
8. **Shymanski V. I**. Surface and Coatings Technology, 278 (2015) 183–189.

MULTIFUNCTIONAL SETUP FOR EXPERIMENTS ON ADVANCED APPLICATIONS OF ELECTRON-BEAM PLASMA

T. Vasilieva[1], A. Diaz Mesa[1], M. Vasiliev[2]

[1]Moscow Institute of Physics and Technology (National Research University), Institutsky per. 9, 141700, Dolgoprudny, Moscow region, Russia, vasileva.tm@mipt.ru
[2]Joint Institute for High Temperatures, Russian Academy of Sciences, Izhorskaya 13 Bd. 2, 125412, Moscow, Russia,

Among the numerous methods for generating low temperature plasmas, Electron Beam plasma (EBP) excited by the injection of electron beams into dense gaseous media attracts attention due to its unique peculiarities that are perspective for materials processing and "green" environment safe technologies [1].

The generation principle and general properties of EBP are described in detail in [1, 2]. The observed physical phenomena and patterns of processes in beam-plasma systems have pronounced specificity and can be demonstrated easily enough. For such demonstrations multifunctional laboratory setup was developed. The setup is capable of reproducing the conditions most often occuring in real beam-plasma systems during research and technological experiments, namely:

1. Continuous and intermittent generation of EBP in free space and in a closed volume at forevacuum pressure;
2. Thermal and nonthermal interaction of EBP with the surface of macroscopic solids and with fine aerosol particles as well as the emission of radiation of various kinds during such interactions;
3. Electrophysical phenomena that are observed in beam-plasma systems and are often critical for their functioning.

The adjustment ranges for the setup operating modes are as follows: initial electron energy E_b = 20–30 keV, beam current I_b = 1–100 mA, and plasma generating gas pressure $P_m = 10^{-2}$–10^2 Torr. The scheme of the experimental setup is illustrated in Fig. 1. Focused electron beam (EB) *3* formed in a high vacuum chamber *2* of EB gun *1*. Then the EB is transported through injection window *4* into working chamber *8* filled with plasma generating gas and an EBP cloud *7* is formed. Inside working chamber *8*, containers *6* with various geometries can be installed.

Figure 1 shows a variant of a cylindrical tube container. An EB is injected along the tube through one of its ends. A nozzle is installed on the end of the container closest to the injection window *5*, which forms a flow of plasma generating gas in it. Various injector options have been developed, both for mechanical atomization in a stationary gas (centrifugal nozzles, vibrating sieves,

ultrasonic atomizers, etc.) and for atomization with a gas flow (jet nozzles, pneumatic dispersing devices). A programmable gas flow rate controller sets gas consumption amount G_g. Through the opposite open end of the container, gas is released into the working chamber connected to a vacuum pump by line *9* through PID regulator *10*, which controls pumping performance G_0.

A system of electrical probes is provided to measure the potential accumulated by aerosol particles or a macroscopic bodies placed in an EBP (Fig.1 shows a diagnostic module with a stationary probe located directly in the plasma cloud and an external probe: a metal ring covering a dielectric container).

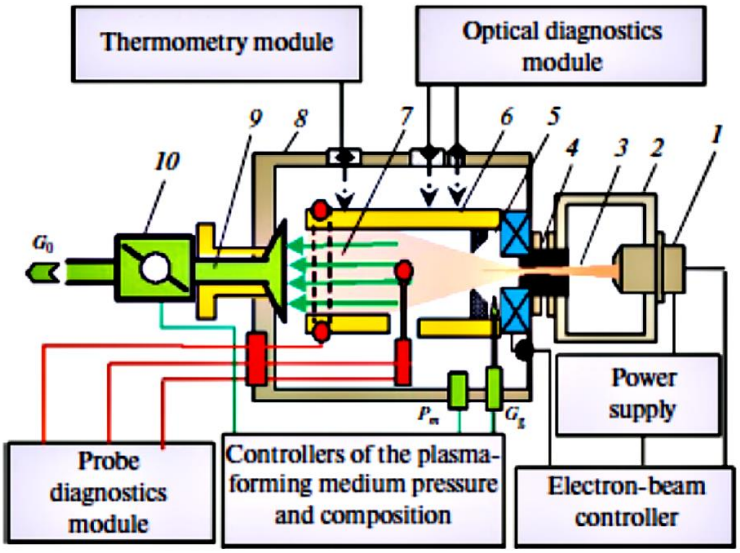

Fig. 1. Experimental setup diagram: (*1*) electron gun, (*2*) high vacuum chamber, (*3*) electron beam, (*4*) injection window, (*5*) gas nozzle, (*6*) container, (*7)* EBP, (*8*) working chamber, (*9*) vacuum pump line, (*10*) gas flow regulator

The heating of bodies placed in an EBP volume can be detected by thermal sensors that are installed at various points on the container wall or on the target surface. To demonstrate nonstationary thermal processes in EBP, signals from thermal sensors come to a multichannel analog-to-digital converter (ADC) operating in real time. By using interchangeable containers and targets, it is possible to demonstrate:

1. Heating dynamics of solid samples of various geometries placed in EBP and phase transitions on their surfaces;

2. Plasma-stimulated synthesis of chemical compounds on the surface of materials (for example, synthesis of titanium oxides and nitrides on a flat surface and on the inner surface of pipes);

3. Low-temperature modification of the surface of materials (for example, changing the hydrophilic hydrophobic properties of the surface of polymers and

biopolymers).

To register the emission spectra of EBP and objects in contact with it fiber optic spectrometers operating in the ultraviolet, visible, and near-infrared ranges are used. In addition to spectrometers, the optical diagnostics module contains LCD photo and video cameras, images from which are also transferred to a computer.

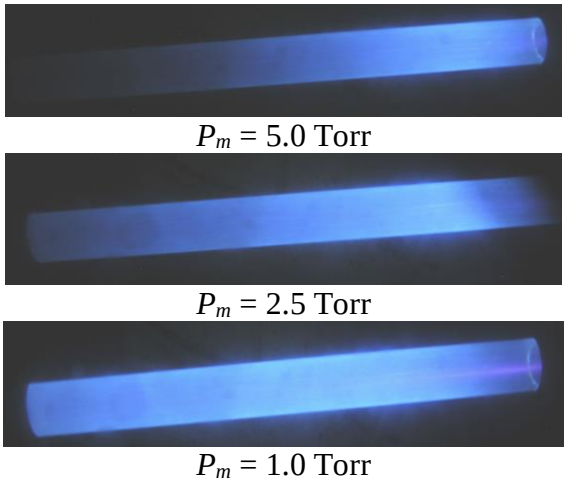

(a)

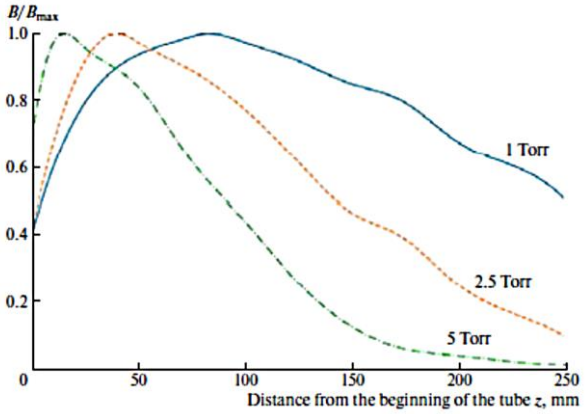

(b)

Fig. 2. (a) Generation of EBP air in a quartz tube with a diameter of 20 mm, (b) Longitudinal profiles of EBP glow intensity in a quartz tube with a diameter of 20 mm at different air pressure values (computer processing of experimental data)

The generation of EBP inside a transparent cylindrical container is illustrated in Fig. 2. The zone of the plasma cloud with the maximum glow intensity, i.e., zone of maximum volumetric energy release. The position of this zone relative to the EB injection plane depends on the pressure of the plasma generating gas: with increasing P_m, it shifts in the direction of the injection window.

Fig. 3 shows a recording of the potential of a macroscopic body inserted in the EBP at variable P_m pressure. Curves *2* and *3* correspond to signals from a spherical probe installed inside the container and from an external ring probe surrounding the quartz tube; curve *1* is a signal taken from the vacuum transducer (VSM 7XDL).

Almost all experiments with EBP are accompanied by the emission of radiation of various wavelengths. Fig. 4 presents the initial emission spectrum of nitrogen EBP excited in a quartz tube. The superposition of the plasma line spectrum and the continuous quartz luminescence spectrum in the range of 400–600 nm is clearly visible.

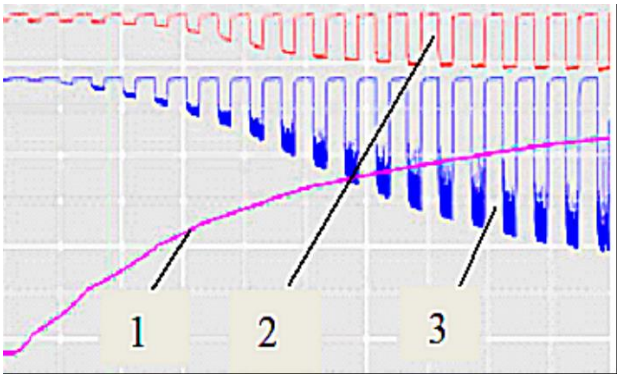

Fig. 3. ADC monitor screen when measuring the potential of a (*3*) spherical probe and (*2*) ring probe when generating EBP air in a quartz tube at (*1*) variable (falling) pressure of the plasma generating gas

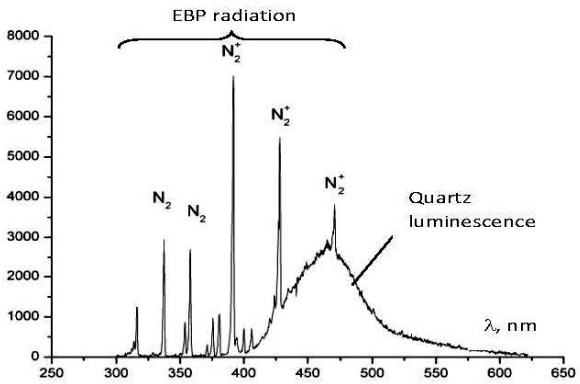

Fig. 4. Optical spectrum of nitrogen EBP radiation excited in a quartz tube

Plasma chemical reactor was tested in experiments with crab shell high molecular weight chitosan destruction. Water-soluble chitooligosaccharides with weight-average molecular mass M_w = 800–2000 Da and polymerization degree varying from dimeres to heptamers were obtained; trimeres being the most predominant. Some increase in oxygen-containing carbonyl C=O and carboxyl –COOH groups and slight increase in deacetylation degree were observed after chitosan processing by the EBP of oxygen. Water solutions of the produced chitosan oligomers enhanced germination in peas and decreased their microbial and fungal contamination [3].

References

1. **Vasiliev M. and Vasilieva T.** Encyclopedia of Plasma Technology (Ed.: J. Leon Shohet). Boka Ralton, FL, USA: Taylor & Francis Inc. (2016).
2. **Vasiliev M. and Vasilieva T.** X International Conference "Plasma Physics and Plasma Technology", September 12-26 (2022) 370-373.
3. **Vasilieva T.M., Naumova I.K., Galkina O.V., Udoratina E.V., Kuvschinova L.A., Vasiliev M.N., Khin Maung Htay and Htet Ko Ko Zaw.** IEEE Transactions Plasma Science, 48 (2020) 1035-1041.

METAL-PUFF Z-PINCH BASED ON FOIL EVAPORATION AND IONIZATION

A. Zhigalin, A. Rousskikh, V. Oreshkin, A. Shishlov, R. Cherdizov, V. Kokshenev, N. Kurmaev.

Institute of High Current Electronics of the Siberian Branch of the Russian Academy of Sciences, Akademichesky Avenue 2/3, Tomsk 634055, Russia
E-mail: zhigalin@ovpe2.hcei.tsc.ru

Fast Z-pinches, are widely used to produce high-density, high-temperature plasmas /1,2/. A Z-pinch is compressed under the action of a high-power current pulse, which creates a high magnetic field pressure at the plasma–vacuum interface. There are several methods of forming liners, such as wire arrays liners /3,4/, gas-puff liners /5,6/, or metal-puff Z-pinches /7/, in which the plasma shell is formed using an arc discharge system.

To study the dynamics of implosion and the development of MRT instabilities during compression of a metal-puff Z-pinch, experiments were carried out in which the liner plasma shell the was formed during the evaporation and ionization of a metal foil in a vacuum arc discharge. Experiments were carried out on the GIT-12 Arkad'ev-Marx pulse-power generator. The pulse-power generator provides the current of 4.7 MA with the current rise time of 1.7 μs with the short-circuit load /8/. Scheme of the experimental load is shown in the figure 1.

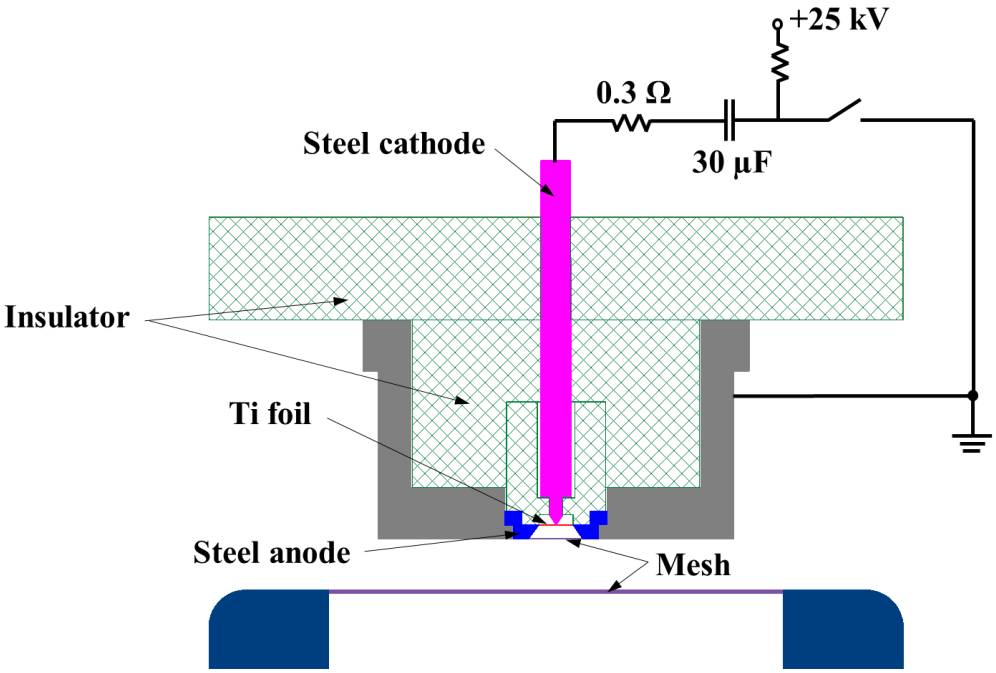

GIT-12 High voltage electrode (cathode)

Figure 1. Scheme of the GIT-12 load.

Previously in work Rousskikh et al. /9/ it was proposed to use a metal-puff Z-pinch to obtain an initially highly ionized plasma column, in which the pinch plasma was produced when the electrodes evaporate as a result of the arc burning. In this work, plasma is formed during the combustion of an arc discharge between a central steel cone cathode and a titanium foil. In the experiments, Ti foil with a thickness of 12.5 μm was used. At the exit of the conical collimator (steel anode) there was a steel mesh with a transparency of 68%. As the foil evaporates, a plasma flow is formed, which is used as the Ti liner. An arc discharge is formed when is switched a capacitor bank with a capacity of 30 μF charged to a voltage of 25 kV. A damping resistance of 0.3 Ohm is installed in the discharge circuit. The Z-pinch length was 20 mm in experiment.

The following types of diagnostics were used in the experiments:

- inductive voltage divider measured the voltage drop on the pinch;
- B-dots measured the derivative of the current flowing through the liner;
- the radiation power was measured with two x-ray vacuum diodes with a copper cathode;
- B-dots, installed of at distances 90, 60, 46 и 30 mm from the pinch axis, were used to obtain information about the dynamics of the current sheet motion.
- High Speed Framing Camera (HSFC-Pro 12-bit ultra-speed /10/) recorded the pinch image with a frame exposure time of 3 ns.

Figure 2 presents the waveforms of the GIT-12 generator current flowing through the load that were obtained by integrating signals from the B-dot probe and the K-shell radiation power.

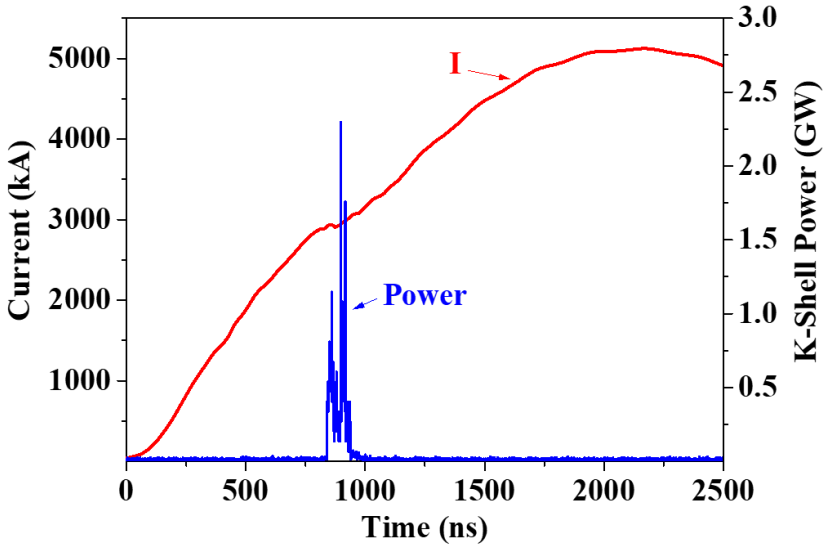

Figure 2. Load current waveforms and the K-shell radiation power.

Images of a titanium metal-puff Z-pinch obtained using an HSFC-Pro camera at different times are shown in figure 3. In shot#3254, the amplitude of the load current, I_{max}, was about 2.74 MA, and the pinch implosion time T_{impl} was about 898 ns relative to the beginning of the GIT-12 current pulse. For a shot#3255 similar parameters were $I_{max} \approx 2.19$ MA, and the pinch implosion time $T_{impl} \approx 713$ ns. The images given in figures 3(a)–(d) were obtained, respectively, 655, 695, 735 and 775 ns after the beginning of the current pulse. The images given in figures 3(e)–(h) were obtained, respectively, 629, 669, 709 and 749 ns after the beginning of the current pulse.

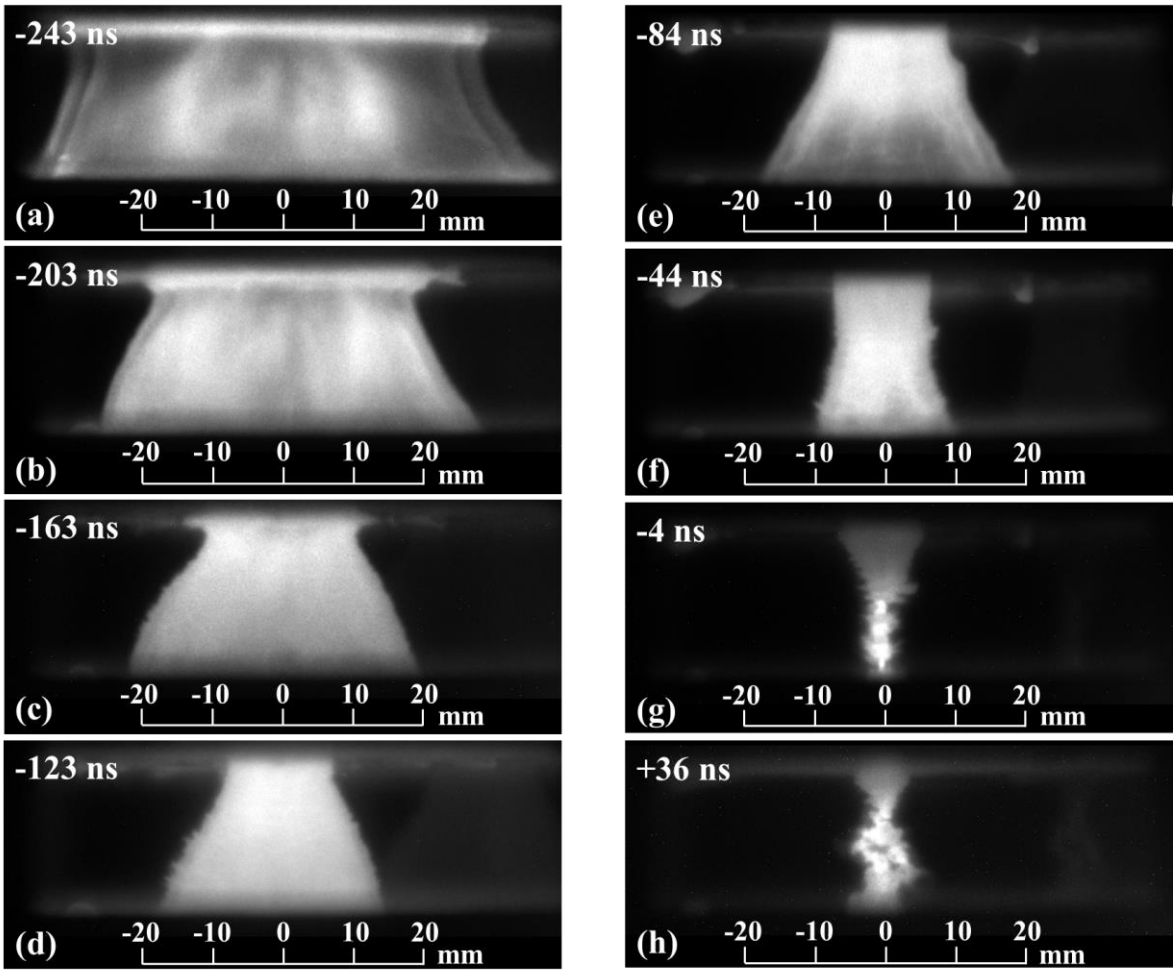

Figure 3. Images of an imploding Mg metal-puff Z-pinch, obtained in experiments on the GIT-12 high-current pulse generator. The images given in figures shot#3254 (a)–(d) 665, 695, 735 and 775 ns and shot#3255 (e)–(h) 629, 669, 709 and 749 ns after the beginning of the current pulse.

Figure 3 show that, in our case, at the initial stage of the pinch acceleration process and up to the beginning of the stagnation phase, the pinch compression

is stable, that is, large-scale instabilities do not develop. From figure 3g, it can be concluded that Rayleigh-Taylor instabilities begin to develop only at the moment of formation of the plasma column on the system axis, at a moment close to the implosion time.

Acknowledgements. This work was supported by the Russian Science Foundation (grant No. 22-19-00686П).

References

1. **Ryutov D.D., Derzon M.S. and Matzen M.K.** The physics of fast Z-pinches Reviews of Modern Physics, 72(2000) 167.
2. **Giuliani J.L. and Commisso R.J.** IEEE Transactions on Plasma Science, 43(2015) 2385.
3. **Spielman R.B., Deeney C., Chandler G.A., et al.** Phys. Plasmas, 5(1998) 2105.
4. **Lebedev S.V., Ampleford D.J., Bland S.N., Bott S.C., Chittenden J.P., Goyer J., Jennings C., Haines M.G., Hall G.N., Hammer D.A., Palmer J.B., Pikuz S.A., Shelkovenko T.A. and Christoudias T.** Plasma Physics and Controlled Fusion, 47(2005) 91-108.
5. **Baksht R.B., Fedunin A.V., Labetsky A.Y., Oreshkin V.I., Rousskikh A.G. and Shishlov A.V.** Plasma Physics and Controlled Fusion, 43(2001) 849.
6. **Chaikovsky S.A., Labetsky A.Y., Oreshkin V.I., Shishlov A.V., Baksht R.B., Fedunin A.V. and Rousskikh A.G.** Laser and Particle Beams 21(2003) 255.
7. **Rousskikh A.G., Zhigalin A.S., Oreshkin V.I., Chaikovsky S.A., Labetskaya N.A. and Baksht R.B.** Physics of Plasmas, 18(2011) 092707.
8. **Shishlov A.V., Baksht R.B., Chaikovsky S.A., Fedunin A.V., et al** Laser Physics, 16(2006) 183-193.
9. **Rousskikh A.G., Zhigalin A.S., Oreshkin V.I., Labetskaya N.A., Chaikovsky S.A., Batrakov A.V., Yushkov G.Yu., and Baksht R.B.**, Physics of Plasmas, 21(2014) 052701.
10. Specifications of HSFC PRO camera (available at: https://spegroup.ru/upload/wikifiles/1223250.pdf)

EXPERIMENTAL STUDY OF COMBINED COOLING SYSTEM USING EHD STREAMS

A.S. Kirillov, V.Yu. Khomich, O.I. Korzhova, S.I. Moshkunov, V.V. Voevodin, Ya.E. Zharkov

IEE RAS, Russia, Saint-Petersburg, Palace Embankment, 18a, 191181,
E-mail: caduceus.kas@gmail.com

Abstract: An experimental study of combined (blower and corona) cooling of two aluminum plates heated to 100 °C in a rectangular channel was carried out. A cathode wires were positioned equidistantly between plates. A temperature measurement at different corona and a blower power supply voltages showed the plate surface temperature decreasing by tens of degrees under combined cooling and increasing by 1-3 degrees under solely electric wind with strong dependency on the interelectrode distance. The results are applicable for standard «heat sink-fan» cooling systems modernization.

During the operation of any electrical device, a certain amount of heat is generated, which increases significantly with increasing power and supply frequency. The tendency to miniaturize electronic components and devices, coupled with high packaging density, leads to increased surface heating due to higher energy density. However, most standard cooling methods (heat sinks, fans, heat pipes, etc.) suffer from several disadvantages, such as dependence of heat dissipation capacity on cooling system size, noise generation, inefficient airflow distribution (dead zones) and insufficient heat pipe contact area. Consequently, there is a need to develop and implement novel cooling systems that combine compactness, noiseless operation, and operational safety. For a long time, the idea of cooling thermally stressed components using electric wind generated by corona or dielectric barrier discharges has remained relevant, yet it has not been fully implemented in practical applications.

Electric wind is a phenomenon, when neutral molecules of a working gas enter a state of directional accelerated motion due to collision with charged particles in a a strong electric field region, creating an electrohydrodynamic (EHD) gas flow /1/. One of the most effective ways to create an EHD flow in air is to use a corona discharge (CD) of negative polarity /2/. In general, CD is considered in the literature as an independent means of cooling, inferior in terms of heat removal intensity to devices for creating forced convection. Researchers pay little attention to combined cooling systems, especially in the conditions of closed cooling channels typically used in practice.

To evaluate the effectiveness of combining EHD flow with forced convection in cooling process, we developed the experimental setup shown in Fig.

1. It consisted of modular rectangular channel ABS plastic (115×55×2d_{wp} mm^3) connected to the blower through a laminizer. Aluminum plates (anodes), insulated from the outside, acted as the grounded walls of channel. For CD generation six copper wires with a 50 microns diameter (cathodes) were placed perpendicular to the flow direction, spaced at 1 cm intervals and equidistant from plates. The top parts of plates were heated using ceramic film resistors, the heating power varied in the range of 23,5-28,2 W to maintain the plates temperature at 100 °C in their center. The temperature was controlled using a type K thermocouple. A Spellman SL20*2000 high-voltage power supply was used for corona discharge generation, QJE PS3010 was used for resistors heating and QJE QJ5003C was used for blower operation.

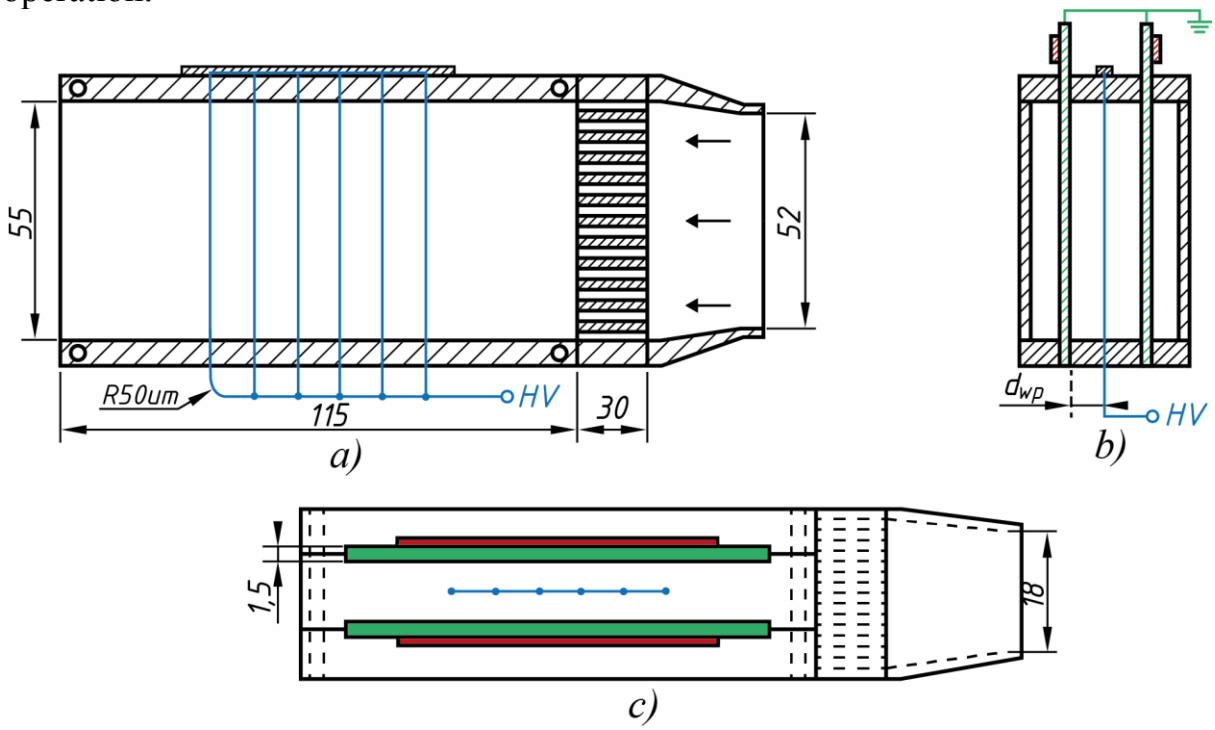

Fig. 1 – Experimental setup scheme: a) side cross–sectional view without plates; b) front cross-sectional view; c) top view (red indicates heating resistors, green – plates-anodes, blue - wires-cathodes)

Modeling of such channel systems has been previously performed /3/, yet practical experiments remain necessary. The initial experiment was conducted for corona discharge only at an interelectrode distance d_{wp} = 5 mm with a time step Δt = 5 min. Subsequent measurements employed a stepwise variation of corona power P_{corona}, with values corresponding to the points of most significant temperature difference observed in the first experiment. The most notable results of this study are presented in Fig. 2. Each graph shows that solely electric wind cooling in studied range of power supply leads to plates heating.

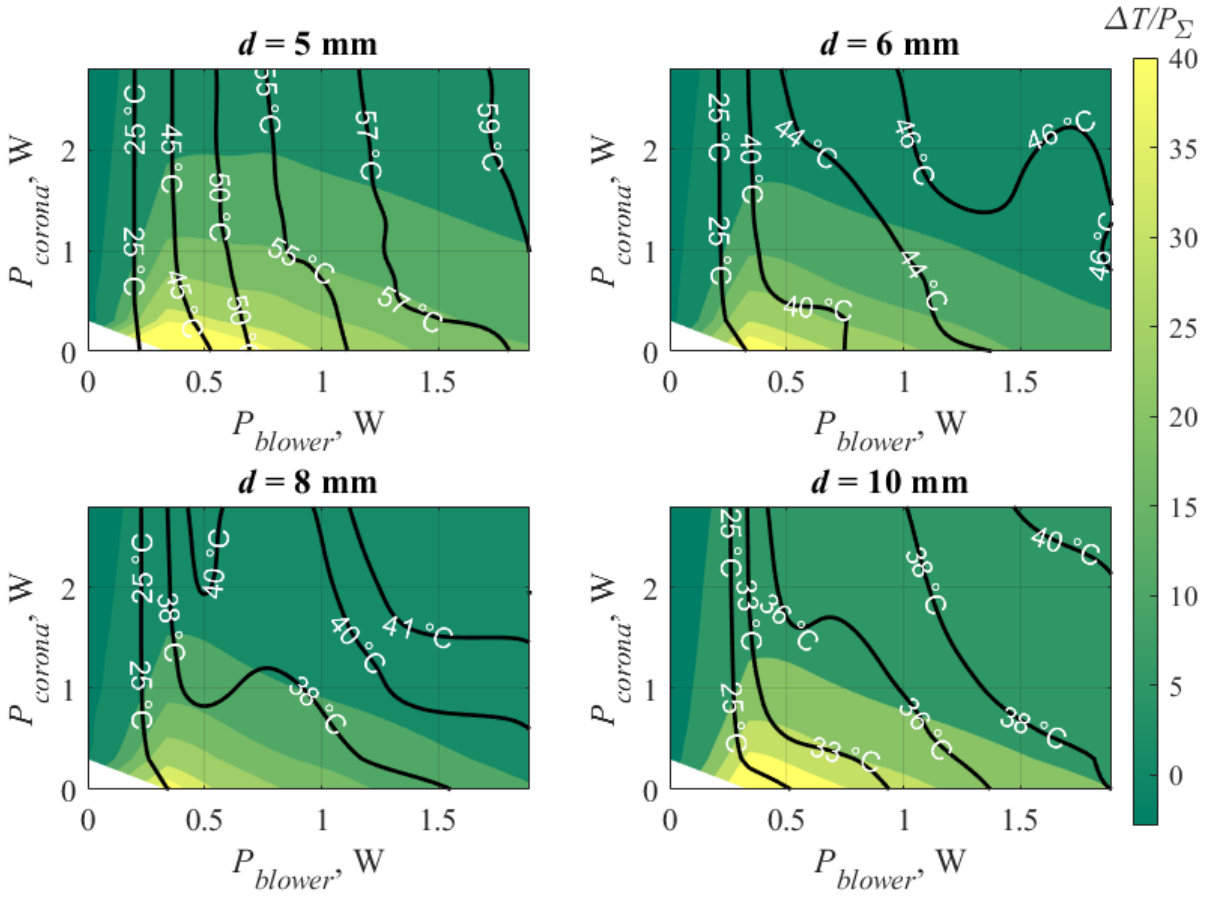

Fig. 2 – Temperature difference isolines between uncooled and combined cooling cases with color separation of energy efficiency zones at different corona and blower powers

Fig. 2 demonstrates that achieving 25°C cooling requires nearly identical total power consumption across all tested interelectrode distances d_{wp}. In addition, cooling with CD only in the absence of blower operation led either to a slight cooling of 0,2-0,5 degrees for d_{wp} = 7-8 mm, which is close to the thermometer measurement error, or to heating up to 103,2 ° C. An increase in the interelectrode distance also led to blower cooling intensity decreasing: at P_{cooler} = 0,34 W, the temperature difference was 38 °C for d_{wp} = 5 mm and 18,4 °C for d_{wp} = 10 mm. At the same time, there was the intensity increasing of combined cooling: the maximum temperature difference between blower cooling and combined cooling methods was 5,9 °C and 15,3 °C for similar cases. Analysis of the isotherm shapes revealed that the contribution of electric wind to heat transfer increased with overall temperature reduction. However, in the absence of forced convection generated by the blower, the plate temperature rose. The obtained results suggest that the heated air radially dispersed from the wires underwent mixing without being effectively exhausted through the channel outlet, thereby impairing natural convection. Consequently, the implementation of the "wire-plate" system in a

partially sealed channel proves impractical without external airflow generation in the present configuration.

From the point of pure energy efficiency view, the blower became the best option, reaching $\Delta T/P_{\Sigma}$ = 40 °C/W. The electric wind utilization in this configuration enable to additional reduce temperature ranging from 1,1 to 15,3 °C and may be practically relevant if dimensional constrains the inlet of the installation cooled section limits blower effectivity.

The obtained results demonstrate the feasibility of using corona discharge to enhance heat transfer in a partially sealed rectangular channel when combined cooling with blower using. However, the wire-plate system cannot be employed as a sole cooling method in the selected configuration.

Acknowledgements. This study was supported by the Russian Ministry of Science and Higher Education (grant No. 075-15-2024-543 dated 24.04.2024) under the Large-Scale Projects Program in priority areas of scientific and technological development.

References

1. **Nebogatkin S.V., Rebrov I.E., Khomich V.Yu., Yamshchikov V.A.** Powerful electrohydrodynamic flow on the basis of the high-frequency barrier discharge in gas. Uspekhi Prikladnoi Fiziki, vol. 2, no. 6 (2014) 595-604.
2. **Qu, J., Zeng, M., Zhang, D., Yang, D., Wu, X., Ren, Q., & Zhang, J.** A review on recent advances and challenges of ionic wind produced by corona discharges with practical applications. Journal of Physics D: Applied Physics, vol. 55 (2021), P. 153002.
3. **Tian-Hu Wang, Ming Peng, Xiao-Dong Wang, Wei-Mon Yan.** Investigation of heat transfer enhancement by electrohydrodynamics in a double-wall-heated channel. International Journal of Heat and Mass Transfer, vol. 113 (2017), 373-383.

CAPABILITIES OF LIQUID-ASSISTED LASER AND PLASMA METHODS FOR SYNTHESIS OF COMPOSITE NANOSTRUCTURES

N. Tarasenko[1], V. Kornev[1], N. Tarasenka[1,2], A.Nevar[1], M. Nedelko[1]

[1] B.I. Stepanov Institute of Physics, National Academy of Sciences of Belarus, Belarus, n.tarasenko@ifanbel.bas-net.by
[2] University of Strathclyde, Glasgow, UK

Nanocomposite materials exhibiting optical, electronic and catalytic properties different from those of component materials are promising for a number of applications that implies a development of novel efficient techniques for their synthesis and deposition into thin film and ordered structures. In recent years, liquid assisted plasmas have attracted increasing attention due to their high potential in the field of material processing and nanotechnology. In plasma-liquid systems, plasma is generated at atmospheric pressure, exists, as a rule, in a non-equilibrium state, contains various highly reactive particles, and thus is well suited for the synthesis of composite nanomaterials such as hybrid, alloyed, and doped ones. Non-equilibrium processes (laser-induced, plasma-enhanced etc.) involve both locally and temporally extreme conditions of temperature and pressure (and their gradients) that could not be attained otherwise. Particles of complex composition are formed due to the chemical reactions of evaporated atoms with each other and with the environmental species.

In this paper, capabilities of a number of combined approaches based on laser ablation plasma in liquid as well as electric discharges inside and in contact with liquid are discussed. By combining various types of targets and liquids, it was possible to control both composition and structure as well as chemical and physical properties of synthesized nanomaterials. The examples of proposed novel schemes suitable for the synthesis of NPs of alloys (Si-Sn, Ge-Sn) /1/, compounds (SiC, ZnO, CuO) /2,3/, doped (ZnO:Nd) /4/ nanocrystals and hybrid (ZnO/C, Si-Ag, Si-Cu and Si-Ag-Au) /5,6/ structures are illustrated by experimental schemes presented in Figure 1.

In particular, one of the combined laser-plasma approaches is based on sequential laser ablation of targets in liquids. The proposed method can be used as a tool for obtaining binary or ternary nanocomposites, as well as for doping of nanocrystals. Another method for obtaining nanoparticles (NPs) of complex composition is based on laser processing of nanoparticle mixtures. Particular attention has been paid to the production of NPs of metastable compounds and alloys, since their formation is favorable under dense plasma conditions with high temperature and pressure. For this purpose, a combined plasma-laser approach was developed based on the electric discharge treatment of a suspension of micropowders in liquids followed by laser irradiation of the

resulting colloids, which has been shown to be suitable for the formation of Cu-Zn, Ag-Cu, Ge-Sn and Si-Sn NPs, as well as binary and ternary compounds such as Gd_5Si_4, $Gd_5Si_2Ge_2$ and $CuInSe_2$.

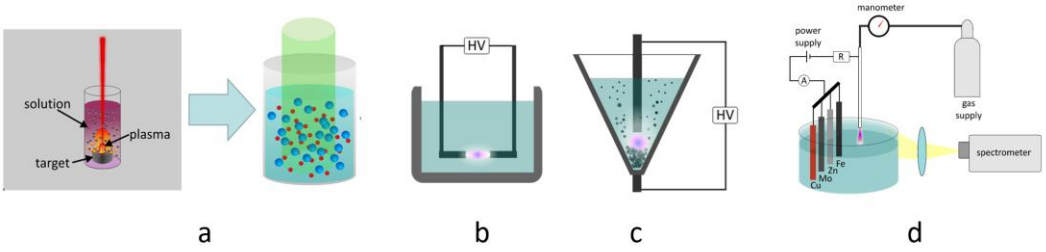

Figure 1 – Illustration of laser ablation and electrical plasma-based approaches developed for the synthesis of composite nanoparticles: a) laser ablation in liquid with an additional laser-induced modification, b) submerged discharge and c) electrical discharge treatment of micropowders in liquid, d) the experimental setup for the synthesis of multimetallic nanomaterials based on plasma in contact with a liquid

To obtain core-shell nanostructures, an approach based on laser ablation of a target (core) in a salt solution or a colloidal solution of another element (shell) was tested. It should be noted that laser ablation of metal targets in water, as a rule, forms NPs coated with an oxide shell. The wider possibilities for controlling size, composition and structure configuration of hybrid nanomaterials obtained by the laser-plasma method are achieved with laser ablation in an external electric field. As experiments have shown, when an electric field is applied to an ablated target immersed in a liquid, nanomaterials of non-spherical morphology are formed. Depending on the applied voltage and polarity, as well as the composition of a liquid, laser ablation of zinc in an external electric field allows the creation of nanoflowers and nanodisks in the case of laser ablation in water or sponge-like structures when ablation was carried out in a solution of carbon NPs. Application of the electric field to the target and substrate during laser ablation in liquids has been shown to be capable both of varying the NPs morphology and of their simultaneous deposition into ordered hierarchical nanostructures on the counter electrode. The fabrication of nanostructures with a developed surface is important for applications of the obtained nanomaterials in the fields of energy generation and storage.

Also, various approaches based on electrical discharges in liquids such as discharge between two electrodes made of different materials (Figure 1b), discharge processing of mixtures of two or more colloidal solutions or micropowders under a liquid layer (Figure 1c); successive discharges with post-discharge laser treatment of the resulting NPs have demonstrated to be efficient tools for the synthesis of alloyed and doped NPs, including alloys of elements immiscible under equilibrium conditions. Another NPs synthetic route utilizing electrical discharges in contact with a liquid (Figure 1d) has been shown to be

capable of not only synthesis of composite NPs but also of NPs deposition during synthesis, as well as modification of the NPs surface that is important for improving their properties such as solubility, biocompatibility, and photoluminescence. In this case, the composition of a solvent is the decisive factor influencing the surface composition of the NPs produced.

Special attention has been paid to the development of methods for the formation of silicon NPs, as well as doped and hybrid Si- based nanostructures. This interest is explained by the fact that modern progress in such areas as opto- and microelectronics, photovoltaics and thermoelectric applications relies on the use of silicon, that requires development of new efficient technologies for the synthesis and processing of such structures. In this work, a new method based on variation of laser beam energy distribution on a target surface has been adopted for the synthesis of silicon-based nanostructures. To form hybrid silicon NPs decorated with silver and/or gold NPs, an approach has been developed based on the ablation of a Si target using a laser radiation focused using a combination of an axicon and a collecting lens. The idea is to form a ring-shaped distribution of light on the target surface. A mixture of gold and silver NPs, preliminarily prepared by laser ablation of the corresponding targets in acetone, was used as a solvent. As shown by the TEM images, hybrid NPs were obtained, having a quasi-spherical shape with a diameter of 30-50 nm, and decorated with NPs of a smaller size. For doped silicon structures formation, a method based on laser ablation of silicon plate covered by thin tin film under ethanol layer has been shown to be applicable. Furthermore, the synthesis of silicon-tin composite NPs has been initiated both in a solution above the treated substrate, as well as on the surface of the treated substrate with the formation of composite metal-silicon structures.

Among the novel developed methods, those applicable for the fabrication of perovskite and multielement NPs are of special interest. As an example, a new approach based on simultaneous plasma-induced anodic dissolution of metal electrodes in plasma for the synthesis of NPs and thin films of gadolinium ferrite perovskite is proposed and tested. In the developed synthesis scheme, metal plates of gadolinium and iron are used as solid precursors, and NPs are generated as a result of the reactions induced by atmospheric pressure plasma at the boundary of the capillary cathode and water surface. Characterization of the NPs by SEM, EDX, XRD, FTIR, and Raman spectroscopy confirmed the formation of gadolinium ferrite with an orthorhombic structure. EDX mapping showed a uniform distribution of Gd, Fe, and O in the NPs and thin films with a Gd:Fe ratio close to the stoichiometric value expected for $GdFeO_3$. The developed approach allows combining NPs synthesis with their simultaneous assembly into thin nanostructured antiferromagnetic films of $GdFeO_3$, that opens

the way to the production of complex nanostructures of metal oxides and their practical applications.

Similarly, a combined plasma-laser method for the synthesis of multimetallic oxide nanomaterials based on non-equilibrium plasma in contact with a liquid with additional laser-induced modification of the resulting NPs is proposed and tested (Figure 1d). A distinctive feature of the approach is simultaneous anodic dissolution of several solid metal plates immersed in a liquid and subjected to plasma-activated electrolysis. The developed approach has been used to obtain a nanomaterial composed of Zn, Fe, Mo, Cu and Mn oxides and can be extended to nanomaterials of other compositions, demonstrating the capabilities of a universal nanomaterials synthesis tool applicable for production of nanomaterials of complex multi-element composition for applications as electrodes of new generation energy storage devices. Based on the results obtained, it can be assumed that the mechanism for the formation of multimetallic NPs in the developed approach includes dissolution of the anode material followed by the processes of reduction of metal ions by electrons and radicals formed during the interaction of the plasma cathode jet with the liquid surface.

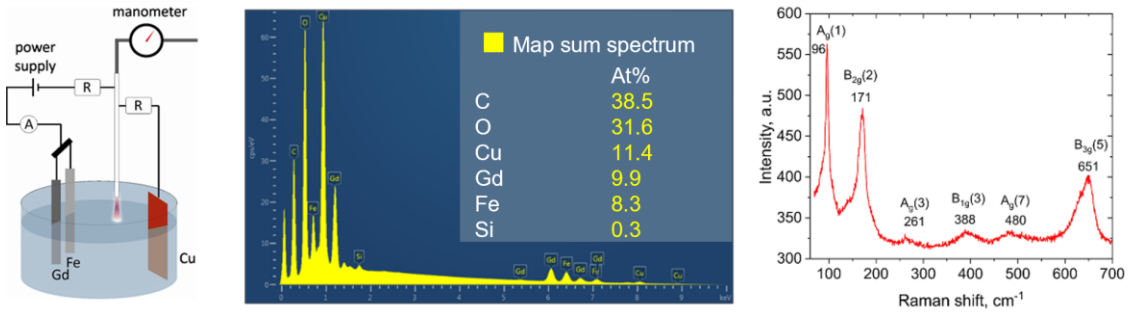

Figure 2 - a) Schematic of the experimental setup used for the synthesis and simultaneous deposition of perovskite $GdFeO_3$ NPs; b) EDX spectrum and elemental composition (at.%) of the film averaged over several points; c) Raman spectrum of $GdFeO_3$ NPs deposited on the substrate during the synthesis process

Acknowledgements. The work was supported by the National Academy of Sciences of Belarus under project Convergence 2.2.05 and by the Belarusian Foundation for Fundamental Researches under Grants F23RNF-156.

References

1. **Tarasenka N.N.** et al Intern. J. of Nanoscience, 18(2019) 1940049.
2. **Tarasenka N.N.** et al Applied Physics A 128 (2022) 749.
3. **Tarasenka N.N.** et al Appl. Surface Science 554 (2021) 149570.
4. **Tarasenka N.N**. et al Heliyon, 8 (2022) e09554.
5. **Tarasenka N.N**. et al ACS Appl. Nano Mater. 6 (2023) 5918.
6. **Tarasenka N.N.** et al J. of Appl. Spectroscopy 90 (2023) 253.

OPTICALLY PUMPED RARE GAS LASER

Yu.A. Adamenkov, M.A. Gorbunov, A.A. Kalacheva, V.A. Shaidulina, A.V. Yuriev

FSUE «RFNC-VNIIEF», Sarov, Russia
e-mail: oefimova@otd13.vniief.ru

Abstract: This paper presents the results of experiments on the study of optical pumped rare gas laser (OPRGL). Dependences of generation power on repetition frequency of discharge pulses and on gas mixture flow rate for medium 2% Ar + 98% He are presented. Result of generation of second harmonic at wavelength 456 nm is presented.

Keywords: optical pumped rare gas laser (OPRGL), rare gases, diode pump, diode laser spectroscopy, metastable atoms.

1. INTRODUCTION

Optical pumped rare gas lasers (OPRGL) are new promising lasers in which high quantum efficiency is combined with excellent optical quality of the output beam. The optical medium of the laser consists of a mixture of gases containing a buffer gas (usually helium) and a gas on the atoms of which generation occurs - Ne, Ar, Kr or Xe. The content of generating gas in the mixture varies from 1 to 5%. Since receiving the first generation on inert gas atoms (Kr) in 2012 /1/, studies of the active medium /2,3/ have been carried out aimed at optimizing laser parameters, such as increasing the generation output and the efficiency of using optical pumping. The production of metastable atoms has been studied, which can be organized using an electron beam /4/. Optical pumping of the active medium can be carried out by a diode laser or a dye laser /5/. work /6/ presents the achieved level of output radiation power at Ar atoms (912 nm) of 4 W using longitudinal pumping.

This paper presents the results of experiments to measure the output power of OPRGL, both with transverse and longitudinal optical pumping. Optical pumping was a 120 W diode laser at a wavelength of 811.53 nm. During the experiments, the following parameters were varied: pressure and flow rate of the gas medium, transmission coefficient of the mirrors of the optical resonator, repetition rate of electric discharge pulses. The maximum generation power obtained in the experiments is 4.5 watts. Experiments to convert OPRGL radiation into a second harmonic were carried out.

2. THEORY AND EXPERIMENT

The energy levels of inert gas atoms involved in the laser cycle are shown on Fig. 1.

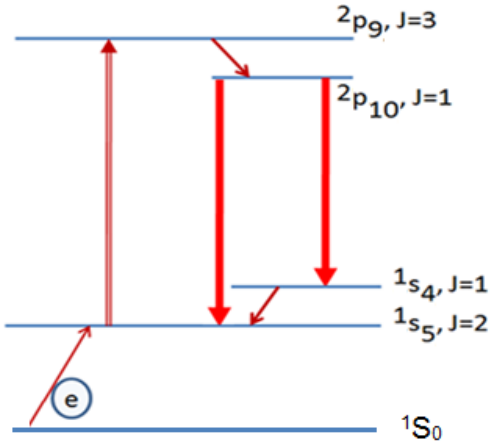

Figure 1 – Excited levels of rare gas atoms involved in laser cycle

The lower laser level is the first excited level np5 (n + 1) s (or $^1s_5$ in Paschen notation), the occupation of which occurs when an electric discharge passes. The energy of this level for an argon atom is 11.55 eV. The OPRGL laser cycle includes optical excitation of the transition between $^1s_5$ and $^2p_9$, collision relaxation to the $^2p_{10}$ level, and laser generation at the transition between $^2p_{10}$ and $^1s_5$. Since the level np_5 (n + 1) s is split into 4 levels, laser generation is possible both in a three-level (at the level [3/2] 0, J = 2) and in a four-level scheme.

Fig. 2 represents our OPRGL experimental setup. The pre-prepared gas mixture enters the system from a volume. The rate of gas supply and the pressure of the gas medium are controlled by the leak valves located before and after the laser volume. The pressure of the gas medium in the region of the discharge chamber was measured by electronic pressure sensor. The key element of the laser, in which metastable atoms are produced and laser generation occurs, is the discharge chamber, where an electric discharge occurs. The discharge chamber is a system of quartz tubes welded together, to which electrode holders and windows for introducing optical pumping are soldered in pairs. The electrodes are made of tungsten (anode) and tantalum (cathode) foil measuring 15 × 3 × 0.5 mm. The distance between the electrodes was 3 mm. A laboratory handmade power supply was used to create a pulse-periodic discharge. Single discharge pulse is shown in Fig. 3. A diode laser with a wavelength of 811.53 nm and a power of 120 W was used as optical pump. To focus the pumping radiation into the discharge area was used a cylindrical lens. The optical resonator consisted of a spherical mirror with a radius of curvature of 50 cm (dull) and a flat output mirror. Output mirrors with reflectance of 55%, 67%, 75%, 88% and 95% were used. The distance between the mirrors was 16.5 cm. The radiation power of OPRGL was measured using an optical power meter.

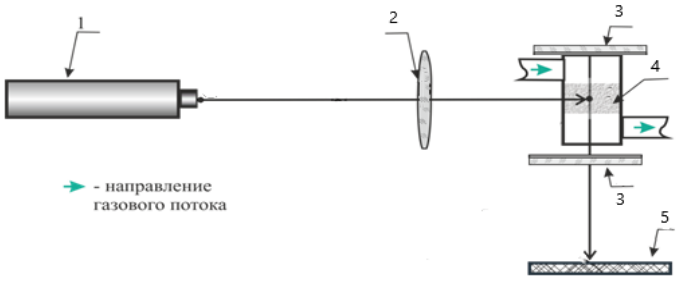

1 – pump laser, 2 – focusing lens, 3 – optical resonator, 4 – discharge area, 5 – power meter

Figure 2 – Experimental setup

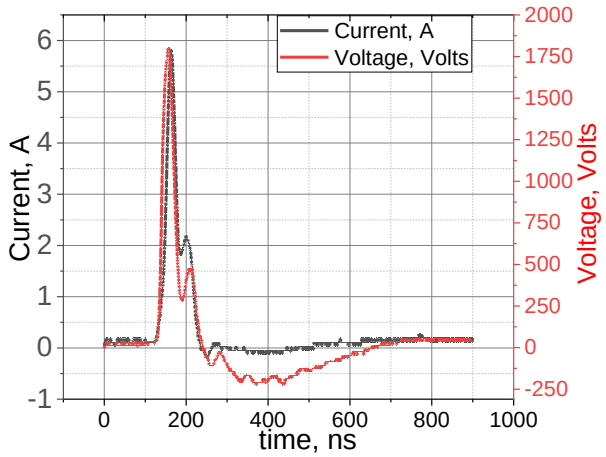

Figure 3 – Voltage and current of single pulse of discharge

3. RESULTS

The main recorded parameter of the experiments was the generation power. Variable parameters were: pressure and flow rate of the gas mixture in the discharge chamber, reflection coefficient of the output mirror of the (flat) optical resonator, frequency of repetition of discharge pulses. In experiments gas flew free via discharge area; after the discharge chamber, the gas mixture exhausted freely into the ambient atmosphere.

Fig, 4 shows the dependence of the output power (normalized) on the gas mixture flow rate. In the case of transverse pumping, the maximum laser generation power is achieved with a gas mixture flow rate of about 10 l/min, longitudinal pumping - at 4 l/min. Preliminary cooling of the gas mixture with liquid nitrogen (LN_2) increases the generation power by 0.5 - 1 W. The maximum lasing power achieved was 4.5 watts at the frequency of repetition of discharge pulses of 120 kHz.

To convert OPRGL radiation into a second harmonic, a non-linear LBO crystal with dimensions of 3x3x315 mm was used, placed inside the optical resonator. Radiation at 456 nm was obtained. The radiation power was less than 1 mW, but was clearly visible to the naked eye.

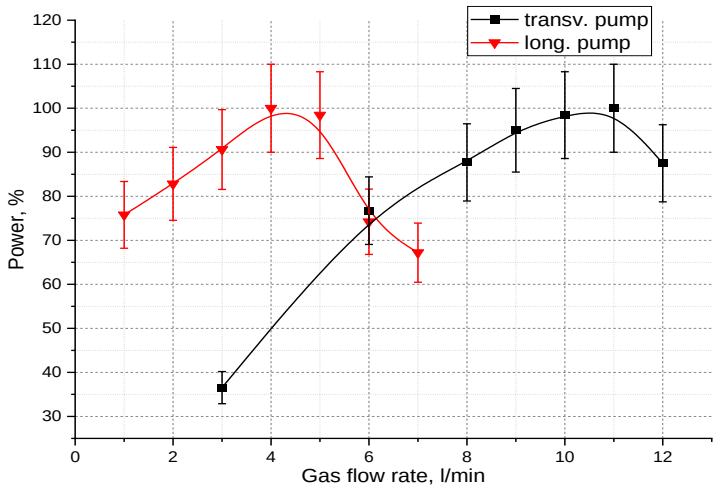

Figure 4 – Output laser power vs. gas flow rate

CONCLUSION

Experiments to measure the output optical power of OPRGL with a change in such parameters as: pressure and flow rate of the gas medium, transmission coefficient of the mirrors of the optical resonator, repetition rate of electric discharge pulses were carried out. For a mixture of 2% Ar + 98% He, the maximum achieved lasing power was 4.5 W at a pressure of 1.25 atm and a mixture flow rate of 9 l/min. Generation of second harmonic of Ar* lasing at wavelength 456 nm was obtained.

REFERENCES

1 J. Han, M.C. Heaven. Gain and lasing of optically pumped metastable rare gas atoms // Optics Letters. – 2012. - Vol. 37, No. 11, pp 2157-2159

2 Sun P., Zuo D., Mikheyev P.A., Han J., Heaven M.C. Time-dependent simulations of a CW pumped, pulsed DC discharge Ar metastable laser system // Opt. Express., 27, 22289 (2019)

3 P.A. Mikheev // Quantum Electronics – 2015, 45, № 2

4 P.A. Mikheev, A.K. Chernyshov, M.I. Svistun, et.al. // Optics Express. - 2019. – V.27, № 26, c. 38759-38767

5 Rawlins W.T., Galbally-Kinney K. L., Davis S. J., Hoskinson A. R., Hopwood J. A., Heaven M. C., Optically pumped microplasma rare gas laser // Opt. Express.,23(4), 4804 (2015)

6 J. Han, M.C. Heaven, P.J. Moran. Demonstration of a CW diode-pumped Ar metastable laser operating at 4 W // Optics Letters. – 2017. - Vol. 42, No. 22, pp 4627-4630

ON THE INFLUENCE OF ELECTRON VELOCITY SPREAD ON THE OPERATION OF COMPTON FELS DRIVEN BY LASER PLASMA ACCELERATORS

S. Anishchenko

Research Institute for Nuclear Problems,
Bobruiskaya street 11, 220006, Minsk, Belarus
sanishchenko@mail.ru

One of the most important challenges in modern physics is the investigation of fast processes on atomic space-time scales using ultrashort pulses of electromagnetic radiation. In this regard, the development and commissioning of X-ray free electron lasers (XFELs) is of great importance /1/. Over the past 20 years, since the first lasing in the soft X-ray range, the progress achieved in this area has been truly impressive. During this time, the radiation wavelength has decreased by two orders of magnitude, from 13.7 to 0.634 Å, the duration of X-ray pulses has stepped into the attosecond range, and the peak power has exceeded 1 TW, and the pulse repetition rate has increased significantly. Moreover, to reduce the size and therefore the cost of XFELs, new methods for accelerating particles and generating electromagnetic radiation have been proposed. In particular, XFELs driven by laser-plasma accelerators are being actively developed /2/. Futhermore, sources of induced parametric radiation, which arises when electron bunches pass through $\sim 100\ \mu$m thick crystals, are proposed as an alternative to undulator FELs /3/.

Progress in XFELs is largely due to a deep understanding of particle-field interaction and statistical phenomena (shot noise and velocity spread) /1, 4/. To date, software packages are available that take all of these phenomena into account in simulations. However, there is still a need for simple models that help us better understand the physical processes occurring in FELs /5, 6/. Unfortunately, the main attention is paid to models that do not take into account electron velocity spread which, as numerical simulations show, plays an important role in FEL operation /6/.

In this regard, the present article is devoted to a simple FEL model that allows for a detailed study the weakly nonlinear particle-field interaction in the presence of electron velocity spread. Namely, using numerical solutions of the derived nonlinear equation for the field amplitude a /7/, we will calculate frequency detuning spectra for XFELs driven by laser-plasma accelerators and compare the spectra with those obtained using particle simulations.

When neglecting radiation slippage and diffraction effects, the amplification in a Compton FEL is described by the following system of equations /5/:

$$\frac{d\phi_j}{d\bar{z}} = \eta_j,\ \frac{d\eta_j}{d\bar{z}} = ae^{i\phi_j} + a^* e^{-i\phi_j}, \quad (1)$$

$$\frac{da}{d\bar{z}} = -\langle e^{-i\phi_j}\rangle + i\delta a, \quad (2)$$

where a is the scaled radiation field, $\phi_j = (k + 2\pi/\lambda_u)z_j - ckt$ and $\eta_j = \frac{\gamma_j - \gamma_0}{\rho\gamma_r}$ are the j^{th} electron phase and scaled energy, $\bar{z} = 4\pi\rho z/\lambda_u$ denotes the scaled distance along the undulator, and $\delta = \frac{\gamma_0 - \gamma_r}{\rho\gamma_r}$ is the frequency detuning. The scaled quantities in (1) and (2) are expressed through the undulator period λ_u, the speed of light c, the electron position z_j in the undulator, the wave vector k of electromagnetic field propagating along the system axis, the Pierce parameter ρ. In the case of a helical undulator, the quantities k and λ_u are related with each other by the expression $k\lambda_u/4\pi = \gamma_r^2/(1 + K^2)$. For a planar undulator, the relationship can be written as $k\lambda_u/4\pi = \gamma_r^2/(1 + K^2/2)$. In the above formulas, K is a dimensionless parameter proportional to the amplitude of the spatially variable magnetic field of the undulator, while γ_0 and $\gamma_r \approx \gamma_0$ are the average Lorentz factor of electrons and the resonance Lorentz factor, respectively.

The quantities η_j are responsible for the phase change along the undulator axis. If there is no initial spread of electron velocities, then $\eta_{0j} = \eta_j(0)$ are equal to zero at $\bar{z} = 0$. Otherwise /4/, the electron velocities and η_{0j} acquire random values $\Delta\beta_{zj}c$ and

$$\eta_{0j} \approx \frac{k\lambda_u\Delta\beta_{zj}}{4\pi\rho}. \quad (3)$$

respectively. If the beam is monoenergetic, then $\Delta\beta_{zj} \approx -\theta_j^2/2$ is valid /4/. (The symbol θ_j denotes the angle between the undulator axis and the velocity of the j^{th} particle at the moment of entry into the system.)

We will assume that, when entering the undulator, there is no field acting on the particle ($a(0) = 0$). Then, the radiative instability begins to grow from small perturbations of the beam density, which are caused by shot noise and (or) e-beam pre-modulation. The magnitude of these perturbations is determined by the initial value of the bunching factor $b_0 = b(0) = \langle e^{-i\phi_j(0)}\rangle \neq 0$ ($|b_0| \ll 1$) /5/.

Averaging (1)—(2) over initial η_{0j} and ϕ_{0j} leads to the following integro-differential equation /7/

$$\frac{da}{d\bar{z}} = i\delta a + iJ_1(2|A|)e^{i\arg A}. \quad (4)$$

Here, A is equal to

$$A = \int_0^{\bar{z}} \int_0^{\bar{z}_2} a(\bar{z}_1) \frac{e^{-\sigma^2(\bar{z}-\bar{z}_1)^2/2}}{1-i\sigma_\theta(\bar{z}-\bar{z}_1)} d\bar{z}_1 d\bar{z}_2 + b_0 \frac{e^{-\sigma^2\bar{z}^2/2}}{1-i\sigma_\theta\bar{z}}, \quad (5)$$

The quanities

$$\sigma = \frac{\Delta\gamma}{\gamma\rho} \quad (6)$$

and

$$\sigma_\theta = \frac{k\lambda_u}{4\pi\rho}\langle\theta_j^2\rangle \quad (7)$$

are responsible for the energy and angle variations, respectively. The typical values of σ and σ_θ are tenths of unity /7/.

To solve (4), it is necessary to set four parameters: the initial value of bunching factor b_0, the frequency detuning δ, as well as σ and σ_θ. Let us note that the linearization (4) leads to an equation different from that derived in /4/, since the latter deals with different boundary conditions. The integral kernels in (5) and /4/ coincide completely.

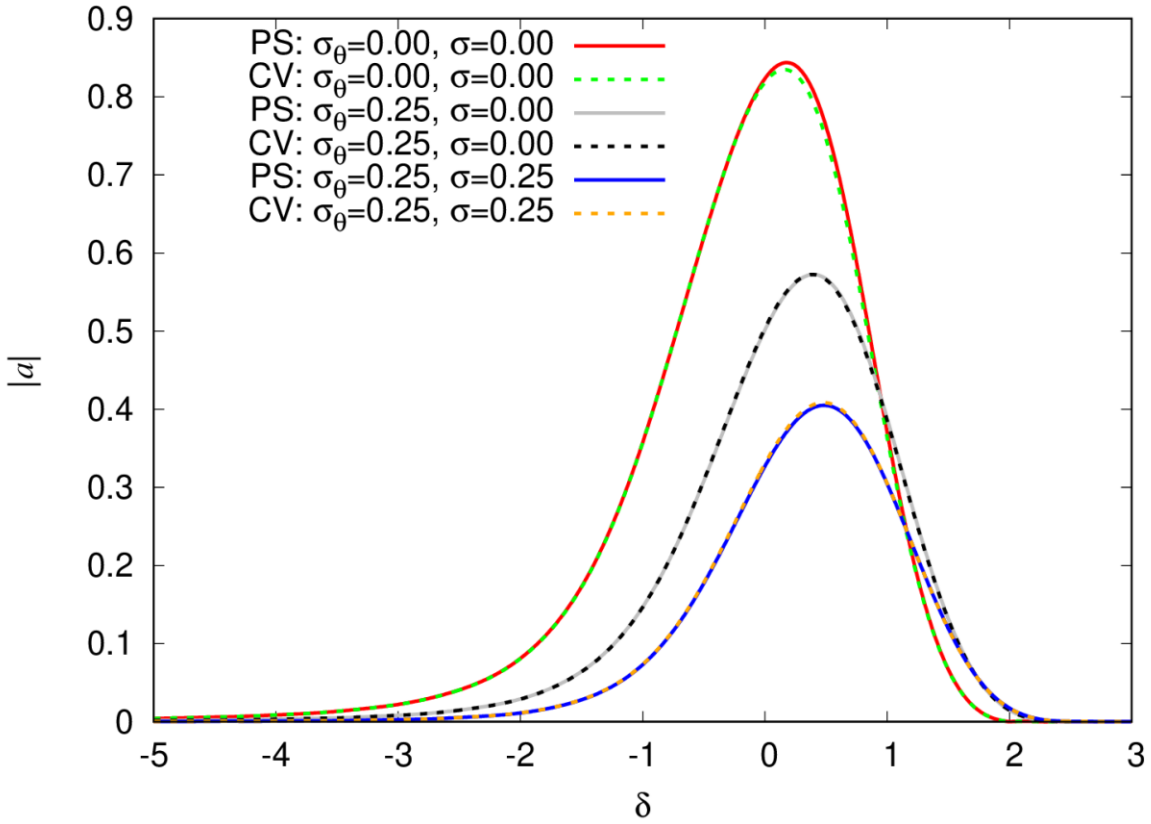

Fig. 1 – Frequency detuning spectra for $\bar{z} = 10$

Using numerical solutions of the integro-differential equation (IDE), we will calculate frequency detuning spectra for different values of σ and σ_θ. To do this,

following /5/, we choose $b_0 = 5 \cdot 10^{-4}$ as the initial value of the bunching parameter. Fig. 1 shows frequency detuning spectra for $\bar{z} = 10$. (The similar case with no velocity spread was considered in /5/.) The choice of $\bar{z} = 10$ is not accidental: at larger $\bar{z}$, discrepancies in the bunching factor b with particle simulations (PS) arise. (When solving the integro-differential equation (4), the maximum value of the bunching parameter is limited by the maximum value of the Bessel function $\max(J_1(x)) \approx 0.582$.) At the same time, the frequency detuning spectra calculated using the two approaches are still in good agreement with each other. This circumstance is primarily due to the short transition time from the linear stage to saturation /7/. During the transition, the inaccuracy in b does not have a noticeable effect on the field amplitude a.

We can conclude that an integro-differential equation for the field amplitude was derived to describe the operation of a Compton FEL in the presence of electron velocity spread that is typical for modern facilities. The solutions of the equation demonstrate a good agreement with the results obtained from particle simulations for the bunching factor below 0.6. Moreover, the solutions reproduce the frequency detuning spectrum near its maximum and describe the radiation amplification in the FEL up to saturation even for higher $\bar{z}$ /7/. The agreement with particle simulations is primarily due to the short transition time from the linear stage to saturation. During the transition, the inaccuracy in the bunching factor, which determines the degree of saturation, has little effect on the field amplitude.

Acknowledgements. The author thanks Professor V.G. Baryshevsky for valuable comments and discussions of the results obtained.

References

1. Seldon E.A., et al. Rep. Progr. Phys. 80 (2017) 115901.
2. Nguyen F., et. al. NIM A 1074 (2025) 170291.
3. Baryshevsky V.G., Phys. Rev. Accel. Beams 27 (2024) 120701.
4. Colson W.B., et al. Phys. Rev. A 34 (1986) 4875.
5. Hemsing E., Phys. Rev. Accel. Beams 23 (2020) 120703.
6. Robles R.R., Giannessi L., Mainelli A. Phys. Rev. Res. 6 (2024) 033158.
7. Anishchenko S.V. ArXiv: 2503.01552 [physics.acc-ph] (2025).

X-RAY RADIOGRAPHY OF SUBSTANCE STRUCTURE OF ALUMINUM TUBE DURING EXPLOSION ON THE GIT-12 FACILITY

A. Artyomov, A. Rousskikh, V. Oreshkin, A. Zhigalin

Institute of High Current Electronics SB RAS,
Akademichesky Ave. 2/3, Tomsk, 634055, Russia, E-mail: artyomov@ovpe.hcei.tsc.ru

In the physics of Z-pinches, the phenomenon of stratification is known, when in the process of an electrical explosion of a conductor (metal wire, tube or foil) a structure of alternating regions with dense and rarefied plasma is formed /1-3/. Moreover, this structure changes over time. Traditional spectroscopic diagnostic methods for measuring the substance density in strata are not suitable because they do not allow measurements to be made in local regions and with the necessary time resolution. A good alternative in this sense is the method of pulse radiography, where an X-pinch is used as a source of probing X-ray radiation /2-4/.

Experiments on X-ray radiography of the explosion of an aluminum cylinder were carried out on the pulse power generator GIT-12 (current amplitude of 5 MA and current rise rate of 2 μs) /5/. The GIT-12 load was an aluminum tube with outer and inner diameters of 10 and 8 mm, respectively. The compact pulse power generator XPG (current amplitude 240 kA and current rise rate 240 ns) was used for X-ray radiography of the object under study /3, 4/. The XPG load was an X-pinch consisting of four 25 μm diameter molybdenum wires. The experimental diagnostic scheme is shown in Fig. 1. The XPG vacuum chamber with an X-pinch was connected to the GIT-12 vacuum chamber. The camera with the film was connected to the vacuum chamber GIT-12 on the opposite side to X-pinch. The photographic film was placed behind a 0.4 μm thick aluminum filter applied to 4 μm thick kymfoil film, and a 12 μm thick polypropylene film filter. This composite filter transmitted radiation with an energy of $h\nu > 1.3$ keV. An aluminum step-wedge consisting of four steps of 250, 500, 750, and 1000 nm thick was sprayed to the polypropylene film using magnetron sputtering. In the experiment, an image of an aluminum tube and a step-wedge was simultaneously recorded on the photographic film.

Since the explosion of aluminum tubes creates a flow of flying matter that inevitably destroys filters and photographic film, they must be protected. For this purpose, an electromagnetic shutter was developed, which was installed in the optical path directly in front of the camera. The shutter closed immediately after the generation of the X-ray pulse of the radiograph. The operating principles of the shutter are described in /6/.

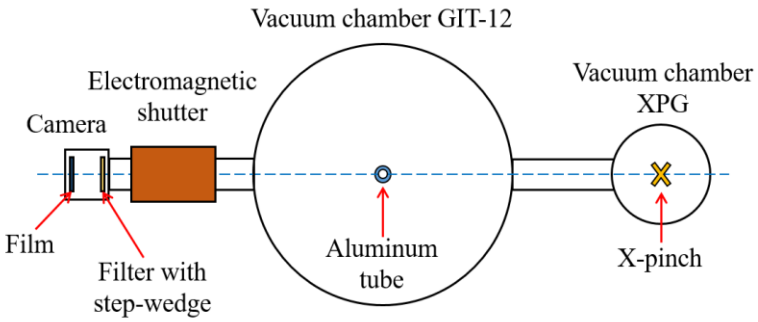

Fig. 1. The experimental diagnostic scheme.

The method for determining the density of plasma formed during the explosion of an aluminum tube is a development of the method for analyzing radiographic images described in /4/. Fig. 2a shows a radiographic image of an explosion of an aluminum tube. The observed dense areas of matter in the boundary layer of the plasma of the exploded tube are strata. The experimental image on the right shows a step-wedge. Additionally, a piece of aluminum foil 6 μm thick was installed in front of the step-wedge to expand the range of optical density values of the step-wedge image. The optical density values of the wedge steps were used to find the relationship between the optical density D_{film} of the film and the photon range in the substance Q:

$$Q = \int_0^h \rho dx \approx \rho \cdot h, \tag{1}$$

where ρ and h are the density and thickness of the substance layer, respectively. The relationship between Q and D_{film} was represented as a second-order polynomial /4/:

$$Q = a \cdot D_{film}^2 + b \cdot D_{film} + c, \tag{2}$$

where the coefficients a, b, and c were determined by the X-ray spectrum and its intensity.

The optical density distribution across an image of the aluminum tube, $D_{\text{film}}(r)$, was determined for cross sections Z_1 and Z_2 with thickness h at the required point along the z axis (fig. 2a). The thickness of the cross-section h was chosen to be equal to the sampling step of the experimental distribution of the optical density of the tube image by radius. The sampling step was determined by the optical resolution of the film scanner CanoScanFS4000US and was equal to: $h = 2.85 \cdot 10^{-4}$ cm. Thus, the value h specifies the size of the elementary area of the substance through which the probing X-ray radiation passes. Let us assume that the slice cross-sections are azimuthally symmetrical relative to the z axis. Let us also assume that the location of the outer boundary of the slice cross-section corresponds to the radius at which the probing X-ray radiation ceases to be absorbed, which was $R \approx 6.3$ mm (fig. 2). In this case, the thickness of the absorption layer is equal to the length of the chord of the cross section of

the plasma cylinder. In this way, the dependence of the range of the probe radiation photons in the material on the aluminum tube radius $Q(r)$ was obtained (Fig. 2b). Note that at a radius of $r < R_{in} \approx 4$ mm, the aluminum tube substance became opaque to the X-pinch X-ray radiation.

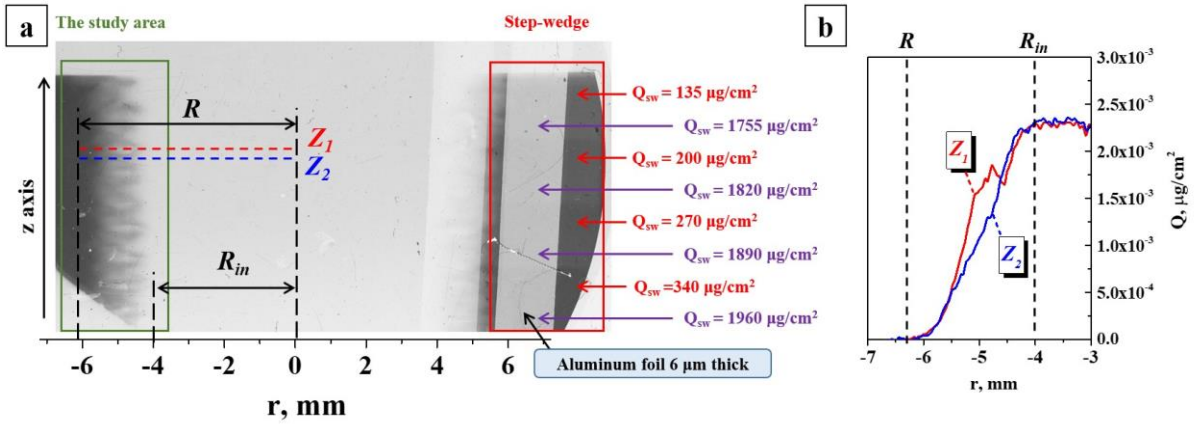

Fig. 2. Radiographic image of an exploding aluminum tube (a) and distributions of the photons range Q along the radius of the cross-sections Z_1 and Z_2 (b).

The task of the work was to obtain the distribution of the substance density by radius in the plasma shell of the aluminum tube. For this purpose, the studied region, enclosed between the radii R and R_{in}, was divided into ring layers. The scheme of the division of the cross section into ring layers is shown in Fig. 3a. The width of each ring was equal to h. Further calculations were made based on the assumption that the density of the substance inside each ring was a constant value. The calculation starts from the outer radius of the plasma cylinder R and moves to the radius R_{in}.

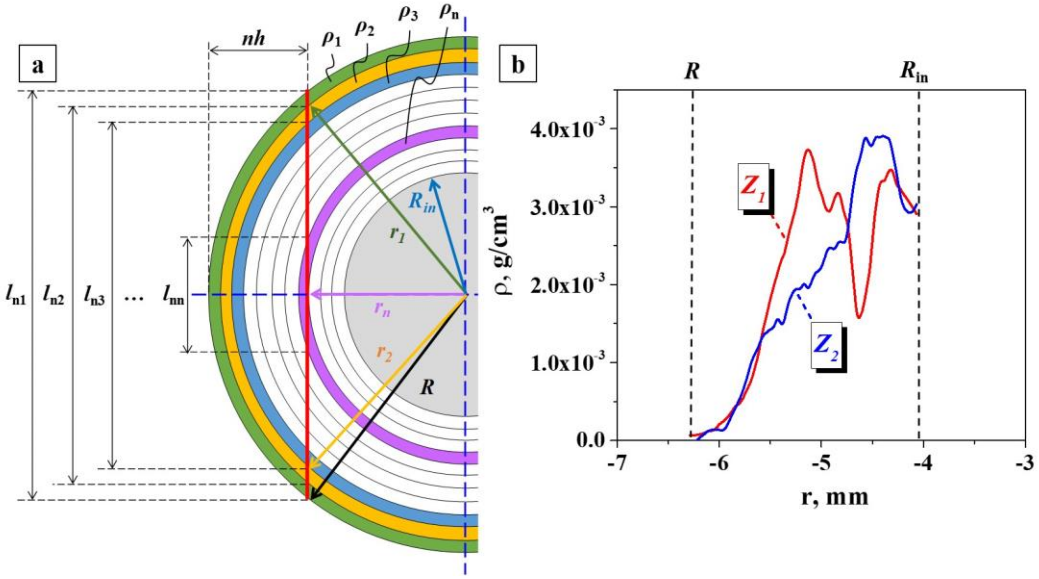

Fig. 3. Scheme of division of the cross-section into ring layers (a) and distributions of the substance density ρ along the radius of the cross-sections Z_1 and Z_2 (b).

Let us consider the chord l_{n1}, shown by the red line in Fig. 3a. It passes through rings from 1 to n inclusive. The substance density inside ring n can be estimated from the expression:

$$\rho_n = q_n / l_{nn}, \tag{3}$$

where q_n is the local range of the photon range along a substance layer of thickness equal to the chord l_{nn}. The local range of photons can be found from the expression:

$$q_n = Q_n - \sum_{k=1}^{n-1} \int_{l_{nk+1}}^{l_{nk}} \rho_k dl, \tag{4}$$

where Q_n is the total value of the photon range along a layer of thickness l_{n1}, measured in the experiment, ρ_k is the substance density calculated for rings with numbers from 1 to n-1 in previous iterations, and the chord lengths l_{nk} are determined as:

$$l_{n1} = 2\sqrt{R^2 - r_n^2}, \; l_{n2} = 2\sqrt{r_1^2 - r_n^2}, \ldots l_{nn} = 2\sqrt{r_{n-1}^2 - r_n^2}, \tag{5}$$

where $r_n = R - n \cdot h$ is the radius of ring n. In this way, the substance density can be estimated at a point corresponding to the radius r_n.

As a result, the method described above made it possible to reconstruct the distribution of the substance density from the radius of the exploded aluminum tube (Fig. 3b). The hump of the substance density distribution Z_1 in fig. 3b corresponds to the stratum observed in fig. 2a. The plasma density in this region reaches a value of $3.9 \cdot 10^{-3}$ g/cm^3, which corresponds to an ion concentration in the plasma of $8 \cdot 10^{19}$ cm^{-3}. The plasma density in the rarefaction region (curve Z_2) at the point where the radius $r = 5$ mm was $2 \cdot 10^{-3}$ g/cm^3, which corresponds to an ion concentration of $4.5 \cdot 10^{19}$ cm^{-3}, which is almost two times less than in the striation region.

Acknowledgements. This work was supported by the Russian Science Foundation (grant No. 25-19-00352).

References

1. **Baksht R.B.** Technical Physics, 58(2013) 1129-1137.
2. **Sinars D.B.** Physics of Plasmas, 8(2001) 216-229.
3. **Baksht R.B.** Physics of Plasmas, 22(2015) 103521.
4. **Rousskikh A.G.** Current Applied Physics, 19(2019) 704-708
5. **A. A. Kim.** Matter and Radiation at Extremes, 1(2016) 201-206.
6. **Zhigalin A.S.** Proceedings of 9th International Congress on Energy Fluxes and Radiation Effects. Tomsk, Russia (2024) 160-163.

OPTIMIZATION OF THE ELECTROLYTIC PLASMA POLISHING PROCESS OF TC4 ALLOY USING TAGUCHI METHOD

S.I. Bahayeu, I.P. Smyaglikov, A.A. Parshuto, E.A. Klimova

Physical-Technical Institute of NAS of Belarus,
220141 Minsk, 10 Kuprevich str., sibahaev@rambler.ru

Titanium and its alloys have a good combination of mechanical and corrosion-resistant characteristics, resistance to high temperatures and biocompatibility. Due to this, they have found wide application in the chemical industry, aerospace, mechanical engineering and medicine /1/. It should be noted that titanium alloys are characterized by poor mechanical workability due to their low thermal conductivity and elastic modulus, tendency to cold-work hardening and sticking to the cutting tool /2, 3/. Particularly difficult is the finishing of titanium parts, where the requirements for surface quality are increased. For example, in the aviation industry, parts must have high reliability, which is characterized by surface integrity. Surface integrity is determined by such parameters as surface roughness, residual stresses, microstructure and microhardness /3/. In articles /4, 5/, it was shown that a decrease in surface roughness directly affects the fatigue strength of parts. In articles /6, 7/, it was shown that a decrease in the roughness of implants below 0.1 μm significantly reduces the risk of postoperative complications. In most cases, traditional methods of mechanical processing as finishing methods are not effective enough, since they form a defective surface layer in which stresses and microcracks are concentrated /2, 3/. An alternative method of finishing (polishing) the surface is electrolytic plasma polishing (EPP). EPP allows achieving high surface quality with minimal material degradation /8, 9/. Different processing modes and electrolyte compositions are used for EPP of titanium and its alloys /10, 11, 12/. The aim of our work is to investigate the EPP process of titanium alloy TC4 and optimize its processing modes according to the combined criterion of reducing surface roughness and metal removal *ΔRa-h*: achieving the maximum change in surface roughness with minimal metal removal.

The experimental samples were flat rectangular plates with dimensions of 24×24×2 mm, made of TC4 alloy. EPP was carried out in the anodic potentiostatic mode at a voltage on the electrodes of 320–340 V and a processing time of 4–6 min. The samples were processed in a solution based on potassium fluoride and ammonium fluoride, with a total concentration of fluoride ions of 0.45–0.55 mol/l. The solution temperature was maintained in the range of 80–90 °C. In this work, the Taguchi method /13/ was used to optimize the multifactorial EPP process according to the *ΔRa-h* criterion. This method allows one to obtain the required result with a minimum number of experiments. An orthogonal matrix L_9 was used with four control factors at three levels each: A – Voltage (V), B – Solution temperature (°C), C – EPP time (min), D – Ammonium fluoride concentration (mol/l) (Table 1).

Table 1. Experimental factors and their levels

Factor	Level 1	Level 2	Level 3
A: Voltage EPP, V	320	330	340
B: Temperature of solution, °C	80	85	90
C: Time EPP, min	4	5	6
D: Concentration of NH_4F, mol/l	0,15	0,20	0,25

The optimization criterion of the EPP process *ΔRa-h* was to obtain the maximum reduction in surface roughness ($\Delta Ra \rightarrow \max$) of the titanium sample with minimum metal removal ($h \rightarrow \min$).

$S/N_{\Delta Ra\text{-}h}$ was calculated using formula 1:

$$S/N_{\Delta Ra\text{-}h} = (S/N_{\Delta Ra} + S/N_h)/2 \quad (1)$$

where

$$S/N_{\Delta Ra} = -10 \cdot \log_{10}(1/\Delta Ra^2) \quad (2)$$

$$S/N_h = -10 \cdot \log_{10}(h^2) \quad (3)$$

Table 2 shows the L_9 experiment matrix and the results obtained.

Table 2. L_9 planning matrix with experimental data

№ experiment	A (V)	B (°C)	C (min)	D (mol/l)	ΔRa (μm)	h (μm)	$S/N_{\Delta Ra}$ (dB)	S/N_h (dB)	$S/N_{\Delta Ra\text{-}h}$ (dB)
1	320	80	4	0,15	0,34	21,17	-9,37	-26,51	-17,94
2	320	85	5	0,20	0,34	21,81	-9,37	-26,77	-18,07
3	320	90	6	0,25	0,39	21,56	-8,18	-26,67	-17,43
4	330	80	5	0,25	0,4	25,75	-7,96	-28,22	-18,09
5	330	85	6	0,15	0,39	26,62	-8,18	-28,50	-18,34
6	330	90	4	0,20	0,27	14,06	-11,37	-22,96	-17,17
7	340	80	6	0,20	0,44	32,07	-7,13	-30,12	-18,63
8	340	85	4	0,25	0,39	18,49	-8,18	-25,34	-16,76
9	340	90	5	0,15	0,46	18,33	-6,74	-25,26	-16,00

Next, based on the obtained data, the average S/N for each factor level (Fig. 1) for the *ΔRa*, *h*, *ΔRa-h* criteria were calculated. Regardless of the criterion, a higher S/N value corresponds to a better result. Therefore, the optimal level of processing parameters is the level with the highest S/N value. From the data in Fig. 1, based on the S/N ratio, it can be seen that the maximum change in surface roughness *ΔRa* occurs at a voltage of 340 V, 80 °C for 6 min of processing, with an ammonium fluoride concentration of 0.15 mol/l. The minimum metal removal *h* occurs at a voltage of 330 V, 90 °C for 4 min. of processing, with an ammonium fluoride concentration of 0.2 mol/l. With the combined *ΔRa-h* criterion, the best result is achieved at a voltage of 340 V, 90°C for 4 min of treatment, at an ammonium fluoride concentration of 0.15 mol/l.

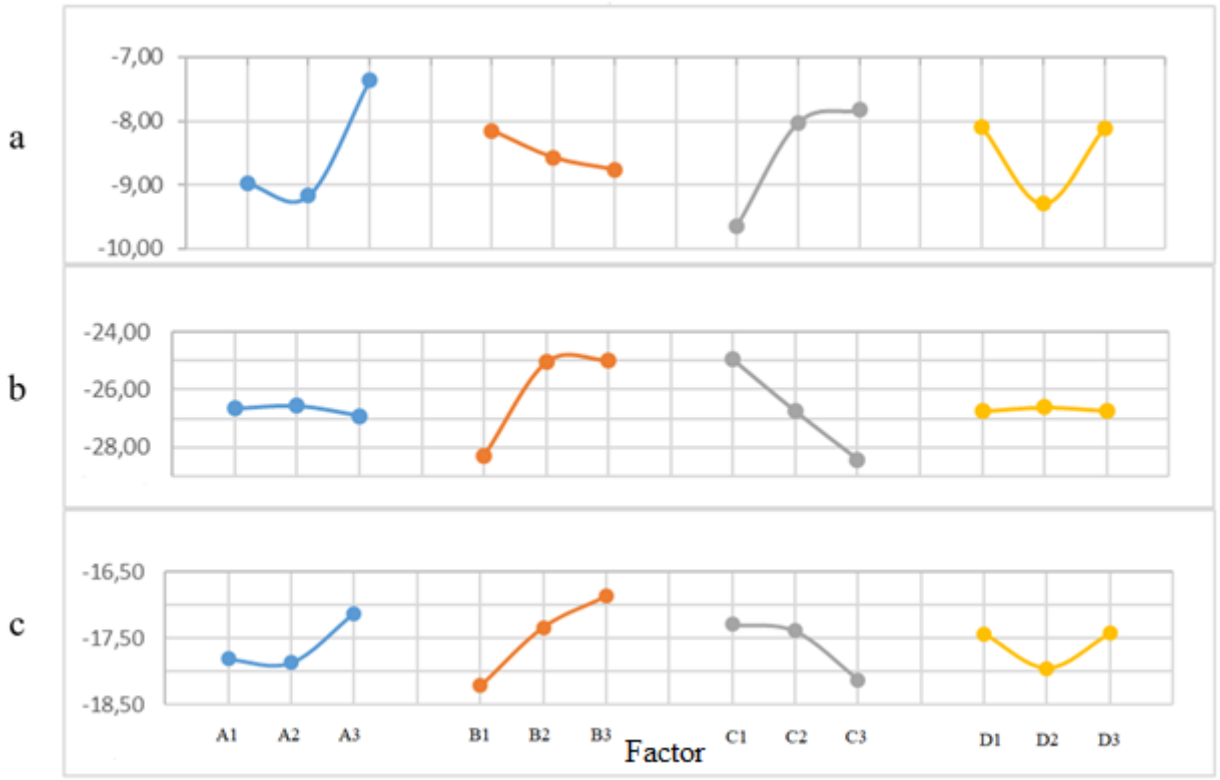

Fig. 1. Main effects for average S/N factors influencing the criterion *ΔRa* (a), *h* (b), *Ra-h* (c)

To identify the degree of influence of factors on *ΔRa*, *h* and *ΔRa-h* during the course of EPP, an analysis of variance (ANOVA) was performed /14/. The results of the analysis are presented in Table 3.

Table 3. ANOVA results for *ΔRa*, *h* and *Ra-h* criteria

Factor	SS (sum of squares)	df	MS (middle square)	F-ratio	Influence, %
For the criterion *ΔRa*					
A (V)	5,98	2	2,99	10,15	39,0
B (°C)	0,59	2	0,29	1,00	3,8
C (min)	5,93	2	2,96	10,07	38,7
D (mol/l)	2,83	2	1,42	4,81	18,5
Error	0,59	-	0.29	-	-
For the criterion *h*					
A (V)	0,41	2	0,20	1,64	1,0
B (°C)	23,57	2	11,78	94,46	55,1
C (min)	18,55	2	9,27	74,35	43,4
D (mol/l)	0,25	2	0,12	1,00	0,6
Error	0,25	-	0,12	-	-
For the combined criterion *ΔRa-h*					
A (V)	1,02	2	0,51	1,80	17,6
B (°C)	2,92	2	1,46	5,15	50,5
C (min)	1,28	2	0,64	2,26	22,1
D (mol/l)	0,57	2	0,28	1,00	9,8
Error	0,57	-	0,28	-	-

The following conclusions can be drawn from the data in Table 3:

1. The *ΔRa* criterion is most strongly influenced by the processing voltage (39%) and the duration of the EPP (39%). The concentration of ammonium fluoride has a moderate effect (18.5%). The temperature of the solution has a minor effect – 4%.

2. The maximum effect on metal removal *h* is exerted by the temperature of the solution (55%) and the duration of the processing (43%). The processing voltage (1%) and the composition of the solution (1%) have a minor effect.

3. The greatest influence on the combined *ΔRa-h* criterion is the temperature of the solution (50%). The duration of the EPP and the processing voltage are comparable in their effect and amount to 22% and 18%, respectively. The composition of the solution has an effect of less than 10%.

Thus, as a result of the study using the Taguchi method, the optimal conditions for electrolytic-plasma polishing of the TC4 alloy were determined taking into account the maximum surface roughness decreasing of the titanium sample with minimal metal removal: at a voltage of 340 V, a solution temperature of 90 °C for 4 min of processing, with an ammonium fluoride concentration of 0.15 mol/l. In this case, the solution temperature has the main influence on the *ΔRa-h* criterion.

References

1. **Leyens C. and Peters M**. Titanium and Titanium Alloys: Fundamentals and Applications. – Weinheim: Wiley-VCH, 2003.
2. **Davim J. P.** (ed.), Machining of Titanium Alloys, Materials Forming, Machining and Tribology. – Springer-Verlag Berlin Heidelberg, 2014.
3. **Moussaoui K. [et al**.]. Advanced Materials Research, 698 (2013) 127-136.
4. **Wycisk, E. [et al.].** Advanced Materials Research. 816-817 (2013). 134-139.
5. **Chastand V. [et al.].** Materials Characterization, 143 (2018) 76-81.
6. **Geetha M. [et al.].** Progress in Materials Science, 54 (2018) 397-425.
7. **Pazos L., Corengia P., Svoboda H.** Journal of the Mechanical Behavior of Biomedical Materials, 3, No. 6 (2010) 416-424.
8. **Kulikov I.S., Vazhenko S.V., Kamenev A.Y.** Electrolytic plasma treatment of materials. – Minsk: Belarusian Science, 2010. (In Russian).
9. **Belkin P., Kusmanov S., Parfenov E.** Applied Surface Science Advances, 1 (2020) 100016.
10. **Bahayeu S. I. and Smyaglikov I. P.** Plasma physics and plasma technology: IX International conference, Minsk (2018) 421–424.
11. **Huang Y. [et al.].** The International Journal of Advanced Manufacturing Technology. 114 (2021) 1893-1912.
12. **Dongliang Yang [et al.].** Coatings 2024, 14(5), 615.
13. **Ross P.J.** Taguchi Techniques for Quality Engineering, 2nd ed., McGraw-Hill, New York, USA, 1996.
14. **Montgomery D. C.** Design and Analysis of Experiments. 9th Edition – Hoboken, NJ: John Wiley & Sons, Inc, 2017.

DIFFUSION FLUX ENHANCEMENT IN DEPOSITION PROCESS

D.A. Butniakov[1], I.A. Sorokin[1,2], D.V. Kolodko[1,2]

[1]National Research Nuclear University Moscow Engineering Physics Institute, Moscow, Russia, email: butnyakovda@yandex.ru
[2]Kotel'nikov Institute of Radio Engineering and Electronics (Fryazino Branch), Russian Academy of Sciences, Fryazino, Russia

In high-pressure sputtering systems (>10 Pa), the transport of sputtered material diverges significantly from high-vacuum conditions due to frequent atomic collisions and thermalization. While Monte Carlo models are effective for low-pressure magnetron sputtering, where the mean free path exceeds target-substrate distances, computational demands increase at higher pressures. For instance, a 3D model required 90 minutes on a 56-core server /1/, prompting the use of alternative methods, such as PDE-based finite element modeling /2/. Accurate simulation must account for system, vessel and substrate geometry.

We have solved the stationary diffusion equation ($\nabla^2 c = 0$) with a finite-element model that uses the full geometry of ion-plasma sputtering systems (IPSS) based on planar asymmetrical hollow cathode discharge (HCD) /3/ (both aperture and target diameters 50 mm and 168 mm), taking into account chamber walls and substrate holder. Experimental validations were conducted using those two setups. The first one had a 50 mm diameter of output aperture /4/ was used for tungsten coating deposition on copper substrate (40 Pa Ar, 1400 eV ions) placed 5 cm from the sputtering system. The second one had a 168 mm diameter of output aperture and was used for nickel coating deposition on a tantalum substrate (18 Pa Ar, 1900 eV ions) placed 4 cm from the sputtering system. Film thickness profiles, analyzed with EPMA /5/ and EDS, revealed a significant increase in deposition rate at substrate edges (Fig. 1a and 1b), consistent across high-pressure conditions. This edge deposition flux enhancement mirrors the electrostatics problem, where convex geometries amplify electric field strength due to analogous Laplace-type equations ($\Delta c=0$ and $\Delta\varphi=0$) governing concentration gradients that define both fluxes and strength of electric fields.

The following qualitative description of the observed phenomenon is proposed (Fig. 2) /4/. Near the edge of the substrate, particles can move into empty space and then return to their original place due to Brownian motion. Consequently, the areas of constant concentration c are located closer to the edge of the substrate compared to the space above the flat surface. On the contrary, a lower concentration is expected to be near the concave geometry, since there are more surface areas around the particle on which it can settle. Alternatively, this phenomenon can be explained by considering the solid angle covered by the constant concentration curve for each point on the surface of the

substrate. This angle is proportional to the deposition probability of a particle and, therefore, proportional to the final flux in the considered point on the substrate. However, it should be noted that this curve is considered only at distances comparable to several mean free path lengths. As a result, Fig. 1 shows the result of a larger flux coming to the edge due to the displacement of the line of constant concentration closer to the substrate (j ~ ∇c, and on the surface, it can be assumed for simplicity that $c = 0$).

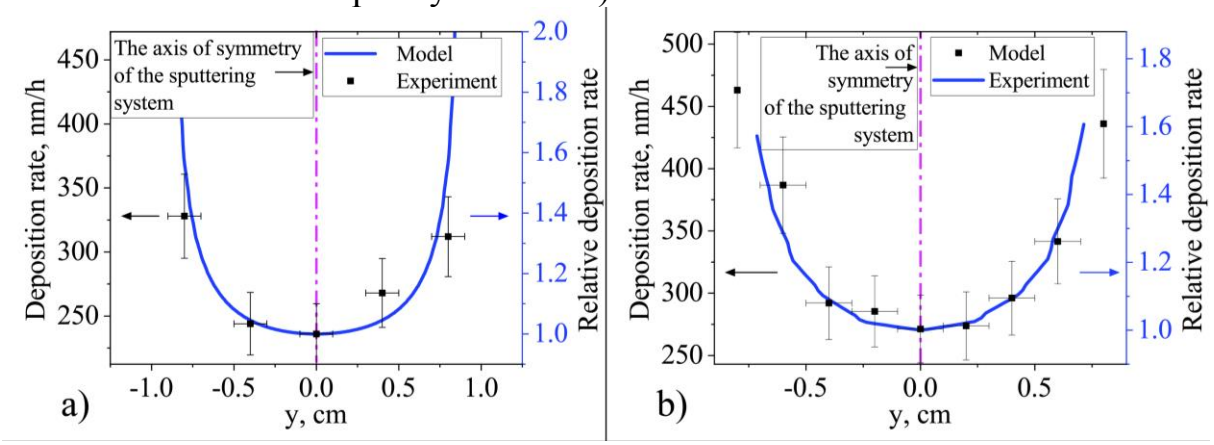

Fig. 1 Profiles of deposition rate on the substrate with diffusion flux enhancement at the edges achieved with IPSS based on planar asymmetrical HCD with diameter of target: a) 50 mm /4/; b) 168 mm

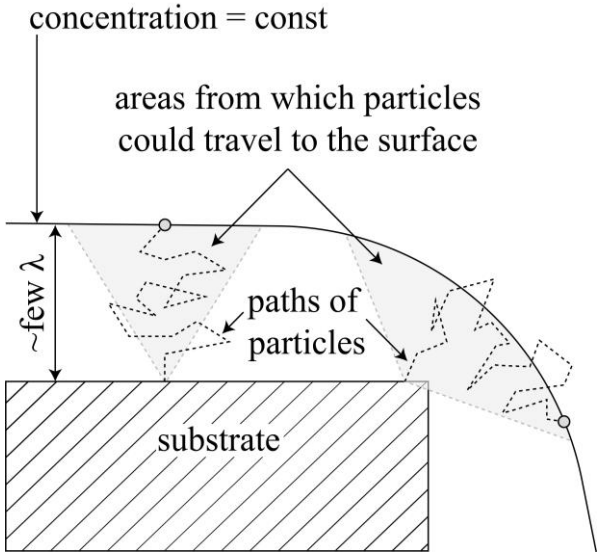

Fig. 2 Diffusion flux enhancement scheme

At low pressures (>10 Pa), when the free path is comparable to the size of the vacuum chamber (or more than it) and greater than the size of the substrate, the deposition profile will have a Gaussian-shaped curve with a maximum at the area where sputtering rates are highest. As an example, in magnetron deposition,

when the substrate is close to the target, coatings formed with the greatest thickness take the form of coating opposite the racetrack.

The observed edge effect of enhanced diffusion flux occurs in various operating modes when the mean free path length at the pressure used is much smaller than the characteristic linear dimensions of the system. Moreover, the nonuniformity of the plasma density distribution inside the discharge gap has no significant effect on the resulting thickness profile of the coating. Fig. 3 shows several measurements of plasma density by a single Langmuir probe along the diameter inside the discharge gap between two plane-parallel cathodes in the sputtering system with an output aperture (and target) diameter of 168mm. Profiles diverge from each other in many different parameters – working gas pressure, voltages applied to the electrodes. It can be seen in Fig. 3a that the working modes of the used IPSS can vary significantly. Sometimes plasma can effectively shield the potentials of the cathodes in the entire discharge gap (Profile 1). And sometimes it cannot, and in the center of the discharge gap, there is a very significant drop in the plasma density distribution (Profiles 2 and 3). However, these differences have no effect on the shape of the deposition rate on the substrate at all. Fig. 3b shows the experimental deposition rate distribution across the substrate and the calculated ones with 4 different plasma density profiles (profiles 1-3 correspond to those shown in Fig. 3a).

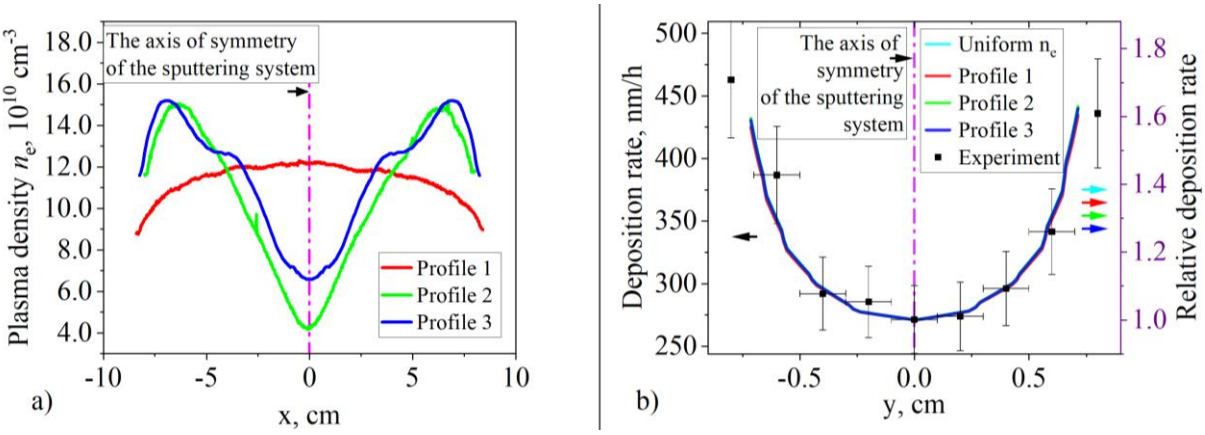

Fig. 3 a) Plasma density profiles along the diameter of the IPSS based on the asymmetrical planar HCD; b) Comparison of deposition rates calculated by model with different ne profiles and experimental data

The similarity in deposition rate shapes is explained by the diffusive nature of the transport of the sputtered atoms. Multiple collisions blur the initial particle flux, and it takes on a similar shape on the substrate for all four profiles. Thus, when films are deposited at pressures >10 Pa, measurements of local plasma parameters are unnecessary for calculations of the transport and thickness profiles of the resulting coatings. Measurements of plasma parameters

to determine the ionic saturation current can be replaced by measuring the total current on the target. It is proportional to the average values of the plasma parameters (according to the Bohm formula).

Additionally, non-thermalized sputtered atoms (several eV initial energy) introduce complexities, as diffusion models assume thermalization and smallness of the deviation from equilibrium. Studies suggest replacing the thermalization calculations by the Monte-Carlo method with a virtual particle source /6/, similar to the Child-Langmuir law's virtual cathode /7/.

Diffusion flux enhancement phenomenon could help to form a thin film with nonuniform, inhomogeneous, predictable, and controllable thickness across the surface of the substrate. It could be used in optics or to produce wear-resistant edge parts for tools. Finally, it is possible to use developments in the field of electrostatics and transfer them to diffusion issues - the solutions will have the same appearance due to the similarity of the mathematical formulation of the problems.

Acknowledgements. The study of diffusion flux enhancement in deposition process was carried out within the framework of the state task "Physico-chemical fundamentals of the development of lithium components facing plasma" (FSWU – 2025-0004).

References

1. **J. Li, Q. An, H. Fang,** Monte Carlo simulation of deposition uniformity in the triple-target magnetron co-sputtering system, Appl. Surf. Sci. 646 (2024) 158914. https://doi.org/10.1016/J.APSUSC.2023.158914.
2. **T. Smy, L. Tan, S.S. Winterton, S.K. Dew, M.J. Brett,** Simulation of sputter deposition at high pressures, J. Vac. Sci. Technol. A 15 (1997) 2847–2853. https://doi.org/10.1116/1.580838.
3. **I.A. Sorokin, D.V. Kolodko**, Planar hollow cathode sputtering with asymmetrical voltage supply, Vacuum 207 (2023) 111570. https://doi.org/10.1016/j.vacuum.2022.111570.
4. **D.A. Butnyakov, I.A. Sorokin, D. V. Kolodko**, Diffusion Transport of Target Material for a Planar Asymmetrical Hollow Cathode Sputtering System, Plasma Chem. Plasma Process. (2025). https://doi.org/10.1007/s11090-025-10550-7.
5. **I.A. Sorokin, D. V. Kolodko**, On the possibility of indirect measurement of the thin carbon films thickness using energy-dispersive analysis, Thin Solid Films 737 (2021) 138937. https://doi.org/10.1016/J.TSF.2021.138937.
6. **A.G. Zhiglinski, V. V Kuchinskiy, E.G. Sheikin**, TRANSFER OF SPUTTERED ATOMS IN GAS-DISCHARGE PLASMA, Zhurnal Tekhnicheskoi Fiz. 56 (1986) 1718–1723.
7. **C.D. Child**, Discharge From Hot Cao, Phys. Rev. (Series I) 32 (1911) 492–511. https://doi.org/10.1103/PhysRevSeriesI.32.492.

ACCOUNTING FOR THE MARANGONI EFFECT DURING ELECTROMAGNETIC MIXING IN AN ELECTRIC ARC LIQUID METAL MELT

M.Yu. Dokukin
Bauman Moscow State Technical University, 2-nd Baumanskaya St. 5,
Moscow, 105005 Russian Federation
E-mail: DMU252@yandex.ru

The necessity of studying the mixing processes of liquid metal components to obtain homogeneous alloys is substantiated. A mathematical model of the processes of electromagnetic mixing of alloys produced in an electric arc furnace, taking into account the Marangoni effect, has been developed. A numerical method is proposed to solve the problem. A special experiment is planned to test the proposed model.

Keywords: *modeling, experimental research, equations of hydro- and electrodynamics, magnetic field, metal melt, Marangoni effect, arc furnace*

Introduction

The relevance of the problems of studying the mixing processes of a liquid metal bath is dictated by the requirements of modern production of homogeneous alloys with special properties. Such tasks have been set and solved to varying degrees in [1-4]. The experimental verification of the present study is supposed to be carried out on a small-sized electric arc melting furnace described in [5].

We reported on the results of an experimental study conducted on a small-sized electric arc furnace with an external solenoid in order to study the effect of an external axial magnetic field on dynamics in a liquid metal and on the results of theoretical modeling of working processes in a melt produced in an electromagnetic crystallizer at the conference on Plasma Physics and Plasma Technology (PPPT-4) [6], and a more detailed analysis of these results was given in the article [7].

In this paper, the theory of the main operating processes in this furnace is developed by including the Marangoni effect in a previously developed model. This effect may be caused by a possible temperature dependence of the surface tension coefficient under the conditions of the forming liquid metal melt. The Marangoni effect leads to the appearance of convective movements on the surface directed from areas with lower surface tension to areas where the value of this coefficient is higher, which ultimately causes the generation and propagation of initial disturbances in the form of so-called Marangoni instability circulation cells. The system of such cells, which is physically related to convection, temperature gradient, and a corresponding change in surface tension, is a typical dissipative structure [8]. It is believed that thermocapillary convection (or the Marangoni effect) is caused by the temperature dependence of the surface tension of a liquid

(in this case, a liquid metal melt) and the intensity of mixing of the melt is comparable to thermogravitational convection.

In addition, when reviewing and analyzing the well-known experiments of Thomson [9], it was noted that the Marangoni effect can affect the interphase surface if the penetration depth of interphase convection is commensurate with the thickness of the liquid layers. It is also expected that the Marangoni effect is responsible for a significant change in the phase contact surface in devices where part of the interfacial surface exists as unsupported or supported thin films. Under these conditions, the processes of mass and heat transfer can lead to the establishment of a gradient of interfacial tension and, as a result, to the movement of the interfacial surface itself.

Experiments show that the surface deformation has a stabilizing effect on existing films in the melt. With local thinning of the film, the surface tension increases. The appearance of a surface tension gradient causes the solution to flow from the area of low surface tension to the thinning points of the film. It is as if the weakened areas are healing.

In connection with the above, we have a question about an additional study of the effect of the thermocapillary effect in an electric arc liquid metal melt on the formation of homogeneous ingots, and, first of all, there was a need to modernize (taking into account this effect) the previously developed mathematical model of the main operating processes in a small-sized electric arc furnace.

Theoretical model and solution method

Modeling of the processes that occur in the metal melt included numerical integration of the system of equations of motion, continuity and energy, i.e., respectively:

$$\rho\left(\frac{\partial\vec{v}}{\partial t}+\left(\vec{v}\nabla\right)\vec{v}\right)=\left(-\vec{\nabla}p-\vec{\nabla}\left(\frac{\sigma_{st}}{r_s}\right)+\vec{j}\times\vec{B}\right)+\rho\vec{g}+\overrightarrow{rot}\,\mu\;rot\,\vec{v}$$

$$\frac{\partial\rho}{\partial t}+div\left(\rho\vec{v}\right)=0 \qquad \frac{\partial H}{\partial t}=\frac{1}{\rho}div\,\overrightarrow{grad}\,Kh-\left(\vec{v}\nabla\right)H,$$

where ρ is the density of the alloy, is the velocity of the melt particles, p is the pressure, σ_{st} is the surface tension coefficient for the melt, r_s is the radius of curvature of the melt surface, $\vec{g}$ is gravity acceleration, μ is dynamic viscosity, $\vec{j}$ is current density, $\vec{B}$ is magnetic field induction, $rot\mu\,rot\vec{v}$ is internal friction force, H is enthalpy, Kh is The Kirchhoff function ($Kh=\int\lambda\,dT$, where λ is the coefficient of thermal conductivity). These equations were solved together with the equations of the medium: $T=T\left(H\right), Kh=Kh\left(T\right), \rho=\rho\left(T\right), \sigma_{st}(T),$ where T is the temperature of the melt, with the Laplace equation $div\overrightarrow{grad}\varphi=0$, where φ is the electric potential, with Ohm's law $\vec{j}=\sigma\vec{E}=-\sigma\vec{\nabla}\varphi$, where σ is the electrical

conductivity, E is the electric field strength, with Maxwell's equation $rot\,\vec{B} = \mu_0\,\vec{j}$, where $\mu_0 = 4\pi\cdot10^{-7}$ Gn/m.

The boundary conditions for particle velocity were established based on the conditions of adhesion and non-breakage at the solid boundaries of a water-cooled mold and on the condition that the stress tensor is equal to the external pressure tensor on the free surface of the melt. The boundary conditions for the electric potential assumed the equipotential of the mold walls, taking into account the resistance of the transition layer (garnissage), as well as the normal Gaussian distribution of current density on the surface of the melt (ingot). The boundary conditions for the Kirchhoff function were established taking into account the coefficients of heat transfer through the metal wall of the mold to the cooling water. The heat flux density on the melt surface was chosen to be proportional to the current density with some concentration factor.

The state of the melt was determined by the value of the enthalpy H (a function of $T(H)$ taking into account the heat of the phase transition).

It is proposed to use a numerical approach to solving the problem based on the method of markers and cells with a number of additions [10]. Similarly, in [11-12], the processes in a metal bath were modeled, taking into account impurities, and our previous work [7].

The calculations are supposed to be carried out for the process of melting a titanium alloy with a garnissage in a water-cooled copper crystallizer with a diameter of $2R$ = 100 mm in order to obtain an ingot with a height of h = 12 mm (Fig. 1). Melting is assumed in an argon medium at a pressure of 2.66 kPa and an interelectrode gap of 23 mm. The focus is on the current modes of the arc I = 400

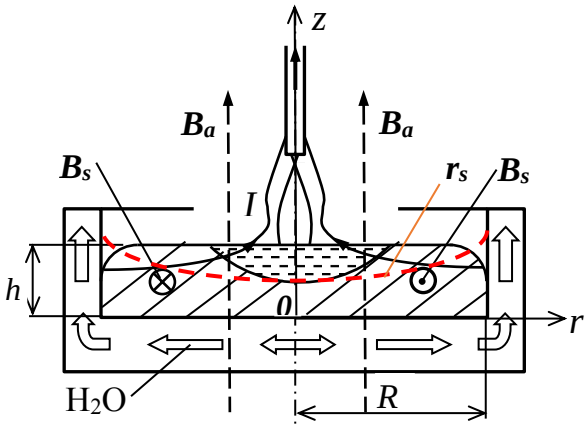

Fig. 1. The model of arc melting of an ingot under an external magnetic field: B_s is the intrinsic magnetic field of currents in the arc and in the metal; B_a is the external axial magnetic field; I is the arc current; r_s is the radius of curvature of the formed free surface of the melt (red dotted line)

A and 500 A in the presence and absence of an external magnetic field with an induction of B_a = 11 mT.

References

1. **Jeng S.-L., Su D.-P., Lee J.-T., Huang J.-Y.** Metals, (8)2018 630.
2. **Smirnov S.A., Kalaev V.V., Hekhamin S.M. etc**. High Temperature, (1)2010 68–76. DOI: 10.1134/S0018151X10010116
3. **Швыдкий Е. Л., Бычков С. А., Захаров В. В., Соколов И. В., Тарасов Ф. Е.** Электрометаллургия, (10)2018 11–17.
4. **Poliakov S.N., Korotchenko A.Yu., Timchenko S.L.** Journal of Physics: Conference Series, (918)2017. DOI: 10.1088/1742-6596/918/1/012001
5. **Anikeev V.**N., **Dokukin M.Yu.** Russian Metallurgy (Metalle), (6)2019 576-580.
6. **Dokukin M.Yu., Pshenichnikov A.A.** Plasma Physics and Plasma Technology: IV Intern. Conference, Minsk, 15-19 Sept. 2003 “PPPT-11”: Contr. Papers, (2)2003 799-802.
7. **Аникеев В.Н., Докукин М.Ю.** Электрометаллургия, (6)2020 27 – 31. DOI: 10.31044/1684-5781-2020-0-6-27-31.
8. **Николис Г., Пригожин И.** Самоорганизация в неравновесных системах: Пер. с англ. М.: Мир (1979).
9. **Thomson** J. Philosophical Magazine, (10)1855 330.
10. **Hirt C.W., Nichols B.D.** Journal of Computational Physics, (39)1981 201-225. doi.org/10.1016/0021-9991(81)90145-5
11. **Dimitrienko Yu.I.** Journal of Physics: Conference Series, (1141)2018 DOI: 10.1088/1742-6596/1141/1/012098
12. **Dimitrienko Yu.I., Bogdanov I.O.** Journal of Physics: Conference Series, (1141)2018 DOI: 10.1088/1742-6596/1141/1/012099

PLASMA-CHEMICAL PROCESS OF RESTORING THE PROPERTIES OF METAL POWDERS AFTER THEIR USE IN ADDITIVE MANUFACTURING

A.A. Fadeev, A.V. Samokhin, N.V. Alekseev, M.A. Sinaisky, D.E. Kirpichev, A.A. Dorofeev, I.V. Kulbakin

Institute of Metallurgy and Materials Science of the Russian Academy of Sciences, Russia
119334 Moscow Leninsky Prospekt-49, fadeev@imet.ac.ru;

The reuse of powders in additive manufacturing (AM) of metals is a key factor in ensuring economic efficiency under industrial conditions /1/. AM powders must meet specific physicochemical requirements, including particle size distribution, morphology, and gas impurity content /2/. Powder Bed Fusion (PBF) is a major AM technology, accounting for 54% of all AM systems /3/. In PBF, powder near the melt pool undergoes intense thermal exposure, altering its size distribution, shape, surface, and chemical composition /3/. Since the powder volume is determined by the build chamber size rather than the part itself, only a small fraction is used in the final product, while the rest—though altered—remains unused /3/. Given the high cost of powders, restoring their properties for reuse is essential. An effective method for regenerating Fe-, Ni-, Co-, W-, Mo-, and Re-based powders degraded in PBF is treatment in a hydrogen-containing thermal plasma, commonly used to produce spherical AM powders /4/.

In the experimental studies of the powder regeneration process, metallic micropowders that had undergone multiple reuse in additive manufacturing (AM) processes were used as research objects (precursors). These powders varied in particle size distribution and primarily contained elements whose oxides are reducible by hydrogen. The powders studied included: heat-resistant nickel-chromium alloy powders IN-718 (“+20–63” μm) and IN-625 (“+53–150” μm); precipitation-hardened stainless steel powder PS-Kh15N5D4B (“+25–71” μm); cobalt-chromium alloy powder PS-KhKM (“+25–63” μm); cobalt-based alloy powder VLK-1 (“+10–63” μm); and heat-resistant nickel alloy powder VZh-159 (“+10–63” μm). Figure 1 presents optical (OM) and scanning electron microscopy (SEM) images of the precursor powders. All samples show a common degradation feature—morphological changes, including particle sintering, formation of agglomerates, irregular shapes, and satellite particles. Table 1 summarizes the gaseous impurity content and technological characteristics of the precursor powders.

Experimental studies of the powder regeneration process were conducted using a plasma spheroidization and regeneration unit developed at the A.A. Baikov Institute of Metallurgy and Materials Science of the Russian Academy of Sciences (IMET RAS) /5, 6/.

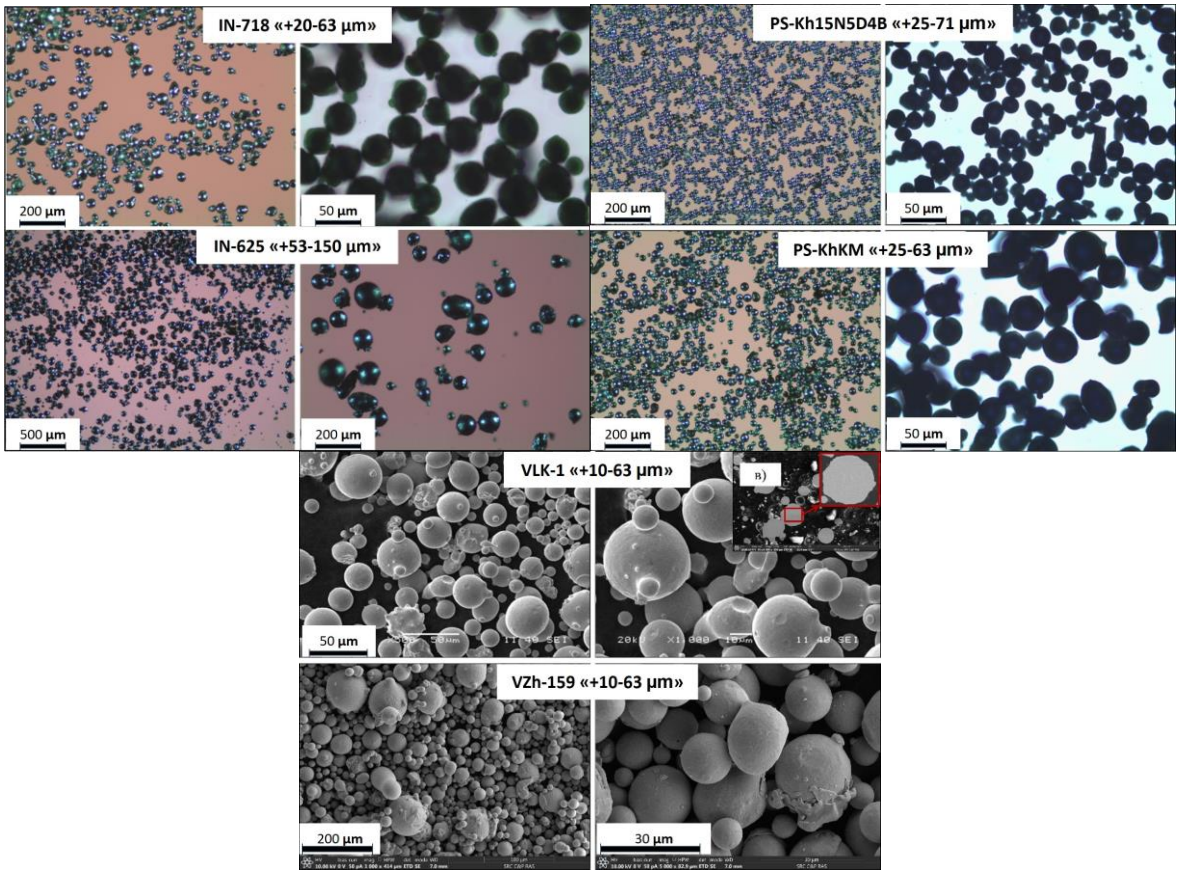

Figure 1. OM and SEM images of the precursor powder.

Table 1. Gaseous impurities and technological characteristics of the studied precursor samples.

Sample	[O], wt.%	[N], wt.%	Flowability, s/50 g	Bulk density, g/cm³
IN-718	0,031	0,14	19	4,6
IN-625	0,08	0,053	16	4,9
PS-Kh15N5D4B	0,079	0,111	15	4,4
PS-KhKM	0,063	0,128	14,3	4,9
VLK-1	0,030	0,0083	no	4,3
VZh-159	0,0256	0,0070	no	4,4

The spheroidization/regeneration process of powders in the IMET RAS plasma system involves intensive heating of precursor particles carried by a gas into the plasma jet, their melting, and formation of spherical droplets driven by surface tension forces /5,6/. This process enables regeneration, including morphological transformation and refinement of gaseous impurities (O_2, N_2). The main goal of plasma treatment is the significant modification or restoration of particle morphology and potential gas impurity reduction. Key process parameters influencing product quality (particle morphology) and productivity include plasma torch power, plasma flow specific enthalpy (defining its average

mass temperature), and material feed rate. Table 1 shows the parameter ranges used for plasma regeneration of the studied powders.

Table 1 – Powder Regeneration Parameters in Thermal Plasma.

Parameter	Value Range
Plasma torch power (N), kW	10 ÷ 31
Plasma-forming gas flow rate (G_{pl}), Ar, Ar + (up to 6 vol.%) H_2, Nm^3/h	2 ÷ 3,5
Plasma flow enthalpy (I_{pl}), kWh/m^3	1,45 ÷ 5,3
Carrier gas flow rate (G_{tr}), Ar, Nm^3/h	0,3 ÷ 1,0
Precursor powder feed rate (G_{pow}), kg/h	0,6 ÷ 11,2

Experimental results showed that increasing the plasma flow enthalpy from 1.45 to 5.3 kWh/m^3 during plasma regeneration of the studied powders increased the degree of particle spheroidization from 50% to 98%, with a circularity coefficient between 1 and 1.02. No surface defects such as satellites were observed (Fig. 2). A side effect of maximizing spheroidization is the formation of nanosized particles via partial evaporation of the particle surface. The nanosized fraction in the product ranges from 0 to 2 wt%. Across the precursor feed rates tested (0.6 to 11.2 kg/h), significant particle morphology changes occurred, with optimal spheroidization at 5–6 kg/h. To enhance plasma jet thermal conductivity and create a reducing atmosphere for plasma-chemical reduction of oxides, up to 6 vol.% hydrogen was added to the argon plasma-forming gas. Hydrogen presence facilitated refinement from gaseous impurities (O_2, N_2) (Table 6), with hydrogen levels in the treated product matching those in the precursors (<0.0008 wt.%) (Table 2).

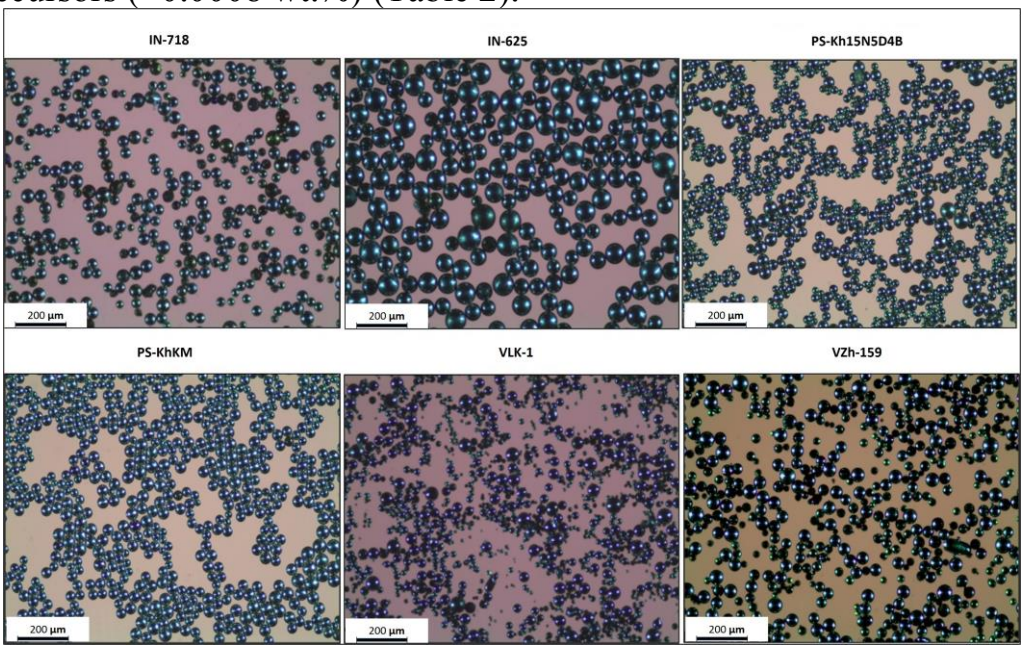

Figure 2. OM images of powders after plasma regeneration and nanosized fraction removal

Table 2. Gaseous impurities and technological characteristics of powders after plasma regeneration and removal of the nanosized fraction.

Sample	[O], wt.%	[N], wt.%	Flowability, s/50 g	Bulk density, g/cm³
IN-718	0,019	0,067	15	4,9
IN-625	0,055	0,039	14	5,1
PS-Kh15N5D4B	0,028	0,024	15	5
PS-KhKM	0,010	0,012	14	5
VLK-1	0,014	0,0053	14	5,2
VZh-159	0,019	0,0066	13	5

Acknowledgements. This work was carried out within the framework of the state assignment of the Ministry of Science and Higher Education of the Russian Federation (project No. 075-00319-25-00).

References

1. **Vojislav Petrovic, Rubén Niñerola.** Powder recyclability in electron beam melting for aeronautical use. Aircraft Engineering and Aerospace Technology: An International Journal, 2015, 87, 2, p. 147 – 155.
2. **Silvia Vock, Burghardt Klöden, Alexander Kirchner, et al.** Powders for powder bed fusion: a review. Prog Addit Manuf. 4, 383–397, (2019).
3. **Daniel Powell, Allan E.W. Rennie, Louise Geekie, Neil Burns.** Understanding powder degradation in metal additive manufacturing to allow the upcycling of recycled powders. Journal of Cleaner Production. 268, (2020), 122077.
4. **A.N.D. Gasper, D. Hickman, I. Ashcroft, et al.** Oxide and spatter powder formation during laser powder bed fusion of Hastelloy X. Powder Technology, 354, (2019), 333–337.
5. **Russian Patent No. RU2779558C1.** Samokhin A.V., Alekseev N.V., Fadeev A.A., Zavertyaev I.D., Kirpichev D.E., Sinaiskiy M.A. Method for regeneration of used metal powders from additive manufacturing in thermal plasma. Year of publication: 2022.
6. **Russian Patent No. RU2756327C1.** Samokhin A.V., Fadeev A.A., Kirpichev D.E., Alekseev N.V., Berestenko V.I., Astashov A.G., Zavertyaev I.D. Plasma apparatus for spheroidization of metal powders in a thermal plasma flow. Year of publication: 2021.

SIMULTANEOUS GENERATION AT THREE WAVELENGTHS IN OPTICALLY PUMPED HE-AR-KR MEDIUM

A.A. Kalacheva, Yu.A. Adamenkov, M.A. Gorbunov,
V.A. Shaydulina, A.V. Yuriev

FSUE «RFNC-VNIIEF» (Russia, Sarov, Mira prosp, 37)
E-mail: oefimova@otd13.vniief.ru

Abstract

The paper presents laser generation of optically pumped rare gas laser (OPRGL) simultaneously at wavelengths 912.3 nm and 893.1 nm using a gas mixture consisting of 98% He (buffer gas), 1.5% Ar and 0,5% Kr . Dependence of generation power and ratio of intensities of separate lines in overall generation on flow rate of gas mixture, pressure in cavity and repetition rate of discharge pulses is experimentally investigated. In the experiments carried out, the ratio of laser generation intensities on argon and krypton atoms was practically equal at the repetition rate of discharge pulses - from 80 to 100 kHz, mixture flow rate - from 8 to 9 l/min, mixture pressure - from $1.2 \cdot 10^5$ to $1.4 \cdot 10^5$Pa. The maximum achieved laser power level (total at all wavelengths) was about 8 mW.

Keywords: *optically pumped rare gas laser (*OPRGL*), argon, krypton, laser technologies*

Introduction

An optical pumped laser on metastable inert gas atoms (OPRGL) /1/. is a promising type of laser with high power, quantum efficiency and radiation wavefront quality. For the first time, generation on atoms of inert gases (IG) was obtained in 2012 /2, 3/. Currently, generation on Ar, krypton, neon and xenon atoms has been obtained. The paper /4/ reported on simultaneous generation at wavelengths of 893.1 nm and 877.7 nm at Kr atoms, while the generation at a wavelength of 893.1 nm was an order of magnitude higher than the generation at 877.7 nm. There are currently no publications reporting the simultaneous generation of inert gases on two or more atoms.

This paper presents the results of studies of OPRGL working according to the transverse scheme, the description of which is given in /5/ with simultaneous pumping at wavelengths of 811.5 nm and 811.3 nm and simultaneous generation at 912.3 nm, 893.1 nm and 877.7 nm /6/.

Theory

Figure 1 shows the electron levels of argon and krypton atoms involved in the laser cycle. Generation at wavelengths of 912.3 nm in argon and 893.1 in krypton occurs by the same mechanisms. The lower laser level 1s5 (in Paschen

notation) is occupied due to electron impact in discharge. The 2p9 level is filled by absorption of pump radiation at 811.5 nm in argon and 811.3 nm in krypton. The upper laser level 2p10 is filled by non-radiative collision relaxation from the pump level 2p9.

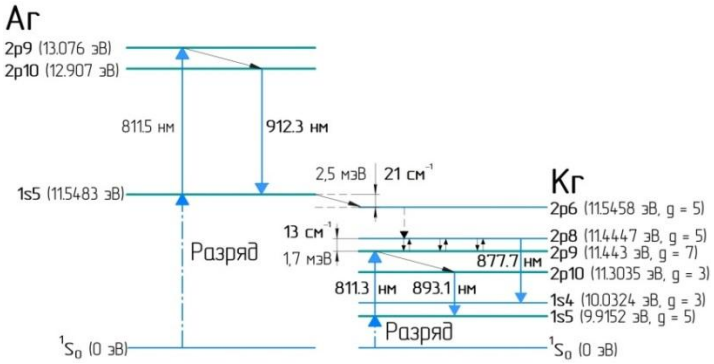

Figure 1 - Electron levels of argon and krypton atoms involved in the laser cycle

The energy of levels 1s5 of the argon atom and 2p6 of the krypton atom differ by 21 cm^{-1}, this contributes to the resonant transfer of excitation from level 1s5 of the argon atom to level 2p6 of the krypton atom in collisions. The concentration of krypton atoms excited to the level of 2p6 and, as a result of radiation and collision relaxation, metastable krypton atoms increases.

Description of pilot plant

Simultaneous generation at wavelengths of 912.3 nm and 893.1 nm was obtained using a transverse optical pumping scheme. The experimental design is shown in Figure 2.

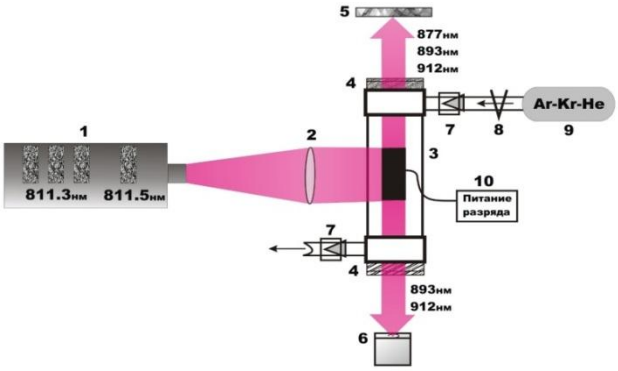

Figure 2 - Experimental procedure
1 - pump laser, 2 - lens (cylindrical lens), 3 - discharge area, 4 - optical resonator mirrors (a - spherical, b - flat), 5 - screen, 6 - calorimeter, 7 - leak valves, 8 - gearbox, 9 - cylinder with gas mixture, 10 - power supply unit

Optical pumping consists of four identical diode emitters (1), the total power is 120 W. One emitter was tuned to a central wavelength of 811.5 nm to pump argon atoms, and the other three to 811.3 nm to pump krypton atoms. The pumping radiation was focused by the lens (2) into the electric discharge region of the discharge chamber (3) in which the active medium was created. The

discharge was powered by a power supply unit (10). The discharge chamber was a quartz tube into which electrodes (tantalum) were soldered, windows and units for pumping the gas mixture were soldered. Mirrors of optical resonator (4) are tightly fixed in ends of units. Optical resonator consists of spherical (4a) (R = 50 cm) and flat (4b) mirrors. Optical coating of a spherical mirror is dichroic - reflection at a wavelength of 811 less than 2%, reflection at wavelengths of 912.3 nm and 893.1 nm - more than 98%. The generation power was determined using an optical calorimeter (5).The generation intensities at wavelengths of 912 nm and 893 nm were determined using a portable spectrometer by radiation scattered from the receiving site of the calorimeter. The pressure and flow rate of the gaseous medium in the discharge chamber were controlled by means of two leak valves (7) located upstream and downstream of the discharge chamber, a reducer (8). Parameters were measured using a pressure sensor and a rotameter. For experiments, the gas mixture is prepared in advance (9).

Receive simultaneous generation

Simultaneous generation at three wavelengths was obtained using a mixture with the ratio [He]: [Kr]: [Ar] = 98: 0.5: 1.5. Figure 3 shows the spectrum of generation from the side of the dichroic mirror. For each series of experiments, the total generation power and the contribution of each line to the total generation were measured. In each series of experiments, parameters such as the pressure and flow rate of the gas mixture and the repetition rate of the discharge pulses varied.

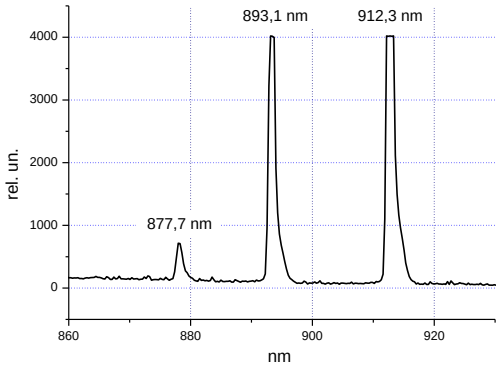

Figure 3 - Spectrum of generation from the side of dichroic mirror

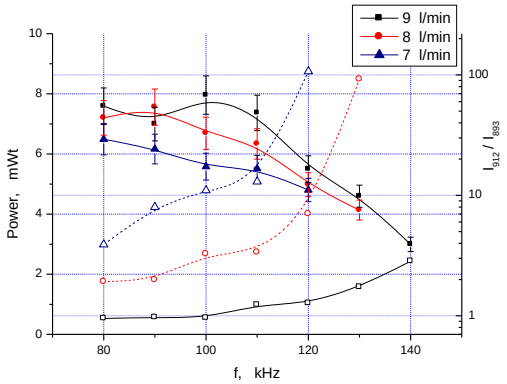

Figure 4 - Generation power depending on pulse repetition rate

Figure 4 shows the results of measuring the output power of laser generation and the ratio of the generation intensity at a wavelength of 912.3 nm to the generation intensity at a wavelength of 893.1 nm, depending on the repetition frequency of the discharge pulses. The results are given for the values of the mixture flow rate from 7 to 9 l/min, pressure 1.16 to $1.30 \cdot 10^5$ Pa. The results demonstrate that the maximum generation power in the experiments was achieved at a discharge pulse repetition rate of (90 ± 10) kHz. At these

frequencies (at a flow rate of 9 l/min), the line intensities at 912.3 nm and 893.1 nm are approximately equal. With an increase in the pulse repetition rate, generation at a wavelength of 912.3 nm begins to prevail over generation at a wavelength of 893.1 nm until it is completely suppressed. When the pulse frequency decreased below 70 kHz, the total generation power decreased by more than 3 times.

Discussion of results

During the experiments, simultaneous laser generation was obtained at wavelengths of 912.3 nm (Ar), 893.1 nm (Kr) and 877.7 nm (Kr) on a mixture of He: Kr: Ar = 98: 0.5: 1.5 on OPRGL. In the work, the dependence of the total generation power on the flow rate of the working mixture, the pressure of the gaseous medium in the discharge chamber and the repetition rate of electric discharge pulses was studied. The maximum achieved level of total radiation power at wavelengths 893.1 nm and 912.3 nm was ~ 8 mW.

The results obtained show that it is possible to obtain simultaneous generation of inert gases on two atoms while simultaneously pumping them. In the experiments carried out, the ratio of laser generation intensities on argon and krypton atoms was practically equal at the repetition rate of discharge pulses - from 80 to 100 kHz, mixture flow rate - from 8 to 9 l/min, mixture pressure - from $1{,}2\cdot10^5$to $1{,}4\cdot10^5$Pa.

A laser device that can generate radiation at two close wavelengths of equal intensity can be useful for generating radiation in the terahertz range, since the difference frequency of wavelengths 912.3 nm and 893.1 nm is 7 THz. Since both beams (893.3 nm and 912.3 nm) come from the same resonator and follow the same path, it is much easier to adjust the position and phase of each of the beams on the nonlinear crystal to obtain the difference frequency.

REFERENCES

1. **Михеев П.А.** Quantum Electronics. **45**(2), 2015.
2. **Han J., Heaven M.C.,** *Opt. Lett.,* **37**, 2157 (2012).
3. **J. Han, M.C. Heaven, P.J. Moran, et al.** *Opt. Lett*. **42** (22), pp 4627-4630 **(**2017).
4. **Quingshan Liu, Rui Wang, Zining Yang et.al.,** *High Power Laser Science and Engineering*, **11**, e87 (2023).
5. **Адаменков А.А., Адаменков Ю.А., Волков М.А. и др.** Quantum Electronics. **52**(8), pp. 695-697. 2022.
6. **Адаменков Ю.А., Горбунов М.А., Калачева А.А., Шайдулина В.А., Юрьев А.В. и др.** Quantum Electronics. **54**(2), pp. 84-88, 2024.

PLASMA-CHEMICAL MICROWAVE METHOD FOR ONE-STAGE SYNTHESIS OF HETEROGENEOUS CATALYSTS

N.K. Kharchev[1], N.N. Skvortsova[1], N.S. Akhmadullina[1,2], V.D. Borzosekov[1], N.G. Gusein-zade[1], E.M. Konchekov[1], D.V. Malakhov[1], E.A. Obraztsova[3], V.D. Stepakhin[1], O.N. Shishilov[1,4]

[1]Prokhorov General Physics Institute of the Russian Academy of Sciences, Moscow 119991, Russia, Vavilova st. 38, mukudori@mail.ru
[2]A.A. Baikov Institute of Metallurgy and Material Science of Russian Academy of Sciences, Moscow, 119991, Russia, Leninsky avenue 49, nakhmadullina@mail.ru
[3]Moscow Institute of Physics and Technology, Dolgoprudny, Moscow Region, 141700, Russia, Institutsky Per. 9, brenka@mail.ru
[4]MIREA – Russian Technological University, Institute of Fine Chemical Technologies, Moscow, Russia, Vernadskogo pr., 86, oshishilov@gmail.com

1. Introduction

Modern chemical industry and environmental technologies require the development of efficient and cost-effective catalysts /1,2/. One promising direction is the creation of heterogeneous catalysts composed of microparticles of dielectric materials coated with nanoscale metal particles. The Plasma Physics Department of GPI RAS has developed an innovative one-step synthesis method for such materials, opening new possibilities for catalytic processes /3/.

Heterogeneous catalysts based on dielectric materials (e.g., aluminum oxide, silicon oxide, or zeolites) with metallic nanoparticles (platinum, palladium, gold, etc.) exhibit high activity, selectivity, and stability. Their key advantages include:

- Enhanced surface area of metal nanoparticles ensures high catalytic activity.
- Dielectric support stabilizes nanoparticles, preventing aggregation and deactivation.
- Controlled morphology allows tuning catalytic properties for specific reactions.

Traditional methods for producing such catalysts involve multi-stage processes: carrier synthesis, metal impregnation, reduction, and activation. The method combines these steps into one, offering significant benefits:

- Time and resource efficiency – reducing the number of stages lowers costs.
- Precise control over nanoparticle size and distribution – achieved by optimizing synthesis parameters (temperature, pressure, reaction mixture composition).
- Reproducibility – a single-step process is easier to standardize.
- Potential applications.

Thus, this method holds considerable scientific and practical potential, contributing to the advancement of green chemistry and sustainable industrial processes.

2. Experimental setup and methodology

The synthesis of micron-sized dielectric particles coated with nanoscale metal catalysts was achieved through plasma-chemical reactions of mixed dielectric-metal powders, activated by high-power microwave irradiation /4,5/.

The laboratory setup (Fig. 1) consisted of: gyrotron (5): generated microwave radiation at 75 GHz with adjustable power (50-400 kW), quasi-optical system: including mirrors (1,3) for beam guidance and a directional coupler (2) for monitoring forward/reflected power via detector heads (6,7), plasma-chemical reactor (4), transmitted power measured by detector for energy balance calculations /6,7/.

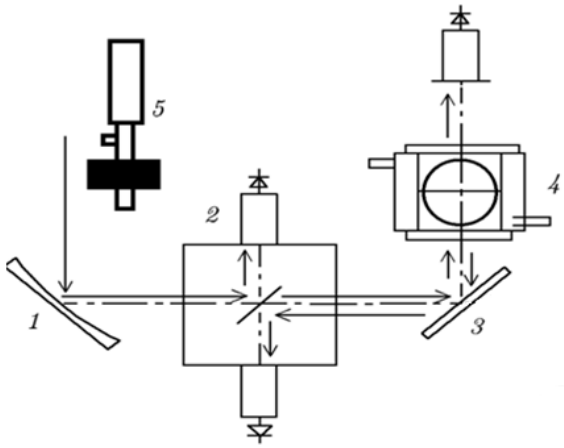

Fig. 1. Microwave plasma synthesis setup schematic: 1, 3 - beam steering mirrors, 2 - power monitoring couple, 4 - reaction chamber, 5 - microwave generator (gyrotron)

3. Reactor and diagnostic configuration.

The layered reactant arrangement in the plasma reactor comprised: quartz plates containing the reaction volume, dielectric powder layer (base material $Al_2O_3/TiO_2/SiO_2$), metal-dielectric mixed layers (precursors for nanoparticle formation), plasma zone (generated by microwave absorption), process gas (controlled atmosphere environment).

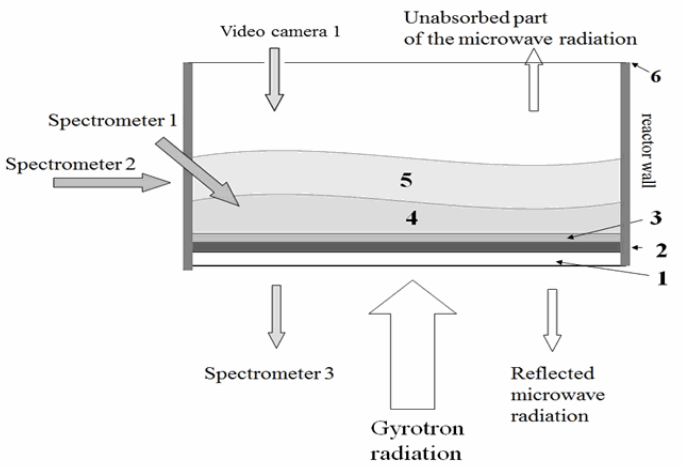

Fig. 2. Schematic of the plasma-chemical reactor assembly: 1, 6 - quartz containment windows, 2 - base dielectric material bed, 3 - composite metal-dielectric precursor strata, 4 - microwave-generated plasma region, 5 - reactive/process gas medium

Irradiation protocol: pulse mode operation - single microwave pulses (2-4 ms duration) with ≥ 30s inter-pulse intervals, treatment cycles - 10-30 pulses per sample batch, power parameters - gyrotron output: 300-450 kW; powder intensity:

~8-10 kW·cm^{-2}; Gaussian beam profile (40 mm characteristic radius); energy absorption: microwave energy dissipated in ceramic absorbers 60 cm.

Key process features:

- Non-equilibrium plasma generation: enables simultaneous dielectric particle structuring and metal nanoparticle deposition
- Precise energy control: power monitoring system ensures reproducible plasma conditions
- Layer-by-layer processing: facilitates controlled composition gradients in final catalysts

This advanced microwave plasma technique demonstrates exceptional capability for one-step production of high-performance heterogeneous catalysts with tunable metal-support architectures. The method's scalability is supported by its energy-efficient pulsed operation and compatibility with industrial microwave systems.

3. Materials Used for Catalyst Synthesis Experiments Introduction

Modern catalysis research requires careful selection of materials that determine the efficiency and selectivity of catalytic processes. Various dielectric supports and catalytic metals are used for the synthesis of heterogeneous catalysts. These substances are chosen based on their chemical, structural, and functional properties, enabling the creation of highly efficient catalytic systems. The laboratory employs oxides of aluminum (Al_2O_3), titanium (TiO_2), and silicon (SiO_2) as catalyst supports. These dielectric materials ensure stable anchoring of metal nanoparticles and prevent their sintering during catalytic processes.

Catalytic metals – active centers

To impart catalytic activity, the following metals are deposited on the dielectric surfaces:

- Platinum (Pt) and palladium (Pd) – Highly active in hydrogenation, dehydrogenation, and exhaust gas purification reactions.
- Silver (Ag) – used in selective oxidation processes and antibacterial coatings.
- Copper (Cu) – effective in reduction reactions and methanol synthesis.

The use of these metals in nanoparticle form significantly enhances their activity due to the increased surface area. /8,9/

The combination of dielectric supports and metals enables the creation of catalysts with tailored properties:

- Control over nanoparticle size and distribution ensures high activity and selectivity.
- The choice of support affects catalyst stability under high temperatures and aggressive environments.
- Surface modification of oxides (e.g., through doping) expands the range of catalyst applications.

4. Conclusion

The series of studies conducted at the Plasma Physics Department of GPI RAS has yielded significant scientific and practical results in the development of next-generation heterogeneous catalysts. The most important achievement has been

the successful development of an innovative one-step synthesis method that, even without additional optimization (such as particle size fractionation or improvement of metal nanoparticle distribution), enables production of catalysts with efficiency parameters comparable to industrial analogues.

Comprehensive studies have confirmed that:

1. The developed catalytic systems based on Al_2O_3, TiO_2 and SiO_2 with nanoparticles of Pt, Pd, Ag and Cu demonstrate:
   - High activity (up to 98% conversion in model reactions)
   - Excellent stability (>90% activity retention after 5 cycles)
   - Competitive performance relative to commercial catalysts
2. Biological studies revealed:
   - An acceptable safety profile for Pt-containing systems
   - The promise of Ag-catalysts for antimicrobial applications
3. The synthesis methodology proved effective by:
   - Ensuring good distribution of metal nanoparticles
   - Providing reproducible results without complex optimization

Future development prospects include:

1. Synthesis method optimization (fractionation, improved metal distribution)
2. Expansion of catalytic material range (incorporation of other metals)
3. Development of specialized modifications for petrochemical processes, environmental applications, medical technologies
4. Conducting trials under real industrial conditions

Thus, the developed one-step synthesis method opens new possibilities for creating efficient and safe catalytic systems. Even at the current development stage, the obtained catalysts demonstrate performance close to industrial samples, confirming the promise of this research direction and its high potential for practical implementation. The integrated results demonstrate that our synthesis approach combines methodological simplicity with production efficiency, offering a viable alternative to conventional multi-stage catalyst preparation methods while maintaining competitive catalytic performance characteristics. A patent was obtained for the plasma-chemical microwave method of one-stage synthesis of heterogeneous catalysts: Method of applying metal nanoparticles to the surface of ceramic carriers using a microwave discharge /3/.

References

1**. Romanovsky B. V.** Fundamentals of catalysis. Binom. (2020).
2. **Krylov O. V.** Heterogeneous catalysis. ICC "Akademkniga" (2004).
3. **Gusein-zade N.G.** et al. Russian Patent No. 2772704 (2022, May 24).
4. **Polak L. S.** et al. Theoretical and applied plasma chemistry. Nauka. (1975).
5. **Skvortsova N. N.** et al. Fusion Science and Technology, (2023). 882–892.
6. **Kharchev N.K.** et al. Plasma and Fusion Research. (2011). 2402142.
7. **Kharchev N. K.** et alReview of Scientific Instruments, *84*(1), . (2013). 013507.
8. **Akhmadullina N. S.** et al. IV Russian Congress on Catalysis "ROSKATALYSIS", Kazan, Russia. (2021).
9. **Skvortsova, N. N.** et al.. Int. Journal of Molecular Sciences, (2024). 5326.

COMPARISON OF PARTIAL LEAST SQUARES (PLS) AND THE ORIGINAL MULTIPARAMETRIC CALIBRATION FOR THE ANALYSIS OF STEELS WITH HIGH COMPOSITIONAL VARIABILITY USING LASER-INDUCED BREAKDOWN SPECTROSCOPY (LIBS)

V. Kiris, M. Belkov

Institute of Physics, National Academy of Sciences of Belarus, Nezalezhnasci Ave. 68-2, 220072 Minsk, Belarus, yavasya@yandex.ru

This study compares Partial Least Squares (PLS) with a novel multiparametric calibration (MPC) for quantifying elements in highly variable steels via Laser-Induced Breakdown Spectroscopy (LIBS). Quantitative LIBS analysis, particularly for highly alloyed steels, is challenging due to complex nonlinearities and matrix effects. Both methods were validated using the dataset from the LIBS 2022 contest /1/.

The spectra of this set were acquired using a conventional nanosecond LIBS system. For a comprehensive account of the experimental methodology, including the detailed setup, data acquisition protocols, and sample characteristics, please refer to /1/. Briefly, a 1064 nm Nd:YAG laser with a 10 ns pulse duration was focused to a 0.2 mm spot on the sample. Plasma emission was collected by an echelle spectrometer, providing a spectral range of 236–1000 nm with a resolving power of 6000. Detection was temporally resolved with a 1.5 μs delay and a 50 μs gate width. To ensure representative data, 50 spectra were acquired from various locations on each sample. The training set, described in reference /1/, included concentrations of chromium, nickel, manganese, molybdenum, carbon, silicon, and copper, with iron constituting the remainder. The elemental composition of the studied samples varied significantly. Iron concentration, as the main matrix component, ranged from ~41% to 98%. The correlation matrix (see Table 1) reveals predominantly low to moderate inter-element correlations, indicating limited multicollinearity within the dataset. This statistical structure is generally favorable for a wide range of analytical modeling approaches—both linear and nonlinear—since it allows individual variables to contribute more distinctly to the model without significant redundancy. Low correlations reduce the risk of overfitting and enhance model stability, especially in multivariate calibration or prediction tasks. Moreover, such independence between variables can improve the performance of variable selection algorithms and increase the robustness of models when applied to complex real-world samples.

In addition to the elements indicated by the authors /1/, spectral lines of the following elements were also detected in the spectra: titanium, vanadium,

cobalt, aluminum, and calcium. Furthermore, lines of nitrogen and oxygen, being air components, were observed, but these were not included in the model.

To minimize spectral line position instability, a preprocessing technique was utilized, involving interpolation, shifting, and stretching of spectra. This approach ensured maximal alignment of each spectrum with the first spectrum in the dataset by maximizing correlation.

Spectral preprocessing and MPC model development were performed in Matlab® R2022b. The PLS model was developed in Unscrambler X (CAMO Software AS) using the Nonlinear Iterative Partial Least Squares (NIPALS) algorithm.

The following spectral lines (in the case of PLS, areas with a width of ±6 pixels centered on the line) were selected for model building: Si I 281.16 nm, Mn II 293.31 nm, Cr II 318.07 nm, Mo I 386.41 nm, Mo II 281.62 nm, Ni II 241.61 nm, Cu I 327.40 nm, Fe II 275.57 nm, Ti II 324.20 nm, V II 311.84 nm, Al I 394.40 nm, Co I 340.51 nm, Co I 350.23 nm, Ca II 393.42 nm, and C 909.48 nm.

As demonstrated in works /2–3/, PLS was shown to be effective for the analysis of low-alloy steels, particularly when the variability of the matrix composition is insignificant. In such cases, the assumption of linear or approximately linear relationships between spectral intensities and elemental concentrations holds reasonably well, allowing PLS to deliver robust and accurate predictions.

Table 1. Correlation coefficient matrix for the main alloying elements

	C	Si	Mn	Cr	Mo	Ni	Cu
C	-	0.47	0.38	-0.06	-0.23	-0.09	-0.24
Si	0.47	-	0.51	-0.30	-0.37	0.08	-0.16
Mn	0.38	0.51	-	-0.10	-0.22	0.21	-0.11
Cr	-0.06	-0.30	-0.10	-	0.31	0.01	0.37
Mo	-0.23	-0.37	-0.22	0.31	-	-0.13	0.33
Ni	-0.09	0.08	0.21	0.01	-0.13	-	-0.14
Cu	-0.24	-0.16	-0.11	0.37	0.33	-0.14	-

However, this assumption may break down in the case of highly alloyed steels. These materials typically exhibit stronger matrix effects and more pronounced nonlinearities due to interactions among multiple alloying elements.

The increased complexity in the LIBS spectra further challenges the linear modeling approach inherent in PLS. Consequently, while PLS may still yield acceptable performance in limited scenarios, it may fail to generalize well across highly variable compositions, leading to degraded prediction accuracy. This limitation motivates the investigation of alternative approaches, such as MPC /4/, which are explicitly designed to account for matrix effects. Therefore, the present study aims to assess whether MPC can outperform PLS under broader analytical conditions.

Calibration functions in the MPC approach were formulated as follows:

$$C_{el} = \frac{a_1 * I_{el} + a_1 * I_1 + \ldots + a_n * I_n + a}{I_{Fe} + b_1 * I_1 + \ldots b_k * I_k + b}$$

where C_{el} is the target element concentration, I_n are the spectral line intensities of various elements, and a_i, b_i are calibration coefficients. The initial model always included the intensity of the target element's spectral line and a constant term in the numerator, while the denominator initially contained only the intensity of a normalization iron line (I_{Fe}), without a coefficient.

Calibration was performed using a stepwise approach. At each iteration, candidate spectral lines from other elements were added to the numerator or denominator. The line that yielded the largest reduction in the root mean square error (RMSE) during leave-one-out cross-validation was retained. This process continued iteratively, each time considering the addition of one more line, until no further decrease in RMSE was observed or a maximum of eight calibration parameters was reached.

This calibration structure was chosen to account for both spectral and non-spectral effects. For example, the intensity of the iron normalization line may decrease not due to instrumental instability but because of real compositional effects, such as the reduction of iron concentration on the sample surface due to enrichment by other elements. The approach is partly inspired by the logic of the calibration-free LIBS method, in which relative concentrations are estimated by normalizing to the total signal contribution from all detectable elements.

While general multivariate calibration guidelines recommend a minimum of ten samples per parameter—which would suggest a limit of four parameters for a dataset of forty samples—the use of leave-one-out cross-validation (in which each sample serves iteratively as both training and validation data) allowed us to relax this constraint. As long as the cross-validation RMSE continued to decrease, up to eight parameters were permitted in the model.

The results for the different analytical methods are presented in Table 2.

Table 2. Comparison of RMSE (%) for different methods on the test set

	Cr	Ni	Mn	Mo
Classical calibr. (Fe norm.)	3.93	2.33	0.460	0.351
PLS	3.67	2.38	0.306	0.572
PLS (Fe norm.)	3.03	1.26	0.278	0.402
MCP	0.785	1.02	0.0942	0.150

As shown in Table 2, under conditions of high matrix variability, PLS calibration with normalization to the iron line proved to be more effective than PLS without normalization. This result is somewhat counterintuitive, as the iron concentration in the dataset varies by more than a factor of two. It is possible that a model in which both intensities and concentrations are normalized could yield even better results. However, such an approach would require a full analysis of all alloying elements to revert normalized concentrations back to their original values when analyzing unknown samples.
The results demonstrate that MPC not only improves accuracy over classical calibration but also significantly outperforms PLS in the analysis of highly alloyed steels—achieving notably lower RMSE values.

Acknowledgements. This research was conducted as part of the Republic of Belarus State Program of Scientific Research, Photonics and Electronics for Innovations, task 1.5. The authors gratefully acknowledge Erik Képeš and Jakub Vrábel for providing the dataset used in this study.

References

1. **E. Képeš, J. Vrábel, P. Siozos, et al.** Spectrochimica Acta Part B: Atomic Spectroscopy 206 (2023) 106710.
2. **M. Belkov, V. Kiris, K. Catsalap** J. Appl Spectrosc., 89 (2023) 1040–1046.
3. **V. Kiris, K. Catsalap, M. Belkov** J. Appl Spectrosc., 92 (2025) 240-248,
4. **Kiris, V. V., Belkov, M. V.** (2025). Compensation of interelement effects in the analusis of alloy steels by laser-induced breakdown spectroscopy. In P. V. Kuchinsky (Ed.), *Applied problems of optics, informatics, radiophysics, aerospace technologies, and condensed matter physics: Proceedings* of *the 8th International Scientific and Practical Conference (Minsk, May 22–23, 2025)* (pp. 19–21). Minsk: StroyMediaProject. *(In Russian)*
5. **Ciucci A, Corsi M, Palleschi V, et al.** Appl Spectrosc. 53 (1999) 960–964.

SYNTHESIS OF COMPLEX OXIDES UNDER THE INFLUENCE OF AIR PLASMA OF PULSED HIGH-VOLTAGE DISCHARGE ON A MECHANICAL MIXTURE OF SIMPLE OXIDES AND ON METAL ELECTRODES AND THEIR MAGNETIC PROPERTIES

V.G. Kuryavyi, I.A. Tkachenko, A.V. Gerasimenko

Institute of Chemistry, Far Eastern Branch of the Russian Academy of Sciences, Vladivostok, Russia, kvg@ich.dvo.ru

Introduction

It is known that complex oxides can have many useful properties [1] including high-temperature superconductivity. Of interest to exploration are rapid methods for synthesizing complex oxides of various compositions. This article demonstrates two such methods using air plasma of a pulsed high-voltage discharge.

1. Experimental Methodology

Two experimental variants were used. The schemes of the variants are shown in Fig. 1. In both variants, a plasma cord was used, which appeared between the electrodes after applying a high-voltage pulse to them. The pulse amplitude was 9 kV, the pulse repetition frequency was 2000 Hz, and the pulse width at half-height was about 1 μs. In the first variant (Fig. 1a), the initial powder sample was poured onto a flat electrode.

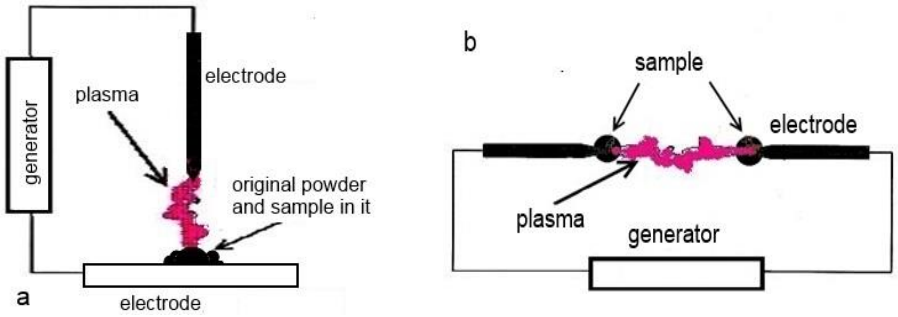

Fig. 1. Experimental schemes: variant 1 (a) and variant 2 (b)

The second rod electrode was placed above the powder surface. The plasma cord was scanned above the powder surface by moving the electrode. Melted granules of about 0.5 mm in size were formed at the plasma entry points. The granules were selected from the powder and ground in an agate mortar. The resulting powder was the sample for research.

In the second variant (Fig. 1 b), the plasma was initiated between two wire electrodes with a diameter of about 0.5 mm. When voltage was applied between

the electrodes, a plasma cord was formed. At the points of plasma entry, the electrode material underwent rapid melting and structural reorganization, forming individual globules. After the plasma was turned off, the globules were separated from the electrode surface and studied.

The structure and composition of the obtained samples were studied using X-ray diffraction (on a D8 ADVANCE diffractometer (Germany) using the PDF-2 powder data bank), SQUID (on a MPMS-XL-5 SQUID magnetometer from Quantum Design (USA), and Raman spectroscopy (on a WiTec alpha500 confocal Raman microscope (Germany)).

2. Experimental results

2.1 Sample 1, obtained according to variant 1

According to X-ray diffraction data, by direct action of pulsed high-voltage discharge plasma on a powder mixture of Y_2O_3, BaO_2 and CuO oxides, a composite $CuO/Cu_2O/Y_2O_3/Y_2BaCuO/YBa_2Cu_3O_{6.32}$ was obtained, which included complex oxides.

2.2 Sample 2 obtained by annealing sample 1

According to the XRD data, by annealing sample 1 at 1173 K, the $CuO/YBa_2Cu_3O_{6.91}$ composite was obtained, which includes the known high-temperature superconductor $YBa_2Cu_3O_{6.91}$. The presence of a superconducting phase in the obtained composite at T < 87 K is confirmed by SQUID magnetometry data. The field dependence of the magnetization of sample 2 measured at T = 4 K has a form characteristic of a superconductor - Fig. 2a. The characteristic form of the temperature dependence of the magnetization indicates the beginning of the transition to the superconducting phase at T = 87 K (according to the beginning of the dependence decay) - Fig. 2b.

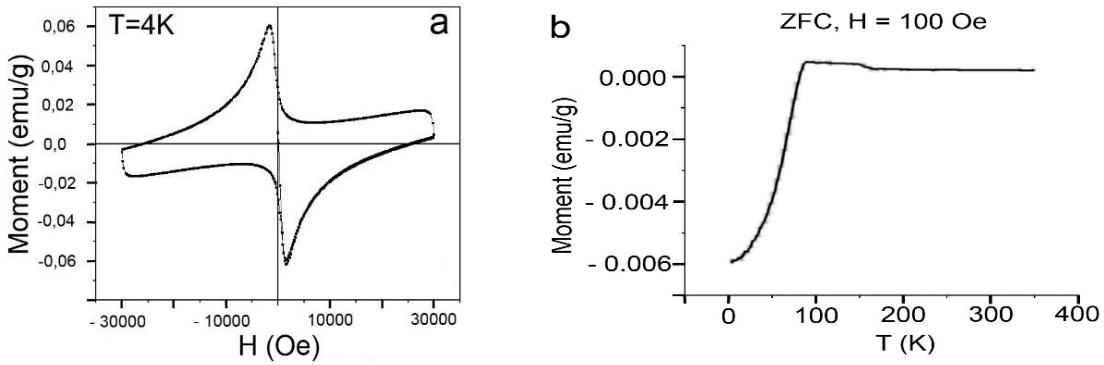

Fig. 2. Field (a) and temperature (b) dependences magnetization of sample 2

2.3 Sample 3, obtained according to variant 2

Granules were obtained by melting nichrome wire electrodes with plasma. X-ray diffraction data measured for the powder obtained by grinding the granules in an agate mortar indicate its composition is $NiCr_2O_4$/NiO/Ni - Fig. 3a. The synthesized sample strongly exhibits the effect of shifting the magnetic hysteresis loop (Fig. 3), indicating the alternation of FM and AFM regions in it. According to literature data, such an effect can find application in spintronics [2].

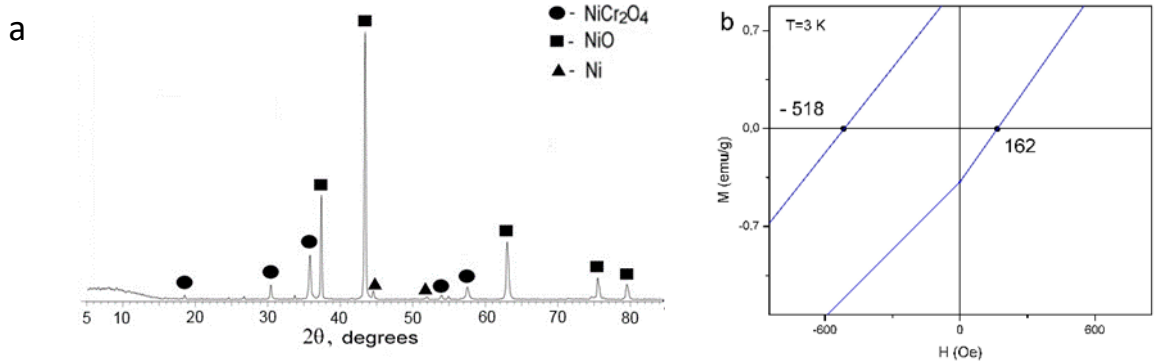

Fig. 3. X-ray diffraction spectrum (a) and the middle part of the field dependence of magnetization (b) of sample 3

2.4 Sample 4, obtained according to variant 2.

By melting copper wire electrodes with plasma, granules containing a core consisting mainly of Cu_2O covered with a shell of CuO were obtained. This structure is indicated by Raman spectroscopy data (Fig. 4).

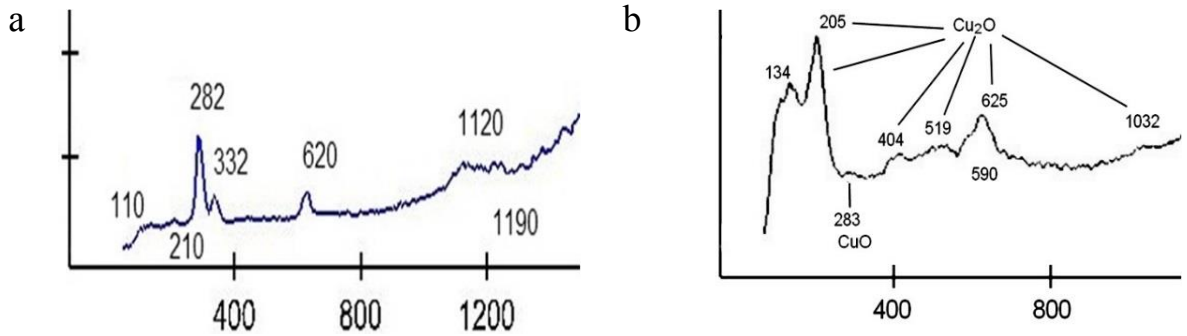

Fig. 4. Raman spectra of the surface of the granule of sample 4 (a) and the inner part of the cleaved granule (b). The spectrum of the surface completely corresponds to the spectrum of CuO. The spectrum of the inner part corresponds to the spectrum of Cu_2O with a slight admixture of CuO [3, 4]

The temperature dependence of the granule magnetization in the temperature range of 35 K - 300 K has a form characteristic of the temperature dependence of CuO samples containing small amount of foreign impurities [5] and shifted to the

diamagnetic region. However, at temperatures below 35 K, the temperature dependence has a form similar to that of superconductors - the magnetization drops sharply to the diamagnetic region. Such behavior could be explained by the occurrence of a superconducting phase in the sample at temperatures below 35 K. However, in this temperature range, a pronounced field hysteresis of the magnetic susceptibility is observed, characteristic of the ferromagnet - Fig. 5. Therefore, the nature of the state of sample 4 at temperatures below 35 K requires further clarification. Based on the Raman data, it can be assumed that the unusual behavior of the temperature dependence of the magnetization of sample 4 is caused by the presence of interface regions between CuO and Cu_2O.

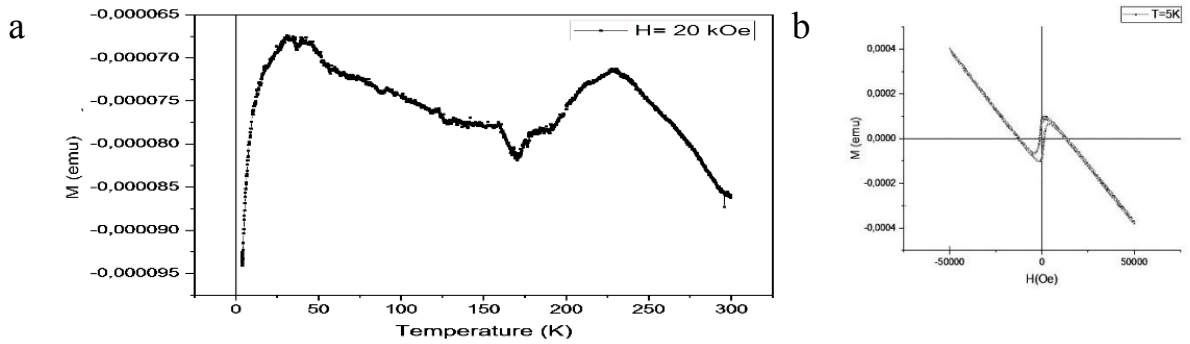

Fig. 5. Temperature (a) and field dependences of magnetization (b) of sample 4

Conclusions

The plasma-chemical methods used are promising for exploratory work on the synthesis of various complex oxides and new functional materials.

References

[1] Abakumov A.M., Antipov E.V., Kovba L.M., Kopnin E.M., Putilin S.N., Panchenko R.V. Uspekhi Chem., 64 (8) (1995) 769-780.

[2] Jesús G. Ovejero, Vanda Godinho, Bertrand Lacroix, Miguel A. García, Antonio Hernando, Asunción Fernández Materials & Design, 171(2019). 107691.

[3] Xu, W. Ji, Z.X. Shen, W.S. Li, S.H. Tang, X.R. Ye, X.Q. Xin. J. Raman spectroscopy, 30 (5) (1999) 413-415,

[4] Sander T., Reindl C. T., Klar P. J. MRS Online Proceedings Library (OPL), 1633 (2014) 81-86.

[5] Arbuzova T.I., Smolyak I.B., S. V. Naumov S.V., Samokhvalov A.A. Phys. Solid State, 40 (10), October 1998 P. 1702-1705.

APPLICATION OF PLASMA AND MICROWAVE TECHNIQUES FOR FABRICATION OF ADVANCED LUMINESCENT CARBON NANODOTS

V.A. Lapina, A.A. Nevar, T.A. Pavich, A.R. Shumejko, N.V. Tarasenko

B.I. Stepanov Institute of Physics of the National Academy of Sciences of Belarus,
68-2 Nezavisimosti Ave., 220072 Minsk, Belarus,
v.lapina@ifanbel.bas-net.by, a.nevar@ifanbel.bas-net.by,
pavich@imaph.bas-net.by, al.shumejko@gmail.com

Luminescent carbon nanoparticles (CNPs) – carbon quantum dots or carbon nanodots (CNDs) – are widely used in various fields of science and technology due to their unique optical, chemical and physical properties: in biomedicine - for diagnostics and imaging of cells and tissues, targeted delivery of pharmaceuticals, in sensorics - to create sensitive sensors for detecting metals, organic compounds, bacteria and other harmful substances, in optoelectronics - to create light sources, in energy - to increase the efficiency of energy conversion in solar cells and photovoltaic devices.

Among the variety of plasma-chemical methods for producing CNPs, electrical discharge in liquid can be distinguished. Advantages of this technique include the ability to control the parameters of the final product by changing the discharge regimes, environmental safety, and a possibility to scale-up the synthesis process.

Doping of CNPs with rare earth ions, in particular europium Eu^{3+}, is described in /1/. The specificity of the luminescence mechanism of lanthanide ions is known, i.e. odd-even prohibition of transitions within the same electron configuration within 4f shells, which leads to low absorptivity of f-f transitions ($\varepsilon < 10$ L·mol^{-1}·cm^{-1}) and, as a consequence, to low efficiency of luminescence of free ions /2,3/. The solution of this problem is the synthesis of organic complexes of lanthanides with strongly absorbing organic ligands. Obviously, the efficiency of energy transfer to the radiative levels of lanthanide ions depends primarily on the type of ligands associated with them. Therefore, the search for organic ligands capable of coordinating with lanthanide atoms to form stable luminescent compounds and the study of the dependence of the luminescent properties of such compounds on their structure are especially relevant today. Combining rare earth ions with an appropriate ligand to form a complex also leads to an increase in the absorption coefficient of each ion and solves the problem of concentration quenching due to the large intermolecular distance.

In this regard, the targeted synthesis of mixed-ligand rare earth compounds, where Ln^{3+} ions are coordinated with organic compounds having a developed system of conjugated bonds that intensely luminescent in a wide spectral range

with a high quantum yield of luminescence and improved photochemical characteristics, is of considerable interest /4/.

The aim of this study is to investigate the possibilities of using plasma-chemical and microwave methods for the synthesis of organo-inorganic complexes based on CNDs, europium ions, and the organic dye α,α′-dipyridyl (Dipy) as a ligand, which is an optically active compound and can promotes the formation of favorable conditions for complexation and the formation of effective donor-acceptor complexes based on solid carrier.

Spherical CNDs with diameter about 5 nm were synthesized by electrical discharge in liquid. More details about the experimental setup can be found in /5/. The experimental system included a high-voltage pulse supply, a reactor chamber with electrodes, electrodes holders and a working liquid. The alternating current spark discharge was initiated by applying a high frequency voltage of 11 kV. The peak current of the high-voltage spark was about 17 A with a duration of a single discharge pulse of 50 μs. The discharge was ignited in 75 ml of liquid between two 6 mm diameter graphite rods being immersed to a depth of 3 cm. Aqueous and ethanol solutions of europium salts (1.0×10^{-3} m/l $Eu(NO_3)_3$) and α,α′-dipyridyl 3.0×10^{-3} m/l were used as working fluids.

During the discharge the electrode material is heated, melted and vaporized in the region of the discharge generated. At the same time, the liquid near the electrodes also evaporates and forms gas bubble. The extremely sharp temperature gradient in it from ~ 4200 °C in the discharge zone between graphite electrodes to the boiling temperature of the liquid ~ 80 °C at the gas-liquid boundary – causes rapid condensation of the vaporized carbon with CNDs formation /6/.

Heating of the working liquid leads to its thermal decomposition, dissociation of C-C or C-O bonds, and the formation of by-products and radicals, which can then be passivated on the surface of the formed CNDs or participate in chain reactions with formation of organo-inorganic complexes and compounds.

Fig. 1a presents the PL spectra (λ_{ex} = 320 nm) of CNDs synthesized in water and ethanol, with and without the addition of europium ions. Samples synthesized in water exhibit a narrow luminescence band with a maximum at 358 nm, whereas CNDs synthesized in ethanol display relatively intense luminescence over a broad wavelength range (350–450 nm). In the presence of europium ions, the luminescence spectra show peaks at 591 nm and 616 nm, characteristic of Eu^{3+} transitions $^5D_0 \rightarrow {}^7F_1$ and $^5D_0 \rightarrow {}^7F_2$, respectively. It is noteworthy that the presence of europium ions in aqueous synthesis does not affect the luminescence intensity, while in ethanol their presence results in luminescence quenching – the peak intensity decreases by nearly a factor of two.

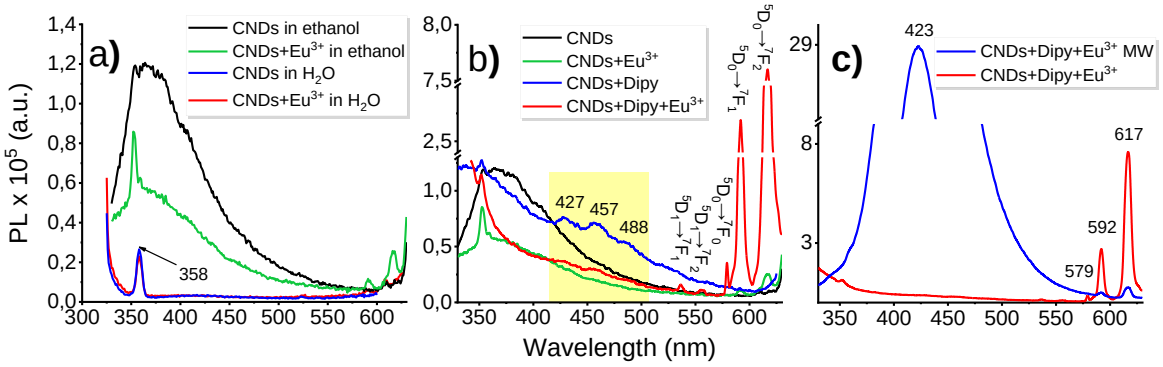

Fig.1. PL spectra (λ_{ex} = 320 nm) of CNDs synthesized by electric discharge in water and ethanol (a), in ethanol with the addition of europium ions (Eu^{3+}) and α,α′-dipyridyl (b), CND–$Eu(NO_3)_2$–$(Dipy)_2$ complex systems prepared by electrical discharge and microwave techniques (c)

The addition of Dipy to the ethanol during CNDs electrical discharge synthesis leads to the appearance of shoulders in the visible region of PL spectrum with maxima at 427, 458, and 486 nm, as shown in Fig. 1b. This spectral response can be attributed to the interaction of Dipy with surface states of the nanoparticles.

In the ternary system comprising Eu^{3+}, Dipy, and CNDs, the spectral properties are determined by the competition of energy transfer pathways in the emitting centers. Dipy has a high coordination capacity and forms a complex with europium with charge transfer from organic ligands to the Eu^{3+} ion, since it has a suitable triplet level. This is evidenced by the enhancement of characteristic europium emission lines in the α,α′-dipyridyl-containing sample compared with the system containing only CNDs and Eu^{3+}. Probably the role of the CNDs in this case is secondary: they act as energy donors to the europium-ligand complex, which is reflected in a decrease in the emission intensity in the 350–450 nm region. This mechanism is consistent with observations in other hybrid systems /7/, where CNDs are primarily used to broaden the excitation window and stabilize the europium–ligand complex, while the antenna effect is provided by the molecular ligand with a stable triplet state.

The possibility of forming an organo-inorganic complex of europium with Dipy based on CNDs under the influence of microwave radiation was also investigated. The synthesis of the complex was carried out in two stages: at the first stage, CNDs were synthesized by the electrical discharge in distilled water; at the second stage, the complex was synthesized by the interaction of the carbon substrate with europium nitrate and Dipy under the influence of microwave radiation at 200 W with a radiation frequency of 2.45 GHz. As a result, the organo-inorganic europium complex CND–$Eu(NO_3)_2$–$(Dipy)_2$ was obtained.

Fig. 1c shows the PL spectra of CND–$Eu(NO_3)_2$–$(Dipy)_2$ complex systems prepared by plasma-chemical and microwave methods. For the microwave-

treated sample, an exceptionally intense and broad emission band with a maximum at 423 nm appears, the integral intensity of which is many times greater than the luminescence intensity of the sample not treated with microwave radiation. At the same time, the processes of resonance energy transfer to the Eu^{3+} centers are suppressed, which explains the pronounced weakening of the characteristic europium peaks. Such spectral changes indicate a deep rearrangement of the structure of the emitting centers in the europium complexes with nanoparticles and their local environment under microwave irradiation. It can be assumed that microwave action in a solution leads to the generation of new electronically excited states that catalyze the course of chemical reactions, as well as the occurrence of a thermal effect of overheating, which significantly affect the nature and kinetics of chemical processes and the formation of the final product.

Thus, we have made the first attempt to synthesize effective nanocarbon luminescent materials under conditions of plasma-chemical synthesis and in combination with the capabilities of microwave radiation. The combination of thermodynamic conditions achieved by plasma and microwave methods leads to the formation of hybrid organo-inorganic carbon light-emitting nanocomplexes in the process of self-organization. Research results demonstrate that the emission properties of the CND–$Eu(NO_3)_2$–$(Dipy)_2$ system can be effectively tuned by modifying the synthesis conditions and the nanoparticle environment. Such light-emitting nanocarbon complexes with high quantum efficiency and absorption capacity in the UV-blue region of the spectrum were fabricated, indicating the prospects for their use as UV converters, as well as for detecting the ionizing radiation. These studies seem promising and require further detailed study.

Acknowledgements. This work was supported by the National Academy of Sciences of Belarus under project Convergence 2.2.05.

References

1. **В.А. Лапина, Т.А. Павич, П.П. Першукевич** Оптика и спектроскопия 22 (2017) 76-85.
2. **М.А. Ельяшевич**. Атомная и молекулярная спектроскопия. - М.: "Эдиториал УРСС", 2001. - 896 с.
3. **J.M. Lehn** // Angew. Chem. Int. Ed. Engl. 29 (1990) 1304-1319.
4. **L.D. Carlos, R.A.S. Ferreira, V. Deermudez, S.J.L. Ribeiro**. Adv. Mater. 21 (2009), 509 - 534.
5. **A.Nevar, N. Tarasenka, M. Nedelko, N. Tarasenko**. Carbon Lett. 31 (2021) – 39-46.
6. **N. Sano, et al.** J. Appl. Phys. 92 (2002) 2783–2788.
7. **S. Tuhin, H. Chanchal, M. Venkataramanan**. New J. Chem. 39 (2015) 106-109.

EFFECTS OF PLASMA TREATMENT ON THE SOME PHYSICOCHEMICAL PROPERTIES OF TECHNOGENIC SALINE SOIL

V. A. Lyushkevich [1], I. I. Filatova[1], S. V. Goncharik[1], J.N. Kalatskaja[2], I.A. Ovchinnikov[2], D.A. Kotov[3], A.V. Aksiuchyts[3]

[1] B.I. Stepanov Institute of Physics of the National Academy of Sciences of Belarus, 68-2 Nezavisimosti Ave., 220072 Minsk, Belarus, v.lyushkevich@ifanbel.bas-net.by
[2] V. F. Kuprevich Institute of Experimental Botany of the National Academy of Sciences of Belarus, Academicheskaya Str., 27, 220072 Minsk, Belarus, kalatskayaj@mail.ru
[3]Belarusian State University of Informatics and Radioelectronics, P. Brovki Str.,6, 220013 Minsk, Belarus, kotov@bsuir.by

Introduction

The research and development of remediation and improvement technologies for contaminated agricultural soils and the greening of food crops is an urgent issue to ensure global food security. Non-thermal plasma technology (NTP) has the potential to effectively degrade organic pollutants in soil and improve soil properties without the addition of any chemical agents /1, 2/. This technology can simultaneously meet the needs of crops in several issues such as soil remediation and improvement /3/, inactivation of pathogenic bacteria /4/, nitrogen fixation /5/ and plant promotion /6/.

Salinization of areas associated with the production of potash fertilizers is one of the most complex regional environmental problems in our country. The main raw material base of the potash industry in Belarus is the Starobin deposit. Another major problem is the deterioration of roadside vegetation due to man-made pollution of soils and plants by anti-icing reagents used in winter.

In this paper, changes in the physical and chemical properties of technogenically saline soil (from roadside areas of highways and the Starobin potash deposit) as a result of treatment with air and argon plasma jets were studied in order to develop a new method for remediation of the ecological functions of contaminated soils.

Experimental part

For all treatment options, including control option (without treatment), soil samples were collected containing a mixture of soils from both roadside areas and the Starobin potash deposit. Two plasma sources were used for soil treatment: an argon plasma jet of a dielectric barrier discharge (PJ-argon) and an air plasma jet generated by a direct current glow discharge (PJ-air).

The following conditions were used for PJ-argon treatment: discharge power of 15-16 W with an argon flow rate of 143 l/hour. The soil was poured

into a round container with a diameter of 17.5 cm. The thickness of the soil layer was about 2-3 mm. The container with soil was moved evenly by hand during treatment. The soil surface was located at a distance of 15 mm from the nozzle exit; the plasma torch diameter was about 1 cm. The treatment was carried out once (1 treatment cycle). The duration of one cycle (treatment of one portion) was 4 min.

The following conditions were used for PJ-air treatment: discharge current of 30 mA with an air flow rate of 1 l/min. The soil was poured into a round container with a diameter of 26 cm and a volume of 2.8 l. The thickness of the soil layer was about 2–3 mm. The container with soil was closed with a lid contained a hole through which the plasma jet exhaust was uniformly supplied. Gas exchange in the container was carried out due to the natural outflow of air from the volume through the slits between the container and the lid. The treatment duration was 10 min.

Results and discussion

It was found that plasma treatment generally contributed to a reduction in the number of large particles (Fig.1). In the treated soil, the number of small aggregate particles with sizes of 0.5–0.25 mm and less than 0.25 mm increased significantly. It is expected that the increase in soil dispersion will provide uniform penetration of the produced active plasma species into the soil volume.

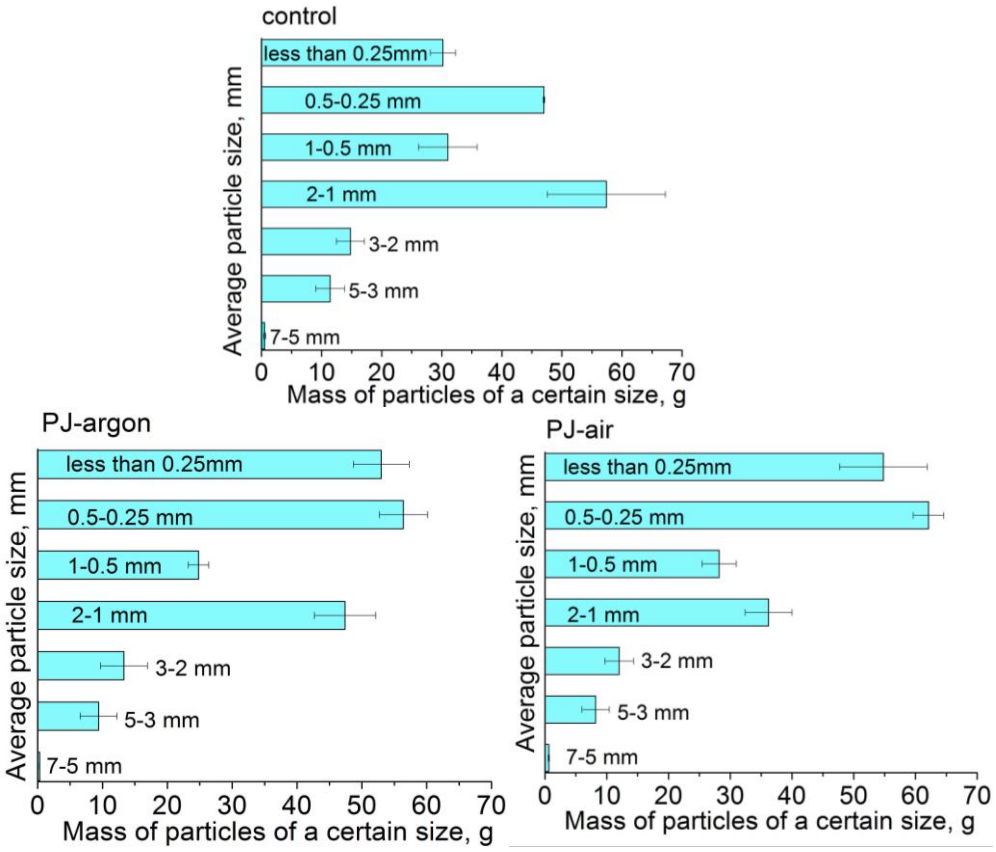

Fig.1. Particle size of soil samples before and after plasma exposure

The effectiveness of plasma treatment might improve due to increase of specific surface area. Laboratory tests showed that plasma treatment did not affect the hygroscopic moisture content of soil samples and porosity, but reduced the total moisture capacity of the studied soil samples by 11–12%.

It is known that the level of soil acidity affect the supply of micro- and macro elements to plants. In agriculture, soil electrical conductivity has been used principally as a measure of soil salinity, but, factors influencing the electrical conductivity of soils include the amount and type of soluble salts in solution, porosity, soil texture, soil moisture and soil temperature. Cation exchange capacity is the sum total of the exchangeable cations that a soil can absorb or hold. Factors that affect the total charge of a soil are the type of clay minerals, the total clay content, organic matter content and the soil pH. The properties of the particulate surface attribute the overall electrostatic charge, so the finest soil particles, both organic and inorganic, determine the total exchange capacity.

Active and exchange acidity, electrical conductivity and cation exchange capacity of control and treated soil samples were determined. It was found that plasma treatment generally increases acidity and reduces electrical conductivity of the soil (Fig. 2) without considerable affecting the cation exchange capacity of the sample (data not shown).

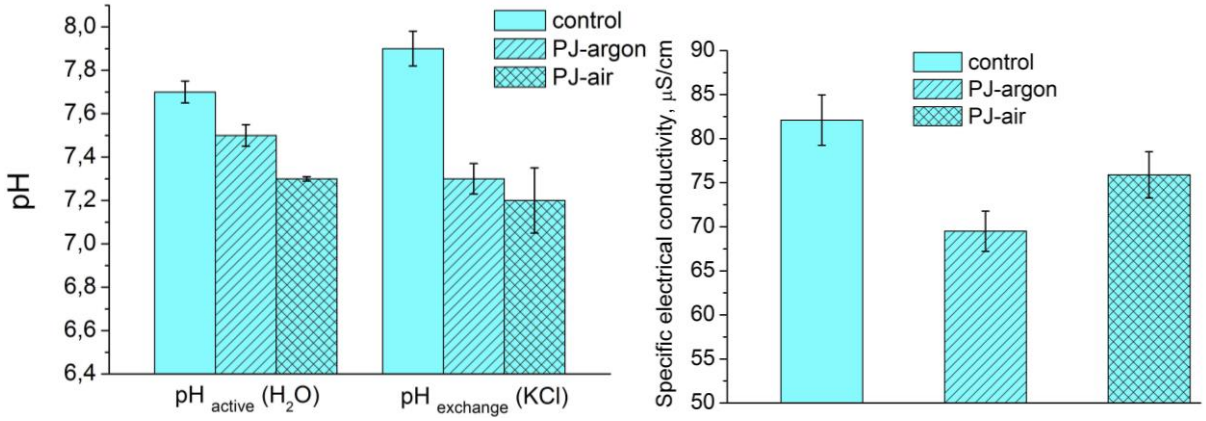

Fig.2. Selected physicochemical characteristics of soil samples before and after plasma exposure

This result is controversial since it is known that with an increase of soil dispersion, its specific surface area and surface energy increase too. Therefore, the exchange capacity and chemical activity should increase. It requires additional research to clarify it.

Conclusions

Thus, it was shown that plasma treatment of technogenically disturbed soil using various plasma sources changes its physical and chemical characteristics. The aggregate state of the soil changes towards an increase in its dispersity (an increase in the content of small particles). The total moisture capacity and electrical conductivity of the soil decrease by 11–12%, while the cation exchange capacity remains at the control level. Soil pH slightly decreased to a value close to neutral. In general, air jet treatment has a more significant effect on the physical and chemical properties of technogenically saline soil than argon plasma.

Acknowledgements. This work was supported by the Belarusian Republican Foundation for Fundamental Research (grant No F24KITG-012).

References

1. **Zhu D. et al.** Environmental Science & Technology, 56 (2022) 349-360.
2. **J. Zhao et al.** Chemical Engineering Journal, 459 (2023) 141632.
3. **Zhang H., Li P., Liu Y. et al**. Environmental Science and Technology, 55 (2021) 16067-16077.
4. **Lee Y. et al.** Journal of Ginseng Research, 45 (4) (2021) 519-526.
5. **Klimek, A. et al.** Processes, 12 (2024), 786.
6. **Staric, P. et al.** Int. J. Mol. Sci., 23 (2022), 7369.

THE STUDY OF THE OSCILLATIONS AND STRUCTURE OF A FLOW INTERACTING WITH A SECONDARY GAS TRANSVERSE JET IN THE PRESENCE OF SPARK DISCHARGES

Y. Miroshnikov*, L. Volkov, A. Firsov, I. Moralev

Joint Institute for High Temperatures, Moscow, Russia
*defourk@yandex.ru

This work is devoted to the study of the influence of periodic spark discharges with different frequencies on the formation of disturbances in the shear layer at the boundary of the secondary transverse jet within a freestream. Two cases of flow structure were considered: the case of a subsonic jet injected into a subsonic flow and the case of a transonic jet injected into a supersonic flow with M = 2. The discharges are localized in the separation zone on the windward side of the injector. For both subsonic and supersonic cases the experiments were performed in the absence and in the presence of a pulsed-periodic local energy release caused by a spark discharge on the windward side of the injector. Also, for supersonic case the computer simulation of the flow was performed by the URANS method using the FlowVision software package.

The subsonic experiments were performed in the subsonic wind tunnel D-2 of Laboratory 21.3 at the JIHT RAS. Both the oncoming flow and the jet flow were dry air treated as an incompressible gas. The instantaneous velocity profiles of the flow were experimentally obtained by the particle image velocimetry (PIV) method for different volumetric flow rates and velocities of the incident subsonic flow. For selected injection parameters the excitation of the jet by the periodic spark discharge at certain frequencies was performed. The spectrum of pulsations was obtained by methods of Fourier transform and spectral proper orthogonal decomposition (SPOD). The operating parameters of the experiment were as follows: the oncoming flow velocity 10-20 m/s; the volumetric air flow rate in the secondary jet 5-15 l/min; jet-to-crossflow momentum flux ratio $J = (u_{jet}/u_{flow})^2$ was set in the range 0.09-2.9. The frame rate for PIV snapshots was 10’000 frames per second, and the resolution was 512×352 pixels.

The supersonic experiments were performed in the wind tunnel IADT-50 of Laboratory 21.3 at the JIHT RAS. The information about flow structure and its dynamics was obtained by means of high-speed schlieren video recording. The oncoming flow was dry air with the operating parameters of the experiment as follows: Mach number M = 2, the oncoming flow velocity 500 m/s, static temperature 170 K, static pressure 22 kPa. The secondary jet was carbon dioxide with the operating parameters of the experiment as follows: mass flow rate was

2 and 4 g/s; jet-to-crossflow momentum flux ratios $J = (\rho u)_{jet}^2/(\rho u)_{flow}^2$ were 0.6 and 1.3 correspondingly. To minimize the influence of boundary layer, a special plate with a sharp front edge was used for jet injection. The frame rate for high-frequency schlieren video recording was 160'000 frames per second, and the resolution was 126×96 pixels.

In both cases the diameter of the injector orifice was 4 mm. Spark discharges were located between flat electrodes mounted in the plate at the windward side of the orifice. The discharges were powered by a pulse voltage generator with a frequency of 7-10 kHz and an average energy release in the discharge of ~20 mJ.

In the subsonic case, the jet's most distinct disturbance modes were identified by means of SPOD analysis. The most energy containing velocity oscillations were identified by means of Fourier transform. It is assumed that these frequencies can be used to force the jet by spark discharge /1, 2/. At the values of J for which the SPOD method was able to identify the most distinct disturbance modes, the jet was subjected to pulsed periodic heating by means of a spark discharge (Fig. 1).

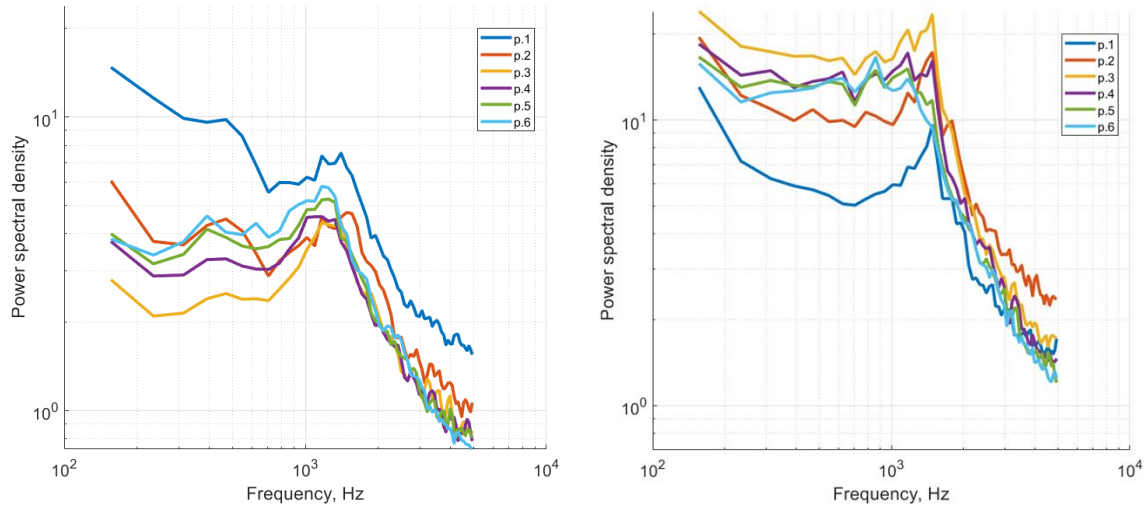

a) b)

Fig. 1 – The Fourier spectra in six points at the windward side of the transverse jet: a) without excitation; b) with excitation by spark discharges at the frequency of 1400 Hz.

In the supersonic case, the results show that at a small value of the jet-to-crossflow momentum flux ratio (J = 0.6), the spark discharges cause the formation of transverse vortices in the shear layer at the windward side of the secondary jet. At a larger value of the jet-to-crossflow momentum flux ratio (J = 1.3) such disturbances arise independently in the absence of discharges. It was shown that periodic spark discharges at J = 1.3 are capable of influencing the

frequency of disturbances in such a way that the characteristic frequency of vortices becomes a multiple of the discharge frequency (Fig. 2).

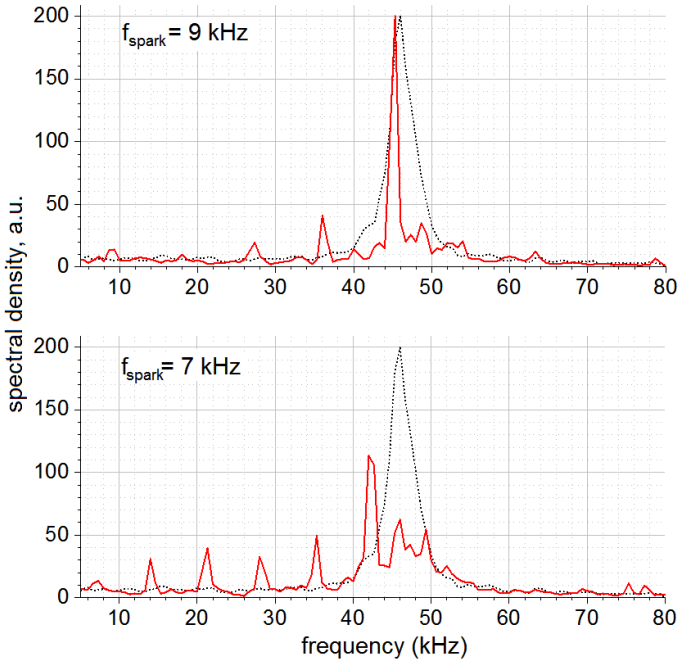

Fig. 2 – Periodograms for cases without discharge (dashed line) and with discharges at frequencies of 9 and 7 kHz (red solid lines).

It was shown that spark discharges are capable of initiating the formation of disturbances in the shear layer at the windward side of the jet and influencing their frequency. The data obtained will be used to analyze the physical mechanisms of intensification of gas mixing in a supersonic flow using electrical discharges.

Acknowledgements. This work was supported by the Ministry of Science and Higher Education of the Russian Federation (State Assignment).

References

1. **Volkov L.S., Firsov A.A.** Computer Research and Modeling // V.15, № 4, 2023, pp. 845–860.
2. **Zheltovodov A.A., Pimonov E.A.** Technical Physics Letters // V. 39, № 11, 2013, pp. 1016–1018.

CONTROL OF THE INSTABILITIES IN SHEAR FLOWS USING PLASMA ACTUATORS

I. Moralev

Joint Institute for High Temperatures, Moscow, Russia
morler@mail.ru

Surface dielectric barrier discharge was extensively studied in the last decades as an actuator for flow control application. It is assumed that plasma actuators have a high frequency response, robust and require small modification of the streamlined surfaces. However, the limited thrust and efficiency of the EHD flow acceleration at atmospheric pressures limited the application of these devices for the low velocities or the problems where the control efficiency itself is high and the mentioned plasma actuator advantages are crucial. One of these applications is the control of the flow instabilities in shear flows. Two key examples of these flows are the boundary layer, where the instability development leads to the transition to turbulence and the mitigation of noise, emitted by turbulent jets of airplane engines. In the convectively unstable shear flow, amplification of the disturbances can attain 10^4, thus the initial forcing can be weak relative to the final amplitude of the pulsations. Still, other issues are present that affect the actuator performance, including discharge unsteadiness, lifecycle against the system degradation and miniaturization of the discharge systems.

The first example is the transition to turbulence in the boundary layer. Transition to turbulence occurs due to development of the travelling or stationary primary disturbances that are amplified as they propagate downstream and eventually break out into a turbulent spot. One of the approaches for the control of these disturbances is so-called wave cancellation, when using the network of sensor and actuators the primary disturbances are removed from the flow in the counter-phase manner. Fig. 1 shows the layout of such system for the transition control in the boundary layer over a swept wing [1,2]. The dominant instability driving the transition in this flow is the cross-flow instability vortices. Initial disturbances can be forced either by oncoming flow turbulence of by surface roughness, then the turbulence level is low. In the latter case, the vortices are stationary and can be controlled by the feed-backward control loop. The system layout is shown in Fig.1a. Flow was organized on a flat plate with a sweep angle of 40^0. Bump on the upper wall was used to accelerate the flow to mimic the conditions on the leading part of the swept wing. Disturbances were excited by an isolated or distributed roughness at the distance of 70-100 mm from the leading edge. Plasma actuator was installed at the position 110 mm from the leading edge and consisted of 16 isolated electrodes, mounted under

the surface of the ceramic layer. External electrode was common and was formed of 4 strips of metal foil. Encapsulated electrodes were powered individually by resonant transformers with HF voltage at frequency of 60-80kV. Effect of the plasma actuator on the flow is assumed to be due to the volume force in each section, therefore, voltage distribution across the actuator led to variation in the spatial spectra of the introduced vortices. The optimal distribution was found using gradient descent method, with transversal flow modulation amplitude used as a gain function. Fig. 1b shows the result of this control at flow velocity of 25m/s and flat plate Reynolds number on the order of 10^6. One can see that cancellation of the primary disturbances can lead to the damping of the natural disturbances and shift of the transition to turbulence by up to 100mm, which is up to 15% of the model chord.

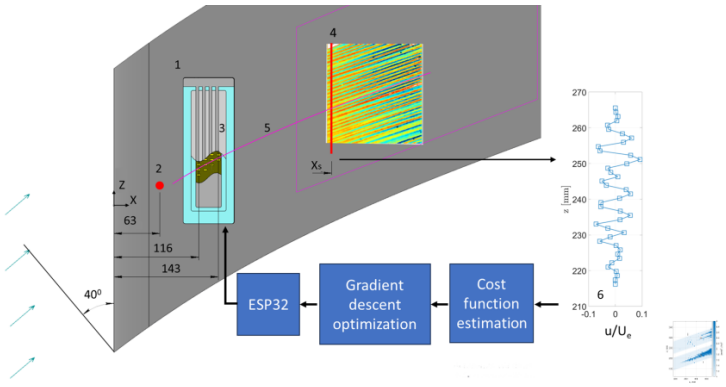

(a) (b)

Fig. 1. Transition to turbulence control in the swept wing boundary layer. (a) Experiment scheme, 1- swept plate, 2-roughness, 3- plasma actuator, 4- velocity field in the boundary layer, 5- line of constant phase for stationary cross-flow vortices. (b) Visualization of the turbulent wedge. 1- uncontrolled case, 2- controlled case [1]

It is known that carrier discharge at atmospheric pressures operates as an ensemble of microdischarges, stochastically moving along the edge of the electrode. Discharge unsteadiness creates hydrodynamic “noise” that affects the performance of the control system. Structure of the stochastic wavepackets induced by microdischarges was analyzed both in 2D and 3D boundary layers. A simple theory was developed for the prediction of the noise level, based on the correlation properties of microdischarges formation and model of ionic wind generation by discharge [3].

At higher velocities instability waves control was demonstrated for turbulent jets at Mach number up to 0.8 [4, 5]. Plasma actuator was placed on the inner surface of the nozzle, at the distance of 5 mm from the leading edge

and was powered by the high frequency voltage with an amplitude of 5-9 kV and frequency of 100-150 kHz. The typical power dissipation in the discharge was as high as 300 W/m, the discharge voltage was modulated by the controller. Feed-backward control was implemented using real time processor. Goal of the control was to minimize the pressure pulsations in the near field of the jet, measured by microphone (Fig. 2). Control law was designed offline using the particle swarm, optimization procedure. Spectra of the pulsations in the shear layer for the reference and controlled case are shown in Fig. 2b. It is obtained that damping of the disturbances in the shear layer can be obtained in the wide range of Strouhal numbers 0.2-0.5 for unexcited jets and in the whole frequency band for the stochastically excited jets. The factor limiting the system performance in this case appeared not to be the actuator properties but loss of the coherence between the microphones due to distributed excitation of instability waves and a waterbed effect, typical for the feed-backward control systems.

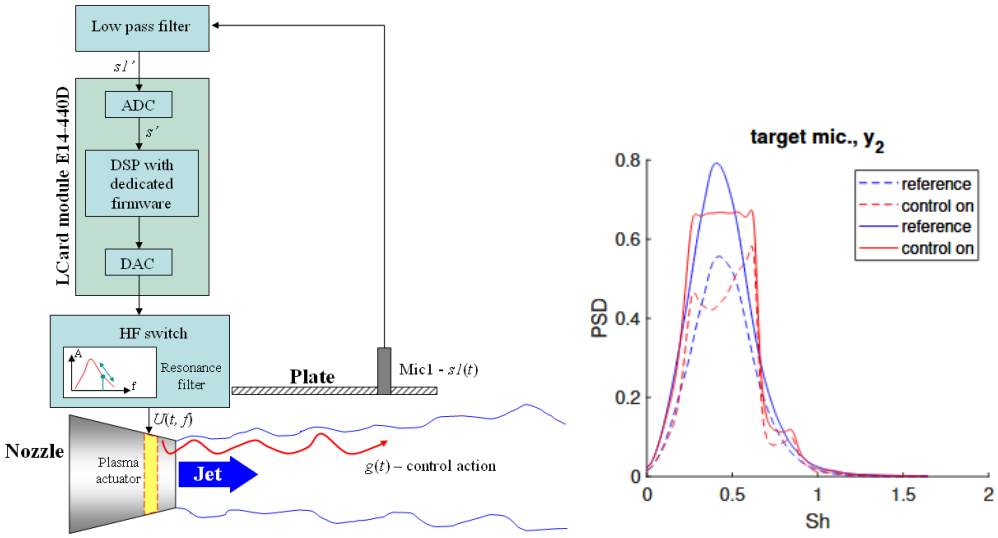

(a) (b)

Fig. 2. Control of the instability waves in the high velocity turbulent jet. (a) setup scheme, [4] (b)- spectra of pressure pulsations on the target microphone, M=0.4

Acknowledgements. The work was partly supported by the Russian Science Foundation within the framework of scientific project № 24-19-00627

References

1 А. Я. Котвицкий, А. А. Абдуллаев, М. В. Устинов, and И. А. Моралев, "Затягивание ламинарно-турбулентного перехода в пограничном слое на скользящем крыле методом подавления

стационарных возмущений с помощью плазменного актуатора,” ПЖТФ, vol. 51, no. 12, pp. 19–23, 2025.

2 **A. Abdullaev, A. Kotvitskii, I. Moralev, and M. Ustinov,** “On the Possibility of Cross-Flow Vortex Cancellation by Plasma Actuators,” Aerospace, vol. 10, no. 5, p. 469, May 2023.

3 **В. Ф. Копьев, О. П. Бычков, В. А. Копьев, Г. А. Фараносов, И. А. Моралев, and П. Н. Казанский,** “Активное управление шумом взаимодействия струи и крыла с помощью плазменных актуаторов в узкой полосе частот,” Акустический Журнал, vol. 69, no. 2, pp. 1–14, 2023.

4 **I. Moralev, M. Ustinov, A. Kotvitskii, I. Popov, I. Selivonin, and P. Kazanskii,** “Stochastic disturbances, induced by plasma actuator in a flat plate boundary layer,” Phys. Fluids, vol. 34, no. 5, 2022.

5 **И. А. Моралёв, Котвицкий, А.Я, and О. П. Бычков**, “Подавление волн неустой- чивости в стохастически возбужденной турбулентной низкоскоростной струе с использованием упреждающего управления,” Теплофизика Высоких Температур, vol. 62, no. 4, pp. 632–636, 2024.

6 **V. Kopiev, G. Faranosov, O. Bychkov, V. Kopiev, I. Moralev, and P. Kazansky,** “Active control of jet-plate interaction noise for excited jets by plasma actuators,” J. Sound Vib., vol. 484, p. 115515

LIBS ANALYSIS OF CARBON-CONTAINING SAMPLES BASED ON MOLECULAR SPECTRA REGISTRATION

M.I. Nedelko, A.A. Nevar, A.O. Radomtsev, N.V.Tarasenko

B.I. Stepanov Institute of Physics of National Academy of Sciences of Belarus , 68-2 Nezalezhnasti Ave., 220072 Minsk, Belarus

Abstract

Spatial and temporal resolved spectroscopic studies of the carbon and steel laser ablation plasmas in nitrogen were performed. The contribution of the emission of carbon-nitrogen diatomic molecules to the spatial-temporal characteristics of the whole plasma glow was determined. The spatial-temporal plasma regions suitable for the detection of molecular emission spectra in the LIBS analysis were established.

Introduction

The emission spectrum of the ablation plasma changes over time when the target is irradiated with pulsed laser radiation. At the initial stage of plasma development, broadband emission occurs due to bremsstrahlung and recombination processes. As the plasma cools, line spectra of ions and then atoms appear. At the final stage, molecular bands remain in the emission spectrum. In traditional LIBS spectroscopy, the elemental composition of a substance is analyzed by processing atomic spectra. In some cases, when analyzing difficult-to-excite elements or when the analytical lines of different elements overlap, this approach cannot provide a reliable result. In order to increase the sensitivity of LIBS, the use of dual- and multi-pulse excitation is of interest. The advantages of multi-pulse excitation include an increase in the plasma volume or heating of the plasma with a second pulse, which improves the detection limits of LIBS by 10 - 100 times. Over the last decade, a significant boost to the development of LIBS methods and new areas of application has been given by the use of molecular spectra in laser plasma emission for isotope analysis. The technique is based on the fact that molecules that differ only in the isotopic composition of the atoms they consist of have isotopic spectral shifts that are significantly greater than in atomic spectra, and therefore the former can be measured using conventional spectrometers with lower resolution. In general, LIBS still lags behind traditional methods of spectrochemical analysis in sensitivity and detection limit, as compared in particular, to inductively coupled plasma. A promising solution to the problem is additional analysis of molecular emission bands that arise in the plasma cooling phase.

1. Experimental

Laser plasma was formed by exposing graphite and steel to YAG:Nd^{3+} laser radiation with local displacement of air by a nitrogen flow. The setup diagram is shown in Fig. 1. The laser beam diameter was about 4 mm, and the divergence was 1.5 mrad.

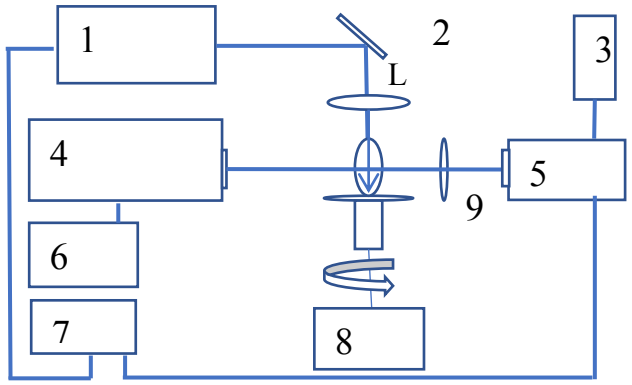

Fig. 1 – Setup diagram:
1 – laser, 2 – rotating mirror,
3 – photomultiplier,
4 – monochromator/spectrograph,
5 – monochromator, 6 – computer,
7 – oscilloscope,
8 – motor with reducer and target,
9 - lens

The laser beam was focused by a lens (F=280 mm) onto the surface of a graphite or steel disk used as a targets. To avoid crater formation on the sample surface and, consequently, changes in the linear dimensions of the erosion plasma, the disk was set in motion by a motor with a gearbox (8). Rotation of the target also made it possible to avoid its rapid destruction. A telescope was used to focus the plasma emission onto the slit of a GSM-850 Lotis TII monochromator/spectrograph (4), made according to the Czerny-Turner scheme with a flat diffraction grating of 600 lines/mm. The entrance slit size was 15 μm. The emission spectra were recorded by a CCD Hamamatsu detector C10416.

The plasma image was also projected in the opposite direction by a quartz lens (quartz, F=75 mm, achromat) onto a small diaphragm (0.5 × 0.5 mm) adjacent to the monochromator (5). The monochromator bandwidth at half intensity was 1.8 nm. A photomultiplier-84 (3) was placed behind the monochromator to record the intensity of the selected plasma emission line over time. The signal from the photomultiplier was fed to the input of a BORDO-422 digital oscilloscope (7) coupled with a personal computer (6). The radiation was collected at the right angle to the laser beam exciting the plasma.

2. Results and Discussion

In LIBS analysis based on molecular spectra, the interpretation of the obtained data only becomes more complicated, since the formation of molecules occurs only under certain conditions: the simultaneous presence of atoms of the corresponding elements in the same plasma zone, the presence of the necessary pressure, temperature, etc., the implementation of which in a non-stationary laser plume /1/ requires information about the spatio-temporal distribution of excited molecules in the laser plume. A typical temporal distribution of CN molecules emission in the region of the edge of the (0,0) band in the laser plume with the background subtracted is shown in Fig. 2.

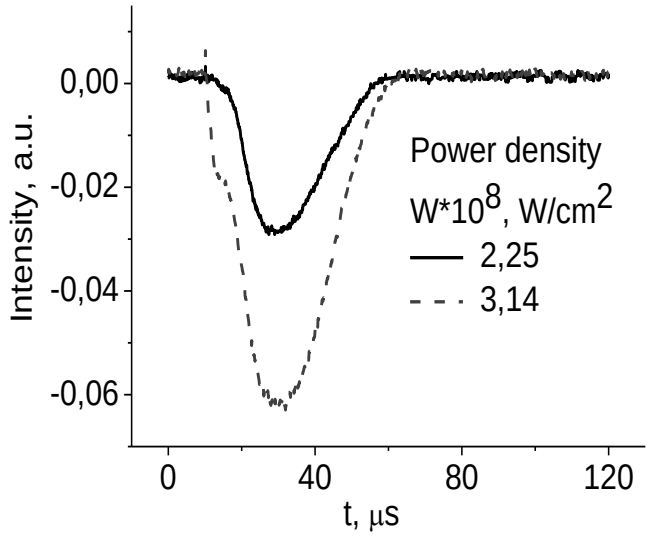

Fig. 2 – Oscillogram of the emission of the CN(0,0) molecule at a distance of 2 mm from the target surface at a wavelength of 388 nm with background subtraction

As the observation zone moves away from the target surface, the maximum intensity of the molecule emission in the plasma spectrum is observed at increasingly later stages of plasma evolution, while the intensity of the continuous background decreases. It turned out that the region of maximal amplitude values of the CN (0.0) emission intensity at the 388 nm with variation in the values of the laser radiation power density from 225 to 371 MW/cm^2 does not depend on the exposure power and is located at a distance of 1.5 mm from the target surface (Fig. 3).

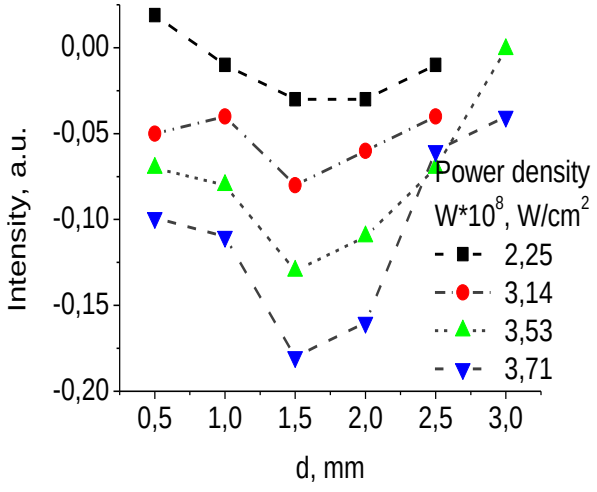

Fig. 3 – Amplitude values of the emission intensity of CN (0,0) at the 388 nm line depending on the distance to the target and the power density of the laser pulse

Fig. 4 shows oscillograms of the emission of laser-induced plasma recorded from the plasma region located at a distance of 1.5 mm from the target surface during ablation of cast iron and the standard steel 65-2

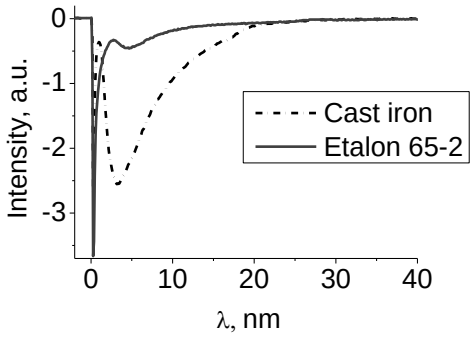

Fig. 4. Oscillograms of plasma emission during laser ablation of cast iron and standard steel 65-2 (%C=0.0034%)

(%C=0.0034%). It is evident from Fig. 4 that the molecular spectrum of cyanogen in the region of the band edge ~ 421 nm is observed even at low values of carbon content in the studied samples. The registered molecular emission of cyanogen molecules during ablation of low-carbon steel samples demonstrated a sufficiently high sensitivity of the method. For comparison, the plasma spectra of cast iron and graphite samples excited by the action of neodymium laser radiation (wavelength 1064 nm, power density on the target $3.71 \cdot 10^8$ W/cm^2) were also registered. In the cast iron plasma spectrum (Fig. 5), no lines of cyanogen molecules were detected when spectra were recorded by a LIBS spectrometer with a CCD array. This fact indicates insufficient sensitivity of the traditional approach for analyzing carbon in steels and cast irons by using the laser-induced plasma spectroscopy.

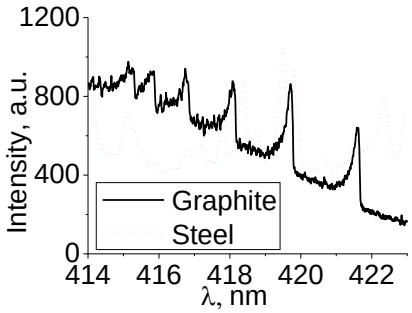

Fig. 5 – Normalized plasma spectra of steel (dotted) and graphite (solid) in the region of 415-422 nm at a laser power density of $3.71 \cdot 10^8$ W/cm^2

Conclusion

The registered molecular emission of cyanogen molecules during ablation of low-carbon steel samples demonstrated the possibility of increasing the sensitivity of the LIBS method by recording molecular emission spectra of laser-induced plasma with spatiotemporal resolution, which opens up prospects for the development of a LIBS spectrometer with the increased analytical characteristics. The work was carried out within the framework of task 2.2.05 of the Convergence program.

References

1. Parigger C.G. et al Trends in Appl. Spectr.11 (2014) 13.

FORMATION OF SUBMICRON TITANIUM CARBIDE PARTICLES BY ELECTRICAL DISCHARGE TREATMENT OF TITANIUM TC4 MICROPOWDERS

A.Shumeijko[1], A. Nevar[1], V. Aniskevich[1], M. Nedelko[1], N. Tarasenko[1], Y. Song[2]

[1]B.I. Stepanov Institute of Physics of the National Academy of Sciences of Belarus,
68-2 Nezavisimosti Ave., 220072 Minsk, Belarus,
al.shumejko@gmail.com, a.nevar@ifanbel.bas-net.by
[2]International Center of Future Science, Jilin University, China

The use of submicron titanium carbide particles in additive manufacturing technologies offers significant advantages in enhancing the mechanical properties of fabricated components. Specifically, incorporating TiC particles into metallic matrices can substantially increase hardness and wear of coatings, which are critical for applications subjected to abrasive conditions. Additionally, the presence of these submicron titanium carbide particles contributes to improved strength and impact toughness, thereby extending the service life and reliability of the final products.

In this study, we investigate the possibility of obtaining submicron TiC particles through high-voltage electrical discharge treatment of titanium (TC4) micropowders dispersed in ethanol. The results of the morphological, compositional and structural analysis of the synthesized material are presented.

A modified power source operating in high-voltage spark mode was used to perform electric discharge processing of TC4 powder. The discharge was initiated by applying a high-frequency voltage of 8.5 kV. The power source supplied alternating current to the spark discharge with a repetition rate of 100 Hz. The relaxation time pulse generator produced a typical oscillating discharge current with a high peak intensity (10-12 A) and a single discharge pulse duration of 2-5 μs. The total duration of the plasma treatment process was 10 and 30 minutes.

The experimental setup is described in detail in /1/. Electric discharges were initiated between two titanium electrodes: one fixed at the bottom of a conical container filled with TC4 micropowder and ethanol, and the other movable, allowing for regulation of the interelectrode gap. The shape of the cuvette allowed particles ejected from the discharge zone to settle on the inclined walls and, under the influence of gravity, re-enter the discharge zone. This configuration enabled intensive mixing: some particles, after being lifted from the electrode surface by the shock wave, entered the bulk liquid volume and formed vortex flows confined by the chamber walls. Heating of the liquid during the discharge eventually led to its intensive boiling, in which case the experiment was temporarily stopped and resumed after the liquid had cooled. The optimal distance between the electrodes is maintained constant at approximately 1.5 mm to ensure stable discharge conditions.

The resulting colloidal solution was separated into two fractions: the top fraction – a colloidal suspension containing fine particles, and the sediment –

consisting of larger particles.

Analysis of SEM images (Fig. 1) and particle size distributions before and after electric discharge modification showed that plasma treatment led to significant fragmentation of the micropowder, resulting in the formation of multiple particle size fractions.

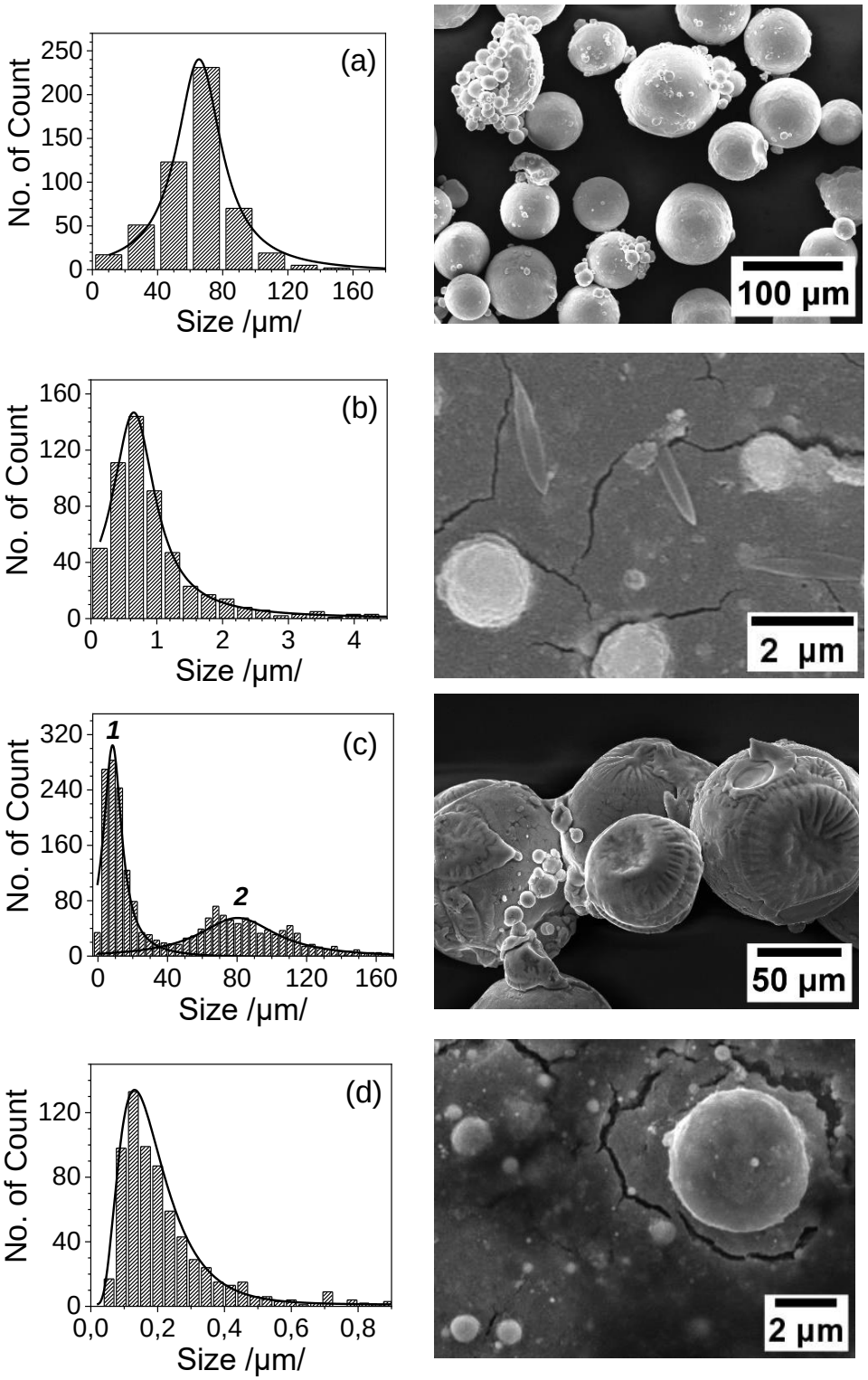

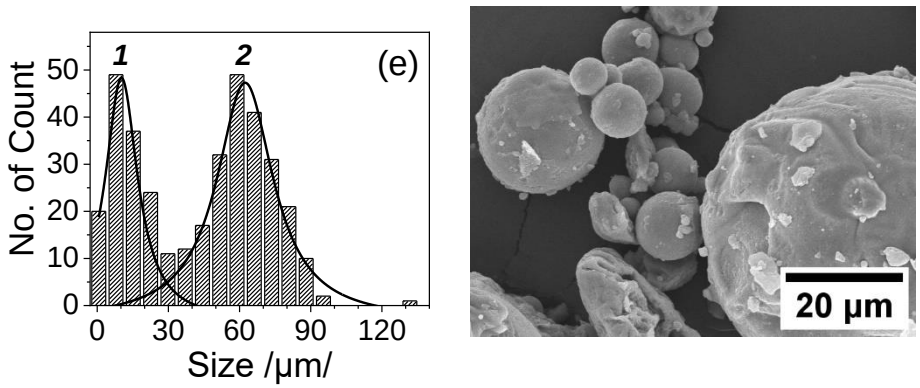

Fig. 1 – SEM images and particle size distribution histograms for the original TC4 powder (a), top (b, d) and sediment (c, e) fractions of the TC4 powder after 10 min (b, c) and 30 min (d, e) of EDM

The size of particles in the top fraction depended on the treatment duration: 0.6 μm after 10 minutes of treatment (Fig.1b) and 0.1 μm after 30 minutes (Fig. 1d). It is worth noting that in both cases, a small number of larger particles (~11.6 μm) were still present.

The sediment of the treated TC4 sample was dominated by two particle size ranges: 11.6 μm and 62.9 μm (marked as 1 and 2 in Fig. 1c and 1e, respectively). The latter size is comparable to that of the original powder (65.3 μm, Fig. 1a), indicating partial retention of large fragments.

Similar bimodal distributions were also observed during electric discharge treatment of other α+β titanium alloys in various dielectric media, including kerosene /2/.

For the top fraction of the TC4 sample, pronounced bands were recorded in the Raman spectra (Fig. 2a) at 264, 420, and 608 cm^{-1}, along with two broad maxima at 1349 cm^{-1} and 1587 cm^{-1}. The first three peaks, according to the literature /3/, correspond to titanium carbide, which was subsequently confirmed by XRD study. The D-band at 1349 cm^{-1} and the G-band at 1587 cm^{-1} are characteristic of defective and graphitic carbon, respectively.

X-ray diffraction analysis (Fig. 2b) of the products obtained after electric discharge treatment of titanium-containing micropowders in ethanol revealed the presence of metallic titanium, as well as compounds with carbon and oxygen.

The appearance of the hexagonal phase of titanium (α-Ti) may be associated with the decomposition of intermetallic bonds in the TC4 alloy under the influence of high temperatures. Titanium carbide was detected in both fractions of the plasma-treated TC4 sample. The formation of TiC can be attributed to the reaction of titanium with active carbon radicals released during the pyrolysis of ethanol under electric discharge conditions.

During electric discharge treatment of titanium in the presence of oxygen-containing components, the most likely oxidation product is titanium dioxide. However, under conditions of limited oxygen availability and the simultaneous

presence of reducing agents such as hydrogen and carbon released during ethanol pyrolysis, TiO_2 can be reduced to suboxides, particularly Ti_2O_3 or Ti_2O /4/.

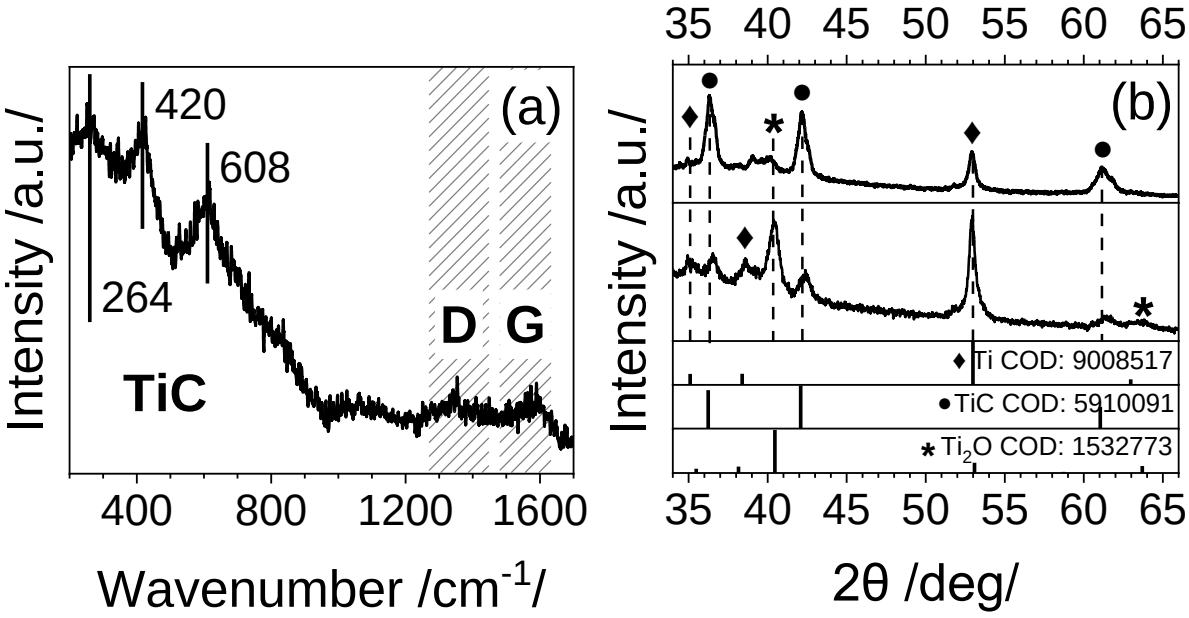

Fig. 2 – Raman spectra (a) of the top fraction of plasma treated TC4 powder; XRD patterns (b) of the top and sediment fraction of plasma treated TC4 powder

The decrease in total crystallinity in the sediment compared to the top fraction further indicates the accumulation of amorphous components and an increased proportion of oxides.

Comprehensive analysis of the morphology, phase composition, and Raman spectra revealed that the electrical discharge treatment leads to degradation of the initial structure, accompanied by the formation of α-Ti, TiC, and titanium suboxides. The synthesized material comprises particles spanning both submicron and micron-scale dimensions. Future studies will focus on elucidating the mechanisms of phase formation, as well as the specific pathways of titanium carbidization and oxidation under conditions of localized high-energy input in a carbon-containing liquid medium.

Acknowledgements. This work was supported by the by the National Academy of Sciences of Belarus under project Convergence 2.2.05.

References

1. **Tarasenka N., Nomine Al., Nevar A.,** et al**.** Phys.Rev.Appl., 13 (2020) 014021.
2. **Khilji I.A., Saffe S.N.B.M., Pathak S**., et al. JOM 74 (2022) 448–455.
3. **Huanhuan Du, Yurong Wang, Dongyang Xiao, et al.** Nanoscale Adv. 4 (2022) 2444–2451.
4. **Zhang Yu-Wen, Ding Wei-Zhong, Lu Xiong-Gang**, et. al. Trans. Nonferrous Met. Soc. China 15 (2005) 594-599.

USING OF THE PLASMA ARC EJECTOR FOR WASTE TREATMENT

P. Petrenko[1,2], A. Pereslavtsev[1], A. Artemov[1],
S. Voschinin1, N. Chemodanov[1]

[1]National Research Center «Kurchatov Institute», Akademika Kurchatov Square, 1, Moscow, 123098, Russia, nrcki@nrcki.ru, petrenko_pi@nrcki.ru
[2]National Research Nuclear University MEPhI (Moscow Engineering Physics Institute), Kashirskoe shosse, 31, Moscow, 115409, Russia info@mephi.ru, ppiu4@mail.ru

The plasma ejector for waste treatment is used in the well-known PAWDS (Plasma Arc Waste Destruction System) /1/. The key patented process is that it first shreds and then mills waste into a lint-like material so that it is transformed into a highly efficient fuel. This milled waste is then rapidly gasified in Plasma fired Eductor. The resulting synthesis gas is then mixed with air in lightweight Combustion Chamber, resulting in a fully oxidized off-gas, comprised of carbon dioxide and water. This off-gas is then shock cooled from above 1,100 °C to approximately 80 °C, using a Water-Quench, preventing the reformation of dioxins and furans. The system consists of three basic sub-systems (Fig. 1): waste preparation, thermal destruction and off-gas treatment.

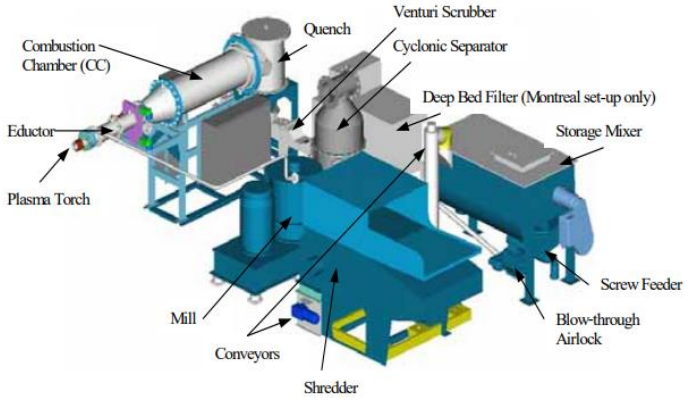

Fig. 1. PAWDS System Overview

In the process, combustible waste such as food, paper, textiles, wood, cardboard and plastics are pre-treated through a series of size reducing equipment and converted to “lint”. The waste pre-processing subsystem is composed of a Shredder, Shredded Waste Conveyors, a Storage Mixer, and a Mill. Waste is fed into the Shredder where its size is reduced. The waste is then transported to the Storage Mixer using Shredded Waste Conveyors.

The waste lint, which becomes the “fuel” to the system, is conveyed by air and injected into the Plasma-fired Eductor (Fig. 2) /2/. In the Eductor, the waste fuel or “lint” is exposed to a high temperature of approximately 1,000 °C that results in rapid gasification of the solid waste into a synthesis gas composed primarily of carbon monoxide (CO) and hydrogen (H_2). This gas then flows into

the Combustion Chamber, where additional air is used to complete the combustion and convert the synthesis gas into carbon dioxide (CO_2) and water vapour (H_2O). The gas temperature in the Combustion Chamber is typically about 1,100°C. Any traces of inorganic substances are transformed into an inert ash. A feature of the PAWDS technology is its use of air and/or water-cooled walls instead of heavy refractory for the Eductor and Combustion Chamber. Internal to the water-cooled jacket for the Combustion Chamber is an air-cooled liner made of superalloy.

This process shows the complexity of equipment implementation and maintenance, as well as the high cost. Due to the complexity of operation, this technology has not been widely used commercially, but it is planned to be implemented on aircraft carriers of the US Navy.

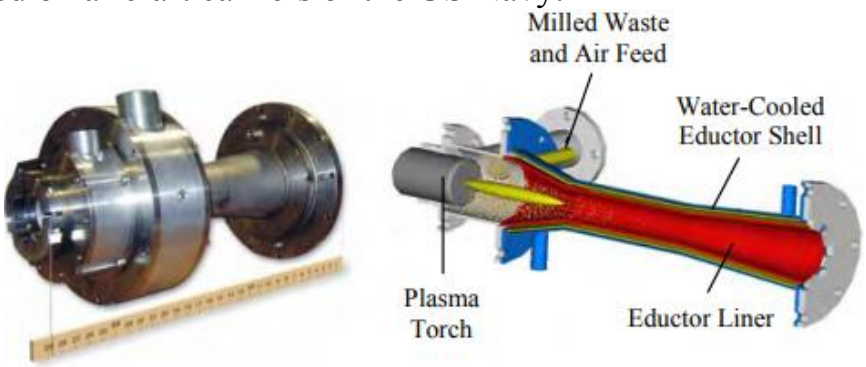

Fig. 2. Photograph and schematic of the Plasma-Fired Eductor Plasma Torch Water-Cooled Eductor Shell

Inspired by this research, our research team decided to conduct our own research in this area. The concept of a system based on a plasma arc ejector for processing liquid or granular solid waste was created. A mathematical model has been created to describe the processes occurring in an arc ejector.

This work is aimed at creating a mathematical model of a plasma-arc ejector as the main component of a mobile plasma installation. The objectives of this work are as follows:

- to analyze of existing and currently used plasma installations;
- to study the main physical and chemical processes in the plasma waste treatment;
- to justify of the chosen disposal method and calculation of the necessary characteristics and parameters of the plasma torch and ejector;
- to calculate the material and heat flow of the process in the ejector;
- to perform the mathematical modeling of the process in a plasma-arc ejector chamber.

The ejector is a chamber-type installation (Fig. 3) with an EDP-200 plasma torch and gas and water supply system. Depending on the composition of the municipal solid waste, 1 kg can produce 1.5 to 15 Nm^3 of gas. The gas is cooled

and released into the atmosphere. The electric arc plasma torch for heating air with a nominal power of 200 kW has a continuous operation time up to 350 hours with the ability to quickly replace the electrodes.

Tasks:
1. To obtain the temperature distribution
2. To obtain the velocity distribution
3. To obtain the current lines.

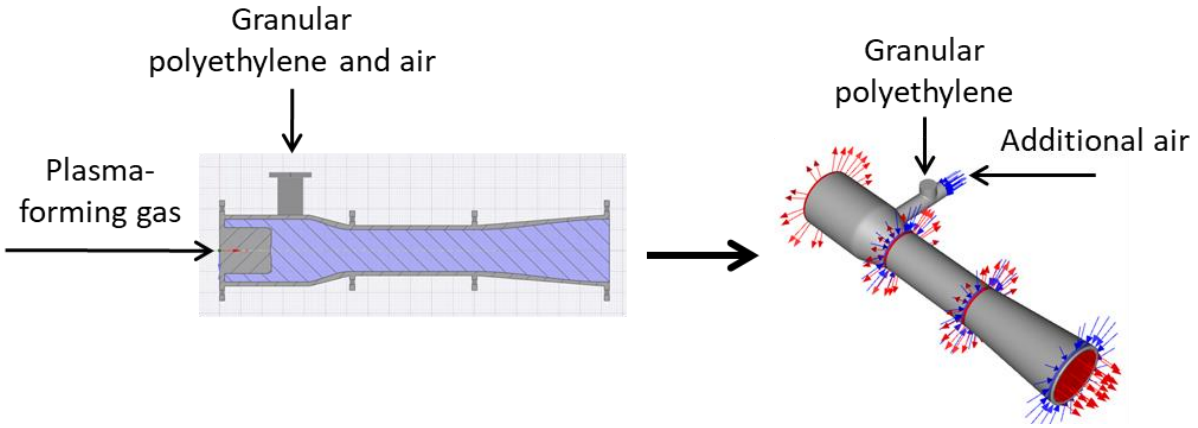

Fig. 3. General view of the ejector model. The figure on the left shows the cross section of the model's grid. The figure on the right shows a general view (blue arrows indicate incoming water into the cooling system; red arrows indicate discharge from the installation).

The basis of the chamber is a steel bell, preheated plasma-forming gas is supplied to the plasma torch from the end for further ignition. The feed of the processed material occurs tangentially to the axis of the chamber. Within the framework of this model, at the exit from the ejector it is necessary to provide a pressure vacuum up to 2000 Pa. In the ejector chamber, the process of high-temperature pyrolysis takes place, but the temperature in the chamber reaches such values that the organic substances are completely decomposed. Then, according to the laws of chemical kinetics, simple chemical compounds are formed.

Basic reactions:

$$(C_2H_4)_n + 1{,}5O_2 = 2CO + H_2 + H_2O$$
$$CO_2 = CO + 0{,}5O_2$$
$$CO + H_2O = CO_2 + H_2$$

Adverse reactions:

$$H_2 + 0{,}5O_2 = H_2O$$
$$N_2 + O_2 = 2NO$$

The energy (heat) balance of any apparatus can be represented in the form of an equation that relates the input and output of the process (apparatus) energy. The energy balance is based on the law of conservation of energy, which states that the sum of all types of energy is constant in a closed system.

To model the flow dynamics the system of equations is solved using the k-ε turbulence model /3/ with the Non-Premixed Combustion and Species Transport chemical kinetics models.

The k-ε turbulence model considers two equations: the kinetic energy of turbulence (k) and the dissipation of turbulent energy (ε):

$$\frac{\partial}{\partial t}(\rho_m k) + \nabla(\rho_m \vec{v}_m k) = \nabla\left(\frac{\mu_{t,m}}{\sigma_k}\nabla k\right) + G_{k,m} - \rho_m \epsilon$$

$$\frac{\partial}{\partial t}(\rho_m \epsilon) + \nabla(\rho_m \vec{v}_m \epsilon) = \nabla\left(\frac{\mu_{t,m}}{\sigma_k}\nabla \epsilon\right) + \frac{\epsilon}{k}\left(C_{1\epsilon} G_{k,m} - C_{2\epsilon}\rho_m \epsilon\right)$$

The equation for k describes the energy carried by turbulent vortices, while the equation for ε describes the rate at which this energy is dissipated.

The k-ε turbulence model is based on the assumption of a local equilibrium between the production and dissipation of turbulent energy. It provides information about the distribution of velocities and directions in the flow. This makes it possible to more accurately predict the behavior of turbulent flows.

The equation for k describes the energy carried by turbulent vortices, while the equation for ε describes the rate at which this energy is dissipated.

Based on the calculations of the material and heat balances and the developed geometry, a mathematical model of the ejector vortex dissipation was created. A dynamic model was calculated with a flow of 40 kg/h of polyethylene particles, a flow of water to the cooling system, and a time interval of 5 seconds.

Preliminary calculations of the material and heat balances have been carried out. The calculation of the material balance is consistent with the results of mathematical modeling, with discrepancies of 5-7%.

In conclusion, the following results were obtained: a model of a plasma arc ejector was developed. The decomposition process of polyethylene particles is modeled. The distribution of temperatures, velocities, and current lines is obtained. The recycling process is consistently calculated both in stationary and dynamic modes, taking into account the movement of waste particles and chemical reactions.

References

1. **Chronopoulos C. et al.** The Plasma Arc Waste Destruction System–One Year of Maritime Experience // Proceedings of the IT3 2005 conference, Galveston, Texas. 2005.
2. **Alexakis T. et al.** A Plasma-Arc-Assisted Thermal Treatment System For Shipboard Waste // Proceedings of the 21st Conference on Incineration and Thermal Treatment Technologies. 2002.
3. **Pashchenko D. I., Naplekov I. S.** CFD-modelirovanie goreniia sinteticheskogo topliva v zakruchennom fakele //Matematicheskie metody v tekhnike i tekhnologiiakh-MMTT. 2019. T. 9. pp. 104-110.

OZONE-HYDROXYL MIXTURE FOR WATER PURIFICATION AND DISINFECTION

I.M. Piskarev[1] , N.A. Aristova[2] , I.P. Ivanova[4] , I.I. Vasina[3]

[1]Skobeltsyn Institute of Nuclear Physics, Lomonosov Moscow State University, Russia, i.m.piskarev@gmail.com
[2]Nizhny Tagil Institute of Technology, Ural Federal University, Russia, aristova-na@mail.ru
[3]Ural State University of Physical Culture, Russia, vasina_irina@mail.ru
[4]Lobachevsky State University of Nizhny Novgorod, Russia, ivanova.ip@mail.ru

Abstract

The possibilities of cold plasma from a corona electric discharge in the geometry of a point electrode-plane under negative voltage polarity on the point electrode for the creation of ozone-hydroxyl mixture generators have been considered. The ozone-hydroxyl mixture is formed during the corona electric discharge in air and in water vapor. The lifetime of hydroxyl radicals under these conditions is approximately 0.12 seconds; ozone is consumed to sustain the life of hydroxyl radicals. The parameters of the power supply chain for point discharge electrodes are analyzed. As an example, a functional diagram of a closed-type generator with a treated liquid volume of 50 ml and a total discharge current of 0.5 mA is considered, along with a flow reactor with a discharge current of 5 mA, a capacity of 250 l/h, and a flow-circulation reactor with a capacity of 25 – 250 l/h. The flow-circulation reactor allows for an increase in the dose generated in the liquid by reducing the water throughput. The energy costs for generating hydroxyl radicals in a corona discharge are about 500 eV per radical. It is not economically viable to treat heavily contaminated water. To remove resistant impurities, such as antibiotics, it is necessary to pre-treat the water and then carry out further purification with an ozone-hydroxyl mixture. For each reactor, the doses created in the processed liquid are determined. The advantages and disadvantages of each design variant are compared.

Specific schemes of corona discharge generators and their characteristics

Processing a fixed volume of water in a closed reactor

The block diagram of the closed generator is shown in Fig. 1. The reactor body is made of glass, and a 500 ml vessel was used. 50 ml of the processing liquid was poured into the bottom of the vessel. The liquid was grounded through an electrode introduced from the bottom. Electrodes made of stainless steel with a diameter of 2 mm were introduced through the top cover, to which a voltage of 11 kV negative polarity was applied through a ballast resistor. A

corona discharge ignites on the electrodes above the water surface. To achieve maximum electric field intensity, the distance between the electrodes was at least 20 mm. The negative polarity of the voltage was chosen to ensure the stability of the corona discharge. The distance between each discharge electrode and the water surface was 6.5 mm. Active particles are generated in the area of maximum electric field intensity.

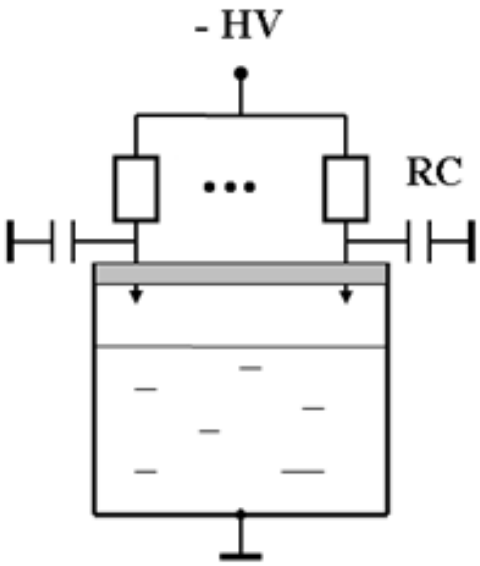

Fig. 1. Block diagram of a closed-type corona discharge cold plasma generator

The obtained values of active particle yields using the methodology described above are normalized to the total current from all electrodes of the reactor. The yield of ozone was obtained as 130 ± 10 mol/(mol of electrons), which corresponds to an ozone production rate of 25 g/(kW·hour), the yield of OH• radicals is 26 ± 4 mol/(mol of electrons), and the yield of H_2O_2 is 2 ± 0.4 mol/(mol of electrons). Thus, the output of hydrogen peroxide is small, and it can be disregarded, especially considering that it is consumed in interactions with hydroxyl radicals. Ozone interacts with OH• radicals, forming an ozone-hydroxyl mixture, in which ozone is consumed to maintain the concentration of hydroxyl radicals.

Flow generator of corona electric discharge

The block diagram of the flow generator of corona discharge is shown in Fig. 2. A high voltage of negative polarity of 11 kV is applied to the resistor matrix. In the considered design, the corona discharge is ignited at 49 point

electrodes above the flat surface of the grounded electrode 3. The discharge current was 5 mA. The power scheme for each electrode is the same as for the reactor in Fig. 1. Hydroxyl radicals are generated in the discharge gap. The treated water is supplied to the inlet of ejector 1. The ozone-hydroxyl mixture produced in the discharge gap is sucked in by the ejector and mixed with water. Hydroxyl radicals immediately interact with the impurities in the water, while some ozone remains. From the ejector, the water flows into the generator cavity. Here, ozone is separated from the water and mixed with a stream of fresh air.

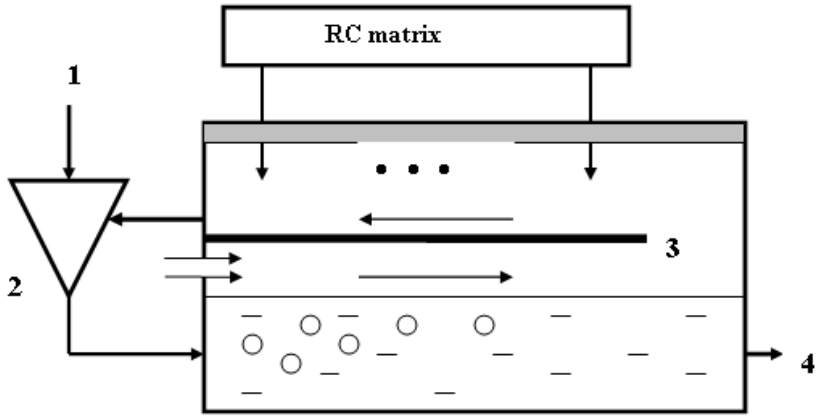

Fig. 2. Flow generator of cold plasma from a corona electric discharge. The numbers denote: 1 - inlet for treated water; 2 - ejector; 3 - grounded electrode; 4 - outlet for treated water

A gas mixture containing ozone, air, and water vapor surrounds the grounded electrode, passes through the discharge chamber where an ozone-hydroxyl mixture is formed again, and is sucked back in by the ejector. Thus, the gas mixture circulates within the generator. The concentration of ozone gradually increases and reaches a steady state after 15 minutes. The treated water flows out through opening 4. After treatment, the water becomes saturated with dissolved oxygen up to the limit of solubility at this temperature. Air is trapped in water in the form of small bubbles that slowly rise over the course of several days. Gas bubbles in the treated water were directly observed using a microscope.

Continuous circulation generator of corona electric discharge

The generator scheme is shown in Fig. 3. In the flow-type generator discussed above (Fig. 2), the delay time of the treated liquid in the cavity of the generator, where the liquid is directly exposed to the active particles, can be 1.5 minutes. During this time, a certain amount of hydroxyl radicals is generated, which can interact with water impurities. If there are many

impurities, then, despite the high oxidative capacity of the hydroxyl radicals, their amount may be insufficient to purify the water. Therefore, a circulation scheme is considered, in which water can undergo treatment multiple times. The flow of incoming water should be reduced, but the residence time in the chamber will increase. The productivity decreases, but the dose generated by the active particles increases. The generator uses two ejectors: one for the incoming water flow, and the other for circulation.

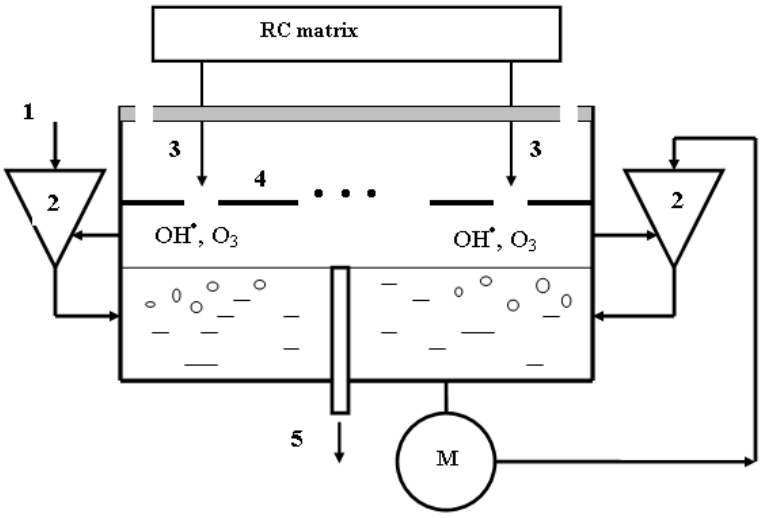

Fig. 3. Flow-circulation generator of cold plasma of corona discharge. The numbers indicate: 1 - inlet of the treated water; 2 - ejectors; 3 - discharge electrodes; 4 - grounded electrode; 5 - outlet of treated water

The water level in the generator chamber is determined by the height of tube 5, through which the processed liquid is drained. The thickness of the gas layer between the surface of the water is at a level of 4 - 5 cm. Unlike the design in Fig. 2, there are holes with a diameter of 7 mm opposite each conductive electrode 3 in the grounded electrode 4. The electronic wind, carrying active particles, passes through the opening and enters the gas cavity above the water.

The study was conducted under the state assignment of Lomonosov Moscow State University.

SYNCHRONOUS PURIFICATION OF DIESEL ENGINE EXHAUST GASES FROM NITROGEN OXIDES AND SOOT USING NANOSECOND CORONA DISCHARGE PLASMA SYSTEMS

A.Z.Ponizovsky, S.G.Gosteev, O.S.Kuzhel, S.P.Kryuchkov, V.A.Maevsky, A.S.Smirnov, I.G. Agrelov, S.N.Filippov

FMDB "Horizont", Moscow region, Dzerzhinsky, Energetikov st. 7, horizontL56@rambler.ru

Despite the fact that there is a large number of studies related to the use of low-temperature nonequilibrium plasma (LSTP) for cleaning diesel engine exhaust (DEE) gases (DEE) from nitrogen oxides (NOx) /1,2/ and soot /3/, currently there is not a single standard operating installation installed on the car. The reason for this is, firstly, the relatively high energy consumption for cleaning the DEE, secondly, the significant dimensions of the pilot plants, and thirdly, the design differences between NOx and soot purification plants. This paper describes the design of the installation, which makes it possible to carry out both processes in a single volume of the reactor chamber by using a nanosecond corona discharge (NSCD) and HVDC. In addition, it has been shown in experiments with real diesel engines that the use of NSCD in jointly with a sorbent and an active catalyst at an DEE temperature of no more than 70°C can dramatically reduce energy consumption during the purification from NOx. In this case, the catalyst was activated by exposure to HV pulse and HVDC. The results of experiments on a prototype of a mobile installation for the of cleaning of DEE from NOx, located in the back of a FORD TRANSIT car in the parking lot and driving through the streets of the city, are also presented.

1. Experimental. Stationary and automotive DEE were cleaned using pilot installations consisting of a three-stage generator according to the Fitch scheme (HVGPF)/3/ and a set of reactor chambers (RC), systems for measuring electrical and gas parameters. The basic version of the RC (Fig.1a) is a grounded pipe with a multi-pointed HV electrode coaxially located in it. In the variant (Fig.1.b), a chamber (KC) filled with a catalyst (V_2O_5) was placed between the two RC, which also had a coaxial design in which the catalyst was located between a tubular HV electrode and a grounded electrode - the inner wall of the RC, insulated from them by ceramic tubes. In a number of experiments, an external chamber (SC) filled with Al_2O_3 sorbent was installed at the outlet of the RC. Volume SC and KC are 2L. Figure 1c shows the oscillograms of the electrical parameters during the operation of the treatment plant. The principle of operation of pulse generator according to the Fitsh scheme (HVPGF) /3/ is that HV pulses are superimposed on a HVDC equal to the charging voltage (Uch). In this case, the pulse amplitude is Up≈3Uch. In the RC at the moment of pulse NSCD with current (Ip) and power (Pp) are generated and NNTP are created. Under the action of NNTP nitrogen oxides are converted into an aerosol of nitric acid. In the pause between passes, the RC works as an electrostatic precipitator and the DEE is

cleaned of aerosols and a soot. The Upl and Uch voltages were measured with a DVN-80I divider; current (Ipl) by current transformer CT-3-0.1. The Upl and Ipl pulses were recorded by a Tektronix 2114 oscilloscope, which synchronously calculated the power of the NSCD Pp = Up•Ip, which made it possible to calculate the energy embedded in the pulse (Wp) as Wp≈ Pp•Δt/2, where Δt is the pulse duration. Concentration NO, NO_2 and NOx = NO+NO_2 (C_{NOx}) were measured with TESTO 335 and 350 gas analyzers. The value of the soot number (FSN) was measured by the Testo 308 (fig 4c), followed by conversion to the concentration of soot Cs =16*FSN^2 [mg/m^3]. Since the engine differed in working volume (Vd [L]), speed (ω [1/min]), and C_{NOx}, the parameters used to compare of results were the purification efficiency ή=($C_{NOx\ initional}$–$C_{NOx\ finish}$)/$C_{NOx\ initional}$,[%], specific energy Ws=60Wp•f/Vd [J/L], and the energy efficiency of NOx removal R= Ws/C_{NOx} [J/L*ppm].

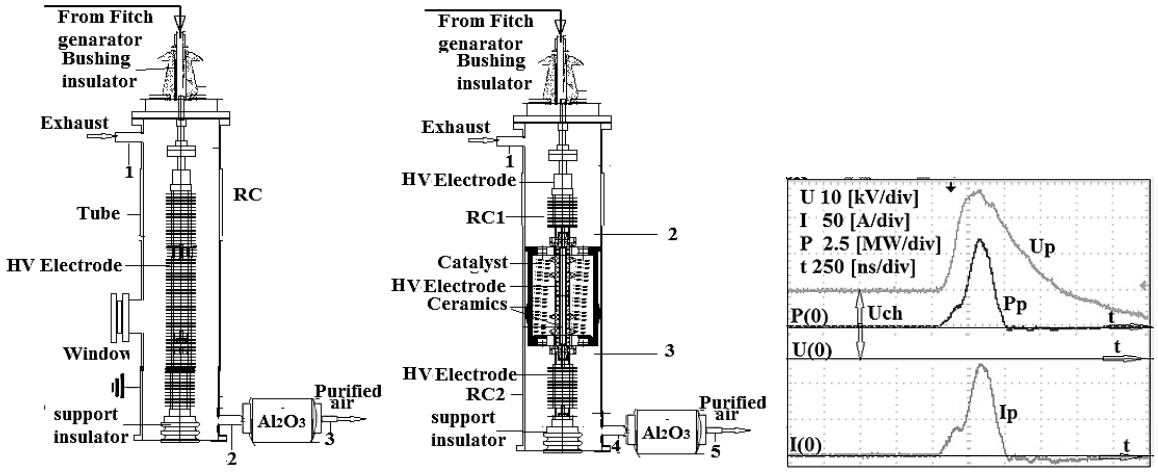

(a) (b) (c)

Fig. 1 Design of RC (a),(b), oscillograms of electrical parameters of NSCD (c)

The main parameters of the DD subjects are presented in Table 1.

Engine type	Vd [L]	Power [kW/hp]	ω [1/min]	Vd*30ω [m^3/h]
GP5-DE	0.418	4.5/5.4	3000	36
Volvo tao532	4.8	110/150	1500	216
KIA Sportage	2	136/184	800	48
Ford "Transit"	2	91/125	800-2500	48-150

The main parameters of the treatment plants are shown in Table 2.

Parameters		X4	X1a	X1б	X2
Stage capacity,	nF	6	4	4	4
Switchboard		TGI 1- 1000/25			TPI1-1к/35
Charging voltage	kV	30	21	21	30
Parameters of pulse. t_f/t_p,	ns	200/350	120/300	120/300	100/150
Pulse frequency	Hz	1000	1000	1000	850
Number of RC		4	fig 1a	fig 1b	1
Length,	m	1.5	1	0.8	2
Inner diameter	mm	219	120	120	120

2. Experimental results. Fig.3a. shows the time diagram of exhaust purification of GP5-DE from NO, ,NO_2, NOx, as well as the concentration of oxygen O_2 by used the X1a installation, in Fig.3b – the same by the X1b installation, in both cases at a constant value of Ws. Fig.3c–dependence of purification efficiency (η), C_{NOx}, Cs and R from Ws.

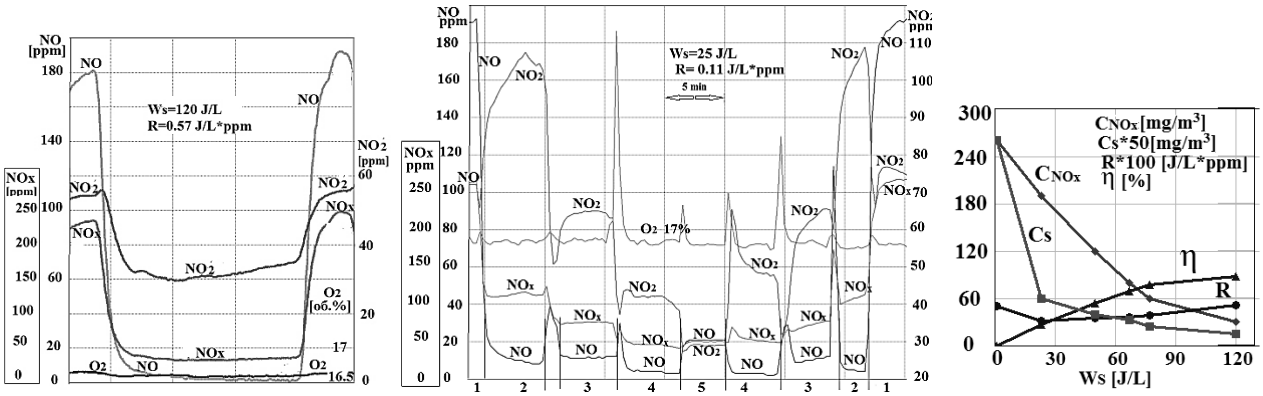

(a) (b) (c)

Fig.3 Cleaning the GP5-DE engine decoding the symbols – in the text

Fig.3c shows that when NOx is removed with increasing Ws, η decreases, , while the R values remain almost unchanged, equal to ~ 0.5 J/L*ppm. At the same time, a comparison of the data in Fig. 3 and a and b shows that the use of an active catalyst and a sorbent makes it possible to reduce Ws from 120 to 25 J/L at close values of ή. Interestingly, until the exhaust is completely cleared of NO, there is no ozone in the NTP. This means that all atomic oxygen produced in plasma chemical reactions is used for the additional oxidation of NO, so the reaction rate coefficient (K) $NO+O=NO_2$ (logK=16.31) is almost 5 orders of magnitude higher than the reaction of $O+O_2=O_3$ (logK=11.84) /5/.

Figure 4a shows a block diagram, and Figure 4b shows a photo of the X1a installation in the FORD Transit body. The power supply was provided from a rechargeable battery through a DC/AC converter.

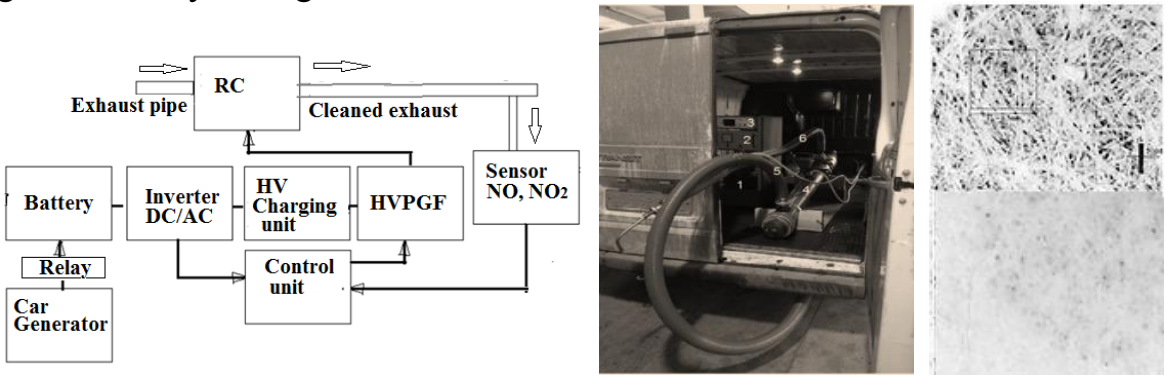

(a) (b) (c)

Fig.4 Block diagram (a) and photo of equipment placement in FORD Transit (b): 1–GINF, 2–HVcharge unit, 3–GIVF 4–RC 5–DEE supply hose; (c) FSN without cleaning (upper) and cleaning Ws=80J/L (lower)

Table 3 shows the results of experiments from which it follows that the NSCR can dramatically reduce the concentration of NOx in the DEE, and an installation with a large volume of RC allows you to achieve a minimum value of R.

Engine/cleaning method	P_{NSCD}	NO	NO_2	NOx	O_2	η	R
	kW	mg/m^3	$мг/m^3$	$мг/m^3$	%	%	J/L*ppm
Volvo Penta /Init.mode	0	417	60	477	15.5	0	0
NSCD	3	154	78	232	15.4	63	0.12
KIA «Sportage /Init. mode	0	140	12	152	17.6	0	0
NSCD only	0.8	30	2	32	17.6	80	0.3
NSCD +CS	0.8	15	1.5	16.5	17.6	89	0.29
FORD Transit/Init. mode	0	80	27	107	17.5	0	0
NSCD No movement	0.8	15	27	40	17.5	62	0.44
NSCD +CS -"-	0.8	10	17	22	17.5	79	0.35
In motion/Init. mode	0	100	18	118	14.5	0	0
NSCD in motion	0.8	20	20	40	14.5	66	0.18

The results of experiments on simultaneous purification of diesel exhaust from NOx and soot, shown in Figures 3c and 4c, show that the use of HVPGF allows simultaneous purification of diesel exhaust from both harmful components in the same RC without additional energy costs up to EURO 6.

Conclusions.

1. Devices have been developed and tested for cleaning emissions from stationary and cars diesel engines from NOx and soot, using NSCD, sorbent and catalyst activated by HV pulses and HVDC.
2. It has been shown that when using only NSCP, NOx can be reduced by 85% at and soot by 90% an energy consumption of 120 J/L. The use of an active catalyst and sorbent reduces energy consumption by 3 times.
3. A flowchart and a photograph of a prototype sewage treatment plant for use on motor vehicles are presented. Testing of the device in normal mode when driving at a speed of 60 km/h showed the possibility of reducing pollution levels to EURO 6.

References

1.Jun Jie Chong University of Birmingham July 2012 152 pp.
2. Ponizovskiy A.Z. Kuzhel T.V. Smirnov A.S.Rindin A.E. 2018.11th International Symposium on Non-thermal/Thermal Plasma Pollution Control Technology & Sustainable Energy (ISNTPT 11)
3.Guo, X.; Ha, K.H.; Du, D. Catalysts 2021, 11, 29.
4. A.Z.Ponizovsky, S.G.Gosteev, O.S.Kuzhel, A.S.Smirnov. The Chemical Safety Science, 2018, Vol. 2, № 2, 212-228 (in Russian).
5. V.N.Kondratiev. Rate constants of gas-phase reactions 1970 Moscow ."Nauka"

OPTIMIZATION OF PLASMA FURNACE DESIGN FOR LOW RADIOACTIVE WASTE PROCESSING

V.Sauchyn[1], A. Liavonchyk[1], I. Khvedchyn[1], U. Skavysh[1], Hr. Dalholenka[1], M. Polkanov[2], I. Kadyrov[2]

[1]A.V. Luikov Heat and Mass Transfer Institute of the National Academy of Sciences of Belarus, Minsk, Belarus

[2]RADON FSUE, State Atomic Energy Corporation Rosatom, the Russian Federation

The traditional method of incinerating low-level radioactive waste (RAW) is used only for combustible waste. For processing waste of mixed morphology plasma technology has been developed. It allows obtaining a glass-like product in one stage, suitable for long-term safe storage. Since 2007, RADON FSUE has been operating the Pluton pilot plant, designed for plasma-pyrolytic processing of radioactive waste.

Plasma technology allows processing of solid radioactive waste of complex morphological composition, containing both combustible and non-combustible components. The product of plasma processing of radioactive waste is molten slag, which has high chemical durability. Plasma technology is applicable to solid radioactive waste (SRW) generated during operation and decommissioning of nuclear power plants and other nuclear facilities, rehabilitation of their territories, as well as previously accumulated in RW repositories.

Main characteristics of the plasma processing plant for SRW

Unlike the most common grate incineration furnaces, the shaft furnace of the Pluton unit processes also non-organic materials (construction debris, thermal insulation, glass, soil, asphalt, turf, etc.), bulk and powdered materials, thermoplastic polymers, and waste with high humidity: ion exchange resins, silt, and sludge. The productivity of the plasma plant depends on the morphology, ash content, humidity and a number of other indicators of SRW. The plant's capacity is about 150-250 kg/h, and operating temperature in the melter is maintained in the range of 1300-1400°C.

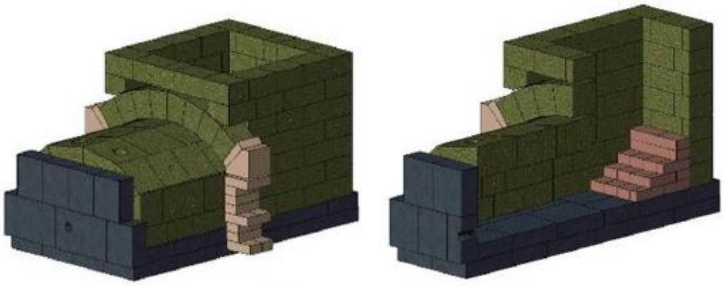

Figure 1 – Scheme of the melter

Melter is heated using two plasma torches of 85-130 kW each. Waste volume decreases in tens times after processing. Figure 1 shows a diagram of the melting device.

The Pluton plant includes a shaft furnace with SRW loading unit and product discharge device (slag melt), a pyrolysis gas combustion chamber and a multi-stage gas cleaning system. DC arc plasma torches are used as heating sources for the shaft furnace melter and the pyrolysis gas combustion chamber. Two plasma torches provide heating, melting and homogenization of the slag melt, which is drained into metal receiving containers and cooled in them. The plasma technology for processing radioactive waste provides maximum volume reduction factors, allowing processing SRW pre-pressed in metal barrels.

Numerical modeling of the temperature distribution during plasma processing of solid radioactive waste

A number of experimental and modeling researches have been carried out to improve the design of high-temperature devices and operating regimes of plasma processing of SRW. It was shown /1/ that during operation of the existing shaft furnace, the plasma torch insertion zone is exposed to the greatest thermal and gas-dynamic loads. The gas flow velocity there can reach 40-50 m/s at temperatures above 3000°C.

Based on the results of experimental studies and comparison of experimental and calculated data /2, 3/, recommendations for changing the design of the melter are proposed.

Changing the angle of the plasma torch input plane into the melter significantly affects the gas dynamics of the device. Plasma torches installed at an angle to the vertical axes (30 and 90 degrees – horizontal) allow greater free path for high-temperature flow, thereby reducing the erosive effect on the melter refractories in the areas of plasma torch installation and slag melt drainage, as well as increasing the share of heat transfer by radiation. Gas vortices move to the area of transition of the coke-slag residue into the melt, intensifying the mixing of gas flows and the oxidation of coke and heavy hydrocarbons in the slag. In the zone of transition of the melter into the shaft, areas of vortices of lower intensity are observed compared to the original version.

Figure 2 shows the results of thermal and gas-dynamic calculations of the furnace melter with horizontal plasma torch input through the front wall.

The modeling results showed a uniform distribution of the temperature field inside the melter and the absence of a local overheating zones with large temperature gradients. Reverse gas flows are observed in the dome part of the melter, but their speed is insignificant, and they should not have an erosive effect on the refractory material. The power of the heat flow through the lining material is small and ranges from 1.5 to 5 kW/m^2.

Figure 3 shows the results of thermal and gas-dynamic calculations of the furnace melter with plasma torch input of 30º angle through the front wall.

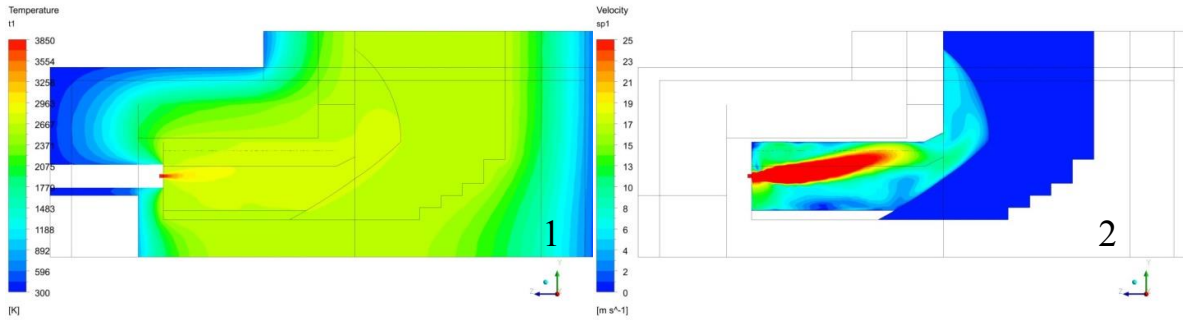

Figure 2 – Distribution of temperature and velocity fields in the central section with horizontal plasma torch installation

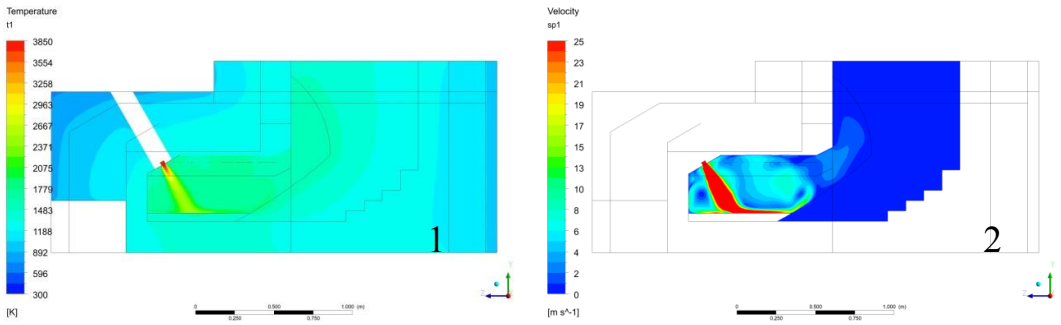

Figure 3 – Distribution of temperature and velocity fields in the central section with plasma torch installation at 30°

The modeling results showed the local overheating zone formation in the area of interaction of the plasma jet with the surface of the molten slag. In general, the temperature field distribution does not have large gradients. This indicates a uniform distribution of the heat flow into the walls of the melter.

In the area close to the front wall, vortex zones are observed. However, most of the flow moves above the surface of the molten slag towards the furnace shaft. The high velocity of gas flow along the surface of the melt intensifies the convective heat exchange between the gas medium and the slag. In this case, heat loss to the environment for this option is approximately 20% higher than with a horizontal plasma torch.

For operation in the nominal stationary mode, it is enough to use one plasma torch with a power of 100-120 kW. In this case, input power is enough to maintain the temperature in the internal volume above 1500 °C. To reduce the erosive gas-dynamic effect of the plasma flow on the refractory materials of the

melter, it is recommended to change the organization of the plasma jet input into the internal volume of the melter: to install the plasma torch through the front wall horizontally.

An alternative way to organize the plasma jet input into the melter is to install the plasma torch in the central plane of the melter at an angle to the vertical. In this case, the flame flow is directed to the bottom and, accordingly, to the surface of the slag melt. Reflecting from the horizontal surface of the melt, the plasma flow moves towards the furnace shaft. The vortices formed in the contact zone are less directed towards the front wall compared to the case of vertical installation of plasma torches.

Conclusions

Based on the results of experimental and calculation researches, options for changing the organization of the internal space of the melter of the "Pluton" plant are proposed. It is shown that one plasma torch with a power of 100-120 kW is enough to maintain the operating temperature up to 1500°C. To ensure uniform heating of the internal volume of the melter, it is recommended to install the plasma torch in the axial plane through the front wall horizontally or at a slight angle to the horizontal axis. On the other hand, it is recommended to introduce the plasma torch at an angle of 30° to the vertical axis to intensify the process of heating the slag melt.

In both cases, small-scale vortices with high speed will be absent in the near-wall zones of the melter. The main mechanism of heat exchange is radiation in both cases. The results of the research will be used to create a promising plasma plant for processing of radioactive waste of various morphologies as part of the second stage of the Radioactive Waste Processing Complex, currently being created at the site of the Sergiev Posad branch of the RADON FSUE.

References

1. **A.I. Liavonchyk, V.V. Sauchyn, I.V. Khvedchyn, I.I. Kadyrov, M.A. Polkanov** Plasma shaft furnace of the Pluton facility modeling. FSUE RADON (2021)
2. **A.I. Liavonchyk, J.V. Zhukava, V.S. Skavysh,V.V. Sauchyn** Numerical modeling of the heat transfer processes in plasma furnace with multilayer wall. Minsk: HMTF-17 (2024)
3. **A.I. Liavonchyk, H.V. Dalgolenka, V.S. Skavysh,V.V. Sauchyn** Effect of accounting radiation heat transfer in numerical modeling of partial oxydation of hydrocarbons in a plasma reactor. High Temperature Material Processes 25(1) (2021) 15–23

PLASMA TECHNOLOGY FOR SEWAGE SLUDGE PROCESSING

V.Sauchyn, U. Skavysh, A. Liavonchyk, I. Khvedchyn, Hr. Dalholenka, N. Kurbanov

A.V. Luikov Heat and Mass Transfer Institute of the National Academy of Sciences of Belarus, Minsk, Belarus, E-mail: sauchyn@itmo.by

Introduction.

During the process of wastewater treatment at sewage facilities, significant volumes of sludge sediments are inevitably formed. Traditionally, their treatment is limited to natural dewatering on sludge beds. Although this method is economically advantageous (requires minimal capital and operating costs) and even allows the use of drained sludge in agriculture, its environmental inconsistency is obvious. Key problems include excessive consumption of land resources, low dewatering rates, seasonal restrictions, high costs of subsequent reclamation of territories, as well as negative impacts on the environment (pollution of the atmosphere, soil and aquifers). In this regard, many regions are gradually abandoning outdated technology in favor of more modern solutions /1/.

The aim of this work is a theoretical study of plasma-thermal processing of wastewater sludge by oxidation to obtain synthesis gas with minimal energy costs.

In the process of plasma-thermal gasification by partial oxidation, the carbon contained in the feedstock is converted primarily into carbon monoxide (CO), and partially into carbon dioxide (CO_2). Hydrogen released from hydrocarbons partially remains in the form of H_2, and partially oxidizes to water vapor (H_2O). The resulting gas mixture, consisting mainly of CO and H_2, is called synthesis gas and can be used for energy production or chemical synthesis /2/. The inorganic components of the feedstock are melted and removed from the reactor as liquid slag /3/.

To calculate the mass and energy balance of the gasification process, sludge with parameters shown in Table 1 was used. For sludge dehydration filter press, vacuum filter and centrifugation is the optimal option /4/.

Table 1. Chemical composition of sludge in mass fractions

Name	Water	Ash	C	H	O	S	Cl	N
%	8,9	39,7	26,5	3,8	15,5	1,3	0	4,3

Two variants of the plasma gasification process were considered. Electric arc jet

plasma torch is used as plasma flow generators, in which the gas (air) consumption is 1 g/s for every 10 kW of thermal power. The thermal efficiency of the reactor is 90%. The calorific value of the feedstock is calculated using Mendeleyev's formula.

Single-stage gasification

In this variant, the entire process takes place in a single reaction volume, where the air flow is used as an oxidizer. The minimum oxygen excess coefficient for this type of gasification is 1.5. Part of the air flow specified in the "Air flow through the plasma torch" parameter is supplied as a plasma jet using an electric arc plasma torch. The remaining air, corresponding to the "Blast air" parameter, enters the reaction volume through separate channels. The maximum temperature (1400 °C) is achieved in the lower (bottom) part of the reactor, where the plasma torches are installed and the ash of the feedstock material melts. The slag temperature at the reactor outlet is 1400 °C. The synthesis gas temperature at the reactor outlet is 1200 °C.

Two-stage gasification

In this case the facility consists of three modules (reactors): a pyrolysis reactor, a coke-ash residue processing reactor, and a final gasification reactor. Air is used as an oxidizer.

A pyrolysis reactor (e.g., screw reactor) operates without access of the oxidizer. The feedstock is heated to 600 °C by the heat of hot synthesis gas coming from the final gasification reactor. As a result of pyrolysis, the feedstock is broke down into a gaseous phase (volatile hydrocarbons and water vapor) and a solid coke-ash residue consisting of carbon and mineral ash. The gaseous products are sent to the final gasification reactor, and the coke-ash residue is sent to the reactor for processing.

The reactor for processing the coke-ash residue is equipped with a plasma torch, providing a temperature in the reaction zone up to 1400 °C. Part of the air ("Air flow through the plasma torch") enters as a plasma jet through an electric arc plasma torch, and the remaining one ("Blast air") is supplied separately. Due to the high temperature and excess oxygen, the carbon is completely oxidized, and the ash melts and is removed in vitrified form. The gas is sent to the final gasification reactor.

There are two gas flows in final gasification reactor:
- pyrolysis gas (600 °C) from the pyrolysis reactor;
- hot gas (1400 °C) from the coke-ash residue processing reactor.

When these flows mix and react, synthesis gas with a temperature 1150 °C is

formed. Then it passes through the heat exchange jacket of the pyrolysis reactor, and enters the cleaning system.

The oxygen excess coefficient for this type of reactor is taken to be 1.2. The slag temperature at the reactor outlet is 1400 °C. The synthesis gas temperature at the reactor outlet is 1150 °C.

Results

The following parameters were calculated: mass-energy balance of the process (Table 2), composition of synthesis gas at the reactor outlet (Table 3), calorific value of synthesis gas, thermal power of the plasma torch.

Table 2. Mass-energy balance of the process

	Single-stage gasification		Two-stage gasification	
Reactor input parameters	kg/h	kW	kg/h	kW
Sludge to be processed	100	310	100	310
Air flow through the plasma torch	58	175	30	60
Blast air	70		53	
Total	228	485	182	370
Reactor output parameters	kg/h	kW	kg/h	kW
Chemical energy of synthesis gas	188	180	142	305
Thermal energy of synthesis gas		250		25
Slag (thermal energy)	40	30	40	30
Reactor heat losses		25		10
TOTAL	228	485	182	370

In single-stage gasification, the calorific value of synthesis gas is 4.9 MJ/m^3. It is determined by minimum content of "ballast" gases N_2, H_2O, CO_2. The required electric power is 250 kW. The required plasma torch power can be reduced by recuperation: heating the blast air to 600 °C by using the thermal energy of syn-gas. As a result, the required electric power can be decreased to 230 kW.

In two-stage gasification, the calorific value of synthesis gas is 6.9 MJ/m^3, and the required electric power is 90 kW.

Table 3. Composition of syngas at the reactor outlet

	Single-stage gasification		Two-stage gasification	
Name	Wet (mol %)	Dry (mol %)	Wet (mol %)	Dry (mol %)
N_2+Air	44,4	48,8	34,3	35,8
CO	22,4	24,7	29,5	30,9
H_2	19,3	21,3	29,2	30,5
H_20	9,1	0	4,3	0
CO_2	4,2	4,6	1,9	2
H_2S	0,5	0,5	0,6	0,6
Other	0,1	0,1	0	0

Conclusions

According to the results of the study, multi-stage plasma gasification of dewatered wastewater sludge has significant advantages over the single-stage process. In particular, a more reasonable use of plasma flow energy is ensured, which allows for a significant reduction in the required plasma torch power. In addition, the resulting synthesis gas has a higher calorific value.

Acknowledgements. This work was supported by State program of scientific research for 2021-2025 "Energy systems, processes and technologies" subprogram "Efficient thermophysical processes and technologies" (EP-2.5).

References

1. **Nasyrov I.A., Mavrin G.V., Sokolov M.P.** Problems of pyrolysis processing of carbon-containing waste // Kazan (Volga Region) Federal University. Access mode**:** https://kpfu.ru/portal/docs/F1448255442/Nasyrov.Mavrin_Sokolov_pdf. Date of access: 5.06.2025.
2 **Mountouris, A. et al**. Solid waste plasma gasification: Equilibrium model development and exergy analysis*. Energy Conversion and Management, 49(2), 281-290. (2008).
3 **M.T. Munir, I. Mardon, S. Al-Zuhair, A. Shawabkeh, N.U. Saqib,** Plasma gasification of municipal solid waste for waste-to-value processing, Renewable and Sustainable Energy Reviews, Volume 116,2019, ISSN 1364-0321,
4 **Shashkin R. Yu.** MODERN METHODS OF SEWAGE SLUDGE DEWATERING // Forum of Young Scientists. 2018. No. 5-3.

SIMULATION THE GAS DYNAMICS IN THE FLAT REACTOR WITH RECTANGULAR CROSS-SECTION FOR THIN FILM DEPOSITION BY CVD

V. Shakialeuski[1], N. Leonovich[1], D. Kotov[1]

[1] Belarusian State University of Informatics and Radioelectronics, 6 Petrusya Brovki str., Minsk, Republic of Belarus, nickxz51@gmail.com

Abstract. This study presents numerical modeling of gas dynamics in a planar reactor designed for thin film formation using the chemical vapor deposition (CVD) method. The objective of the modeling is to analyze the distribution of gas flows and reactant concentrations within the reactor chamber in order to minimize non-uniformity in the deposition of iron oxide films. A 3D geometric model of the reactor was developed, including substrates, a substrate holder, and a gas distribution system operating under sub-atmospheric pressure. The results are important for the development of masking coatings for photomasks.

Introduction. The chemical vapor deposition (CVD) method is widely used in microelectronics, optoelectronics, and the production of functional coatings to create thin films with specific physicochemical properties [1]. One of the key challenges in implementing the CVD process is ensuring uniform material deposition thickness across the substrate, which directly depends on the gas dynamics within the reaction chamber [2]. Non-uniform distribution of gaseous reagents leads to significant thickness variations in the resulting coating, which is unacceptable in the fabrication of masking layers for photomasks [3].

To optimize gas flow in the reactor without resorting to experimental studies, we conducted a simulation of the gas dynamics and thermodynamics in a flat reactor with a rectangular cross-section, designed for iron oxide film deposition via CVD at sub-atmospheric pressure. The main focus is on analyzing the distribution of working gas flows and temperature above the substrate surface. The study relies on modern modeling approaches implemented in COMSOL Multiphysics, which allow for consideration of complex multiphysics interactions, including laminar flows and heat transfer [4].

When solving problems involving laminar flow and heat transfer, COMSOL Multiphysics employs the finite element method. From a practical perspective, the finite element method can be described as follows: the original domain of the function is divided, using a generally non-uniform mesh, into separate subdomains—finite elements—after which the desired continuous function is approximated by a piecewise-continuous function defined over the

set of finite elements. This approximation can be defined arbitrarily, but most often polynomials are used, selected in such a way as to ensure continuity of the target function at the nodes located at the boundaries of the elements.

Experimental setup. The first stage of the study involved modeling the gas flow inside the reaction chamber. The initial conditions were as follows: the pressure inside the reaction chamber was 1 atm, the initial temperature of the working gas was 30 °C, and the initial temperature of the chamber and internal components was 20 °C. The flow velocity of the gas mixture was set to U = 1.18 m/s, which corresponds to a carrier gas flow rate of 6 L/min, taking into account the diameter of the gas inlet and the presence of three inlet ports. As a result of the gas dynamics simulation for the simplified model of the reaction chamber, Fig. 1 shows the distribution of gas flow at a height of 2 mm above the substrate surface. Fig. 2 presents the velocity distribution of the gas flow above the substrate surface in a cross-section of the reactor at the same height of 2 mm.

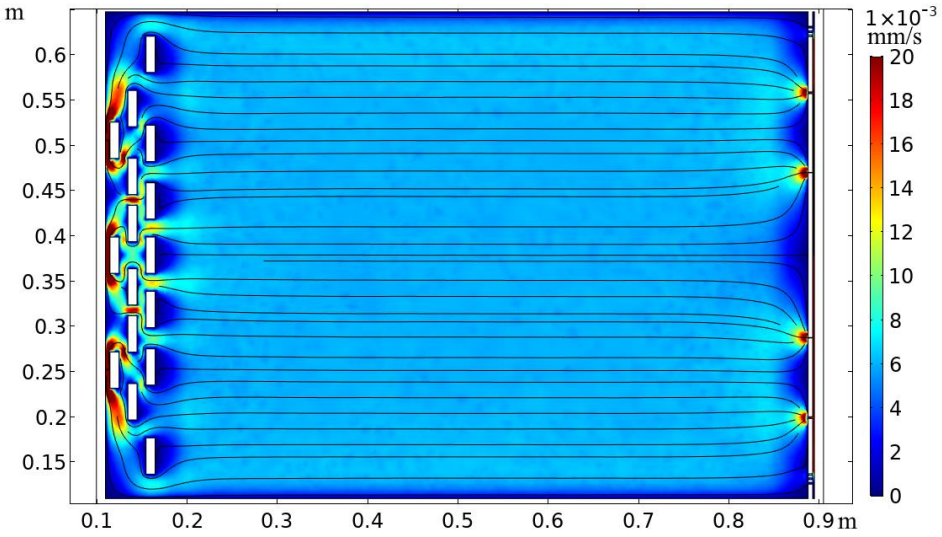

Fig. 1 – Gas flow distribution above the substrate surface at a height of 2 mm

Based on the results of the gas dynamics modeling, it can be noted that the formation of a uniform laminar flow over the substrate surface was achieved due to the optimized design of the chamber. As seen in Fig.s 1 and 2, the flow velocity along the substrate holder remains stable with minimal fluctuations, which contributes to the uniform distribution of reagents. The maximum flow velocity is reached near the center of the flow, and the absence of turbulence confirms the stability of the flow regime.

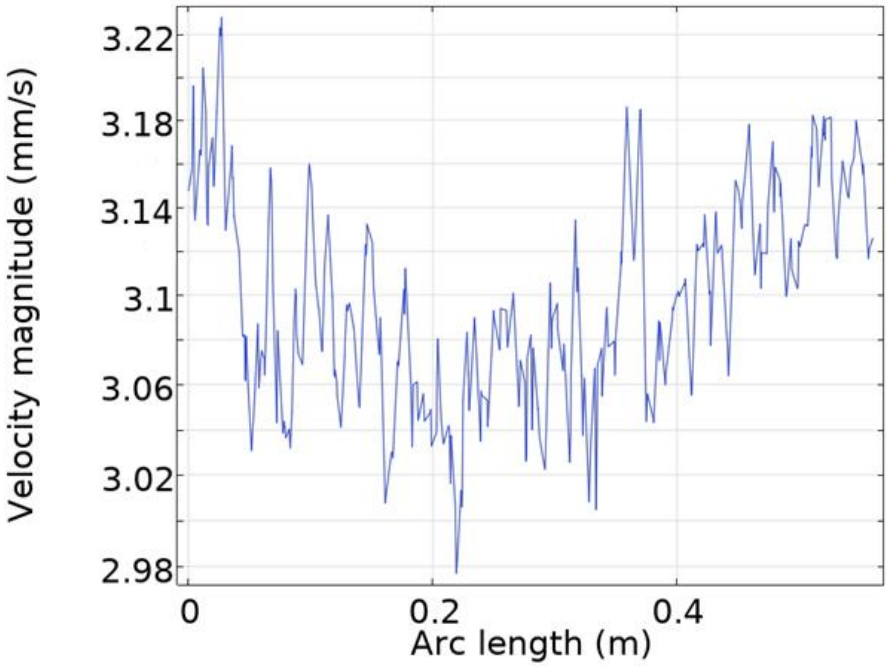

Fig. 2 – Gas flow velocity distribution above the substrate surface in a cross-section of the reactor at a height of 2 mm

The next stage involved calculating heat transfer between the gas medium, the substrates, and the chamber walls, based on the data obtained from the gas flow distribution simulation. A more detailed analysis of the temperature distribution was carried out by constructing temperature profiles. Fig. 3 presents the temperature profile of the gas flow in the direction perpendicular to the flow. Temperature fluctuations are minimal, indicating a high degree of uniformity in heat transfer within the thermal decomposition zone.

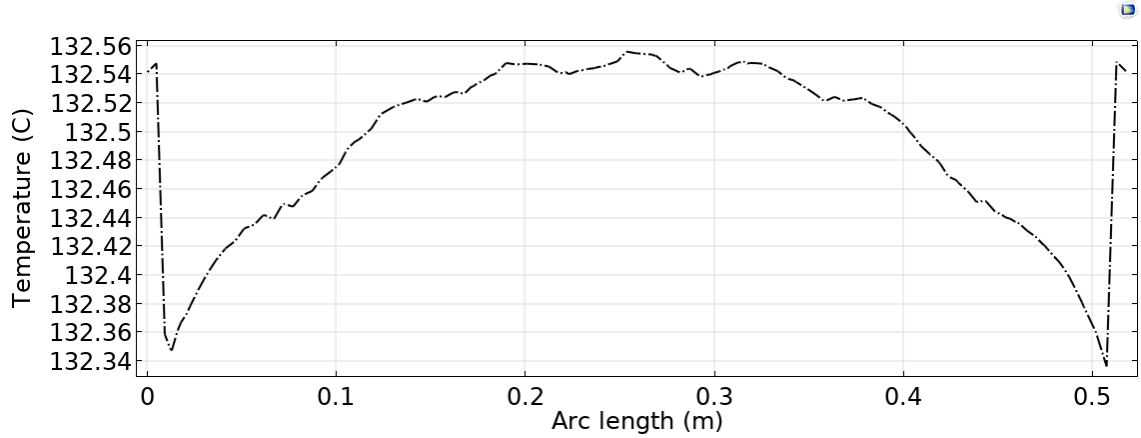

Fig. 3 – Temperature profile of the gas flow in a cross-section of the reactor above the substrate surface at a height of 2 mm

Fig. 4 shows the temperature profile along the direction of the gas flow. Minor temperature fluctuations within ±0.11 °C confirm the stability of the thermal regime across the entire length of the substrate holder, which is critically important for achieving uniform film thickness during the deposition process.

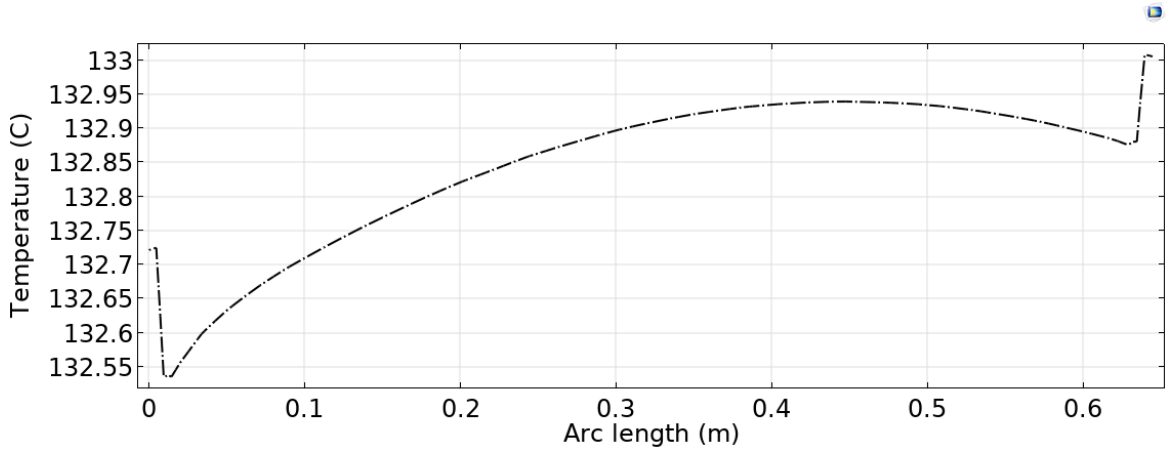

Fig. 4 – Temperature profile of the gas flow along the length of the substrate holder above the substrate surface at a height of 2 mm

Conclusions. Thus, as a result of this study, numerical modeling was employed to optimize gas flow and heat distribution over the surface of the substrate holder inside the chamber. Subsequent design improvements to the reactor led to the formation of a laminar gas flow with a velocity non-uniformity of ±3.87% and a uniform temperature distribution with a deviation of ±0.11%. Consequently, the finite element method proves to be essential for modeling the physical processes occurring inside the reaction chamber, such as heat and mass transfer.

References

1. **Pierson H.O.** Handbook of Chemical Vapor Deposition (CVD): Principles, Technology, and Applications. Norwich, NY: William Andrew Publishing (1999).
2. **Jensen K.F.** Journal of Crystal Growth, 130(1993) 373–388.
3. **Hitchman M.L. and Jensen K.F.** Chemical Vapor Deposition: Principles and Applications. London: Academic Press (1993).
4. **Kleijn C.R.** Thin Solid Films, 365(2000) 294–306.

ESTIMATION OF PLASMA DENSITY AND ENERGY OF ELECTRONS AT ANOMALOUS ABSORPTION OF ORDINARY MICROWAVE IN A PLASMA FILAMENT

M.S. Usachonak[1], L.V. Simonchik[1], E.Z. Gusakov[2], A.Yu. Popov[2]

[1]Institute of Physics of NAS of Belarus, 68-2 Nezavisimostsi Ave., 220072 Minsk, Belarus
[2]Ioffe Institute, 26 Polytekhnicheskaya St., 194021 St. Petersburg, Russia
E-mail: m.usachonak@dragon.bas-net.by

Introduction

In experiments on electron-cyclotron resonant (ECR) plasma heating by extraordinary microwaves a large number of various anomalous effects (anomalous backscattering, anomalously accelerated ions) are observed [1-2]. As it was shown in [3], similar effects (anomalous absorption) can be exited at non-monotonous density profile for pump wave of ordinary polarization. The initial experimental results of the investigation of ordinary microwave absorption at plasma filament at magnetic field level higher than the ECR for half-frequency of pump we was reported in [4]. So in present work the time behavior of density and energy of electrons in plasma filament at this anomalous absorption of ordinary microwave are under investigation.

Experimental setup and results

Similar to [5], the experiment is performed at the linear plasma device "Granite" where a plasma filament is produced by a RF discharge in a long glass tube (1) with the inner diameter of 2a = 22 mm oriented along the magnetic field direction (Fig. 1, *a*) and filled with argon (at pressure about 1.5 Pa). The magnetic field created by the external electromagnet (2) can be varied from 0 to 630 G (controlled by SH1-8, instrumental error 2%). The glass tube passes through the waveguide (3) (72×34 mm2) perpendicularly to the wide walls through the hole in it and in parallel to the narrow walls. The continuous RF power about 100 W at frequency of 27 MHz is supplied to the ring electrodes (4) placed outside of the tube and disposed on both sides of the waveguide at a distance of about 30 cm. The microwave pulses at frequency f_0 = 2.385 GHz (power up to 600 W) were incident onto the plasma along the waveguide (3) (Fig, 1). Vector of electric field of a microwave in waveguide is along to external magnetic field. It is a case of O-mode.

Time behavior of incident P_0, transmitted P_t, reflected P_r power pulses and the integral plasma luminosity I at anomalous absorption of ordinary microwave in plasma filament is shown by corresponding waveforms in Fig. 1, *b*. The initial conditions for it are the average electron density in plasma about $\langle n_e \rangle = 4\times10^9$ cm^{-3} and magnitude of the magnetic field about H = 570 Oe. As it's seen,

absorption is accompanying by huge integral plasma luminosity increase.

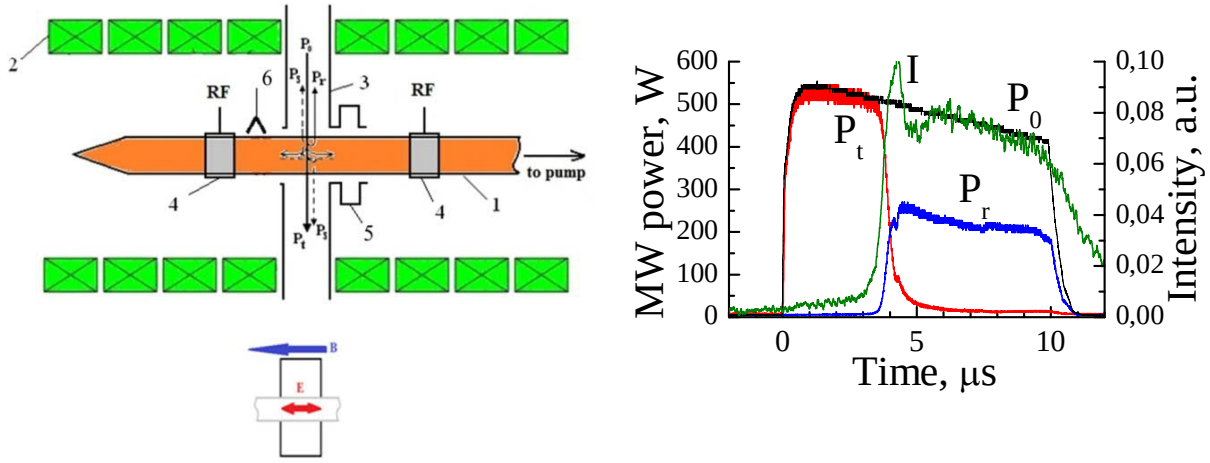

Fig. 1. Schematic of experimental setup and of microwave electric field vector in waveguide orientation to external magnetic field, and (*b*) the waveforms of incident P_0, transmitted P_t, reflected P_r power pulses and the integral plasma luminosity I inside the waveguide at $\langle n_e \rangle = 4 \cdot 10^9$ cm^{-3} at H= 570 Oe.

The electron density evaluation at the observed microwave absorption was estimated by probe wave transmission method. Main idea of the method is to determine dielectric constant (electron density) of the investigated plasma by transmission of the probe wave through it. For instance, in [6] it is proposed to use this method with utilizing rectangular waveguides for localized plasma fro which $d_p < 0.2a$, where d_p – plasma column diameter and a – width of the waveguide wide wall. In our experiments this is not the case due to d_p = 22 mm and a = 72 mm. Additionally the plasma filament placed in the external magnetic field and its dielectric constant got tensor form for incident pump microwave. Therefore we proposed to use this method with preliminary calibration of waveguide section. For this purpose additional microwave signal (probe wave) on shifted frequency (2600 MHz) fed in the waveguide (3) (see Fig. 1, *a*). Power of the probe wave (about 600 mW) was much lower than the threshold of

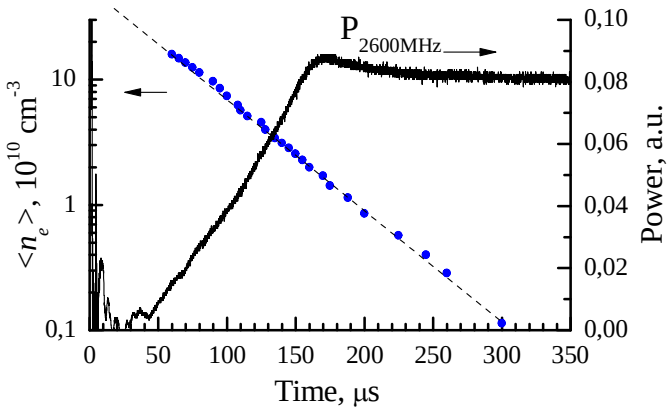

Fig. 2. The time dependence of the afterglow plasma electron density and the probe wave signal waveform $P_{2600MHz}$. during the afterglow plasma decay.

anomalous absorption appearing. For pump suppression in the waveguide, where the probe wave signal is measured, a narrow band rejection filter was used. It should be noted that initial experimental conditions don't affect on the probe wave transmission.

In first step we obtained the dependence of the waveguide transmission at the probe wave frequency on electron density in plasma filament without absorption $T(<n_e>)$. For this, we used afterglow plasma of the high voltage pulse discharge, as in [5]. We measured the afterglow plasma density time dependence $<n_e>(t)$ by using microwave cavity (5) (Fig. 1, *a*) and the probe wave transmission time dependence during the afterglow plasma decay $T(t)$ (see Fig. 2), and compared them in different time points to excluding time (see Fig. 3, *a*). Next we measured the waveform of the probe wave signal to obtained the dependences of its transmission on time during the microwave anomalous absorption, and compared it with the dependence $T(<n_e>)$, which allowed us to exclude the transmission level and to find $<n_e>(t)$ (stars in Fig. 3, *b*).

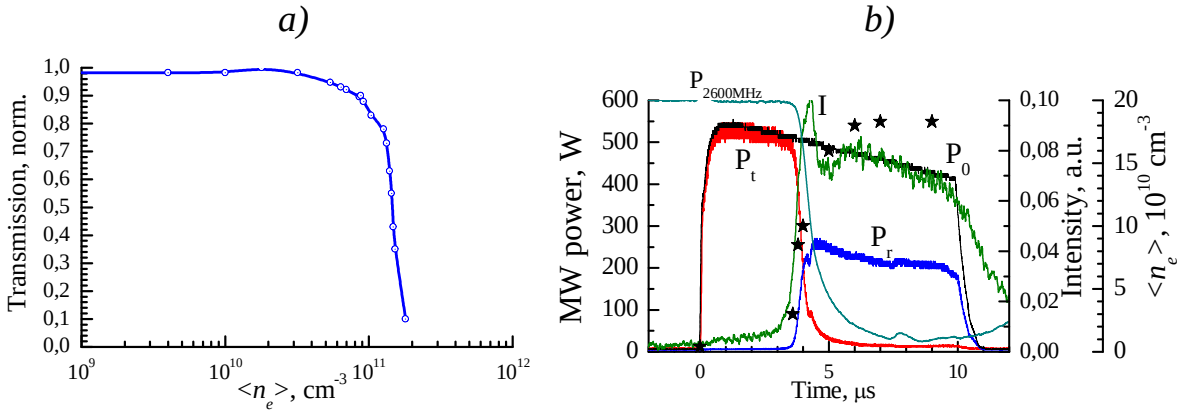

Fig. 3. *(a)* The normalized waveguide transmission dependence on the afterglow plasma electron density for the probe wave frequency. *(b)* The waveforms of P_0, P_t, P_r , probe wave $P_{2600MHz}$, plasma luminosity I and the electron density time behavior estimation.

As can be seen, the observed absorption is accompanying by a electron density increasing over one order of magnitude during about 1 microsecond and its saturation at about $17 \cdot 10^{10}$ cm^{-3}.

Also we estimated the energy of electrons in the plasma filament at some experimental conditions. It was performed similarly to [5] by the relative intensity of atomic lines of argon ArI (λ_1 = 430.0 nm ($4s[1^1/_2]^o$-$5p[2^1/_2]$) and λ_2 = 451.1 nm ($4s'[^1/_2]^o$-$5p[^1/_2]$), due to its dependence on electron energy *Te*, that was calculated in the frames of coronal model [7]. A time behavior of argon lines ArI (430.0 nm and 451.1 nm) and ArII (480.6 nm) intensities was measured by using the monochromator MDR-23, PMT-79 and digital oscilloscope GDS-72204E (GwInstek, 200 MHz, 1 GS/s) and was shown at Fig. 4, *a*. As can be seen, the electron temperature was reached 8 eV at time

point 4.3 microsecond (Fig. 4, *b*), that is corresponds to the time point for huge microwave absorption and maximum integral plasma luminosity (see Fig. 2, *b*). Also excitation ion line ArII (480 nm) indicates the emergence of superthermal electrons.

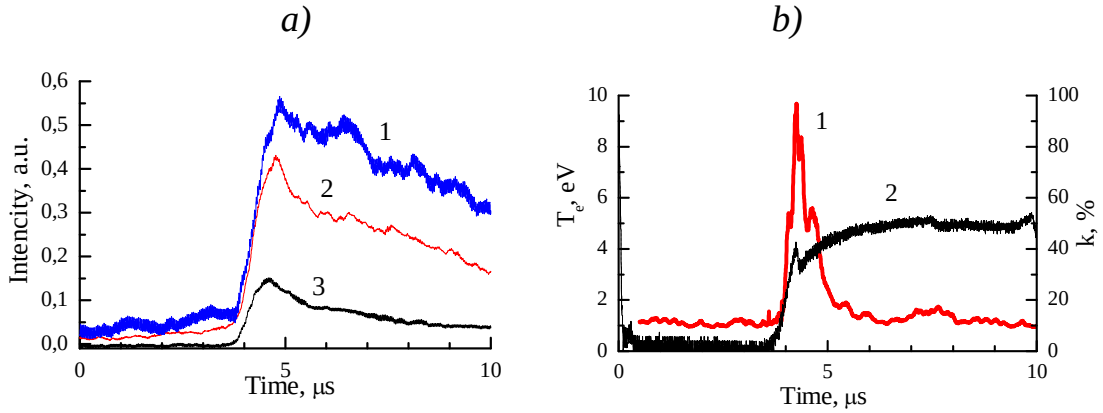

Fig. 4. *(a)* Waveforms of Ar lines intensity: 1 – 430 nm, 2 – 451.1 nm, 3 – 480.6 nm (multiplied by 10) and *(b)* electron temperature (1) and absorption coefficient (2) time dependencies.

The absorption coefficient was determined by $k = (1 - (\frac{P_t + P_r}{P_0})) \cdot 100\%$, where P_0, P_t and P_r were obtained from waveforms. Microwave power irradiation along the glass tube through the holes in the waveguide was not taking in to account due its very low level (several watts).

Conclusions

In present work the estimation of electron density and energy at anomalous absorption of ordinary microwave in plasma filament was performed. It was shown that the absorption is accompanied by an increase of electron temperature up to 8 eV and by the electron density increasing over one order of magnitude. Obtained experimental results may be useful for development a theoretical model of the anomalous ordinary microwave absorption in plasma filament at magnetic field level higher than the ECR for half-frequency of pump.

Acknowledgements. Financial support of the contract № 23-RB-02-06 and BRFFR grant F24SPbG-005 is acknowledged.

References

1. **S.K. Nielsen, M. Salewski, et al.**, Plasma Phys. Control. Fusion 55, 115003 (2013)
2. **S. K. Hansen, et. al.**, Nucl.Fusion. 60, 106008 (2020).
3. **A.Yu. Popov, et. al.**, ZhETF, 166, 748-754 (2024)

4. **E. Z. Gusakov, A.Yu. Popov, L.V. Simonchik, and M.S. Usachonak**, 21th Int. workshop «Complex systems of charge particles and their interactions with electromagnetic radiation», 111 (2025)
5. **E. Z. Gusakov, A.Yu. Popov, L.V. Simonchik, and M.S. Usachonak**, Physics of Plasmas, 32, 092101 (2025)
6. В.Е. Голант, Сверхвысокочастотные методы исследования плазмы. М.: Наука, 1968.
7. V. I. Arkhipenko, L. I. Kiselevskii, V. E. Plyuta, I. A. Romanchuk, and L. V. Simonchik, Izv. Acad. Sci. BSSR, Phys. Mat. Ser. (Russ.) 1, 88 (1979).

Научное издание

Материалы докладов XI Международной конференции «ФИЗИКА ПЛАЗМЫ И ПЛАЗМЕННЫЕ ТЕХНОЛОГИИ»
Минск, Беларусь, 15 – 19 сентября 2025 г.

На английском языке

Составители:
Тарасенко Николай Владимирович
Невар Елена Аркадьевна
Усачёнок Максим Сергеевич

Материалы опубликованы в виде,
представленном авторами – участниками Конференции

Plasma physics and plasma technology (PPPT-11) : XI International Conference, Minsk, Belarus, September 15—19, 2025 : contributed papers / [editors: N. V. Tarasenko [et al.]. — Minsk : Kovcheg, 2025. — 525 p.

Электронное издание

Институт физики НАН Беларуси
220072 г. Минск, пр. Независимости, 68.

Оформление ООО «Ковчег» Свидетельство о ГРИИРПИ
№ 1/381 от 01.07.2014
Ул. Л. Беды, 11/1-205, 220040 г. Минск
Тел./факс: (017) 379 19 81. E-mail: kovcheg_info@tut.by
Instagram: kovcheg_info, Facebook: infoKOVCHEG

ISBN 978-985-884-542-1